

AUGUST 2021

**AJNR**

VOLUME 42 • PP 1359–1556

# AJNR

## AMERICAN JOURNAL OF NEURORADIOLOGY

AUGUST 2021  
VOLUME 42  
NUMBER 8  
[WWW.AJNR.ORG](http://WWW.AJNR.ORG)

THE JOURNAL OF DIAGNOSTIC AND  
INTERVENTIONAL NEURORADIOLOGY

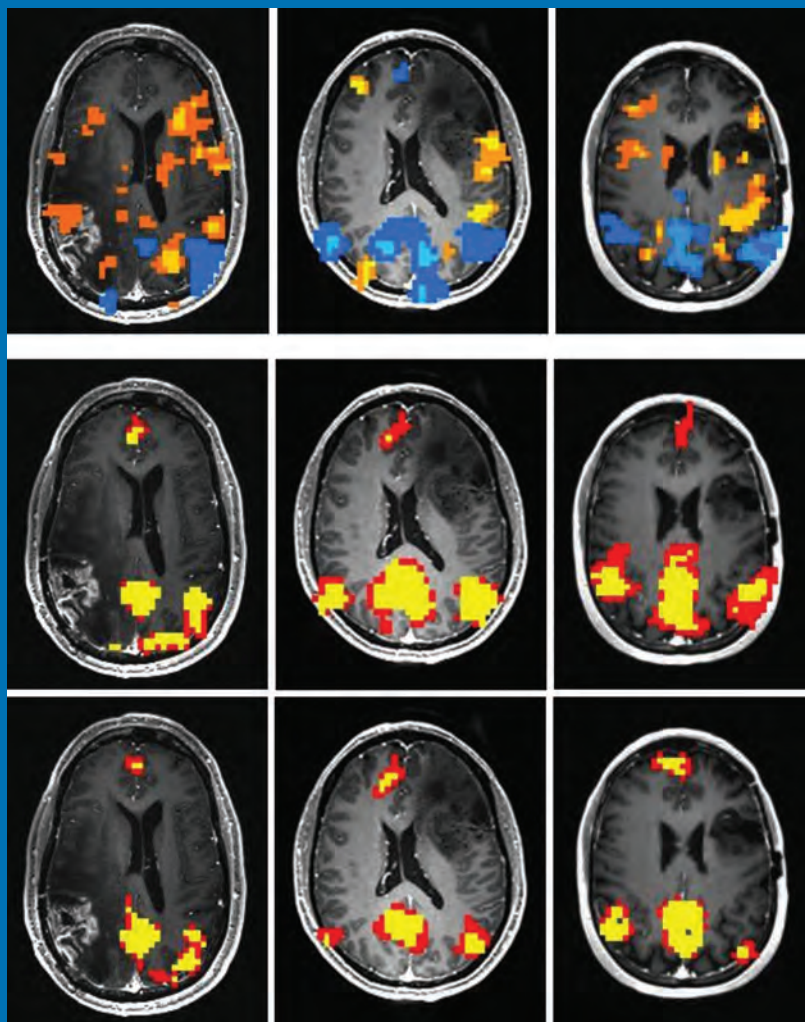
Perfusion CT imaging predictor of SAH outcome

Response criteria for CNS lymphoma

Scoring of basilar occlusion angiographic results

Dural AVF of the foramen magnum region

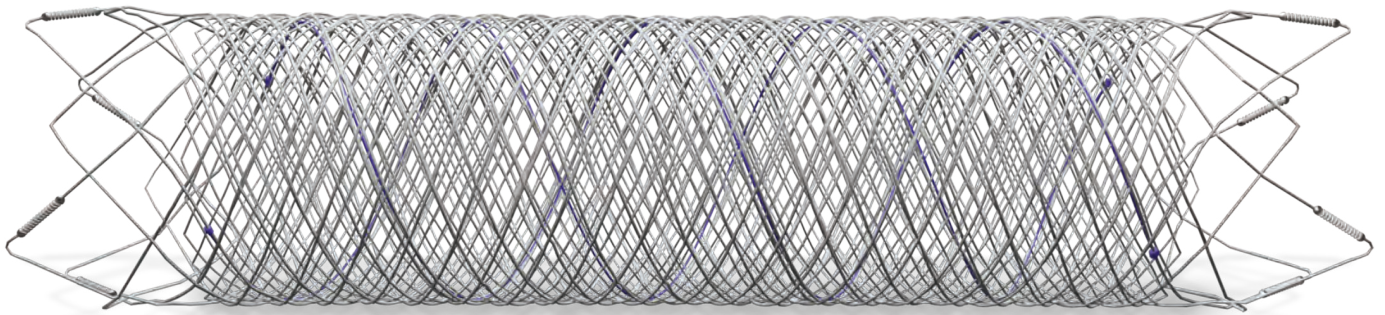
Official Journal ASNR • ASFNR • ASHNR • ASPNR • ASSR



# FRED™

Flow Re-Direction  
Endoluminal Device

## FLOW DIVERSION.



## SIMPLIFIED.

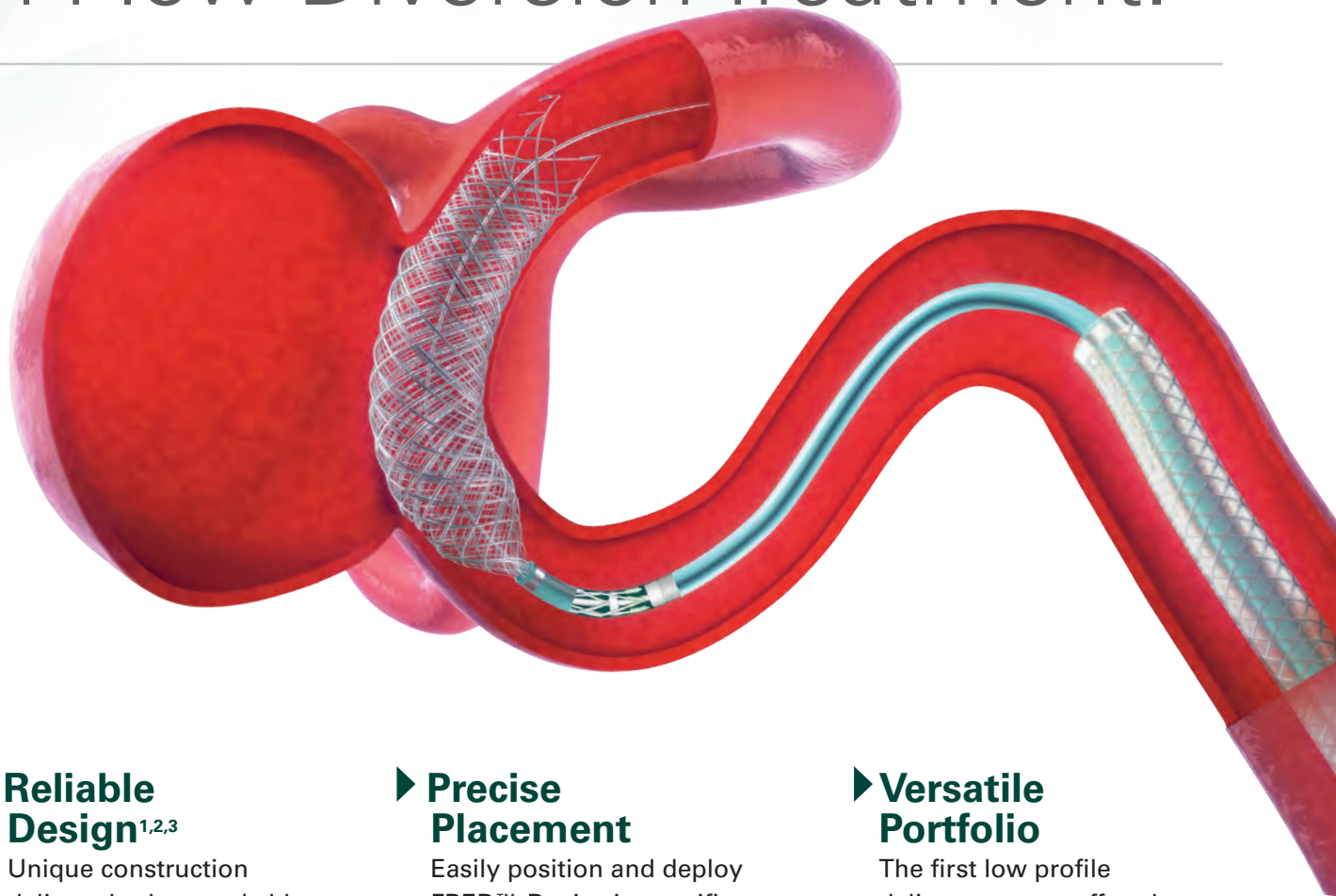


**MicroVention Worldwide**  
**Innovation Center**  
35 Enterprise  
Aliso Viejo, CA 92656 USA  
**MicroVention UK Limited**  
**MicroVention Europe S.A.R.L.**  
**MicroVention Deutschland GmbH**  
**Web**

PH +1 714.247.8000

PH +1 44 (0) 191 258 6777  
PH +33 (1) 39 21 77 46  
PH +49 211 210 798-0  
[microvention.com](http://microvention.com)

# The New Standard of **Ease and Simplicity** in Flow Diversion Treatment.



## ► **Reliable Design**<sup>1,2,3</sup>

Unique construction delivers both remarkable ease of use and excellent flow diversion<sup>1,2,3</sup>

## ► **Precise Placement**

Easily position and deploy FRED™ Device in specific, targeted locations<sup>4,5,6</sup>

## ► **Versatile Portfolio**

The first low profile delivery system offered in combination with large diameter and long length options

#### References:

1. TR11-211 2. TR13-171 3. TR15-055 4. TR13-192 5. TR15-072 6. TR19-145

The Flow Re-Direction Endoluminal Device (FRED™) System is indicated for use in the internal carotid artery from the petrous segment to the terminus for the endovascular treatment of adult patients (22 years of age or older) with wide-necked (neck width  $\geq 4$  mm or dome-to-neck ratio  $< 2$ ) saccular or fusiform intracranial aneurysms arising from a parent vessel with a diameter  $\geq 2.0$  mm and  $\leq 5.0$  mm.

Use of the FRED™ System is contraindicated under these circumstances: Patients in whom anticoagulant, anti-platelet therapy, or thrombolytic drugs are contraindicated. Patients with known hypersensitivity to metal such as nickel-titanium and metal jewelry. Patients with anatomy that does not permit passage or deployment of the FRED™ System. Patients with an active bacterial infection. Patients with a pre-existing stent in place at the target aneurysm. Patients in whom the parent vessel size does not fall within the indicated range. Patients who have not received dual anti-platelet agents prior to the procedure. For complete indications, contraindications, potential complications, warnings, precautions, and instructions, see instructions for use (IFU provided in the device).

**RX Only:** Federal (United States) law restricts this device to sale by or on the order of a physician.

MICROVENTION™ and FRED™ are registered trademarks of MicroVention, Inc. in the United States and other jurisdictions. © 2020 MicroVention, Inc. 04/2020.





## Medical Imaging in the Fight against COVID-19 Call for Contributions

[illegible]

- To ensure success, MIDRC encourages all institutions and hospitals, both small and large, to donate their COVID-19 medical images and data to the cause.
- MIDRC provides a HIPAA-compliant mechanism to securely submit medical images and clinical metadata, and is committed to helping institutions throughout the submission process.

Visit [midrc.org](http://midrc.org) for more information





# AJNR *go green*

***AJNR* urges American Society of Neuroradiology members to reduce their environmental footprint by voluntarily suspending their print subscription.**

The savings in paper, printing, transportation, and postage directly fund new electronic enhancements and expanded content.

The digital edition of *AJNR* presents the print version in its entirety, along with extra features including:

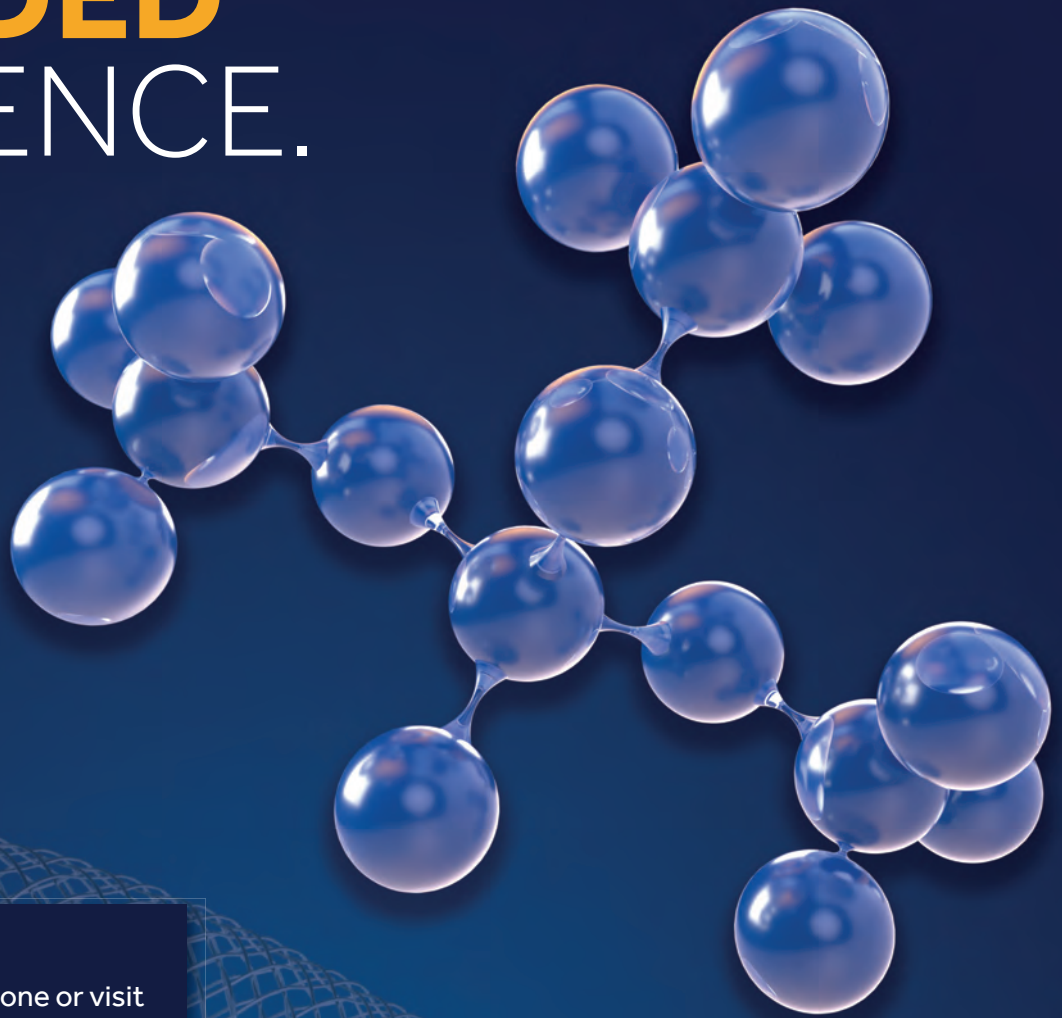
- Publication Preview
- Case Collection
- Podcasts
- The *AJNR* News Digest
- The *AJNR* Blog

It also reaches subscribers much faster than print. An electronic table of contents will be sent directly to your mailbox to notify you as soon as it publishes.

Readers can search, reference, and bookmark current and archived content 24 hours a day on [www.ajnr.org](http://www.ajnr.org).

ASNR members who wish to opt out of print can do so by using the *AJNR* Go Green link on the *AJNR* Website (<http://www.ajnr.org/content/subscriber-help-and-services>). Just type your name in the email form to stop print and spare our ecosystem.

# SHIELDED BY SCIENCE.



## See SHIELD in action.

Scan code with your smart phone or visit  
[medtronic.com/ShieldedByScience](https://www.medtronic.com/ShieldedByScience)



## Pipeline™ Flex Embolization Device with Shield Technology™

Shield Technology™ builds on the clinically proven Pipeline™ Flex Embolization Device by introducing an innovative surface modification. Scan code to learn more.

**CAUTION:** Federal (USA) law restricts this device to sale, distribution and use by or on the order of a physician. Indications, contraindications, warnings and instructions for use for the Pipeline™ Flex Embolization Device with Shield Technology™ can be viewed at <https://www.medtronic.com/manuals>

UC202200467 EN © 2021 Medtronic. All Rights Reserved. Medtronic, Medtronic logo and Further, Together are trademarks of Medtronic. All other brands are trademarks of a Medtronic company. 9775 Toledo Way, Irvine, CA 92618

# Medtronic



# AJNR

## AMERICAN JOURNAL OF NEURORADIOLOGY

AUGUST 2021  
VOLUME 42  
NUMBER 8  
WWW.AJNR.ORG

Publication Preview at [www.ajnr.org](http://www.ajnr.org) features articles released in advance of print.  
Visit [www.ajnrblog.org](http://www.ajnrblog.org) to comment on AJNR content and chat with colleagues  
and AJNR's News Digest at <http://ajnrdigest.org> to read the stories behind the  
latest research in neuroimaging.

1359 **PERSPECTIVES** *M. Hauben*

### EDITORIAL

- 1360 **Digital Didactics: Introducing the New ASNR Neuroradiology Fellowship Curriculum** *P.M. Bunch, et al.*

### REVIEW ARTICLE

- 1362 **Head CT: Toward Making Full Use of the Information the X-Rays Give** *K.A. Cauley, et al.*

ADULT BRAIN

### RADIOLOGY-PATHOLOGY CORRELATION

- 1370 **Hypothalamic Pilomyxoid Astrocytoma in a Child with Lipodystrophy** *J.C. Benson, et al.*

PEDIATRICS

### GENERAL CONTENTS

- 1375 **Strength of Association between Infarct Volume and Clinical Outcome Depends on the Magnitude of Infarct Size: Results from the ESCAPE-NAI Trial** *J.M. Ospel, et al.* ADULT BRAIN
- 1380 **Hypoperfusion Intensity Ratio Correlates with CTA Collateral Status in Large-Vessel Occlusion Acute Ischemic Stroke** *D. Lyndon, et al.* ADULT BRAIN FUNCTIONAL
- 1387 **MTT Heterogeneity in Perfusion CT Imaging as a Predictor of Outcome after Aneurysmal SAH** *B.B. Hofmann, et al.* ADULT BRAIN FUNCTIONAL
- 1396 **MTT and Blood-Brain Barrier Disruption within Asymptomatic Vascular WM Lesions** *B.E. Dewey, et al.* ADULT BRAIN FUNCTIONAL
- 1403 **Diagnostic Accuracy of Screening Arterial Spin-Labeling MRI Using Hadamard Encoding for the Detection of Reduced CBF in Adult Patients with Ischemic Moyamoya Disease** *K. Setta, et al.* ADULT BRAIN FUNCTIONAL
- 1410 **Collicular Hyperactivation in Patients with COVID-19: A New Finding on Brain MRI and PET/CT** *A. Chammas, et al.* ADULT BRAIN FUNCTIONAL
- 1415 **Comparison of Measurement Techniques and Response Criteria for MR Imaging Follow-up in Adult Primary Central Nervous System Lymphoma** *K. Massicotte-Tisluck, et al.* ADULT BRAIN
- 1421 **Is Contrast Medium Really Needed for Follow-up MRI of Untreated Intracranial Meningiomas?** *J. Boto, et al.* ADULT BRAIN

AJNR (Am J Neuroradiol ISSN 0195–6108) is a journal published monthly, owned and published by the American Society of Neuroradiology (ASNR), 800 Enterprise Drive, Suite 205, Oak Brook, IL 60523. Annual dues for the ASNR include approximately 21% for a journal subscription. The journal is printed by Intellicor Communications, 330 Eden Road, Lancaster, PA 17601; Periodicals postage paid at Oak Brook, IL and additional mailing offices. Printed in the U.S.A. POSTMASTER: Please send address changes to American Journal of Neuroradiology, P.O. Box 3000, Denville, NJ 07834, U.S.A. Subscription rates: nonmember \$410 (\$480 foreign) print and online, \$320 online only; institutions \$470 (\$540 foreign) print and basic online, \$935 (\$1000 foreign) print and extended online, \$380 online only (basic), \$825 online only (extended); single copies are \$35 each (\$40 foreign). Indexed by PubMed/MEDLINE, BIOSIS Previews, Current Contents (Clinical Medicine and Life Sciences), EMBASE, Google Scholar, HighWire Press, Q-Sensei, RefSeek, Science Citation Index, SCI Expanded, Meta/CZI, ReadCube, and Semantic Scholar. Copyright © American Society of Neuroradiology.



		1429	Prognostic Utility of Disproportionately Enlarged Subarachnoid Space Hydrocephalus in Idiopathic Normal Pressure Hydrocephalus Treated with Ventriculoperitoneal Shunt Surgery: A Systematic Review and Meta-analysis <i>H.Y. Park, et al.</i>	ADULT BRAIN	
		1437	Simultaneous Multislice for Accelerating Diffusion MRI in Clinical Neuroradiology Protocols <i>M.J. Hoch, et al.</i>	ADULT BRAIN	
		1444	Linking Stage-Specific Plasma Biomarkers to Gray Matter Atrophy in Parkinson Disease <i>W.-C. Lin, et al.</i>	ADULT BRAIN	
		1452	A Multicenter Preliminary Study of Cangrelor following Thrombectomy Failure for Refractory Proximal Intracranial Occlusions <i>G. Marnat, et al.</i>	INTERVENTIONAL	
		1458	Interobserver Agreement in Scoring Angiographic Results of Basilar Artery Occlusion Stroke Therapy <i>M. Findler, et al.</i>	INTERVENTIONAL	
		1464	Clinical and Procedural Outcomes with or without Balloon Guide Catheters during Endovascular Thrombectomy in Acute Ischemic Stroke: A Systematic Review and Meta-analysis with First-line Technique Subgroup Analysis <i>A. Podlasek, et al.</i>	INTERVENTIONAL	
		1472	Infarct Growth despite Successful Endovascular Reperfusion in Acute Ischemic Stroke: A Meta-analysis <i>F. Bala, et al.</i>	INTERVENTIONAL	
		1479	Impact of A1 Asymmetry on the Woven EndoBridge Device in Anterior Communicating Artery Aneurysms <i>J. Cortese, et al.</i>	INTERVENTIONAL	
			1486	Dural Arteriovenous Fistulas of the Foramen Magnum Region: Clinical Features and Angioarchitectural Phenotypes <i>M.T. Caton, et al.</i>	INTERVENTIONAL
		1492	Transradial Neuroendovascular Procedures in Adolescents: Initial Single-Center Experience <i>H. Alshehri, et al.</i>	INTERVENTIONAL	
		1497	Prevalence of Cervical Artery Abnormalities on CTA in Patients with Spontaneous Coronary Artery Dissection: Fibromuscular Dysplasia, Dissection, Aneurysm, and Tortuosity <i>J.C. Benson, et al.</i>	EXTRACRANIAL VASCULAR	
		1503	<b>Commentary</b> Look beyond the Heart: Extracoronary Vascular Manifestations of Spontaneous Coronary Artery Dissection <i>R. Ramcharitar, et al.</i>		
		1505	Functional MRI Shows Altered Deactivation and a Corresponding Decrease in Functional Connectivity of the Default Mode Network in Patients with Gliomas <i>Y.M. Maniar, et al.</i>	FUNCTIONAL	
		1513	Convolutional Neural Network to Stratify the Malignancy Risk of Thyroid Nodules: Diagnostic Performance Compared with the American College of Radiology Thyroid Imaging Reporting and Data System Implemented by Experienced Radiologists <i>G.R. Kim, et al.</i>	HEAD & NECK	
		1520	Neuroaxial Infantile Hemangiomas: Imaging Manifestations and Association with Hemangioma Syndromes <i>T. Feygin, et al.</i>	PEDIATRICS	
		1528	The Fetus with Ganglionic Eminence Abnormality: Head Size and Extracranial Sonographic Findings Predict Genetic Diagnoses and Postnatal Outcomes <i>S.K. Goergen, et al.</i>	PEDIATRICS	
		1535	Diffusion MRI Microstructural Abnormalities at Term-Equivalent Age Are Associated with Neurodevelopmental Outcomes at 3 Years of Age in Very Preterm Infants <i>M.N. Parikh, et al.</i>	PEDIATRICS FUNCTIONAL	
		1543	Cystlike Lesions as a Late Sequela of Radiotherapy in Pediatric Patients <i>M.G.D. Veiga, et al.</i>	PEDIATRICS	
		1550	Diagnostic Accuracy and Failure Mode Analysis of a Deep Learning Algorithm for the Detection of Cervical Spine Fractures <i>A.F. Voter, et al.</i>	SPINE	

## ONLINE FEATURES

### WHITE PAPER

- E48 **The Updated Neuroradiology Milestones: Synapsing from 1.0 to 2.0** *A.A. Bhatt, et al.*

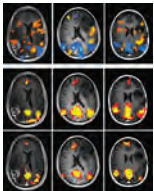
### LETTERS

- 🔑 E53 **COVID-19 Stroke Apical Lung Exam Study: Is it Really an Accurate Diagnostic Method?** *S. Marquez, et al.*
- 🔑 E54 **Reply** *F. Bala, et al.*
- E56 **Do Prior Iodine Contrast Injections Affect Cerebral Blood Flow Measurement on CT Perfusion Studies of Patients with Large-Vessel Occlusions?** *S.A. Amukotuwa, et al.*
- E58 **Reply** *M.R. Amans, et al.*

### BOOK REVIEWS

*R.M. Quencer, Section Editor*

Please visit [www.ajnrblog.org](http://www.ajnrblog.org) to read and comment on Book Reviews.



Examples of correlation maps in an axial view for patients with gliomas in different locations (Maniar, et al.).



Indicates Editor's Choices selection



Indicates Fellows' Journal Club selection



Indicates open access to non-subscribers at [www.ajnr.org](http://www.ajnr.org)



Indicates article with supplemental online data



Indicates article with supplemental online video



Evidence-Based Medicine Level 1



Evidence-Based Medicine Level 2

### EDITOR-IN-CHIEF

**Jeffrey S. Ross, MD**

Professor of Radiology, Department of Radiology,  
Mayo Clinic College of Medicine, Phoenix, AZ

### SENIOR EDITORS

**Harry J. Cloft, MD, PhD**

Professor of Radiology and Neurosurgery,  
Department of Radiology, Mayo Clinic College of  
Medicine, Rochester, MN

**Christopher G. Filippi, MD**

Professor and Alice Ettinger-Jack R. Dreyfuss  
Chair of Radiology,  
Tufts University School of Medicine,  
Radiologist-in-Chief  
Tufts University Medical Center, Boston, MA

**Thierry A.G.M. Huisman, MD**

Radiologist-in-Chief, Texas Children's Hospital,  
Houston, TX

**Yvonne W. Lui, MD**

Associate Professor of Radiology,  
Chief of Neuroradiology,  
New York University School of Medicine,  
New York, NY

**C.D. Phillips, MD, FACR**

Professor of Radiology, Weill Cornell Medical  
College, Director of Head and Neck Imaging,  
New York-Presbyterian Hospital, New York, NY

**Lubdhra M. Shah, MD, MS**

Professor of Radiology and Director of Spine  
Imaging, University of Utah Department of  
Radiology and Imaging Sciences, Salt Lake City, UT

### STATISTICAL SENIOR EDITOR

**Bryan A. Comstock, MS**

Senior Biostatistician,  
Department of Biostatistics,  
University of Washington, Seattle, WA

### ARTIFICIAL INTELLIGENCE DEPUTY EDITOR

**Peter D. Chang, MD**

Assistant Professor-in-Residence,  
Departments of Radiological Sciences,  
Computer Sciences, and Pathology,  
Director, Center for Artificial Intelligence in  
Diagnostic Medicine (CAIDM),  
University of California, Irvine, Irvine, CA

### EDITORIAL BOARD

Ashley H. Aiken, Atlanta, GA

Lea M. Alhilali, Phoenix, AZ

Mohammed A. Almekhlafi, Calgary, Alberta,  
Canada

Joachim Berkefeld, Frankfurt, Germany

Aashim Bhatia, Pittsburgh, PA

Waleed Brinjikji, Rochester, MN

Judah Burns, New York, NY

Danielle Byrne, Dublin, Ireland

Federico Cagnazzo, Montpellier, France

J. Levi Chazen, New York, NY

James Y. Chen, San Diego, CA

Gloria C. Chiang, New York, NY

Daniel Chow, Irvine, CA

Kars C.J. Compagne, Rotterdam, The Netherlands

Arturo Consoli, Suresnes, France

Seena Dehkharghani, New York, NY

Nilesh K. Desai, Houston, TX

Yonghong Ding, Rochester, MN

Birgit Ertl-Wagner, Toronto, Ontario, Canada

Clifford J. Eskey, Hanover, NH

Massimo Filippi, Milan, Italy

Nils D. Forkert, Calgary, Alberta, Canada

Ana M. Franceschi, New York, NY

Frank Gaillard, Melbourne, Australia

Joseph J. Gemmete, Ann Arbor, Michigan

Wende N. Gibbs, Phoenix, AZ

Philipp Göltz, Erlangen, Germany

Brent Griffith, Detroit, MI

Joseph M. Hoxworth, Phoenix, Arizona

Raymond Y. Huang, Boston, MA

Gábor Janiga, Magdeburg, Germany

Christof Karmonik, Houston, TX

Timothy J. Kaufmann, Rochester, MN

Hillary R. Kelly, Boston, MA

Toshitomi Kinoshita, Akita, Japan

Alexander W. Korutz, Chicago, IL

Stephen F. Kralik, Houston, TX

Alexander Lerner, Los Angeles, CA

Yinsheng Li, Madison, WI

Franklin A. Marden, Chicago, IL

Markus A. Möhlenbruch, Heidelberg, Germany

Kambiz Nael, Los Angeles, CA

Renato Hoffmann Nunes, Sao Paulo, Brazil

Sasan Partovi, Cleveland, OH

Johannes A.R. Pfaff, Salzburg, Austria

Laurent Pierot, Reims, France

Alireza Radmanesh, New York, NY

Prashant Raghavan, Baltimore, MD

Eytan Raz, New York, NY

Paul M. Ruggieri, Cleveland, OH

Sebastian Schafer, Madison, WI

Maksim Shapiro, New York, NY

Timothy Shepherd, New York, NY

James Shin, New York, NY

Mark S. Shiroishi, Los Angeles, CA

Bruno P. Soares, Baltimore, MD

Jason F. Talbot, San Francisco, CA

Ruth Thiex, Everett, Washington

Vincent Thijs, Melbourne, Victoria, Australia

Anderanik Tomasian, Los Angeles, CA

Fabio Triulzi, Milan, Italy

Anja G. van der Kolk, Utrecht, the Netherlands

Arastoo Vossough, Philadelphia, PA

Elysa Widjaja, Toronto, Ontario, Canada

Leonard Yeo, Singapore

Woong Yoon, Gwangju, South Korea

David M. Yousem, Evergreen, CO

Carlos Zamora, Chapel Hill, NC

Chengcheng Zhu, Seattle, WA

### EDITORIAL FELLOW

Vivek Yedavalli, Baltimore, MD

### SPECIAL CONSULTANTS TO THE EDITOR

**AJNR Blog Editor**

Neil Lall, Denver, CO

**Case of the Month Editor**

Nicholas Stence, Aurora, CO

**Case of the Week Editors**

Matylda Machnowska, Toronto, Ontario, Canada

Anvita Pauranik, Calgary, Alberta, Canada

Vinil Shah, San Francisco, CA

**Classic Case Editor**

Sandy Cheng-Yu Chen, Taipei, Taiwan

**Health Care and Socioeconomics Editor**

Pina C. Sanelli, New York, NY

**Physics Editor**

Greg Zaharchuk, Stanford, CA

**Podcast Editor**

Courtney Tomblinson, Nashville, TN

**Deputy Podcast Editor**

Kevin Hiatt, Winston-Salem, NC

**Twitter Editor**

Roger Jordan, Houston, TX

### Official Journal:

American Society of Neuroradiology

American Society of Functional Neuroradiology

American Society of Head and Neck Radiology

American Society of Pediatric Neuroradiology

American Society of Spine Radiology

Founding Editor  
Juan M. Taveras

Editors Emeriti  
Mauricio Castillo, Robert I. Grossman,  
Michael S. Huckabee, Robert M. Quencer

Managing Editor  
Karen Halm

Assistant Managing Editor  
Laura Wilhelm

Executive Director, ASNR  
Mary Beth Hepp



Title: Fire Breather, Prague. This image, spontaneously recorded with an iPhone 6, reinforces my feeling that photography is a singularly life-enhancing art. It allows us to see, contemplate, and marvel at things that do not normally register on the retina or occipital cortex. In this instance, note the beautiful, radiating incandescent spikes concentrated at the distal end of the flame plume that I did not perceive when observing with the naked eye. My hypothesis is that these correspond to statistical outliers in the velocity/position distribution of the incandescent particles. A Maxwell-Boltzmann type distribution interacting with the breath flow profile of the fire breather might be a good explanatory model. The appearance is not dissimilar to some starburst plots that I have generated in statistical outlier analysis.

*Manfred Hauben, MD, MPH, Pfizer Inc and NYU Langone Health, New York City*



# Digital Didactics: Introducing the New ASNR Neuroradiology Fellowship Curriculum

 P.M. Bunch,  C.M. Tomblinson,  A.H. Aiken, and  T.A. Kennedy 

In 2020, the American Society of Neuroradiology (ASNR) Fellowship Directors Committee and Young Professionals Section collaborated to curate the ASNR Neuroradiology Fellowship Digital Curriculum.<sup>1</sup> The objective of this curated curriculum is to supplement the existing educational offerings at individual neuroradiology fellowship programs. This curriculum is composed primarily of video lectures selected from a variety of sources, including annual meetings and webinar series of the ASNR and Radiological Society of North America as well as regional (Eastern Neuroradiological Society) and subspecialty (American Society of Head and Neck Radiology) societies of the ASNR. Highly relevant journal articles are also included. The new curriculum builds on a 2017 initiative led by the ASNR Education Committee to create lists of topics with which all neuroradiology trainees should be familiar at their respective level of training (junior resident,<sup>2</sup> senior resident,<sup>3</sup> and fellow<sup>4</sup>). The purpose of this editorial is to summarize the Neuroradiology Fellowship Digital Curriculum development process and to provide an introduction to this new electronic resource that is freely available to all ASNR members.

Recently updated Accreditation Council for Graduate Medical Education guidelines<sup>5</sup> outline requirements related to providing a neuroradiology curriculum for trainees. Although previously developed neuroradiology curricular topic lists<sup>2-4</sup> are useful, a limitation of these lists is that they shift the responsibility of finding, choosing, and vetting the specific content covering the topics of interest to the learner. Such an approach leaves room for error, omission, or misinterpretation on the part of the learner with respect to deciding what is or could be important in preparing for independent neuroradiology practice and the neuroradiology subspecialty certification examination. Thus, there is substantial potential for heterogeneity of educational content encountered at the individual learner level with some learners likely selecting high-quality resources and others inadvertently choosing lesser quality resources in the absence of a trustworthy endorsement.

Furthermore, there is also the potential for heterogeneity of educational content and trainee experience at the fellowship program level, as many programs are likely to excel at teaching certain topics more than others, depending on program faculty expertise. For example, some programs may not have in-house health policy or artificial intelligence experts, whereas others may not have expertise with some advanced imaging techniques (eg, fMRI, DTI, arterial spin-labeling, MR spectroscopy). Despite inevitable relative strengths and weaknesses in educational content areas, neuroradiology

fellowship training programs have a responsibility to provide a comprehensive curriculum to their trainees. Finally, the sheer number of educational resources can be overwhelming, leaving both learners and training programs alike uncertain as to which resources are the highest yield and most accurate.

For these reasons, there is a need for expert content curation to identify trainee-appropriate resources mapped to the previously developed neuroradiology fellowship curriculum topics that can be used to supplement educational offerings at each neuroradiology fellowship program.

## The Process


The national shift to virtual radiology meetings and the proliferation of other online educational material in response to the coronavirus disease 2019 pandemic provided the opportunity to curate high-quality resources from ample available digital content created by recognized experts. To select content for inclusion in the digital fellowship curriculum, subject matter-based teams (eg, brain, spine, head and neck) were formed. Each team (Table) was led by a member of the ASNR Fellowship Directors Committee. Teams included ASNR Young Professionals Committee Regional and Subspecialty Society Liaisons, additional Fellowship Directors Committee volunteers, and selected trainees representing a variety of neuroradiology training programs and educational backgrounds. One of the major benefits of including team members at different career stages is that the curriculum perspectives of both the program director and learner were represented through mutual collaboration rather than a top-down or bottom-up approach.

Each subject matter team reviewed relevant content from the ASNR, subspecialty society, and regional society annual meetings plus webinars and relevant online content from other organizations in the following topic areas: 1) Advanced Imaging, 2) Brain, 3) Head and Neck, 4) Interventional Neuroendovascular, 5) Noninterpretive/Finance, 6) Pediatric, and 7) Spine. The availability of virtual meeting recorded lecture content (eg, the ASNR 2020 Annual Meeting) for several months after the meeting enabled the teams to be thoughtful and deliberate in the content-selection process rather than rushed. Following each team's review of available content in the respective content areas, the highest quality, highest yield material was recommended for inclusion in the curriculum.

Moving forward, the digital curriculum will be refined annually through a similar team-based process. These future iterations will ensure that the digital curriculum remains relevant and up-to-date, incorporating additional topics and even higher quality resources when available.

## The Result

The result of this team-based collaborative effort between the ASNR Fellowship Directors Committee and Young Professionals Section is the Neuroradiology Fellowship Digital Curriculum (Figure). This new, curated online curriculum supplements the core educational curriculum of individual neuroradiology fellowship programs and decreases heterogeneity of the educational experience for individual learners at different programs. The full digital

 Indicates article with online supplemental data.  
<http://dx.doi.org/10.3174/ajnr.A7150>

# Topic leads and additional volunteer contributors to the ASNR neuroradiology fellowship digital curriculum

Topic Area	Topic Lead	Other Team Members
Advanced Imaging Brain	Alex Korutz Aparna Singhal	Anna Trofimova Michelle Miller Thomas, Harp Bedi, Kiran Talekar, Mari Hagiwara, Richard Beegle
Head and Neck Interventional Neuroendovascular Noninterpretive/Finance	Nancy Fischbein Paul Jacobson Vinil Shah	Ashley Aiken, Bruno Policeni, Asha Sarma Scott Raymond Tabby Kennedy, Evan Calabrese, Priya Rajagopalan, Ashwani Gore, Melissa Chen, Paul Bunch, Courtney Tomblinson
Pediatric Spine	Stephen Kralik Vikas Agarwal	Julie Guerin Jennifer McCarty, Miriam Peckham, Amit Aggarwal



**FIGURE.** Graphic demonstrates the ASNR Neuroradiology Fellowship Digital Curriculum accessible to all ASNR members through the ASNR Education Connection. When logged in to Education Connection with a member account, click “Launch” (oval) to access the full curriculum.

curriculum is freely available to all ASNR members through the ASNR Education Connection (<https://www.asnr.org/education/education-connection/>) and includes 189 video lectures. Details of the curated video lecture content within each of the 7 topic areas are summarized in Online Supplemental Data.

Benefits of the curated online curriculum from the neuroradiology fellow’s perspective include the following: 1) confidence that content curated by ASNR experts is accurate and up-to-date, 2) access to topics and content experts that may be missing from the individual’s home program, 3) additional perspectives on topics already covered by the fellow’s home program, 4) free to use with a no-cost in-training ASNR membership, and 5) the ability to access it from the comfort of one’s own home. The new online curriculum benefits individual neuroradiology fellowship programs by supplementing the institutional curriculum, particularly in areas where a program may lack local expertise or where quality educational material is relatively sparse.

## CONCLUSIONS

Through a collaborative effort of the ASNR Fellowship Directors Committee and the Young Professionals Section, an online neuroradiology fellowship digital curriculum of high-quality content that learners can trust to be accurate and up-to-date was curated by volunteer experts. This digital curriculum is intended to

supplement the educational offerings of each individual neuroradiology fellowship program and is freely available to all ASNR members. Furthermore, ASNR membership is offered at no cost to residents, fellows, and others in training.

## ACKNOWLEDGMENTS

We thank the committee volunteers who participated in curriculum curation and the Radiological Society of North America, the American Society of Head and Neck Radiology, and the Eastern Neuroradiological Society for generously supporting this project by sharing their educational content.

## REFERENCES

1. Neuroradiology Fellowship Curriculum. <http://asnr.mycrowdwisdom.com/diweb/catalog/item?id=6099490>. Accessed January 31, 2021
2. R1 to R3 Curriculum. <https://www.asnr.org/wp-content/uploads/2018/06/FINAL-ASNR-R1-to-R3-Curriculum.pdf>. Accessed January 31, 2021
3. R4 Curriculum. <https://www.asnr.org/wp-content/uploads/2018/06/Fourth-Year-R4.pdf>. Accessed January 31, 2021
4. Fellowship Curriculum. [https://www.asnr.org/wp-content/uploads/2018/06/FINAL-ASNR-Fellow-Curriculum.ver\\_06.21.18-2.pdf](https://www.asnr.org/wp-content/uploads/2018/06/FINAL-ASNR-Fellow-Curriculum.ver_06.21.18-2.pdf). Accessed January 31, 2021
5. ACGME Program Requirements for Graduate Medical Education in Neuroradiology. [https://www.acgme.org/Portals/0/PFAssets/ProgramRequirements/423\\_Neuroradiology\\_2020.pdf?ver=2020-06-29-164131-690](https://www.acgme.org/Portals/0/PFAssets/ProgramRequirements/423_Neuroradiology_2020.pdf?ver=2020-06-29-164131-690). Accessed January 31, 2021

# Head CT: Toward Making Full Use of the Information the X-Rays Give

K.A. Cauley, Y. Hu, and S.W. Fielden



## ABSTRACT

**SUMMARY:** Although clinical head CT images are typically interpreted qualitatively, automated methods applied to routine clinical head CTs enable quantitative assessment of brain volume, brain parenchymal fraction, brain radiodensity, and brain radiomass. These metrics gain clinical meaning when viewed relative to a reference database and expressed as quantile regression values. Quantitative imaging data can aid in objective reporting and in the identification of outliers, with possible diagnostic implications. The comparison to a reference database necessitates standardization of head CT imaging parameters and protocols. Future research is needed to learn the effects of virtual monochromatic imaging on the quantitative characteristics of head CT images.

*“... it became apparent that the conventional methods were not making full use of all the information the x-rays could give.”*

G. Hounsfield, Nobel Lecture, 1979<sup>1</sup>

CT scans serve a unique and necessary role in clinical medicine with approximately 82 million CT scans performed in the United States in 2018, and 11.5 million of those being head CTs.<sup>2,3</sup> Despite these numbers, the radiation exposure from CT largely precludes prospective human subjects research. In addition, low soft tissue contrast has resulted in relatively little published clinical research in head CT imaging relative to MR imaging. In the clinical setting, CT is used to diagnose gross structural pathology, to be followed by MR imaging as clinically indicated. Where the signal intensity of MR imaging is largely uncalibrated, the image intensity of CT is a scaled and calibrated metric that reflects the radiodensity of the material imaged and offers a quantitative tissue measure, which is not assessed by MR imaging. In this review, we discuss current methods and applications of quantitative analysis of head CT imaging.

## Methods of Analysis

Volumetric analysis of brain CT imaging entails removal of non-brain tissue from the head imaging series, an image-processing step termed “brain extraction” or “skull stripping.” Brain extraction is often performed in postprocessing of brain MR images and has been less applied to CT imaging. Several author groups have found that the MR imaging postprocessing software FSL (<http://fsl.fmrib.ox.ac.uk/fsl/fslwiki/FSL>)<sup>4</sup> can be used to process head CT imaging.<sup>5,6</sup> By means of FSL, the skull can be subtracted from head CT images by thresholding, and the residual nonbrain tissue can be removed using the FSL Brain Extraction Tool (<http://fsl.fmrib.ox.ac.uk/fsl/fslwiki/BET>). The CSF space can be subtracted to permit the calculation of the ratio of the brain volume to intracranial volume, to yield the brain parenchymal fraction.<sup>7,8</sup>

## Volumetrics

Digital images are acquired as signal intensities with voxel coordinates. The routine CT brain protocol at our institution results in voxels that are  $0.5 \times 0.5$  mm and are typically displayed and stored at 5-mm section thickness, with the consequence that the spatial resolution is very high in-plane (“x” and “y” dimension on an axial section) but low in the “z” dimension. After brain extraction, the volume of the brain parenchyma can be obtained by a simple voxel count, which is easily performed with FSL. The average adult brain size is approximately  $1200 \text{ cm}^3$ , or on the order of 1,000,000 voxels.

Changes in brain volume as a function of age have been a popular topic of imaging literature, largely investigated with MR imaging of healthy volunteers.<sup>9–12</sup> Abnormalities of total brain volume have been associated with congenital and acquired pathology. In the pediatric population, congenital conditions are

Received February 8, 2021; accepted after revision February 19.

From the Departments of Radiology (K.A.C.) and Biomedical & Translational Informatics (Y.H.) Geisinger Medical Center, Danville, Pennsylvania, and Geisinger Autism & Developmental Medicine Institute (S.W.F.), Lewisburg, Pennsylvania.

This work was supported by a Geisinger clinical research fund to K.A.C. and S.W.F., SRC-L-58.

Please address correspondence to Keith A. Cauley, MD, PhD, Geisinger Medical Center, Department of Radiology, Danville, PA 17821; e-mail: [keithcauley@hotmail.com](mailto:keithcauley@hotmail.com)

Indicates open access to non-subscribers at [www.ajnr.org](http://www.ajnr.org)

<http://dx.doi.org/10.3174/ajnr.A7153>

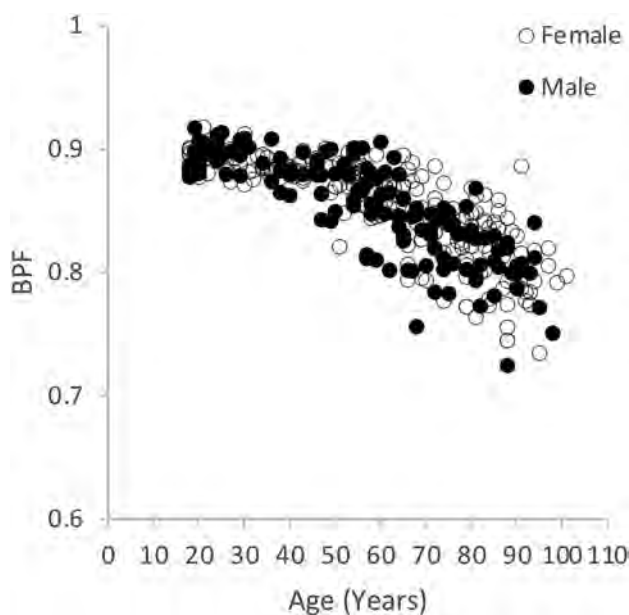


**FIG 1.** Change in brain parenchymal fraction through the life span, men (filled) and women (unfilled). This figure summarizes the findings further detailed in Cauley et al.<sup>7</sup>

associated with macrocephaly and microcephaly, with accompanying abnormalities of brain volume. Among adults, abnormalities of global brain volume have been described in multiple sclerosis,<sup>8</sup> amyotrophic lateral sclerosis,<sup>13</sup> and Alzheimer disease and age-related dementia.<sup>14,15</sup> Head CT has been used for the investigation of brain volume measures in Alzheimer disease and age-related dementias well before the advent of MR imaging. Early studies focused on CT brain volumetrics as derived or inferred from linear measurements, such as sulcal width or ventricular volume.<sup>16</sup> Recent advances in computer software enable automated, statistical modeling of digital methods of analysis of head CT images. Quantitative assessment of brain volume could aid in the characterization of pathology associated with global brain volume loss.

### The Brain Parenchymal Fraction

Where brain volume varies widely among healthy individuals, the ratio of the brain volume to the intracranial volume, or brain parenchymal fraction, reduces the intrasubject variability.<sup>8,17</sup> Accurate estimation of the brain parenchymal fraction requires estimation of the intracranial volume and the brain volume, the latter measure achieved by segmenting the CSF from the brain parenchyma. The brain parenchymal fraction increases sensitivity for correlation with pathology, is decreased in multiple sclerosis, and has been used to distinguish different phenotypes in amyotrophic lateral sclerosis.<sup>8,13</sup> The brain parenchymal fraction shows consistent decline with age after the second decade, with decreased variance relative to the brain volume measure (Fig 1 and Cauley et al<sup>7,18</sup>).

### Radiodensity

During CT imaging, the radiodensity of each voxel is recorded as the signal intensity and is scaled and calibrated in terms of the Hounsfield unit (HU), a scale that defines “zero” for distilled

water and  $-1000$  for air.<sup>1</sup> More precisely, the HU scale “is a linear transformation of the original linear attenuation coefficient measurement into one in which the radiodensity of distilled water at standard pressure and temperature is defined as  $0$  HU, while the radiodensity of air at [standard pressure and temperature] is defined as  $-1000$  HU.” For materials of higher attenuation, the HU for bone is on the order of  $1000$ – $2000$  HU and for metal,  $> 3000$  HU.<sup>19</sup>

In a voxel with average linear attenuation coefficient  $\mu$ , the corresponding HU value is therefore given by

$$HU = 1000 \times \frac{\mu - \mu_{\text{water}}}{\mu_{\text{water}} - \mu_{\text{air}}},$$

where  $\mu_{\text{water}}$  and  $\mu_{\text{air}}$  are the linear attenuation coefficients of water and air, respectively. This definition is true for CT scanners that are calibrated with reference to water.

Although the radiodensity value is only infrequently used in routine image interpretation, the accuracy of the radiodensity determines the image quality, and it is monitored and calibrated as part of the American College of Radiology quality control program (ACR.org). In our studies using standard clinical CT scanners, the Hounsfield units of water and of an attenuation phantom are recorded daily and drift or trending were rarely observed. In a typical month, the HU of water or the tissue attenuation plug is found to vary by less than  $1$  HU.

Radiodensity assessment of the brain enables objective, quantitative assessment of findings which are typically described in qualitative terms. Such quantitation enables the detection of subtle changes that might otherwise be overlooked. Radiodensity measures of specific pathologies, such as hemorrhage or cerebral edema after infarct, have been investigated with claims of prognostic implication.<sup>20,21</sup> There are few reports on the radiodensity of nonfocal or global parenchymal pathology.<sup>22</sup> Using automated, digital methods, a decline in global radiodensity of the brain as a function of aging has been reported.<sup>7</sup> Using digital methods a higher global brain radiodensity was found in multiple sclerosis.<sup>23</sup> Others report a globally decreased brain radiodensity associated with elevated intracranial pressure.<sup>24</sup> Global radiodensity values in the context of quantile regression, as described below, may aid in the identification and characterization of conditions involving abnormalities of global brain radiodensity.

### Radiomass

Tissue volume is arguably the most common metric assessed from imaging. The corresponding postmortem metric is brain tissue weight or mass. The weight might be estimated from the measured volume, provided that the specific gravity (grams/milliliter) of brain tissue is constant.<sup>11</sup> This would not appear to be the case, however, as the radiodensity increases in early life<sup>25</sup> and decreases with age.<sup>7</sup> An alternative weight estimation for CT imaging is the product of the volume and the radiodensity, or the “radiomass.” Although the radiomass has the cryptic units of  $HU \times cm^3$  and has been little explored in the literature, the measure may have clinical meaning. Study results vary, but whereas the brain volume declines approximately  $11\%$  throughout the adult life span,<sup>26</sup> the brain weight declines  $20\%$ – $22\%$ . Compared



with postmortem literature, the measured relative decline in radiomass as a function of age is highly correlated with direct measures of brain weight (unpublished data). Disease states may also show changes in brain radiomass, though this has not been investigated. In multiple sclerosis, for example, brain volume and radiodensity are both affected by the disease.<sup>8,23</sup> Future studies will be needed to investigate correlations between abnormalities of radiomass and various global brain pathologies.

### **Gray and White Matter Segmentation**

Imaging research is facilitated by segmentation of tissue types and anatomic regions. Where tissue class segmentation is relatively straightforward for MR imaging, low image contrast poses a challenge for gray-white matter segmentation of CT images. When displayed as a voxel histogram, MR imaging is of sufficient image contrast that gray and white matter are represented as separate peaks of a bimodal distribution of signal intensity (Fig 2).<sup>27</sup> For clinical brain CT images, however, the signal intensity histogram of the brain is unimodal, without separation between gray and white matter peaks (Fig 2 and Cauley et al<sup>6</sup>). Tissue class segmentation of head CT images requires a more sophisticated methodology than a simple radiodensity cutoff.

Segmentation of CT images can be direct, based on the signal intensities of individual voxels<sup>6</sup> or based on image masking using an MR imaging template.<sup>28</sup> Newer techniques propose machine learning algorithms for CT image segmentation.<sup>29</sup> Although MR imaging represents a current “gold standard” for segmentation, gray and white matter segmentation of MR images can vary with segmentation technique.<sup>30</sup> A given voxel may include a mix of tissue classes, and accurate segmentation entails subvoxel segmentation. Direct segmentation, as described using software such as FSL, has both binary and partial volume options. A comparison of the outputs of binary and partial volume segmentation is shown in Fig 2. Gray and white matter volumes derived from brain CT segmentation are likely to differ from MR imaging results, though a direct comparison of segmentations from the different modalities has yet to be conducted.

Segmentation of brain CT images enables measurements of gray and white matter radiodensity, which may have clinical implications. In cases of global anoxic injury seen in cardiac arrest, for example, the gray matter radiodensity decreases and consequently the ratio between gray and white matter densities is decreased.<sup>31</sup> Automated segmentation can facilitate this calculation.<sup>32</sup> It has recently been suggested that such measures may prove useful in forensic medicine to aid in determining the cause or time of death.<sup>33</sup>

**The Normative Clinical Database. Quantile Regression.** A patient’s medical data become meaningful only through comparison to reference values. Existing reference imaging databases of human brain data largely comprise MR imaging studies with relatively small numbers of healthy volunteers. As CT scans entail a radiation exposure, the recruitment of healthy volunteers into a CT study for this purpose would be difficult to justify. However, in the clinical setting, the threshold for CT imaging is very low,

and the PACS includes large numbers of studies with essentially normal findings. Radiographic studies with normal findings can be narrowed to studies of patients without significant medical history or without systemic disease. In this way, large databases can be subject to statistical analysis to identify normative parameters.

A criticism of a database generated from the clinical archive is that because patients are always scanned for a reason, no study within the database can be presumed to have truly normal findings, and therefore, such a database cannot serve as a reference. This reasoning should be questioned. First, many studies within the archive are performed for nonspecific symptoms or for minor trauma without traumatic finding and have essentially normal findings. As the database increases in size, the mean values will approach normalcy. Second, our goal is not to identify the healthy patients, but to identify the patients with abnormal findings. In the clinical setting, a patient’s condition is judged as more or less urgent. In this sense, the metrics of a given study need not be identified as healthy or unhealthy, but rather “at the 97th percentile” or “at the 23rd percentile” (of brain volume for age and sex, for example), as is often done for other types of clinical data. This can be achieved through quantile regression (Fig 3). This is the reasoning by which the diagnosis is made for microcephaly (head circumference  $> 2$  SD below the mean for sex and age)<sup>34</sup> or macrocephaly (head circumference of  $> 2$  SD above the mean for age and sex).<sup>35</sup> Databases could be continuously expanded as studies meeting criteria for “negative” or healthy are added. Finally, the PACS archive offers a huge database of both sexes across the life span. Such a cohort would be difficult to obtain through the recruitment of healthy volunteers. As a prospective study is not likely to happen, the PACS database is the only information available for the generation of a reference database for CT images.

### **Caveats and Current Limitations of Quantitative CT**

**Manipulation of CT Images.** Popular MR image processing techniques, such as image registration (warping), are not as easily applied to CT imaging due to typically highly anisotropic voxel geometry and changes in the partial volume calculation. Changing the positioning or angulation of the CT brain image after acquisition can alter volume measurement (Fig 4A, -B). Registering CT images to a target image can alter the CT image histogram (Fig 4A, -C) and erode the image integrity. Warping the images while maintaining the integrity of the signal intensity may be a complex task.<sup>36</sup> As an alternative, mask or standard images can be registered to the CT scan enabling gross registration of standard atlas images.

**Beam-Hardening by the Skull.** Since the initial development of head CT imaging, it has been noted that the high attenuation of the skull creates a significant beam-hardening artifact, which greatly limits image quality.<sup>37,38</sup> This artifact is greater for thicker skulls, and can impact image interpretation.<sup>6,39</sup> Modifications in machine design have enabled prehardening of the beam, reducing the effects of beam-hardening on the images;<sup>40,41</sup> however, the effects can still be seen on many current acquisitions (Fig 5 and Cauley et al<sup>6</sup>). Radiologists tend to associate beam-hardening

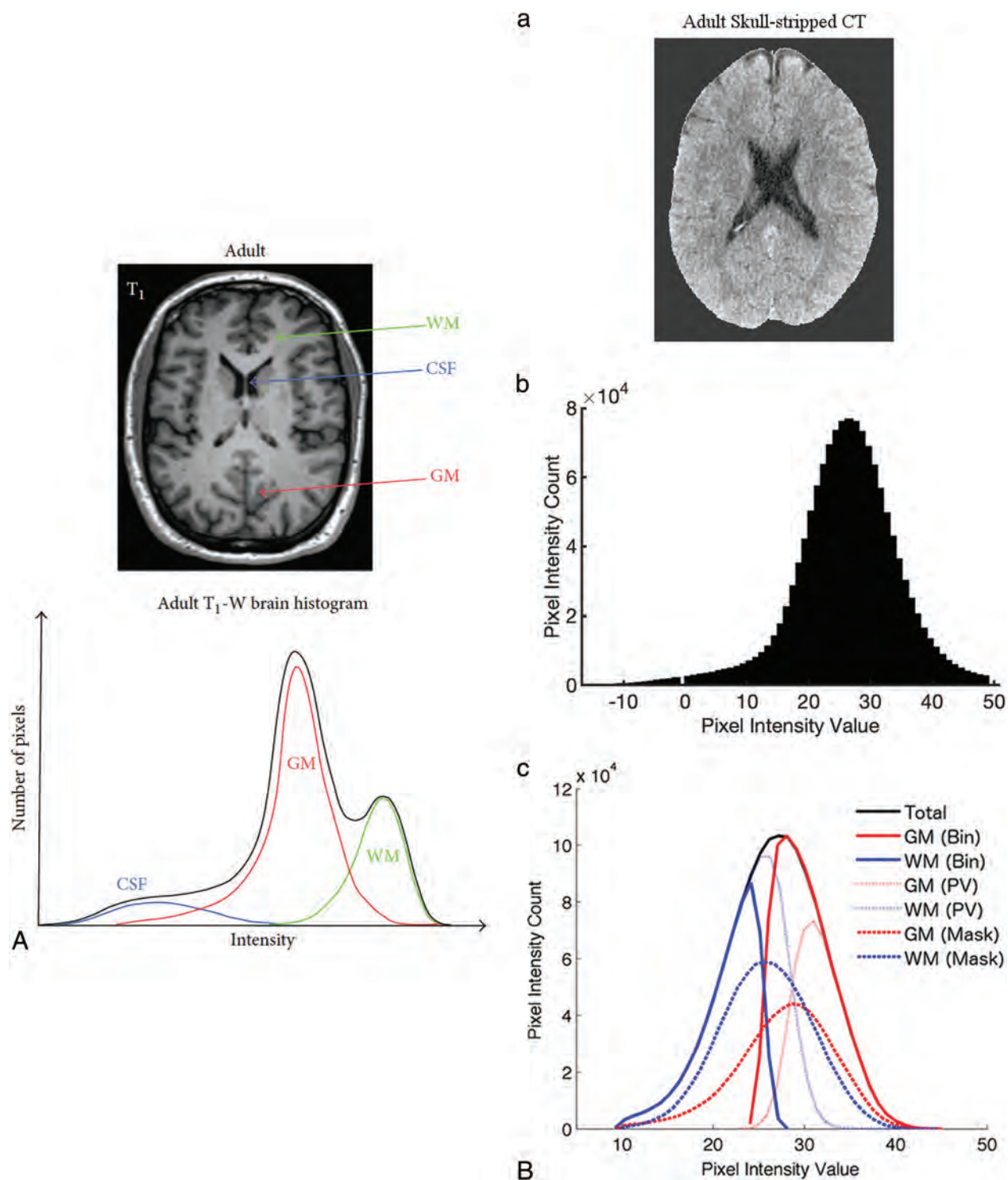


**FIG 2.** A, Segmentation of T1-weighted MR image of the brain, reprinted with permission from Despotović et al.<sup>27</sup> B, Segmentation of a brain CT image, reprinted with permission from Cauley et al.<sup>6</sup>

with streak artifacts, which are caused by focal skull thickening or by sharp attenuation transitions between air and skull, as in the paranasal sinuses. Beam-hardening is a far more universal phenomenon in head imaging, as the skull filters all x-rays that pass through it and increases the mean beam energy reaching the brain (increasing the kilovolt peak). This in turn results in a decrease in the measured HU as the brain tissue has less stopping

power for higher energy x-rays. This broadly affects the measured HU of brain tissue and draws attention to the fact that HU measures are not absolute. The effects of beam-hardening are reduced by a monochromatic x-ray source.<sup>42</sup>

In MR imaging, field inhomogeneities can give rise to image intensity inhomogeneities, which can undermine image quality and preclude accurate image processing, such as registration and

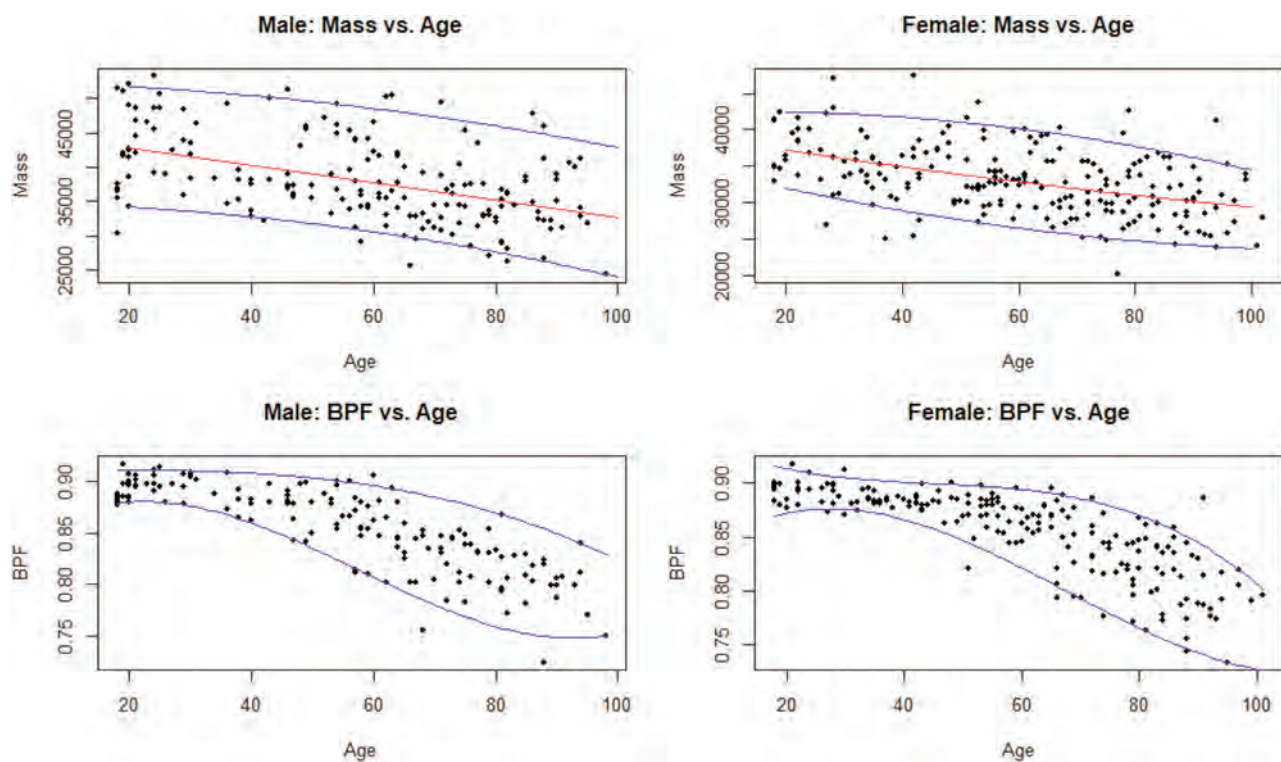


**FIG 3.** Quantile regression of adult brain parenchymal fraction (men, *left* and women, *right*) as a function of age. Quantile regression of adult brain mass (men, *left* and women, *right*) as a function of age.

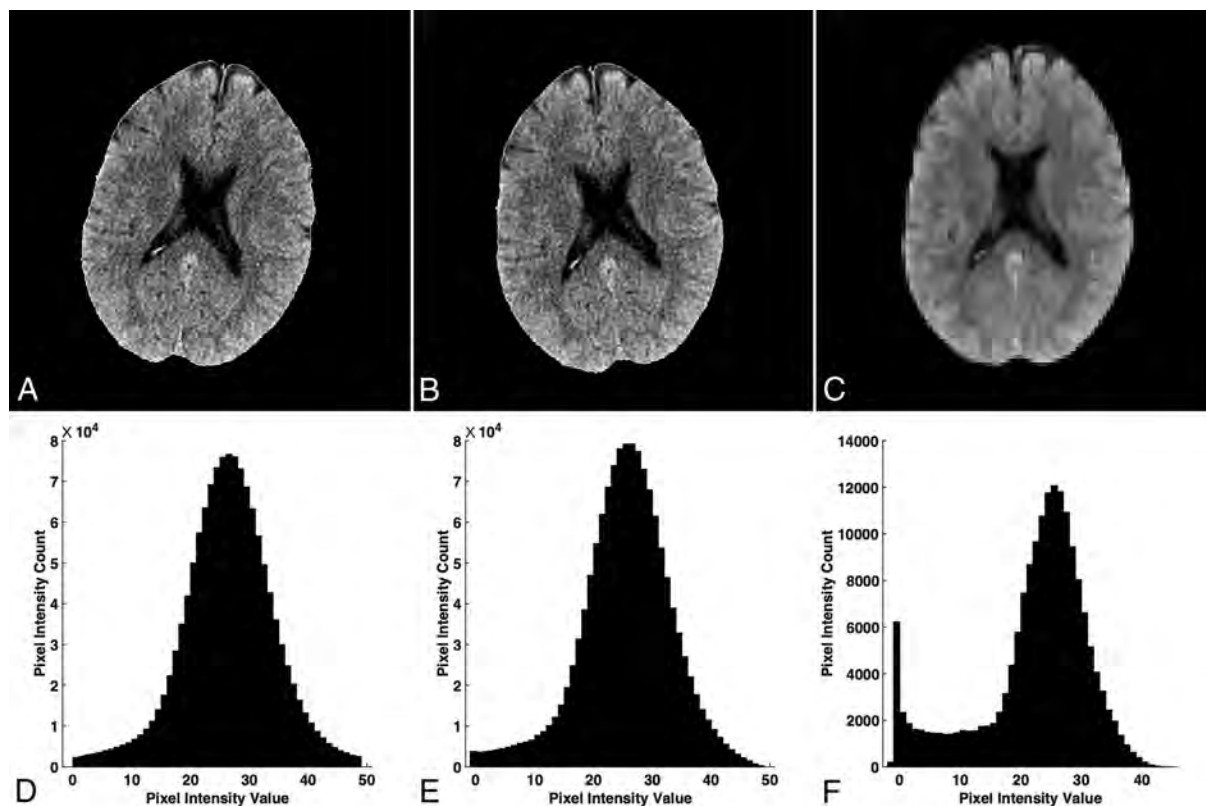


**FIG 4.** The effects of image rotation on radiodensity histogram and volumetrics of brain CT images. A, Original image. Volume calculated 1565 mL. B, Image rotated 15° to the right. Volume calculated 1602 mL. C, Rotated image registered to standard brain MR imaging template in FSL to restore image to nonrotated orientation. Volume calculated 2022 mL.



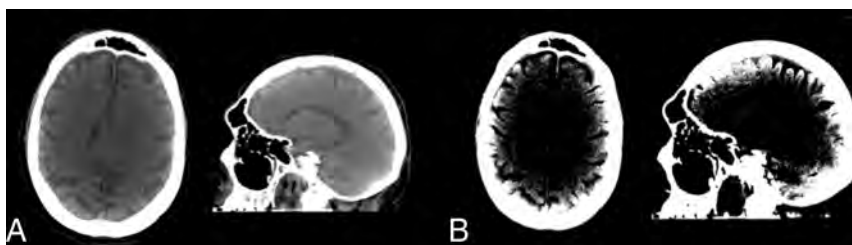


**FIG 5.** Beam-hardening by the skull is seen in routine clinical head CT. These images were acquired on 11/14/2018 from a standard hospital GE Healthcare scanner for acute trauma. For the image pair on the left the default display window settings were used (window width/window length 125/40). For the image pair on the right (same case), the display window settings were window width/window length 17/42. This persistent beam-hardening artifact can impact the interpretation of cortical lesions and is particularly important when performing quantitative, digital analysis.

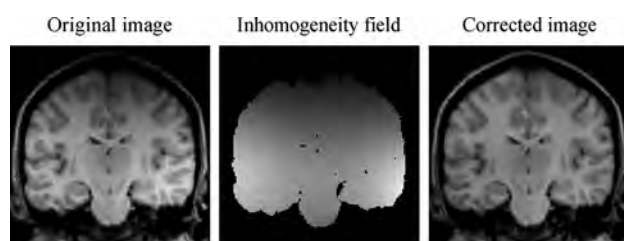


**FIG 6.** Image inhomogeneity seen on routine MR images of the brain, with image intensity inhomogeneity-corrected image on the right. Reproduced with permission from Vovk et al.<sup>44</sup>

segmentation (Fig 6). Postprocessing software has been developed for image intensity inhomogeneity correction of MR images and has been used to facilitate automated segmentation algorithms.<sup>43,44</sup> We found that ictal-interictal continuum algorithms developed for use in MR imaging can identify the global signal inhomogeneity of head CT imaging caused by the beam-hardening of the skull (Fig 7). Examples include the ITK N4BiasFieldCorrection Filter ([https://simpleitk.readthedocs.io/en/master/link\\_N4BiasFieldCorrection\\_docs.html](https://simpleitk.readthedocs.io/en/master/link_N4BiasFieldCorrection_docs.html)), as well as the correction factor that is engineered into the FSL Automated Segmentation Tool (<http://fsl.fmrib.ox.ac.uk/fsl/fslwiki/FAST>), which facilitates CT segmentation in much the same way as it facilitates MR imaging segmentation.<sup>6</sup> Because beam-hardening by the skull is dependent upon the thickness of the skull through which the beam passes, head positioning in the scanner can influence the beam-hardening, and therefore, influence the measured radiodensity. The head position can be “corrected” as a postprocessing step at the console, but the beam-hardening effects will persist in the image. For this reason, the use of a head holder and attention to patient positioning are advised for quantitative CT.

**Machine Calibration.** There is calibration drift within individual scanners, as well as small differences in measured radiodensity between scanners from the same manufacturer running the same protocol, though data trends appear consistent.<sup>25</sup>

Greater differences might be expected from machines from different vendors or using different protocols. Until more rigorous standards are established, statistical methods of normalization may

be necessary for the adaptation of a universal database to a particular setting.

**The Role of Quantitative Assessment in Clinical Medicine.** As with most quantitative diagnostic tools, quantitative CT must be interpreted in a clinical context. There has been considerable investigation into the value of the gray and white attenuation ratio in assessing the degree of hypoxic-ischemic injury in the setting of cardiac arrest.<sup>31,32,45–47</sup> Brain volume, radiodensity, or radio-mass identified as statistically higher or lower than a comparative peer group may have normal findings, or it may raise suspicion for a particular pathology,

or serve to support an existing suspicion of a particular pathology. In cases of known disease, quantitative CT may be used to monitor disease status.

### Future Directions

**Machine Calibration.** American College of Radiology guidelines for the calibration of CT scanners are sufficient for the maintenance of image quality, but may not be optimal for quantitative imaging. At our institution, daily machine calibrations are recorded and note little (typically less than 1 HU) variation; however, calibration is performed in the same way and at the same time every day. Drift of HU values throughout the day or after high usage is not typically evaluated. Calibration values are recorded but not rigorously reset to zero when small drifts are observed. The range of radiodensities of brain tissue is relatively narrow, with the bulk of the brain tissue radiodensities falling between 15 and 40 HU, and small differences in mean radiodensity may represent significant tissue differences, as a 3-HU difference in mean brain tissue radiodensity was found between control subjects and patients with multiple sclerosis. Higher standards for machine calibration would not be difficult to achieve. The measured HU could be zeroed daily, rather than be permitted to drift between accepted values. A water standard could be included with each imaging study, perhaps as part of the imaging apparatus, such that the image intensity could be referenced to an internal zero standard.

**Anatomic Segmentation.** A large body of research in MR imaging has focused on volumetric changes that occur in specific anatomic brain regions.<sup>48–51</sup> The relatively low image contrast of CT has precluded this type of analysis of head CT images. Although it is possible to localize brain regions using MR imaging-based atlas images to mask CT images, further research in this area is needed before reliable regional measures can be derived from head CT images. Although still in its early stages, machine learning may prove useful in this regard.<sup>52</sup> If gray and white matter have discrete radiodensities, the radiodensity of a given lobe or anatomic segment of brain would be expected to largely reflect the percentages of gray and white matter in a particular substructure, though this idea has yet to be verified empirically.



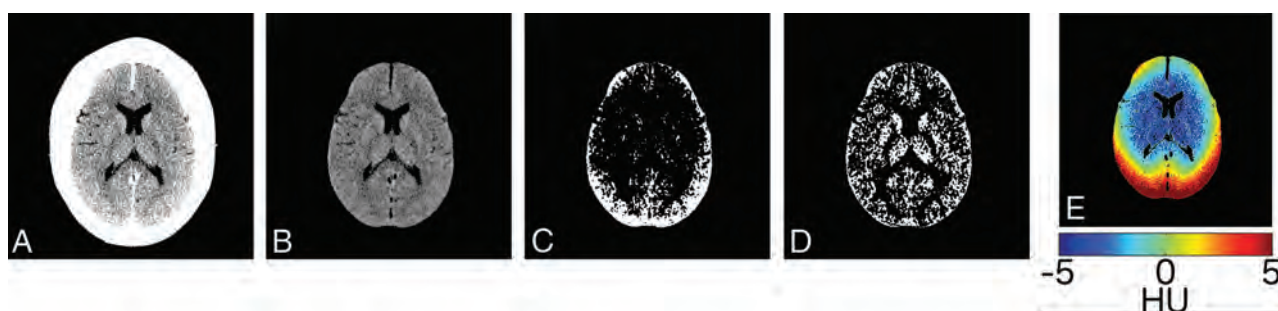


**FIG 7.** FSL “Bias field reduction” corrects for the attenuation and scatter artifacts seen on routine clinical head CT images. Subject with a thick skull and normal head CT (A). Brain-extracted image (B). Segmented GM images with “bias field correction” “turned off” (C), and with bias field “on” at default settings (D). The magnitude of the correction in HU, color-scaled as per the color bar at the bottom (E). Reproduced with permission from Cauley et al.<sup>6</sup>

**Dual Source CT.** As discussed above, the beam-hardening artifact from the skull has long posed a problem for head CT imaging. Beam-hardening by the skull is the result of filtering of lower energies of the x-ray energy spectrum. Dual Source CT (Siemens) has been advocated for metal artifact reduction<sup>53</sup> and dual source virtual monochromatic imaging has the potential to reduce beam-hardening caused by the skull,<sup>54</sup> though this too has yet to be fully investigated. Reduction in beam-hardening could result in more reliable quantitative imaging, with the caveat that changes in image acquisition may confound comparison with previously acquired images using conventional methods. Similarly, standardization of protocols (kilovolt peak and milli-ampere settings, pulse width [milliseconds], helical versus axial imaging) should broaden the application of quantitative imaging.

## CONCLUSIONS

Godfrey Hounsfield noted that the quantitative capability of CT is one of its major advantages over 2D x-ray,<sup>1</sup> yet the quantitative capabilities of clinical head CT remain largely unexplored. Automated methods together with a clinical database and quantile regression techniques could enable quantitative assessment of head CT parameters to augment qualitative image interpretation.

## REFERENCES

- Hounsfield GN. **Computed medical imaging. Nobel lecture, December 8, 1979.** *J Comput Assist Tomogr* 1980;4:665–74 CrossRef Medline
- Hess EH, Shah ND, Stroebe RJ, et al. **Trends in computed tomography utilization rates: a longitudinal practice-based study.** *J Patient Saf* 2014;10:52–58 CrossRef Medline
- The IMV Medical Imaging MasterFile.** IMV. <https://imvinfo.com/>. Accessed May 22, 2021
- Jenkinson M, Beckmann CF, Behrens TE, et al. **FSL.** *Neuroimage* 2012;62:782–90 CrossRef Medline
- Muschelli J, Ullman NL, Mould WA, et al. **Validated automatic brain extraction of head CT images.** *Neuroimage* 2015;114:379–85 CrossRef Medline
- Cauley KA, Och J, Yorks PJ, et al. **Automated segmentation of head computed tomography images using FSL.** *J Comput Assist Tomogr* 2018;42:104–10 CrossRef Medline
- Cauley KA, Hu Y, Fielden SW. **Aging and the brain: a quantitative study of clinical CT images.** *AJNR Am J Neuroradiol* 2020;41:809–14 CrossRef Medline
- Rudick RA, Fisher E, Lee JC, et al. **Use of the brain parenchymal fraction to measure whole brain atrophy in relapsing-remitting MS.** *Neurology* 1999;53:1698–704 CrossRef Medline
- Blatter DD, Bigler ED, Gale SD, et al. **Quantitative volumetric analysis of brain MR: normative database spanning 5 decades of life.** *AJNR Am J Neuroradiol* 1995;16:241–51 Medline
- Condon B, Grant R, Hadley D, et al. **Brain and intracranial cavity volumes: in vivo determination by MRI.** *Acta Neurol Scand* 1988;78:387–93 CrossRef Medline
- Courchesne E, Chisum HJ, Townsend J, et al. **Normal brain development and aging: quantitative analysis at in vivo MR imaging in healthy volunteers.** *Radiology* 2000;216:672–82 CrossRef Medline
- Matsumae M, Kikinis R, Mórocz IA, et al. **Age-related changes in intracranial compartment volumes in normal adults assessed by magnetic resonance imaging.** *J Neurosurg* 1996;84:982–91 CrossRef Medline
- Rajagopalan V, Pioro EP. **Brain parenchymal fraction: a relatively simple MRI measure to clinically distinguish ALS phenotypes.** *Biomed Res Int* 2015;2015:693206 CrossRef Medline
- Fjell AM, McEvoy L, Holland D, et al. **Brain changes in older adults at very low risk for Alzheimer's disease.** *J Neurosci* 2013;33:8237–42 CrossRef Medline
- Bin Zahid A, Mikheev A, Srivatsa N, et al. **Accelerated brain atrophy on serial computed tomography: potential marker of the progression of Alzheimer disease.** *J Comput Assist Tomogr* 2016;40:827–32 CrossRef Medline
- Förstl H, Zerfass R, Geiger-Kabisch C, et al. **Brain atrophy in normal ageing and Alzheimer's disease. Volumetric discrimination and clinical correlations.** *Br J Psychiatry* 1995;167:739–46 CrossRef Medline
- Vågberg M, Granäs G, Svenningsson A. **Brain parenchymal fraction in healthy adults—a systematic review of the literature.** *PLoS One* 2017;12:e0170018 CrossRef Medline
- Cauley KA, Hu Y, Fielden SW. **Pediatric head CT: automated quantitative analysis with quantile regression.** *AJNR Am J Neuroradiol* 2021;42: 382–88 CrossRef Medline
- Haggstrom M. **Hounsfield unit.** [http://radlines.org/Hounsfield\\_unit](http://radlines.org/Hounsfield_unit). Accessed May 22, 2021
- Nguyen HS, Li L, Patel M, et al. **Radiodensity of intraventricular hemorrhage associated with aneurysmal subarachnoid hemorrhage may be a negative predictor of outcome.** *J Neurosurg* 2018;128:1032–36 CrossRef Medline
- Wagner I, Volbers B, Hilz MJ, et al. **Radiopacity of intracerebral hemorrhage correlates with perihemorrhagic edema.** *Eur J Neurol* 2012;19:525–28 CrossRef Medline
- Kim H, Kim GD, Yoon BC, et al. **Quantitative analysis of computed tomography images and early detection of cerebral edema for pediatric traumatic brain injury patients: retrospective study.** *BMC Med* 2014;12:186 CrossRef Medline

23. Cauley KA, Fielden SW. **A radiodensity histogram study of the brain in multiple sclerosis.** *Tomography* 2018;4:194–203 CrossRef Medline
24. Inaba K, Teixeira PG, David JS, et al. **Computed tomographic brain density measurement as a predictor of elevated intracranial pressure in blunt head trauma.** *Am Surg* 2007;73:1023–26 CrossRef Medline
25. Cauley KA, Hu Y, Och J, et al. **Modeling early postnatal brain growth and development with CT: changes in the brain radiodensity histogram from birth to 2 years.** *AJNR Am J Neuroradiol* 2018;39:775–81 CrossRef Medline
26. Scallan RI, Frost C, Jenkins R, et al. **A longitudinal study of brain volume changes in normal aging using serial registered magnetic resonance imaging.** *Arch Neurol* 2003;60:989–94 CrossRef Medline
27. Despotović I, Goossens B, Philips W. **MRI segmentation of the human brain: challenges, methods, and applications.** *Comput Math Methods Med* 2015;2015:450341 CrossRef Medline
28. Kemmling A, Wersching H, Berger K, et al. **Decomposing the Hounsfield unit: probabilistic segmentation of brain tissue in computed tomography.** *Clin Neuroradiol* 2012;22:79–91 CrossRef Medline
29. Furat OW, Neumann M, Petrich M, et al. **Machine learning techniques for the segmentation of tomographic image data of functional materials.** *Front Mater* 2019;6:1–17 CrossRef
30. Eggert LD, Sommer J, Jansen A, et al. **Accuracy and reliability of automated gray matter segmentation pathways on real and simulated structural magnetic resonance images of the human brain.** *PLoS One* 2012;7:e45081 CrossRef Medline
31. Lee BK, Jeung KW, Song KH, et al. **Prognostic values of gray matter to white matter ratios on early brain computed tomography in adult comatose patients after out-of-hospital cardiac arrest of cardiac etiology.** *Resuscitation* 2015;96:46–52 CrossRef Medline
32. Hanning U, Sporns PB, Lebedez P, et al. **Automated assessment of early hypoxic brain edema in non-enhanced CT predicts outcome in patients after cardiac arrest.** *Resuscitation* 2016;104:91–94 CrossRef Medline
33. Berger N, Ampanozi G, Schweitzer W, et al. **Racking the brain: detection of cerebral edema on postmortem computed tomography compared with forensic autopsy.** *Eur J Radiol* 2015;84:643–51 CrossRef Medline
34. Hanzlik E, Gigante J. **Microcephaly.** *Children (Basel)* 2017;4:47 CrossRef Medline
35. Purugganan OH. **Abnormalities in head size.** *Pediatr Rev* 2006;27:473–76 CrossRef Medline
36. Gillebert CR, Humphreys GW, Mantini D. **Automated delineation of stroke lesions using brain CT images.** *Neuroimage Clin* 2014;4:540–48 CrossRef Medline
37. Di Chiro G, Brooks RA, Dubal L, et al. **The apical artifact: elevated attenuation values toward the apex of the skull.** *J Comput Assist Tomogr* 1978;2:65–70 CrossRef Medline
38. Gado M, Phelps M. **The peripheral zone of increase density in cranial computed tomography.** *Radiology* 1975;117:71–74 CrossRef Medline
39. Craddock C, Chen MY, Dixon RL, et al. **The effect of skull volume and density on differentiating gray and white matter on routine computed tomography scans of the head.** *J Comput Assist Tomogr* 2006;30:734–38 CrossRef Medline
40. Barrett JF, Keat N. **Artifacts in CT: recognition and avoidance.** *Radiographics* 2004;24:1679–91 CrossRef Medline
41. Boas EF, D. **CT artifacts: causes and reduction techniques.** *Imaging in Medicine* 2012;4:229–40
42. Cauley KA, Yorks PJ, Flora S, et al. **The effects of the skull on CT imaging of the brain: a skull and brain phantom study.** *BR J Radiol* 2021;94:20200714 CrossRef Medline
43. Hou Z. **A review on MR image intensity inhomogeneity correction.** *Int J Biomed Imaging* 2006;2006:49515 CrossRef Medline
44. Vovk U, Pernus F, Likar B. **A review of methods for correction of intensity inhomogeneity in MRI.** *IEEE Trans Med Imaging* 2007;26:405–21 CrossRef Medline
45. Choi SP, Park HK, Park KN, et al. **The density ratio of grey to white matter on computed tomography as an early predictor of vegetative state or death after cardiac arrest.** *Emerg Med J* 2008;25:666–69 CrossRef Medline
46. Metter RB, Rittenberger JC, Guyette FX, et al. **Association between a quantitative CT scan measure of brain edema and outcome after cardiac arrest.** *Resuscitation* 2011;82:1180–85 CrossRef Medline
47. Torbey MT, Selim M, Knorr J, et al. **Quantitative analysis of the loss of distinction between gray and white matter in comatose patients after cardiac arrest.** *Stroke* 2000;31:2163–67 CrossRef Medline
48. Carne RP, Vogrin S, Litewka L, et al. **Cerebral cortex: an MRI-based study of volume and variance with age and sex.** *J Clin Neurosci* 2006;13:60–72 CrossRef Medline
49. Xu J, Kobayashi S, Yamaguchi S, et al. **Gender effects on age-related changes in brain structure.** *AJNR Am J Neuroradiol* 2000;21:112–18 Medline
50. Bozzali M, Cercignani M, Caltagirone C. **Brain volumetrics to investigate aging and the principal forms of degenerative cognitive decline: a brief review.** *Magn Reson Imaging* 2008;26:1065–70 CrossRef Medline
51. Geuze E, Vermetten E, Bremner JD. **MR-based in vivo hippocampal volumetrics: 2. Findings in neuropsychiatric disorders.** *Mol Psychiatry* 2005;10:160–84 CrossRef Medline
52. Cai JC, Akkus Z, Philbrick KA, et al. **Fully automated segmentation of head CT neuroanatomy using deep learning.** *Radiol: Artificial Intelligence* 2020;2:e190183 CrossRef
53. Pessis E, Campagna R, Sverzut JM, et al. **Virtual monochromatic spectral imaging with fast kilovoltage switching: reduction of metal artifacts at CT.** *Radiographics* 2013;33:573–83 CrossRef Medline
54. Pomerantz SR, Kamalian S, Zhang D, et al. **Virtual monochromatic reconstruction of dual-energy unenhanced head CT at 65–75 keV maximizes image quality compared with conventional polychromatic CT.** *Radiology* 2013;266:318–25 CrossRef Medline

# Hypothalamic Pilomyxoid Astrocytoma in a Child with Lipodystrophy

J.C. Benson, J. Trejo-Lopez, S.E. Bach, J. Schwartz, T.J. Kaufmann, L. Eckel, and J. Guerin

## ABSTRACT

**SUMMARY:** Pilomyxoid astrocytoma is a rare form of pediatric CNS malignancy first classified in 2007 by the World Health Organization. The tumors are similar to pilocytic astrocytomas, sharing both some imaging and histologic traits. However, pilomyxoid astrocytomas portend a more ominous prognosis, with more aggressive local tendencies and a greater proclivity for leptomeningeal spread. Although tissue sampling is ultimately required to differentiate pilocytic astrocytomas and pilomyxoid astrocytomas, some imaging features can be used to suggest a pilomyxoid astrocytoma, including homogeneous enhancement, leptomeningeal seeding, and lack of intratumoral cysts. In this article, a case of a hypothalamic pilomyxoid astrocytoma is described, in which the presenting disorder was profound generalized lipodystrophy. The aforementioned imaging characteristics of pilomyxoid astrocytomas are reviewed, as are the pathologic features of such tumors, including their angiocentric cellular arrangement and myxoid background.

**ABBREVIATION:** PMA = pilomyxoid astrocytoma

The patient was a 2-year-old boy who presented with a history of poor weight gain with loss of adipose tissue despite normal growth in height during the previous 12 months. His symptoms ultimately culminated in hospitalization for failure to thrive. Physical examination revealed a scarcity of subcutaneous fat with relative prominence of his musculature and vasculature (Fig 1). A comprehensive genetic screen for congenital lipodystrophy performed at an outside institution had negative findings. Given the association between CNS tumors and generalized lipodystrophy, the patient's endocrinologist requested a brain MR imaging to assess an intracranial mass.

## Imaging

MR imaging demonstrated a well-circumscribed lobulated mass arising from the hypothalamic/optic chiasmatic region, measuring up to 3.0 cm in maximum diameter. Intralesional signal was uniformly hyperintense on T2-weighted and FLAIR images and was prominently hypointense on T1-weighted images. The mass avidly and uniformly enhanced following contrast administration.

Displacement occurred in adjacent structures: The optic chiasm and pituitary infundibulum were pushed anteriorly, the midbrain was deviated dorsally, and the optic tracts draped around the lateral aspects of the mass. Inferiorly, the mass extended into both the suprasellar and prepontine cisterns (Fig 2), and the lesion extended superiorly into the third ventricle. Remote from the mass were a few smaller enhancing lesions along the surface of the right temporal lobe, medulla, and cerebellum, consistent with leptomeningeal spread. Imaging of the remainder of the neuraxis revealed several additional enhancing foci along the thoracic spinal cord and cauda equina, concerning for additional leptomeningeal tumor dissemination (Fig 3).

The imaging characteristics were thought to be consistent with a hypothalamic glioma, either a pilocytic astrocytoma or a pilomyxoid astrocytoma (PMA). The diffuse leptomeningeal seeding seen along the neuraxis is more common in PMA. Other tumors typically found in this region were less likely. For example, germinomas more frequently demonstrate intratumoral cysts and restricted diffusivity, hypothalamic hamartomas lack enhancement, and neither craniopharyngiomas nor gangliogliomas are expected to have diffuse subarachnoid seeding.

## Subsequent Clinical Course

On the basis of imaging characteristics of a probable low-grade glioma and the expected risk of morbidity associated with surgical biopsy, the decision was made to forgo pathologic sampling in favor of a chemotherapy regimen. The patient was treated with

Received December 30, 2020; accepted after revision February 16, 2021.

From the Departments of Radiology (J.C.B., T.J.K., L.E., J.G.), Laboratory Medicine and Pathology (J.T.-L.), and Pediatric and Adolescent Medicine (J.S.), Mayo Clinic, Rochester, Minnesota; and Department of Laboratory Medicine and Pathology (S.E.B.), OSF Saint Francis Medical Center, Peoria, Illinois.

Please address correspondence to John C. Benson, MD, 723 6th St. SW, Department of Radiology, Mayo Clinic, Rochester, MN 55902; e-mail: [benson.john3@mayo.edu](mailto:benson.john3@mayo.edu) <http://dx.doi.org/10.3174/ajnr.A7136>





**FIG 1.** Photographs of the patient demonstrate clinical sequelae of lipodystrophy, with profound loss of subcutaneous fat. Printed with authorization from the patient's parents.

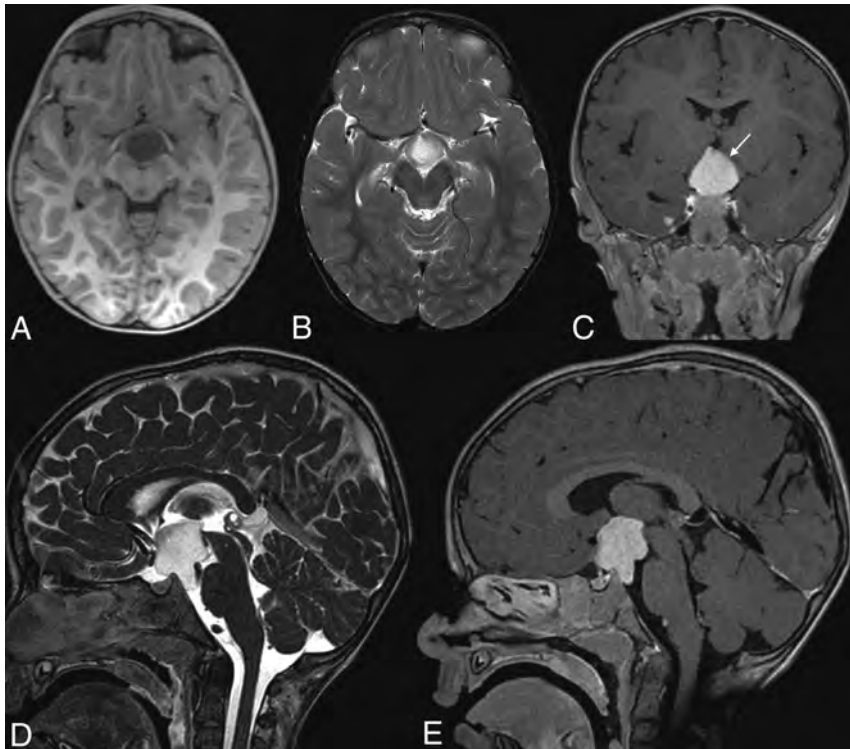


**FIG 2.** Tumor appearance on axial MPRAGE (A) and T2WI (B), coronal postgadolinium T1-weighted Cube (GE Healthcare) (C), and sagittal FIESTA (D) and postgadolinium T1-weighted Cube (E). Images demonstrate an enhancing lobulated mass arising from the hypothalamic/chiasmatic region, with indistinct borders between the tumor and adjacent left hypothalamic parenchyma (arrow).

vincristine and carboplatin, the current standard of care for patients with low-grade gliomas (single lesion or multifocal) that are not amenable to surgical resection.

MR imaging performed approximately 3 months after chemotherapy initiation demonstrated a slight increase in size of the primary hypothalamic tumor, measuring 1.9 cm in the

maximum axial diameter along its superior margin compared with 1.5 cm on the initial examination. Partially related to travel restrictions at the time of the coronavirus disease 2019 pandemic, the patient continued his care at an outside facility with continued consultation from our institution. A radiologist's interpretation of a follow-up MR imaging, performed at the outside hospital, expanded the differential to include craniopharyngioma and metastasis. Because of concerns related to diagnostic uncertainty and apparent lack of response to treatment, a biopsy was performed.

### Pathology

Histologic examination of the tumor revealed a population of overall monomorphous neoplastic cells embedded in a myxoid background and demonstrating prominent angiocentric arrangements (Fig 4). No substantial mitotic activity, necrosis, or microvascular proliferation was identified in the material, histologically supporting a low-grade neoplasm.

Immunohistochemical studies revealed tumor cells diffusely and strongly reactive for glial fibrillary acidic protein, consistent with glioma, as opposed to nonglial processes such as germ cell tumor, lymphoma, and metastatic disease. A neurofilament study revealed, overall, few axons in the tumor background; this finding was compatible with an expansile rather than infiltrative growth pattern, a feature seen in noninfiltrative tumors such as pilocytic astrocytoma, and less consistent with tumors characterized by extensive infiltrative growth such as diffuse astrocytoma and oligodendroglioma. Also inconsistent with these latter entities, neoplastic cells were negative for the *IDH1 R132H* mutation on surrogate immunohistochemistry. By current 2016 World Health Organization criteria, the definitive diagnosis of oligodendroglioma requires the identification of

both an isocitrate dehydrogenase (*IDH*) mutation as well as whole-arm chromosomal codeletion of 1p and 19q.<sup>1</sup> *IDH* mutations also define a category of infiltrating astrocytoma commonly arising in younger adults; such *IDH*-mutant astrocytomas commonly also have mutations of *ATRX* and *p53*, though these mutations are not required for the diagnosis.<sup>2</sup>



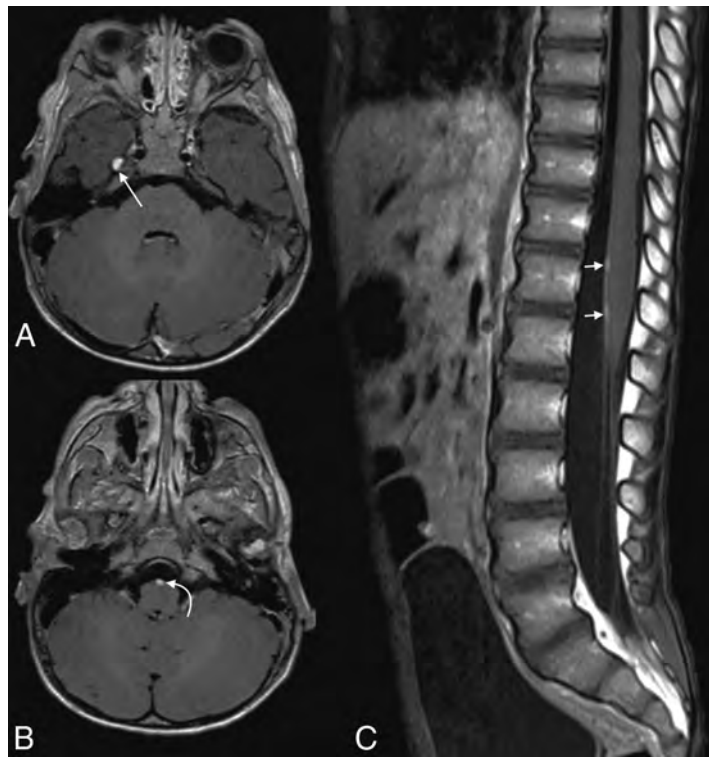


**FIG 3.** Leptomeningeal seeding seen on axial postgadolinium T1 Cube (A and B) and sagittal postgadolinium T1 images of the lower spine (C). Multiple enhancing foci are noted, including along the right temporal lobe (*long straight arrow* in A), ventral medulla (*curved arrow* in B), and ventral conus medullaris (*short straight arrows* in C). There is near-complete absence of subcutaneous fat, compatible with the patient's known lipodystrophy.

While the tumor was negative for the *BRAF* V600E mutation by immunohistochemistry, fluorescence in situ hybridization studies revealed that the tumor had a duplication of *BRAF* (at the 7q34 chromosome locus), an alteration that serves as a surrogate for the detection of *KIAA1549-BRAF* fusion. This latter fusion alteration is a well-described molecular event in pilocytic astrocytoma and its histologic variant, PMA. Pilocytic astrocytoma is classically described as a glioma exhibiting a biphasic histologic pattern, with compact areas of bipolar cells containing Rosenthal fibers and eosinophilic granular bodies alternating with areas of loose-textured background containing multipolar cells and microcysts. PMA is histologically differentiated from classic pilocytic astrocytoma by angiocentric arrangements of bipolar tumor cells, as well as the presence of a markedly myxoid background, a morphologic appearance well-represented by this neoplasm and thus favoring this diagnosis.

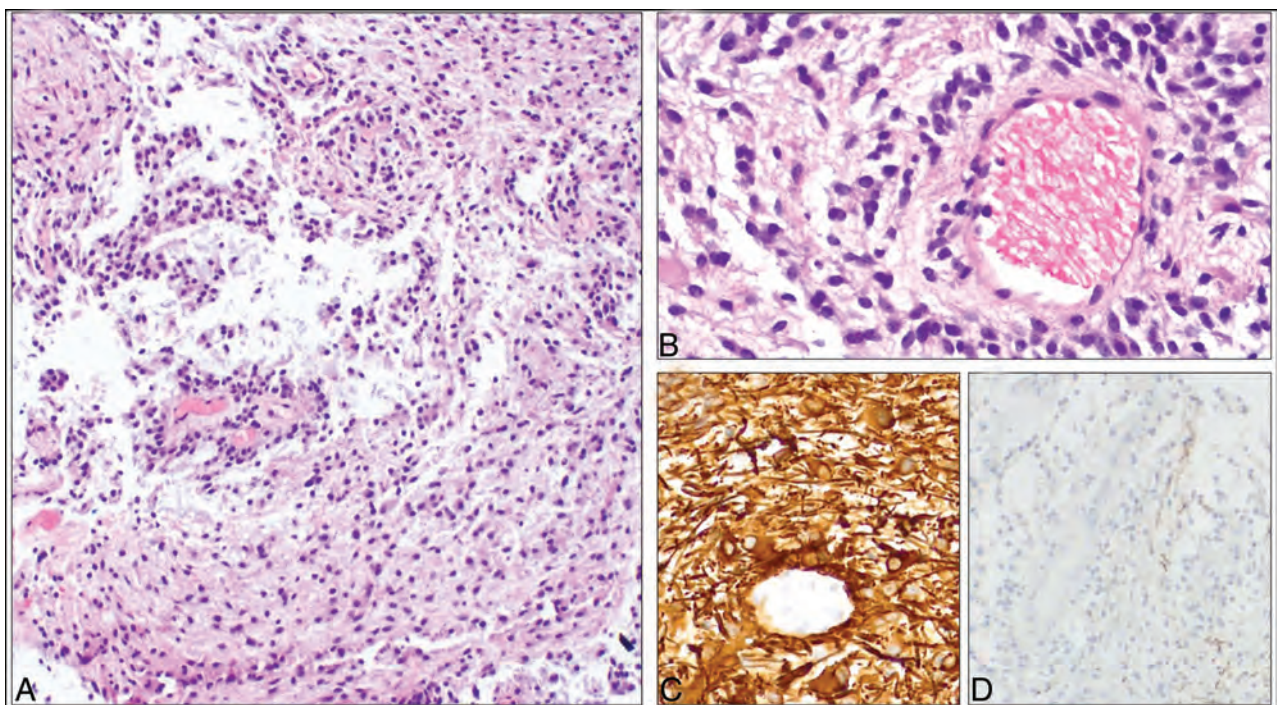


**FIG 4.** Photomicrographs of the tumor reveal a glioma composed of overall monotonous neoplastic cells embedded in a myxoid background (A, H&E,  $\times 100$  magnification) and exhibiting prominent angiocentric arrangements (B, H&E,  $\times 200$  magnification). Neoplastic cells demonstrate immunoreactivity for glial fibrillary acidic protein. C, Glial fibrillary acidic protein immunohistochemistry,  $\times 200$  magnification. Neurofilament reveals, overall, few background axons, compatible with a predominantly expansile growth pattern (D, neurofilament immunohistochemistry,  $\times 100$  magnification).

## DISCUSSION

Pilomyxoid astrocytomas are rare pediatric CNS tumors, accounting for approximately 2% of childhood astrocytomas.<sup>3</sup> First introduced in 1999 and classified by the World Health Organization in 2007, PMAs were originally identified as a variant of pilocytic astrocytomas.<sup>4</sup> The discovery of PMAs partially helped explain what had been a befuddling attribute of pilocytic astrocytomas: Though most exhibited indolent growth and favorable prognoses, a subset of pilocytic astrocytomas demonstrated unexpected aggressiveness. PMAs fit nicely into this diagnostic puzzle, offering an explanation for the observed clinical variability.<sup>5</sup> Patients with PMAs have higher rates of local recurrence and CSF dissemination and shorter progression-free and overall survival than those with pilocytic astrocytomas.<sup>6,7</sup>

Given the variability of its clinical behavior and prognosis, in 2007, the World Health Organization had classified this tumor as a grade II disease. However, in its 2016 classification, they removed the grade assignments to PMAs.<sup>5</sup> PMAs typically occur in younger patients; an average age of onset for PMAs is 18 months, compared with 58 months for pilocytic astrocytomas, leading to early labels of an “infantile” subtype.<sup>4,6</sup> However, cases have been identified across a broad age range, even among adults.<sup>8</sup> Clinical presentations vary and include developmental delay, failure to thrive, vomiting, feeding difficulties, and generalized weakness.<sup>6</sup> In infants, the initial clinical manifestations can be more subtle, such as increased head size or bulging fontanelle from increased intracranial pressure.<sup>5</sup>

On imaging, PMAs have an idiosyncratic proclivity for the hypothalamic/chiasmatic region (60%–75% of cases), though they may occur anywhere along the neuraxis, particularly the cerebral hemispheres.<sup>9,10</sup> The tumors are typically well-circumscribed, predominantly solid tumors, with high homogeneous

intralesional signal on T2-weighted and T2-weighted FLAIR images and iso- to hypointense signal on T1-weighted imaging, reflecting their myxoid matrix (Fig 5).<sup>9</sup> The reported frequency of central necrosis varies; some authors believe it to be rare, while a large review of cases noted necrosis in nearly one-third of tumors.<sup>8,11</sup> Peritumoral edema is infrequently seen.<sup>12</sup> PMAs tend to be devoid of calcifications and do not demonstrate reduced diffusivity, helping distinguish them from craniopharyngiomas and germinomas, respectively.<sup>12</sup> Obstructive hydrocephalus may be present, though usually in a minority of patients.<sup>5</sup>

Prior studies have sought to distinguish between PMAs and pilocytic astrocytomas on the basis of imaging features. In general, PMAs demonstrate more homogeneous enhancement, are more susceptible to intratumoral hemorrhage, and are less prone to intralesional cystic changes (Table).<sup>12,13</sup> PMAs are also more prone to leptomeningeal spreading, occurring in approximately 20% of tumors in 1 study; none of the pilocytic astrocytomas in the same study demonstrated such spread.<sup>6</sup> However, considerable overlap exists between the entities. Even in the hypothalamic/chiasmatic region, most pediatric low-grade tumors are pilocytic astrocytomas.<sup>6</sup> In this area, about 20%–50% of pilocytic astrocytomas are associated with neurofibromatosis type 1.<sup>14,15</sup> Fernandez et al<sup>11</sup> found a higher rate of intratumoral necrosis in PMAs—not surprising, given their relative aggressiveness—though this has not been reported elsewhere. Alkonyi et al<sup>12</sup> found no difference in the size, margins, or intralesional T1 and T2 signal characteristics between PMAs and pilocytic astrocytomas. Ultimately, in its most classic form, a solid hypothalamic mass with leptomeningeal spread in a young pediatric patient, imaging alone might help favor a PMA over a pilocytic astrocytoma. Nevertheless, pathologic analysis is still required to confidently make such a distinction.<sup>16</sup>

The tumor in this case was discovered because of the astute diagnostic capabilities of the patient’s endocrinologist. Although rare, the connection between hypothalamic astrocytomas and lipodystrophy has been long known.<sup>17</sup> In its original description, “diencephalic syndrome” is characterized by emaciation, normal linear growth, locomotor overactivity, and somewhat incongruous pleasantness and euphoria.<sup>18,19</sup> However, many afflicted patients present with isolated lipodystrophy.<sup>20</sup> The mechanism by which hypothalamic astrocytoma results in such a profound loss of subcutaneous fat remains uncertain. Some authors have opined that the pathophysiology may be paraneoplastic, in which either antiadipocyte autoantibodies induce cytotoxicity or hormones/cytokines induce lipolysis. Others have suggested that growth hormone dysregulation and resistance may play a role. Regardless, the symptoms have been described in the setting of both pilocytic (and anaplastic) astrocytomas and PMAs.<sup>21,22</sup> It

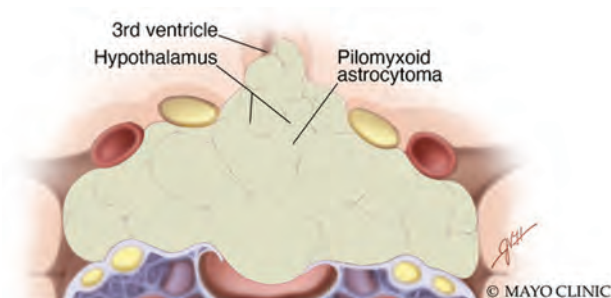


**FIG 5.** Artistic illustration of a PMA extending from the hypothalamus, with involvement of the suprasellar region and adjacent structures. PMAs tend to be solid and are typically devoid of both calcifications and intratumoral cysts. Used with permission of Mayo Foundation for Medical Education and Research. All rights reserved.

### Comparison of typical PMA and pilocytic astrocytoma clinical and imaging features

	PMA	Pilocytic Astrocytoma
Age	Younger (mean age, 1.5 yr)	Older (mean age, 4.8 yr)
Location	Hypothalamic/chiasmatic region	Cerebellum > hypothalamic/chiasmatic region
Enhancement	Homogeneous	Heterogeneous
Intratumoral contents	Most solid, with minimal tumoral cysts	Most have cystic content
Intratumoral hemorrhage	12%–25%	1%–8%
Evidence of leptomeningeal seeding	More frequent (up to 20%)	Exceedingly rare



remains unknown whether certain types of hypothalamic tumor, eg, PMA or pilocytic astrocytoma, are particularly prone to causing sequelae of the diencephalic syndrome.

The patient presented here recently completed his chemotherapy regimen of vincristine and carboplatin and had decreased tumor size on his most recent examination, measuring 1.9 cm in maximum axial diameter compared with 2.2 cm when at its largest size. Serial MRIs will be used to continue to observe the tumor. Currently, his prognosis is considered guarded-but-favorable, particularly given the recent decrease in tumor size. Nevertheless, the patient's body weight continues to be suboptimal. Although his family has reported that he is able to gain some weight during intermittent breaks in chemotherapy, it tends to fall off following re-initiation of treatment, and he continues to exhibit considerable symptoms of lipodystrophy.

### Case Summary

- Generalized lipodystrophy may be caused by a hypothalamic glioma. In its classic form, the clinical presentation includes additional elements of diencephalic syndrome: emaciation, euphoria, and locomotor hyperactivity.
- PMAs typically arise from the hypothalamic/chiasmatic region but may appear anywhere along the neuraxis.
- Pathologic confirmation is required for diagnosis, though radiographically, a PMA may be suggested over pilocytic astrocytoma when a solid composition, homogeneous enhancement, and leptomeningeal seeding are present.
- Histologically, PMA is currently defined by the 2016 World Health Organization as a variant of pilocytic astrocytoma, exhibiting a prominent myxoid background and perivascular arrangement of tumor cells, and demonstrates molecular alterations similar to those of classic pilocytic astrocytoma (including KIAA1549-BRAF fusion).

### REFERENCES

- Louis DN, Perry A, Reifenberger G, et al. **The 2016 World Health Organization Classification of Tumors of the Central Nervous System: a summary.** *Acta Neuropathol* 2016;131:803–20 CrossRef Medline
- Kannan K, Inagaki A, Silber J, et al. **Whole-exome sequencing identifies ATRX mutation as a key molecular determinant in lower-grade glioma.** *Oncotarget* 2012;3:1194–1203 CrossRef Medline
- Stiller CA, Bayne AM, Chakrabarty A, et al. **Incidence of childhood CNS tumours in Britain and variation in rates by definition of malignant behaviour: population-based study.** *BMC Cancer* 2019;19:139 CrossRef Medline
- Tihan T, Fisher PG, Kepner JL, et al. **Pediatric astrocytomas with monomorphous pilomyxoid features and a less favorable outcome.** *J Neuropathol Exp Neurol* 1999;58:1061–68 CrossRef Medline
- Burger PC, Khandji AG, Tihan T, et al. **Pilomyxoid astrocytoma: a review.** *Medscape Gen Med* 2004;6:42. <https://www.ncbi.nlm.nih.gov/pmc/articles/PMC1480592/>. Accessed October 9, 2020
- Komotar RJ, Burger PC, Carson BS, et al. **Pilocytic and pilomyxoid hypothalamic/chiasmatic astrocytomas.** *Neurosurgery* 2004;54:72–80; discussion 79–80 CrossRef Medline
- Lee IH, Kim JH, Suh YL, et al. **Imaging characteristics of pilomyxoid astrocytomas in comparison with pilocytic astrocytomas.** *Eur J Radiol* 2011;79:311–16 CrossRef Medline
- Pruthi SK, Chakraborti S, Naik R, et al. **Pilomyxoid astrocytoma with high proliferation index.** *J Pediatr Neurosci* 2013;8:243–46 CrossRef Medline
- Arslanoglu A, Cirak B, Horska A, et al. **MR imaging characteristics of pilomyxoid astrocytomas.** *AJNR Am J Neuroradiol* 2003;24:1906–08 Medline
- Ho CY, Supakul N, Patel PU, et al. **Differentiation of pilocytic and pilomyxoid astrocytomas using dynamic susceptibility contrast perfusion and diffusion weighted imaging.** *Neuroradiology* 2020;62:81–88 CrossRef Medline
- Fernandez C, Figarella-Branger D, Girard N, et al. **Pilocytic astrocytomas in children: prognostic factors—a retrospective study of 80 cases.** *Neurosurgery* 2003;53:544–553; discussion 554–55 CrossRef Medline
- Alkonyi B, Nowak J, Gnekow AK, et al. **Differential imaging characteristics and dissemination potential of pilomyxoid astrocytomas versus pilocytic astrocytomas.** *Neuroradiology* 2015;57:625–38 CrossRef Medline
- White JB, Piepgras DG, Scheithauer BW, et al. **Rate of spontaneous hemorrhage in histologically proven cases of pilocytic astrocytoma.** *J Neurosurg* 2008;108:223–26 CrossRef Medline
- Poussaint TY. **Magnetic resonance imaging of pediatric brain tumors: state of the art.** *Top Magn Reson Imaging* 2001;12:411–33 CrossRef Medline
- Plaza MJ, Borja MJ, Altman N, et al. **Conventional and advanced MRI features of pediatric intracranial tumors: posterior fossa and suprasellar tumors.** *AJR Am J Roentgenol* 2013;200:1115–24 CrossRef Medline
- Karthigeyan M, Singhal P, Salunke P, et al. **Adult pilomyxoid astrocytoma with hemorrhage in an atypical location.** *Asian J Neurosurg* 2019;14:300–03 CrossRef Medline
- Fleischman A, Brue C, Poussaint TY, et al. **Diencephalic syndrome: a cause of failure to thrive and a model of partial growth hormone resistance.** *Pediatrics* 2005;115:e742–48 CrossRef Medline
- British Paediatric Association. **Proceedings of the twenty-second general meeting of the British Pediatric Association.** *Arch Dis Child* 1951;26:270–25 CrossRef
- Addy DP, Hudson FP. **Diencephalic syndrome of infantile emaciation.** *Arch Dis Child* 1972;47:338–43 CrossRef Medline
- Patni N, Alves C, von Schnurbein J, et al. **A novel syndrome of generalized lipodystrophy associated with pilocytic astrocytoma.** *J Clin Endocrinol Metab* 2015;100:3603–06 CrossRef Medline
- Singh G, Wei XC, Hader W, et al. **Sustained response to weekly vinblastine in 2 children with pilomyxoid astrocytoma associated with diencephalic syndrome.** *J Pediatr Hematol Oncol* 2013;35:e53–56 CrossRef Medline
- Stival A, Lucchesi M, Farina S, et al. **An infant with hyperalertness, hyperkinesis, and failure to thrive: a rare diencephalic syndrome due to hypothalamic anaplastic astrocytoma.** *BMC Cancer* 2015;15:616 CrossRef Medline

# Strength of Association between Infarct Volume and Clinical Outcome Depends on the Magnitude of Infarct Size: Results from the ESCAPE-NA1 Trial

J.M. Ospel, M.D. Hill, B.K. Menon, A. Demchuk, R. McTaggart, R. Nogueira, A. Poppe, D. Haussen, W. Qiu, A. Mayank, M. Almekhlafi, C. Zerna, M. Joshi, M. Jayaraman, D. Roy, J. Rempel, B. Buck, M. Tymianski, and M. Goyal, for the ESCAPE-NA1 investigators



## ABSTRACT

**BACKGROUND AND PURPOSE:** Infarct volume is an important predictor of clinical outcome in acute stroke. We hypothesized that the association of infarct volume and clinical outcome changes with the magnitude of infarct size.

**MATERIALS AND METHODS:** Data were derived from the Safety and Efficacy of Nerinetide in Subjects Undergoing Endovascular Thrombectomy for Stroke (ESCAPE-NA1) trial, in which patients with acute stroke with large-vessel occlusion were randomized to endovascular treatment plus either nerinetide or a placebo. Infarct volume was manually segmented on 24-hour noncontrast CT or DWI. The relationship between infarct volume and good outcome, defined as mRS 0–2 at 90 days, was plotted. Patients were categorized on the basis of visual grouping at the curve shoulders of the infarct volume/outcome plot. The relationship between infarct volume and adjusted probability of good outcome was fitted with linear or polynomial functions as appropriate in each group.

**RESULTS:** We included 1099 individuals in the study. Median infarct volume at 24 hours was 24.9 mL (interquartile range [IQR] = 6.6–92.2 mL). On the basis of the infarct volume/outcome plot, 4 infarct volume groups were defined (IQR = 0–15 mL, 15.1–70 mL, 70.1–200 mL, >200 mL). Proportions of good outcome in the 4 groups were 359/431 (83.3%), 219/337 (65.0%), 71/201 (35.3%), and 16/130 (12.3%), respectively. In small infarcts (IQR = 0–15 mL), no relationship with outcome was appreciated. In patients with intermediate infarct volume (IQR = 15–200 mL), there was progressive importance of volume as an outcome predictor. In infarcts of >200 mL, outcomes were overall poor.

**CONCLUSIONS:** The relationship between infarct volume and clinical outcome varies nonlinearly with the magnitude of infarct size. Infarct volume was linearly associated with decreased chances of achieving good outcome in patients with moderate-to-large infarcts, but not in those with small infarcts. In very large infarcts, a near-deterministic association with poor outcome was seen.

**ABBREVIATION:** IQR = interquartile range

In acute ischemic stroke, the larger the irreversibly damaged area is, the more severe and permanent the clinical deficits will be. Infarct size is predictive of clinical outcome in acute ischemic stroke<sup>1</sup> and has been used as a surrogate outcome in several studies.<sup>2</sup> However, human brain architecture leads to an exquisite structure-function relationship so that even small lesions may

cause specific disability. As a corollary, recent studies have shown that the correlation between infarct volume and clinical outcome is only moderate.<sup>3,4</sup> Anterior choroidal infarcts, for example, are very small but frequently lead to severe disability due to the specific structures damaged.<sup>5</sup> We explored the relationship between infarct volume and outcome, hypothesizing that the association of infarct volume and clinical outcome is nonlinear and varies by the magnitude of infarct size.

Received December 30, 2020; accepted after revision March 17, 2021.

From the Departments of Clinical Neurosciences (J.M.O., M.D.H., B.K.M., A.D., W.Q., A.M., M.A., C.Z., M.G.) and Radiology (M.D.H., B.K.M., A.D., M.A., M. Joshi, M.G.), University of Calgary, Calgary, Alberta, Canada; Department of Radiology (J.M.O.), University Hospital of Basel, Basel, Switzerland; Department of Interventional Radiology (R.M., M. Jayaraman), Warren Alpert Medical School of Brown University, Providence, Rhode Island; Department of Neurology (R.N., D.H.), Emory University School of Medicine, Atlanta, Georgia; Centre Hospitalier de l'Université de Montréal (A.P., D.R.), Montreal, Quebec, Canada; University of Alberta Hospital (J.R., B.B.), Edmonton, Alberta, Canada; and NoNO Inc (M.T.), Toronto, Ontario, Canada.

The ESCAPE-NA1 trial was funded by the Canadian Institutes for Health Research, AB Innovates, and NoNO Inc.

Please address correspondence to Mayank Goyal, MD, PhD, Departments of Clinical Neurosciences and Diagnostic Imaging, University of Calgary, 1079 A, 29th St NW, Calgary, AB, Canada, T2N 2T9; e-mail: mgoyal@ucalgary.ca; @johanna\_ospel; @mayank\_GO

Indicates open access to non-subscribers at www.ajnr.org

Indicates article with online supplemental data.

<http://dx.doi.org/10.3174/ajnr.A7183>



## MATERIALS AND METHODS

### Patient Population

Data are from the Safety and Efficacy of Nerinetide in Subjects Undergoing Endovascular Thrombectomy for Stroke (ESCAPE-NA1) trial, a multicenter randomized, double-blind, placebo-controlled trial that evaluated the efficacy and safety of the neuroprotectant nerinetide<sup>6</sup> in patients with acute ischemic stroke who underwent endovascular treatment. Patients were randomized to a single, 2.6-mg/kg dose of intravenous nerinetide or a placebo. All patients received endovascular treatment and best medical care, including intravenous alteplase if indicated. Noncontrast CT and multiphase CTA<sup>7</sup> at baseline were performed in all patients. Patients were eligible for the trial only if they had a large-vessel occlusion (intracranial internal carotid artery, M1 occlusion or functional M1 occlusion [occlusion of both M2 branches]), moderate or good collaterals (defined as filling of  $\geq 50\%$  of the middle cerebral artery territory), and an ASPECTS of  $\geq 5$ . The remaining inclusion criteria were as follows: 1) 18 years of age or older, 2) baseline NIHSS score  $> 5$ , functional independence before the ischemic stroke (Barthel Index score  $> 90$ ), and 3) time since last known well  $< 12$  hours.

### Image Analysis

All imaging data (baseline noncontrast CT and multiphase CTA, conventional angiography, follow-up noncontrast CT, and DWI) were reviewed in consensus readings by an independent core lab that was blinded to clinical outcomes. Final infarct volumes were measured by summation of the manual planimetric demarcation of the infarct on axial NCCT or diffusion-weighted MR imaging at 24 hours using the open-source software ITK-SNAP (<http://www.itksnap.org>).

### Outcomes of Interest

The primary outcome was good outcome, which was defined as an mRS 0–2 at 90 days. Additional outcomes were mRS 0–1 and mortality at 90 days.

### Statistical Analysis

Because final infarct volume was not normally distributed (Fig 1), the relationship between infarct volume and good outcome was plotted with volume examined as a continuous variable, log-transformed in deciles, quartiles, and tertiles. On the basis of visual inspection, we defined final infarct volume groups at the curve shoulders of the infarct volume/outcome plot. Patient baseline characteristics and clinical outcomes were reported for each of the infarct volume groups. Adjusted probabilities of good outcome were obtained from a generalized linear model using a Poisson distribution with Huber-White robust sandwich variance estimation to allow direct estimation of risk ratios.<sup>8</sup> The model was adjusted for a priori variables, including key treatment and pretreatment variables used in the minimization algorithm (age, sex, baseline NIHSS, ASPECTS, occlusion location, alteplase treatment, nerinetide treatment) as independent variables. We displayed the relationship between adjusted probability of good outcome, derived from the multivariable model, and infarct volume as a panel of plots showing volume as a continuous variable, log-transformed volume, and then by volume groups. The

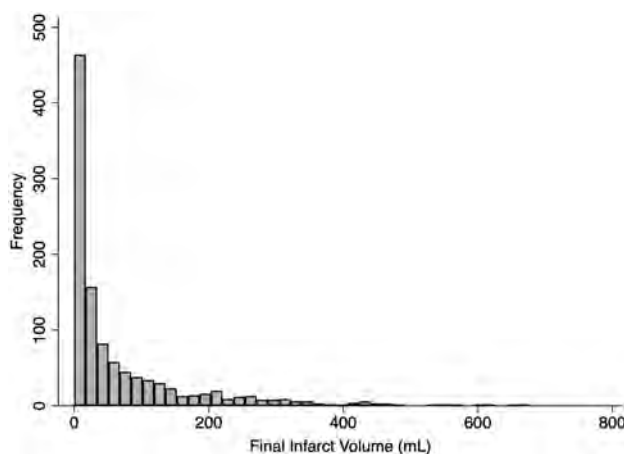


FIG 1. Distribution of infarct volumes in the patient sample.

relationship between final infarct volume by volume group and the adjusted probability of good outcome was then fitted with a linear or polynomial function as appropriate. All statistical tests were 2-sided, and conventional levels of significance ( $\alpha = .05$ ) were used for interpretation. All analysis was performed using STATA 16.1 (StataCorp).

## RESULTS

Infarct volume was available for 1099/1105 patients who were included in the analysis. Infarct volume was measured on CT ( $n = 652$ , 59.3%) and MR imaging ( $n = 447$ , 40.7%). Median infarct volume was 24.9 mL (IQR = 6.6–92.2 mL). Good functional outcome was achieved by 666/1105 (60.3%) at 90 days, while 147/1105 (13.3%) patients died within 90 days. On the basis of visual assessment of the infarct volume/outcome plot (Fig 2A, -B), 4 infarct volume groups were defined (0–15 mL, 15.1–70 mL, 70.1–200 mL,  $> 200$  mL). The Online Supplemental Data show patient baseline characteristics and workflow variables for the 4 groups. As expected, the ASPECTS was lower, and successful recanalization, less common in patients with larger infarcts. Clinical outcomes for the 4 groups are shown in the Table. When the relationship of infarct volume and the adjusted probability of good outcome was modelled in each infarct volume group, it became apparent at low volumes (group 1: IQR = 0–15 mL) that infarct volume had no clear relationship with outcome (Fig 2C). In volume groups 2 and 3 with volumes from 15 to 200 mL, there was progressive importance of volume as a predictor of outcome (Fig 2D, -E). When infarct volume was very large (group 4:  $> 200$  mL), the volume of infarct seemed to be the dominant factor in predicting outcome, and probabilities of achieving good outcome were generally very low (Fig 2F).

## DISCUSSION

The relationship between infarct volume and clinical outcome varies nonlinearly with the magnitude of infarct size. In small infarcts, on average, volume did not predict clinical outcome, while in moderate-to-large infarcts, larger infarct volume was linearly associated with decreased chances of achieving good outcome. When infarcts were very large, there

# Infarct Volume-Outcome Relationship

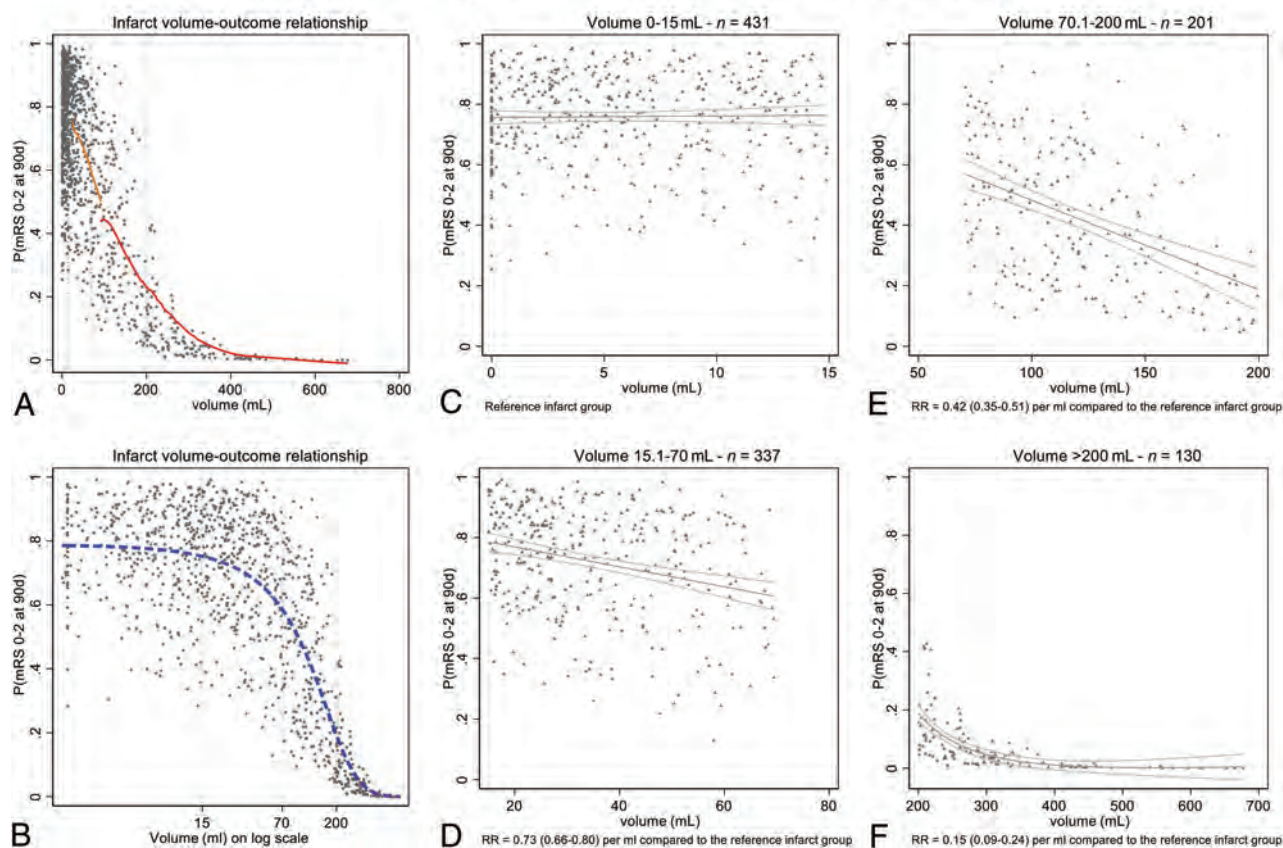


**FIG 2.** Probability of mRS 0–2 at 90 days adjusted for infarct volume and key baseline variables (age, sex, NIHSS, ASPECTS, occlusion location, alteplase treatment, nerinetide treatment). A, *Lines of best fit* for volume groups 3 and 4, modelled within each volume group using a LOWESS function (red line). *Lines of best fit* are not shown for groups 1 and 2 because the volumes are so compressed by the x-axis scale. B, Volumes on a log scale better show the relationship at low infarct volumes (dashed blue line). Dashed vertical gray lines indicate curve shoulders that have been used to define infarct volume groups. C–F, Volume grouping according to visually-defined groupings at the curve shoulders. The graphs illustrate that at low volumes (IQR = 0–15 mL), the infarct volume has no relationship with outcome (C); other factors are deterministic of outcome. In volume groups 2 and 3 with volumes from 15 to 200 mL (D and E), there is progressive importance of volume as a predictor of outcome. At volumes of  $\geq 200$  mL (F), a large infarct volume is the determinant factor in predicting outcomes, which are generally poor. RR indicates risk ratio; 90d, ninety days; P, probability.

## Clinical outcomes in each infarct volume group

Variable	Infarct Volume 0–15 mL (n = 431)	Infarct Volume 15.1–70 mL (n = 337)	Infarct Volume 70.1–200 mL (n = 201)	Infarct Volume >200 mL (n = 130)
Primary outcome mRS 0–2 at 90 days (No.) (%)	359 (83.3)	219 (65.0)	71 (35.3)	16 (12.3)
Additional outcomes mRS 0–1 at 90 days (No.) (%)	269 (62.4)	142 (42.1)	31 (15.4)	5 (3.8)
Mortality at 90 days (No.) (%)	18 (4.2)	26 (7.7)	34 (16.9)	64 (49.2)

was a near-deterministic relationship with poor outcome. This nonlinear relationship and the widely scattered infarct volumes we observed suggest that reliable prediction of clinical outcome based on infarct volume is not feasible for individual patients.

In prior work using mediation analysis, reduction of infarct volume explains only roughly 10% of the treatment benefit of endovascular treatment,<sup>3</sup> possibly because of confounding factors

such as brain eloquence, infarct patterns (eg, white matter sparing infarcts<sup>9</sup>), and selective neuronal loss.<sup>10</sup> This result might be particularly true when infarct volumes are small, in which case the location and eloquence of the affected tissue plays an even more critical role.

The result has relevant clinical and research implications. Infarct volume is often used as an imaging outcome in clinical trials.<sup>2</sup> However, the association with clinical outcome is imperfect

and of limited value for individual outcome prediction.<sup>4</sup> Clinically, small infarct volumes measured at 24 hours poststroke can be considered as directly related to patient selection and treatment success. If a small infarct volume is achieved, then outcome will be determined, not by the infarct, but by complications in the follow-up period, meaning that attention to stroke unit care, stroke work-up, and prevention posttreatment will be deterministic in outcome.<sup>11</sup> Furthermore, involvement of certain anatomic structures and the eloquence of the affected brain parenchyma probably play a role in clinical outcome in patients with small infarcts. Those with very large infarcts have so much injury that postprocedural care, while important for compassionate and palliative goals of care, may simply not be substantially important in predicting good outcome. It will remain important clinically all across the patient spectrum to work quickly and obtain high-quality reperfusion to reduce infarct volumes. When infarcts are already very large (>200 mL) or if ASPECTS is very low (0–2), the prognosis may already be so poor that intervention is likely to be futile.

Use of infarct volume as a surrogate outcome can be refined on the basis of these data. Volume may only be a useful surrogate measure in the middle range of infarcts. Work on lesion-mapping with a goal of understanding structure-function relationships, similarly, may be useful only in smaller infarcts because of the floor effects on outcome associated with large infarcts.

### Strengths and Limitations

The strengths of this study are its large and inclusive randomized patient sample, which resulted in a wide spectrum of infarct volumes, which were manually measured by an independent core lab. The study also has several limitations: Infarct volumetry on non-contrast head CT can be challenging, particularly because follow-up imaging was performed relatively early at 24 hours, a time at which infarcted tissue is often not yet sharply demarcated. Only patients with baseline ASPECTS of  $\geq 5$  were included in the ESCAPE-NA1 trial, and this feature might have limited the number of patients with very large infarcts, obscuring more detailed understanding of the relationship between very large infarcts and outcome. Neither NCCT nor DWI can distinguish between pan-necrosis and incomplete infarction;<sup>12</sup> in other words, we cannot be sure that what we think of as “infarct” on imaging is indeed irreversibly injured tissue. Measurement inaccuracy is relatively higher in smaller infarcts.<sup>13</sup> Last, this study was a post hoc study of a patient sample of the ESCAPE-NA1 rather than a prespecified analysis and, therefore, should be considered purely exploratory. Further prospective studies to confirm our findings are needed.

### CONCLUSIONS

Overall, the relationship between infarct volume and clinical outcome depends nonlinearly on the magnitude of infarct size. Within small and very large infarct groups, outcome does not vary by volume, but there is a linear relationship between larger volume and poorer outcome in moderate-sized infarcts. Our analysis further dissects and quantitates the volume-outcome relationship and provides direction on when infarct volume could be used as a surrogate outcome.

### ACKNOWLEDGMENTS

The authors are most grateful to all enrolling sites.

Disclosures: Michael D. Hill—*RELATED: Grant:* NoNO Inc, Canadian Institutes for Health Research, AB Innovates, *Comments:* grants to the University of Calgary for the ESCAPE-NA1 trial\*; *UNRELATED: Board Membership:* Circle NVI, Canadian Neuroscience Federation, Canadian Stroke Consortium; *Consultancy:* Boehringer Ingelheim; *Grants/Grants Pending:* Alberta Innovates, Canadian Institutes for Health Research, National Institute of Neurological Disorders and Stroke, Stryker, Medtronic, Biogen, *Comments:* grants to the University of Calgary\*; *Patents (Planned, Pending or Issued):* US Patent office No. 62/086,077; *Stock/Stock Options:* Circle CVI, PureWeb Inc. Bijoy K. Menon—*UNRELATED: Board Membership:* Circle NVI; *Patents (Planned, Pending or Issued):* Systems of Triage in Acute Stroke; *Stock/Stock Options:* shares in Circle NVI. Andrew Demchuk—*RELATED: Grant:* Canadian Institutes of Health Research, *Comments:* The ESCAPE-NA1 was funded and supported by a grant from the Canadian Institutes for Health Research\*; *Consulting Fee or Honorarium:* Medtronic, *Comments:* I have received honoraria for consulting to Medtronic; *UNRELATED: Employment:* University of Calgary; *Patents (Planned, Pending or Issued):* Circle NVI; *Stock/Stock Options:* Circle NVI. Raul Nogueira—*OTHER RELATIONSHIPS:* consulting fees for advisory roles with Anaconda, Biogen, Cerenovus, Genentech, Imperative Care, Medtronic, phenox, Prolong Pharmaceuticals, and Stryker Neurovascular and stock options for advisory roles with Astrocyte, Brainomix, Cerebrotech, Ceretrieve, Corindus Vascular Robotics, Vesalio, Viz.ai, and Perfuse. Alexandre Poppe—*UNRELATED: Grants/Grants Pending:* CaSTOR networking grant, Stryker. Diogo Haussen—*UNRELATED: Consultancy:* Stryker, Vesalio, Cerenovus; *Stock/Stock Options:* Viz.ai. Manish Joshi—*UNRELATED: Employment:* University of Calgary, Canada. Mahesh Jayaraman—*UNRELATED: Payment for Lectures Including Service on Speakers Bureaus:* Medtronic, *Comments:* payment for lecture at International Stroke Conference 2018. Mayank Goyal—*RELATED: Grant:* NoNO Inc, *Comments:* unrestricted research grant to University of Calgary for the ESCAPE-NA1 trial\*; *UNRELATED: Consultancy:* Stryker, Medtronic, MicroVenture, Mentice, Michael Tymianski—*UNRELATED: Employment:* NoNO Inc, *Comments:* Sponsor of ESCAPE-NA1; *Stock/Stock Options:* I own NoNO Inc stock; *OTHER RELATIONSHIPS:* I am CEO of NoNO Inc, the sponsor of the ESCAPE-NA1 trial. \*Money paid to the institution.

### REFERENCES

1. Al-Ajlan FS, Goyal M, Demchuk AM, et al. for the ESCAPE Trial Investigators. **Intra-arterial therapy and post-treatment infarct volumes: insights from the ESCAPE randomized controlled trial.** *Stroke* 2016;47:777–81 CrossRef Medline
2. Zaidi SF, Aghaebrahim A, Urra X, et al. **Final infarct volume is a stronger predictor of outcome than recanalization in patients with proximal middle cerebral artery occlusion treated with endovascular therapy.** *Stroke* 2012;43:3238–44 CrossRef Medline
3. Boers AM, Jansen IG, Brown S, et al. **Mediation of the relationship between endovascular therapy and functional outcome by follow-up infarct volume in patients with acute ischemic stroke.** *JAMA Neurol* 2019;76:194–202 CrossRef Medline
4. Boers AM, Jansen IG, Beenen LF, et al. **Association of follow-up infarct volume with functional outcome in acute ischemic stroke: a pooled analysis of seven randomized trials.** *J Neurointerv Surg* 2018;10:1137–42 CrossRef Medline
5. Hupperts RM, Lodder J, Heuts-van Raak EP, et al. **Infarcts in the anterior choroidal artery territory: anatomical distribution, clinical syndromes, presumed pathogenesis and early outcome.** *Brain* 1994;117:825–34 CrossRef Medline
6. Aarts M, Liu Y, Liu L, et al. **Treatment of ischemic brain damage by perturbing NMDA receptor-PSD-95 protein interactions.** *Science* 2002;298:846–50 CrossRef Medline
7. Menon BK, d'Este CD, Qazi EM, et al. **Multiphase CT angiography: a new tool for the imaging triage of patients with acute ischemic stroke.** *Radiology* 2015;275:510–20 CrossRef Medline
8. Ospel JM, Singh N, Almekhlafi MA, et al. **Early recanalization with alteplase in stroke because of large-vessel occlusion in the ESCAPE trial.** *Stroke* 2021;52:304–07 CrossRef Medline



9. Kleine JF, Kaesmacher M, Wiestler B, et al. **Tissue-selective salvage of the white matter by successful endovascular stroke therapy.** *Stroke* 2017;48:2776–83 CrossRef Medline
10. Baron JC, Yamauchi H, Fujioka M, et al. **Selective neuronal loss in ischemic stroke and cerebrovascular disease.** *J Cereb Blood Flow Metab* 2014;34:2–18 CrossRef Medline
11. Ganesh A, Menon BK, Assis ZA, et al. **Discrepancy between post-treatment infarct volume and 90-day outcome in the ESCAPE randomized controlled trial.** *Int J Stroke* 2020 June 9 [Epub ahead of print] CrossRef Medline
12. Garcia JH, Lassen NA, Weiller C, et al. **Ischemic stroke and incomplete infarction.** *Stroke* 1996;27:761–65 CrossRef Medline
13. Ospel JJ, Schulze-Zaachau V, Kozerke S, et al. **Spatial resolution and the magnitude of infarct volume measurement error in DWI in acute ischemic stroke.** *AJNR Am J Neuroradiol* 2020;41:792–97 CrossRef Medline

# Hypoperfusion Intensity Ratio Correlates with CTA Collateral Status in Large-Vessel Occlusion Acute Ischemic Stroke

 D. Lyndon,  M. van den Broek,  B. Niu,  S. Yip,  A. Rohr, and  F. Settecase



## ABSTRACT

**BACKGROUND AND PURPOSE:** Collateral blood supply is a key determinant of outcome in large-vessel occlusion acute ischemic stroke. Single- and multiphase CTA collateral scoring systems have been described but are subjective and require training. We aimed to test whether the CTP-derived hypoperfusion intensity ratio is associated with CTA collateral status and whether a threshold hypoperfusion intensity ratio exists that predicts poor CTA collaterals.

**MATERIALS AND METHODS:** Imaging and clinical data of consecutive patients with large-vessel occlusion acute ischemic stroke were retrospectively reviewed. Single-phase CTA and multiphase CTA scoring were performed by 2 blinded neuroradiologists using the Tan, Maas, and Calgary/Menon methods. CTP was processed using RAPid processing of Perfusion and Diffusion software (RAPID). Hypoperfusion intensity ratio = ratio of brain volume with time-to-maximum >10 seconds over time-to-maximum >6-second volume. Correlation between the hypoperfusion intensity ratio and CTA collateral scores was calculated using the Pearson correlation. The optimal threshold of the hypoperfusion intensity ratio for predicting poor collaterals was determined using receiver operating characteristic curve analysis.

**RESULTS:** Fifty-two patients with large-vessel occlusion acute ischemic stroke were included. Multiphase CTA collateral scoring showed better interrater agreement ( $\kappa = 0.813$ ) than single-phase CTA (Tan,  $\kappa = 0.587$ ; Maas,  $\kappa = 0.273$ ). The hypoperfusion intensity ratio correlated with CTA collateral scores (multiphase CTA:  $r = -0.55$ ; 95% CI,  $-0.67$  to  $-0.40$ ;  $P \leq .001$ ). The optimal threshold for predicting poor multiphase CTA collateral status was a hypoperfusion intensity ratio of  $>0.45$  (sensitivity = 78%; specificity = 76%; area under the curve = 0.86). Patients with high hypoperfusion intensity ratio/poor collateral status had lower ASPECTS/larger infarcts, higher NIHSS scores, and larger hypoperfused volumes.

**CONCLUSIONS:** The hypoperfusion intensity ratio is associated with CTA collateral status in patients with large-vessel occlusion acute ischemic stroke. The hypoperfusion intensity ratio is an automated and quantitative alternative to CTA collateral scoring methods for both clinical and future stroke trial settings.

**ABBREVIATIONS:** AIS = acute ischemic stroke; DCA = diagnostic cerebral angiography; EVT = endovascular thrombectomy; HIR = hypoperfusion intensity ratio; IQR = interquartile range; LVO = large-vessel occlusion; mCTA = multiphase CTA; rCBF = relative cerebral blood flow; ROC = receiver operating characteristic; sCTA = single-phase CTA; Tmax = time-to-maximum

Endovascular thrombectomy (EVT) is the standard of care for eligible patients with large-vessel occlusion (LVO) acute ischemic stroke (AIS) up to 24 hours from symptom onset.<sup>1-4</sup> During LVO AIS, brain tissue in the territory of an acute LVO progresses with time through varying states of ischemia (penumbra) to infarction if untreated, with retrograde leptomeningeal collateral flow supplying the ischemic brain tissue


(penumbra) beyond the LVO. The quality of collateral blood supply to the affected hemisphere in LVO AIS is a significant predictor of infarct size and growth, patient functional outcome,<sup>5,6</sup> and the rate of hemorrhagic transformation.<sup>7-9</sup> As a result, collateral status may impact eligibility for EVT as well as appropriateness for patient transfer to an EVT-capable hospital.<sup>10,11</sup>

Received September 24, 2020; accepted after revision February 19, 2021.

From the Neuroradiology Division (D.L., M.v.d.B., A.R., F.S.), Vancouver General Hospital, Vancouver, British Columbia, Canada; Departments of Radiology (D.L., M.v.d.B., A.R., F.S.) and Neurology (S.Y.), University of British Columbia, Vancouver, British Columbia, Canada; and Vancouver Imaging Inc (B.N.), Vancouver, British Columbia, Canada.

Preliminary findings previously presented at: Annual Meeting of the American Society of Neuroradiology, May 30 to June 4, 2020; Virtual.

Please address correspondence to Fabio Settecase, MD, MSc, FRCPC, Vancouver General Hospital, 899 West 12th Ave, G861, Vancouver, BC V5Z 1M9, Canada; e-mail: fabio.settecase@vch.ca

 Indicates article with online supplemental data.  
<http://dx.doi.org/10.3174/ajnr.A7181>

Currently, imaging triage of collateral status is most commonly performed using CTA, and several CTA scoring systems have been devised. The Tan and Maas scoring systems were designed to evaluate collaterals on single-phase CTA (sCTA).<sup>12-14</sup> Multiphase CTA (mCTA), which includes additional late arterial and late venous phase CTAs, is the most widely studied and validated.<sup>15</sup> The Calgary/Menon mCTA scoring system takes into account delayed filling of the MCA territory, which may be seen only in the late arterial or late venous phases. A limitation of these visual scoring systems, however, is their reliance on qualitative assessment, resulting in the need for additional training, susceptibility to reader bias, and interrater variability.<sup>16</sup>

CTP is a widely used neuroimaging technique in the work-up of LVO AIS. Maps derived from CTP can be used to estimate the size of established infarct core relative to the volume of hypoperfused brain at risk of infarction (commonly referred to as penumbra).<sup>17,18</sup> Measuring infarct core volume and penumbra from sCTA or mCTA techniques is limited by temporal resolution. CTP acquisitions track the contrast density–bolus time curve for 45–60 seconds versus only 1–3 acquisition time points of sCTA or mCTA.

The time for brain tissue to progress from ischemic penumbra to irreversibly infarcted core varies. Collateral status is the main determinant of how quickly the penumbral tissue will progress to irreversible infarct core. This progression can happen within an hour in some patients and in others it can take >24 hours because collateral status varies from patient to patient, as well as with changes in cerebral perfusion pressure during work-up, transfer, and treatment (eg, induction/intubation) of the patient. Obtaining a quantitative measure of collateral status from the CTP acquisition may obviate the need to measure it from a CTA (single-phase or multiphase) and help prognosticate the rate of progression of the penumbral volume to irreversible infarction.

The hypoperfusion intensity ratio (HIR), defined as the ratio of the volume of tissue with a time-to-maximum (Tmax) of >10 seconds divided by the volume of tissue with a Tmax of >6 seconds,<sup>19</sup> can be quantitatively derived from CT perfusion datasets. The HIR is a potential objective measure of collateral status<sup>19</sup> and may be a surrogate for CTA scoring methods. This has been supported in post hoc analyses of small subcohorts of large randomized controlled trials primarily aimed at assessment of the effectiveness of EVT.<sup>20,21</sup> Recently, for M1 segment MCA occlusions, the HIR was found to correlate well with collateral scoring using the criterion standard diagnostic cerebral angiography (DCA) scoring (American Society of Interventional and Therapeutic Neuroradiology/Society of Interventional Radiology method) at the time of EVT.<sup>22,23</sup>

The purpose of this study was to assess whether the HIR correlates with sCTA and mCTA collateral status in patients presenting acutely with anterior circulation LVO AIS. We also aimed to determine whether a threshold HIR exists to indicate good-versus-poor mCTA collateral status.

## MATERIALS AND METHODS

The study protocol was approved by the University of British Columbia institutional review board. Informed consent was

waived due to the observational and retrospective analysis of anonymized data, acquired prospectively as part of routine clinical care at our institution.

### Patient Population

We retrospectively identified patients presenting to our comprehensive stroke center between March and September 2019 with anterior circulation LVO AIS. Most patients presenting to our institution with suspected LVO AIS during this time period were imaged with NCCT of the head, mCTA, and CTP acquired before consideration for EVT. Inclusion criteria for patients in this study were the following: 1) NCCT, mCTA, and CTP, and 2) presenting with an acute neurologic deficit due to anterior circulation LVO (ICA terminus and M1 segment MCA). We excluded patients with LVO in other locations. Isolated occlusions of the distal MCA segments (M2 and M3) also have a less clear effect on collateral blood supply, given that part of the MCA territory remains perfused via anterograde flow from other MCA branches rather than via anterior cerebral artery–MCA or posterior cerebral artery–MCA retrograde collaterals. Isolated occlusions of the anterior cerebral artery or posterior circulation were not included because they may also differ physiologically and most data regarding CTA collateral scoring methods pertain to MCA and ICA terminus occlusions.<sup>12</sup> Additional exclusion criteria were the following: 1) poor image quality due to patient motion, significant foreign body artifacts, or inadequate acquisition; 2) pre-existing flow-limiting arterial stenosis or occlusion in the head or neck; and 3) patients in whom CT perfusion analysis failed (Fig 1).

Clinical and technical data were collected from the patient's medical records and a prospectively maintained institutional stroke data base, including age, sex, the presence of stroke risk factors, the interval between symptom onset and neuroimaging, the initial NIHSS score, and the use of intravenous tPA (alteplase).

### Imaging Protocol and Imaging Reconstruction

Images were acquired using a standardized institutional acute stroke protocol (Online Supplemental Data) on 1 of 3 CT scanners at our institution: a 192-section multidetector dual-source scanner (Somatom Force; Siemens) and 1 of two 128-section multidetector dual-source scanners (Definition Flash; Siemens).

Single-phase and multiphase CTAs were reconstructed at the CT acquisition workstation running Somatom Somari 7 (Siemens). Time-density curves for the input artery and output vein were automatically obtained from the contralateral ICA and superior sagittal sinus, respectively; then perfusion maps were automatically derived using automated RAPID processing of Perfusion and Diffusion software (RAPID; ISchemaView). Infarct core volume was defined as the volume of tissue with a cerebral blood flow of <30% relative to the unaffected hemisphere on CTP (relative CBF [rCBF] <30%). Hypoperfusion volumes were quantitatively measured by the perfusion delay on the Tmax maps. HIR was defined as the ratio of the Tmax >10-second lesion volume divided by the Tmax >6-second lesion volume.<sup>20</sup> Mismatch volume (reflecting the hypoperfused penumbra around the infarct core) was defined as the Tmax >6-second



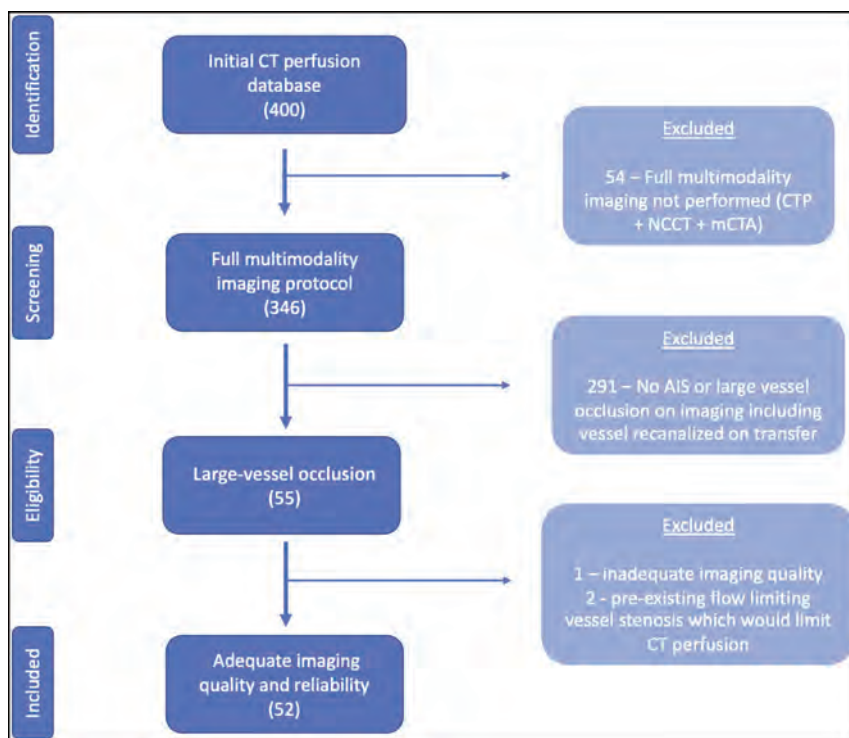


**FIG 1.** Flow chart of patient selection.

volume minus the rCBF <30% volume. No manual correction of processed CTP images was performed.

### Imaging Analysis

CTA collateral scoring was performed by 2 fellowship-trained diagnostic neuroradiologists, each with 5 years of experience, both blinded to clinical information and CTP output (including the HIR). Previously validated scoring systems were used, designed to assess collateral status on sCTA (Tan et al,<sup>13</sup> and Maas et al<sup>14</sup>), and mCTA (Calgary/Menon scoring system),<sup>15</sup> respectively. Correlation with DCA collateral status was not performed because DCA collateral scoring methods are limited to M1 occlusions, and not all patients were taken to angiography and thrombectomy. For sCTA collateral scoring methods, the initial (early arterial) phase of mCTA was used.

The Tan scoring system is a 4-point scale for sCTA: grade 0, zero collateral filling in the affected territory; grade I, filling in the affected territory, <50% of the contralateral side; grade II, filling >50% but <100% than in contralateral territory; grade III, filling equal to the contralateral territory. The Maas scoring system is a 5-point scale for sCTA: grade I, zero filling in the affected territory; grade II, filling less in the affected territory than in the contralateral territory; grade III, filling equal to the contralateral territory; grade IV, filling greater than in the contralateral territory; and grade V, exuberant filling in the affected territory. The Calgary/Menon scoring system is a 6-point scale for mCTA: grade 0, zero filling in any phase in the affected territory; grade I, just a few vessels visible in any phase; grade II, delay of 2 phases and decreased prominence or number of vessels, or delay of 1 phase and some ischemic areas with no vessels; grade III, delay of

2 phases but the same prominence or number of vessels, or delay of 1 phase with the prominence or number of vessels significantly decreased; grade IV, delay of 1 phase but prominence and extent are the same; and grade V, no delay and normal or increased number or prominence of vessels.

### Statistical Analysis

Nominal variables were summarized using frequency descriptive analysis and then compared using the Fisher exact test. Continuous variables were assessed for normality using histogram analysis and then summarized using mean (SD), median, and interquartile range (IQR) as appropriate and then tested using the Mann-Whitney *U* test. The sCTA and mCTA scores calculated by each of the 2 raters were tested for interrater reliability using square-weighted  $\kappa$  analysis (Cohen  $\kappa$ ).<sup>24</sup> Patients were then dichotomized into 2 subgroups on the basis of collateral score of good and poor collaterals as follows: Tan sCTA score, 2–3 = good, 0–1 = poor;<sup>13</sup> Maas sCTA score, 3–5 = good, 1–2 = poor;<sup>14</sup> Calgary/Menon mCTA score, 4–5 = good, 0–3 = poor.<sup>25</sup> Univariate analysis was performed to compare initial stroke severity assessed by the NIHSS score, core infarct volume, Tmax volumes, mismatch volume, and perfusion mismatch ratio between good and poor mCTA collateral groups using the Mann-Whitney *U* test. The correlations between the HIR and the CTA collateral scores were calculated using the Pearson correlation. Receiver operating characteristic (ROC) curve analysis was performed to assess the diagnostic performance of the HIR in predicting poor mCTA collateral status (scores of 0–3). The Youden index was used to determine the optimal threshold HIR from the ROC curve for predicting poor mCTA collateral status. The corresponding specificity and sensitivity of the optimal HIR thresholds for poor-versus-good CTA collateral status were also calculated. Similarly, ROC curve analyses determining of the optimal HIR thresholds for predicting poor-versus-good Tan sCTA collateral status (scores of 0–1) and poor Maas sCTA collateral status (scores of 1–2), and specificity and sensitivity of the optimal HIR thresholds were also performed.

Statistical analysis was performed using the R statistical and computing software (<http://www.r-project.org/>) and SPSS Statistics, Version 24 (IBM). Statistical tests were considered significant at a *P* value < .05.

## RESULTS

### Patient Population

Between March and September 2019, four hundred patients were assessed with multimodality neuroimaging for suspected AIS, including mCTA and CTP at our center. A total of 52 patients were included in this study (Fig 1). There were no significant

differences in the age, sex, or vascular risk factors between the groups with good and poor mCTA collaterals (Table 1).

There was no significant difference in the location (ICA versus M1) of the LVO between groups with good and poor collateral status ( $P = .97$ ) and no difference in the laterality of the LVO between groups ( $P = .26$ ). The median NIHSS at presentation was lower in those with good collateral scores (15; IQR = 8–19) versus poor scores (19; IQR = 14–21;  $P = .05$ ). The median ASPECTS was 7 (IQR = 5–8) for all patients, with a higher baseline ASPECTS seen in patients with good collaterals on mCTA ( $P = .003$ ).

The median time between symptom onset and CT/CTA/CTP was significantly longer in the group with good mCTA collaterals

(median, 374 minutes; IQR = 191–598 minutes) versus poor collaterals (median, 116 minutes; IQR = 67–285 minutes). The time from last known well to administration of IV tPA was not significantly different between groups.

### Image Analysis

Interrater agreement was excellent when using the Calgary/Menon mCTA scoring method ( $\kappa = 0.813$ ), moderate using the Tan sCTA scoring method ( $\kappa = 0.587$ ), and fair using the Maas sCTA scoring method ( $\kappa = 0.273$ ).<sup>24</sup>

**Calgary/Menon mCTA Scores.** The HIR was significantly greater in those with poor-versus-good mCTA collateral scores (HIR = 0.60; IQR = 0.40–0.70 versus 0.30; IQR = 0.10–0.45;  $P \leq .001$ ) (Table 2). The HIR showed a strong correlation with Calgary/Menon mCTA scores (Pearson correlation coefficient =  $-0.55$ ; 95% CI,  $-0.67$  to  $-0.40$ ;  $P \leq .001$ ). ROC curve analysis showed a significant association between poor collaterals and the HIR ( $P \leq .001$ ) with an area under the curve of 0.86. The optimal HIR threshold for prediction of poor-versus-good mCTA collateral status (scores of 0–3) was 0.45 (specificity = 76%, sensitivity = 78%) (Fig 2).

**Tan sCTA Scores.** HIR ratios were significantly greater in those with poor-versus-good Tan sCTA collateral scores (HIR = 0.60; IQR = 0.50–0.80 versus 0.30; IQR = 0.15–0.50;  $P < .001$ ) (Online Supplemental Data). The HIR showed a strong correlation with Tan sCTA scores (Pearson correlation coefficient =  $-0.54$ ; 95% CI,  $-0.67$  to  $-0.39$ ;  $P < .001$ ). ROC curve analysis showed a significant association between poor collaterals and HIR ( $P < .001$ ), with an area under the curve of 0.87. The optimal HIR threshold for prediction of good-versus-poor collateral status was 0.55 (specificity = 89%, sensitivity = 67%).

**Maas sCTA Scores.** HIR ratios were significantly greater in those with poor-versus-good Maas sCTA collateral scores (HIR = 0.50; IQR = 0.4–0.6 versus 0.20; IQR = 0.05–0.40);

**Table 1: Baseline characteristics for all patients according to Calgary/Menon mCTA collateral scale**

Characteristics	All	Poor Collaterals (mCTA Scores 0–3)	Good Collaterals (mCTA Scores 4–5)	P Value
No. of patients	<i>n</i> = 52 (100%)	<i>n</i> = 18 (35%)	<i>n</i> = 34 (65%)	
Age (median) (IQR) (yr)	72 (59–79)	74 (65–79)	71 (58–80)	.77
Female	22 (42%)	5 (28%)	17 (50%)	.15
Medical history				
Dyslipidemia	22 (42%)	9 (50%)	13 (38%)	.56
Hypertension	29 (56%)	12 (67%)	17 (50%)	.38
Atrial fibrillation	17 (33%)	7 (39%)	10 (29%)	.54
Diabetes	9 (17%)	5 (27%)	4 (12%)	.25
Smoking history				
Yes	14 (27%)	4 (22%)	10 (29%)	1.00
No	38 (73%)	14 (78%)	24 (71%)	1.00
Stroke presentation				
Initial NIHSS (median) (IQR)	17 (9–21)	19 (14–21)	15 (8–19)	.05 <sup>a</sup>
ASPECTS (median) (IQR)	7 (5–8)	5 (3–7)	7 (6–9)	.003 <sup>a</sup>
IV tPA given	21 (40%)	7 (39%)	14 (41%)	1.00
Left-sided occlusion	23 (44%)	10 (56%)	13 (38%)	.26
Right-sided occlusion	29 (56%)	8 (44%)	21 (62%)	.26
Clot location				
ICA terminus	18 (35%)	7 (39%)	11 (32%)	.97
M1	34 (65%)	11 (61%)	23 (68%)	.97
Time metrics (median) (IQR) (min)				
Symptom onset to imaging	273 (120–445)	116 (67–285)	374 (191–598)	<.0001 <sup>a</sup>
Symptom onset to tPA	155 (108–285)	111.0 (93–237)	212.0 (116–375)	.20

<sup>a</sup> Statistically significant,  $P \leq .05$ .

**Table 2: HIR, rCBF <30%, and Tmax volumes depending on collateral score using the Calgary/Menon method**

Characteristics	All	Calgary/Menon mCTA Score		P Value
		Poor Collaterals (Scores 0–3)	Good Collaterals (Scores 4–5)	
No. of patients	<i>n</i> = 52 (100%)	<i>n</i> = 18 (34.6%)	<i>n</i> = 34 (65.4%)	
Perfusion characteristics				
Volume of rCBF < 30% (median) (IQR) (mL)	15.60 (5.6–37)	60 (14.0–92.0)	11 (0.0–22.0)	<.001 <sup>a</sup>
Volume of Tmax > 6 seconds (median) (IQR) (mL)	131.00 (83.3–192)	195 (135.0–256.0)	105 (74.5–151.0)	<.001 <sup>a</sup>
Volume of Tmax > 10 seconds (median) (IQR) (mL)	58.0 (19.3–110.3)	108 (66.0–151.0)	26 (11.0–71.5)	<.001 <sup>a</sup>
Mismatch volume (median) (IQR) (mL)	99.00 (70.5–150.0)	113 (78.0–182.0)	94 (64.5–144.5)	.19
HIR assessment				
HIR (median) (IQR)	0.40 (0.23–0.60)	0.60 (0.40–0.70)	0.30 (0.10–0.45)	<.001 <sup>a</sup>

<sup>a</sup> Statistically significant,  $P \leq .05$ .

$P < .001$ ) (Online Supplemental Data). The HIR showed a strong correlation with Maas sCTA scores (Pearson correlation coefficient =  $-0.38$ ; 95% CI,  $-0.53$  to  $-0.20$ ;  $P < .001$ ). ROC curve analysis showed a significant association between poor collaterals and HIR ( $P < .001$ ) with an area under the curve of 0.82. The optimal HIR threshold for prediction of

good-versus-poor collateral status was 0.25 (specificity = 55%, sensitivity = 94%).

## DISCUSSION

In this study, CTP-derived HIR correlated well with sCTA and mCTA collateral scoring methods. In addition, this study identified an HIR threshold of  $>0.45$  as an optimal predictor of poor collateral status on mCTA and demonstrated a significant association between favorable collaterals and a better baseline imaging profile (smaller penumbra/hypoperfused volume and infarct core volumes).<sup>20,23</sup> This study is the first primary analysis comparing the HIR with several CTA collateral scoring methods in the setting of anterior circulation LVO AIS. Our study population included patients from both the early and late windows and supports the use of the HIR in assessing collateral status.<sup>26</sup> For institutions routinely performing CTP with appropriate postprocessing software for LVO AIS work-up, the capability of CTP to assess collaterals in addition to mapping mismatch between infarct volume and penumbra may obviate the need for multiphase CTA for collateral assessment, despite the slight increase in radiation dose. In addition, poor interrater agreement was observed in this study for sCTA collateral scoring methods (Tan and Maas), suggesting that sCTA alone for collateral assessment is suboptimal.

The ability to automatically derive an objective measure of collateral status using CTP may have important clinical implications for triage and decision-making for EVT. The HIR is a measure of collateral blood flow within ischemic brain tissue using CT or MR perfusion imaging.<sup>12,15,20</sup> Traditionally, non-invasive evaluation of collateral status in LVO AIS has focused primarily on CTA techniques. Several scales have been developed for assessing collateral status on CTA on the basis of the degree of contrast opacification of the MCA branches distal to the occlusion.<sup>17,18,27</sup>

There may be significant advantages in using the HIR for collateral assessment compared with these CTA visual scoring systems. The HIR is a quantitative assessment, requiring no additional training for scoring scales (Fig 3), thereby eliminating susceptibility to reader bias and interrater variability (the latter particularly pronounced for sCTA methods in this study). Although the interrater agreement for mCTA scores in this study was high and in keeping with other mCTA studies, this finding is based on data generated by trained/experienced neuroradiologist interpretations of mCTA. A large portion of CTAs are read by non-neuroradiologists, however, and mCTA use is not widespread. In contrast, after the DWI or CTP

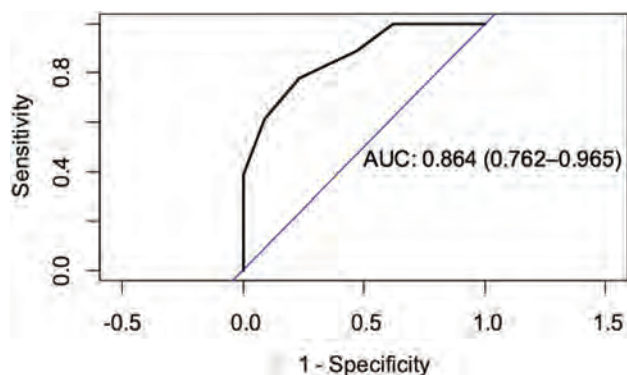


**FIG 2.** ROC analysis of the HIR to predict poor collaterals (Calgary/Menon mCTA scores 0–3) with an area under curve (AUC) of 0.864. An HIR of 0.45 was the optimal threshold that predicted poor-versus-good mCTA collaterals, with sensitivity = 78%, specificity = 76%.

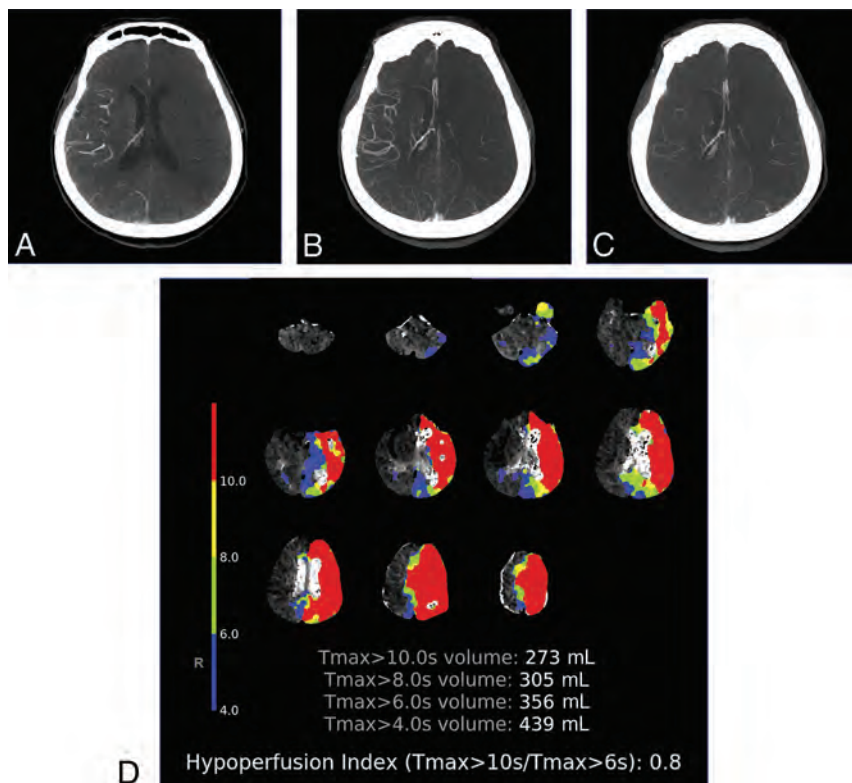


**FIG 3.** Patient with acute occlusion of the left terminal ICA and poor collateral blood supply. A–C, Multiphase CTA images show early arterial (A), late arterial (B), and late venous (C) phases, respectively, with only a small number of left MCA territory branches filling in any phase. D, HIR Color map shows color coded areas of increased Tmax in the left MCA territory with the HIR calculated as 0.8 (red =  $T_{max} > 10$  seconds, yellow =  $> 8$  seconds, blue =  $> 6$  seconds, green =  $> 4$  seconds). S indicates seconds.



Assessment with Clinical Mismatch in the Triage of Wake-Up and Late Presenting Strokes Undergoing Neurointervention with Trevo (DAWN)<sup>4</sup> trial and the Endovascular Therapy Following Imaging Evaluation for Ischemic Stroke (DEFUSE3)<sup>3</sup> trial, use of CTP has grown significantly. In addition, there is recent evidence of a benefit of CTP in the first 9 hours of AIS for selecting patients with LVO as well as non-LVO to receive intravenous tPA.<sup>28</sup>

Because the HIR can be derived from routine CTP acquisitions, it can be quickly integrated in LVO AIS stroke imaging workflow. Moreover, commercially available software platforms that automate the derivation and reporting of the HIR may provide valuable time-savings and rapid availability of results via messaging platforms to the entire multidisciplinary stroke team, expediting the decision-making process. These features may also be particularly useful for facilitating referrals from primary stroke centers with physicians less experienced in assessing collateral status on CTA during initial stroke imaging work-up. In addition, rapid assessment of collateral status using the HIR may be also useful in “spoke” centers for selecting eligible candidates and preventing futile transfers to “hub” EVT-capable centers because patients with poor collateral status (high HIR) are less likely to undergo EVT, have higher stroke severity and infarct growth, increased risk of hemorrhagic infarct transformation, and worse functional outcomes.<sup>10,11,19,20,23,29-32</sup>

While CT-based AIS imaging work-up has become more widespread due to logistic and resource advantages, some centers use MR imaging. However, time-of-flight MRA in the setting of an LVO AIS does not allow evaluation of the distal vascular bed, preventing collateral assessment by MRA. In a study by Guenego et al,<sup>23</sup> 53% (52/98) of patients had MR imaging before EVT, and collateral assessment on MRA was not possible in these patients. Because the HIR can be derived from MR perfusion, centers that favor MR imaging for EVT triage may also benefit from the HIR as a measure of collateral status.

Our findings are consistent with recently reported data correlating the HIR with criterion standard DCA-derived collateral scores for patients with M1 occlusion (ICA occlusions excluded) assessed during EVT as a primary analysis<sup>23</sup> and with CTA collateral scores as secondary analyses.<sup>15</sup> DCA is considered the criterion standard method for dynamically assessing the cerebral arteries, yet this assessment can be derived only during EVT, which limits its utility on LVO AIS decision-making. The same study of DCA-derived collateral scores of patients with M1 occlusion found a similar cutoff of <0.4 for predicting good collateral status.<sup>23</sup> While it is expected that the HIR would correlate with CTA collateral status because it correlates with DCA, it is important to validate it against CTA. Collateral status on DCA may differ from that on CTA, for example, if the patient’s blood pressure changes due to the hypotensive effects of medications or anesthesia.

Previous studies comparing the HIR with sCTA have also reported similar findings. A post hoc analysis of a small subcohort of the Solitaire With the Intention For Thrombectomy as Primary Endovascular Treatment (SWIFT-PRIME) trial found that CTP-derived HIR correlates with sCTA-based collateral status, with good collaterals having a median HIR value of 0.4 and excellent collaterals having a median HIR value of 0.3.<sup>21</sup> Similar

post hoc analysis of the DEFUSE-3 trial found that a lower HIR correlates with slower infarct growth and smaller final infarct volume.<sup>20</sup> These studies were, however, limited by potential selection bias as well as heterogeneous neuroimaging protocols due to their post hoc nature and large multicenter design.

This study is limited by its retrospective design, with data from a single center. We chose not to compare the HIR with DCA collateral status because it has already been shown to correlate well<sup>16</sup> and we did not want to restrict analysis to solely M1 occlusions. We also restricted our analysis to some commonly used CTA scoring methods; however, we acknowledge that several alternative subjective CTA collateral scoring methods exist. We did not include other vessel-occlusion locations (ie, isolated M2, M3, anterior cerebral artery, posterior cerebral artery, or basilar artery occlusions). The HIR thresholds derived from this retrospective dataset need to be further validated. We also acknowledge that currently only 1 CTP processing software vendor has automated HIR output, which limits use of this technique. Further study of the correlation of the HIR with initial and final infarct volume, hemorrhagic transformation, and patient functional outcome is also warranted and may encourage additional vendors to incorporate this tool into future iterations of their software packages.

## CONCLUSIONS


The HIR is associated with CTA collateral status in patients presenting with LVO AIS. As an automated and quantitative tool, it may be rapidly obtained and is easier to interpret than subjective CTA collateral scoring methods. Current clinical practice and future clinical LVO AIS trials may consider use of the HIR for assessment of patient collateral status at the time of initial stroke imaging work-up.

## REFERENCES

1. Goyal M, Menon BK, van Zwam WH, et al. **Endovascular thrombectomy after large-vessel ischaemic stroke: a meta-analysis of individual patient data from five randomised trials.** *Lancet* 2016;387:1723–31 CrossRef Medline
2. Palaniswami M, Yan B. **Mechanical thrombectomy is now the gold standard for acute ischemic stroke: implications for routine clinical practice.** *Interv Neurol* 2015;4:18–29 CrossRef Medline
3. Albers GW, Marks MP, Kemp S, et al. **Thrombectomy for stroke at 6 to 16 hours with selection by perfusion imaging.** *N Engl J Med* 2018;378:708–18 CrossRef Medline
4. Nogueira RG, Jadhav AP, Haussen DC, et al. **Thrombectomy 6 to 24 hours after stroke with a mismatch between deficit and infarct.** *N Engl J Med* 2018;378:11–21 CrossRef Medline
5. Berkhemer OA, Jansen IGH, Beumer D, et al. MR CLEAN Investigators. **Collateral status on baseline computed tomographic angiography and intra-arterial treatment effect in patients with proximal anterior circulation stroke.** *Stroke* 2016;47:768–76 CrossRef Medline
6. Menon BK, Qazi E, Nambiar V, et al. Interventional Management of Stroke III Investigators. **Differential effect of baseline computed tomographic angiography collaterals on clinical outcome in patients enrolled in the Interventional Management of Stroke III Trial.** *Stroke* 2015;46:1239–44 CrossRef Medline
7. Bang O, Saver J, Buck B, et al. UCLA Collateral Investigators. **Impact of collateral flow on tissue fate in acute ischaemic stroke.** *J Neurology Neurosurg Psychiatry* 2008;79:625–29 CrossRef Medline

8. Bang OY, Saver JL, Kim SJ, et al. **Collateral flow predicts response to endovascular therapy for acute ischemic stroke.** *Stroke* 2011;42:693–99 CrossRef Medline
9. Bang OY, Saver JL, Kim SJ, et al. UCLA-Samsung Stroke Collaborators. **Collateral flow averts hemorrhagic transformation after endovascular therapy for acute ischemic stroke.** *Stroke* 2011;42:2235–39 CrossRef Medline
10. Liebeskind DS, Tomsick TA, Foster LD, et al. IMS III Investigators. **Collaterals at angiography and outcomes in the Interventional Management of Stroke (IMS) III trial.** *Stroke J Cereb Circulation* 2014;45:759–64 CrossRef Medline
11. Vagal A, Menon BK, Foster LD, et al. **Association between CT angiogram collaterals and CT perfusion in the Interventional Management of Stroke III Trial.** *Stroke* 2016;47:535–38 CrossRef Medline
12. Seker F, Potreck A, Möhlenbruch M, et al. **Comparison of four different collateral scores in acute ischemic stroke by CT angiography.** *J Neurointerv Surg* 2016;8:1116–18 CrossRef Medline
13. Tan IYL, Demchuk AM, Hopyan J, et al. **CT angiography clot burden score and collateral score: correlation with clinical and radiologic outcomes in acute middle cerebral artery infarct.** *AJNR Am J Neuroradiol* 2009;30:525–31 CrossRef Medline
14. Maas MB, Lev MH, Ay H, et al. **Collateral vessels on CT angiography predict outcome in acute ischemic stroke.** *Stroke* 2009;40:3001–05 CrossRef Medline
15. Menon BK, d'Esterre CD, Qazi EM, et al. **Multiphase CT angiography: a new tool for the imaging triage of patients with acute ischemic stroke.** *Radiology* 2015;275:510–20 CrossRef Medline
16. Hassen WB, Malley C, Boulouis G, et al. **Inter- and intraobserver reliability for angiographic leptomeningeal collateral flow assessment by the American Society of Interventional and Therapeutic Neuroradiology/Society of Interventional Radiology (ASITN/SIR) scale.** *J Neurointerv Surg* 2019;11:338–41 CrossRef Medline
17. Albers GW, Thijs VN, Wechsler L, et al. for the DEFUSE Investigators. **Magnetic resonance imaging profiles predict clinical response to early reperfusion: the Diffusion and Perfusion Imaging Evaluation for Understanding Stroke Evolution (DEFUSE) study.** *Ann Neurol* 2006;60:508–17 CrossRef Medline
18. Lansberg MG, Lee J, Christensen S, et al. **RAPID automated patient selection for reperfusion therapy: a pooled analysis of the Echoplanar Imaging Thrombolytic Evaluation Trial (EPITHET) and the Diffusion and Perfusion Imaging Evaluation for Understanding Stroke Evolution (DEFUSE) Study.** *Stroke J Cereb Circulation* 2011;42:1608–14 CrossRef Medline
19. Bang OY, Saver JL, Alger JR, et al. UCLA Collateral Investigators. **Determinants of the distribution and severity of hypoperfusion in patients with ischemic stroke SYMBOL.** *Neurology* 2008;71:1804–11 CrossRef Medline
20. Olivot J, Mlynash M, Inoue M, et al. **Hypoperfusion intensity ratio predicts infarct progression and functional outcome in the DEFUSE 2 cohort.** *Stroke* 2014;45:1018–23 CrossRef Medline
21. Arenillas JF, Cortijo E, García-Bermejo P, et al. **Relative cerebral blood volume is associated with collateral status and infarct growth in stroke patients in SWIFT PRIME.** *J Cereb Blood Flow Metab* 2018;38:1839–47 CrossRef Medline
22. Higashida RT, Furlan AJ, Roberts H, et al. Technology Assessment Committees of the American Society of Interventional and Therapeutic Neuroradiology and the Society of Interventional Radiology. **Trial design and reporting standards for intraarterial cerebral thrombolysis for acute ischemic stroke.** *J Vasc Interv Radiol* 2003;14:E1–31 CrossRef Medline
23. Guenego A, Fahed R, Albers GW, et al. **Hypoperfusion intensity ratio correlates with angiographic collaterals in acute ischemic stroke with M1 occlusion.** *Eur J Neurol* 2020;27:864–70 CrossRef Medline
24. McHugh ML. **Interrater reliability: the kappa statistic.** *Biochem Medica* 2012;22:276–82 Medline
25. Flores A, Rubiera M, Ribó M, et al. **Poor collateral circulation assessed by multiphase computed tomographic angiography predicts malignant middle cerebral artery evolution after reperfusion therapies.** *Stroke* 2015;46:3149–53 CrossRef Medline
26. de Havenon A, Mlynash M, Kim-Tenser MA, et al. DEFUSE 3 Investigators. **Results From DEFUSE 3.** *Stroke* 2019;50:632–38 CrossRef Medline
27. Raymond SB, Schaefer PW. **Imaging brain collaterals: quantification, scoring, and potential significance.** *Top Magn Reson Imag* 2017;26:67–75 CrossRef Medline
28. Ma H, Campbell BC, Parsons MW, et al. **Thrombolysis guided by perfusion imaging up to 9 hours after onset of stroke.** *N Engl J Med* 2019;380:1795–1803 CrossRef Medline
29. Guenego A, Mlynash M, Christensen S, et al. **Hypoperfusion ratio predicts infarct growth during transfer for thrombectomy: HIR predicts infarct growth.** *Ann Neurol* 2018;84:616–20 CrossRef Medline
30. Rabinstein AA. **Collateral flow predicts response to endovascular therapy for acute ischemic stroke.** *Yearbook Neurology Neurosurg* 2011;2011:26–28 CrossRef
31. Fanou EM, Knight J, Aviv RI, et al. **Effect of collaterals on clinical presentation, baseline imaging, complications, and outcome in acute stroke.** *AJNR Am J Neuroradiol* 2015;36:2285–91 CrossRef Medline
32. Guenego A, Marcellus DG, Martin BW, et al. **Hypoperfusion intensity ratio is correlated with patient eligibility for thrombectomy.** *Stroke* 2019;50:917–22 CrossRef Medline

# MTT Heterogeneity in Perfusion CT Imaging as a Predictor of Outcome after Aneurysmal SAH

 B.B. Hofmann,  I. Fischer,  A. Engel,  K. Jannusch,  D.M. Donaldson,  C. Karadag,  J.H. van Lieshout,  K. Beseoglu,  S. Muhammad,  B. Turowski,  D. Hänggi,  M.A. Kamp, and  C. Rubbert



## ABSTRACT

**BACKGROUND AND PURPOSE:** Impairment of tissue oxygenation caused by inhomogeneous microscopic blood flow distribution, the so-called capillary transit time heterogeneity, is thought to contribute to delayed cerebral ischemia after aneurysmal SAH but has so far not been systematically evaluated in patients. We hypothesized that heterogeneity of the MTT, derived from CTP parameters, would give insight into the clinical course of patients with aneurysmal SAH and may identify patients at risk of poor outcome.

**MATERIALS AND METHODS:** We retrospectively analyzed the heterogeneity of the MTT using the coefficient of variation in CTP scans from 132 patients. A multivariable logistic regression model was used to model the dichotomized mRS outcome. Linear regression was used to eliminate variables with high linear dependence. *T* tests were used to compare the means of 2 groups. Furthermore, the time of the maximum coefficient of variation for MTT after bleeding was evaluated for correlation with the mRS after 6 months.

**RESULTS:** On average, each patient underwent 5.3 CTP scans during his or her stay. Patients with high coefficient of variation for MTT presented more often with higher modified Fisher ( $P = .011$ ) and World Federation of Neurosurgical Societies grades ( $P = .014$ ). A high coefficient of variation for MTT at days 3–21 after aneurysmal SAH correlated significantly with a worse mRS score after 6 months ( $P = .016$ ). We found no correlation between the time of the maximum coefficient of variation for MTT after bleeding and the patients' outcomes after 6 months ( $P = .203$ ).

**CONCLUSIONS:** Heterogeneity of MTT in CTP after aneurysmal SAH correlates with the patients' outcomes. Because the findings are in line with the pathophysiologic concept of the capillary transit time heterogeneity, future studies should seek to verify the coefficient of variation for MTT as a potential imaging biomarker for outcome.

**ABBREVIATIONS:** aSAH = aneurysmal SAH; CTH = capillary transit time heterogeneity; cvMTT = coefficient of variation for MTT; cvMTT-peak = maximum cvMTT after bleeding; DCI = delayed cerebral ischemia; EVD = external ventricular drainage; ICP = intracranial pressure; RTH = relative transit time heterogeneity; Tmax = time-to-maximum; WFNS = World Federation of Neurosurgical Societies

From the 9 in 100,000 individuals with an aneurysmal SAH (aSAH) per year, up to 40% die within 1 month despite improved intensive care and current treatment strategies.<sup>1–4</sup> Subsequent physical impairment, cognitive impairment, and secondary long-term psychosocial deterioration mean that most survivors cannot return to their former work life.<sup>5,6</sup>

The etiology of the detrimental long-term changes after SAH remains poorly understood. In terms of temporal progression, 2 distinct harmful phases of pathophysiologic changes can be distinguished. The term “early brain injury” describes initial pathophysiologic changes within the first 3 days, whereas “delayed cerebral ischemia” (DCI) represents a complex of reactions that occur later during the course of the disease.<sup>7</sup>

During DCI, various pathophysiologic reactions and mechanisms result in cerebral ischemia and neuronal energy depletion. DCI likely involves microvascular dysfunction; disturbances in cerebral microcirculation; angiographic vasospasms; thrombosis of cerebral, primarily cortical, vessels; cortical spreading depolarization and ischemia; as well as inflammatory reactions.<sup>7–10</sup> Finally, DCI may lead to cerebral infarction and, therefore, irreversible loss of function.

Received January 22, 2021; accepted after revision March 9.

From the Departments of Neurosurgery (B.B.H., I.F., A.E., D.M.D., C.K., J.H.v.L., K.B., S.M., D.H., M.A.K.) and Diagnostic and Interventional Radiology (K.J., B.T., C.R.), Medical Faculty, Heinrich-Heine-University Düsseldorf, Düsseldorf, Germany.

Please address correspondence to Björn B. Hofmann, MD, Departments of Neurosurgery, Medical Faculty, Heinrich-Heine-University Düsseldorf, Medical Faculty, Department of Neurosurgery, Moorenstr 5, D40225 Düsseldorf, Germany; e-mail: bjoern.hofmann@med.uni-duesseldorf.de

<http://dx.doi.org/10.3174/ajnr.A7169>



In general, the important factors for brain tissue survival are adequate oxygenation and glucose supply, among others. Historically, it was assumed that oxygenation mainly relies on the CBF, and previously macroscopic, angiographically visible vasospasms were assumed to be the main driver of DCI. However, it turned out that for this simplified assumption, the blood flow in capillaries must be identical throughout the whole capillary bed, which is not the case. In addition to the CBF, the microvascular blood distribution across capillaries, also known as the capillary transit time heterogeneity (CTH), was found to be a crucial factor for the oxygenation of brain tissue.<sup>11,12</sup> Recently, Østergaard et al<sup>11</sup> presumed that the CTH also contributes to DCI-related ischemia. According to the group's model, an increased CBF can lead to better tissue oxygenation as long as the CTH has not crossed a critical threshold. If the threshold is exceeded, any further increase in CBF will lead to a reduced oxygen extraction efficacy in brain tissue, due to capillary shunting in hyperemic areas, resulting in hypoxic brain tissue.<sup>12</sup> Østergaard et al defined this state as malignant CTH.<sup>11,12</sup> In such a case, adequate oxygenation of the brain tissue may be achieved only by reducing the CBF and thereby slowing the flow of erythrocytes through the shunting capillaries. This mechanism could be an explanation for the occurrence of vasospasm in patients with aSAH.<sup>11</sup>

CTH has been mainly evaluated in simulations, rodent models, and humans predominately with ischemic stroke or neurodegenerative diseases, such as Alzheimer disease. In the patient population, evaluation has so far mainly relied on MR imaging. Moreover, Østergaard et al<sup>11</sup> recently established the relative transit time heterogeneity (RTH) as the ratio of CTH to MTT.<sup>13</sup> In doing so, the inherent dependency of CTH on the MTT was removed, making the RTH an improved indicator of the capillary transit heterogeneity.<sup>13</sup> Furthermore, Østergaard et al have based the calculation of CTH and RTH on elaborated Bayesian approaches, and CTH evaluation is not readily available in clinical software for perfusion evaluation. Hence, to date, there is no routinely available radiologic readout for the CTH or RTH in the clinical setting of aSAH.

So far, the concept of capillary transit time heterogeneity has not been systemically evaluated in patients with aSAH. We hypothesized that the higher heterogeneity of MTT derived from CTP parameters will allow us to gain insight into the clinical course of patients with aSAH and to predict a worse outcome. In the present study, we, therefore, retrospectively analyzed the heterogeneity of MTT in CTP scans obtained within 3 weeks after SAH and assessed a potential association with the initial neurologic status on admission and clinical outcome after 6 months.

## MATERIALS AND METHODS

All procedures performed in studies involving human participants were in accordance with the ethical standards of the institutional committee and with the 1964 Helsinki declaration and its later amendments. For this type of study formal consent is not required. The study was approved by the local ethics committee (study ID: 5760R). Data will be made available on reasonable request. We prepared the manuscript according to the Strengthening the Reporting of Observational Studies in Epidemiology (STROBE) guidelines.

## Inclusion Criteria

We retrospectively included all patients with SAH admitted to our hospital between January 2008 and December 2015 who met the following inclusion criteria: 1) SAH present on initial nonenhanced CT, 2) admission within 24 hours after ictus, 3) subsequent CTP scans with at least 2 CTP scans in addition to the initial CTP imaging after aneurysm occlusion, and 4) documented clinical follow-up examination 6 months after discharge to assess the functional outcome. Patients were excluded from the study on the basis of following criteria: 1) nonaneurysmal SAHs, 2) unknown onset of aSAH, 3) patients with unevaluable CTP (eg, due to severe motion), or 4) patients with a history of cranial neurosurgical or endovascular intervention.

## SAH Management

We managed patients according to the applicable aSAH guidelines.<sup>14</sup> SAH was graded according to the modified Fisher scale based on initial noncontrast CT imaging.<sup>15</sup> In all patients, systolic arterial blood pressure was adjusted between 100 and 140 mm Hg, and the partial pressure of carbon dioxide (pCO<sub>2</sub>) was maintained in the range of 35 to 40 mm Hg for all intubated patients. External ventricular drainage (EVD) was established in intubated patients and patients with poor World Federation of Neurosurgical Societies (WFNS) grades (Glasgow Coma Scale  $\leq 12$  according to our internal guidelines), as well as patients with exacerbated intracranial pressure after initial imaging (CT + CTA) and before subsequent angiography and aneurysm treatment. If a patient showed secondary-progressive deterioration of awareness before or after aneurysm treatment, even leading to insufficient neurologic assessability (Glasgow Coma Scale  $\leq 12$  according to our internal guidelines), an increase in intracranial pressure was suspected after exclusion of other causes and an EVD was placed. General care followed a standardized protocol, including surgical or endovascular occlusion of the aneurysm within 24 hours after admission. A CTP scan was performed routinely 6 hours after aneurysm treatment and on days 4, 7, and 10 after bleeding or in case of clinical suspicion of DCI (defined as previously described<sup>16</sup>). CTP was not performed only when CT was not possible due to critical situations such as a cardiopulmonary instability of a patient or if there was a treatment-resistant absolute contraindication for the administration of the contrast agent (allergy, high-grade renal insufficiency).

## Perfusion CT Analysis

CTP data were acquired with a multisection CT scanner (Somatom Volume Zoom, Definition Flash or AS; Siemens) (80 kV, 120 mAs, 2 adjacent slices, 10-mm section thickness, 1 image/s for 35 seconds).<sup>17-19</sup> Three seconds after starting the CT, contrast-enhancing medium (30 mL, 400 mg iodine/mL) followed by a saline chaser (30 mL) was injected with a flow rate of 5 mL/s. Intravenous access of  $\leq 18$  gauge in a cubital vein or a high-flow central venous catheter was required for contrast administration. Slices were positioned at the level of the central parts of lateral ventricles, parallel to a plane through the orbital floor and the external auditory meatus, thereby sampling the anterior, middle, and posterior cerebral artery territories as well as the anterior and posterior borderzones.<sup>20</sup> Calculation of the parameter images

(MTT, CBF, CBV, and time-to-maximum [Tmax]) was performed using STROKETOOL-CT (Digital Image Solutions), which processes data using singular value decomposition.<sup>21</sup> We used the software Angiotux CT 2D (ECCET 2006, Beck A. Aurich V., <http://www.eccet.de/>) for standardized parameter value extraction from the different cortical brain regions.<sup>18</sup> A 10-mm-wide band was automatically delineated along the cortex, omitting outer CSF spaces, the rostral falx cerebri, and the superior sagittal sinus. The automated definition of the ROI was reviewed and potential deviations were corrected as needed. A running average spanning 10° of the ROI was computed in 2° steps for each perfusion parameter, yielding 180 measurements per parameter per CTP scan (Fig 1). We assessed the heterogeneity of cerebral perfusion by the coefficient of variation (cv), also called the relative SD, of the MTT (cvMTT) for each individual scan. The cv is a measure of the dispersion of a probability distribution independent of the mean of the examined variable:

$$cvMTT = \frac{SD}{Expected\ Value} = \frac{SD\ MTT}{Mean\ MTT}.$$

The statistical analysis of this study included all late CTP scans gathered in the nonacute phase of a patient, thus all CTP scans between days 3 and 21 postbleeding. To further evaluate the impact of very large heterogeneity, we determined the point in time of the maximum cvMTT across all CTP scans from an individual patient during the entire clinical course, including the CTP scans in the first 3 days after ictus.

#### Definition of Grading/Outcome Measures

We dichotomized the initial neurologic condition using the WFNS grading system.<sup>22</sup> A WFNS score of I–III represents a good neurologic grade on admission, whereas a WFNS score of IV–V is considered a poor grade. The functional outcome was assessed using the mRS 6 months after ictus.<sup>23</sup> An mRS score of 0–2 was considered a favorable outcome, and a score of 3–6, an unfavorable outcome. The Fisher score was used without dichotomization.<sup>24,25</sup>

#### Statistical Analysis

We analyzed presenting variables for correlation with cvMTT as well as Rankin outcomes. A multivariable logistic regression model would be used to model the dichotomized patient outcome according to the mRS (good versus poor). In a first step, to avoid multicollinearities in predictor variables, we used pair-wise linear regression among numeric variables to eliminate variables with high linear dependence. The remaining predictors, including sex (binary indicator, male or female), age (numeric), WFNS score (undichotomized, treated as a continuous numeric variable), Fisher score (undichotomized, treated as continuous numeric variable), and the logarithm of the cvMTT (numeric), were later used in the logistic regression. We used the logarithm of cvMTT because cvMTT is, by definition, always positive and thus non-normally distributed. Logistic regression, by definition, assumes log-odds to linearly depend on predictor variables. This condition is automatically satisfied when the 2 outcome groups are normally distributed

with the same variance. In our case, the variances of cvMTT between the 2 groups, mRS ≤ 2 and mRS ≥ 3, differed strongly (0.0044 versus 0.0072). Using the logarithm achieved a more similar distribution (0.11 and 0.16), thus leading to more reliable predictions. For the outcome variable, we dichotomized patient mRS scores to 2 values: 0, representing mRS ≤ 2, and 1 representing mRS ≥ 3. We applied both forward and backward selection of predictor variables. The fitted logistic regression model was used to assess the effect of predictor variables on the patient outcome. To examine the difference in the means of a numeric variable between the 2 groups, we used the Student *t* test, and to compare multiple groups, ANOVA.

## RESULTS

### Patients

From the initial 476 patients with SAH, a total of 344 were excluded due to various factors, including those with a nonaneurysmal SAH, <2 follow-up CTP scans being performed, the onset of SAH being unknown, aneurysm occlusion not performed within 24 hours after SAH, mRS after 6 months not recorded, or the patient already having a history of cranial neurosurgical intervention. One hundred thirty-two patients were included in the analysis. The mean age was 54 (SD, 11) years, and 69% were women (Table 1).

On admission, 64 patients (48%) were of good neurologic grade (WFNS III), and 68 patients (52%) presented with a poor grade (WFNS IV–V). Twenty-three patients (17%) had minor SAH (modified Fisher grade 1–2), and 109 (83%) had severe SAH (modified Fisher grade 3–4) (Table 1). Eighty-seven patients (66%) received an EVD during their treatment, and 45 patients (34%) did not need an EVD implantation. Sixty-six patients (50%) received endovascular aneurysm treatment, 60 patients (45%) were treated surgically, 2 patients (2%) received neither treatment, and 4 patients (3%) received both endovascular and surgical treatment. On average, patients were discharged at day 22 (SD), and each patient included in this study underwent 5.3 (SD, 2.1) CTP scans (Table 2).

Six months after ictus, 25 patients (19%) had died (mRS 6), a further 27 patients (20%) had an unfavorable outcome (mRS 3–5), and 80 patients (61%) were in a favorable clinical condition (mRS 0–2) (Table 2).

### CTP Data

The late perfusion data showed that the MTT was 3.5 (SD, 0.79) seconds. The MTT did not correlate with either the initial WFNS grade ( $\beta = 0.59$ ; 95% CI,  $-0.26$ – $1.43$ ;  $P = .18$ ) or the Fisher grade ( $\beta = -0.13$ ; 94% CI,  $-1.53$ – $1.27$ ;  $P = .86$ ) (Fig 2A). Besides age ( $\beta = 0.077$ ; 95% CI,  $0.043$ – $0.111$ ;  $P \leq .001$ ) and Fisher grade ( $\beta = 0.98$ ; 95% CI,  $0.61$ – $1.35$ ;  $P \leq .001$ ), the dichotomized mRS after 6 months also positively correlated with the MTT (logistic regression: OR = 1.05; 95% CI,  $1.004$ – $1.103$ ;  $P = .034$ ) (Fig 2C, upper graph).

### CTP Heterogeneity Correlates with 6-Month mRS

The cvMTT correlated significantly with the WFNS ( $\beta = 0.010$ ; 95% CI,  $0.002$ – $0.019$ ;  $P = .014$ ) and the Fisher grade ( $\beta = 0.018$ ;

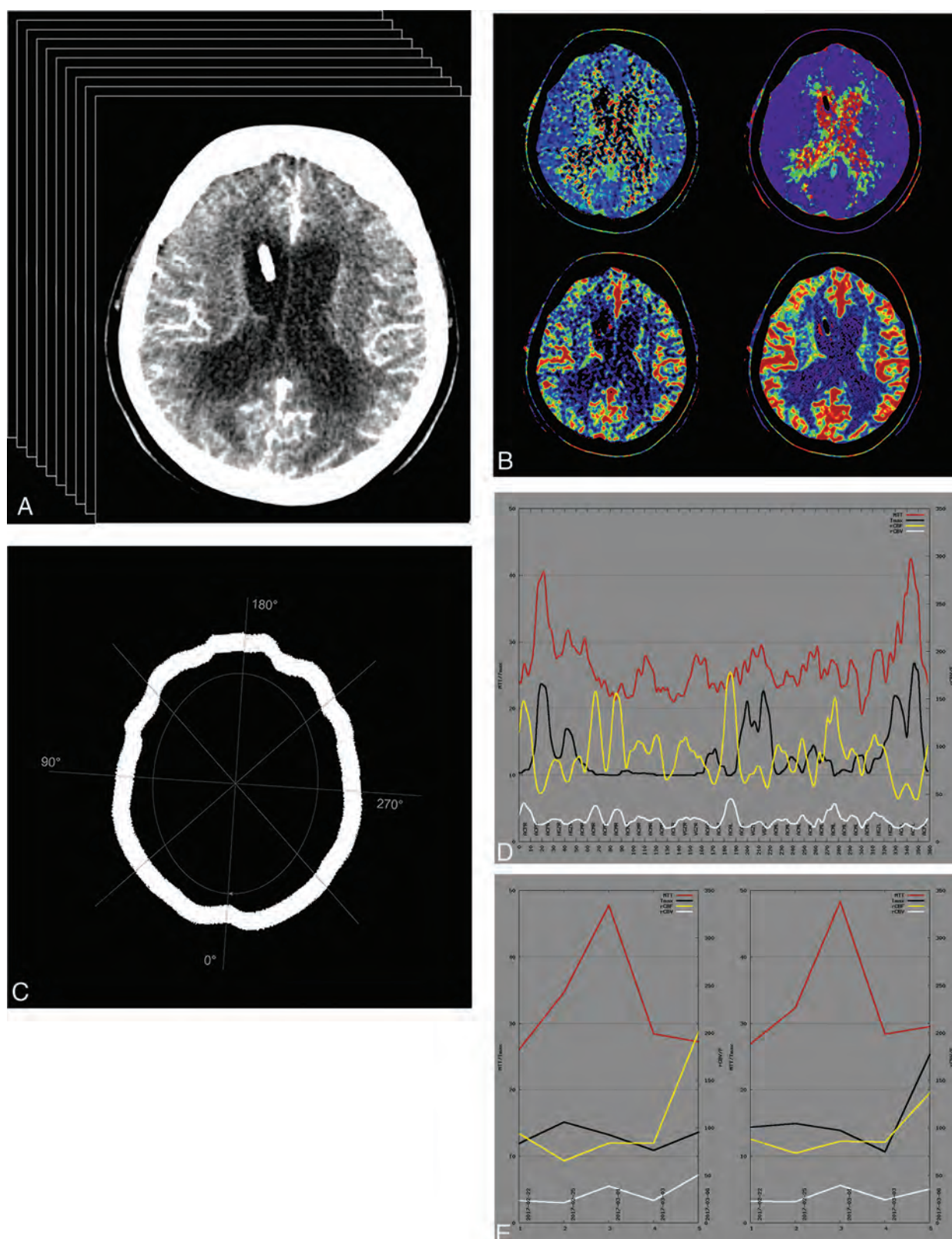


**FIG 1.** Exemplary illustration of CTP imaging in patients with SAH. *A*, A series of axial CTP scans at the level of the cella media of the lateral ventricles, parallel to the orbitomeatal plane, thereby representing 6 supratentorial vessel territories. *B*, Calculated perfusion parameter maps in clockwise order from top left: MTT, Tmax, and semi-quantitative relative CBF (rCBF) as well as CBV (rCBV). *C*, Depiction of the ROI automatically defined along the cortex. Readout starts in the territory of the right posterior cerebral artery and is carried out in a clockwise manner using a sliding-window approach (mean across 10° in 2° steps). *D*, Display of 180 measurements across 360° (red, MTT; black, Tmax; yellow, rCBF; white, rCBV). *E*, Mean perfusion parameters over 5 CTP scans for the left hemisphere on the left and the right hemisphere on the right side. Note the marked pathologic elevation of MTT (red) in the third scan.



**Table 1: Descriptive statistics**

	All Patients	mRS <3	mRS ≥3
	No. (%)	No. (%)	No. (%)
Age			
Younger than 50 yr	41 (31.06)	34 (42.5)	7 (13.5)
50 Years or older	91 (68.94)	46 (57.5)	45 (86.5)
Sex			
Female	91 (68.9)	57 (71.2)	34 (65.4)
Male	41 (31.1)	23 (28.8)	18 (34.6)
WFNS grade			
I–III	64 (48.48)	50 (62.5)	14 (26.9)
IV–V	68 (51.52)	30 (37.5)	38 (73.1)
Fisher grade			
0–2	23 (17.42)	20 (25)	3 (5.8)
3–4	109 (82.58)	60 (75)	49 (92.2)
Aneurysm location			
ACA	1 (0.76)	0 (0)	1 (1.9)
AcomA	53 (40.15)	31 (38.8)	22 (42.3)
BA	13 (9.85)	8 (10)	5 (9.6)
ICA	6 (4.55)	3 (3.75)	3 (5.8)
MCA	21 (15.91)	12 (15)	9 (17.3)
PcaA	4 (3.03)	1 (1.25)	3 (5.8)
PcomA	18 (13.64)	15 (18.8)	3 (5.8)
PICA	9 (6.82)	5 (6.25)	4 (7.7)
SCA	2 (1.52)	2 (2.5)	0 (0)
VA	3 (2.27)	1 (1.25)	2 (3.8)
Other	2 (1.52)	2 (2.5)	0 (0)

**Note:**—ACA indicates anterior cerebral artery; AcomA, anterior communicating artery; BA, basilar artery; PcaA, pericallosal artery; PcomA, posterior communicating artery; VA, vertebral artery; SCA, superior cerebellar artery.

**Table 2: Treatment modalities and outcome after 6 months**

	No. (%)
Extraventricular drainage	
Yes	87 (65.9)
No	45 (34.1)
Endovascular treatment	66 (50)
Surgical treatment	60 (45.5)
Combined/no treatment	6 (4.5)
mRS 6 mo	
0–2	80 (60.6)
3–5	27 (20.5)
6	25 (18.9)

95% CI, 0.004–0.031;  $P = .011$ ) at admission (Fig 2B). The cvMTT significantly correlated with the mRS after 6 months (logistic regression: OR = 5.09; 95% CI, 1.46–17.77;  $P = .011$ ) (Fig 2C, lower graph). A higher cvMTT was associated with a worse mRS after 6 months (Fig 2D). Further statistical tests revealed a positive association of the cvMTT with the presence of an EVD ( $t$  test; 95% CI,  $-0.054$ – $0.007$ ;  $P = .012$ ). cvMTT also remained a significant predictor for the outcome when only patients with an EVD were considered (logistic regression: OR = 7.15; 95% CI, 1.51–33.9;  $P = .013$ ). No significant correlation was found between the aneurysm location and the cvMTT (ANOVA,  $F_{10,121} = 1.315$ ,  $P = .23$ ).

### CTP Heterogeneity Peak

The peak of the MTT heterogeneity occurred most frequently at 7.3 (SD, 5.1) days after bleeding (Fig 3A). We found no significant correlation between the maximum cvMTT after bleeding (cvMTT-peak) and the dichotomized patient outcomes after

6 months (logistic regression: OR = 1.03; 95% CI, 0.55–1.93;  $P = .4$ ) (Fig 3B). There was no correlation between the outcome after 6 months and the number of CTP scans obtained in an individual patient (OR = 1.01; 95% CI, 0.85–1.20;  $P = .89$ ).

## DISCUSSION

This retrospective study in patients with SAH has 3 main findings:

1. The heterogeneity of MTT, as defined by cvMTT in late CTP imaging, correlates significantly with the initial WFNS or Fisher grade
2. The heterogeneity of MTT, as defined by cvMTT in late CTP imaging, correlates significantly with the dichotomized outcome after 6 months
3. The point in time of the MTT heterogeneity peak does not correlate with the outcome after 6 months.

CTP is an essential diagnostic tool in the detection of hypoperfused areas of the brain in acute stroke and is gaining increasing relevance in aSAH management as a diagnostic tool for delayed cerebral ischemia.<sup>18,26,27</sup> A prolonged MTT and TTP in an early CTP after aSAH is known to correlate with the initial neurologic status and clinical outcome.<sup>17,19,26–28</sup> Furthermore, these might serve together with additional imaging markers, such as a large intracerebral blood clot in the early noncontrast cranial CT scan, as a surrogate for DCI and as a predictive feature of neurologic outcome.<sup>19</sup> While the aforementioned studies evaluated early CTP scans, with various definitions of “early” ranging from  $\leq 6$  hours to  $\leq 72$  hours after ictus, our study focused on late CTP scans in the phase when a patient is more susceptible to DCI ( $> 72$  hours after ictus).<sup>17,19,27,28</sup>

Increased CTH is considered an important feature of DCI.<sup>7,11,12</sup> Elevated CTH during DCI results in a decreased net oxygen supply to cerebral tissue and, therefore, in tissue hypoxia, resulting in a poor clinical outcome.<sup>11</sup>

Recently, the RTH was established for MR imaging in stroke, representing the CTH without the inherent dependency of CTH on MTT.<sup>13</sup> In our opinion, this further developed parameter is even better for displaying changes in the microvascular blood flow than the CTH itself, and we followed the approach by determining the heterogeneity of the MTT using the coefficient of variation, resembling the approach of the previously discussed RTH. Mathematically, the cvMTT represents the dispersion of MTT values around the brain cortex of individual patients. Falsification of the normal SD by extraordinarily high or low MTT values is thereby diminished, further underlining the potential use of the cvMTT as an imaging biomarker. While previously discussed,<sup>11,29</sup> the current study is the first to systematically assess CTP heterogeneity in patients with SAH. While Østergaard et al<sup>11</sup> applied an elaborated Bayesian statistical model to derive CTH and RTH, our approach is based on the widely clinically available singular value decomposition.

From the various values measured in CTP imaging, the MTT has been established as the surrogate parameter for changes in the microvasculature perfusion. Furthermore, the MTT has the greatest practical relevance in the context of SAH because the indication for an endovascular intervention (spasmolysis) or, in general, intensified DCI-protective therapy is often based on MTT values.<sup>19,30,31</sup>

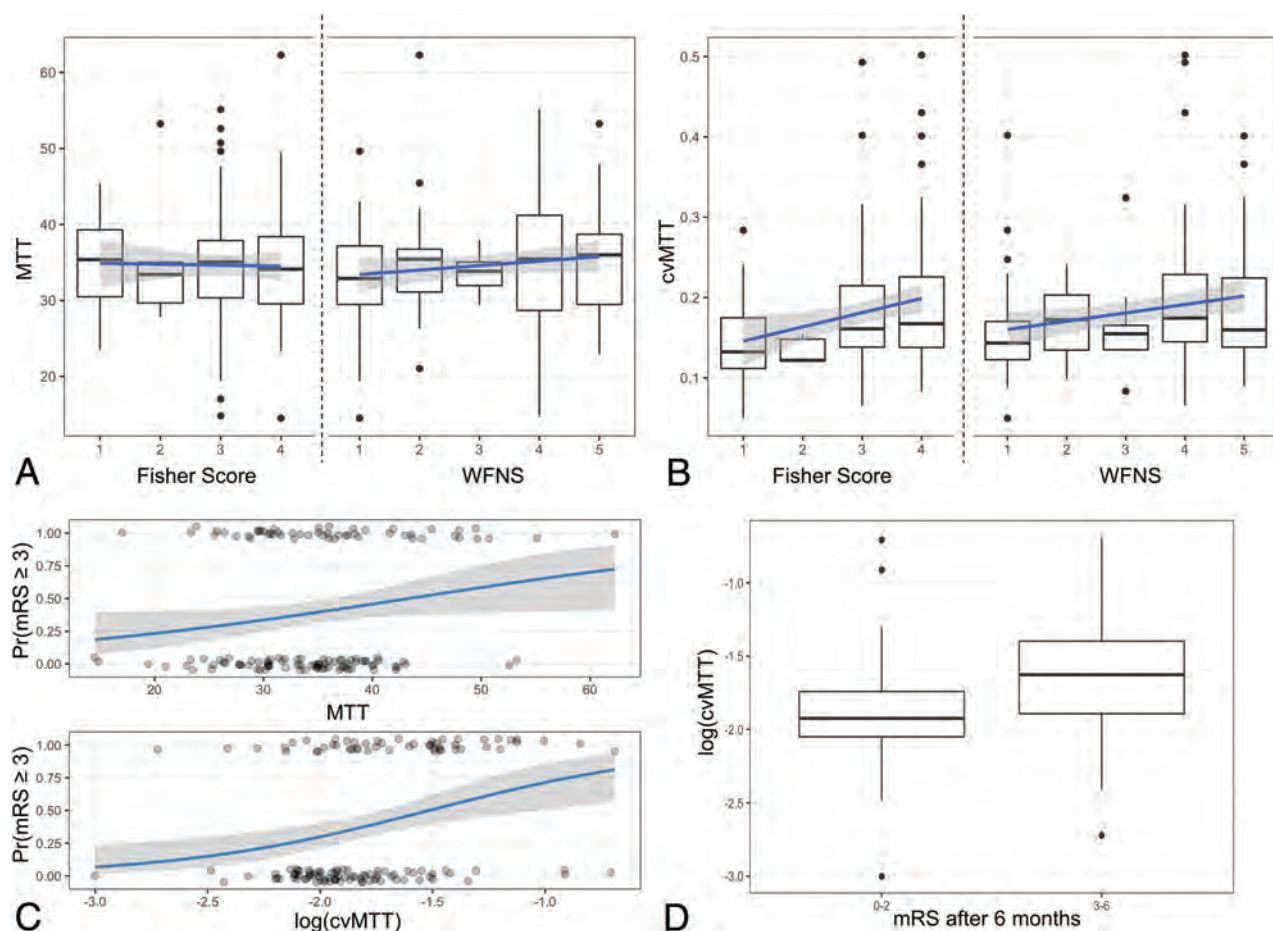


**FIG 2.** Correlation of MTT and the cvMTT with the dichotomized outcome after 6 months. *A*, Mean MTT distribution of the Fisher grade (left) and the WFNS grades (right). The MTT did not correlate with the initial WFNS grade ( $P = .18$ ) or Fisher grade ( $P = .86$ ) at admission. *B*, cvMTT distribution for the Fisher grade (left) and the WFNS grades (right). The cvMTT correlates significantly with the WFNS ( $P = .014$ ) and the Fisher grade ( $P = .011$ ) at admission. *C*, *Upper graph*: MTT as a predictor of the dichotomized mRS after 6 months (logistic regression: OR = 1.05, 95% CI, 1.004–1.103;  $P = .034$ ); *lower graph*: cvMTT as a predictor of the dichotomized mRS after 6 months (logistic regression: OR = 5.09; 95% CI, 1.46–17.77;  $P = .011$ ). *D*, cvMTT for favorable and unfavorable outcomes (mRS after 6 months  $\leq 2$  and  $\geq 3$ , respectively). Pr(mRS  $\geq 3$ ) indicates probability (mRS  $\geq 3$ ).

Overall, in our opinion, the MTT of CTP imaging is the most likely correlation to detect changes in the microvascular blood flow in the clinical setting of aSAH. As previously mentioned, we did not simply use the SD of MTT as a correlate of CTH but went 1 step further. To exclude the influence of MTT on the measured heterogeneity, we calculated the cvMTT. The coefficient of variation, also known as the relative SD, depicts the heterogeneity of MTT independent of the absolute numeric value of MTT.

The main result of this study is the correlation between the heterogeneity of MTT, as measured by the cvMTT, and the outcome of the patient. We have shown that a higher cvMTT, ie, a more nonuniform cerebral capillary blood flow, correlates with an unfavorable mRS after 6 months. We can set this result in the context of the numerous previous works by Østergaard et al.<sup>11</sup> As previously mentioned, the group hypothesized that the presence of malignant CTH results in decreased oxygenation of the brain, resulting in a worse outcome.<sup>12,29</sup> This hypothesis fits well with patients with an increased cvMTT in this study also more likely having a poor outcome. It is conceivable that the increased cvMTT

is a surrogate of decreased oxygenation of the brain, resulting in brain tissue damage and thus leading to a worse outcome.

Most interesting, this study also reveals a correlation between the cvMTT and the WFNS and the Fisher grades. Like the cvMTT, both of these parameters are related to the outcome after SAH. The Fisher score, in particular, predicts “symptomatic vasospasms.” Therefore, it is understandable that there is a mutual relationship, though it is unclear whether and which physiopathologic mechanisms are the basis for this. Yet, even the combination of both WFNS and Fisher score is not sufficient to predict the outcome very well,<sup>32</sup> in contrast to the cvMTT.

A further result of this study is the correlation of the cvMTT with the presence of an EVD. Taking into consideration that the patients with an EVD are predominantly those with a worse initial WFNS and/or Fisher grade associated with a more severe clinical course and worse outcome, a possible reason for this correlation becomes appreciable. We consider it unlikely that the EVD itself influences the cvMTT. At the scanning level, the EVD component may cross the imaging plane, though the ribbonlike ROI generally does not include the EVD; therefore, an artifact due to the EVD is

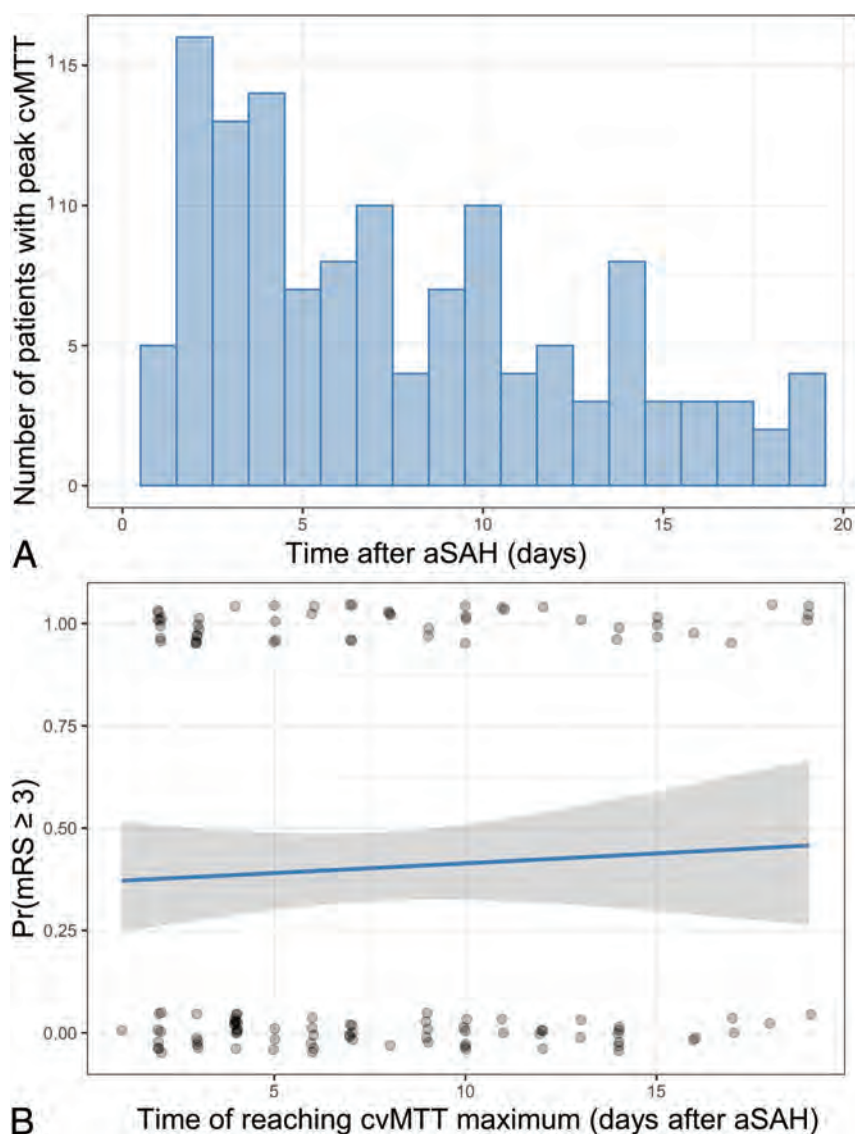


**FIG 3.** The time of cvMTT-peak does not correlate with the outcome after 6 months. *A*, Histogram shows the number of patients with the cvMTT-peak with respect to the days after SAH. *B*, No significant correlation between the time of reaching the cvMTT-peak and the dichotomized patient outcomes after 6 months could be observed (logistic regression: OR=1.03; 95% CI, 0.55–1.93;  $P = .4$ ). Pr(mRS  $\geq 3$ ) indicates probability (mRS  $\geq 3$ ).

almost impossible. For the patients without an EVD, a minimal Glasgow Coma Scale of 13 and normal wakefulness were required. Therefore, in these patients, a physiologic intracranial pressure was assumed. In patients with secondary-progressive deterioration of awareness, even leading to insufficient neurologic assessability (Glasgow Coma Scale  $\leq 12$  according to our internal guidelines), an increase of intracranial pressure was suspected and an EVD was subsequently placed. For patients with an EVD, the intracranial pressure was adjusted to a physiologic level of  $<18$  mm Hg by cerebrospinal fluid drainage. As a result, a significant effect of intracranial pressure on our results seems unlikely. The finding that cvMTT also remained a significant predictor for the outcome when only patients with an EVD were considered supports the assumption.

Caspers et al<sup>33</sup> demonstrated, in 2017, that the point in time of maximum mean MTT after aSAH is of importance for the outcome of a patient. An earlier peak of mean MTT was associated with an unfavorable outcome. We, therefore, examined a possible connection between the point in time of the greatest MTT heterogeneity (cvMTT-peak) and the outcome. In contrast to the earlier findings, however, no evidence for a correlation was detected for cvMTT.

Our study has several limitations:

1. Data were retrospectively collected, and to obtain a study group with a comparable timeline of therapeutic and diagnostic procedures in the pathophysiologic sequence occurring after SAH,<sup>7</sup> very strict inclusion and exclusion criteria were necessary, which meant that many patients could not be included in this study. Nevertheless, the study population is relatively large for a single-center study and is overall well-balanced, for example, regarding patients with good- and poor-grade SAH according to their WFNS score. We believe it is unlikely that our inclusion/exclusion criteria introduced a relevant bias. Larger prospective, preferably multicentric, and more inclusive future studies would need to be conducted to validate our results.
2. Some of the results might be affected by alteration of the intracranial pressure (ICP). However, the MTT is primarily a correlate for microvascular perfusion, whereas Tmax (as a modification of the TTP) is thought to best reflect the intracranial pressure—ie, studies hinting at a Tmax decrease after EVD placement or decompressive hemicraniectomy.<sup>34,35</sup> Therefore, we consider a decisive influence of the ICP on our results unlikely. Additionally, at the time of imaging, the ICP was controlled and maintained at physiologic values by means of an EVD in most patients. Patients without an EVD in place had a Glasgow Coma Scale score of at least 13 and were, therefore, likely to have a physiologic ICP. The influence of ICP should, therefore, be limited.
3. We correlated heterogeneity of cerebral perfusion with the mid-term outcome 6 months after discharge.
4. Other factors such as comorbidities, intracerebral hemorrhage, secondary brain edema, or seizures might additionally



influence the outcome. These potential confounders were not taken into account in the present analysis. Furthermore, even larger studies are required to confirm the heterogeneity of the MTT in CTP scans after aSAH as an independent risk factor for poor outcome.

5. This is one of the first studies addressing the value of cortical perfusion heterogeneity in CTP imaging. Standard values for normal brain tissue have, therefore, not yet been established. Due to the high variation in the CTP protocols and postprocessing, our results may not be translatable one-to-one to other setups.
6. The influence of confounding factors on the maximum heterogeneity of MTT, such as diagnosed or undiagnosed diseases affecting the microvasculature such as diabetes, atherosclerosis, or hypertension, are unknown. However, this study is the first to investigate the heterogeneity of MTT as a predictor of outcome in SAH. Future prospective studies should, therefore, conduct subgroup analyses with a greater number of patients.

## CONCLUSIONS

In the present cohort of 132 patients with aSAH, heterogeneity of the late cerebral perfusion (cvMTT) correlated with the initial WFNS and Fisher grades. The cvMTT has prognostic value because it correlated significantly with the dichotomized outcome after 6 months. A high degree of heterogeneity was associated with an unfavorable outcome, making the cvMTT an attractive candidate as a robust imaging biomarker for further studies.

## REFERENCES

1. van Gijn J, Kerr RS, Rinkel GJ. **Subarachnoid haemorrhage.** *Lancet* 2007;369:306–18 CrossRef Medline
2. de Rooij NK, Rinkel GJ, Dankbaar JW, et al. **Delayed cerebral ischemia after subarachnoid hemorrhage: a systematic review of clinical, laboratory, and radiological predictors.** *Stroke* 2013;44:43–54 CrossRef Medline
3. Lovelock CE, Rinkel GJ, Rothwell PM. **Time trends in outcome of subarachnoid hemorrhage: population-based study and systematic review.** *Neurology* 2010;74:1494–1501 CrossRef Medline
4. Kamp MA, Lieshout JHV, Dibue-Adjei M, et al. **A systematic and meta-analysis of mortality in experimental mouse models analyzing delayed cerebral ischemia after subarachnoid hemorrhage.** *Transl Stroke Res* 2017;8:206–19 CrossRef Medline
5. Kreiter KT, Copeland D, Bernardini GL, et al. **Predictors of cognitive dysfunction after subarachnoid hemorrhage.** *Stroke* 2002;33:200–08 CrossRef Medline
6. Hutter BO, Kreitschmann-Andermahr I, Mayfrank L, et al. **Functional outcome after aneurysmal subarachnoid hemorrhage.** *Acta Neurochir Suppl* 1999;72:157–74 CrossRef Medline
7. van Lieshout JH, Dibue-Adjei M, Cornelius JF, et al. **An introduction to the pathophysiology of aneurysmal subarachnoid hemorrhage.** *Neurosurg Rev* 2017;41:917–30 CrossRef Medline
8. Friedrich B, Muller F, Feiler S, et al. **Experimental subarachnoid hemorrhage causes early and long-lasting microarterial constriction and microthrombosis: an in-vivo microscopy study.** *J Cereb Blood Flow Metab* 2012;32:447–55 CrossRef Medline
9. Dreier JP. **The role of spreading depression, spreading depolarization and spreading ischemia in neurological disease.** *Nat Med* 2011;17:439–47 CrossRef Medline
10. Schneider UC, Davids AM, Brandenburg S, et al. **Microglia inflict delayed brain injury after subarachnoid hemorrhage.** *Acta Neuropathol* 2015;130:215–31 CrossRef Medline
11. Østergaard L, Aamand R, Karabegovic S, et al. **The role of the microcirculation in delayed cerebral ischemia and chronic degenerative changes after subarachnoid hemorrhage.** *J Cereb Blood Flow Metab* 2013;33:1825–37 CrossRef Medline
12. Jespersen SN, Østergaard L. **The roles of cerebral blood flow, capillary transit time heterogeneity, and oxygen tension in brain oxygenation and metabolism.** *J Cereb Blood Flow Metab* 2012;32:264–77 CrossRef Medline
13. Engedal TS, Hjort N, Hougaard KD, et al. **Transit time homogenization in ischemic stroke: a novel biomarker of penumbral microvascular failure?** *J Cereb Blood Flow Metab* 2018;38:2006–20 CrossRef Medline
14. Connolly ES Jr, Rabinstein AA, Carhuapoma JR, et al. **Guidelines for the management of aneurysmal subarachnoid hemorrhage: a guideline for healthcare professionals from the American Heart Association/American Stroke Association.** *Stroke* 2012;43:1711–37 CrossRef Medline
15. Frontera JA, Claassen J, Schmidt JM, et al. **Prediction of symptomatic vasospasm after subarachnoid hemorrhage: the modified Fisher scale.** *Neurosurgery* 2006;59:21–27; discussion 21–27 CrossRef Medline
16. Vergouwen MD, Vermeulen M, van Gijn J, et al. **Definition of delayed cerebral ischemia after aneurysmal subarachnoid hemorrhage as an outcome event in clinical trials and observational studies: proposal of a multidisciplinary research group.** *Stroke* 2010;41:2391–95 CrossRef Medline
17. Kamp MA, Heiroth HJ, Beseoglu K, et al. **Early CT perfusion measurement after aneurysmal subarachnoid hemorrhage: a screening method to predict outcome?** *Acta Neurochir Suppl* 2012;114:329–32 CrossRef Medline
18. Turowski B, Haenggi D, Wittsack J, et al. **Cerebral perfusion computerized tomography in vasospasm after subarachnoid hemorrhage: diagnostic value of MTT [in German].** *Rofo* 2007;179:847–54 CrossRef Medline
19. Etminan N, Beseoglu K, Heiroth HJ, et al. **Early perfusion computerized tomography imaging as a radiographic surrogate for delayed cerebral ischemia and functional outcome after subarachnoid hemorrhage.** *Stroke* 2013;44:1260–66 CrossRef Medline
20. Turowski B, Haenggi D, Wittsack HJ, et al. **Computerized analysis of brain perfusion parameter images [in German].** *Rofo* 2007;179:525–29 CrossRef Medline
21. Wittsack HJ, Wohlschläger AM, Ritzl EK, et al. **CT-perfusion imaging of the human brain: advanced deconvolution analysis using circulant singular value decomposition.** *Comput Med Imaging Graph* 2008;32:67–77 CrossRef Medline
22. Teasdale GM, Drake CG, Hunt T, et al. **A universal subarachnoid hemorrhage scale: report of a committee of the World Federation of Neurosurgical Societies.** *J Neurol Neurosurg Psychiatry* 1988;51:1457 CrossRef Medline
23. Rankin J. **Cerebral vascular accidents in patients over the age of 60.** *Scott Med J* 1957;2:200–15 CrossRef Medline
24. Claassen J, Bernardini GL, Kreiter K, et al. **Effect of cisternal and ventricular blood on risk of delayed cerebral ischemia after subarachnoid hemorrhage: the Fisher scale revisited.** *Stroke* 2001;32:2012–20 CrossRef Medline
25. Fisher CM, Kistler JP, Davis JM. **Relation of cerebral vasospasm to subarachnoid hemorrhage visualized by computerized tomographic scanning.** *Neurosurgery* 1980;6:1–9 CrossRef Medline
26. Mathys C, Martens D, Reichelt DC, et al. **Long-term impact of perfusion CT data after subarachnoid hemorrhage.** *Neuroradiology* 2013;55:1323–31 CrossRef Medline
27. Beseoglu K, Etminan N, Haenggi D. **The value of perfusion computed tomography (PCT) imaging after aneurysmal subarachnoid hemorrhage: a review of the current data.** *Acta Neurochir Suppl* 2015;120:35–38 CrossRef Medline

28. Murphy A, Manoel AL, Burgers K, et al. **Early CT perfusion changes and blood-brain barrier permeability after aneurysmal subarachnoid hemorrhage.** *Neuroradiology* 2015;57:767–73 CrossRef Medline
29. Anzabi M, Angleys H, Aamand R, et al. **Capillary flow disturbances after experimental subarachnoid hemorrhage: a contributor to delayed cerebral ischemia?** *Microcirculation* 2019;26:e12516 CrossRef Medline
30. Wintermark M, Ko NU, Smith WS, et al. **Vasospasm after subarachnoid hemorrhage: utility of perfusion CT and CT angiography on diagnosis and management.** *AJNR Am J Neuroradiol* 2006;27:26–34 Medline
31. Mir DI, Gupta A, Dunning A, et al. **CT perfusion for detection of delayed cerebral ischemia in aneurysmal subarachnoid hemorrhage: a systematic review and meta-analysis.** *AJNR Am J Neuroradiol* 2014;35:866–71 CrossRef Medline
32. Rosen DS, Macdonald RL. **Subarachnoid hemorrhage grading scales: a systematic review.** *NCC* 2005;2:110–18 CrossRef Medline
33. Caspers J, Rubbert C, Turowski B, et al. **Timing of mean transit time maximization is associated with neurological outcome after subarachnoid hemorrhage.** *Clin Neuroradiol* 2017;27:15–22 CrossRef Medline
34. Fragata I, Alves M, Papoila AL, et al. **Temporal evolution of cerebral computed tomography perfusion after acute subarachnoid hemorrhage: a prospective cohort study.** *Acta Radiol* 2020;61:376–85 CrossRef Medline
35. Philipp JS, Marcel AK, Thomas B, et al. **The influence of decompressive craniectomy for major stroke on early cerebral perfusion.** *J Neurosurg* 2015;123:59–64 CrossRef Medline

# MTT and Blood-Brain Barrier Disruption within Asymptomatic Vascular WM Lesions

 B.E. Dewey,  X. Xu,  L. Knutsson,  A. Jog,  J.L. Prince,  P.B. Barker,  P.C.M. van Zijl,  R. Leigh, and  P. Nyquist



## ABSTRACT

**BACKGROUND AND PURPOSE:** White matter lesions of presumed ischemic origin are associated with progressive cognitive impairment and impaired BBB function. Studying the longitudinal effects of white matter lesion biomarkers that measure changes in perfusion and BBB patency within white matter lesions is required for long-term studies of lesion progression. We studied perfusion and BBB disruption within white matter lesions in asymptomatic subjects.

**MATERIALS AND METHODS:** Anatomic imaging was followed by consecutive dynamic contrast-enhanced and DSC imaging. White matter lesions in 21 asymptomatic individuals were determined using a Subject-Specific Sparse Dictionary Learning algorithm with manual correction. Perfusion-related parameters including CBF, MTT, the BBB leakage parameter, and volume transfer constant were determined.

**RESULTS:** MTT was significantly prolonged (7.88 [SD, 1.03] seconds) within white matter lesions compared with normal-appearing white (7.29 [SD, 1.14] seconds) and gray matter (6.67 [SD, 1.35] seconds). The volume transfer constant, measured by dynamic contrast-enhanced imaging, was significantly elevated (0.013 [SD, 0.017] minutes<sup>-1</sup>) in white matter lesions compared with normal-appearing white matter (0.007 [SD, 0.011] minutes<sup>-1</sup>). BBB disruption within white matter lesions was detected relative to normal white and gray matter using the DSC-BBB leakage parameter method so that increasing BBB disruption correlated with increasing white matter lesion volume (Spearman correlation coefficient = 0.44;  $P < .046$ ).

**CONCLUSIONS:** A dual-contrast-injection MR imaging protocol combined with a 3D automated segmentation analysis pipeline was used to assess BBB disruption in white matter lesions on the basis of quantitative perfusion measures including the volume transfer constant (dynamic contrast-enhanced imaging), the BBB leakage parameter (DSC), and MTT (DSC). This protocol was able to detect early pathologic changes in otherwise healthy individuals.

**ABBREVIATIONS:** cSVD = cerebrovascular small-vessel disease; DCE = dynamic contrast-enhanced; Gd = gadolinium;  $K_2$  = BBB leakage parameter;  $k^{trans}$  = volume transfer constant; WML = white matter lesion

Understanding vascular contributions that influence cognitive decline and dementia is a national research priority.<sup>1,2</sup> Cerebrovascular small-vessel disease (cSVD) is associated with stroke and dementia and is potentially modifiable.<sup>3-5</sup> Many aspects of vascular disease of the brain can be detected with MR

imaging. Features associated with cSVD include small subcortical (lacunar) infarcts, white matter hyperintensities, dilated perivascular spaces, microbleeds, brain atrophy, and increased BBB permeability.<sup>6,7</sup> White matter lesions (WMLs) seen on T2-weighted MR imaging are the most common feature of cSVD, estimated to represent 40% of cSVD disease burden.<sup>6</sup> WMLs are accompanied by many pathologic changes, including BBB disruption.<sup>8-17</sup> While other multifactorial pathophysiologic mechanisms are undoubtedly involved, including hypertension, genetic factors, and inflammation,<sup>18-25</sup> changes in CBF and


Received October 16, 2020; accepted after revision March 13, 2021.

From the Departments of Electrical and Computer Engineering (B.E.D., J.L.P.) and Radiology and Radiological Science (X.X., L.K., J.L.P., P.B.B., P.C.M.v.Z.), Division of MRI Research, and Department of Neurology (R.L., P.N.), Johns Hopkins University, Baltimore, Maryland; F.M. Kirby Research Center for Functional Brain Imaging (B.E.D., X.X., P.B.B., P.C.M.v.Z.), Kennedy Krieger Institute, Baltimore, Maryland; Department of Medical Radiation Physics (L.K.), Lund University, Lund, Sweden; and Athinoula A. Martinos Center for Biomedical Imaging (A.J.), Harvard University Medical School, Boston Massachusetts.

B.E. Dewey and X. Xu contributed equally to this work.

This work was supported by funding from the National Institutes of Health—National Institute of Neurological Disorders and Stroke (R01NS062059) and the Johns Hopkins Department of Anesthesia, Stimulating and Advancing ACCM Research award.

Please address correspondence to Paul Nyquist, MD, Johns Hopkins, Department of Neurology, 416 Phipps, 600 N Wolfe St, Baltimore MD 21287; e-mail: pnyquist@jhmi.edu

 Indicates open access to non-subscribers at [www.ajnr.org](http://www.ajnr.org)

 Indicates article with online supplemental data.

<http://dx.doi.org/10.3174/ajnr.A7165>



increasing BBB permeability have been implicated as markers of WML progression and may have a causative role.<sup>13,26</sup>

Quantifying different measures of hemodynamics such as CBF, CBV, and BBB disruption directly within WMLs has been difficult. Previous studies have shown decreased CBF in larger brain regions associated with WMLs but not within WMLs themselves.<sup>6,7,17,26-32</sup> These studies have also identified increased regional nonlesional volume transfer constant ( $K^{trans}$ ) using gadolinium (Gd)-based dynamic contrast-enhanced (DCE) MR imaging, but these methods have drawbacks such as decreased signal discrimination within and without WMLs and a dependence on adequate correction for decreased perfusion within WMLs.<sup>7,31,33</sup> Some studies have detected decreased CBF within lesions using arterial spin-labeling,<sup>34</sup> while others have detected these changes within regions surrounding WMLs and within ROIs within WMLs.<sup>26,35</sup>

Presently, new imaging approaches and data-processing pipelines are needed to allow us to segment WMLs and measure subtle intralesion changes in CBF, MTT, and BBB disruption. Measures of BBB permeability incorporate MR imaging surrogates, which detect Gd extravasation outside the microvasculature due to disruption of the BBB related to microvascular injury.<sup>7,31</sup> In the current study, on a voxel-by-voxel basis, we quantify 2 different parameters related to tissue abnormality:  $K^{trans}$  from DCE MR imaging and the BBB leakage parameter ( $K_2$ ) from DSC MR imaging,<sup>28,29</sup> which can relate changes in BBB transport and/or CBF.<sup>36</sup> These values can then be assessed for WMLs to get insight into changes in BBB functioning and tissue perfusion. In addition, we assessed MTT, which reflects tissue perfusion.

In the Genetic Study of Atherosclerosis Risk (GeneSTAR) cohort study, we have identified individuals with a family history of early-onset coronary vascular disease with earlier WMLs detected in midlife,<sup>37</sup> with a concomitant impact on measures of cognitive-motor function.<sup>38</sup> In this relatively young high-risk subgroup (average age, 54.1 [SD, 3.5] years) of 21 participants with repeat MR imaging, we have observed rapid rates of WML progression associated with cognitive decline.<sup>39</sup> In this study, we present a data-analysis pipeline that incorporates segmentation of WMLs<sup>40,41</sup> and quantification of perfusion-based measures of MTT, CBF,  $K_2$ , and  $K^{trans}$  from both DSC and DCE MR imaging. This work builds on previous work measuring microvascular perfusion and Gd extravasation in different regions of the brain.<sup>31,42</sup> We propose that these Gd-based representations of BBB disruption in WMLs, with knowledge of the CBF, may enable identifying WMLs at risk of progression at a stage at which they may respond to strategies of disease prevention.<sup>3,4,6</sup>

## MATERIALS AND METHODS

### Patient Recruitment

The 21 participants in this repeat imaging study were healthy family members of relatives with known early-onset coronary artery disease who were randomly selected (2008–2013) from a previous GeneSTAR WML study and recruited.<sup>43</sup> The study was approved by the institutional review board and was conducted at the Johns Hopkins medical campus in Baltimore, Maryland.<sup>44</sup> The parent study was designed to characterize the genetic and biologic traits associated with incident cardiovascular disease.<sup>38</sup> In the larger GeneSTAR study, probands were identified during

hospitalization for an acute coronary syndrome or acute myocardial infarction or with angiographic evidence of a flow-limiting stenosis before 60 years of age. Probands did not participate in the final study by design. Apparently healthy asymptomatic siblings, their offspring, and the offspring of the probands were eligible if they were 29–75 years of age and had no personal history of coronary artery disease, stroke, or TIAs. The 21 participants in this study were recruited from a cohort of 714 participants in a previous MR imaging substudy from the larger GeneSTAR study population (54.1 [SD, 3.5] years, 45% hypertensive). Written consent was obtained from each participant.

### MR Imaging

The participants were examined using a 3T Achieva MR imaging scanner (Philips Healthcare) with a 32-channel head coil. The examination protocol is illustrated in the Online Supplemental Data. The structural series included axial T1-weighted MPRAGE and axial turbo spin-echo FLAIR as follows: The MPRAGE sequence was chosen over other T1WI sequences due to its excellent GM/WM contrast. The sequence parameters are the following: 1) axial T1-weighted MPRAGE: flip angle = 8°, TR = 10 ms, TE = 6 ms, voxel size = 1.0 × 1.0 × 1.0 mm, contiguous slices, FOV = 240 × 240 × 160 mm, and reconstruction matrix = 320 × 320 × 160; and 2) axial turbo spin-echo FLAIR: TR = 11,000 ms, TI = 2800 ms, TE = 68 ms, voxel size = 0.98 × 0.98 × 3.0 mm, contiguous slices, FOV = 240 × 240 × 132 mm, and reconstruction matrix = 512 × 512. The Online Supplemental Data show an example of the MPRAGE, FLAIR, precontrast baseline DCE, and DSC images from 1 participant. The structural images were reviewed by the Principal Investigator to ascertain any health concerns. The examinations were follow-up MRIs obtained after a prior MR imaging that had been reviewed by a neuroradiologist and were deemed to have normal findings with the exception of signs of WM hyperintensity and age-related microvascular disease. No lacunar infarcts were detected in this study cohort by clinical radiologists and the study investigator.

T1 mapping was performed before contrast agent injection with an inversion recovery Look-Locker sequence at resolution of 2 × 2.2 × 4 mm<sup>3</sup> with a flip angle of 4° and a TR of 2.6 seconds. The first TI was 38.5 ms, and the spacing between successive time points was 69 ms. Thirty-eight images with different TIs were recorded for a total of 11 slices. The total scan time was 112 seconds.

A T1-weighted gradient-echo sequence was used for DCE imaging using the following parameters: flip angle = 26°, TE = 2.5 ms, TR = 5.1 ms, resolution = 22 × 2.22 × 4 mm<sup>3</sup>. Gadoteridol (ProHance; Bracco Diagnostics) was given at a dosage of 0.1 mmol/kg via a power injector. The contrast agent was injected with an injection delay of 30 seconds (14 precontrast baseline images) at a speed of 5 mL/s, followed by a 20-mL saline rinse with the same speed. The time for acquiring each dynamic scan was 2.5 seconds for 11 slices, and a total of 150 dynamic series were acquired. A postcontrast MPRAGE image was acquired after the Gd contrast injection.

Approximately 6 minutes after the DCE scan, DSC imaging was performed using single-shot EPI with TE = 29 ms, TR = 1500 ms, flip angle = 90°, and resolution = 2 × 2.2 × 4 mm.<sup>3</sup> A

second dose of gadoteridol was injected with a 15-second injection delay (10 precontrast baseline images) at a speed of 5 mL/s, followed by a 20-mL saline rinse with the same speed. The time for acquiring each dynamic scan was 1.5 seconds, and a total of 80 dynamic series were acquired for 25 slices covering most of the brain. As a direct comparison with the precontrast image, the MPAGE sequences were repeat postcontrast, with the same parameters as those in precontrast, for direct identification of any lesion enhancement.

### Data Processing

Anatomic volumes of discrete brain regions and tissue types were determined with MPAGE images, and WML volumes were determined using FLAIR images coregistered into Montreal Neurological Institute space.<sup>45</sup> Spatial normalization of coregistered MPAGE and FLAIR images into Montreal Neurological Institute space was performed via affine transformation. MPAGE images were skull-stripped and coregistered to FLAIR images. Within this pilot study, there was some enlargement of perivascular spaces observed, but they were not systematically quantified.

### DCE and DSC Postprocessing

DSC, DCE dynamic images, and T1 maps were processed using nordicICE (NordicNeuroLab). For each participant, first, a precontrast T1 map was calculated by fitting the Look-Locker inversion recovery images to a model. The DCE dynamic images were motion-corrected, and the  $K^{\text{trans}}$  maps were calculated using the extended Tofts model.<sup>46</sup> The arterial input function used in the extended Tofts model was defined by taking the average of semi-automatically selected voxels (2 or 3 voxels) within the anterior cerebral arteries for each participant in the DCE images.

To calculate the CBF and MTT maps, we processed the DSC images for perfusion parameters using delay-insensitive singular value deconvolution with a threshold of 0.15 for regularization.<sup>47</sup> The arterial input function was defined by taking the average of semi-automatically selected voxels (5 voxels) within the branches of the middle cerebral artery around the Sylvian fissure. The reason for not choosing the same arteries as in DCE is that DSC is subjected to distortions due to the EPI readout in the frontal part of the brain due to susceptibility artifacts. No leakage correction was applied for the postprocessing.

The pre-infusion images from the DCE and DSC scans were averaged and coregistered to the MPAGE image using a fully automated pipeline, BrainMap (<http://brainmap.org/software.html>).<sup>48</sup> The pipeline performed image registration using the Advanced Normalization Tools (ANTs; <http://stnava.github.io/ANTs>) software package,<sup>49</sup> skull removal using Multi-contrast brain STRipping (MONSTR; <https://www.nitrc.org/projects/monstr/>),<sup>50</sup> whole-brain gray/white matter segmentation using Multi-Atlas Cortical Reconstruction Using Implicit Surface Evolution (MaCRUISE; <https://github.com/MASILab/MaCRUISE>),<sup>51</sup> and lesion segmentation using the Subject-Specific Sparse Dictionary Learning (S3DL; [http://iacl.ece.jhu.edu/index.php?title=Subject\\_Specific\\_Sparse\\_Dictionary\\_Learning\\_for\\_Atlas\\_Based\\_Brain\\_MRI\\_Segmentation](http://iacl.ece.jhu.edu/index.php?title=Subject_Specific_Sparse_Dictionary_Learning_for_Atlas_Based_Brain_MRI_Segmentation)).<sup>41</sup> Automatically segmented lesion masks were manually edited to remove false-positives common to this

process. Segmentation masks were eroded (except for lesion masks) and applied to parameter maps to extract ROIs representing normal-appearing WM, GM, and WMLs. To extract parameter values for each participant, we took the median voxel value in each ROI from the CBF, MTT, and  $K^{\text{trans}}$  maps.

In addition to calculating perfusion metrics, DSC images were also separately processed to calculate  $K_2$  values.<sup>52</sup> DSC images are T2\*-weighted, and intravascular gadolinium causes a decrease in signal due to its susceptibility artifacts. However, DSC images also have some T1-weighting that is proportional to the concentration of gadolinium in the tissue.<sup>32</sup> During a DSC acquisition, the measured change in signal is due to both intravascular gadolinium (flow-dependent) and parenchymal gadolinium (leak-dependent).<sup>53</sup> Using normal tissue as a reference, one can isolate the signal due to gadolinium leakage from the signal due to intravascular gadolinium.<sup>52</sup> Normal tissue can be identified by excluding voxels that exhibit signal changes due to gadolinium leakage.<sup>28</sup> In our case, in which leakage is small and limited to a few white matter regions, a “normal brain DSC response curve” was defined from a whole-volume analysis (about 3000 voxels). Subsequently, arrival time correction<sup>52</sup> was applied to each individual voxel by scaling (width and height of the initial response) and shifting (position of the peak maximum of the initial response) the DSC dynamic curves.  $K_2$  in each voxel was then determined using

$$\Delta\tilde{R}2^*(t)_{ATC} = \overline{\Delta R2^*}(t) - K_2 \int_0^t \overline{\Delta R2^*}(t') dt',$$

in which  $\Delta\tilde{R}2^*(t)_{ATC}$  is the corrected change in relaxivity and  $\overline{\Delta R2^*}(t)$  is the average signal of the normal brain. Thus,  $K_2$  reflects the proportion of the recorded signal that is due to gadolinium leakage. The resulting voxel-by-voxel measure of  $K_2$  was used to generate a blood-brain permeability image in which voxels were assigned as normal when the fitted  $K_2$  was  $<0.1\%$ .

FLAIR images were coregistered to the DSC source images using a diffeomorphic registration pipeline.<sup>54</sup> By means of the combined transforms, the WML ROIs were moved from FLAIR space to DSC space. The mean  $K_2$  value for all voxels within the WML ROIs that demonstrated elevated BBB permeability (gadolinium leakage) was calculated for each patient and used in the subsequent analysis. The  $K_2$  analysis was performed on the DSC acquisition that occurred during the second dose of gadolinium administration.  $K_2$  is largely a first-pass measure as opposed to  $K^{\text{trans}}$ , which is measured in steady-state. Thus, for this study, the measured  $K_2$  reflects gadolinium leakage that occurred during the second injection and beyond steady-state background from the first injection.

### Statistical Analysis

All statistical analyses were performed using R statistical and computing software (<http://www.r-project.org/>).<sup>55</sup> Linear mixed effects modeling was used for statistical comparison among WM, GM, and WMLs based on the ROI level. Significance levels were assessed using paired Wilcoxon signed rank tests. Spearman correlations coefficients were calculated between lesion volumes and subjects.

## RESULTS

All scans were read by the investigator and then read formally by a clinical neuroradiologist. There were no lacunar infarcts detected in this small study. Within this small group included in the pilot study, there was a significant quantity of atrophy observed and there was some enlargement of perivascular spaces observed, but these were not systematically quantified.

T1 MPRAGE images were used for GM and WM segmentation, and FLAIR images were used for lesion assignment. Notice that some lesions are not highlighted due to the size of the lesions and the detection limitations of the algorithm. The nonsegmented lesions were not included in the analysis. None of the subjects' images showed any contrast enhancement on the post-contrast MPRAGE. Two subjects were excluded due to technical problems in the contrast agent administration. Representative images for the CBF, MTT, and  $K^{trans}$  maps, and their overlays on anatomic images of 1 participant are presented in the Online Supplemental Data. The perfusion images were interpolated to match the FLAIR resolution. MTT values are elevated within and around the clusters of WMLs (Online Supplemental Data). While all ROIs followed an approximately normal distribution, given the limited sample size, the median values were calculated instead of the mean. The boxplot in the Online Supplemental Data shows the median and interquartile range of MTT in the GM, WM, and WMLs of all participants. Paired Wilcoxon signed rank tests reveal that the MTT is significantly prolonged ( $P < .001$ ) in WMLs (7.88 [SD,  $\pm 1.03$ ] seconds, median + interquartile range) compared with normal-appearing WM (6.67 [SD, 1.35] seconds), suggesting that these areas of the brain have associated vascular pathology. We also see that there is a small-but-significant difference ( $P < .001$ ) in MTT for the reference WM and GM (7.29 [SD, 1.14] seconds) ROIs. CBF values were also calculated, and we found that there is no significant difference in CBF between WMLs and WM ( $P = .62$ ).

The Online Supplemental Data show boxplots of the mean values for each ROI for  $K^{trans}$  for all participants.  $K^{trans}$  showed a much larger variance between subjects with smaller difference between ROIs. The  $K^{trans}$  values were significantly different ( $P < .001$ ) between the WMLs (0.013 [SD, 0.017] minutes<sup>-1</sup>) and the normal-appearing WM (0.007 [SD, 0.011] minutes<sup>-1</sup>).

The Online Supplemental Data show an example of color-coded  $K_2$  values overlaid on a gray-scale DSC source image. Voxels in the WMLs are shown in color, with increasing BBB disruption going from green (least severe) to yellow to orange to red (most severe). The Online Supplemental Data show the signal change ( $\Delta R$ ) with time (at each dynamic) of the recorded signal (red dashed lines) and the normal average signal (solid blue lines) before and after applying the arrival time correction. The Online Supplemental Data are for a voxel with a  $K_2$  of 0.1% (a green voxel from panel A). The Online Supplemental Data are for a voxel with a  $K_2$  value of 3.5% (a red voxel in panel A). Note that in the setting of BBB disruption, the dashed line is pulled down below the baseline due to the T1 effects from contrast leakage into the tissue. Using the DSC- $K_2$  technique, we averaged voxels within segmented WMLs with elevated  $K_2$ . The average  $K_2$  value across the cohort was 2.67 [SD, 2.33%]. This value was correlated with 3 variables: total WML volume, subcortical WML volume,

and periventricular WML volume. Increasing average  $K_2$  was significantly correlated with total WML volume (Spearman correlation = 0.44;  $P < .046$ ), and there was a trend toward correlation with periventricular WML volume (Spearman correlation = 0.44;  $P < .071$ ). No significant correlation with subcortical WML volume (Spearman correlation = 0.0078;  $P < .973$ ) was found.

## DISCUSSION

The underlying pathophysiology causing cSVD and WMLs has been attributed to intermittent ischemia due to microvascular narrowing and altered compliance leading to transient hypoperfusion in vulnerable watershed zones.<sup>4,26,31</sup> Exogenous contrast-based perfusion MR imaging has been used extensively to image hemodynamic changes in the microvasculature of ischemic white matter disease.<sup>4,27,31,32,34,35,42,56,57</sup> Most studies have taken the strategy of quantifying perfusion parameters in different regions of the whole brain, as opposed to measuring these parameters within WMLs, and comparing them with overall WML burden.<sup>14,27,34,35,42</sup> While a few studies have separately used arterial spin-labeling<sup>34</sup> and Gd-based perfusion MR imaging within lesions,<sup>4,27,35,42,56</sup> these lesion studies differ from ours in that they either used strategies focused on limited ROIs, including nonlesional white matter, or determined the WML volume using manual readers.<sup>25,27,31,54,58</sup>

Our approach is different from the approaches in these other studies in that we used an automated WML segmentation pipeline allowing us to determine the CBF, MTT,  $K_2$ , and  $K^{trans}$  within individual WMLs and compare them with normal-appearing WM and GM.<sup>41,45,59</sup> Automated technology is required to study perfusion parameters and BBB disruption in large epidemiology studies to ensure consistency and speed in analysis.<sup>4,6,13</sup> Our study design allows one to obtain perfusion parameters such as CBF, MTT,  $K_2$ , and  $K^{trans}$  in the same scan session. We found significant increases in MTT and  $K^{trans}$ , but no significant change in CBF within WMLs compared with unaffected GM and WM. Gd leakage detected with  $K_2$  indicated more severe BBB disruption in subjects with a larger burden of WMLs.

The measurement of absolute CBF using DSC is difficult due to the lack of a direct linear relationship between contrast concentration and the signal change and partial volume effects in the arterial input function.<sup>36</sup> Therefore, it is common to use relative values, making it difficult to make comparisons among different studies and cohorts. MTT reflects the average time for the blood to pass through a given region of brain tissue, and it is calculated by dividing the CBV by the CBF or using the Zierler area-to-height relationship.<sup>60,61</sup> The MTT is measured in seconds, and the reverse MTT reflects the local cerebral perfusion pressure.<sup>30</sup> MTT removes the need for obtaining absolute values of CBF and CBV; therefore, MTT has the potential to serve as a marker of hemodynamic change in white matter diseases. Tissue with decreased cellularity or metabolic activity could have decreased CBF; for example, Promjunyakul et al<sup>62</sup> reported reduced CBF in WMLs as well as the adjacent normal-appearing WM regions beyond the WMLs, using the arterial spin-labeling technique in elderly volunteers (mean age, 84.1 years).

Our study has some differences compared with this article: First, the CBF in our article was measured using DSC MR



imaging. DSC MR imaging has better contrast-to-noise in white matter than arterial spin-labeling, in which the lower SNR makes the detection of changes less sensitive.<sup>63</sup> Also, the resolution in the above article is  $3 \times 3 \times 4 \text{ mm}^3$  compared with  $2 \times 2.2 \times 4 \text{ mm}^3$  in our study. Therefore, we could better place the voxels without the risk of partial volume effects. There should not have been a significant contribution of a perilesional zone, if any. Second, because we did not find decreased CBF within WMLs in the current study, it is not likely that the perilesional zone would have decreased the CBF. One significant difference between this article and most other literature is that the patient cohort is relatively young and asymptomatic. We found no change in CBF between WMLs and normal-appearing WM, while the MTT (CBV/CBF) was elevated, indicating compensatory vasodilation and reduced cerebrovascular resistance due to autoregulation. The elevated MTT observed in the WMLs before CBF changes may be an early indicator of asymptomatic cSVD.

Gadoteridol is a macrocyclic gadolinium-based contrast agent that is approved for multidose application. It was recommended that one-fourth-dose to 1 full-dose contrast agent preload be given 5–10 minutes before the DSC scan to reduce the T1 effect caused by contrast agent extravasation.<sup>64</sup> In our study, one full dose of gadoteridol was injected, which served as a preload for DSC and also allowed us to perform the DCE experiment. We studied  $K^{\text{trans}}$  derived from the DCE experiment using the extended Tofts model to provide more information about BBB disruption.  $K^{\text{trans}}$  is a combination parameter that includes both permeability and perfusion. In a perfusion-limiting situation, the measured  $K^{\text{trans}}$  may reflect perfusion instead of permeability. It has been shown that during a low-leakage situation, there is a risk that  $K^{\text{trans}}$  will be overestimated using the extended Tofts model.<sup>65</sup> Because we did not observe any visible enhancement, we believe that the risk of overestimation was avoided. We have also found that the CBF was maintained in the WMLs, and the elevated  $K^{\text{trans}}$  can be attributed to increased permeability in the WMLs compared with the normal-appearing WM. However, the T1-based DCE experiment is inherently noisier, and the calculation of  $K^{\text{trans}}$  requires fitting that may not be robust. In addition,  $K^{\text{trans}}$  itself cannot be used to reflect permeability without knowledge of CBF.

In our study, we performed 2 gadolinium injections. DSC images are used to measure perfusion parameters. The signal change on the R2\*-weighted DSC source images during the passage of a gadolinium bolus is dominated by susceptibility effects from the intravascular contrast agent. However, in the presence of gadolinium leakage, the recorded signal is augmented by a T1 effect, acting in the opposite direction, which is proportional to the concentration of gadolinium leakage (Online Supplemental Data). Thus, after arrival time correction, the effect of gadolinium leakage can be isolated as  $K_2$  (Online Supplemental Data).  $K_2$  reflects the signal change due to gadolinium leakage through the BBB during the first (and, to a lesser extent, the second) pass of the gadolinium bolus through the brain. Using the DSC- $K_2$  approach has the advantage that the effects of blood flow and BBB permeability are being collected simultaneously during a first pass as opposing signals. In contrast, the DCE- $K^{\text{trans}}$  approach requires interpreting a separately acquired perfusion

metric with a steady-state model of T1 signal change in which the effect may not be large enough to be measured in the setting of reduced blood flow. In addition, when the second gadolinium injection was given, the first injection was considered to be at steady-state. Therefore, any leakage detected by  $K_2$  for the second injection reflects first-pass effects beyond the background steady-state signal. Using the DSC- $K_2$  method, we found that higher  $K_2$  values were significantly correlated with total WML volume, suggesting that in these asymptomatic patients, increasing WML volume is associated with increasing disruption of the BBB.

A recent article by Wong et al<sup>26</sup> demonstrated that increased extravasation of Gd correlated with declines in CBF in the perilesional zone of WMLs. This approach solidifies the association of hypoperfusion with lesion progression and BBB disruption. The Patlak graphic method used in the article to measure Gd transition into the lesion is perfusion-dependent. Even though  $K_2$  is a dimensionless, relative measure, it has the advantage that  $K_2$  is not dependent on perfusion and is suited for detection of smaller BBB breakdown effects in regions of lower CBF. In our study, manual detection of increasing  $K_2$  was observed in proximity to WML borders as well but was not quantifiable in an automated fashion and could not be associated with declining perfusion in proximity to the WML border. Imaging techniques to simultaneously assess MTT, CBF, CBV,  $K^{\text{trans}}$ , and  $K_2$  are essential to study how changes in perfusion affect WML progression<sup>14,27,31,34</sup> and allow investigation of how subsequent BBB breakdown with associated increases in measured BBB disruptions may precede brain parenchymal injury in WMLs.<sup>4,31,42</sup> It has been previously observed in other studies that BBB disruption in gray matter and normal-appearing white matter is increased with increasing WML burden and other signs of small-vessel disease and this has been studied extensively in white matter hyperintensities and Alzheimer disease.

Our study was not powered or designed to detect changes BBB disruption/permeability in normal-appearing white matter in general but only to compare existing WMLs and normal-appearing white matter BBB disruption using our combined imaging approach. Finding a control group without WMLs within the original study sample is very difficult because 90% of all participants in this study have signs of white matter hyperintensities, regardless of risk factors. The patients were selected across the 800 or so included in the study. They were selected for the following reasons: high or low white matter hyperintensity burden, age, sex, the presence of hypertension, and ethnicity. They were balanced to reflect the age, race, sex, and relative demographic composition of the original sample. Currently, it is difficult to know how BBB disruption could be used to predict WML progression without a study involving repeat imaging of the participant at 2 separate points in time. In future prospective studies with a larger sample size, one may have the statistical power to establish a permeability threshold above which the WMLs are at risk of expansion or the WM is at risk of lesion formation.

There are several limitations to our study. Our technique incorporated coregistration of segmented lesions of brain WMLs with brain perfusion images. The large section thickness of perfusion scans relative to the higher-resolution FLAIR images may

have resulted in a partial volume effect. Additionally, some of the smaller lesions were too small to allow accurate measurement of the perfusion characteristics and, thus, were not picked up by the automatic analysis. Due to the small sizes of the lesions and the difficulty in obtaining adequate segmentation in such small areas, lesion masks were not eroded and may include some partial volume on the edges of lesions. Finally, the  $K_2$  values depend on a time integration of the difference signal for the  $\Delta R_2^*$  curves. A disadvantage of this approach is that  $K_2$  depends on the MR imaging parameters and number of dynamics (length of the curve) used in the analysis. Thus, while the  $K_2$  values will provide an accurate reflection of BBB breakdown when used consistently within a study, they can differ in absolute value among studies.

## CONCLUSIONS

The results show that MTT was increased significantly within WMLs compared with normal-appearing GM and WM, while no significant CBF alteration was found between WMLs and normal-appearing WM. These findings indicate vasodilation within the WMLs to maintain normal blood flow. Significantly elevated  $K^{trans}$  was observed within WMLs compared with the normal-appearing WM. IntraleSION BBB patency was also evaluated in terms of  $K_2$  using DSC data demonstrating increasing BBB disruption within WMLs with increased total WML volume. These findings suggest that DSC perfusion provides valuable information in assessing cSVD because MTT may be an early marker for an asymptomatic stage of the ischemic disease before CBF is affected and the value of BBB disruption as measured by  $K_2$  may shine light on the process of disease progression.

Disclosures: Linda Knutsson—RELATED: Grant: Swedish Research Council, Swedish Cancer Society\*; Support for Travel to Meetings for the Study or other Purposes: Swedish Research Council, Swedish Cancer Society.\* Jerry L. Prince—UNRELATED: Grants/Grants Pending: Biogen, Comments: contract on brain image processing of people with multiple sclerosis.\* Peter C.M. van Zijl—UNRELATED: Grants/Grants Pending: Philips Healthcare, Comments: research, support/equipment; Payment for Lectures Including Service on Speakers Bureaus: Philips Healthcare, Comments: lectures; Patents (Planned, Pending or Issued): Philips Healthcare, Comments: patents licensed; Travel/Accommodations/Meeting Expenses Unrelated to Activities Listed: Philips Healthcare, Comments: travel to give lectures. \*Money paid to the institution.

## REFERENCES

- Corriveau RA, Bosetti F, Emr M, et al. **The science of vascular contributions to cognitive impairment and dementia (VCID): a framework for advancing research priorities in the cerebrovascular biology of cognitive decline.** *Cell Mol Neurobiol* 2016;36:281–88 CrossRef Medline
- Corriveau RA, Koroshetz WJ, Gladman JT, et al. **Alzheimer's disease-related dementias summit 2016: national research priorities.** *Neurology* 2017;89:2381–91 CrossRef Medline
- Bath PM, Wardlaw JM. **Pharmacological treatment and prevention of cerebral small vessel disease: a review of potential interventions.** *Int J Stroke* 2015;10:469–78 CrossRef Medline
- Wardlaw JM, Smith C, Dichgans M. **Mechanisms of sporadic cerebral small vessel disease: insights from neuroimaging.** *Lancet Neurol* 2013;12:483–97 CrossRef Medline
- Edrissi H, Schock SC, Cadonic R, et al. **Cilostazol reduces blood brain barrier dysfunction, white matter lesion formation and motor deficits following chronic cerebral hypoperfusion.** *Brain Res* 2016;1646:494–503 CrossRef Medline
- Wardlaw JM, Smith EE, Biessels GJ, et al. **Neuroimaging standards for research into small vessel disease and its contribution to ageing and neurodegeneration.** *Lancet Neurol* 2013;12:822–38 CrossRef Medline
- Thrippleton MJ, Backes WH, Sourbron S, et al. **Quantifying blood-brain barrier leakage in small vessel disease: review and consensus recommendations.** *Alzheimers Dement* 2019;15:840–58 CrossRef Medline
- Tsai CF, Thomas B, Sudlow CL. **Epidemiology of stroke and its subtypes in Chinese vs white populations: a systematic review.** *Neurology* 2013;81:264–72 CrossRef Medline
- Maillard P, Carmichael O, Fletcher E, et al. **Coevolution of white matter hyperintensities and cognition in the elderly.** *Neurology* 2012;79:442–48 CrossRef Medline
- Traylor M, Lewis CM. **Genetic discovery in multi-ethnic populations.** *Eur J Hum Genet* 2016;24:1097–98 CrossRef Medline
- Vermeer SE, Longstreth WT Jr, Koudstaal PJ. **Silent brain infarcts: a systematic review.** *Lancet. Neurol* 2007;6:611–19 CrossRef Medline
- Li Y, Li M, Zuo L, et al. **Compromised blood-brain barrier integrity is associated with total magnetic resonance imaging burden of cerebral small vessel disease.** *Front Neurol* 2018;9:221 CrossRef Medline
- Luciano M, Marioni RE, Valdes HM, et al. **Structural brain MRI trait polygenic score prediction of cognitive abilities.** *Twin Res Hum Genet* 2015;18:738–45 CrossRef Medline
- Habes M, Erus G, Toledo JB, et al. **White matter hyperintensities and imaging patterns of brain ageing in the general population.** *Brain* 2016;139:1164–79 CrossRef Medline
- Maki T, Hayakawa K, Pham LD, et al. **Biphasic mechanisms of neurovascular unit injury and protection in CNS diseases.** *CNS Neurol Disord Drug Targets* 2013;12:302–15 CrossRef Medline
- Lo EH, Rosenberg GA. **The neurovascular unit in health and disease: introduction.** *Stroke* 2009;40:S2–3 CrossRef Medline
- DeBette S, Markus HS. **The clinical importance of white matter hyperintensities on brain magnetic resonance imaging: systematic review and meta-analysis.** *BMJ* 2010;341:c3666 CrossRef Medline
- Jagust W. **Vulnerable neural systems and the borderland of brain aging and neurodegeneration.** *Neuron* 2013;77:219–34 CrossRef Medline
- Fornage M, DeBette S, Bis JC, et al. **Genome-wide association studies of cerebral white matter lesion burden: the charge consortium.** *Ann Neurol* 2011;69:928–39 CrossRef Medline
- Turner ST, Jack CR, Fornage M, et al. **Heritability of leukoaraiosis in hypertensive sibships.** *Hypertension* 2004;43:483–87 CrossRef Medline
- Verhaaren BF, DeBette S, Bis JC, et al. **Multiethnic genome-wide association study of cerebral white matter hyperintensities on MRI.** *Circ Cardiovasc Genet* 2015;8:398–409 CrossRef Medline
- Raina A, Zhao X, Grove ML, et al. **Cerebral white matter hyperintensities on MRI and acceleration of epigenetic aging: the Atherosclerosis Risk in Communities Study.** *Clin Epigenetics* 2017;9:21 CrossRef Medline
- Silbert LC, Lahna D, Promjunyakul NO, et al. **Risk factors associated with cortical thickness and white matter hyperintensities in dementia free Okinawan elderly.** *J Alzheimers Dis* 2018;63:365–72 CrossRef Medline
- Walker KA, Power MC, Hoogveen RC, et al. **Midlife systemic inflammation, late-life white matter integrity, and cerebral small vessel disease: the Atherosclerosis Risk in Communities Study.** *Stroke* 2017;48:3196–3202 CrossRef Medline
- Nam KW, Kwon HM, Jeong HY, et al. **High neutrophil to lymphocyte ratio is associated with white matter hyperintensity in a healthy population.** *J Neurol Sci* 2017;380:128–31 CrossRef Medline
- Wong SM, Jansen JF, Zhang CE, et al. **Blood-brain barrier impairment and hypoperfusion are linked in cerebral small vessel disease.** *Neurology* 2019;92:e1669–77 CrossRef Medline
- Markus HS, Lythgoe DJ, Ostegaard L, et al. **Reduced cerebral blood flow in white matter in ischaemic leukoaraiosis demonstrated using quantitative exogenous contrast-based perfusion MRI.** *J Neurol Neurosurg Psychiatry* 2000;69:48–53 CrossRef Medline

28. Arba F, Leigh R, Inzitari D, et al. **Blood-brain barrier leakage increases with small vessel disease in acute ischemic stroke.** *Neurology* 2017;89:2143–50 CrossRef Medline
29. Gupta N, Simpkins AN, Hitomi E, et al. **White matter hyperintensity-associated blood-brain barrier disruption and vascular risk factors.** *J Stroke Cerebrovasc Dis* 2018;27:466–71 CrossRef Medline
30. Schumann P, Touzani O, Young AR, et al. **Evaluation of the ratio of cerebral blood flow to cerebral blood volume as an index of local cerebral perfusion pressure.** *Brain* 1998;121:1369–79 CrossRef Medline
31. Shi Y, Thrippleton MJ, Makin SD, et al. **Cerebral blood flow in small vessel disease: a systematic review and meta-analysis.** *J Cereb Blood Flow Metab* 2016;36:1653–67 CrossRef Medline
32. Zaharchuk G. **Theoretical basis of hemodynamic MR imaging techniques to measure cerebral blood volume, cerebral blood flow, and permeability.** *AJNR Am J Neuroradiol* 2007;28:1850–58 CrossRef Medline
33. Patlak CS, Blasberg RG, Fenstermacher JD. **Graphical evaluation of blood-to-brain transfer constants from multiple-time uptake data.** *J Cereb Blood Flow Metab* 1983;3:1–7 CrossRef Medline
34. Brickman AM, Zahra A, Muraskin J, et al. **Reduction in cerebral blood flow in areas appearing as white matter hyperintensities on magnetic resonance imaging.** *Psychiatry Res* 2009;172:117–20 CrossRef Medline
35. Sachdev P, Wen W, Shnier R, et al. **Cerebral blood volume in T2-weighted white matter hyperintensities using exogenous contrast-based perfusion MRI.** *J Neuropsychiatry Clin Neurosci* 2004;16:83–92 CrossRef Medline
36. Knutsson L, Stahlberg F, Wirestam R. **Absolute quantification of perfusion using dynamic susceptibility contrast MRI: pitfalls and possibilities.** *MAGMA* 2010;23:1–21 CrossRef Medline
37. Nyquist PA, Bilgel M, Gottesman R, et al. **Age differences in periventricular and deep white matter lesions.** *Neurobiol Aging* 2015;36:1653–58 CrossRef Medline
38. Nyquist PA, Yanek LR, Bilgel M, et al. **Effect of white matter lesions on manual dexterity in healthy middle-aged persons.** *Neurology* 2015;84:1920–26 CrossRef Medline
39. Nyquist PA, Yanek LR, Kral BG, et al. **White matter lesion progression and cognitive function over 5 years in a young susceptible population.** *Neuroepidemiology* 2017;49:62–63 CrossRef Medline
40. Roy S, He Q, Sweeney E, et al. **Subject-specific sparse dictionary learning for atlas-based brain MRI segmentation.** *IEEE J Biomed Health Inform* 2015;19:1598–1609 CrossRef Medline
41. Roy S, Carass A, Prince JL, et al. **Subject-specific sparse dictionary learning for atlas based brain MRI segmentation.** *Mach Learning Med Imaging* 2014;8679:248–55 CrossRef Medline
42. O'Sullivan M, Lythgoe DJ, Pereira AC, et al. **Patterns of cerebral blood flow reduction in patients with ischemic leukoaraiosis.** *Neurology* 2002;59:321–26 CrossRef Medline
43. Becker DM, Yook RM, Moy TF, et al. **Markedly high prevalence of coronary risk factors in apparently healthy African-American and White siblings of persons with premature coronary heart disease.** *Am J Cardiol* 1998;82:1046–51 CrossRef Medline
44. Nyquist PA, Wityk R, Yanek LR, et al. **Silent small-vessel cerebrovascular disease and silent myocardial ischemia in families with premature coronary disease.** *Neuroepidemiology* 2009;33:66–67 CrossRef Medline
45. Shiee N, Bazin PL, Ozturk A, et al. **A topology-preserving approach to the segmentation of brain images with multiple sclerosis lesions.** *Neuroimage* 2010;49:1524–35 CrossRef Medline
46. Sourbron SP, Buckley DL. **On the scope and interpretation of the Tofts models for DCE-MRI.** *Magn Reson Med* 2011;66:735–45 CrossRef Medline
47. Wu O, Østergaard L, Weisskoff RM, et al. **Tracer arrival timing-insensitive technique for estimating flow in MR perfusion-weighted imaging using singular value decomposition with a block-circulant deconvolution matrix.** *Magn Reson Med* 2003;50:164–74 CrossRef Medline
48. Dewey B. *ECTRIMS ONLINE LIBRARY*. 2017. <https://www.ectrims.eu/online-library/>. Accessed March 1, 2020
49. Avants BB, Tustison NJ, Song G, et al. **A reproducible evaluation of ANTS similarity metric performance in brain image registration.** *Neuroimage* 2011;54:2033–44 CrossRef Medline
50. Roy S, Butman JA, Pham DL. **Robust skull stripping using multiple MR image contrasts insensitive to pathology.** *Neuroimage* 2017;146:132–47 CrossRef Medline
51. Huo Y, Plassard AJ, Carass A, et al. **Consistent cortical reconstruction and multi-atlas brain segmentation.** *Neuroimage* 2016;138:197–210 CrossRef Medline
52. Leigh R, Jen SS, Varma DD, et al. **Arrival time correction for dynamic susceptibility contrast MR permeability imaging in stroke patients.** *PLoS One* 2012;7:e52656 CrossRef Medline
53. Boxerman JL, Schmainda KM, Weisskoff RM. **Relative cerebral blood volume maps corrected for contrast agent extravasation significantly correlate with glioma tumor grade, whereas uncorrected maps do not.** *AJNR Am J Neuroradiol* 2006;27:859–67 Medline
54. Oishi K, Faria A, Jiang H, et al. **Atlas-based whole brain white matter analysis using large deformation diffeomorphic metric mapping: application to normal elderly and Alzheimer's disease participants.** *Neuroimage* 2009;46:486–99 CrossRef Medline
55. R Core Team. *R: A Language and Environment for Statistical Computing*. <https://cran.r-project.org/doc/manuals/r-release/fullrefman.pdf>. Accessed March 1, 2020
56. Marstrand JR, Garde E, Rostrup E, et al. **Cerebral perfusion and cerebrovascular reactivity are reduced in white matter hyperintensities.** *Stroke* 2002;33:972–76 CrossRef Medline
57. Perkio J, Aronen HJ, Kangasmaki A, et al. **Evaluation of four post-processing methods for determination of cerebral blood volume and mean transit time by dynamic susceptibility contrast imaging.** *Magn Reson Med* 2002;47:973–81 CrossRef Medline
58. Mazziotta J, Toga A, Evans A, et al. **A probabilistic atlas and reference system for the human brain: International Consortium for Brain Mapping (ICBM).** *Philos Trans R Soc Lond B Biol Sci* 2001;356:1293–22 CrossRef Medline
59. Bazin PL, Cuzzocreo JL, Yassa MA, et al. **Volumetric neuroimage analysis extensions for the MIPAV Software Package.** *J Neurosci Methods* 2007;165:111–21 CrossRef Medline
60. Zierler KL. **Equations for measuring blood flow by external monitoring of radioisotopes.** *Circ Res* 1965;16:309–21 CrossRef Medline
61. Rempp KA, Brix G, Wenz F, et al. **Quantification of regional cerebral blood flow and volume with dynamic susceptibility contrast-enhanced MR imaging.** *Radiology* 1994;193:637–41 CrossRef Medline
62. Promjunyakul NO, Lahna DL, Kaye JA, et al. **Comparison of cerebral blood flow and structural penumbras in relation to white matter hyperintensities: a multi-modal magnetic resonance imaging study.** *J Cereb Blood Flow Metab* 2016;36:1528–36 CrossRef Medline
63. van Osch MJ, Teeuwisse WM, van Walderveen MA, et al. **Can arterial spin-labeling detect white matter perfusion signal?** *Magn Reson Med* 2009;62:165–73 CrossRef Medline
64. Welker K, Boxerman J, Kalnin A, et al. **ASFNR recommendations for clinical performance of MR dynamic susceptibility contrast perfusion imaging of the brain.** *AJNR Am J Neuroradiol* 2015;36:E41–51 CrossRef Medline
65. Barnes SR, Ng TS, Montagne A, et al. **Optimal acquisition and modeling parameters for accurate assessment of low  $K^{\text{trans}}$  blood-brain barrier permeability using dynamic contrast-enhanced MRI.** *Magn Reson Med* 2016;75:1967–77 CrossRef Medline



# Diagnostic Accuracy of Screening Arterial Spin-Labeling MRI Using Hadamard Encoding for the Detection of Reduced CBF in Adult Patients with Ischemic Moyamoya Disease

K. Setta, T. Matsuda, M. Sasaki, T. Chiba, S. Fujiwara, M. Kobayashi, K. Yoshida, Y. Kubo, M. Suzuki, K. Yoshioka, and K. Ogasawara



## ABSTRACT

**BACKGROUND AND PURPOSE:** Adult patients with ischemic Moyamoya disease are advised to undergo selective revascularization surgery based on cerebral hemodynamics. The purpose of this study was to determine the diagnostic accuracy of arterial spin-labeling MR imaging using Hadamard-encoded multiple postlabeling delays for the detection of reduced CBF in such patients.

**MATERIALS AND METHODS:** Thirty-seven patients underwent brain perfusion SPECT and pseudocontinuous arterial spin-labeling MR imaging using standard postlabeling delay (1525 ms) and Hadamard-encoded multiple postlabeling delays. For Hadamard-encoded multiple postlabeling delays, based on data obtained from the 7 sub-boluses with combinations of different labeling durations and postlabeling delays, CBF corrected by the arterial transit time was calculated on a voxel-by-voxel basis. Using a 3D stereotaxic template, we automatically placed ROIs in the ipsilateral cerebellar hemisphere and 5 MCA territories in the symptomatic cerebral hemisphere; then, the ratio of the MCA to cerebellar ROI was calculated.

**RESULTS:** The area under the receiver operating characteristic curve for detecting reduced SPECT-CBF ratios ( $<0.686$ ) was significantly greater for the Hadamard-encoded multiple postlabeling delays–CBF ratios (0.885) than for the standard postlabeling delay–CBF ratios (0.786) ( $P = .001$ ). The sensitivity and negative predictive value for the Hadamard-encoded multiple postlabeling delays–CBF ratios were 100% (95% confidence interval, 100%–100%) and significantly higher than the sensitivity (95% CI, 44%–80%) and negative predictive value (95% CI, 88%–97%) for the standard postlabeling delay–CBF ratio, respectively.

**CONCLUSIONS:** ASL MR imaging using Hadamard-encoded multiple postlabeling delays may be applicable as a screening tool because it can detect reduced CBF on brain perfusion SPECT with 100% sensitivity and a 100% negative predictive value in adult patients with ischemic Moyamoya disease.

**ABBREVIATIONS:** ASL = arterial spin-labeling; ATT = arterial transit time; hASL = Hadamard-encoded multiple PLD ASL; MMD = Moyamoya disease; PLD = postlabeling delay; sASL = standard-encoded PLD ASL

Moyamoya disease (MMD) is a chronic, occlusive cerebrovascular disease of unknown etiology that is characterized by bilateral steno-occlusive changes in the terminal portion of the ICA and an abnormal vascular network at the base of the brain.<sup>1,2</sup> The typical treatment for patients with ischemia symptoms is

revascularization surgery, which can involve anastomosis of the superficial temporal artery and MCA.<sup>3</sup> Regardless of the severity of cerebral ischemia, this procedure is universally recommended for pediatric patients with MMD with ischemic symptoms because in such cases, the brain is still developing.<sup>3–5</sup> By contrast, revascularization surgery is selectively recommended for adult patients presenting with ischemic symptoms.<sup>3,6</sup> However, no clear guidelines are available for this selection. Two recent studies used PET and brain perfusion SPECT to measure the oxygen extraction fraction and CBF, respectively, and demonstrated that among adult patients (older than 30 but younger than 60 years of age) receiving medication alone for symptomatic ischemic MMD without hemodynamic compromise, such as misery perfusion or reduced CBF, the incidence of recurrent ischemic events was very low (approximately 1% per year).<sup>7,8</sup> Moreover, the recurrent ischemic episodes were transient ischemic attacks only, and no changes were seen in scores on the modified Rankin Disability

Received December 28, 2020; accepted after revision March 11, 2021.

From the Department of Neurosurgery (K.S., T.C., S.F., M.K., K. Yoshida, Y. Kubo, K.O.), Department of Radiology (M. Suzuki, K. Yoshioka), and Division of Ultrahigh Field MRI, Institute for Biomedical Sciences (T.M., M. Sasaki), Iwate Medical University School of Medicine, Yahaba-cho, Japan.

This study was funded by a Grant-in-Aid for Scientific Research from the Japan Society for the Promotion of Science (JP18K09002).

Please address correspondence to Kuniaki Ogasawara, MD, Department of Neurosurgery, Iwate Medical University, Idaidoori 2-1-1, Yahaba-cho 020-8505, Japan; e-mail: kuogasa@iwate-med.ac.jp

Indicates open access to non-subscribers at www.ajnr.org

Indicates article with online supplemental data.

<http://dx.doi.org/10.3174/ajnr.A7167>

Scale after the recurrence of ischemic symptoms in such patients.<sup>7</sup> In addition, neither cerebral hemodynamics nor cognitive function had deteriorated at 2 years after the last event in patients without recurrent ischemic events.<sup>7</sup> Initial treatment with medication alone may be recommended for adult patients with ischemic MMD without hemodynamic compromise,<sup>7</sup> and the determination of whether hemodynamic compromise exists in the symptomatic cerebral hemisphere is important for the management of such patients.<sup>7,8</sup> However, the clinical use of PET or brain perfusion SPECT to detect misery perfusion or reduced CBF is precluded by its high cost and limited availability in the clinical setting. Other screening modalities for detecting hemodynamic compromise before performing PET or brain perfusion SPECT would therefore be useful.

Arterial spin-labeling (ASL) MR imaging is a noninvasive technique that can quantify CBF.<sup>9-11</sup> A number of studies involving patients with MMD conducted using ASL MR imaging with a single postlabeling delay (PLD) have simply compared CBF measured using ASL MR imaging with brain perfusion parameters measured using other modalities such as PET, SPECT, and dynamic susceptibility contrast perfusion MR imaging.<sup>12-14</sup> However, almost all the cerebral cortical regions in MMD have some degree of perfusion delay, which varies even within individual cerebral cortical regions of a single patient.<sup>15</sup> Therefore, it is difficult to obtain precise CBF measurements using the standard ASL method with a single PLD in MMD.<sup>15</sup> By contrast, theoretically, ASL measurements covering a wide range of PLD times can be interpreted to estimate CBF with practical spatial and temporal resolutions in the clinical setting.<sup>16,17</sup> Actually, multi-PLD ASL MR imaging with corrections using the arterial transit time (ATT) significantly improved CBF quantification compared with single-PLD ASL MR imaging.<sup>18,19</sup> However, the accuracy of multi-PLD ASL MR imaging for detecting hemodynamic compromise has not been reported. Hadamard-encoding techniques have recently been applied to the ASL methods to calculate the ASL signals as multiple PLDs by dividing the ASL signal into sub-boluses of different PLDs.<sup>16</sup> Several investigations have demonstrated that Hadamard-encoded labeling strategies for healthy human subjects provide robust CBF measurements in a time-efficient manner with shorter scan times (<10 minutes).<sup>20</sup> This benefit may be suitable for the detection of reduced CBF in patients with MMD.

Given this background, the aims of this study were to determine the diagnostic accuracy of ASL MR imaging using Hadamard-encoded multiple PLDs for the detection of reduced CBF, a key determinant for revascularization surgery, in adult patients with ischemic MMD, and to propose practical clinical algorithms using ASL MR imaging and subsequent management in such patients.

## MATERIALS AND METHODS

The protocol of the present prospective observational study was reviewed and approved by our institutional ethics committee. Written, informed consent was obtained from all participants or their next of kin before the study began.

### Patients

Patients who were diagnosed as having MMD according to the diagnostic criteria of the Research Committee on Spontaneous

Occlusion of the Circle of Willis of the Ministry of Health, Labor, and Welfare of Japan<sup>1</sup> were prospectively selected for participation in this study if they satisfied the following clinical inclusion criteria: older than 30 but younger than 60 years of age, modified Rankin disability scale score of 0 or 1, presence of episodes of ischemic symptoms in the unilateral carotid territory occurring  $\leq 3$  months before presentation to our department, and absence of infarction in the bilateral cerebral cortices on MR imaging.

### Brain Perfusion SPECT

A brain perfusion SPECT study was performed using *N*-isopropyl-p-[<sup>123</sup>I]iodoamphetamine (<sup>123</sup>I-IMP) and a triple-head gamma camera (GCA-9300R; Toshiba Medical Systems) between 3 weeks and 3 months after the last ischemic event. The spatial resolution of the gamma camera with a high-resolution fan-beam collimator was 8.5-mm full width at half maximum. The SPECT acquisition protocol consisted of a matrix size of 128  $\times$  128 and a 30-minute continuous acquisition (5 minutes/rotation) over 360° in 4° steps. Postacquisition, the data were corrected for scatter using the triple energy window method and then reconstructed by filtered back-projection. A Butterworth preprocessing filter was applied with a cutoff frequency of 0.08 cycles per pixel (1 pixel = 1.72 mm). For attenuation correction, the iterative Chang method was used,<sup>21</sup> and the attenuation map was generated by extracting the skin contour and assuming the inner region side as a uniform attenuation body. The attenuation coefficient was 0.146 cm<sup>-1</sup>.

After delivering a 1-minute intravenous infusions of 222 MBq of <sup>123</sup>I-IMP (5-mL volume) and physiologic saline at a constant rate of 5 mL/min, data were acquired at a midscan time of 30 minutes after the administration of <sup>123</sup>I-IMP with a scan duration of 20 minutes.<sup>22</sup>

### ASL MRI

ASL MR imaging studies were performed using a 3T MR imaging scanner (Discovery MR750; GE Healthcare) with an 8-channel receive head coil and body coil for transmission within 3 days after the brain perfusion SPECT study. Each patient underwent 2 kinds of ASL MR imaging with a 3D pseudocontinuous labeling sequence. At first, the standard ASL (sASL) was performed using the following parameters: labeling duration, 1450 ms; PLD, 1525 ms; TR, 4802 ms; TE, 10.5 ms; section thickness, 4.0 mm; number of slices, 32; sampling points, 8 arms  $\times$  512; FOV, 24  $\times$  24 cm; matrix size, 128  $\times$  128; and voxel resolution, 1.9  $\times$  1.9  $\times$  4.0 mm. The total scan time was 3 minutes 13 seconds. Next, for ASL MR imaging using Hadamard-encoded multiple PLDs (hASL), we performed ASL consisting of 7 sub-boluses<sup>17</sup> with the following combinations of labeling duration and PLDs: labeling duration (ms), PLD (ms) = 286, 700; 330, 998; 370, 1327; 432, 1697; 534, 2128; 732, 2661; and 1308, 3392, with TR, 6141 ms; TE, 24.3 ms; section thickness, 4.0 mm; number of slices, 32; sampling points, 4 arms  $\times$  512; FOV, 24  $\times$  24 cm; matrix size, 128  $\times$  128; and voxel resolution, 1.9  $\times$  1.9  $\times$  4.0 mm. The total scan time was 7 minutes 35 seconds. For each scan, vessel suppression using a velocity-selective saturation sequence was applied to reduce artifactual bright signals by dephasing intravascular labeled spins.<sup>20</sup> On the basis of data obtained from the 7 sub-boluses, CBF

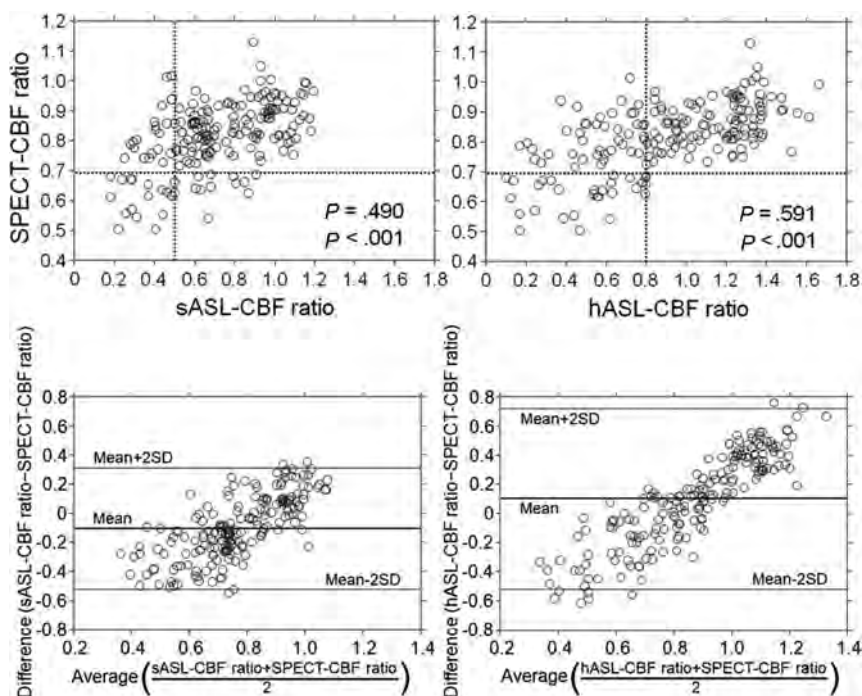


**FIG 1.** Comparisons (*upper graphs*) and Bland-Altman plots (*lower graphs*) of SPECT-CBF and sASL-CBF ratios and sASL-CBF (*left graphs*) or hASL-CBF ratios (*right graphs*) for each MCA ROI in each patient. In the *upper graphs*, each horizontal line denotes the cutoff point for indicating a reduced SPECT-CBF ratio (0.686) and each vertical line denotes the cutoff point lying closest to the upper left corner of the receiver operating characteristic curve for detecting a reduced SPECT-CBF ratio (0.502 for sASL-CBF, 0.801 for hASL-CBF).

corrected by the ATT was automatically calculated on a voxel-by-voxel basis.

#### Data Analysis and Definition of Reduced CBF

All SPECT and ASL MR imaging data were transformed into the standard brain size and shape by linear and nonlinear transformation using statistical parametric mapping (SPM2; <http://www.fil.ion.ucl.ac.uk/spm/software/spm12>) for anatomic standardization.<sup>23</sup> Therefore, the brain images from all participants had the same anatomic format. A total of 318 constant ROIs were automatically placed in both the cerebral and cerebellar hemispheres using a 3D stereotaxic ROI template with SPM2.<sup>24</sup> ROIs were grouped into 10 segments—callosomarginal, pericallosal, precentral, central, parietal, angular, temporal, posterior, hippocampal, and cerebellar—in each hemisphere according to the arterial supply. Of these 10 segments, 5—precentral, central, parietal, angular, and temporal—perfused by the MCA and cerebellar ROI were selected for analyses.<sup>22</sup>

The mean values of the radioactive counts on brain perfusion SPECT images and CBF and ATT on ASL MR images were measured in the 5 MCA ROIs in both cerebral hemispheres and both cerebellar ROIs. For each patient, the mean value in each MCA ROI in the symptomatic cerebral hemisphere relative to that in the ipsilateral cerebellar ROI on brain perfusion SPECT and ASL MR imaging was calculated and defined as the SPECT-CBF, ASL-CBF, and ASL-ATT ratios, respectively.

For each MCA ROI of each patient, the ROI was defined as exhibiting reduced CBF when the SPECT-CBF ratio was  $<0.686$ .<sup>22</sup>

#### Statistical Analysis

Data are expressed as the mean (SD). Correlations between 2 variables were determined using the Spearman rank correlation coefficient. Differences between 2 correlation coefficients were compared using the Meng-Rosenthal-Rubin method. Bland-Altman analysis was performed to confirm the concordance between each CBF ratio. Taking the correlation between different measures in the same patient into account, we evaluated the relationship between SPECT-CBF and ASL-CBF ratios using generalized linear mixed effects models with a subject random intercept. These 2 parameters were assumed to be a normal variable with an identity link. Receiver operating characteristic curves were used to assess the accuracy of the sASL-CBF and hASL-CBF ratios for detecting reduced CBF. Reduced CBF as a criterion standard was defined as a SPECT-CBF ratio of  $<0.686$ .<sup>22</sup>

Pair-wise comparisons of the area

under the receiver operating characteristic curves for the sASL-CBF and hASL-CBF ratios were then performed. For all statistical analyses, significance was set at  $P < .05$ . The exact 95% CIs for sensitivity, specificity, and positive and negative predictive values were computed with binomial distributions. Differences in the sensitivity, specificity, and positive and negative predictive values among the sASL-CBF and hASL-CBF ratios were analyzed using 95% CIs.

#### RESULTS

During the 24-month study period, a total of 40 patients met the inclusion criteria, among whom, 3 declined to participate. The remaining 37 patients (13 men, 24 women; mean age, 45 [SD, 6] years; age range, 31–57 years) underwent brain perfusion SPECT and ASL MR imaging, leading to 185 ( $5 \times 37$ ) MCA ROIs in the symptomatic cerebral hemispheres being included in the final analyses. Among these 37 patients, 29 experienced the onset of transient ischemic attacks alone; 3, a minor stroke alone; and 5, onset of a minor stroke after a transient ischemic attack. In total, 11, 16, and 10 patients were classified into MRA stages 2, 3, and 4, respectively.<sup>1</sup>

A significant positive correlation was observed between SPECT-CBF and sASL-CBF ( $\rho = 0.490$ ;  $P < .001$ ) or hASL-CBF ratios ( $\rho = 0.591$ ;  $P < .001$ ) in the 185 MCA ROIs (Fig 1). The latter coefficient was significantly greater than the former ( $P = .002$ ). A significant positive correlation was also observed between SPECT-CBF ratios and the quantitative values of



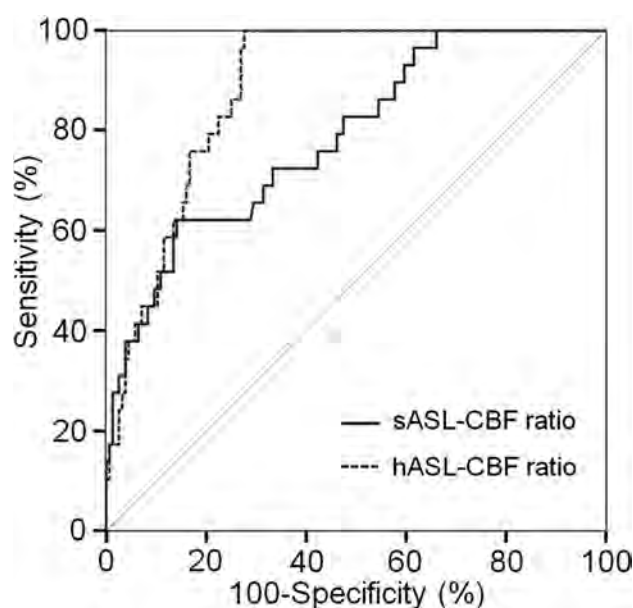


**FIG 2.** Receiver operating characteristic curves used to compare the accuracy of sASL-CBF and hASL-CBF ratios for detecting a reduced SPECT-CBF ratio. Pair-wise comparison analysis shows a significantly greater area under the receiver operating characteristic curve for the hASL-CBF (dotted line) than for the sASL-CBF ratio (solid line).

sASL-CBF ( $\rho = 0.462$ ;  $P < .001$ ) or hASL-CBF ( $\rho = 0.534$ ;  $P < .001$ ) in the 185 MCA ROIs (Online Supplemental Data). Although the former coefficient did not differ from that between SPECT-CBF and sASL-CBF ratios, the latter coefficient was significantly lower than that between SPECT-CBF and hASL-CBF ratios ( $P = .036$ ).

No constant bias was detected for the SPECT-CBF and sASL-CBF (95% CI of difference,  $-0.530$ – $0.319$ ) or hASL-CBF ratios (95% CI of difference,  $-0.510$ – $0.711$ ) by Bland-Altman analysis (Fig 1). However, a proportional bias was identified for SPECT-CBF and sASL-CBF (slope-of-regression equation,  $0.969$ ;  $P < .001$ ) or hASL-CBF ratios (slope-of-regression equation,  $1.242$ ;  $P < .001$ ) (Fig 1). Whereas sASL-CBF ratios showed a propensity toward underestimation at lower CBF ratios, hASL-CBF ratios showed a propensity toward underestimation and overestimation at lower and higher CBF ratios, respectively. Generalized linear mixed effects models with a subject random intercept revealed a significant relationship between SPECT-CBF and sASL-CBF ( $P < .001$ ) or hASL-CBF ratios ( $P < .001$ ).

Of the 185 ROIs analyzed, 29 (16%) were determined to exhibit reduced CBF on brain perfusion SPECT. The areas under the curve for sASL-CBF and hASL-CBF ratios for detecting reduced CBF on brain perfusion SPECT were  $0.786$  (95% CI,  $0.720$ – $0.843$ ) and  $0.885$  (95% CI,  $0.830$ – $0.927$ ), respectively; the latter was significantly greater than the former (difference between areas,  $0.099$ ;  $P = .001$ ) (Fig 2).

The sensitivity and negative predictive value for the hASL-CBF ratio, with the cutoff point lying closest to the upper left corner of the receiver operating characteristic curve for the detection of MCA ROIs with reduced CBF on brain perfusion SPECT, were 100% (cutoff point,  $0.801$ ) and significantly higher than those for the sASL-CBF ratio (cutoff point,  $0.502$ ) (Online

Supplemental Data). The specificity and positive predictive value did not differ between the 2 ASL-CBF ratios.

When the difference between the hASL-CBF and SPECT-CBF ratios (hASL-CBF ratio–SPECT-CBF ratio) was compared with the hASL-ATT ratio for each MCA ROI (Online Supplemental Data), the differences in most MCA ROIs exhibiting nonreduced hASL-CBF ratios ( $\geq 0.801$ ) and nonreduced SPECT-CBF ratios ( $\geq 0.686$ ) were  $>0$ , regardless of the hASL-ATT ratios. By contrast, the differences for most MCA ROIs with reduced hASL-CBF ratios ( $< 0.801$ ) were  $<0$  regardless of the ASL-ATT ratios. In particular, no MCA ROIs with reduced hASL-CBF ratios exhibited reduced SPECT-CBF ratios when they had an hASL-ATT ratio of  $>1.3$ .

Of the 37 patients studied, 1, 3, 6, and 4 patients had 4, 3, 2, and 1 MCA ROIs with reduced CBF on brain perfusion SPECT, respectively. Therefore, 14 patients (38%) were determined to have MCA ROIs with reduced CBF. In the 10 patients with  $\geq 2$  MCA ROIs with reduced CBF, the ROIs were adjacent to one another. The sensitivity and negative predictive value for the hASL-CBF ratio for the detection of patients with MCA ROIs exhibiting reduced CBF on brain perfusion SPECT based on the determination for each MCA ROI were 100% and significantly higher than those for the sASL-CBF ratio (Online Supplemental Data). The specificity and positive predictive value did not differ between these 2 ASL-CBF ratios.

Figures 3 and 4 show representative MRA, brain perfusion SPECT, and ASL MR images in a patient with MCA ROIs exhibiting reduced CBF and in a patient without any MCA ROIs exhibiting reduced CBF, respectively.

## DISCUSSION

The results of this study demonstrate that ASL MR imaging using Hadamard-encoded multiple PLDs can detect reduced CBF on brain perfusion SPECT with 100% sensitivity and negative predictive value in adult patients with ischemic MMD. This diagnostic accuracy may be applicable as a screening test before further examination of cerebral hemodynamics.

In this study, CBF in each MCA ROI in the symptomatic cerebral hemisphere was normalized using CBF in the ipsilateral cerebellar hemisphere. This cerebellar normalization has been commonly applied to brain perfusion SPECT because of its simplicity, objectivity, and reproducibility.<sup>22,25,26</sup> By contrast, the accuracy of the cerebellar normalization for ASL-CBF in patients with MMD remains controversial. One previous study demonstrated improvement of the correlation between sASL-CBF and PET-CBF by cerebellar normalization,<sup>15</sup> whereas another found overestimation of sASL-CBF by cerebellar normalization.<sup>12</sup> Perfusion delay may differ between the cerebral and cerebellar cortices in healthy subjects, and this difference in perfusion delay may vary in patients with MMD. Our data showed a better correlation between SPECT-CBF ratios and hASL-CBF ratios compared with that between SPECT-CBF ratios and sASL-CBF ratios or between SPECT-CBF ratios and quantitative hASL-CBF values. These findings suggest that correcting brain perfusion delay, including the cerebellum using Hadamard-encoded multiple PLDs, may increase the accuracy of cerebellar normalization for ASL-CBF in MMD. However, this correction also underestimated and overestimated ASL-CBF

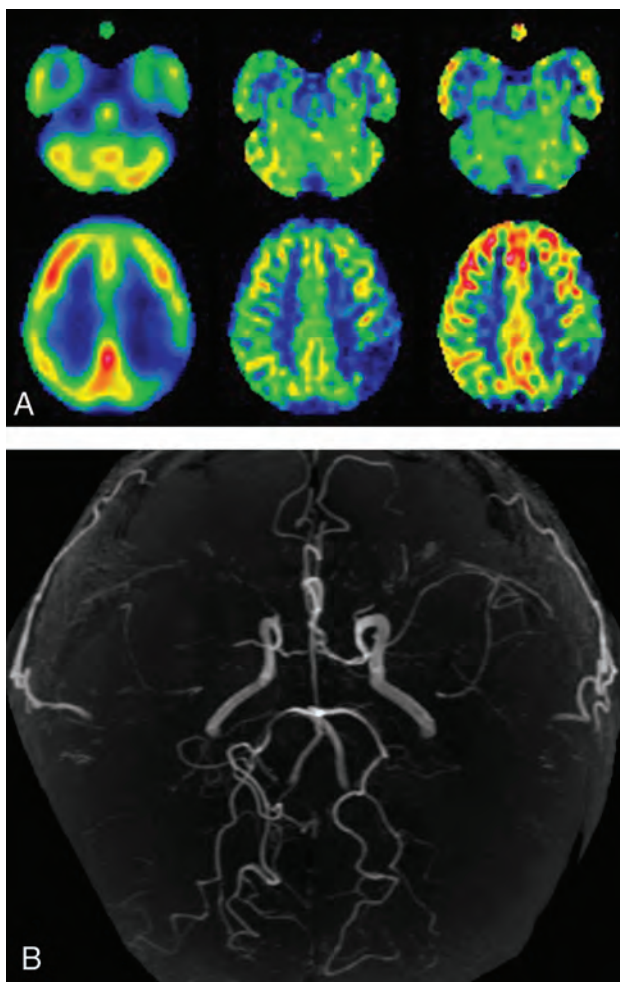


**FIG 3.** MRA (B), brain perfusion SPECT images (A, left), and sASL (A, middle) and hASL (A, right) MR images of a 43-year-old male patient with transient ischemic attacks complicated by right-sided hemiparesis. MRA shows stage 3 Moyamoya disease. On all 3 SPECT and ASL images, the CBF in the left parietal region is severely reduced compared with that in the left cerebellar hemisphere.

ratios at lower and higher CBFs, respectively. We used the vessel-suppression technique for hASL MR imaging to reduce artifactual bright signals by dephasing intravascular labeled spins.<sup>27</sup> However, this technique theoretically prolongs the effective TE, resulting in a reduction in the SNR.<sup>27</sup> Such SNR reductions may be related to the underestimation of hASL-CBF ratios at lower CBFs. Actually, investigators do not necessarily recommend the use of vessel suppression for clinical applications.<sup>27</sup> By contrast, the overestimation of hASL-CBF ratios at higher CBFs may be due to the overcorrection of cerebral perfusion delay using Hadamard-encoded multiple PLDs in cerebral regions with slightly or not prolonged PLDs; these should be considered limitations of hASL MR imaging.

A previous study using PET demonstrated that among adult patients receiving medication alone for symptomatic ischemic MMD without an increased oxygen extraction fraction in all MCA ROIs, the incidence of recurrent ischemic events was very low.<sup>7</sup> Another study showed that SPECT-CBF ratios obtained in the same fashion as in the present study detect increased oxygen

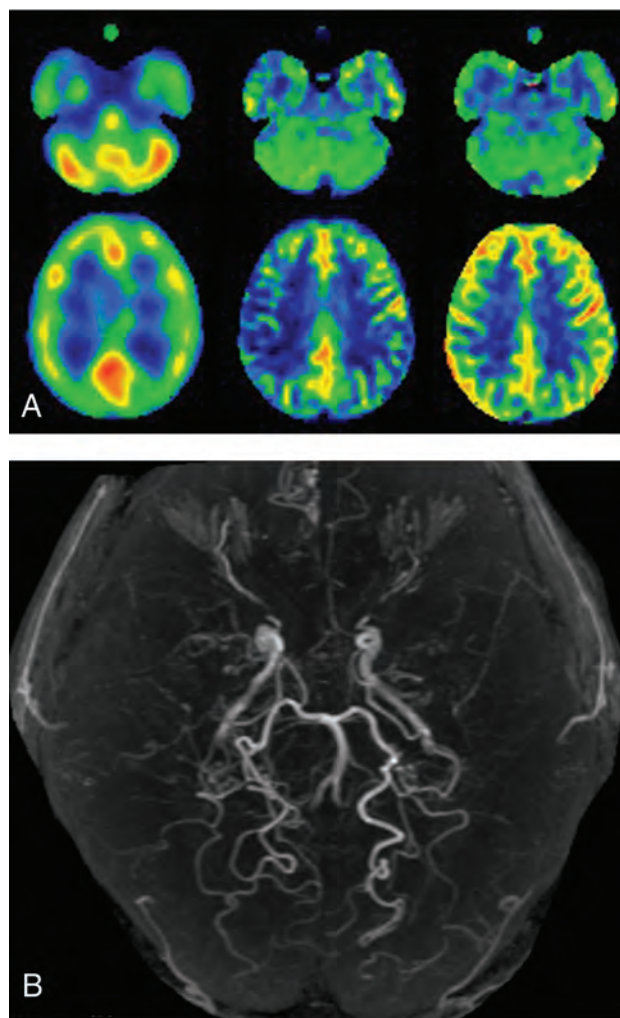


**FIG 4.** MRA (B), brain perfusion SPECT images (A, left), and sALS (A, middle) and hASL (A, right) MR images of a 34-year-old female patient with transient ischemic attacks complicated by left-sided hemiparesis. MRA shows stage 3 Moyamoya disease. On perfusion SPECT images, the CBF in the right MCA territory is slightly reduced compared with that in the right cerebellar hemisphere. The CBF on sASL MR images is severely reduced in the right central, parietal, and angular regions, whereas the CBF on hASL MR imaging is not reduced relative to the right cerebellar hemisphere.

extraction fraction with 100% sensitivity and a 100% negative predictive value in adult patients with ischemic MMD (older than 30 but younger than 60 years of age), and the optimal cutoff point for the SPECT-CBF ratio for detection of increased oxygen extraction fraction is 0.686.<sup>22</sup> The present study, therefore, defined a SPECT-CBF ratio below this cutoff point as reduced CBF. As a result, the sensitivity and negative predictive value of hASL for the detection of reduced CBF on brain perfusion SPECT were 100%. This diagnostic accuracy may be applicable to a screening test before further examination of cerebral hemodynamics. By contrast, the positive predictive value of hASL was low (<50%) and comparable with that of sASL. In particular, reduced CBF on hASL was not corrected when the hASL-ATT ratio was >1.3. This finding suggests that hASL does not

sufficiently correct the longer perfusion delays in the cerebral cortex in patients with MMD, also a limitation of hASL MR imaging.

On the basis of the present data and previous findings,<sup>7,22</sup> we propose practical clinical algorithms for the detection of hemodynamic compromise using ASL MR imaging with Hadamard-encoded multiple PLDs and subsequent management in adult patients with ischemic MMD. Patients who undergo ASL MR imaging using Hadamard-encoded multiple PLDs are determined to not have hemodynamic compromise and should, therefore, receive medication alone, including an antiplatelet drug, if the ASL-CBF ratios in all MCA ROIs in the symptomatic hemisphere are not low ( $\geq 0.801$ ). If the ASL-CBF ratio in any MCA ROI is low ( $< 0.801$ ), the patient may possibly have hemodynamic compromise and, therefore, requires further examinations such as brain perfusion SPECT and/or ( $^{15}\text{O}$ ) gas PET to detect hemodynamic compromise more accurately. If hemodynamic compromise is detected on SPECT or PET, revascularization surgery may be recommended. The introduction of ASL MR imaging using Hadamard-encoded multiple PLDs for screening may reduce the number of patients who undergo PET or brain perfusion SPECT by about two-thirds.

A prospective study<sup>7</sup> reported that during the recurrence of ischemic events in adult patients with MMD, the affected cerebral hemisphere exhibited new misery perfusion. By contrast, cerebral hemodynamics had not deteriorated 2 years after the last event in patients without recurrent ischemic events. Those results suggest that the development of misery perfusion may be a strong predictor of recurrent ischemic events in adult patients with ischemic-onset MMD.<sup>7</sup> The detection of reduced CBF using screening ASL MR imaging with Hadamard-encoded multiple PLDs for such patients may be also recommended for the prediction of recurrent ischemic symptoms during follow-up.

In addition to the limitations listed above, we did not assess stress perfusion such as acetazolamide challenge. A previous study demonstrated that whereas CBF assessed using brain perfusion SPECT detects misery perfusion with high sensitivity and a high negative predictive value in adult patients with ischemic MMD, the accuracy of cerebrovascular reactivity to acetazolamide is significantly lower than that of CBF.<sup>22</sup> Furthermore, cerebrovascular reactivity to acetazolamide in addition to CBF did not increase the accuracy for detecting misery perfusion.<sup>22</sup> These findings suggest that hemodynamic compromise can be sufficiently detected by CBF measurement alone in such patients.<sup>22</sup>

## CONCLUSIONS

ASL MR imaging using Hadamard-encoded multiple PLDs can detect reduced CBF on brain perfusion SPECT with 100% sensitivity and 100% negative predictive value in adult patients with ischemic MMD; therefore, it may be applicable as a screening tool before further examination of cerebral hemodynamics.

Disclosures: Makoto Sasaki—UNRELATED: Grants/Grants Pending: Japan Society for the Promotion of Science-Kakenhi, Hitachi, GE Healthcare\*; Payment for Lectures Including Service on Speakers Bureaus: Hitachi, GE Healthcare. \*Money paid to the institution.

## REFERENCES

1. Research Committee on the Pathology and Treatment of Spontaneous Occlusion of the Circle of Willis; Health Labour Sciences Research Grant for Research on Measures for Intractable Diseases. **Guidelines for diagnosis and treatment of moyamoya disease (spontaneous occlusion of the circle of Willis).** *Neurol Med Chir (Tokyo)* 2012;52:245–66 CrossRef Medline
2. Suzuki J, Takaku A. Cerebrovascular “moyamoya” disease: disease showing abnormal net-like vessels in base of brain. *Arch Neurol* 1969;20:288–99 CrossRef Medline
3. Fujimura M, Tominaga T. Current status of revascularization surgery for moyamoya disease: special consideration for its ‘internal carotid-external carotid (IC-EC) conversion’ as the physiological reorganization system. *Tohoku J Exp Med* 2015;236:45–53 CrossRef Medline
4. Fujimura M, Shimizu H, Mugikura S, et al. Delayed intracerebral hemorrhage after superficial temporal artery-middle cerebral artery anastomosis in a patient with moyamoya disease: possible involvement of cerebral hyperperfusion and increased vascular permeability. *Surg Neurol* 2009;71:223–27 CrossRef Medline
5. Fushimi Y, Okada T, Takagi Y, et al. Voxel based analysis of surgical revascularization for moyamoya disease: pre- and postoperative SPECT studies. *PLoS One* 2016;11:e0148925 CrossRef Medline
6. Guzman R, Lee M, Achrol A, et al. Clinical outcome after 450 revascularization procedures for moyamoya disease. *J Neurosurg* 2009;111:927–35 CrossRef Medline
7. Miyoshi K, Chida K, Kobayashi M, et al. Two-year clinical, cerebral hemodynamic and cognitive outcomes of adult patients undergoing medication alone for symptomatically ischemic moyamoya disease without cerebral misery perfusion: a prospective cohort study. *Neurosurgery* 2018;84:1233–41 CrossRef Medline
8. Nam KW, Cho WS, Kwon HM, et al. Ivy sign predicts ischemic stroke recurrence in adult moyamoya patients without revascularization surgery. *Cerebrovasc Dis* 2019;47:223–30 CrossRef Medline
9. Williams DS, Detre JA, Leigh JS, et al. Magnetic resonance imaging of perfusion using spin inversion of arterial water. *Proc Natl Acad Sci USA* 1992;89:212–16 CrossRef Medline
10. Alsop DC, Detre JA. Reduced transit-time sensitivity in noninvasive magnetic resonance imaging of human cerebral blood flow. *J Cereb Blood Flow Metab* 1996;16:1236–49 CrossRef Medline
11. Detre JA, Samuels OB, Alsop DC, et al. Noninvasive magnetic resonance imaging evaluation of cerebral blood flow with acetazolamide challenge in patients with cerebrovascular stenosis. *J Magn Reson Imaging* 1999;10:870–75 CrossRef Medline
12. Goetti R, Warnock G, Kuhn FP, et al. Quantitative cerebral perfusion imaging in children and young adults with moyamoya disease: comparison of arterial spin-labeling-MRI and H(2)[(15)O]-PET. *AJNR Am J Neuroradiol* 2014;35:1022–28 CrossRef Medline
13. Yun TJ, Sohn CH, Han MH, et al. Effect of delayed transit time on arterial spin labeling: correlation with dynamic susceptibility contrast perfusion magnetic resonance in moyamoya disease. *Invest Radiol* 2013;48:795–802 CrossRef Medline
14. Noguchi T, Kawashima M, Irie H, et al. Arterial spin-labeling MR imaging in moyamoya disease compared with SPECT imaging. *Eur J Radiol* 2011;80:e557–62 CrossRef Medline
15. Hara S, Tanaka Y, Ueda Y, et al. Noninvasive evaluation of CBF and perfusion delay of moyamoya disease using arterial spin-labeling MRI with multiple postlabeling delays: comparison with 15O-gas PET and DSC-MRI. *AJNR Am J Neuroradiol* 2017;38:696–702 CrossRef Medline
16. Gunther M. Highly efficient accelerated acquisition of perfusion inflow series by cycled arterial spin labeling. In: *Proceedings of the 15th Annual Meeting of International Society of Magnetic Resonance in Medicine and the European Society for Magnetic Resonance in Medicine and Biology*, Berlin, Germany; May 19–25, 2007
17. Wells JA, Lythgoe MF, Gadian DG, et al. In vivo Hadamard-encoded continuous arterial spin-labeling (H-CASL). *Magn Reson Med* 2010;63:1111–18 CrossRef Medline



18. Fan AP, Khalighi MM, Guo J, et al. **Identifying hypoperfusion in moyamoya disease with arterial spin labeling and an [15O]-water positron emission tomography/magnetic resonance imaging normative database.** *Stroke* 2019;50:373–80 CrossRef Medline
19. Wang R, Yu S, Alger JR, et al. **Multi-delay arterial spin-labeling perfusion MRI in moyamoya disease: comparison with CT perfusion imaging.** *Eur Radiol* 2014;24:1135–44 CrossRef Medline
20. Guo J, Holdsworth SJ, Fan AP, et al. **Comparing accuracy and reproducibility of sequential and Hadamard-encoded multidelay pseudocontinuous arterial spin-labeling for measuring cerebral blood flow and arterial transit time in healthy subjects: a simulation and in vivo study.** *J Magn Reson Imaging* 2018;47:1119–32 CrossRef Medline
21. Chang LT. **A method for attenuation correction in radionuclide computed tomography.** *IEEE Trans Nucl Sci* 1978;25:638–43 CrossRef
22. Setta K, Kojima D, Shimada Y, et al. **Accuracy of brain perfusion single-photon emission computed tomography for detecting misery perfusion in adult patients with symptomatic ischemic moyamoya disease.** *Ann Nucl Med* 2018;32:611–19 CrossRef Medline
23. Nishimiya M, Matsuda H, Imabayashi E, et al. **Comparison of SPM and NEUROSTAT in voxelwise statistical analysis of brain SPECT and MRI at the early stage of Alzheimer's disease.** *Ann Nucl Med* 2008;22:921–27 CrossRef Medline
24. Takeuchi R, Matsuda H, Yoshioka K, et al. **Cerebral blood flow SPET in transient global amnesia with automated ROI analysis by 3DSRT.** *Eur J Nucl Med Mol Imaging* 2004;31:578–89 CrossRef Medline
25. Soonawala D, Amin T, Ebmeier KP, et al. **Statistical parametric mapping of (99m)Tc-HMPAO-SPECT images for the diagnosis of Alzheimer's disease: normalizing to cerebellar tracer uptake.** *Neuroimage* 2002;17:1193–1202 CrossRef Medline
26. Ohnishi T, Yano T, Nakano S, et al. **Acetazolamide challenge and technetium-99m-ECD versus iodine-123-IMP SPECT in chronic occlusive cerebrovascular disease.** *J Nuc Med* 1997;38:1463–67 Medline
27. Alsop DC, Detre JA, Golay X, et al. **Recommended implementation of arterial spin-labeled perfusion MRI for clinical applications: a consensus of the ISMRM Perfusion Study Group and the European Consortium for ASL in dementia.** *Magn Reson Med* 2015;73:102–16 CrossRef Medline

# Collicular Hyperactivation in Patients with COVID-19: A New Finding on Brain MRI and PET/CT

 A. Chammas,  C. Bund,  F. Lersy,  J.-C. Brisset,  F.-D. Ardellier,  S. Kremer, and  I.J. Namer



## ABSTRACT

**SUMMARY:** Hyperactivation of the colliculi has been observed in some patients with coronavirus disease 2019.

**ABBREVIATIONS:** ASL = arterial spin-labeling; COVID-19 = coronavirus disease 2019; SARS-CoV-2 = Severe Acute Respiratory Syndrome coronavirus 2

Recent publications have described several brain abnormalities in patients with coronavirus disease 2019 (COVID-19), such as cerebral hemorrhage (including intraparenchymal hemorrhage or diffuse microhemorrhage), cerebral infarction, leukoencephalopathy,<sup>1,2</sup> leptomeningeal enhancement, circumscribed or diffuse white matter signal abnormalities, posterior reversible encephalopathy syndrome, and focal intraparenchymal enhancement.<sup>3,4</sup>

In the [<sup>18</sup>F] FDG-PET/CT, several patterns of abnormalities have been described, including frontal hypometabolism and cerebellar hypermetabolism<sup>5</sup> and diffuse cortical hypometabolism (associated with putaminal and cerebellum hypermetabolism, compatible with encephalitis, and especially cerebellitis).<sup>6,7</sup> In most of the cases, the underlying pathophysiological mechanism remains unknown.

Arterial spin-labeling (ASL) is increasingly used in neuroradiology as a diagnostic aid.<sup>8,9</sup> Hyperperfusion is associated with hypermetabolism in PET/CT, suggesting that ASL could be considered as an alternative to [<sup>18</sup>F] FDG-PET/CT.<sup>10</sup>

In the current brief, we report a new neuroradiological finding on MR imaging and PET/CT in patients with COVID-19.

## MATERIALS AND METHODS

This retrospective study was carried out in the University Hospitals of Strasbourg and the Cancer Institute of Strasbourg Europe, from March 6, 2020, to August 13, 2020, on patients with COVID-19.


The study was approved by the ethical standards committee on human experimentation at Strasbourg University Hospital (CE-2020-37) and was in accordance with the Declaration of Helsinki of 1964 and its subsequent amendments. Due to the emergency in the context of the COVID-19 pandemic responsible for the resurgence of acute respiratory and neurologic manifestations, the requirement for written informed consent from patients was waived. The final COVID-19 diagnosis was confirmed by real-time reverse-transcriptase polymerase chain reaction oropharyngeal swab test.

A total of 112 patients with neurologic symptoms who underwent brain 3T MR imaging were retrospectively included (age range, 25–87 years; mean age, 63.03 years; male-to-female ratio, 65%/35%). Inclusion criteria were the following: age 18 years or older, positive Severe Acute Respiratory Syndrome coronavirus 2 (SARS-CoV-2) polymerase chain reaction swab test, and neurologic symptomatology that led to an MR imaging scan in the Strasbourg hospital. The mortality rate was 5%. Patients had impaired consciousness (36 patients, 50%), confusion (31 patients, 43%), pyramidal tract signs (19 patients, 26%), agitation (18 patients, 25%), headaches (14 patients, 19%), pathologic awakening (13 patients, 18%), anosmia and ageusia (5 patients, 7%), and seizures (3 patients, 4%). Among them, 90% were hospitalized in the intensive care unit. The initial cerebral MR imaging was performed an average of 30 days after the onset of respiratory symptoms (SD, 15.92). Clinical, imaging, biologic, treatment, and progression data were collected and are detailed in the Results section (Online Supplemental Data). Categorical data were compared using Fisher exact test. Quantitative data were compared using Student *t* test. A *P* value lower than .05 was considered significant. Brain MR imaging anomalies were classified as follows: leptomeningeal enhancement, multifocal and circumscribed FLAIR white matter hyperintensities, diffuse white matter FLAIR hyperintensities, white matter microhemorrhages, ischemic stroke, focal enhancement, FLAIR hyperintensities involving the mesial temporal lobe, and posterior reversible encephalopathy syndrome.

Received October 14, 2020; accepted after revision March 11, 2021.

From Hôpitaux Universitaires de Strasbourg (A.C., F.L., F.-D.A., S.K.), Service d'Imagerie 2, Hôpital de Hautepierre and Service de Médecine Nucléaire (C.B., I.J.N.), Institut de Cancérologie Strasbourg Europe Strasbourg, France, and Observatoire Français de la Sclérose en Plaques (J.-C.B.) Lyon, France.

Please address correspondence to: Prof Stéphane Kremer; Service d'Imagerie 2, Hôpital de Hautepierre, 1, Ave Molière, 67000 Strasbourg, France; e-mail: stephane.kremer@chru-strasbourg.fr

 Indicates open access to non-subscribers at [www.ajnr.org](http://www.ajnr.org)

 Indicates article with online supplemental data.

<http://dx.doi.org/10.3174/ajnr.A7158>

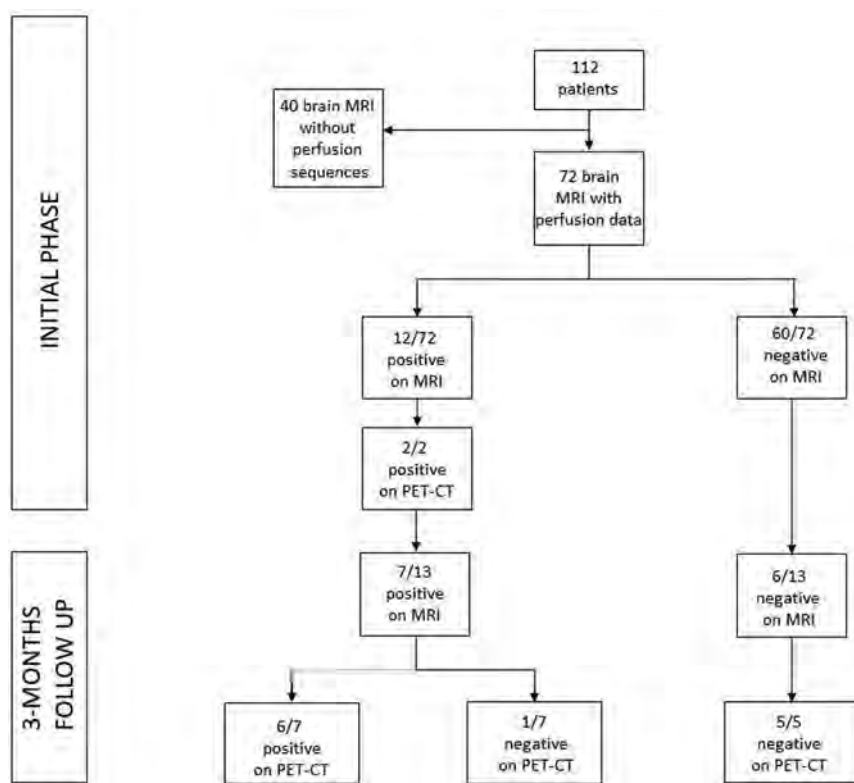


**FIG 1.** In the acute phase of COVID-19 infection, among the 72 patients with the ASL sequence, 12 of them showed hyperperfusion of their colliculi (defined as positive findings on MR imaging) and 60 of them did not (defined as negative findings on MR imaging). Among the 12/72 with positive findings on MR imaging, 2 underwent a PET/CT that showed hyperactivation. At the 3-month follow-up, 13 patients had brain MR imaging with 7 of them showing hyperperfusion of their colliculi, confirmed by PET/CT in 6 patients. Among the 6/13 patients who had no hyperperfusion of their colliculi on MR imaging, all of the PET/CTs that were obtained (5/5) were also negative.

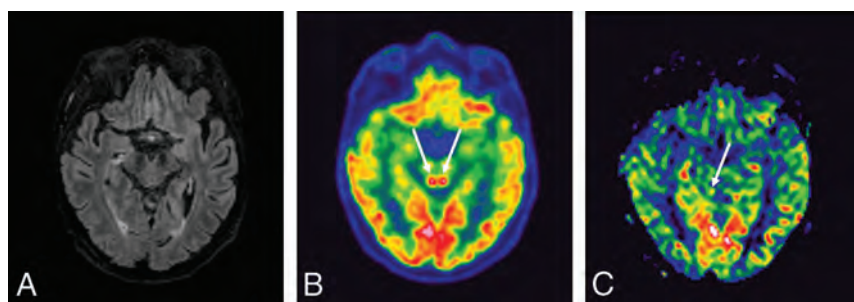


**FIG 2.** A 64-year-old man who had MR imaging for headaches, confusion, pyramidal tract signs, and pathologic awakening under sedation. These 3 images in the same patient showed a hyperactivation of colliculi in  $^{18}\text{F}$  FDG-PET/CT (B), hyperperfusion in the brain perfusion sequence (CBF cartography), less intense and predominantly right-sided hyperperfusion on the follow-up MR imaging at 3 months (C), and no abnormalities on the FLAIR sequence (A).

Perfusion ASL sequences were performed on two 3T MR imaging scanners. On the 3T Achieva dStream (Philips Healthcare), sequence parameters were as follows: 3D perfusion ASL, section thickness of 6 mm, 6-mm spacing between slices,  $80 \times 80$  matrix, 11 ms TE,  $90^\circ$  flip angle, 4235 ms TR, 1 echo, postlabeling delay 2000 ms. On the 3T Signa HD (GE Healthcare), voxel size was  $1.875 \times 1.875 \times 4$  mm, 4599 ms TR,

9.8 ms TE, postlabeling delay 1525 ms. The machine software was used to perform reconstructions (Software release HD23.0\_V03\_1614.b). Postprocessing was performed on MR imaging software and created final gray-scale DICOM images and CBF maps in color JPEG format.

At the time of analysis, the native sequence was first reviewed to ensure its good quality and the absence of artifacts, then systematically reconstructed by windowing with the same scale between the different patients (CBF between 0 and 200). ASL was systematically acquired before gadolinium injection.<sup>11</sup> ASL was available in 72 patients in the acute phase of infection (Fig 1). Colliculi were analyzed qualitatively on CBF maps (for hyperperfusion, hyperintensity, nonhyperperfusion, and intensity indistinguishable from adjacent parenchyma) (Figs 2–4). The images were blindly interpreted independently by 2 neuroradiologists (A.C. and F.L., with 6 and 9 years of experience in neuroradiology, respectively), with total concordance. A brain  $^{18}\text{F}$  FDG-PET/CT was performed for 13 patients on a Vision scanner (Siemens). The  $^{18}\text{F}$  FDG was injected intravenously at 2 MBq/kg, after at least 6 hours of fasting (except ad libitum water intake) and capillary glycemia lower than 6.6 mmol/L. Image acquisition was initiated 30 minutes after the  $^{18}\text{F}$  FDG injection, including low-dose noncontrast transmission CT scan followed by a PET/CT with an acquisition time of 10 minutes. PET data were reconstructed with and without CT-based attenuation correction (TrueX+TOF, 10 iterations, 5 subsets, zoom 2, matrix 880, and Gaussian filter 2). Quantitative measurements were done on the PET/CT data. The metabolism of the right and left colliculi was measured by regions of interest and compared

with that of the mesencephalon. A signal variation of more than 20% between the colliculi and the mesencephalon was considered hypermetabolic.

The PET/CT examinations were carried out on 2 patients during the acute phase of infection and on 12 patients during the 3-month follow-up period (1 patient had an initial PET/CT and follow-up) (Fig 1). The examinations were blindly interpreted independently



by 2 nuclear medicine physicians (C.B. and I.J.N., with 7 and 15 years of experience, respectively) with total concordance.

ASL was acquired prospectively on 25 healthy controls with an age range of 21–61 (mean age, 42.32) on the same 3T Signa HD (GE Healthcare) with the same protocol at the same times, to see the usual collicular appearance.

## RESULTS

Hyperperfusion of the colliculi, predominant in the lower colliculi, was observed in 12/72 (16.7%) patients during the acute

phase of infection. None of the 25 controls had similar findings. Persistent hyperperfusion of the lower colliculi was visually less intense on the follow-up MR imaging than on acute phase imaging and was observed in 7/13 (53.8%) patients.

Brain MRIs were considered normal, unrelated to the current acute event in 30 cases (42%). Among the pathologic brain MRIs (42; 58%), the neuroimaging findings were as follows (also shown in Fig 4):

- 20 (28%) Leptomeningeal enhancement.
- 15 (21%) White matter microhemorrhages.
  - 10 (14%) Circumscribed white matter FLAIR hyperintensities.
  - 10 (14%) Ischemic stroke.
  - 8 (11%) Confluent white matter FLAIR hyperintensities.
  - 4 (5%) FLAIR hypersignal involving the mesial lobe.
  - 2 (3%) Focal enhancement.
  - 0 (0%) Posterior reversible encephalopathy syndrome.

We found a statistical difference between the group with hyperperfusion of the colliculi and the group without

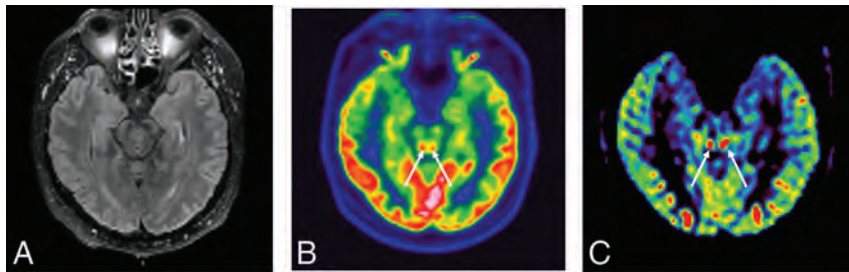


**FIG 3.** A 49-year-old man who had pathologic awakening under sedation and pyramidal tract signs. FLAIR sequence showed no hyperintensity of the colliculi (A). They are hyperactivated in [<sup>18</sup>F] FDG-PET/CT (B) and hyperperfused in perfusion sequence (CBF cartography) (C).

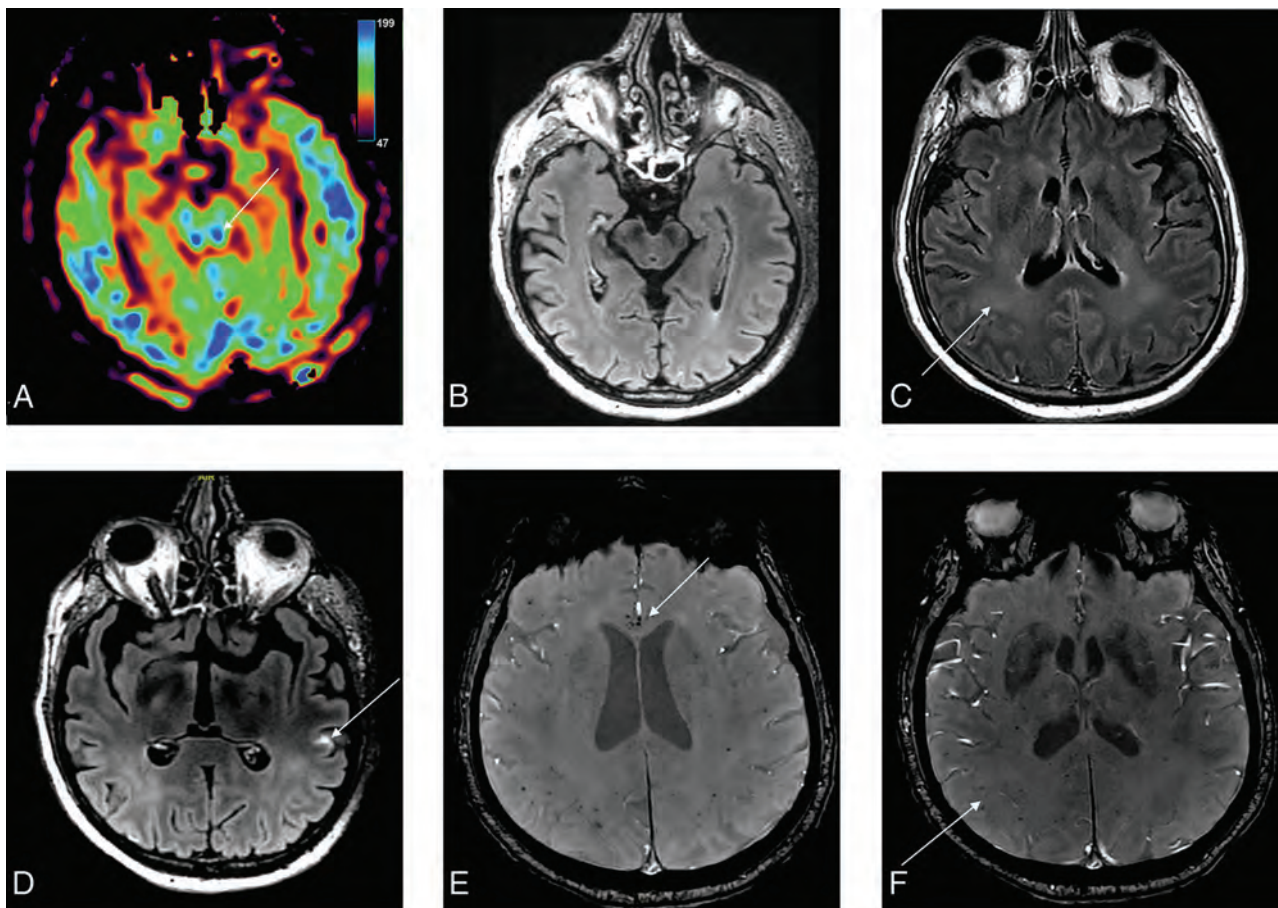


**FIG 4.** A 56-year-old man who presented with delayed awakening under sedation and had colliculi hyperperfusion on ASL perfusion sequence (A) without FLAIR hyperintensity (B). FLAIR postinjection of gadolinium showed diffuse hyperintensities of white matter (C) and leptomeningeal enhancement (D). Magnetic susceptibility sequence showed multiple microhemorrhages of the corpus callosum (E) and of the periventricular white matter (F).

hyperperfusion for the variable “leptomeningeal enhancement” ( $P = .016$ ) (Online Supplemental Data). The colliculi showed no signal anomaly on all the other sequences performed.

Hyperactivation of the lower colliculi was confirmed in the 2 patients (100%) who underwent PET/CT during the acute phase of infection (mean ratio colliculi/mesencephalon, 1.2955), and in 6/7 patients (85.7%) who underwent PET/CT during the 3-month follow-up period (mean ratio colliculi/mesencephalon, 1.2947).

There was no significant difference between the groups with “hyperperfusion of the colliculi” and “no hyperperfusion” for the demographic variables. For clinical variables, seizures were more frequent in the group with hyperperfusion of the colliculi ( $P = .004$ ). Hyperperfusion of colliculi was not associated with a more severe clinical form of the infection nor with a more negative prognosis. However, there was a difference between the 2 groups in the biologic variables concerning the number of leukocytes at admission, which was higher in the group with hyperperfusion of the colliculi ( $P = .02$ ).

## DISCUSSION

Lower colliculi play a role in hearing<sup>12</sup> whereas the upper part contributes to visual coordination.<sup>13</sup>

Recent studies suggest that colliculi might be involved in coordinated autonomic and respiratory responses.<sup>14</sup> The spectrum of pathologies affecting the colliculi is wide, rare, and poorly described. Tumors (glioma) have been described in this region.<sup>15,16</sup> Colliculi can be affected in the context of vasculitis and necrotizing encephalitis.<sup>17</sup> To the best of our knowledge, no examples have been reported in the literature, but inflammatory (neuromyelitis optica spectrum disorder), metabolic (mitochondriopathies), auto-immune (acute disseminated encephalomyelitis), or ischemic (vascular territory of perforating arteries of the basilar trunk) diseases are also possible.

In our study, 16.7% of patients had hyperperfusion of their colliculi during the acute phase of the infection, predominantly in the lower colliculi, without abnormality on the anatomic sequences. We tried to perform quantitative measures on each colliculus and on normal white and gray matter to have as a reference, but the structure of interest was too small to allow reliable measurements in MR imaging. The hyperactivation, well correlated with [<sup>18</sup>F] FDG-PET/CT results, persisted despite discontinuation of sedation and ventilation, which excludes an iatrogenic etiology.<sup>18</sup> This finding has not yet been described in the literature. This study raises the question of the underlying physiopathology of the involvement of the colliculi in COVID-19 infection. The reasons for this overactivation of the predominantly lower colliculi remain poorly understood. Angiotensin-converting enzyme 2, the main receptor for SARS-CoV-2, is expressed by endothelial cells, among others.<sup>19</sup> The presence of angiotensin-converting enzyme 2 receptors within the colliculi has been described in the literature.<sup>20,21</sup> It has been recently described that SARS-CoV-2 can infect endothelial cells with endotheliitis.<sup>22</sup>

This hyperperfusion could reflect a viral gateway into the central nervous system or a direct viral involvement. Hyperleukocytosis could reinforce this hypothesis, but this was not supported by the analysis of the CSF. Lumbar punctures were performed on 7/12 patients, and the SARS-CoV-2 ribonucleic acid was never detected

by reverse-transcriptase polymerase chain reaction. In addition, CSF analyses showed normal or slightly increased white blood cell count ( $< 10/\text{mm}^3$ ). These results do not rule out the diagnosis because lumbar punctures were performed after the SARS-CoV-2 infection (mean, 26.2 days).

CNS immune surveillance and initial immune activation occurred in the subarachnoid space, which is a site for antigen presentation, lymphocyte accumulation and proliferation, and antibodies production.<sup>23</sup> These resulted in an important local inflammatory infiltrate, which may explain the higher prevalence of leptomeningeal enhancement in the hyperperfusion of the colliculi group. Thus, leptomeningeal enhancements can be linked to inflammatory or immunologic responses, as previously described with some neurotropic viruses like human T-cell leukemia and HIV.<sup>24</sup>

One hypothesis would be that the cytokine storm caused by the infection involved these receptors and was responsible for their hyperactivation. This may be supported by the presence of significantly higher leukocyte levels at admission of patients with colliculi hyperperfusion (mean leukocyte rate, 11.069G/L versus 7.522G/L,  $P = .002$ ). Another hypothesis would be that the colliculi are a preferential site for COVID-19 viral encephalitis (not supported by CSF analysis).

Among our 12 patients with colliculi hyperperfusion, 10 were hospitalized in the intensive care unit for severe COVID-19. These patients could have a cytokine release syndrome. It is a consequence of a rapid release of pro-inflammatory cytokines that increase the inflammatory response and could lead to neurotoxicity. The release of cytokines into the CNS increases the local inflammation, which leads to brain cell dysfunctions and edema. Moreover, cytokine release syndrome is associated with blood-brain barrier and brain-CSF barrier breakdown and, therefore, with meningeal inflammation. That could also explain leptomeningeal enhancement.

## CONCLUSIONS

MR imaging and PET revealed hyperactivation of the colliculi in patients with COVID-19 and the CSF analysis performed in a few patients did not detect SARS-CoV-2 ribonucleic acid. Moreover, no biologic or clinical correlation was found with the sign of hyperperfused inferior colliculi, the physiopathologic mechanisms of which remain unclear.

Disclosures: Jean-Christophe Brisset—UNRELATED: Employment: Median Technologies. Stéphane Kremer—UNRELATED: Board Membership: Bayer; Payment for Lectures Including Service on Speakers Bureaus: Roche, Biogen.

## REFERENCES

1. Gulko E, Oleksk ML, Gomes W, et al. **MRI brain findings in 126 patients with COVID-19: initial observations from a descriptive literature review.** *AJNR Am J Neuroradiol* 2020;41:2199–203 CrossRef Medline
2. Yoon BC, Buch K, Lang M, et al. **Clinical and neuroimaging correlation in patients with COVID-19.** *AJNR Am J Neuroradiol* 2020;41:1791–96 CrossRef Medline
3. Kremer S, Lersy F, Anheim M, et al. **Neurologic and neuroimaging findings in COVID-19 patients: a retrospective multicenter study.** *Neurology* 2020;95:e1868–82 CrossRef Medline

4. Kremer S, Lersy F, de Seze J, et al. **Brain MRI findings in severe COVID-19: a retrospective observational study.** *Radiology* 2020;297:E242–51 CrossRef Medline
5. Delorme C, Paccoud O, Kas A, et al. **COVID-19-related encephalopathy: a case series with brain FDG-PET/CT findings.** *Eur J Neurol* 2020;27:2651–57 CrossRef Medline
6. Grimaldi S, Lagarde S, Harle JR, et al. **Autoimmune encephalitis concomitant with SARS-CoV-2 infection: insight from (18)F-FDG PET imaging and neuronal autoantibodies.** *J Nucl Med* 2020;61:1726–29 CrossRef Medline
7. Guedj E, Million M, Dudouet P, et al. **F-FDG brain PET hypometabolism in post-SARS-CoV-2 infection: substrate for persistent/delayed disorders?** *Eur J Nucl Med Mol Imaging* 2020;48:592–95 CrossRef Medline
8. Noguchi T, Yakushiji Y, Nishihara M, et al. **Arterial spin-labeling in central nervous system infection.** *Magn Reson Med* 2016;15:386–94 CrossRef Medline
9. Sachs JR, Zapadka ME, Popli GS, et al. **Arterial spin labeling perfusion imaging demonstrates cerebral hyperperfusion in anti-NMDAR encephalitis.** *Radiol Case Rep* 2017;12:833–37 CrossRef Medline
10. Haller S, Zaharchuk G, Thomas DL, et al. **Arterial spin labeling perfusion of the brain: emerging clinical applications.** *Radiology* 2016;281:337–56 CrossRef Medline
11. Deibler AR, Pollock JM, Kraft RA, et al. **Arterial spin-labeling in routine clinical practice, part 1: technique and artifacts.** *AJNR Am J Neuroradiol* 2008;29:1228–34 CrossRef Medline
12. Speck I, Arndt S, Thurow J, et al. **F-FDG PET imaging of the inferior colliculus in asymmetric hearing loss.** *J Nucl Med* 2020;61:418–22 CrossRef Medline
13. Song JH, McPeck RM. **Neural correlates of target selection for reaching movements in superior colliculus.** *J Neurophysiol* 2015;113:1414–22 CrossRef Medline
14. Müller-Ribeiro FC, Goodchild AK, McMullan S, et al. **Coordinated autonomic and respiratory responses evoked by alerting stimuli: Role of the midbrain colliculi.** *Respir Physiol Neurobiol* 2016;226:87–93 CrossRef Medline
15. **Erratum to too much on your "plate"? Spectrum of pathologies involving the tectal plate.** *Can Assoc Radiol J* 2020;71:NP1 CrossRef Medline
16. Gandhi N, Tsehmaister-Abitbol V, Glikstein R, et al. **Too much on your "plate"? Spectrum of pathologies involving the tectal plate.** *Can Assoc Radiol J* 2020;71:186–94 CrossRef Medline
17. Osborn AG. *Osborn's Brain: Imaging, Pathology, and Anatomy.* Elsevier; 2013
18. Tongjaroenbungam W, Jongkamonwiwat N, Cunningham J, et al. **Opioid modulation of GABA release in the rat inferior colliculus.** *BMC Neurosci* 2004;5:31 CrossRef Medline
19. Catt KJ, Mendelsohn FA, Millan MA, et al. **The role of angiotensin II receptors in vascular regulation.** *J Cardiovasc Pharmacol* 1984;6:S575–86 CrossRef Medline
20. Barnes JM, Steward LJ, Barber PC, et al. **Identification and characterisation of angiotensin II receptor subtypes in human brain.** *Eur J Pharmacol* 1993;230:251–58 CrossRef Medline
21. Song K, Zhuo J, Allen AM, et al. **Angiotensin II receptor subtypes in rat brain and peripheral tissues.** *Cardiology* 1991;79 Suppl 1:45–54 CrossRef Medline
22. Varga Z, Flammer AJ, Steiger P, et al. **Endothelial cell infection and endotheliitis in COVID-19.** *Lancet* 2020;395:1417–18 CrossRef Medline
23. Kivisäkk P, Imitola J, Rasmussen S, et al. **Localizing central nervous system immune surveillance: meningeal antigen-presenting cells activate T cells during experimental autoimmune encephalomyelitis.** *Ann Neurol* 2009;65:457–69 CrossRef Medline
24. Absinta M, Cortese IC, Vuolo L, et al. **Leptomeningeal gadolinium enhancement across the spectrum of chronic neuroinflammatory diseases.** *Neurology* 2017;88:1439–44 CrossRef Medline



# Comparison of Measurement Techniques and Response Criteria for MR Imaging Follow-up in Adult Primary Central Nervous System Lymphoma

 K. Massicotte-Tisluck,  D. Vanderweyen,  J.-F. Vendrell,  D. Fortin, and  G. Gahide



## ABSTRACT

**BACKGROUND AND PURPOSE:** Current guidelines proposed for the measurement of primary central nervous system lymphoma in 2005 have indicated that unidimensional and bidimensional measurements may be used, using the same threshold for response categorization, because no clinical study has evaluated the agreement among the measurement techniques. Hence, our study assessed the agreement among different measurements.

**MATERIALS AND METHODS:** In this retrospective study, primary central nervous system lymphoma lesions were measured with different techniques (longest 1D, axial 1D, 2D, 3D, and the Response Evaluation Criteria in Solid Tumor) on consecutive MR images. Intra- and interobserver correlations were calculated with intraclass correlation coefficients. Correlations between raw measurements and variations in size compared with baseline were evaluated with the Spearman rank correlation, and agreement among response categories was evaluated.

**RESULTS:** A total of 304 examinations obtained in 40 patients was assessed. The intraobserver intraclass correlation coefficient for 3D, 2D, and longest 1D were  $\geq 0.993$ . The interobserver intraclass correlation coefficient was  $\geq 0.967$ . The correlations in raw measurements and size variation in comparison with 3D were respectively; 0.99 and 0.98 for 2D; 0.94 and 0.92 for longest 1D; 0.94 and 0.83 for axial 1D; and 0.90 and 0.79 for Response Evaluation Criteria in Solid Tumor. With 20%–30% and 25%–50% thresholds for unidimensional techniques, response categorizations were 95% and 95% for 2D, 92.5% and 90% for the longest 1D, 87.5% and 82.5% for axial 1D, and 90% and 85% for the Response Evaluation Criteria in Solid Tumor.

**CONCLUSIONS:** Both longest 1D and 2D demonstrated excellent correlations with 3D measurements. The longest 1D could be used for the follow-up of primary central nervous system lymphoma. If unidimensional measurements were used, 20% and 30% cutoffs should be used for defining response categorization instead of the current guidelines.

**ABBREVIATIONS:** CNS = central nervous system; CR = complete response; ICC = intraclass correlation coefficient; PCNSL = primary central nervous system lymphoma; PD = progressive disease; PR = partial response; RECIST = Response Evaluation Criteria in Solid Tumor; SD = stable disease; WBRT = whole brain radiotherapy


Since the first international guidelines were published in 1981 by the World Health Organization,<sup>1</sup> there are currently 2 main coexisting paradigms for clinically assessing tumor responses to treatments. On the one hand, there are unidimensional criteria, mainly represented by the Response Evaluation Criteria in Solid

Tumor (RECIST). These criteria are widely accepted for the assessment of nonneurologic tumors. On the other hand, bidimensional criteria are mainly used for assessing primary cerebral tumors, such as the modified Macdonald criteria and the Response Assessment in Neuro-Oncology Criteria for primary CNS tumors.<sup>2–4</sup> The unidimensional criteria are characterized by partial response (PR), defined as a 30% decrease in size, and progressive disease (PD), defined as a 20% increase in size. The bidimensional criteria are slightly different, with PR defined as a 50% decrease in size and PD corresponding to a 25% increase. The currently accepted guidelines for assessing primary central nervous system lymphomas (PCNSLs) indicate that unidimensional or bidimensional criteria may both be used indiscriminately.<sup>5</sup> Most interesting, the recommended response criteria proposed by the authors were identical, notwithstanding the chosen measurement technique, ie, a 50% decrease in size to define PR and a 25% increase in size to define PD for both unidimensional and bidimensional measurements.

Received November 22, 2020; accepted after revision February 19, 2021.

From the Département d'Imagerie Médicale, (K.M.-T., D.V., G.G.) and Service de Neurochirurgie, Département de Chirurgie (D.F.), Centre Hospitalier Universitaire de Sherbrooke, Sherbrooke, Québec, Canada; and Centre de Recherche du Centre Hospitalier Universitaire de Sherbrooke, Etienne Le Bel (D.F., G.G.), Faculté de Médecine et des Sciences de la Santé (K.M.-T., D.V.), Université de Sherbrooke, Sherbrooke, Québec, Canada and Departments of Neuroradiology (J.-F.V.), Institut de cancérologie de Montpellier, Clinique de val d'Aurelle, Montpellier, France.

Please address correspondence to G rald Gahide, MD, Radiology Department, Centre Hospitalier Universitaire de Sherbrooke, Sherbrooke, Quebec, Canada. 3001 12e Ave N, Sherbrooke, QC J1H 5H3; e-mail: gerald.gahide@usherbrooke.ca; @ggahide

 Indicates article with online supplemental data.

<http://dx.doi.org/10.3174/ajnr.A7132>

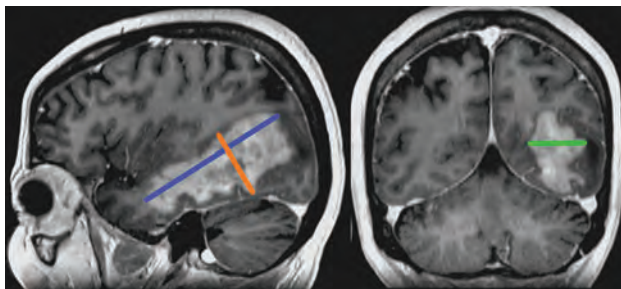


**FIG 1.** 3D measurement example on postcontrast 3D T1 MPRAGE. The blue line represents the longest 1D. The orange line is the longest length perpendicular to the blue line; their product represents 2D. The green line is the longest length perpendicular to the blue and orange lines; those 3 measures are used to calculate the volume for 3D.

Since the publication of the international guidelines in 2005, no clinical study has evaluated the agreement among the different measurement techniques for defining tumor-response categorization in PCNSL.<sup>5</sup> Hence, our study consisted of assessing the agreement among different measurement techniques in a group of patients treated at our institution for PCNSL. We also assessed whether a correlation was observed between response categorization and clinical surrogates.

## MATERIALS AND METHODS

### Patients

All immunocompetent patients presenting to our institution with PCNSL from 2000 to 2019 were considered for inclusion in this study. The inclusion criteria were as follows: 1) biopsy-confirmed PCNSL, 2) naïve patient with no prior treatment, 3) immunocompetency, and 4) 18 years of age or older. The exclusion criteria were as follows: 1) systemic lymphoma with secondary cerebral involvement, 2) relapsing disease, 3) unavailable imaging files, and 4) history of cytoreductive surgery.

### Imaging Techniques

Cerebral MR imaging was performed before each cycle of treatment every 4–6 weeks. MR imaging was performed on a 1.5T scanner (Magnetom Symphony; Siemens) or a 3T scanner (Ingenia; Philips Healthcare). The imaging protocol included axial T1-weighted spin-echo, T2-weighted spin-echo, T2 FLAIR, diffusion-weighted imaging (multisection spin-echo single-shot echo-planar) with generated ADC maps and a T1-weighted gradient-echo acquisition after gadolinium injection (MPRAGE). Images were interpreted on a Barco MDNC 3421 reading station (Barco, Kortrijk, Belgium) with a PACS server.

### Measurements

The measurements were obtained by 2 investigators (K.M.-T. and D.V.).

The axial 1D measurement was obtained by looking solely at the axial plane by adding the sum of the longest diameters of all enhancing lesions visible on axial images. Axial 1D measurements were expressed in millimeters.

The RECIST 1.1 measurement criteria consisted of the summation of the longest axial diameters for a maximum of 2 lesions per organ (lesions of  $\geq 10$  mm at baseline). Because the CNS

equals 1 organ, 2 lesions at maximum were considered target lesions. The other lesions were considered nontarget but could influence the response categorization as recommended by the RECIST 1.1 guidelines.<sup>6</sup> In addition to the relative increase of 20%, the sum must also demonstrate an absolute increase of at least 5 mm.

The longest 1D measurement was the sum of the longest diameters of all enhancing lesions among the measurements obtained on axial, coronal, or sagittal planes (Fig 1, blue line). In other words, the longest 1D measurements were made by adding the length of each lesion's longest axis. The longest 1D measurements were expressed in millimeters.

The 2D measurements corresponded to the sum of the products of the longest length of enhancing lesions with their maximum perpendicular diameter obtained in the same plane (axial, coronal, or sagittal) (Fig 1, orange line). 2D measures were expressed in square millimeters.

The 3D volumes were calculated using the 2 lengths obtained for calculating the 2D measurements and the longest perpendicular diameter (Fig 1, green line). The volume of each lesion was estimated by an ellipsoid formula [ $V = (4 \times \pi \times A \times B \times C) / 3$ ] and expressed in cubic millimeters. If there was  $> 1$  lesion, 3D measurements corresponded to the summation of the different volumes.

As recommended by the guidelines, the size of a measurable lesion needed to be at least twice the thickness of the axial section acquisition and visible on  $\geq 2$  axial slices with 0-mm skip.<sup>6</sup> Considering the potential margin of error when measuring smaller lesions, a minimum of 1 cm in length in 1 axis was required to be considered measurable.<sup>3,6</sup> If an initially measurable lesion decreased to measure less than 5 mm during treatment, it was reported to measure 5 mm until complete resolution. As proposed in the modified Macdonald criteria and Küker et al,<sup>2</sup> a complete response (CR) was a residual enhancing lesion of  $< 5$  mm on 2 consecutive MR images in the absence of edema in the region of the biopsy, hemorrhage, or infection, or, if the initial lesion was  $> 5$  cm for 2 consecutive MR images.<sup>7</sup> Lesions of  $< 1$  cm or having nonnodular enhancement at baseline were reported as a nonmeasurable disease but were considered, and their evolution was noted as stable, increasing, or decreasing. If a nonmeasurable lesion grew and met measurable criteria on follow-up MR imaging, it was then properly measured.<sup>6</sup>

Interobserver variability was assessed by comparing the successive measurements of 19 lesions in 9 patients on 51 MR images. Intraobserver variability was assessed by repeating the measurements of 55 lesions on 20 baseline MR images for 20 patients after a 1-year delay.

### Definition of Response Categories

Patients were classified into 4 groups according to the cutoff values reported in the Online Supplemental Data: PD, stable disease (SD), PR, and CR. The best overall response for each patient was considered to define the response category as recommended.<sup>5,8</sup> To assess the impact on response categorization of using the 25% and 50% cutoffs for unidimensional measurements, as recommended by the international guidelines for PCNSL, we performed a second analysis using these criteria proposed by Abrey et al<sup>5</sup> as reported in the Online Supplemental Data. For each

measurement technique, the lesions were compared with the baseline MR image and classified as CR, PR, SD, or PD according to the percentages indicated in the Online Supplemental Data. Any new lesion was considered a progressive disease except if a

complete response had been obtained beforehand. In this case, the new lesion was considered a relapse. All complete responses had to be confirmed on follow-up imaging.

### Statistical Analysis

Statistical analysis was performed with SPSS software, Version 24 (IBM).

Interobserver and intraobserver correlations were evaluated by intraclass correlation coefficients (ICCs) with a 95% confidence interval. A single-measurement, absolute-agreement, 2-way mixed-effects model was used for calculation. Completely resolved lesions on follow-up MR images were excluded to not artificially increase inter- and intraobserver concordance.

Correlation between raw measurements according to the different methods was realized with the Spearman rank correlation after excluding resolved lesions, as aforementioned, to not artificially increase the coefficients. To determine the concordance among the different methods, we applied a cubic root to volumetric measurements and a square root to the surface area for comparison in the same unit of measurement (so-called root manipulation in the current article).

To assess the response categorization, we calculated the variation in size on follow-up MR images in comparison with the baseline MR image. The correlation coefficients among the different techniques were obtained after applying a cubic root on volumetric measurements and a square root on surface areas. These data were evaluated in pairs with the Spearman rank correlation (axial 1D versus longest 1D, axial 1D versus 2D, and so forth).

Response categories for each measurement technique were classified at each follow-up. The frequency of agreement was evaluated with a contingency table.

## RESULTS

### Population Characteristics

An archive chart review identified 92 patients with a cerebral lymphoma diagnosis. From this population, 5 had a relapse of PCNSL and 17 had systemic lymphoma; 70 patients met the inclusion criteria. Nineteen patients were treated before 2003, and their MR images were not available in the data-storage archives. Eleven patients had a prior surgical resection instead of a biopsy, so 40 patients were included in the study. The mean age was 61.5 (SD, 11) years, with 42.5% women ( $n = 17$ ) (Table 1). A total of 304 MR images were analyzed with a mean number of 7.6 MR images per patient (Fig 2).

### Intraobserver and Interobserver Correlations

Both intra- and interobserver ICCs for 3D, 2D, and longest 1D measurements

**Table 1: Included patient characteristics (N = 40)**

Patient Characteristics	Value (SD)
Mean age (yr)	61.5 (11.1)
Age range (yr)	29–81
Male/female ratio	23:17
Pathology	
Primary CNS large B-cell lymphoma	40
Prior WBRT	5
Median follow-up (yr) <sup>a</sup>	3.01
Total baseline MR imaging	33
Total baseline CT	7
Total follow-up MR imaging	254
Total follow-up CT	10
Mean number of MR images per patient	7.60 (3.49)
Mean number of lesions on baseline MR image	2.33 (1.14)
Disease location	
Superficial	16
Deep	15
Mixed	9
Particular disease distribution	
Midline crossing lesion	10
Multifocal, bilateral lesions	16
Induction response <sup>a</sup>	22
Relapse after induction <sup>a</sup>	12

**Note:**—WBRT indicates whole brain radiotherapy; SD, standard deviation.

<sup>a</sup>One patient was lost to follow-up, and 5 stopped their treatment for palliative care and were not included in this analysis.

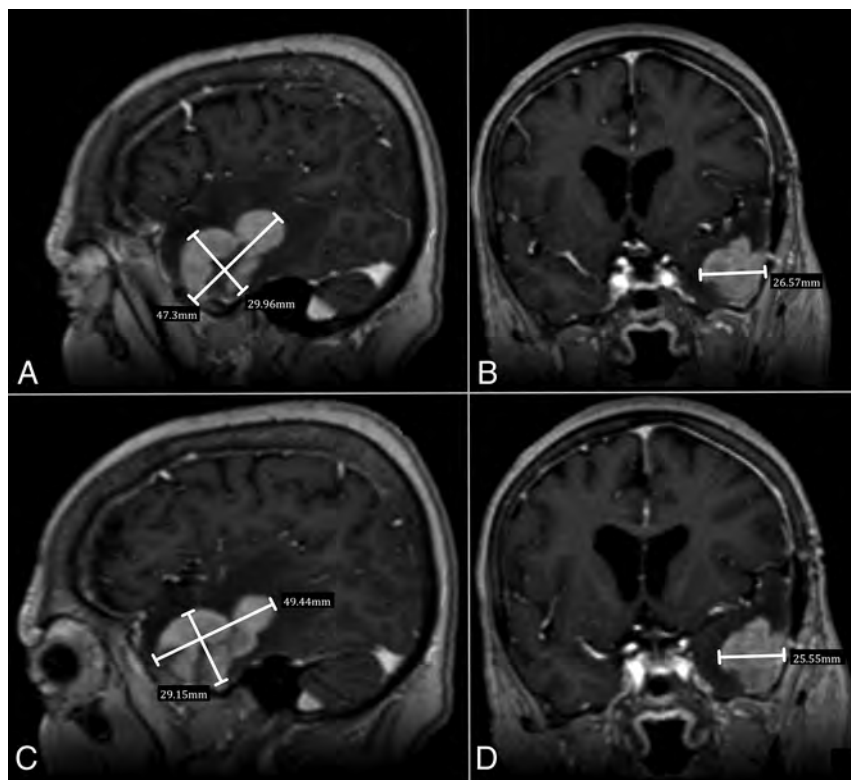


**FIG 2.** Postcontrast 3D T1 MPRAGE in a 56-year-old woman treated for a left temporal PCNSL. Comparison of the 3D measurements performed by the 2 readers (reader 1, A and B; reader 2, C and D).



**Table 2: Intraobserver and interobserver correlations calculated with the ICC for each measurement method in raw units (95% CI)**

Measurement Method	Intraobserver Correlation (95% CI)	Interobserver Correlation (95% CI)
Longest 1D	0.993 (0.985–0.997)	0.967 (0.947–0.979)
2D	0.997 (0.994–0.998)	0.982 (0.969–0.989)
3D	0.993 (0.985–0.997)	0.992 (0.986–0.995)

**Table 3: Correlation between raw measurements with the Spearman rank correlation coefficient**

Measurement Method	Spearman Rank Correlation Coefficient (95% CI)
Longest 1D vs axial 1D	0.977
Longest 1D vs RECIST	0.930
Longest 1D vs 2D	0.965
Longest 1D vs 3D	0.935
Axial 1D vs RECIST	0.915
Axial 1D vs 2D	0.963
Axial 1D vs 3D	0.942
RECIST vs 2D	0.924
RECIST vs 3D	0.898
2D vs 3D	0.990

showed very strong correlations (Table 2). The intraobserver ICC varied from 0.993 to 0.997 in raw units and was calculated to be 0.997 after root manipulation for 2D and 3D measurements. The interobserver ICC varied from 0.967 to 0.992 in raw units and from 0.966 to 0.968 after root manipulation for 2D and 3D, respectively.

### Correlation among Measurement Strategies

The correlations among the different measurement techniques were also strong. If the tridimensional measurements were considered as the reference, the correlations with bidimensional and unidimensional measurements were also excellent, ranging from 0.99 (2D) to 0.90 (RECIST 1.1) (Table 3 and Fig 3).

A decrease in the correlation between RECIST 1.1 and the other techniques was noticed after the fifth MR image (Fig 3). From then on, fewer data were available because several patients were in complete remission or opted for palliative treatment and had thus been excluded from the analysis. As a reference, only 12 of the 40 patients remained at the sixth follow-up MR imaging.

### Correlation among Different Response Measurements

Compared with the baseline MR images, most measurement methods presented with a correlation coefficient of  $\geq 0.80$  (Table 4).

2D had the best correlation with 3D, with a coefficient of 0.980, closely followed by the longest 1D versus 2D with a coefficient of 0.96. Compared with 3D, 2D (0.98) and the longest 1D (0.92) had a better correlation coefficient than axial 1D (0.83) and RECIST (0.79), which were still, nonetheless, excellent.

### Response Categorization

Each patient was categorized as having CR, PR, SD, or PD according to the measurable disease extent evolution in comparison with the baseline. Agreement between each measurement method is presented as contingency tables (Online Supplemental Data). These results demonstrate excellent agreement in categorization between each technique, most being  $>90\%$ , particularly for the first method.

## DISCUSSION

### Background, Reproducibility, and Measurements

One of the particular aspects of PCNSL is its radiologic presentation as a strongly enhanced lesion.<sup>2</sup> This aspect makes PCNSL quite simple to delineate and measure, very likely explaining the excellent inter- and intraobserver correlations reported herein (both being  $>0.96$ ). Nevertheless, PCNSL may behave oddly, growing asymmetrically in several directions and giving a non-spheric aspect to the lesion. This feature implies that there could be some variations in estimating the lesion behavior according to the kind of measurement used (1D, 2D, or 3D).

The response assessment of PCNSL is currently based on the widely accepted international guidelines for standardizing evaluation and response criteria. These guidelines have dramatically improved the quality of patient follow-up and management and have participated in the improvement of scientific publications on the subject, allowing reliable comparisons among studies. One of the interesting points of these guidelines was the decision of the authors not to choose between recommending unidimensional or bidimensional measurements.<sup>5,9,10</sup> This decision was very likely due to the different backgrounds of the authors: Some coming from the 2D neuro-oncologic world used to the modified Macdonald criteria, and the others coming from the 1D solid-tumor world used to the RECIST.

Most interesting, our study demonstrated excellent correlation coefficients among all the different techniques for evaluating the variation in the size of the lesions compared with the baseline MR image. The longest 1D and 2D had excellent correlations with the 3D reference, ranging from 0.92 to 0.94 for the longest 1D and an almost perfect correlation of 0.98 to 0.99 for 2D. This finding could slightly advocate using 2D measurements, given their almost perfect correlations with 3D. Nevertheless, all the other measurement techniques had correlation coefficients greater than acceptable, and, in routine practice, the simplest measurement technique needs particular consideration because it is generally more acceptable for readers and accessible to all clinicians. Many contributing factors to discrepancies have long been recognized, most particularly excessive workload and cognitive overload, particularly in oncologic centers with heavy radiologic CT and MR imaging activities.<sup>11</sup>

One of the other interesting points of these international guidelines was the choice of the authors to recommend 25% and 50% cutoffs to define progressive disease and partial response for both unidimensional and bidimensional measurements. As indicated by Therasse et al<sup>12</sup> in the RECIST 1.0 guidelines, a 25% increase in size for bidimensional measurements corresponds to a 12% increase for unidimensional measures. Due to observer reproducibility issues, a 12% limit was found to be prone to mistakes, and a cutoff of 20% was chosen for the RECIST 1.0 criteria. They also indicated that a 50% decrease in size for bidimensional measurements corresponds to a 30% decrease for unidimensional measurements. Our study tends to confirm that using 25% and 50% cutoffs for unidimensional measurements provides less homogeneous response categorization among the different techniques. This is not readily obvious when just reading the excellent correlation coefficients obtained in both cases, but those coefficients are heavily influenced by

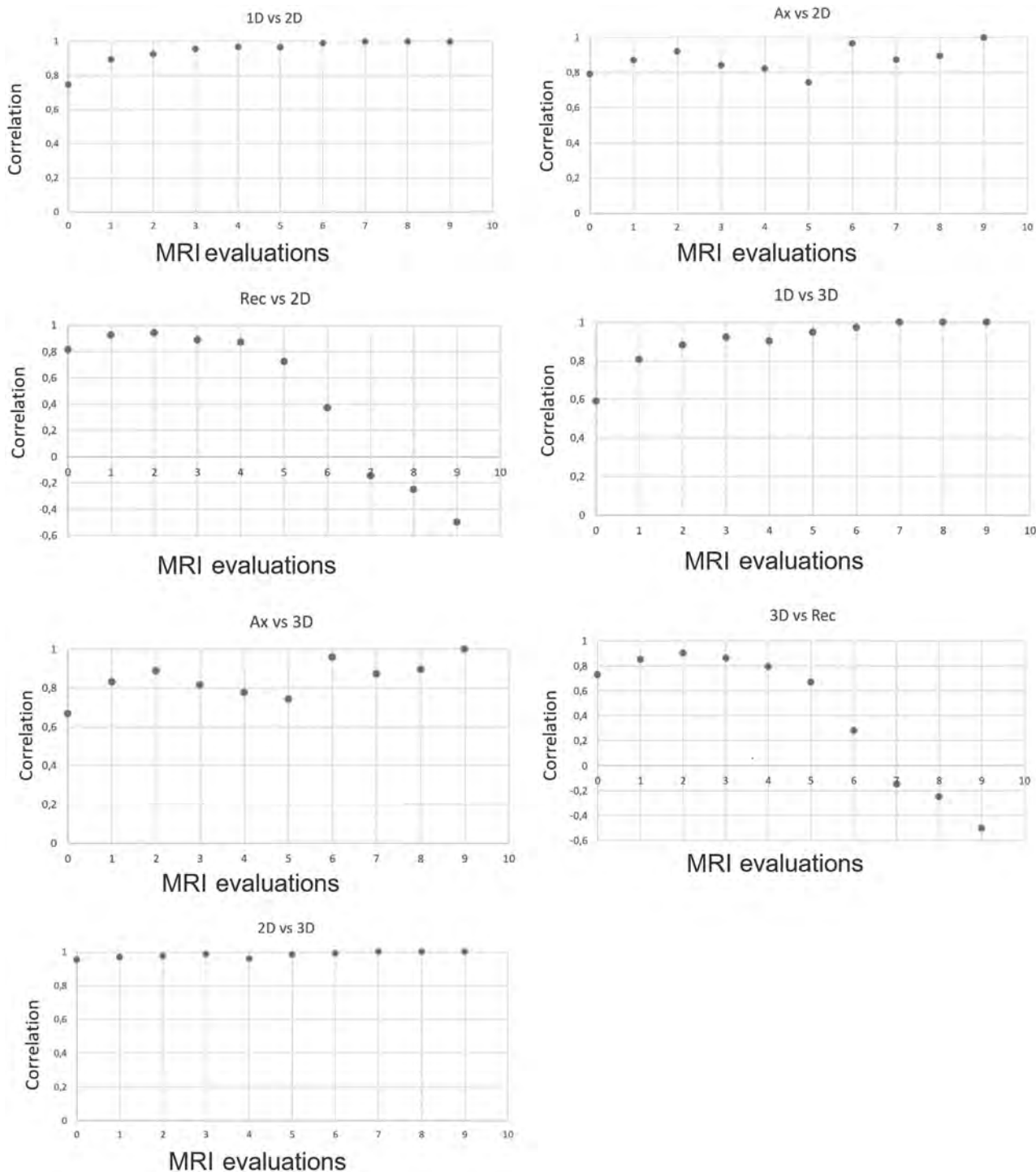


**FIG 3.** Correlation of raw measurements calculated with the Spearman correlation after we applied cubic root on volume calculated with the 3D method and square root on surface area calculated with the 2D methods (exclusion of zero values). Rec indicates RECIST; Ax, axial.

the complete responses encountered for >50% of the patients in our series. These complete responses have perfect agreement, which is obvious because they correspond to the complete disappearance of tumoral enhancement. On the other hand, there was more dispersion for the other categories when using 25% and 50% for unidimensional measurements. Stable disease ranged from 3 to 7 patients, and progressive disease ranged from 6 to 10 with 25% and 50% cutoffs, while ranges were from

4 to 5 patients and 6 to 9 with 20% and 30% cutoffs, respectively. Similarly, the frequencies of agreement were all stronger or equal when using 20% and 30% cutoffs rather than 25% and 50%. This finding advocates using 20% and 30% cutoffs for unidimensional measurements instead of the recommended 25% and 50% cutoffs by Abrey et al.<sup>5</sup>

Axial 1D and longest 1D could both be used as standard measurements for PCNSL, because they showed great correlation

**Table 4: Spearman rank correlation coefficients of the lesion variation in size compared with baseline MR images<sup>a</sup>**

Measurement Method	Spearman Correlation Coefficient (95% CI)
Longest 1D vs axial 1D	0.890
Longest 1D vs RECIST	0.898
Longest 1D vs 2D	0.962
Longest 1D vs 3D	0.918
Axial 1D vs RECIST	0.796
Axial 1D vs 2D	0.872
Axial 1D vs 3D	0.831
RECIST vs 2D	0.847
RECIST vs 3D	0.794
2D vs 3D	0.980

<sup>a</sup>Cubic roots and square roots were applied for 3D and 2D measurements, respectively.

compared with 3D measurements and had an excellent response categorization agreement. However, the longest 1D showed a better performance in all our analyses. According to the literature, 1D, 2D, and 3D measurements are equivalent to volumetric criteria and are easier to perform.<sup>8,13</sup> Many studies have already demonstrated great intraobserver and interobserver reliability using unidimensional measurements.<sup>14,15</sup> Most guidelines suggest unidimensional measurements in oncologic follow-up to assure greater reproducibility and to facilitate follow-up. Our results show that unidimensional measurements could also be applied to PCNSL.

### Limitations

Using the Spearman correlation, the multiplicity of follow-up MR images could induce an overestimation of the correlations obtained with raw measures. This could have affected the results presented in Table 3. However, the presentation of the same results in Fig 2 also expresses this correlation without the potential error of overestimation. Because Table 3 is easier to read, we decided to present both methods.

### CONCLUSIONS

Unidimensional and bidimensional measurements are both reliable techniques to assess the PCNSL response to treatment, though there was a slight advantage of 2D measurements regarding the correlation coefficients obtained in comparison with 1D and 3D measurements and for classifying the response categories. Our study suggests that the longest 1D measurements could be used for the follow-up of PCNSL with high performance and agreement with 3D measurements. Our study also indicated that if unidimensional measurements were to be used, 20% and 30% cutoffs should be used instead of 25% and 50% for defining PD and PR, respectively, contrary to the recommendations of the international guidelines.

### ACKNOWLEDGMENTS

We wish to thank the biostatistics team from Centre Hospitalier Universitaire de Sherbrooke Research Center, and Dr M. St-Amant Beaudoin for his advice.

Disclosures: Gerald Gahide—UNRELATED: Consultancy: Boston Scientific.

### REFERENCES

1. Miller AB, Hoogstraten B, Staquet M, et al. **Reporting results of cancer treatment.** *Cancer* 1981;47:207–14 CrossRef Medline
2. Küker W, Nägele T, Thiel E, et al. **Primary central nervous system lymphomas (PCNSL): MRI response criteria revised.** *Neurology* 2005;65:1129–31 CrossRef Medline
3. Lin NU, Lee EQ, Aoyama H, et al. Response Assessment in Neuro-Oncology (RANO) group. **Response assessment criteria for brain metastases: proposal from the RANO group.** *Lancet Oncol* 2015;16:270–78 CrossRef Medline
4. Vogelbaum MA, Jost S, Aghi MK, et al. **Application of novel response/progression measures for surgically delivered therapies for gliomas: Response Assessment in Neuro-Oncology (RANO) working group.** *Neurosurgery* 2012;70:234–43 CrossRef Medline
5. Abrey LE, Batchelor TT, Ferreri AJ, et al. International Primary CNS Lymphoma Collaborative Group. **Report of an international workshop to standardize baseline evaluation and response criteria for primary CNS lymphoma.** *J Clin Oncol* 2005;23:5034–43 CrossRef Medline
6. Eisenhauer EA, Therasse P, Bogaerts J, et al. **New response evaluation criteria in solid tumours: revised RECIST guideline (version 1.1).** *Eur J Cancer* 2009;45:228–47 CrossRef Medline
7. Macdonald DR, Cascino TL, Schold SC, et al. **Response criteria for phase II studies of supratentorial malignant glioma.** *J Clin Oncol* 1990;8:1277–80 CrossRef Medline
8. Galanis E, Buckner JC, Maurer MJ, et al. **Validation of neuroradiologic response assessment in gliomas: measurement by RECIST, two-dimensional, computer-assisted tumor area, and computer-assisted tumor volume methods.** *Neuro Oncol* 2006;8:156–65 CrossRef Medline
9. Chiavazza C, Pellerino A, Ferrio F, et al. **Primary CNS lymphomas: challenges in diagnosis and monitoring.** *Biomed Res Int* 2018;2018:3606970 CrossRef Medline
10. Grommes C, Rubenstein JL, DeAngelis LM, et al. **Comprehensive approach to diagnosis and treatment of newly diagnosed primary CNS lymphoma.** *Neuro Oncol* 2019;21:296–305 CrossRef Medline
11. Vendrell JF, Frandon J, Boussat B, et al. **Double reading of out-sourced CT/MR radiology reports: retrospective analysis.** *J Patient Saf* 2018 Aug 13. [Epub ahead of print] CrossRef Medline
12. Therasse P, Arbuck SG, Eisenhauer EA, et al. **New guidelines to evaluate the response to treatment in solid tumors.** *J Natl Cancer Inst* 2000;92:205–16 CrossRef Medline
13. Shah GD, Kesari S, Xu R, et al. **Comparison of linear and volumetric criteria in assessing tumor response in adult high-grade gliomas.** *Neuro Oncol* 2006;8:38–46 CrossRef Medline
14. Hopper KD, Kasales CJ, Van Slyke MA, et al. **Analysis of interobserver and intraobserver variability in CT tumor measurements.** *AJR Am J Roentgenol* 1996;167:851–54 CrossRef Medline
15. McElean A, Panicek DM, Zabor EC, et al. **Intra- and interobserver variability in CT measurements in oncology.** *Radiology* 2013;269:451–59 CrossRef Medline
16. Chappell R, Miranpuri SS, Mehta MP. **Dimension in defining tumor response.** *J Clin Oncol* 1998;16:1234 CrossRef Medline



# Is Contrast Medium Really Needed for Follow-up MRI of Untreated Intracranial Meningiomas?

J. Boto, R. Guatta, A. Fetsiori, J. Hofmeister, T.R. Meling, and M.I. Vargas



## ABSTRACT

**BACKGROUND AND PURPOSE:** Recent concerns relating to tissue deposition of gadolinium are favoring the use of noncontrast MR imaging whenever possible. The purpose of this study was to assess the necessity of gadolinium contrast for follow-up MR imaging of untreated intracranial meningiomas.

**MATERIALS AND METHODS:** One-hundred twenty-two patients (35 men, 87 women) with meningiomas who underwent brain MR imaging between May 2007 and May 2019 in our institution were included in this retrospective cohort study. We analyzed 132 meningiomas: 73 non-skull base (55%) versus 59 skull base (45%), 93 symptomatic (70%) versus 39 asymptomatic (30%). Fifty-nine meningiomas underwent an operation: 54 World Health Organization grade I (92%) and 5 World Health Organization grade II (8%). All meningiomas were segmented on T1 3D-gadolinium and 2D-T2WI. Agreement between T1 3D-gadolinium and 2D-T2WI segmentations was assessed by the intraclass correlation coefficient.

**RESULTS:** The mean time between MR images was 1485 days (range, 760–3810 days). There was excellent agreement between T1 3D-gadolinium and T2WI segmentations ( $P < .001$ ): mean tumor volume (T1 3D-gadolinium: 9012.15 [SD, 19,223.03] mm<sup>3</sup>; T2WI: 8528.45 [SD, 18,368.18] mm<sup>3</sup>; intraclass correlation coefficient = 0.996), surface area (intraclass correlation coefficient = 0.989), surface/volume ratio (intraclass correlation coefficient = 0.924), maximum 3D diameter (intraclass correlation coefficient = 0.986), maximum 2D diameter in the axial (intraclass correlation coefficient = 0.990), coronal (intraclass correlation coefficient = 0.982), and sagittal planes (intraclass correlation coefficient = 0.985), major axis length (intraclass correlation coefficient = 0.989), minor axis length (intraclass correlation coefficient = 0.992), and least axis length (intraclass correlation coefficient = 0.988). Tumor growth also showed good agreement ( $P < .001$ ), estimated as a mean of 461.87 [SD, 2704.1] mm<sup>3</sup>/year on T1 3D-gadolinium and 556.64 [SD, 2624.02] mm<sup>3</sup>/year on T2WI.

**CONCLUSIONS:** Our results show excellent agreement between the size and growth of meningiomas derived from T1 3D-gadolinium and 2D-T2WI, suggesting that the use of noncontrast MR imaging may be appropriate for the follow-up of untreated meningiomas, which would be cost-effective and avert risks associated with contrast media.

**ABBREVIATIONS:** Gd = gadolinium; ICC = intraclass correlation coefficient; WHO = World Health Organization

Recent concerns regarding gadolinium (Gd) compounds are fueling a trend to use contrast media in MR imaging less frequently. Notwithstanding the well-established safety profile of Gd compounds, a small number of immediate adverse effects, which may be life-threatening, has been reported<sup>1,2</sup> at a rate of

approximately 0.3%.<sup>2</sup> Furthermore, repeat administration of Gd-based contrast may lead to deposition of Gd in the dentate nucleus and the globus pallidus,<sup>3-7</sup> which seems to be the case with linear rather than macrocyclic Gd compounds,<sup>4</sup> despite a normal renal function<sup>7</sup> and an intact blood-brain barrier.<sup>6</sup> Health care costs should also be considered because they are a heavy burden to modern Western societies,<sup>8-10</sup> and medical imaging accounts for a large proportion of these costs.<sup>10</sup> Gd-based contrast media significantly contribute to the cost of an MR image, due to the price of the contrast medium itself and also because of the prolonged image-acquisition time. Using contrast media more sparingly could, therefore, reduce these costs considerably.

The above-mentioned concerns are particularly pertinent to young patients with incidental or asymptomatic meningiomas in which frequent and long-term follow-up MR imaging is usually

Received September 17, 2020; accepted after revision March 8, 2021.

From the Divisions of Neuroradiology (J.B., A.F., J.H., M.I.V.) and Neurosurgery (T.R.M.), Geneva University Hospital and Faculty of Medicine of Geneva, Geneva, Switzerland; and Division of Neurosurgery (R.G.), Lugano Regional Hospital (Civic), Lugano, Switzerland.

Please address correspondence to José Boto, MD, MSc, Geneva University Hospitals, Division of Neuroradiology, Rue Gabrielle-Perret-Gentil 4, 1205 Genève, Switzerland; e-mail: jose.m.baiaoboto@hcuge.ch



Indicates article with online supplemental data.

<http://dx.doi.org/10.3174/ajnr.A7170>

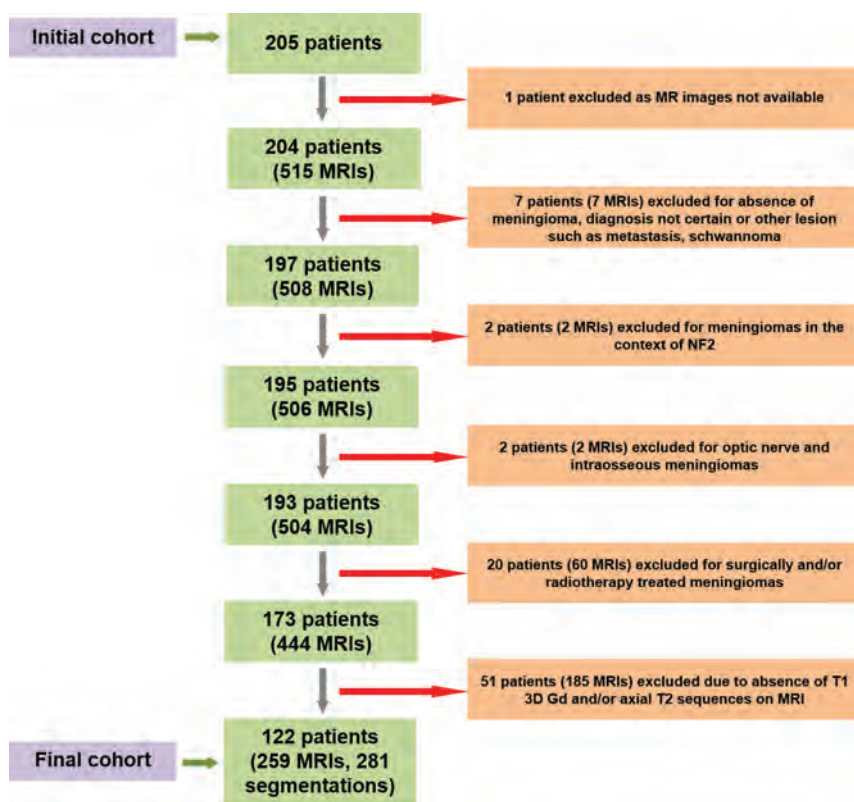


**FIG 1.** Flow diagram showing the steps in patient selection. NF2 indicates neurofibromatosis type 2.

performed, the current standard-of-care being MR with Gd-based contrast media.<sup>11</sup> Intracranial meningiomas are, by and large, benign World Health Organization (WHO) grade I tumors derived from meningothelial cells,<sup>12,13</sup> representing approximately one-third of all primary central nervous system tumors<sup>14</sup> and 15% of symptomatic intracranial masses.<sup>15</sup> They are extra-axial lesions that usually exhibit slow growth (approximately 14%/year for WHO grade I lesions).<sup>16</sup> However, the growth rate can be substantially higher, particularly in WHO grade II and III meningiomas, necessitating frequent MR imaging follow-up. For instance, the European Association of Neuro-Oncology advocates diligent radiologic follow-up of meningiomas. For small asymptomatic meningiomas, the recommendation of this institution is to assess the tumor dynamics with contrast MR imaging at 6 months after the initial diagnosis and then annually as long as the patient remains asymptomatic.<sup>11</sup>

Quantitative MR imaging parameters such as tumor volume<sup>17</sup> are important in predicting tumor growth and behavior. Nakasu and Nakasu,<sup>18</sup> in 2020, identified large tumor size and annual volume change of  $\geq 2.1 \text{ cm}^3$  as the strongest predictors of symptomatic tumor progression. Several other parameters may be important in predicting the potential for rapid tumor growth, such as male sex,<sup>18</sup> younger age,<sup>18</sup> absence of calcification,<sup>18-23</sup> peritumoral edema,<sup>21,22,24</sup> and hyperintensity on T2WI.<sup>18,19,22,25,26</sup>

Considering these points, the purpose of this retrospective cohort study was to assess the hypothesis that size and growth of untreated intracranial meningiomas derived from T1 3D-Gd and

2D-T2WI sequences show good agreement, which would, should this be the case, question the added value of Gd-based contrast media for routine follow-up MRIs of intracranial meningiomas.

## MATERIALS AND METHODS

### Subjects

The Ethics Committee of Geneva University approved this retrospective cohort study. Patient consent was waived. All patients with meningiomas who underwent brain MR imaging with Gd-based contrast media between May 2007 and May 2019 were retrieved from the radiology information system of our institution using the thesaurus feature with the appropriate search terms ("brain MR imaging," "meningioma," "Dotarem"), which searches for exact matches.

The initial search identified 205 patients. Pre-hoc inclusion criteria were adult patients with symptomatic or asymptomatic intracranial meningiomas who had undergone brain MR imaging, including at least T1 3D-Gd and axial 2D-T2WI sequences, in cases in which the radiologic diagnosis

of meningioma was practically certain. Pre-hoc exclusion criteria were uncertain diagnosis of meningioma; meningiomas in the context of a syndrome such as neurofibromatosis type 2, optic nerve, intraosseous, and en plaque meningiomas; and previously treated meningiomas, surgically or otherwise. Eighty-three patients and 256 MR scans were excluded on the basis of these criteria. A total number of 122 patients (35 men, 87 women) was analyzed (Fig 1). The analysis was conducted on the entire cohort as a whole, but a subgroup analysis by meningioma location (skull base versus non-skull base), meningioma size (maximum 3D diameter  $\leq 20$  versus  $> 20$  mm), and symptoms (asymptomatic versus symptomatic) was also performed.

To estimate tumor growth, we included only MRIs in which the time interval between the index scan and subsequent scans was at least 2 years (730 days). Because meningiomas are slow-growing tumors, shorter time periods were excluded to allow detection of tumor growth and to minimize measurement error when calculating annual tumor growth, in which a small error could potentially be multiplied several-fold if a very short time interval was used. Tumor growth was calculated between the index scan and each subsequent scan available for that particular patient. Thirty meningiomas from 26 patients met the time interval criterion of at least 730 days between the index scan and subsequent scans, producing a total of 51 data points. Annual growth for each dimension and geometric parameter was calculated and normalized to annual growth expressed as both the absolute value and percentage change per year to allow comparison.

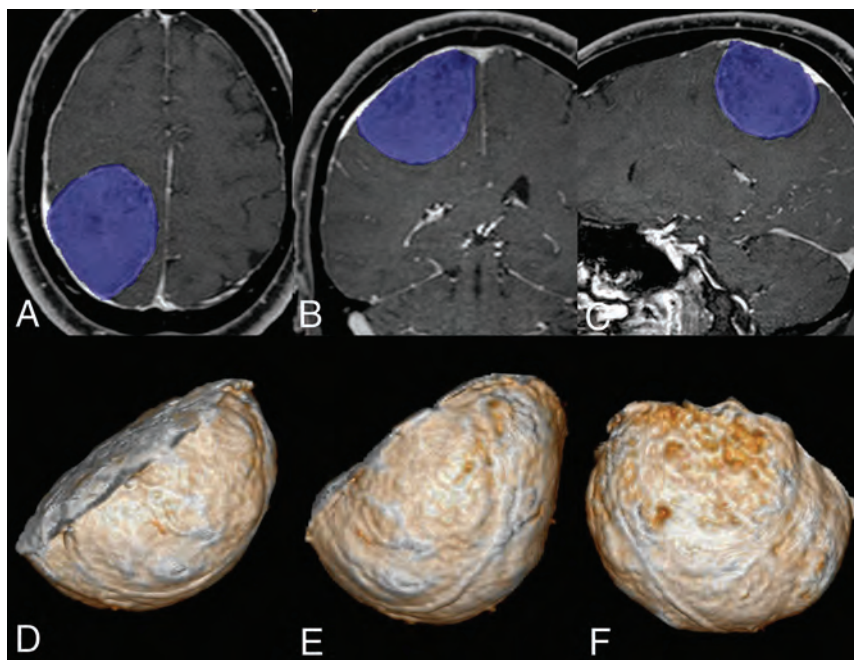


**FIG 2.** A 41-year-old man with a meningioma of the right convexity adjacent to the parietal lobe. Segmentation of the meningioma is achieved by shading the lesion in blue using a semi-automated software (A–C). The voxels outside the shaded volume can be discarded, and the voxels within the volume (shown as 3D-rendering in D, E, and F) can be isolated and exported to the PACS or any other software for further analysis.

The meningioma locations were classified according to studies by Al-Mefty et al<sup>27</sup> and Meling et al,<sup>28</sup> in which cerebral convexity, parasagittal, falcine, intraventricular, and cerebellar convexity meningiomas were considered non-skull base, and all other intracranial locations were considered skull base.

### MR Imaging Protocol

Patients were scanned on 3T and 1.5T Siemens (Siemens Healthcare, Erlangen, Germany), Philips (Philips, Best, The Netherlands), and GE (GE Healthcare, Chicago, Illinois, USA) scanners. As mentioned before, only MR imaging studies that included at least an isotropic, enhanced 3D-T1 sequence (0.6- to 1.1-mm section thickness, no gap between slices) and a conventional axial 2D-T2WI sequence (4-mm section thickness, 0.4-mm gap between slices) were considered. The former was either MP-RAGE or a volumetric interpolated breath-hold examination (VIBE; Siemens), 3D-T1 fast-field echo or T1-weighted high-resolution isotropic volume examination (THRIVE; Philips Healthcare), fast 3D gradient echo brain volume imaging (GRE BRAVO; GE Healthcare), or fast acquisition with multiphase elliptic fast gradient-echo (FAME; GE Healthcare). The technical parameters of these sequences can be found in the Online Supplemental Data. Most scans were obtained in our institution; however, a small number of scans included in this study originated from outside institutions. The technical parameters of the sequences from these institutions were roughly similar to those of our center.

### Segmentation and Morphometry

All meningiomas were segmented using a semi-automated software (advanced visualization platform IntelliSpace Portal [ISP],

Version 10.1; Philips Healthcare) on both the T1 3D-Gd and axial T2WI sequences. This method consists of isolating the voxels of the lesion by gradually shading ROIs that automatically grow according to an algorithm based on pixel intensity and proximity. This process can be repeated in all 3 planes until the operator is satisfied that all the voxels of the mass have been selected. The segmentations were performed by J.B. and R.G. (Fig 2), each author having performed approximately half of all the workload. J.B. is a neuro-radiologist with 5 years' experience, and R.G. is a neurosurgeon who received guidance and training before performing the segmentation. In all cases, the quality of the segmentation was overseen by J.B. Shape and volume features were then automatically computed for all meningiomas using Pyradiomics (Version 2.2.0; <https://github.com/AIM-Harvard/pyradiomics>).<sup>29</sup> The following resulting 10 features were thus obtained for all meningiomas and for the segmentations on the T1 3D-Gd and T2WI sequences: tumor volume, tumor surface area, surface/volume ratio, maximum 3D diameter, maximum 2D diameter in the axial plane, maximum 2D diameter in the coronal plane, maximum 2D diameter in the sagittal plane, major axis length, minor axis length, and least axis length.

### Statistical Analysis

Agreement between the dimensions and geometric parameters obtained from the T1 3D-Gd and T2WI segmentations was assessed by the intraclass correlation coefficient (ICC). Statistical analysis of the data was performed with SPSS Statistics (IBM). A significance level of .05 was used for all statistical tests.

## RESULTS

### Demographics and Descriptive Statistics

The mean patient age at the date of the first available MR imaging scan was 64.7 (SD 17.5) years; range, 22.8–96.0 years). A total of 132 intracranial meningiomas from 122 patients were analyzed. Ninety-three meningiomas (70.5%) were symptomatic, whereas 39 (29.5%) were asymptomatic. Fifty-nine of the 132 meningiomas included underwent surgical resection. Fifty-four of these (91.5%) were WHO grade I, and 5 (8.5%) were grade II. Most patients had a single intracranial meningioma (115/122, 94.3%), 6 patients had 2 meningiomas (4.9%), and 1 patient had 5 meningiomas (0.8%). Two of the 6 patients who had 2 meningiomas on the first MR imaging scan underwent surgical resection of one of the tumors, leaving them with a single lesion on the subsequent follow-up MR imaging. In our cohort, there were 73 non-skull base (55%) and 59 skull base (45%) meningiomas. Distribution of



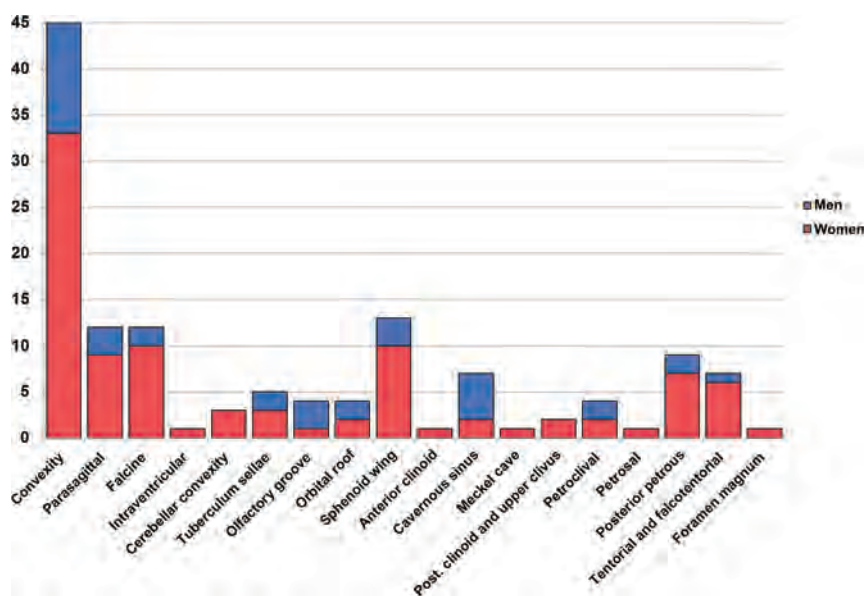


**FIG 3.** Chart showing the number of included intracranial meningiomas by sex and specific location. Cerebral convexity parasagittal, falcine, intraventricular, and cerebellar convexity meningiomas are considered non-skull base. All other locations are considered skull base. Post. indicates posterior.

meningiomas according to sex and specific location are shown in Fig 3 and the Online Supplemental Data.

A total of 259 MR scans were included, 217 (83.8%) from our own center and 42 (16.2%) from outside institutions. A single MR scan was available for 71 of the 132 meningiomas (54%) from 67 of 122 (55%) patients. The remaining 61 meningiomas (46%) from 55 patients were scanned at least twice, enabling analysis of annual tumor growth. Thirty meningiomas (24 from women, 6 from men; 16 non-skull base, 14 skull base) from 26 patients (20 women, 6 men) met the time-interval criterion of at least 730 days between the index scan and subsequent scans, producing a total of 51 data points. The mean time period between scans was 1485 (SD, 864) days (range, 760–3810 days).

### Quantitative Analysis

There was excellent agreement among all parameters derived from the segmentation of meningiomas on the T1 3D-Gd and T2-weighted sequences ( $P < .001$ ): tumor volume (T1 3D-Gd: 9012.15 [SD, 19,223.03] mm<sup>3</sup>; T2WI: 8528.45 [SD, 18,368.18] mm<sup>3</sup>; ICC = 0.996), surface area (ICC = 0.989), surface/volume ratio (ICC = 0.924), maximum 3D diameter (T1 3D-Gd: 26.21 [SD, 15.76] mm, T2WI: 27.49 [SD, 16.02] mm, ICC = 0.986), maximum 2D diameter in the axial plane (ICC = 0.990), maximum 2D diameter in the coronal plane (ICC = 0.982), maximum 2D diameter in the sagittal plane (0.985), major axis length (T1 3D-Gd: 21.92 [SD, 13.16] mm; T2WI: 22.48 [SD, 13.00] mm, ICC = 0.989), minor axis length (ICC = 0.992), least axis length (ICC = 0.988) (Online Supplemental Data). Figures 4 and 5 show examples of T1 3D-Gd- and T2WI-based segmentations of meningiomas in different locations.

The agreement between T1 3D-Gd and T2WI measurements was also excellent in the subgroup analysis of meningiomas according to location, size, and symptoms with ICCs higher than

0.9 in most cases and generally above 0.8 ( $P < .001$ ), including meningiomas with a maximum 3D diameter of  $\leq 20$  mm. Excellent ICCs ( $> 0.9$ ) were found for all subgroups in tumor volume, maximum 3D diameter, and maximum 3D diameter in the axial plane. For example, the ICC for tumor volume for asymptomatic lesions was 0.997 (T1 3D-Gd: 6353.99 [SD, 14,245.73] mm<sup>3</sup>; T2WI: 6022.21 [SD, 14,022.95] mm<sup>3</sup>); and 0.993 for symptomatic meningiomas (T1 3D-Gd: 17,179.23 [SD, 28,322.25] mm<sup>3</sup>; T2WI: 16,228.74 [SD, 26,444.90] mm<sup>3</sup>). As this example shows, this analysis also revealed that symptomatic meningiomas tended to be larger than asymptomatic lesions but also that, despite this difference, the agreement between the 2 different sequences was not meaningfully affected. The results of the subgroup analysis are shown in the Online Supplemental Data.

The data used to assess annual tumor growth showed good-to-excellent agreement (ICC = 0.820–0.989,  $P < .001$ ) between the T1 3D-Gd and T2WI segmentations, expressed both in absolute values and relative change per year when we used the following measurements: tumor volume (T1 3D-Gd: 461.87 [SD, 2704.17] mm<sup>3</sup>/year, 9.24 [SD, 22.55]%/year; T2WI: 556.64 [SD, 2624.02] mm<sup>3</sup>/year, 15.82 [SD, 32.00]%/year), tumor surface area (T1 3D-Gd: 87.03 [SD, 371.66] mm<sup>2</sup>/year, 5.73 [SD, 12.66]%/year; T2WI: 112.01 [SD, 453.59] mm<sup>2</sup>/year, 15.82 [SD, 32.00]%/year), maximum 3D diameter (T1 3D Gd: 0.56 [SD, 1.79] mm/year, 2.38 [SD, 6.12]%/year; T2WI: 0.72 [SD, 1.95] mm/year, 3.16 [SD, 7.02]%/year), and major axis length (T1 3D Gd: 0.51 [SD, 1.57] mm/year, 2.42 [SD, 5.86]%/year; T2WI: 0.67 [SD, 1.64] mm/year, 3.52 [SD, 7.45]%/year). Of note, the T2WI segmentation tended to overestimate tumor-interval growth despite the good agreement with the T1 3D-Gd segmentation. The same analysis performed on other measurements used to evaluate tumor growth (eg, surface/volume ratio, maximum 2D diameter in the axial plane, maximum 2D diameter in the coronal plane, maximum 2D diameter in the sagittal plane, minor axis length, and least axis length) also produced significant results, albeit less striking, with ICCs ranging from 0.631 to 0.901 ( $P < .001$ ). The agreement was generally better when absolute rather relative growth was considered. These results are summarized in the Online Supplemental Data.

### DISCUSSION

In this single-institution, retrospective cohort study of 123 adult patients with symptomatic or asymptomatic intracranial meningiomas with both skull base and non-skull base locations, a total of 282 MR scans were analyzed to assess the value of Gd-based contrast media for routine follow-up MRIs with respect to tumor size and growth.

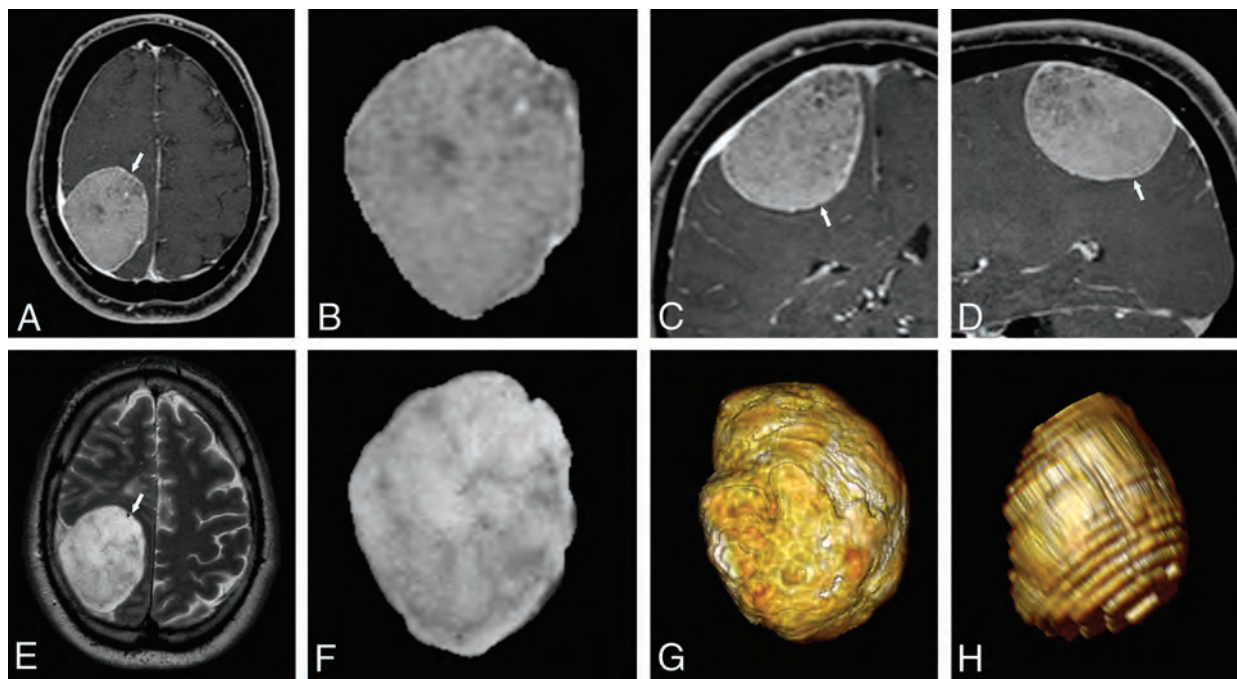


**FIG 4.** Same patient as in Fig 2 with a meningioma of the right convexity adjacent to the parietal lobe. Axial (A), coronal (C) and sagittal (D) THRIVE Gd and axial T2-weighted (E) images depict a meningioma of the right convexity exerting mass effect on the adjacent brain parenchyma of the parietal lobe (arrow, A, C, D, and E). Axial THRIVE Gd (B) and T2-weighted (F) images of the isolated lesion obtained with the semi-automated software, from which 3D-rendering can easily be performed with any DICOM viewer (G, THRIVE Gd. H, T2WI).

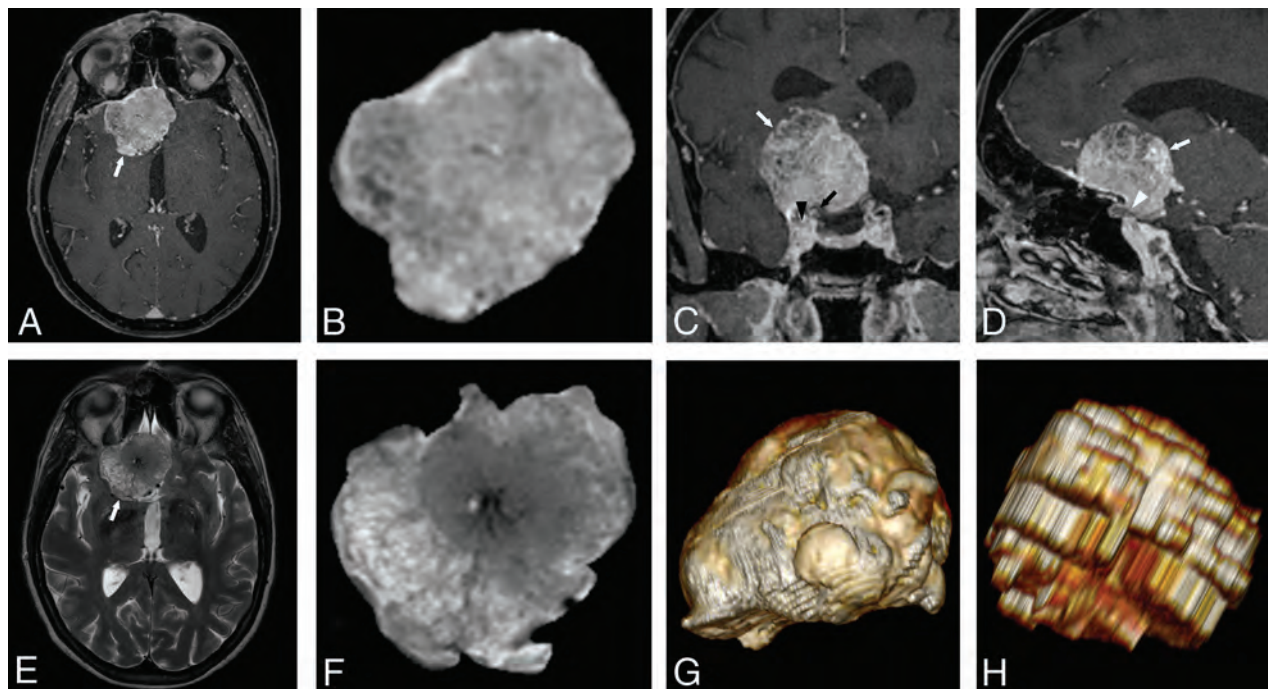


**FIG 5.** A 52-year-old woman. Axial (A), coronal (C) and sagittal (D) THRIVE Gd and axial T2-weighted (E) images show a meningioma arising from the planum sphenoidale and orbital roof on the right (white arrow, A, C, D, and E). The lesion crosses the midline and is in close contact with the cisternal segment of the right optic nerve (white arrowhead in D), the supraclinoid right internal carotid artery (black arrow, C), and cranial aspect of the right cavernous sinus (black arrowhead, C). Axial THRIVE Gd (B) and T2-weighted (F) images of the isolated lesion obtained with the semi-automated software, from which 3D-rendering was performed with our DICOM viewer (G, T1 3D-fat-saturated Gd; H, T2WI). This case illustrates a particularly challenging meningioma for which the skull base location, close contact with other structures, and irregular shape made the segmentation process more difficult.

### Individual Measures and Tumor Growth

Our study demonstrates that the absolute agreement among parameters obtained from the T1 3D-Gd and T2WI sequences with respect to tumor volume, maximum 3D diameter, maximum 2D diameters in 3 planes, and major axis length was near-perfect, despite T2WI sequences being 2D with 4-mm section thickness and a 0.4-mm gap between slices, demonstrating the value of such noncontrast sequences for the follow-up of untreated meningiomas. This feature proved to be the case even across a variety of 9 scanner models from 2 different manufacturers in our institution and also a third scanner manufacturer from outside institutions, thus reinforcing the robustness of the agreement we found between T1 3D-Gd and T2WI segmentations.

An important point is the subgroup analysis we performed to investigate whether the agreement between the 2 sequences remained acceptable if only certain types of meningiomas were considered. The agreement between T1 3D Gd and T2 remained adequate for meningiomas in different locations, smaller-versus-larger meningiomas, and also symptomatic-versus-asymptomatic lesions for all the different single-time-point measurements, including the most important ones such as tumor volume, maximum 3D diameter, and maximum diameter in all 3 planes. The subgroup analysis also found that symptomatic meningiomas tended to be larger than asymptomatic lesions, as expected. These high ICC values provide, in our opinion, further reassurance that our method was consistent and that noncontrast MR imaging could potentially suffice for the follow-up of a wide variety of meningiomas, including symptomatic lesions. We understand, however, that the case could be made for the use of Gd contrast media for a small proportion of aggressive and infiltrative meningiomas in very specific locations, which could hinder an appropriate imaging work-up, at least in the first scan.

The growth rate of intracranial meningiomas is one of the most important factors influencing the decision for surgical treatment, with immediate intervention at diagnosis having the potential for unnecessary treatment.<sup>30</sup> Furthermore, because most asymptomatic meningiomas do not exhibit growth, the best management option may be conservative treatment with imaging follow-up, thus avoiding surgery-related morbidity.<sup>25</sup> Serial imaging allowed us to evaluate tumor growth. A conscious decision was made to include only meningiomas in which the follow-up was at least 2 years, to minimize errors as much as possible. Absolute tumor growth (evaluated as an annual increase in tumor volume, tumor surface area, maximum 3D diameter, and major axis length) obtained from the T1 3D-Gd and T2WI segmentations showed excellent agreement between the 2 sequences with near-perfect ICCs. The agreement for relative annual tumor growth expressed as %/year was slightly lower, probably reflecting that more computation was needed to obtain relative annual growth, but it was still very high with  $P < .001$  in all cases. Because MR imaging follow-up of intracranial meningiomas is primarily performed to assess tumor growth, our results are both encouraging and reassuring, indicating that Gd-based contrast might not add enough value and could potentially be omitted.

An important point is that contrast medium is usually administered in follow-up MR imaging of intracranial meningiomas because it is thought to allow improved delineation of invasion of

the dural venous sinuses by a lesion, such as the sagittal, straight, or cavernous sinuses. Nevertheless, we found that visualization of vascular invasion by meningiomas is often hindered on T1 Gd-weighted sequences, in which enhancement of the meningioma is sometimes difficult to distinguish from opacification of the venous sinus itself, and that vascular invasion is often better depicted on T2WI as an absence of flow void and by direct visualization of the edges of the meningioma itself. This is the case with gradient-echo T1 3D-Gd sequences, which are routinely performed as part of the meningioma follow-up imaging protocol at our institution. While it is true that black-blood Cube (GE Healthcare) or sampling perfection with application-optimized contrasts by using different flip angle evolution (SPACE; Siemens) sequences would mitigate this limitation, they would also depict other anatomic structures in less detail, especially near the skull base, including the meningioma itself and brain tissue. Image-acquisition time would also be prolonged with this type of sequence. Another important point in this respect is that while it is true that the absence of flow voids on T2WI does not always reflect sinus invasion by the meningioma, dural sinus invasion could be evaluated with other noncontrast sequences. Because meningiomas are usually hyperintense on diffusion-weighted imaging due to their high cellularity, this sequence could be used to distinguish slow flow from sinus invasion.

Because one of the advantages of not using contrast media is to reduce imaging time, it seems somewhat counterproductive to include sequences that would increase the image-acquisition time for little gain in quality. At our institution, the actual gain in imaging time if no contrast was used amounts to the time it takes to perform 2D-T1 spin-echo Gd and T1 3D-Gd sequences, which is approximately 8 minutes depending on the scanner. The time savings would be even more striking if we obviated the need for contrast MRV, a sequence usually included in the imaging protocol of meningiomas that invade or compress the dural venous sinuses. However, 3D-T2 sequences can sometimes depict the venous sinuses and structures near the skull base in less detail due to artifacts. In view of these limitations, a sensible compromise could be to keep 2D-T2WI in the imaging protocol and replace the 2D-FLAIR with a 3D-FLAIR sequence.

As mentioned before, health care cost is also an important factor in modern medical practice, not only to patients in private or semi-private health care systems but also to societies. In our center, the direct cost-saving of performing a noncontrast as opposed to a contrast brain MR imaging would be approximately \$500. Indirectly, savings would be even more significant if the reduced image-acquisition time is taken into account. Last and despite the relative safety of Gd contrast media, the short-term and long-term consequences of the administration of contrast media could be avoided and patient safety could be improved.

### Literature

The excellent agreement between absolute annual tumor growth obtained from the T1 3D-Gd and T2WI segmentations strongly suggests that noncontrast MR imaging is adequate for the follow-up of most intracranial meningiomas. Our results are in agreement with those by He et al,<sup>31</sup> in 2020, who assessed the suitability of T2WI sequences for long-term follow-up of asymptomatic



convexity meningiomas. However, our study differs from this one in several points, specifically a larger number of patients (123 versus 18), also including skull base meningiomas as well as both symptomatic and asymptomatic meningiomas, and our study tumor size being assessed by a semi-automated method, thus minimizing interoperator error.

The behavior of skull base meningiomas is different from that of non-skull base meningiomas, and skull base meningiomas have shorter retreatment-free survival.<sup>28</sup> Notwithstanding some difficulties we encountered with the segmentation of skull base meningiomas in certain locations (in the cavernous sinus and near the orbits), we were reasonably confident that our method had adequate accuracy for all intracranial locations, and we also included skull base meningiomas in our study, which are known to behave differently and exhibit faster growth rates than non-skull base meningiomas as observed by Hashimoto et al,<sup>32</sup> in 2012. The fact that the agreement between the two different sequences remained acceptable for skull base meningiomas provided some validation to the decision of including these meningiomas in our study.

### Strengths and Limitations

We believe that one of the strengths of our study is that an accurate semi-automated segmentation method was considered from the early planning stages of this study to minimize subjectivity and operator-related variability as much as possible. Furthermore, we included parameters that are not generally used in routine clinical practice such as the least axis length and minor axis length of the tumor, to further confirm the accuracy of the segmentation and the measurements. Another strong point, in our opinion, is that we did not exclude skull base or symptomatic meningiomas, making our results more generalizable and holding higher external validity than if we had focused only on convexity meningiomas.

The main limitations of this study are its retrospective rather than prospective nature and also the potential bias that was introduced by the segmentation process, which was not blinded between the T1 3D-Gd and T2-weighted images, as each meningioma was segmented by the same operator. The decision to perform the segmentation in this manner was made at the beginning of the study in order to allow the considerable workload to be shared and to expedite the segmentation process. Another limitation is that although some MR imaging studies from external institutions were included, it remains a single-center study. Other limitations relate to the technical aspects of the semi-automated segmentation; we found that delineation of skull base meningiomas in certain locations posed considerable difficulties due to adjacent anatomic structures with similar signal intensities. Although care was taken to perform the segmentation of these meningiomas as thoroughly as possible, we acknowledge that some inaccuracies may have occurred while performing the segmentation of meningiomas of the cavernous sinus, both on T1 3D-Gd and T2WI, and those near the orbits on T2WI. A case of a meningioma for which the segmentation was particularly challenging is illustrated in Fig 5. T2WI-based segmentation tended to overestimate tumor growth. This feature was probably due to the effects of partial volume averaging, which are to be expected when a 2D sequence is used to generate 3D parameters, particularly on lesions that are irregularly shaped. We believe this overestimation could,

however, be easily overcome if a 3D volumetric T2-weighted sequence was used, which could be a topic of future research.

### CONCLUSIONS

Our results show excellent agreement between dimension and geometric parameters of meningiomas derived from T1 3D-Gd and T2-weighted sequences, suggesting that the use of Gd-based contrast agents in follow-up MR imaging of untreated meningiomas should be carefully reviewed because the use of gadolinium might not offer enough added value for assessing tumor size and growth rates. Furthermore, noncontrast MR imaging would avert risks associated with contrast media, be more cost effective, and reduce image-acquisition time.

### REFERENCES

1. Prince MR, Zhang H, Zou Z, et al. **Incidence of immediate gadolinium contrast media reactions.** *AJR Am J Roentgenol* 2011;196:W138–43 CrossRef Medline
2. Granata V, Cascella M, Fusco R, et al. **Immediate adverse reactions to gadolinium-based MR contrast media: a retrospective analysis on 10,608 examinations.** *BioMed Res Int* 2016;2016:3918292 CrossRef Medline
3. Kanda T, Ishii K, Kawaguchi H, et al. **High signal intensity in the dentate nucleus and globus pallidus on unenhanced T1-weighted MR images: relationship with increasing cumulative dose of a gadolinium-based contrast material.** *Radiology* 2014;270:834–41 CrossRef Medline
4. Kanda T, Osawa M, Oba H, et al. **High signal intensity in dentate nucleus on unenhanced T1-weighted MR images: association with linear versus macrocyclic gadolinium chelate administration.** *Radiology* 2015;275:803–09 CrossRef Medline
5. Quattrocchi CC, Mallio CA, Errante Y, et al. **Gadodiamide and dentate nucleus T1 hyperintensity in patients with meningioma evaluated by multiple follow-up contrast-enhanced magnetic resonance examinations with no systemic interval therapy.** *Invest Radiol* 2015;50:470–72 CrossRef Medline
6. Ramalho J, Semelka RC, Ramalho M, et al. **Gadolinium-based contrast agent accumulation and toxicity: an update.** *AJNR Am J Neuroradiol* 2016;37:1192–98 CrossRef Medline
7. Stojanov D, Aracki-Trenkic A, Benedeto-Stojanov D. **Gadolinium deposition within the dentate nucleus and globus pallidus after repeated administrations of gadolinium-based contrast agents—current status.** *Neuroradiology* 2016;58:433–41 CrossRef Medline
8. Huber M, Orosz E. **Health expenditure trends in OECD countries.** *Health Care Financ Rev* 2003;25:1–22 Medline
9. Reinhardt UE, Hussey PS, Anderson GF. **U.S. health care spending in an international context.** *Health Aff (Millwood)* 2004;23:10–25 CrossRef Medline
10. Dunnick NR, Applegate KE, Arenson RL. **The inappropriate use of imaging studies: a report of the 2004 Intersociety Conference.** *J Am Coll Radiology* 2005;2:401–06 CrossRef Medline
11. Goldbrunner R, Minniti G, Preusser M, et al. **EANO guidelines for the diagnosis and treatment of meningiomas.** *Lancet Oncol* 2016;17:e383–91 CrossRef Medline
12. Buetow MP, Buetow PC, Smirniotopoulos JG. **Typical, atypical, and misleading features in meningioma.** *Radiographics* 1991;11:1087–106 CrossRef Medline
13. Russell EJ, George AE, Kricheff II, et al. **Atypical computed tomography features of intracranial meningioma: radiological-pathological correlation in a series of 131 consecutive cases.** *Radiology* 1980;135:673–82 CrossRef Medline
14. Ostrom QT, Gittleman H, Fulop J, et al. **CBTRUS Statistical Report: Primary Brain and Central Nervous System Tumors Diagnosed in**

- the United States in 2012-2016. *Neuro Oncol* 2019;21(Suppl 5):v1-100 CrossRef Medline
15. Wood MW, White RJ, Kernohan JW. **One hundred intracranial meningiomas found incidentally at necropsy.** *J Neuropathol Exp Neurol* 1957;16:337-40 CrossRef Medline
  16. Nakamura M, Roser F, Michel J, et al. **Volumetric analysis of the growth rate of incompletely resected intracranial meningiomas.** *Zentralbl Neurochir* 2005;66:17-23 CrossRef Medline
  17. Lee EJ, Kim JH, Park ES, et al. **A novel weighted scoring system for estimating the risk of rapid growth in untreated intracranial meningiomas.** *J Neurosurg* 2017;127:971-80 CrossRef Medline
  18. Nakasu S, Nakasu Y. **Natural history of meningiomas: review with meta-analyses.** *Neurol Med Chir (Tokyo)* 2020;60:109-20 CrossRef Medline
  19. Niino M, Yatsushiro K, Nakamura K, et al. **Natural history of elderly patients with asymptomatic meningiomas.** *J Neurol Neurosurg Psychiatry* 2000;68:25-28 CrossRef Medline
  20. Nakamura M, Roser F, Michel J, et al. **The natural history of incidental meningiomas.** *Neurosurgery* 2003;53:62-70; discussion 70-71 CrossRef Medline
  21. Hashiba T, Hashimoto N, Izumoto S, et al. **Serial volumetric assessment of the natural history and growth pattern of incidentally discovered meningiomas.** *J Neurosurg* 2009;110:675-84 CrossRef Medline
  22. Oya S, Kim SH, Sade B, et al. **The natural history of intracranial meningiomas.** *J Neurosurg* 2011;114:1250-56 CrossRef
  23. Jadid KD, Feychting M, Höijer J, et al. **Long-term follow-up of incidentally discovered meningiomas.** *Acta Neurochir (Wien)* 2015;157:225-30 CrossRef Medline
  24. Romani R, Ryan G, Benner C, et al. **Non-operative meningiomas: long-term follow-up of 136 patients.** *Acta Neurochir (Wien)* 2018;160:1547-53 CrossRef Medline
  25. Yano S, Kuratsu JI. Kumamoto Brain Tumor Research Group. **Indications for surgery in patients with asymptomatic meningiomas based on an extensive experience.** *J Neurosurg* 2006;105:538-43 CrossRef Medline
  26. Sughrue ME, Rutkowski MJ, Aranda D, et al. **Treatment decision making based on the published natural history and growth rate of small meningiomas.** *J Neurosurg* 2010;113:1036-42 CrossRef Medline
  27. Al-Mefty O, McDermott MW, DeMonte F. *Al-Mefty's Meningiomas*. 2nd ed. Thieme Medical; 2011
  28. Meling TR, Da Broi M, Scheie D, et al. **Meningiomas: skull base versus non-skull base.** *Neurosurg Rev* 2019;42:163-73 CrossRef Medline
  29. van Griethuysen JJ, Fedorov A, Parmar C, et al. **Computational radiomics system to decode the radiographic phenotype.** *Cancer Res* 2017;77:e104-07 CrossRef Medline
  30. Islam AI, Mohan M, Moon RDC, et al. **Incidental intracranial meningiomas: a systematic review and meta-analysis of prognostic factors and outcomes.** *J Neurooncol* 2019;142:211-21 CrossRef Medline
  31. He JQ, Iv M, Li G, et al. **Noncontrast T2-weighted magnetic resonance imaging sequences for long-term monitoring of asymptomatic convexity meningiomas.** *World Neurosurg* 2020;135:e100-05 CrossRef Medline
  32. Hashimoto N, Rabo CS, Okita Y, et al. **Slower growth of skull base meningiomas compared with non-skull base meningiomas based on volumetric and biological studies.** *J Neurosurg* 2012;116:574-80 CrossRef Medline

# Prognostic Utility of Disproportionately Enlarged Subarachnoid Space Hydrocephalus in Idiopathic Normal Pressure Hydrocephalus Treated with Ventriculoperitoneal Shunt Surgery: A Systematic Review and Meta-analysis

H.Y. Park, C.R. Park, C.H. Suh, M.J. Kim, W.H. Shim, and S.J. Kim



## ABSTRACT

**BACKGROUND:** Disproportionately enlarged subarachnoid space hydrocephalus is a specific radiologic marker for idiopathic normal pressure hydrocephalus. However, controversy exists regarding the prognostic utility of disproportionately enlarged subarachnoid space hydrocephalus.

**PURPOSE:** Our aim was to evaluate the prevalence of disproportionately enlarged subarachnoid space hydrocephalus in idiopathic normal pressure hydrocephalus and its predictive utility regarding prognosis in patients treated with ventriculoperitoneal shunt surgery.

**DATA SOURCES:** We used MEDLINE and EMBASE databases.

**STUDY SELECTION:** We searched for studies that reported the prevalence or the diagnostic performance of disproportionately enlarged subarachnoid space hydrocephalus in predicting treatment response.

**DATA ANALYSIS:** The pooled prevalence of disproportionately enlarged subarachnoid space hydrocephalus was obtained. Pooled sensitivity, specificity, and area under the curve of disproportionately enlarged subarachnoid space hydrocephalus to predict treatment response were obtained. Subgroup and sensitivity analyses were performed to explain heterogeneity among the studies.

**DATA SYNTHESIS:** Ten articles with 812 patients were included. The pooled prevalence of disproportionately enlarged subarachnoid space hydrocephalus in idiopathic normal pressure hydrocephalus was 44% (95% CI, 34%–54%). The pooled prevalence of disproportionately enlarged subarachnoid space hydrocephalus was higher in the studies using the second edition of the Japanese Guidelines for Management of Idiopathic Normal Pressure Hydrocephalus compared with the studies using the international guidelines without statistical significance (52% versus 43%,  $P = .38$ ). The pooled sensitivity and specificity of disproportionately enlarged subarachnoid space hydrocephalus for prediction of treatment response were 59% (95% CI, 38%–77%) and 66% (95% CI, 57%–74%), respectively, with an area under the curve of 0.67 (95% CI, 0.63–0.71).

**LIMITATIONS:** The lack of an established method for assessing disproportionately enlarged subarachnoid space hydrocephalus using brain MR imaging served as an important cause of the heterogeneity.

**CONCLUSIONS:** Our meta-analysis demonstrated a relatively low prevalence of disproportionately enlarged subarachnoid space hydrocephalus in idiopathic normal pressure hydrocephalus and a poor diagnostic performance for treatment response.

**ABBREVIATIONS:** DESH = disproportionately enlarged subarachnoid space hydrocephalus; HSROC = hierarchical summary receiver operating characteristic; iNPH = idiopathic normal pressure hydrocephalus; NPV = negative predictive value; PPV = positive predictive value; VP = ventriculoperitoneal

Idiopathic normal pressure hydrocephalus (iNPH) is a potentially reversible disease characterized by the triad of gait disturbance, dementia, and urinary incontinence.<sup>1,2</sup> Currently, the


only effective treatment for iNPH is CSF shunt surgery, with ventriculoperitoneal (VP) shunt surgery being the most commonly performed.<sup>3</sup> However, the procedure is invasive and is associated

Received January 11, 2021; accepted after revision March 17.

From the Department of Radiology and Research Institute of Radiology (H.Y.P., C.H.S., M.J.K., W.H.S., S.J.K.), Asan Medical Center, University of Ulsan College of Medicine, Seoul, Korea; and Department of Medical Science (C.R.P.) Asan Medical Institute of Convergence Science and Technology, University of Ulsan College of Medicine, Seoul, Korea.

H.Y. Park and C.R. Park contributed equally to the manuscript.

Please address correspondence to Chong Hyun Suh, MD, PhD, Department of Radiology and Research Institute of Radiology, University of Ulsan College of Medicine, Asan Medical Center, Olympic-ro 33, Seoul 05505, Korea; e-mail: chonghyunsuh@amc.seoul.kr

 Indicates article with online supplemental data.

<http://dx.doi.org/10.3174/ajnr.A7168>



with complications such as shunt obstruction, which may require multiple revision surgeries.<sup>4,5</sup> Hence, careful selection of patients for this surgery is critical. The CSF tap test or drainage test and CSF infusion test have been proposed to predict treatment response in iNPH.<sup>1,2,6</sup> However, several studies have questioned the predictive values of these tests.<sup>7-9</sup> In addition, these tests are invasive and pose the potential risk of infection.<sup>6,10,11</sup>

Several studies have attempted identifying radiologic markers to predict treatment response in iNPH, including the callosal angle and disproportionately enlarged subarachnoid space hydrocephalus (DESH).<sup>12-15</sup> DESH refers to a morphologic pattern of communicating hydrocephalus that features uneven distribution of CSF between the superior and inferior subarachnoid spaces.<sup>15</sup> DESH has gained recognition for its prognostic and diagnostic utility in iNPH.<sup>1,16-18</sup> Consequently, the third edition of the Japanese Guidelines for Management of Idiopathic Normal Pressure Hydrocephalus adopted DESH as an imaging marker in the diagnostic criteria for iNPH.<sup>19</sup> The seminal study supporting this decision was published in 2010 by Hashimoto et al,<sup>17</sup> which reported a high prevalence of DESH in iNPH and an excellent positive predictive value (PPV) of DESH for treatment response. However, this study had not included a control group (patients negative for DESH) and hence did not report the negative predictive value (NPV). Several studies published since have presented contradictory results.<sup>12,16,20-25</sup> Of note, a few studies have questioned the clinical value of DESH for its poor NPV.<sup>20,21,26</sup> In addition, the reported prevalence of DESH varies widely across studies, ranging from 22% to 96%.<sup>12,16,17,27</sup>

To our knowledge, the diagnostic performance of DESH in the prediction of treatment response and the prevalence of DESH in iNPH have not been systematically evaluated. Therefore, we conducted a systematic review and meta-analysis to investigate the prevalence of DESH in iNPH and evaluate its clinical value in predicting treatment response.

## MATERIALS AND METHODS

### Evidence Acquisition

This study was performed and reported according to the Preferred Reporting Items for Systematic Reviews and Meta-Analyses (PRISMA) guidelines.<sup>28</sup> Neither institutional review board approval nor written informed consent was required owing to the nature of the study.

### Literature Search

A systematic literature search of the MEDLINE and EMBASE databases was conducted to identify studies that reported the prevalence of DESH in iNPH or the diagnostic performance of DESH in predicting treatment response in patients who underwent VP shunt surgery. The search term was ((normal pressure hydrocephalus) OR (NPH)) AND ((disproportionately enlarged subarachnoid space hydrocephalus) OR (DESH)), using the combination of a MESH term and free-text terms. The search was performed on October 10, 2020.

### Inclusion Criteria

DESH was diagnosed when all 3 components, enlarged ventricles, tight high convexity, and dilated Sylvian fissure, were present (Fig



**FIG 1.** Typical imaging features of DESH in a 77-year-old patient who presented with gait disturbance, urinary symptoms, and cognitive impairment. A coronal 3D T1-weighted image shows a dilated Sylvian fissure (arrows), tightened subarachnoid space near the vertex (square), and ventriculomegaly (asterisks).

1).<sup>1</sup> Some studies have used the term “incomplete” DESH to describe a status of features of DESH being partially present.<sup>23,29</sup> However, to maintain consistency among the results of the included studies, we focused on DESH with all 3 features. To investigate the prevalence of DESH, we selected studies if they reported performing brain imaging to evaluate DESH in patients with iNPH. To evaluate the diagnostic performance of DESH for prediction of treatment response, we selected studies if they met all of the following criteria: 1) VP shunt surgery performed for iNPH; 2) brain MR imaging performed for the evaluation of DESH; 3) inclusion of the analysis of treatment response after VP shunt; and 4) availability of adequate information for the reconstruction of  $2 \times 2$  tables to calculate the diagnostic performance of DESH.

### Exclusion Criteria

Studies were excluded if they met any of the following criteria: 1) case reports and case series with  $<5$  patients, 2) conference abstracts, 3) reviews, 4) letters to the editor or editorials, and 5) incomplete data for reconstruction of  $2 \times 2$  tables. Two reviewers (H.Y.P, with 4 years of experience in diagnostic radiology, and C.H.S., with 9 years of experience in diagnostic radiology) independently evaluated the eligibility of each article. Interreviewer disagreements were resolved through discussions to form a consensus.

### Data Extraction and Quality Assessment

A standardized extraction form was used to extract data from the studies. The extracted data included the following: 1) study characteristics: author, year of publication, institution, country of origin, study period, study design, consecutive-versus-nonconsecutive enrollment, reference standards, outcome measures, blinding to

outcome measures, and follow-up periods; 2) patient characteristics: number of patients with iNPH, number of patients responsive to VP shunts, mean age, age range, and male-to-female ratio; and 3) characteristics of brain MR imaging: magnet strength, vendor, scanner, MR image, and image plane for the evaluation of DESH, method of evaluation, and the number and experience of the readers. On the basis of the Quality Assessment of Diagnostic Accuracy Studies-2 (QUADAS-2) tool, we evaluated the quality of the studies.<sup>30</sup> Data extraction and quality assessment were independently conducted by 2 reviewers (H.Y.P. and C.H.S.).

### Data Synthesis and Analysis

The primary outcome of our study was the prevalence of DESH among patients with iNPH. The pooled proportion and its 95% confidence interval were calculated using the DerSimonian and Laird random effects model, and a forest plot was constructed. The Cochran Q test and Higgins inconsistency index ( $I^2$ ) test were used to evaluate heterogeneity, and a funnel plot was constructed to assess publication bias.<sup>31,32</sup> To explain heterogeneity among the studies, we performed subgroup analysis based on which iNPH guidelines were being used for the patient inclusion.

The secondary outcome of our study was the diagnostic performance of DESH in predicting treatment response in patients with iNPH who underwent VP shunt surgery. Pooled sensitivity, pooled specificity, and their corresponding 95% CIs were calculated using a bivariate random effects model, and coupled forest plots were constructed. On the basis of the calculated prevalence of patients responsive to treatment (total number of patients responsive to the shunt/total number of patients with iNPH) and pooled sensitivity and specificity, the PPV and NPV of DESH were obtained using the following formulae:

$$\text{PPV} = (\text{Sensitivity} \times \text{Prevalence} / [\text{Sensitivity} \times \text{Prevalence} + (1 - \text{Prevalence}) \times (1 - \text{Specificity})])$$

$$\text{NPV} = [\text{Specificity} \times (1 - \text{Prevalence})] / [\text{Specificity} \times (1 - \text{Prevalence}) + \text{Prevalence} \times (1 - \text{Sensitivity})].$$

A hierarchical summary receiver operating characteristic (HSROC) curve with 95% confidence and prediction regions was plotted. Sensitivity analyses were performed to explain study heterogeneity. Heterogeneity among the studies was determined using the Cochran Q test and Higgins inconsistency index ( $I^2$ ) test; a Cochran Q test with a  $P < .05$  or  $I^2 > 50\%$  was considered to indicate heterogeneity.<sup>31,32</sup> In addition, the difference between the 95% confidence region and prediction region in the HSROC curve was visually analyzed, with a large difference indicating heterogeneity. A threshold effect (ie, positive correlation between sensitivity and the false-positive rate) was evaluated by visual assessment of the coupled forest plots and the Spearman correlation coefficient. A correlation coefficient of  $>0.6$  indicated a threshold effect.<sup>33</sup> Publication bias was assessed using the Deeks funnel plot, and statistical significance was evaluated using the Deeks asymmetry test.<sup>34</sup> For statistical analysis, the metandi and midas modules in STATA, Version 15.0 (StataCorp), and R, Version 3.6.3 (<http://www.r-project.org>), were used.

## RESULTS

### Literature Search

Figure 2 summarizes our study-selection process. In total, 130 articles were obtained from the systematic search. After we removed 4 duplicate articles, 126 articles were screened for eligibility on the basis of titles and abstracts, and 110 articles were excluded. One additional eligible study was identified from the bibliographies of articles.<sup>12</sup> After full-text reviews of 17 articles, 7 articles were further excluded for the following reasons: Three articles were not in the field of interest,<sup>14,18,35</sup> and 4 articles had insufficient information for reconstruction of  $2 \times 2$  tables.<sup>13,15,17,36</sup> Of the 4 articles, 3 articles reported an association between DESH and postsurgical outcome based on correlation and regression analyses.<sup>13,15,36</sup> However, sensitivity and specificity could not be calculated in these studies, and they were excluded from the analysis. Finally, 10 original articles were included in the study.<sup>12,16,20-27</sup>

### Characteristics of the Included Studies

The study and patient characteristics of the 10 articles are described in the Online Supplemental Data. All studies reported the prevalence of DESH. Of those, 8 studies reported the diagnostic performance of DESH with regard to treatment response.<sup>12,16,20-25</sup> Three studies were prospective,<sup>16,22,25</sup> and 7 studies were retrospective.<sup>12,20,21,23,24,26,27</sup> Consecutive enrollment was performed in 7 studies,<sup>12,16,20-22,24,25</sup> whereas 3 studies did not detail patient enrollment.<sup>23,26,27</sup> Four studies used the international guidelines,<sup>20-22,25</sup> while 3 studies used the second edition of the Japanese guidelines for the diagnosis of iNPH and the selection of patients receiving a VP shunt.<sup>23,24,27</sup> The other 3 studies did not mention the reference standard.<sup>12,16,26</sup> Of note, only patients with positive CSF tap test results underwent VP shunt surgery in 4 studies, possibly causing a selection bias.<sup>12,23-25</sup> For the outcome measurements, 5 studies used either the iNPH grading scale or the NPH Eide scale, which are systematic grading scales that focus on 3 domains: gait, cognitive, and urinary disturbance.<sup>12,16,22-24</sup> The rest of the studies used various quantitative or qualitative methods including the Timed 10-Meter Walk Test or the revised Wechsler Adult Intelligence Scale neuropsychology report.<sup>20,21,25</sup> In 5 studies, readers were blinded to outcome measures.<sup>16,20,21,26,27</sup> The remaining 5 studies did not report on blinding.<sup>12,22-25</sup> Most studies assessed treatment response 12 months after VP shunt surgery.<sup>16,20-22,25</sup> In 1 study, treatment response was evaluated 10 days after VP shunt surgery,<sup>23</sup> whereas another study included long follow-up periods (51.8 months; interquartile range, 22.2–64.2 months).<sup>12</sup> One study did not report the time point for treatment-response evaluation.<sup>24</sup>

The characteristics of brain MR imaging performed in the studies are summarized in the Online Supplemental Data. In 6 studies, T1-weighted imaging was used,<sup>16,20,22,24,25,27</sup> whereas the remaining 4 studies did not mention which MR image was used.<sup>12,21,23,26</sup> Visual qualitative assessment was performed in all studies for the evaluation of DESH based on the axial and/or coronal image plane. The number of readers ranged from 1 to 3.

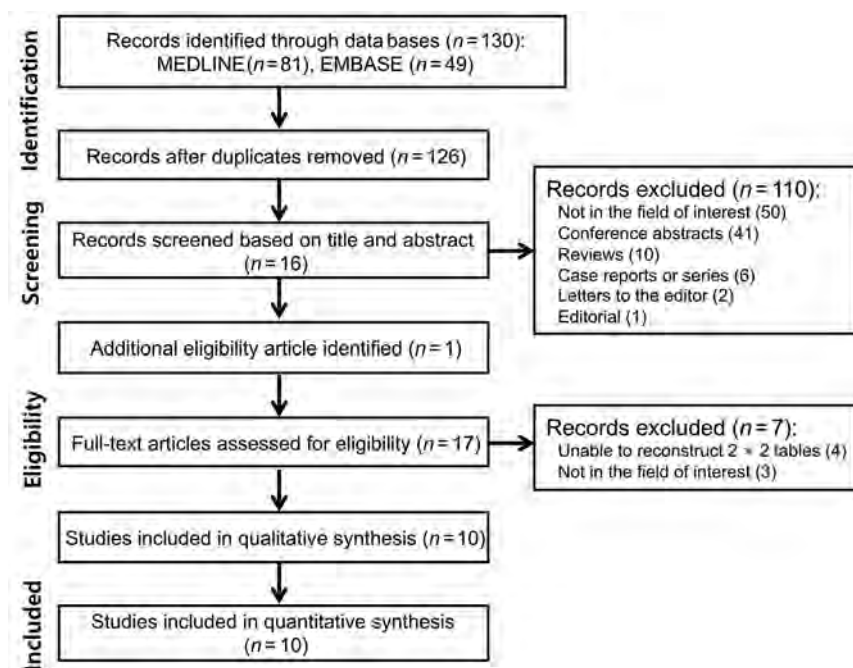


FIG 2. Flow diagram of the study-selection process.

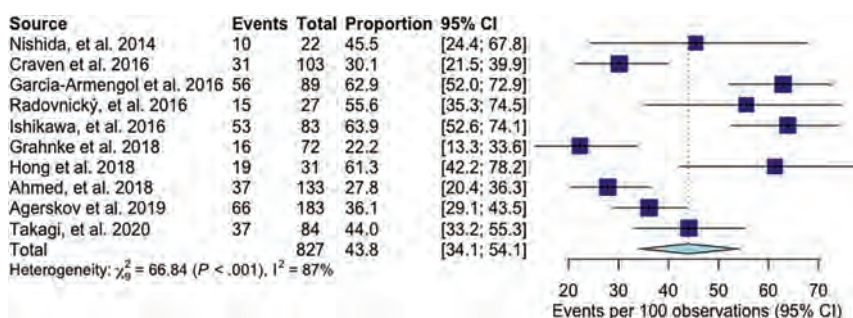


FIG 3. Forest plots of the pooled prevalence of DESH in iNPH. Numbers are pooled estimates with 95% CIs in parentheses. Horizontal lines indicate 95% CIs.

### Quality Assessment

On the basis of the QUADAS-2 criteria, 6 of 10 articles satisfied at least 4 of the 7 items, indicating reasonable analysis quality (Online Supplemental Data). The detailed description of quality assessment is provided in the Online Supplemental Data.

### Prevalence of DESH among Patients with iNPH

Ten studies reported the prevalence of DESH in patients with iNPH, which ranged from 22% to 64%.<sup>12,16,20-27</sup> The pooled prevalence of DESH was 44% (95% CI, 34%–54%) (Fig 3). The Cochran Q test and the  $I^2$  test demonstrated considerable heterogeneity among the studies ( $Q = 66.84$ ;  $P < .001$ ;  $I^2 = 87\%$ ). No significant publication bias was observed on the funnel plot (Online Supplemental Data).

Subgroup analysis demonstrated that the pooled prevalence of DESH was higher in the studies using the second edition of the Japanese guidelines compared with studies using the international

guidelines, but without statistical significance (52% versus 43%,  $P = .38$ ) (Online Supplemental Data). The heterogeneity among the studies was slightly decreased on subgroup analysis (international guidelines:  $I^2 = 77\%$ ; Japanese guidelines:  $I^2 = 72\%$ ).

Four studies used a CSF tap test as a prerequisite for surgical eligibility.<sup>12,23-25</sup> No significant difference was observed in the prevalence of DESH among these 4 studies and the rest of the studies ( $P = .79$ ).

### Diagnostic Performance of DESH for Prediction of Treatment Response

Eight studies reported the diagnostic performance of DESH in predicting treatment response.<sup>12,16,20-25</sup> The sensitivity and specificity of DESH in individual studies ranged from 20% to 93% and 48% to 100%, respectively. The pooled sensitivity and specificity were 59% (95% CI, 38%–77%) and 66% (95% CI, 57%–74%), respectively (Fig 4). The area under the HSROC curve was 0.67 (95% CI, 0.63–0.71) (Fig 5). Based on the pooled estimates, the calculated PPV and NPV were 80% and 41%, respectively.

The Cochran Q test and Higgins  $I^2$  test demonstrated significant study heterogeneity regarding sensitivity ( $Q = 87.25$ ;  $P = .00$ ;  $I^2 = 92\%$ ) and specificity ( $Q = 15.45$ ;  $P = .03$ ;  $I^2 = 55\%$ ). In addition, a notable difference was observed between the 95% confidence region and the prediction region in HSROC, indicating considerable heterogeneity (Fig 5).

Visual analysis of the coupled forest plot showed a high likelihood of the threshold effect (Fig 4), though the Spearman correlation coefficient between the sensitivity and the false-positive rate was not significant (correlation coefficient, 0.336; 95% CI,  $-0.483$ – $0.842$ ). The Deeks funnel plot showed a low likelihood of publication bias ( $P = .26$ ) (Online Supplemental Data).

No significant difference was observed in the diagnostic performance of DESH among the 4 studies depending solely on CSF tap test for surgical eligibility and the rest of the studies ( $P = .74$ ). All except 3 studies evaluated treatment response at 12 months after VP shunt surgery. When a sensitivity analysis was performed excluding those 3 studies,<sup>12,23,24</sup> the diagnostic performance was slightly improved with a pooled sensitivity of 62% (95% CI, 37%–82%) and a specificity of 70% (95% CI, 60%–78%) (Online Supplemental Data). Additional sensitivity analysis was conducted regarding the 5 studies that used systematic grading



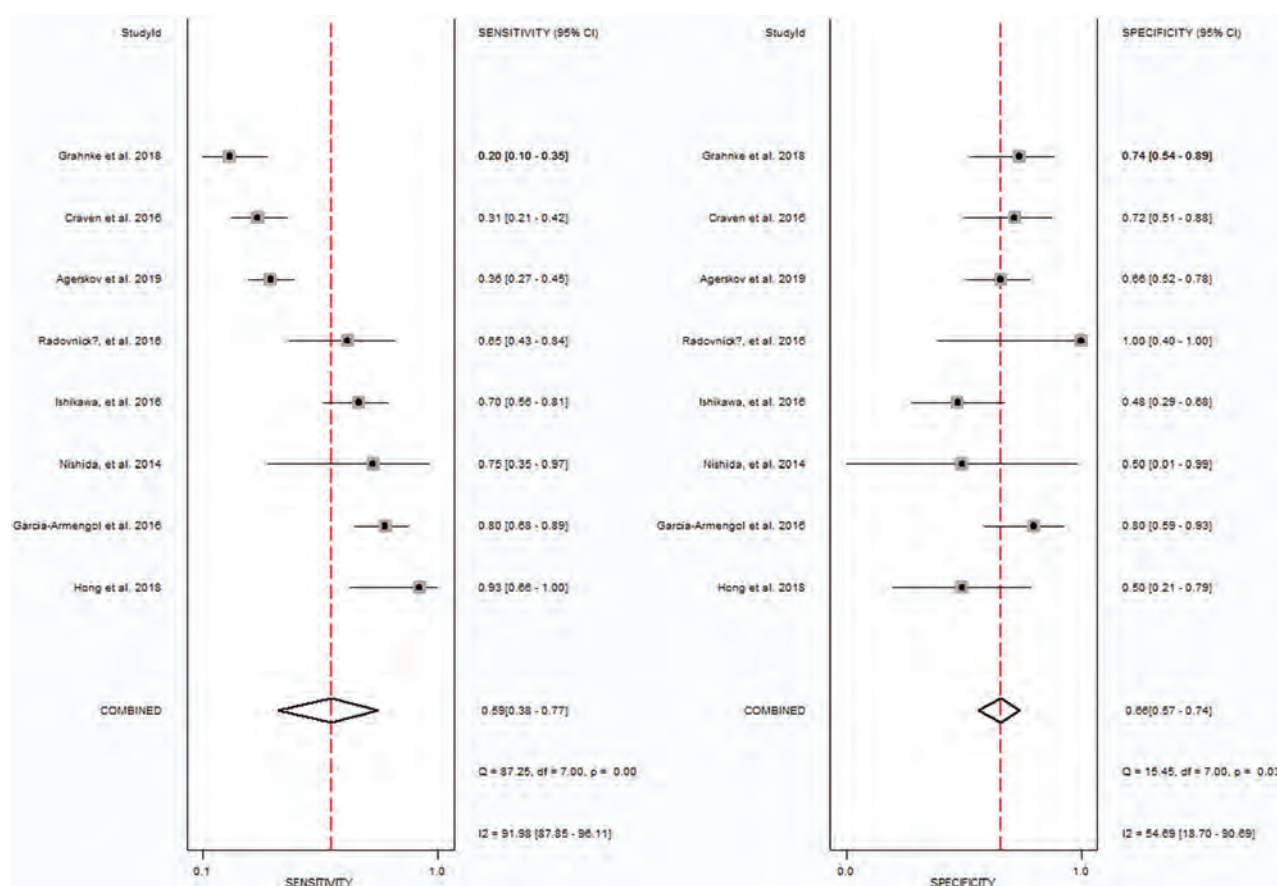


**FIG 4.** Coupled forest plots showing the pooled sensitivity and specificity for the diagnostic performance of DESH in the prediction of treatment response. Numbers are pooled estimates with 95% CIs in parentheses. Horizontal lines indicate 95% CIs.

scales for the evaluation of treatment response.<sup>12,16,22-24</sup> Pooled sensitivity was slightly improved to 70% (95% CI, 41%–88%), but no considerable change was observed in the pooled specificity of 64% (95% CI, 48%–76%) (Online Supplemental Data). The degree of heterogeneity remained similar in both sensitivity analyses.

## DISCUSSION

DESH has been regarded as an imaging marker that aids in the diagnosis of iNPH and the prediction of treatment response after shunt surgery.<sup>1,18,19</sup> However, our study demonstrated poor diagnostic performance of DESH with regard to the prediction of treatment response (pooled sensitivity of 59% and specificity of 66%) and a relatively low prevalence of DESH (44%) in iNPH. In addition, the calculated NPV of DESH based on the pooled estimates was poor (41%), which means that a substantial number of patients in the included studies had improvement of symptoms after the operation even without DESH. Therefore, our study suggests that patients negative for DESH should not be excluded from VP shunt surgery.

The concept of DESH was first introduced in the study by Hashimoto, et al,<sup>17</sup> in which they reported a high prevalence of DESH (96%). However, patients were included in this study only if they showed tight high convexity and ventriculomegaly on brain MR imaging.<sup>17</sup> Therefore, the calculated prevalence of

DESH in the study was inevitably high because the included patients already had at least 2 features of DESH. On the contrary, our study demonstrated a pooled prevalence of DESH of 44% in patients with iNPH. Our results support previous studies reporting that a considerable number of patients had no or partial features of DESH.<sup>20,21,26</sup> Partial features of DESH or incomplete DESH was defined in a few studies as 1 or 2 definite features of the 3 components of DESH.<sup>23,29,37</sup> Currently, the evidence is scarce regarding the prevalence of incomplete DESH in patients with iNPH and its role in the diagnosis.<sup>19</sup> In addition, it is difficult to differentiate incomplete DESH from mere brain atrophy.<sup>19</sup> In our meta-analysis, patients with incomplete DESH were excluded to maintain consistency among the studies, possibly further lowering the prevalence of DESH. Indeed, the prevalence of DESH increased from 64% to 87% in 1 of the included studies<sup>23</sup> when incomplete DESH was taken into account.

We speculated that the prevalence of DESH would be higher in the studies that used the second edition of the Japanese guidelines for patient inclusion, because DESH was part of the diagnostic criteria in the guidelines.<sup>1</sup> In subgroup analysis, a higher pooled prevalence of DESH (52%) was observed in the studies using the second Japanese guidelines but without statistical significance ( $P = .38$ ). The study heterogeneity was slightly decreased on subgroup analysis.

Our study demonstrated poor performance of DESH in predicting treatment response with the pooled sensitivity and specificity

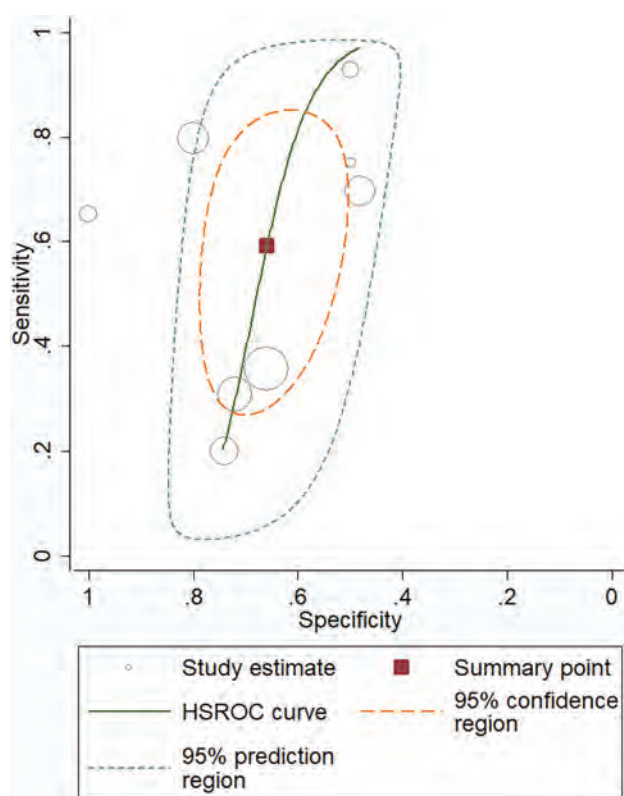


**FIG 5.** HSROC curve of the diagnostic performance of DESH in the prediction of treatment response. A notable difference was observed between the 95% confidence region and the 95% prediction region in HSROC, indicating considerable heterogeneity.

being 59% and 66%, respectively. The area under the HSROC curve was 0.67, which also indicates an unsatisfactory diagnostic performance. The study by Hashimoto, et al<sup>17</sup> established the clinical utility of DESH based on its high PPV in treatment-response evaluation. However, NPV was not provided by this study. Since then, a few studies have reported on the poor performance of DESH with a low NPV.<sup>20,21</sup> The calculated PPV and NPV in our study were 80% and 41%, respectively, which are in line with PPV and NPV in the previous reports.<sup>20,21</sup> The low NPV of DESH suggests that a substantial number of patients who might benefit from a VP shunt surgery will be missed. Therefore, our results indicate that DESH should not be used alone as an exclusionary test. In fact, the third edition of the Japanese guidelines suggested the use of the CSF tap test in patients with negative findings for DESH for determination of surgical eligibility. However, the CSF tap test itself does not accurately predict the surgical outcome, with sensitivities ranging from 26% to 87% and specificities ranging from 33% to 100% on a previous systematic review.<sup>38</sup> Therefore, further studies with large cohorts need to be performed to establish an optimal patient-management algorithm for selection of surgical candidates.

The lack of an established method of assessing DESH served as an important cause of the heterogeneity. Visual analysis of the coupled forest plots demonstrated a high likelihood of the threshold effect in the diagnostic performance of DESH. The threshold effect implies that each study assessed DESH using different standards. All the included studies assessed DESH on the basis of qualitative visual analysis, with most studies failing to detail the

exact evaluation methods.<sup>12,16,20-27</sup> Only 3 studies reported that they adopted the method described by Kitagaki et al,<sup>18</sup> who had used a 4-point scale to assess subarachnoid space enlargement: decreased, normal, mildly or moderately dilated, and severely dilated.<sup>22,24,27</sup> However, these visual analyses are invariably subjective, which may introduce the potential risk of interobserver variability. In fact, a study by Takagi et al<sup>27</sup> showed only moderate agreement among 3 readers in the evaluation of DESH ( $\kappa = 0.522$ ). The absence of a standard method for the evaluation of DESH explains the significant heterogeneity among the results of the included articles. Developing objective evaluation methods should be explored in a future study to reduce heterogeneity. A few recent studies have presented promising results on the quantification of DESH based on the scoring system or the ratio between subarachnoid spaces of the Sylvian fissure and the vertex sulci.<sup>36,39</sup> These quantification methods need to be validated.

Our study has several limitations. First, only 10 studies were included. Because DESH is a relatively recent imaging marker of iNPH, studies on the performance of DESH remain scarce. Nevertheless, >800 patients with iNPH were included in our study. Second, differences existed between the studies with regard to time points and methods of treatment-response evaluation. These may have affected the study heterogeneity. However, study heterogeneity remained unchanged in sensitivity analyses. A slight improvement in diagnostic performance was seen when performing the sensitivity analysis after excluding 3 studies that used different time intervals for the outcome measurement. One of the excluded studies that reported a substantially lower sensitivity of DESH used a very long time interval (mean, 51.9 months).<sup>12</sup> In contrast, another study that used a very short time interval (0.3 months) demonstrated a substantially lower specificity of DESH.<sup>23</sup> We assumed that the follow-up period might have affected the diagnostic performance of DESH, given that that symptom improvements were most remarkable in the short term, with a gradual decline in the long term.<sup>40,41</sup> Our results suggest the need for a large multicenter study including patients with/without DESH subjected to shunt surgery and with outcomes evaluated in a standardized manner.

Third, potential selection bias may be present in the study. Some of the studies used positive findings on the CSF tap tests for the selection of surgical candidates, which might have caused selection bias because patients with negative CSF tap test results could also benefit from VP shunt surgery.<sup>8,9</sup> Moreover, 3 studies demonstrating an association between DESH and favorable post-surgical outcome were excluded because the sensitivity and specificity could not be calculated.<sup>13,15,36</sup> This issue might have resulted in the underestimation of the diagnostic performance of DESH in our study. Finally, patients with incomplete DESH were excluded from the analysis. Despite an additional search performed to incorporate incomplete DESH, no eligible article was found. A previous study reported that patients satisfying DESH features except a dilated Sylvian fissure showed a higher improvement rate after VP shunt surgery than patients satisfying DESH features except for the tight high convexity (87.5% versus 27.2%).<sup>23</sup> Although the evidence is lacking, this finding may suggest that tight high convexity is a more important prognostic factor than the other features of DESH.

## CONCLUSIONS

Our meta-analysis demonstrates a relatively low prevalence of DESH among patients with iNPH and a poor diagnostic performance of DESH with regard to treatment-response prediction.

## REFERENCES

1. Mori E, Ishikawa M, Kato T, et al. **Guidelines for management of idiopathic normal pressure hydrocephalus: second edition.** *Neurol Med Chir (Tokyo)* 2012;52:775–809 CrossRef Medline
2. Relkin N, Marmarou A, Klinge P, et al. **Diagnosing idiopathic normal-pressure hydrocephalus.** *Neurosurgery* 2005;57:(3 Suppl):S4–16; discussion ii–v CrossRef Medline
3. Kazui H, Miyajima M, Mori E, et al. **Lumboperitoneal shunt surgery for idiopathic normal pressure hydrocephalus (SINPHONI-2): an open-label randomised trial.** *Lancet Neurol* 2015;14:585–94 CrossRef Medline
4. Feletti A, d'Avella D, Wikkelsø C, et al. **Ventriculoperitoneal shunt complications in the European idiopathic normal pressure hydrocephalus multicenter study.** *Oper Neurosurg (Hagerstown)* 2019;17:97–102 CrossRef Medline
5. Nassar BR, Lippa CF. **Idiopathic normal pressure hydrocephalus: a review for general practitioners.** *Gerontol Geriatr Med* 2016;2:2333721416643702 CrossRef Medline
6. Marmarou A, Young HF, Aygok GA, et al. **Diagnosis and management of idiopathic normal-pressure hydrocephalus: a prospective study in 151 patients.** *J Neurosurg* 2005;102:987–97 CrossRef Medline
7. Malm J, Kristensen B, Karlsson T, et al. **The predictive value of cerebrospinal fluid dynamic tests in patients with the idiopathic adult hydrocephalus syndrome.** *Arch Neurol* 1995;52:783–89 CrossRef Medline
8. Marmarou A, Bergsneider M, Klinge P, et al. **The value of supplemental prognostic tests for the preoperative assessment of idiopathic normal-pressure hydrocephalus.** *Neurosurgery* 2005;57:(3 Suppl):S17–28; discussion ii–v CrossRef Medline
9. Wikkelsø C, Hellström P, Klinge PM, et al. **The European iNPH Multicentre Study on the predictive values of resistance to CSF outflow and the CSF tap test in patients with idiopathic normal pressure hydrocephalus.** *J Neurol Neurosurg Psychiatry* 2013;84:562–68 CrossRef Medline
10. Williams MA, Malm J. **Diagnosis and treatment of idiopathic normal pressure hydrocephalus.** *Continuum (Minneapolis)* 2016;22:579 CrossRef Medline
11. Greenberg BM, Williams MA. **Infectious complications of temporary spinal catheter insertion for diagnosis of adult hydrocephalus and idiopathic intracranial hypertension.** *Neurosurgery* 2008;62:431–36 CrossRef Medline
12. Grahne K, Jusue-Torres I, Szujewski C, et al. **The quest for predicting sustained shunt response in normal-pressure hydrocephalus: an analysis of the callosal angle's utility.** *World Neurosurg* 2018;115:e717–22 CrossRef Medline
13. Narita W, Nishio Y, Baba T, et al. **High-convexity tightness predicts the shunt response in idiopathic normal pressure hydrocephalus.** *AJNR Am J Neuroradiol* 2016;37:1831–37 CrossRef Medline
14. Otero-Rodríguez A, Sousa-Casasnovas P, Cruz-Terrón H, et al. **Utility of radiologic variables to predict the result of lumbar infusion test in the diagnosis of idiopathic normal pressure hydrocephalus.** *World Neurosurg* 2019;127:e957–64 CrossRef Medline
15. Virhammar J, Laurell K, Cesarini KG, et al. **Preoperative prognostic value of MRI findings in 108 patients with idiopathic normal pressure hydrocephalus.** *AJNR Am J Neuroradiol* 2014;35:2311–18 CrossRef Medline
16. Garcia-Armengol R, Domenech S, Botella-Campos C, et al. **Comparison of elevated intracranial pressure pulse amplitude and disproportionately enlarged subarachnoid space (DESH) for prediction of surgical results in suspected idiopathic normal pressure hydrocephalus.** *Acta Neurochir (Wien)* 2016;158:2207–13 CrossRef Medline
17. Hashimoto M, Ishikawa M, Mori E, et al. **Diagnosis of idiopathic normal pressure hydrocephalus is supported by MRI-based scheme: a prospective cohort study.** *Cerebrospinal Fluid Res* 2010;7:18 CrossRef Medline
18. Kitagaki H, Mori E, Ishii K, et al. **CSF spaces in idiopathic normal pressure hydrocephalus: morphology and volumetry.** *AJNR Am J Neuroradiol* 1998;19:1277–84 Medline
19. Nakajima M, Yamada S, Miyajima M, et al. **Guidelines for Management of Idiopathic Normal Pressure Hydrocephalus: Endorsed by the Japanese Society of Normal Pressure Hydrocephalus.** *Neurol Med Chir (Tokyo)* 2021;61:63–97 CrossRef Medline
20. Agerskov S, Wallin M, Hellström P, et al. **Absence of disproportionately enlarged subarachnoid space hydrocephalus, a sharp callosal angle, or other morphologic MRI markers should not be used to exclude patients with idiopathic normal pressure hydrocephalus from shunt surgery.** *AJNR Am J Neuroradiol* 2019;40:74–79 CrossRef Medline
21. Craven CL, Toma AK, Mostafa T, et al. **The predictive value of DESH for shunt responsiveness in idiopathic normal pressure hydrocephalus.** *J Clin Neurosci* 2016;34:294–98 CrossRef Medline
22. Hong YJ, Kim MJ, Jeong E, et al. **Preoperative biomarkers in patients with idiopathic normal pressure hydrocephalus showing a favorable shunt surgery outcome.** *J Neurol Sci* 2018;387:21–26 CrossRef Medline
23. Ishikawa M, Oowaki H, Takezawa M, et al. **Disproportionately enlarged subarachnoid space hydrocephalus in idiopathic normal-pressure hydrocephalus and its implication in pathogenesis.** *Acta Neurochir Suppl* 2016;122:287–90 CrossRef Medline
24. Nishida N, Nagata N, Toda H, et al. **Association of lipocalin-type prostaglandin D synthase with disproportionately enlarged subarachnoid-space in idiopathic normal pressure hydrocephalus.** *Fluids Barriers CNS* 2014;11:9 CrossRef Medline
25. Radovnický T, Adámek D, Derner M, et al. **Fractional anisotropy in patients with disproportionately enlarged subarachnoid space hydrocephalus.** *Acta Neurochir (Wien)* 2016;158:1495–1500 CrossRef Medline
26. Ahmed AK, Luciano M, Moghekar A, et al. **Does the presence or absence of DESH predict outcomes in adult hydrocephalus?** *AJNR Am J Neuroradiol* 2018;39:2022–26 CrossRef Medline
27. Takagi K, Watahiki R, Machida T, et al. **Reliability and interobserver variability of Evans' index and disproportionately enlarged subarachnoid space hydrocephalus as diagnostic criteria for idiopathic normal pressure hydrocephalus.** *Asian J Neurosurg* 2020;15:107–12 CrossRef Medline
28. Liberati A, Altman DG, Tetzlaff J, et al. **The PRISMA statement for reporting systematic reviews and meta-analyses of studies that evaluate healthcare interventions: explanation and elaboration.** *BMJ* 2009;339:b2700 CrossRef Medline
29. Miyazaki K, Ishii K, Hanaoka K, et al. **The tight medial and high convexity subarachnoid spaces is the first finding of idiopathic normal pressure hydrocephalus at the preclinical stage.** *Neurol Med Chir (Tokyo)* 2019;59:436–43 CrossRef Medline
30. Whiting PF, Rutjes AW, Westwood ME, et al. **QUADAS-2: a revised tool for the quality assessment of diagnostic accuracy studies.** *Ann Intern Med* 2011;155:529–36 CrossRef Medline
31. Higgins JP, Thomas J, Chandler J, et al, eds. **Cochrane Handbook for Systematic Reviews of Interventions, Version 6.0 (updated July 2019).** *Cochrane Training*. 2019. www.training.cochrane.org/handbook. Accessed October 15, 2020
32. Suh CH, Park SH. **Successful publication of systematic review and meta-analysis of studies evaluating diagnostic test accuracy.** *Korean J Radiol* 2016;17:5–6 CrossRef Medline
33. Devillé WL, Buntinx F, Bouter LM, et al. **Conducting systematic reviews of diagnostic studies: didactic guidelines.** *BMC Med Res Methodol* 2002;2:9 CrossRef Medline



34. Deeks JJ, Macaskill P, Irwig L. **The performance of tests of publication bias and other sample size effects in systematic reviews of diagnostic test accuracy was assessed.** *J Clin Epidemiol* 2005;58:882–93 CrossRef Medline
35. Yamada S, Ishikawa M, Yamamoto K. **Optimal diagnostic indices for idiopathic normal pressure hydrocephalus based on the 3D quantitative volumetric analysis for the cerebral ventricle and subarachnoid space.** *AJNR Am J Neuroradiol* 2015;36:2262–69 CrossRef Medline
36. Shinoda N, Hirai O, Hori S, et al. **Utility of MRI-based disproportionately enlarged subarachnoid space hydrocephalus scoring for predicting prognosis after surgery for idiopathic normal pressure hydrocephalus: clinical research.** *J Neurosurg* 2017;127:1436–42 CrossRef Medline
37. Engel D, Adib S, Schuhmann M, et al. **Paradigm-shift: radiological changes in the asymptomatic iNPH-patient to be: an observational study.** *Fluids Barriers CNS* 2018;15:1–7 CrossRef Medline
38. Mihalj M, Dolić K, Kolić K, et al. **CSF tap test—obsolete or appropriate test for predicting shunt responsiveness? A systemic review.** *J Neurol Sci* 2016;362:78–84 CrossRef Medline
39. Benedetto N, Gambacciani C, Aquila F, et al. **A new quantitative method to assess disproportionately enlarged subarachnoid space (DESH) in patients with possible idiopathic normal pressure hydrocephalus: the SILVER index.** *Clin Neurol Neurosurg* 2017;158:27–32 CrossRef Medline
40. Grasso G, Torregrossa F, Leone L, et al. **Long-term efficacy of shunt therapy in idiopathic normal pressure hydrocephalus.** *World Neurosurg* 2019;129:e458–63 CrossRef Medline
41. Wu EM, El Ahmadieh TY, Kafka B, et al. **Ventriculoperitoneal shunt outcomes of normal pressure hydrocephalus: a case series of 116 patients.** *Cureus* 2019;11:e4170 CrossRef Medline

# Simultaneous Multislice for Accelerating Diffusion MRI in Clinical Neuroradiology Protocols

M.J. Hoch, M. Bruno, D. Pacione, Y.W. Lui, E. Fieremans, and T.M. Shepherd



## ABSTRACT

**BACKGROUND AND PURPOSE:** Diffusion MR imaging sequences essential for clinical neuroradiology imaging protocols may be accelerated with simultaneous multislice acquisitions. We tested whether simultaneous multislice–accelerated diffusion data were clinically equivalent to standard acquisitions.

**MATERIALS AND METHODS:** In this retrospective study, clinical diffusion sequences obtained before and after implementation of 2-slice simultaneous multislice acceleration and an altered diffusion gradient sampling scheme using the same 3T MRI scanner and 20-channel coil ( $n = 25$  per group) were independently and blindly evaluated by 2 neuroradiologists for perceived quality, artifacts, and overall diagnostic utility. Diffusion tractography was performed in 13 patients both with and without 2-slice simultaneous multislice acceleration ( $b = 0, 1000, 2000$  s/mm<sup>2</sup>; 60 directions). The corticospinal tract and arcuate fasciculus ipsilateral to the lesion were generated using the same ROIs and then blindly assessed by a neurosurgeon for anatomic fidelity, perceived quality, and impact on surgical management. Tract volumes were compared for spatial overlap.

**RESULTS:** Two-slice simultaneous multislice diffusion reduced acquisition times from 141 to 45 seconds for routine diffusion and from 7.5 to 5.9 minutes for diffusion tractography using 3T MR imaging. The simultaneous multislice–accelerated diffusion sequence was rated equivalent for diagnostic utility despite reductions to perceived image quality. Simultaneous multislice–accelerated diffusion tractography was rated clinically equivalent. Dice similarity coefficients between routine and simultaneous multislice–generated corticospinal tract and arcuate fasciculus tract volumes were 0.78 (SD, 0.03) and 0.71 (SD, 0.05), respectively.

**CONCLUSIONS:** Two-slice simultaneous multislice diffusion appeared clinically equivalent for standard acquisitions and diffusion tractography. Simultaneous multislice makes it feasible to acquire higher angular and  $q$ -space-resolution diffusion acquisitions required for translating advanced diffusion models into clinical practice.

**ABBREVIATIONS:** AF = arcuate fasciculus; CST = corticospinal tract; DSC = Dice similarity coefficient; FA = fractional anisotropy; GRAPPA = generalized autocalibrating partially parallel acquisition; SMS = simultaneous multislice

The diffusion-weighted sequence is essential for clinical protocols in head MR imaging and detecting acute ischemic

stroke.<sup>1</sup> Nervous tissue diffusion properties can be informative for other pathologies, including prognosis in lymphoma,<sup>2</sup> detection of skull lesions,<sup>3</sup> or early diagnosis of Creutzfeldt-Jakob disease.<sup>4</sup> Diffusion tractography has improved our understanding of white matter anatomy, like the arcuate fasciculus (AF), the key pathway for language.<sup>5</sup> Diffusion tractography improves neurosurgical planning and reduces perioperative morbidity for patients with brain tumors<sup>6–8</sup> but requires high-angular-resolution acquisitions that prolong scan time. During the past 15 years, more advanced diffusion models that account for non-Gaussian water diffusion have further improved our understanding of white matter structure<sup>9</sup> but require both high-angular-resolution<sup>10,11</sup> and high  $q$ -space-resolution<sup>12</sup> acquisition strategies; these protocols necessitate relatively long scan times that are much harder for patients to tolerate and thus have not been widely implemented clinically.

Received February 3, 2021; accepted after revision March 4.

From the Department of Radiology (M.J.H.), University of Pennsylvania, Philadelphia, Pennsylvania; Departments of Radiology (M.B., Y.W.L., E.F., T.M.S.) and Neurosurgery (D.P.), New York University Langone School of Medicine, New York, New York; and Center for Advanced Imaging Innovation and Research (E.F.), New York, New York.

Timothy Shepherd received research support from the National Institute of Aging (National Institutes of Health 1K23 AG048622-01). This research was supported, in part, by the Center for Advanced Imaging Innovation and Research, a National Institutes of Health–National Institute of Biomedical Imaging and Bioengineering Biomedical technology resource center (grant P41EB017183).

Please address correspondence to Timothy Shepherd, MD/PhD, Department of Radiology, Room 230D, 660 First Ave, New York, NY 10016; e-mail: timothy.shepherd@nyulangone.org; @tim0shepherd; @RVUhound; @elsfi

Indicates open access to non-subscribers at [www.ajnr.org](http://www.ajnr.org)

Indicates article with online supplemental data.

<http://dx.doi.org/10.3174/ajnr.A7140>

Simultaneous multislice (SMS) is a recent innovation that allows concurrently acquiring multiple image slices during each acquisition,<sup>13</sup> thereby enabling reduced TR and total scan time. Parallel imaging–based SMS uses controlled aliasing with blipped z-direction gradients<sup>14,15</sup> and then reconstructs images individually using a section generalized autocalibrating partially parallel acquisition (GRAPPA) reconstruction<sup>16</sup> with little penalty to the image SNR. This technique has become popular in the radiology research community because it supports ever more complex diffusion MR imaging acquisitions for advanced nervous tissue models and representations.<sup>17–19</sup> Researchers, however, seldom rely on visual interpretation of SMS-diffusion trace images, nor do they depend on the fidelity of diffusion tractography for high-risk clinical decision-making in individual patients. The goal of this study was to evaluate SMS acceleration for clinical neuroradiology diffusion and tractography applications.

## MATERIALS AND METHODS

Initially, volunteers gave consent and were scanned under a prospective, technical development institutional review board (New York University) approval using outpatient 3T MR imaging (Magnetom Skyra; Siemens) with a 20-channel head coil to compare multiple versions of 2-slice SMS-accelerated diffusion sequences to determine an acceptable sequence for common neuroradiology protocols that require trace-weighted and ADC maps, and for a diffusion tractography protocol for patients requiring presurgical planning. The 2-slice SMS-accelerated sequence common to most protocols was then implemented on multiple 1.5T and 3T clinical scanners. Diffusion data for tractography still were obtained with both the original and SMS-accelerated sequences until comparison and approval also could be obtained by the referring neurosurgery service. Data analyzed for this report were collected and analyzed retrospectively from the time period around SMS implementation after institutional review board approval of a Health Insurance Portability and Accountability Act–compliant research study.

### Clinical Neuroradiology Head Protocols

Diffusion trace and ADC images from 25 consecutive patients imaged with neuroradiology head protocols using the hospital 3T MR imaging scanner (Magnetom Skyra) with a 20-channel coil were collected from the first day of the month before and after implementation of the 2-slice accelerated SMS diffusion sequence. Consecutive cases were included regardless of reported diagnoses and included inpatients or patients in the emergency department with infarcts, hemorrhage, or brain tumors. The only exclusion criterion was severe motion degradation, but no studies were excluded. There were 2 key changes to the sequence (Online Supplemental Data): First, we used 2-slice SMS acceleration to reduce the TR from 8200 to 3400 ms. Second, the diffusion-sampling scheme was changed by the following: 1) eliminating  $b = 500 \text{ s/mm}^2$  sampling, 2) increasing gradient directions from 3 to 6 at  $b = 1000 \text{ s/mm}^2$ , and 3) reducing averages from 2 to 1 per direction. If we counted  $b = 0 \text{ s/mm}^2$  images (2 averages), the total diffusion-weighted images were reduced from 14 to 8 (43% reduction in diffusion volumes acquired). Note that 2-slice SMS TR reductions will always be greater than the resulting total scan time reductions because “dummy” scans are required to reach a steady-state before image

acquisition occurs. Overall, these 2 changes reduced scan time from 141 to 45 seconds.

Blinded to the acquisition sequence and alternating side per subject, the senior author used ROIs to extract ADC for the frontal lobe white matter (minor forceps) and frontal horn lateral ventricle CSF (free of the choroid plexus), and to calculate relative SNR for the minor forceps and cerebellar white matter relative to a noise ROI in the same trace-weighted image using previously published methods.<sup>20</sup> Next, 2 board-certified neuroradiologists blinded to the acquisition sequence independently rated 3 features of the diffusion-weighted trace and ADC images: artifacts (motion, fat suppression, skull base susceptibility, geometric distortion), image quality (resolution, edge sharpness, noise, gray-white junction), and overall diagnostic utility (ability to interpret). Each rating used the same ordinal scale, where 1 was poor, needs recall; 2 was suboptimal, but interpretable; 3 was average, lower range of normal quality; 4 was good, higher range of normal quality; and 5 was excellent. Sample size per group was determined a priori specifically to detect a 0.5 change in the ordinal rating scale in which the predicted mean = 4.0 (SD, 0.5),  $\alpha = .05$ , and  $\beta \sim 0.95$ . ROI and ordinal data were compared by unpaired 2-tailed  $t$  tests and Mann-Whitney-Wilcoxon 2-tailed tests, respectively. Confidence intervals and Cohen  $\kappa$  coefficients for interrater reliability were calculated.

### Diffusion Tractography Protocol

Thirteen consecutive brain-mapping cases obtained for neurosurgical planning had both conventional and SMS acquisitions for DTI; this group included 9 glial tumors, 2 seizure foci, 1 cavernous malformation, and 1 epidermoid cyst (mean age, 44 [SD, 36] years, 5 woman). No potential subjects were excluded. Distance documented in the original radiology report between the lesion margin and the visualized corticospinal tract (CST) and/or AF in the ipsilateral hemisphere was 0 cm ( $n = 4$ ), <1 cm ( $n = 5$ ), <2.5 cm ( $n = 3$ ), or  $\sim 4$  cm ( $n = 1$ ). In this latter patient, tractography was requested because the CST was in closer proximity to the planned surgical corridor than the lesion. One patient had a repeat diffusion scan with SMS acceleration 30 days later for a second procedure.

The shared sequence parameters included  $54 \times 3 \text{ mm}$  thick slices with 2.8-mm in-plane resolution (200-cm FOV,  $88 \times 88$  matrix) with identical diffusion parameters (1 average,  $b$ -values = 0, 1000, 2000  $\text{s/mm}^2$ , 30 directions per  $b$ -value, bipolar gradients). Higher  $b$ -value data are part of our institutional protocol but may not be considered necessary at other institutions. TR and TE were 7100/95 and 4700/95 ms for standard and 2-slice SMS acquisitions, respectively. Shorter TEs (with resultant shorter TRs and overall scan time) are possible with monopolar diffusion gradients but may be more affected by eddy currents. Volumetric T1, diffusion, and SMS diffusion acquisitions were coregistered in third-party brain mapping software (Brainlab). Two ROIs per tract were drawn on the direction-encoded color fractional anisotropy (FA) maps derived from the standard diffusion acquisitions to generate CST and AF tracts ipsilateral to the lesion<sup>21</sup> (Online Supplemental Data).

Diffusion data with and without SMS were used separately to generate the tracts while keeping the ROIs constant, thus eliminating manual drawing biases. The minimum tract lengths were 80 and 50 mm for CST and AF, respectively. The lower limit of FA was 0.15 and 0.12 for CST and AF, respectively. Tractography



**Table 1: Quantitative and qualitative comparison of diffusion trace and ADC parameter maps for clinical patients in the emergency department (single single 3T MRI scanner)<sup>a</sup>**

Data	Standard (n = 25)	SMS (n = 25)	95% CI for Difference	P Value
Age (yr)	61.5 [SD, 19.5]	63.2 [SD, 15.4]	NA	.734 <sup>b</sup>
Woman (No.) (%)	52% (13/25)	56% (14/25)	NA	NA
ADC, minor forceps ( $\times 10^{-3}$ mm <sup>2</sup> /s)	0.833 [SD, 0.077]	0.816 [SD, 0.073]	−0.025 to + 0.059	.427 <sup>b</sup>
ADC, CSF ( $\times 10^{-3}$ mm <sup>2</sup> /s)	3.032 [SD, 0.099]	3.015 [SD, 0.080]	−0.033 to + 0.067	.508 <sup>b</sup>
SNR, minor forceps	21.4 [SD, 14.6]	22.5 [SD, 9.6]	−7.9 to + 5.7	.754 <sup>b</sup>
SNR, cerebellum	32.6 [SD, 10.9]	27.3 [SD, 14.8]	−1.9 to + 12.5	.156 <sup>b</sup>
Artifacts <sup>c</sup>	3.5 [SD, 0.5]	3.7 [SD, 0.5]	−0.5 to + 0.1	.070 <sup>d</sup>
Image quality <sup>c</sup>	4.0 [SD, 0.7]	3.3 [SD, 0.5]	−0.4 to + 1.0	.001 <sup>d</sup>
Diagnostic utility <sup>c</sup>	3.8 [SD, 0.4]	3.7 [SD, 0.5]	−0.2 to + 0.4	.187 <sup>d</sup>

**Note:**—NA indicates not applicable

<sup>a</sup> Data are mean (SD), (No.) (%), or 95% CI.

<sup>b</sup> Unpaired, 2-tailed *t* test.

<sup>c</sup> Average of independent, blinded assessment using an ordinal scale 1–5 by 2 board-certified neuroradiologists (no adjudication performed).

<sup>d</sup> Mann-Whitney-Wilcoxon 2-tailed test.

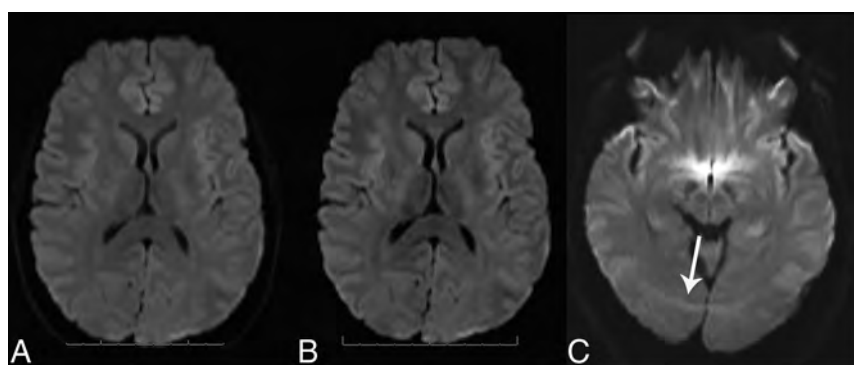


**FIG 1.** Axial diffusion images from standard (A) and SMS diffusion acquisitions (B) in a clinical patient with headaches. There is no appreciable difference in diagnostic utility, even with a reduction in scan time using SMS. An SMS arc-like scalp artifact (C, arrow) is seen in another clinical patient due to poor fat saturation. With SMS, unsaturated fat signal associated with echo-planar acquisitions can alias into all simultaneously acquired slices.

seed density and turning angle limits have fixed values in the clinical software used. While normally part of our clinical practice, here potential spurious tracts were not edited, nor were FA thresholds adjusted for individual cases, to avoid introducing individual bias into the comparisons.

The tract volumes were superimposed on the T1-weighted, volumetric sequences and then retrospectively reviewed in random order separately using Brainlab software by a neurosurgeon with 5 years of experience using tractography for surgical planning (blinded for all assessments). The neurosurgeon evaluated anatomic correctness and preference and whether the tract would alter surgical management. “Anatomically correct” implied that the tract matched known anatomy from previous surgical experience and reports of postmortem white matter dissection.<sup>22</sup> “Different surgical management” implied that a tract changed the surgical approach or planned extent of resection. Finally, in blinded side-by-side comparison, the neurosurgeon determined whether he preferred 1 version of the tract.

The AF and CST length, FA, and volumes were extracted from the tract objects for standard and SMS diffusion tractography and then compared using paired-sample 2-tailed *t* tests. Note that sample size was determined by practical considerations but was

estimated a priori to require approximately 16 to detect a quantitative difference roughly equal to the anticipated variance of the data (ie, a Cohen D value of 1) with 95% statistical power. Confidence intervals also were calculated. The Dice similarity coefficient (DSC)<sup>23</sup> was used to measure the spatial overlap between standard (A) and SMS (B) tract volumes, where  $DSC(A, B) = 2(A \cap B) / (A + B)$  and  $\cap$  is the intersection between the 2 volumes. Spatial misregistration from skull base geometric distortion was characterized by measuring the distance from the anterior margin of the conventional and SMS-derived CST tracts to the anterior margin of the cervicomedullary junction on coregistered volumetric T1 at

the foramen magnum.

## RESULTS

### Clinical Diffusion Trace

At 3T, 2-slice SMS acceleration with an altered diffusion-sampling scheme allowed us to reduce the TR by 59% (from 8.2 to 3.4 seconds), reduce diffusion volumes acquired 43% (from 14 to 8), and reduce overall scan time by 70% (from 141 to 45 seconds). There was an 18% decrease in perceived image quality of the SMS-accelerated scans ( $P = .001$ ). No difference in artifacts or diagnostic utility was detected with 95% confidence interval that true differences, if present, represented  $<0.5$  decrement on the 5-point ordinal scale (Table 1). Representative clinical cases are provided in Figs 1 and 2 for readers to compare sequence results. Readers perceived subtle, lower SNR in the posterior fossa on SMS images (16% absolute quantitative reduction,  $P = .156$ , with a 95% confidence interval to detect an SNR reduction of  $\geq 38\%$ ), but this remained acceptable for diagnostic use in ratings and subsequent clinical cases (Fig 2). Both readers noted a fat-saturation artifact in 1 subject undergoing SMS (Fig 1C); however, the diagnostic utility of this scan was not compromised. Readers did not observe increased T1-weighting to the SMS diffusion trace images; the TR of 3400 ms remained

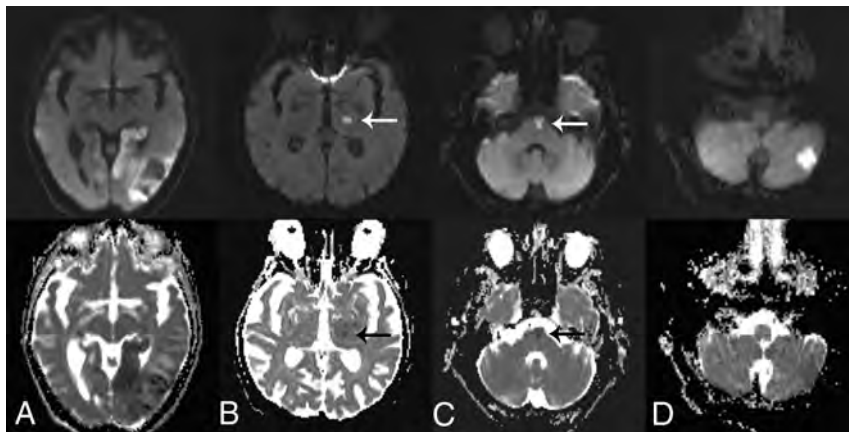


**FIG 2.** Examples of 2-slice SMS-accelerated diffusion trace and ADC maps of 4 different clinical patients. Large acute left-occipital infarct (A) contrasted with a small subacute left-thalamic infarct (B) (arrows). Raters suggested subtle SNR reductions for the posterior fossa using SMS (Table 1); however, small infarcts in the brainstem (C) and cerebellum (D) remain well-visualized.

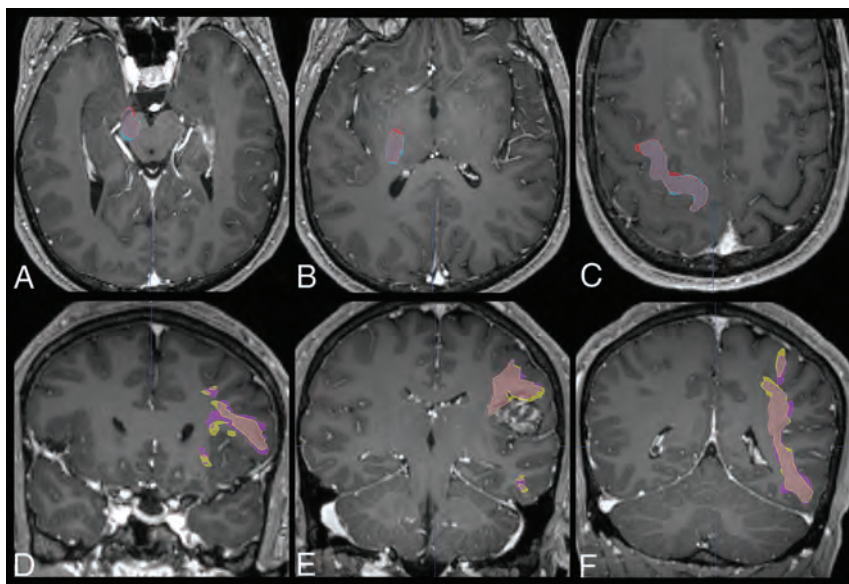


**FIG 3.** Overlap of diffusion tractography between standard and SMS-acquired data in 2 selected patients. *Upper Row:* A 56-year-old man with a multifocal right-cerebral hemisphere glioma. The right corticospinal tract volumes are shown in blue (conventional) and red (SMS) at the levels of the cerebral peduncle (A), posterior limb of the internal capsule (B), and precentral gyrus (C). The DSC between standard and SMS tract volumes is 0.76. *Lower Row:* A 36-year-old man with a left opercular cavernous malformation. The left-arcuate fasciculus volumes are shown in purple (conventional) and yellow (SMS) at the levels of the anterior and posterior frontal projections (D and E) and genu (F). There are slight differences in the edge of the visualized tracts abutting the superior border of the cavernous malformation (E), but these differences would not affect selection of the surgical corridor, and in both situations, the neurosurgeon would be cautious in approaching the superior margin of the lesion. The DSC between standard and SMS tract volumes is 0.75.

3× the reported T1-relaxation times for gray and white matter at 3T.<sup>24</sup> There was no difference in the ADC values of the minor forceps or frontal horn CSF of standard compared with SMS diffusion images (95% confidence to exclude no greater than a 7% difference). There were no callbacks or nondiagnostic diffusion scans attributed to SMS during the subsequent 10 months after widespread adoption.

Rater agreement for artifacts, image quality, and diagnostic utility were 60%, 62%, and 76%, respectively. The Cohen  $\kappa$  values for interrater reliability were 0.216, 0.363, and 0.413, respectively; these may underestimate agreement due to the first kappa paradox<sup>25</sup> because ratings of 3 or 4 represented most scores. Reader agreement for artifacts, image quality, and diagnostic utility became 100%, 88%, and 96% respectively if 3 and 4 ordinal scores from raters were collapsed to 1 value. While it was not part of the rater assessment, a similar 2-slice SMS-accelerated diffusion sequence was implemented on a newer 1.5T MRI scanner with a 20-channel coil (Magnetom Aera; Siemens) at the same hospital, reducing scan time from 165 to 65 ms (Online Supplemental Data); for reader interest, additional clinical examples of SMS-accelerated diffusion images at both field strengths are provided in the Online Supplemental Data. Note that full protocol parameters for 1.5T and 3T MR imaging scanners will be provided to interested readers by contacting the communicating author.

### Diffusion Tractography

2-slice SMS acceleration reduced the TR 34% to 4.7 seconds and reduced overall acquisition time 22% to 5.9 minutes without visual differences in tractography (Fig 3) or quantitative tractography differences for either the CST or AF ipsilateral to clinical lesions (Table 2). The mean DSCs between standard and SMS tract volumes were 0.78 (SD, 0.03) and 0.71 (SD, 0.05) for the CST and AF tracts, respectively ( $n = 13$  subjects). The SMS-acquired CST demonstrated similar spatial misregistration at the skull base (Table 2). The Online Supplemental Data demonstrate reproducibility for CST and AF tracts in the same subject scanned twice 30 days apart.

The neurosurgeon rated 25 of 26 (96%) SMS-generated tracts to be anatomically correct. The exception was the AF in case 11; however, both the conventional and SMS tracts were deemed equally nonanatomic in this case. This outcome was attributed to a porencephalic cavity, which made the standardized 2-ROI tractography approach ineffective and not from any inherent deficiency of the SMS acquisition. Tractography from SMS diffusion was considered equivalent or

**Table 2: Quantitative comparison of DTI tractography for the corticospinal tract and arcuate fasciculus ipsilateral to the lesion in 13 subjects<sup>a</sup>**

Diffusion Technique	Standard	SMS	Mean Individual Difference <sup>b</sup>	95% CI for Difference	P Value
Corticospinal tract					
Volume (mL)	30.7 [SD, 9.1]	32.9 [SD, 9.7]	−2.3 [SD, 4.0]	−9.4 to +5.0	.062 <sup>c</sup>
Length (mm)	125.2 [SD, 13.1]	124.0 [SD, 15.0]	1.2 [SD, 7.0]	−9.6 to +12.0	.537 <sup>c</sup>
Mean FA	0.45 [SD, 0.04]	0.46 [SD, 0.04]	−0.01 [SD, 0.02]	−0.04 to +0.02	.076 <sup>c</sup>
Arcuate fasciculus					
Volume (mL)	25.3 [SD, 5.3]	26.0 [SD, 6.7]	−0.7 [SD, 3.1]	−5.3 to +3.9	.438 <sup>c</sup>
Length (mm)	77.4 [SD, 7.1]	76.5 [SD, 6.7]	0.9 [SD, 4.6]	−4.4 to +6.2	.482 <sup>c</sup>
Mean FA	0.36 [SD, 0.04]	0.36 [SD, 0.04]	0.00 [SD, 0.01]	−0.03 to +0.03	1.000 <sup>c</sup>
Spatial misregistration (mm) <sup>d</sup>	3.4 [SD, 1.6]	2.8 [SD, 1.0]	0.6 [SD, 1.3]	−0.4 to +1.6	.135 <sup>c</sup>

<sup>a</sup> Data are mean (SD) or 95% CI.<sup>b</sup> Difference between measurements in the same individual (standard value minus SMS value).<sup>c</sup> Paired-sample 2-tailed *t* test.<sup>d</sup> Difference between the anterior margin of the cervicomedullary junction at the foramen magnum depicted by volumetric T1 MR imaging versus CST diffusion tractography.

better in 18 of 26 (69%) tracts generated. Reasons for preferring one tract over its counterpart included the following: more robust tract, less spurious fibers, less discontinuities in volume, and less spurious extension into the extracranial soft tissues (removing the latter is normally routine, but not in this investigation to avoid introducing bias). All CST pairs did not change the surgical management (approach and aggressiveness). All AF pairs had no change in surgical approach. Eleven of 13 (85%) AF pairs would have equivalent aggressiveness of resection. The standard AF tract in case 13 was considered a better anatomic representation of projections of the left-frontal operculum adjacent to a left-frontal oligodendroglioma that would result in a less aggressive resection. The SMS AF tract in case 5 was considered a more robust tract adjacent to the cavernous malformation, which would result in a less aggressive resection.

## DISCUSSION

SMS-accelerated neuroradiology protocol diffusion acquisitions appear safe and clinically feasible without large differences in image quality when assessed by 2 neuroradiologists. Raters perceived mild decreases in the SNR of diffusion trace images, particularly in the posterior fossa structures, but characterization of pathologies of different sizes and in different anatomic locations appeared similar between standard and SMS-accelerated diffusion. Aggressive 2-slice-accelerated SMS with 3T MR imaging and a standard 20-channel coil reduced our standard diffusion trace scan time approximately 70%, saving 1.5 minutes per scan. Yokota et al<sup>26</sup> reported a 41% scan time reduction using 3T MR imaging and 2-slice SMS acceleration with 2-mm isotropic resolution, but their final scan time of the SMS-accelerated sequence was still 3× longer than our current data.<sup>26</sup> Given that diffusion imaging is ubiquitous to all neuroradiology protocols, the 1.5-minute time savings obtained here would return sufficient time theoretically for an additional 3 scans per day per magnet at our primary outpatient facility (estimation based on ~67.5 minutes saved; the facility is open 15 hours per day, with 20-minute slots and 100% neuroradiology head protocols). A motion-free 45-second diffusion scan should facilitate more rapid decision-making in acute stroke, decrease motion degradation in patients who are less MR imaging-tolerant, and create more time for additional MR imaging sequences. An additional motivation for our center was to create more time within

the scheduled slots to clean the magnet between patients during the early stages of the coronavirus 19 pandemic.

SMS-accelerated diffusion tractography was considered anatomically equivalent by an experienced neurosurgeon without altering intended surgical management or the aggressiveness of resection. The tractogram volume agreement was good: mean DSCs of 0.78 and 0.71 for CST and AF, respectively. An imperfect DSC may occur due to low spatial resolution (~3-mm isotropic voxels), SNR differences, patient movement (or other causes of misregistration), and/or different spurious tracts not actively edited from the data. In our clinical practice, neuroradiologists freely and subjectively manipulate the tractography parameters more on an individual basis than permitted in this study design to accomplish the goals of presurgical planning. Yokota et al<sup>26</sup> reported that CST tractography appeared similar to radiologists with or without 2-slice SMS acceleration, but most of the data were from nonsurgical patients and not blindly evaluated by a neurosurgeon experienced using tractography. Here, SMS acquisitions in preoperative cases could reduce tractography scan times by ~2 minutes; these studies tend to be long due to the need for coregistered fMRI, tractography, and 3D structural MR imaging. Even more time savings might be possible with 3- or 4-fold slice acceleration using array coils with more receive elements (eg, a 64-channel coil), less angular or *q*-space resolution than in our current institutional protocol, or improved monopolar imaging gradients that reduce TE (and subsequently scan time).

Besides increased throughput on busy clinical MR imaging scanners, SMS acceleration can also be used to increase spatial resolution of clinical diffusion MR imaging protocols; this potential was not emphasized in the current study but could be the subject of future work. SMS-accelerated diffusion images for the current study still had TRs (3200 or 4700 ms) more than 3× the T1-relaxation times of gray and white matter at 3T.<sup>24</sup> More aggressive reductions of TR are possible, particularly with 3- or 4-slice acceleration, which may introduce T1-weighting to diffusion trace images. In preliminary experiments, shortening the TR below 2500 ms also introduced more substantial signal loss and increased the frequency of peripheral nerve stimulation reported by volunteer subjects. With SMS, unsaturated fat signal associated with echo-planar acquisitions can alias into all simultaneously acquired slices and result in spurious tractography. While SMS diffusion is now FDA-approved, readers



should carefully adapt SMS acquisitions with or without acceleration to their local diffusion protocols.

This study has limitations. Due to practical limitations on the time required for detailed assessment by radiologists and a neurosurgeon, the study is underpowered to exclude smaller quantitative differences between sequences (see confidence intervals in Tables 1 and 2). The SMS-accelerated diffusion sequences used here are derived from a single large academic center (New York University) but may differ from other radiology practice locations and settings. Scan time reductions were not just from 2-slice SMS acceleration but also the elimination of the  $b=500$  s/mm<sup>2</sup> images. The external validity of our results is supported by another report of SMS-accelerated diffusion equivalence, albeit with less time savings, using a different sequence (2-mm isotropic resolution,  $b=0$  and 1000 s/mm<sup>2</sup> with 10 directions, a final time of 128 seconds, which was 41% faster than the previous protocol).<sup>26</sup> Hence changes in time savings, perceived image quality, artifacts, and diagnostic utility will vary depending on the local accepted protocol and how it is modified. Another limitation was that tractography results were reviewed retrospectively so that the position of the SMS-derived tracts could not be correlated with operative findings (the standard diffusion data were instead used as an index standard). Intraoperative verification of tractography with or without SMS acceleration in patients requiring surgery is not trivial to obtain, but it could be the subject of a future study. There are additional methods for accelerating diffusion acquisitions that are being translated into clinical practice, including compressed sensing<sup>27</sup> and image denoising with<sup>28</sup> or without deep learning.<sup>29</sup> These techniques are not readily available for clinical implementation, but direct comparison of these diffusion-acceleration techniques and/or their combination also could be the subject of future study.

The characterization of nervous tissue microstructure with advanced diffusion models in clinical patients has been hampered by the time-intensive high-angular and  $q$ -space acquisition requirements that SMS acceleration helps overcome.<sup>30</sup> For instance, as part of an ongoing National Institutes of Health-funded study, we have used SMS to acquire high-spatial and -angular resolution, multi- $b$ -shell diffusion data from 137 patients with multiple sclerosis.<sup>31</sup> We also have used SMS-accelerated acquisitions to generate probabilistic tractography-derived contrast of internal brainstem anatomy.<sup>32</sup> SMS diffusion can complement other means of accelerating clinical neuroradiology MR imaging protocols like compressed sensing,<sup>33</sup> synthetic MR imaging,<sup>34</sup> or MR fingerprinting<sup>35</sup> that have, thus far, been more limited at producing clinically acceptable accelerations or substitutions for conventional diffusion-weighted sequences.<sup>36</sup>

## CONCLUSIONS

Using standard 3T MR imaging hardware and coils, 2-slice SMS acceleration can reduce routine diffusion MR imaging and diffusion tractography acquisition times in clinical patients without compromising image quality, clinical interpretation, or surgical planning. SMS acceleration also should increase the feasibility of translating high spatial and angular resolution diffusion acquisitions to clinical patients.

## ACKNOWLEDGMENTS

The authors thank Matt Young and Benjamin Cohen for performing initial clinical evaluations of the SMS diffusion sequence.

Disclosures: Donato Pacione—UNRELATED: Consultancy: 2nd.MD consulting, Yvonne W. Lui—UNRELATED: Grants/Grants Pending: National Institutes of Health, Lowenstein Foundation, Department of Defense, National Science Foundation.\* Els Fieremans—UNRELATED: Board Membership: MICroStructure Imaging, Comments: no money paid; Grants/Grants Pending: National Institutes of Health, Comments: R01 NS039135, P41 EB017183\*; Royalties: GE Healthcare, Comments: patent licensing; Stock/Stock Options: MICroStructure Imaging, Comments: no money paid. Timothy M. Shepherd—RELATED: Grant: National Institutes of Health, Comments: 1) National Institute of Aging (National Institutes of Health 1K23 AG048622-01), and 2) National Institutes of Health—National Institute of Biomedical Imaging and Bioengineering Biomedical technology resource center (Grant P41EB017183)\*; UNRELATED: Board Membership: MICroStructure Imaging, Comments: founder and equity holder. \*Money paid to the institution.

## REFERENCES

1. Schaefer PW, Grant PE, Gonzalez RG. **Diffusion-weighted MR imaging of the brain.** *Radiology* 2000;217:331–45 CrossRef Medline
2. Barajas RF Jr, Rubenstein JL, Chang JS, et al. **Diffusion-weighted MR imaging derived apparent diffusion coefficient is predictive of clinical outcome in primary central nervous system lymphoma.** *AJNR Am J Neuroradiol* 2010;31:60–66 CrossRef Medline
3. Nemeth AJ, Henson JW, Mullins ME, et al. **Improved detection of skull metastasis with diffusion-weighted MR imaging.** *AJNR Am J Neuroradiol* 2007;28:1088–92 CrossRef Medline
4. Murata T, Shiga Y, Higano S, et al. **Conspicuity and evolution of lesions in Creutzfeldt-Jakob disease at diffusion-weighted imaging.** *AJNR Am J Neuroradiol* 2002;23:1164–72 Medline
5. Rilling JK, Glasser MF, Preuss TM, et al. **The evolution of the arcuate fasciculus revealed with comparative DTI.** *Nat Neurosci* 2008;11:426–28 CrossRef Medline
6. Wu JS, Zhou LF, Tang WJ, et al. **Clinical evaluation and follow-up outcome of diffusion tensor imaging-based functional neuronavigation: a prospective, controlled study in patients with gliomas involving pyramidal tracts.** *Neurosurgery* 2007;61:935–48; discussion 948–49 CrossRef Medline
7. Berman JI, Berger MS, Chung SW, et al. **Accuracy of diffusion tensor magnetic resonance imaging tractography assessed using intraoperative subcortical stimulation mapping and magnetic source imaging.** *J Neurosurg* 2007;107:488–94 CrossRef Medline
8. Jellison BJ, Field AS, Medow J, et al. **Diffusion tensor imaging of cerebral white matter: a pictorial review of physics, fiber tract anatomy, and tumor imaging patterns.** *AJNR Am J Neuroradiol* 2004;25:356–69 Medline
9. Novikov DS, Fieremans E, Jespersen SN, et al. **Quantifying brain microstructure with diffusion MRI: theory and parameter estimation.** *NMR Biomed* 2019;32:e3998 CrossRef Medline
10. Tuch DS. **Q-ball imaging.** *Magn Reson Med* 2004;52:1358–72 CrossRef Medline
11. Wedeen VJ, Hagmann P, Tseng WY, et al. **Mapping complex tissue architecture with diffusion spectrum magnetic resonance imaging.** *Magn Reson Med* 2005;54:1377–86 CrossRef Medline
12. Jensen J, Helpert J, Ramani A, et al. **Diffusional kurtosis imaging: the quantification of non-Gaussian water diffusion by means of magnetic resonance imaging.** *Magn Reson Med* 2005;53:1432–40 CrossRef Medline
13. Larkman DJ, Hajnal JV, Herlihy AH, et al. **Use of multicoil arrays for separation of signal from multiple slices simultaneously excited.** *J Magn Reson Imaging* 2001;13:313–17 CrossRef Medline
14. Setsompop K, Cohen-Adad J, Gagoski BA, et al. **Improving diffusion MRI using simultaneous multi-slice echo planar imaging.** *Neuroimage* 2012;63:569–80 CrossRef Medline
15. Setsompop K, Gagoski BA, Polimeni JR, et al. **Blipped-controlled aliasing in parallel imaging for simultaneous multislice echo**

- planar imaging with reduced g-factor penalty. *Magn Reson Med* 2012;67:1210–24 CrossRef Medline
16. Cauley SF, Polimeni JR, Bhat H, et al. **Interslice leakage artifact reduction technique for simultaneous multislice acquisitions.** *Magn Reson Med* 2014;72:93–102 CrossRef Medline
17. Obele CC, Glielmi C, Ream J, et al. **Simultaneous multislice accelerated free-breathing diffusion-weighted imaging of the liver at 3T.** *Abdom Imaging* 2015;40:2323–30 CrossRef Medline
18. Lau AZ, Tunnicliffe EM, Frost R, et al. **Accelerated human cardiac diffusion tensor imaging using simultaneous multislice imaging.** *Magn Reson Med* 2015;73:995–1004 CrossRef Medline
19. Filli L, Piccirelli M, Kenkel D, et al. **Simultaneous multislice echo planar imaging with blipped controlled aliasing in parallel imaging results in higher acceleration: a promising technique for accelerated diffusion tensor imaging of skeletal muscle.** *Invest Radiol* 2015;50:456–63 CrossRef Medline
20. Gudbjartsson H, Patz S. **The Rician distribution of noisy MRI data.** *Magn Reson Med* 1995;34:910–14 CrossRef Medline
21. Catani M, Howard RJ, Pajevic S, et al. **Virtual in vivo interactive dissection of white matter fasciculi in the human brain.** *Neuroimage* 2002;17:77–94 CrossRef Medline
22. Ludwig E, Klingler J. *Atlas Cerebri Humani*. Karger; 1956
23. Dice LR. **Measures of the amount of ecologic association between species.** *Ecology* 1945;26:297–302 CrossRef
24. Wansapura JP, Holland SK, Dunn RS, et al. **NMR relaxation times in the human brain at 3.0 Tesla.** *J Magn Reson Imaging* 1999;9:531–38 CrossRef Medline
25. Feinstein AR, Cicchetti DV. **High agreement but low kappa, I: the problems of two paradoxes.** *J Clin Epidemiol* 1990;43:543–49 CrossRef Medline
26. Yokota H, Sakai K, Tazoe J, et al. **Clinical feasibility of simultaneous multi-slice imaging with blipped-CAIPI for diffusion-weighted imaging and diffusion-tensor imaging of the brain.** *Acta Radiol* 2017;58:1500–10 CrossRef Medline
27. Ning L, Setsompop K, Michailovich O, et al. **A compressed-sensing approach for super-resolution reconstruction of diffusion MRI.** *Inf Process Med Imaging* 2015;24:57–68 CrossRef Medline
28. Kawamura M, Tamada D, Funayama S, et al. **Accelerated acquisition of high-resolution diffusion-weighted imaging of the brain with a multi-shot echo-planar sequence: deep-learning-based denoising.** *Magn Reson Med Sci* 2021;20:99–105 CrossRef Medline
29. Veraart J, Novikov DS, Christiaens D, et al. **Denoising of diffusion MRI using random matrix theory.** *Neuroimage* 2016;142:394–406 CrossRef Medline
30. Novikov DS, Kiselev VG, Jespersen SN. **On modeling.** *Magn Reson Med* 2018;79:3172–93 CrossRef Medline
31. Gillingham N, Ades-Aron B, Conti B, et al. **Normal appearing white matter damage assessed with diffusion MRI, but not T2 lesion load, correlates with disability and disease duration in multiple sclerosis.** In: *Proceedings of the International Society for Magnetic Resonance in Medicine Workshop on Quantitative MRI in White Matter Disorders: Useful, Usable, Used?* Vancouver, British Columbia, Canada. February 7–10, 2017:15
32. Hoch MJ, Chung S, Ben-Eliezer N, et al. **New clinically-feasible 3T MRI protocol to discriminate internal brain stem anatomy.** *AJNR Am J Neuroradiol* 2016;37:1058–65 CrossRef Medline
33. Lustig M, Donoho D, Pauly JM. **Sparse MRI: the application of compressed sensing for rapid MR imaging.** *Magn Reson Med* 2007;58:1182–95 CrossRef Medline
34. Warntjes JB, Dahlqvist O, Lundberg P. **Novel method for rapid, simultaneous T1, T2\*, and proton density quantification.** *Magn Reson Med* 2007;57:528–37 CrossRef Medline
35. Ma D, Gulani V, Seiberlich N, et al. **Magnetic resonance fingerprinting.** *Nature* 2013;495:187–92 CrossRef Medline
36. Powell HW, Parker GJ, Alexander DC, et al. **Hemispheric asymmetries in language-related pathways: a combined functional MRI and tractography study.** *Neuroimage* 2006;32:388–99 CrossRef Medline

# Linking Stage-Specific Plasma Biomarkers to Gray Matter Atrophy in Parkinson Disease

W.-C. Lin, P.-L. Lee, C.-H. Lu, C.-P. Lin, and K.-H. Chou



## ABSTRACT

**BACKGROUND AND PURPOSE:** The shortcomings of synucleinopathy-based Parkinson disease staging highlight the need for systematic clinicopathologic elucidation and biomarkers. In this study, we investigated associations of proteinopathy and inflammation markers with changes in gray matter volume that accompany Parkinson disease progression.

**MATERIALS AND METHODS:** We prospectively enrolled 42 patients with idiopathic Parkinson disease, subdivided into early-/late-stage groups and 27 healthy controls. Parkinson disease severity and participants' functional and cognitive performance were evaluated. Peripheral plasma  $\alpha$ -synuclein,  $\beta$ -amyloid<sub>42</sub>, and tau were quantified with immunomagnetic reduction assays, and nuclear DNA by polymerase chain reaction, and regional gray matter volumes were determined by MR imaging. Statistical tests identified stage-specific biomarkers and gray matter volume patterns in the early-stage Parkinson disease, late-stage Parkinson disease, and control groups. Correlations between gray matter volume atrophy, plasma biomarkers, Parkinson disease severity, and cognitive performance were analyzed.

**RESULTS:** Patients with Parkinson disease had significantly elevated  $\alpha$ -synuclein, tau, and  $\beta$ -amyloid<sub>42</sub> levels compared with controls; nuclear DNA levels were similar in early-stage Parkinson disease and controls, but higher in late-stage Parkinson disease (all  $P < .01$ ). We identified 3 stage-specific gray matter volume atrophy patterns: 1) control > early-stage Parkinson disease = late-stage Parkinson disease: right midfrontal, left lingual, and fusiform gyri, left hippocampus, and cerebellum; 2) control > early-stage Parkinson disease > late-stage Parkinson disease: precentral, postcentral, parahippocampal, left superior-temporal, right temporal, right superior-frontal, and left cingulate gyri, occipital lobe, and bilateral parts of the cerebellum; 3) control = early-stage Parkinson disease > late-stage Parkinson disease: left midfrontal, superior-frontal and temporal, amygdala, and posterior cingulate gyri, caudate nucleus, and putamen. We discovered stage-specific correlations among proteinopathy, inflammation makers, topographic gray matter volume patterns, and cognitive performance that accompanied Parkinson disease progression.

**CONCLUSIONS:** Identifying associations linking peripheral plasma biomarkers, gray matter volume, and clinical status in Parkinson disease may facilitate earlier diagnosis and improve prognostic accuracy.

**ABBREVIATIONS:**  $A\beta$  =  $\beta$ -amyloid; AD = Alzheimer disease; CASI = Cognitive Abilities Screening Instrument; FDR = false discovery rate; GMV = gray matter volume; HC = healthy control; HY = Hoehn & Yahr; IMR = immunomagnetic reduction; MMSE = Mini-Mental State Examination; nDNA = nuclear DNA; PD = Parkinson disease; PD<sub>E</sub> = early-stage PD; PD<sub>L</sub> = late-stage PD; SE-ADL = Schwab and England Activities of Daily Living scale; T-tau = total tau; UPDRS = Unified Parkinson's Disease Rating Scale

The degree of pathology from the onset of Parkinson disease (PD) to death is conventionally graded according to Braak staging, a neuroanatomic scheme based on the presence and

spread of  $\alpha$ -synuclein deposits in the brain (Lewy pathology).<sup>1</sup> However, the validity of this "pure" synucleinopathy-based staging approach is controversial due to inconsistencies such as

Received October 11, 2020; accepted after revision March 17, 2021.

From the Departments of Diagnostic Radiology (W.-C.L.) and Neurology (C.-H.L.), Kaohsiung Chang Gung Memorial Hospital and Chang Gung University College of Medicine, Kaohsiung, Taiwan; Institute of Neuroscience (P.-L.L., C.-P.L., K.-H.C.), Department of Biomedical Imaging and Radiological Sciences (C.-P.L.), and Brain Research Center (C.-P.L., K.-H.C.), National Yang Ming Chiao Tung University, Taipei, Taiwan.

Statistical analysis was conducted by Wei-Che Lin, MD, PhD, Department of Diagnostic Radiology, Kaohsiung Chang Gung Memorial Hospital, Chang Gung University College of Medicine, 123 Ta-Pei Rd, Niao-Sung, Kaohsiung 83305, Taiwan; e-mail: u64lin@yahoo.com.tw

This study received funding from the Ministry of Science and Technology, (MOST 106-2314-B-182A-031-MY2 to W.-C.L.; CORPG8L0191 to W.-C.L.; and MOST 107-2221-E-010-010-MY3, to K.-H.C.).

Please address correspondence to Kun-Hsien Chou, PhD, Brain Research Center, National Yang Ming Chiao Tung University, 155 Linong St, Section. 2, Taipei 11221, Taiwan; e-mail: dargonchow@gmail.com

Indicates open access to non-subscribers at www.ajnr.org

Indicates article with online supplemental data.

<http://dx.doi.org/10.3174/ajnr.A7171>



discrepancies between the pathologic stage and clinical symptoms.<sup>2</sup> Recent studies have suggested that several coexisting misfolding proteins play important roles in the pathogenesis of PD, including cortical and limbic Lewy bodies,<sup>3</sup> neurofibrillar tangles, senile plaques,<sup>4</sup> and microglia.<sup>5</sup> These heterogeneous etiologic pathways present challenges to formulating a unified staging model that encapsulates the entire disease course. Therefore, the systematic evaluation of sequential pathophysiologic and clinical changes in PD and of their mutual interactions is crucial.

In addition to synucleinopathy, it has been reported that cytoxic intermediates of  $\beta$ -amyloid ( $A\beta$ ) fibril formation and tau protein aggregates lead to neuronal disruption and death, while also causing symptoms commonly observed in Alzheimer disease (AD).<sup>6</sup> Postmortem studies have confirmed the coexistence of AD-related misfolding proteins from early-to-late stage PD, indicating that rapid cognitive decline predicts poor prognosis in early PD.<sup>7,8</sup> Furthermore, studies of CSF and serum biomarkers that indicate both Lewy body and AD pathology have garnered considerable interest.<sup>9-11</sup> Although CSF  $A\beta$  and tau levels in patients with PD have been reported to independently predict cognitive decline,<sup>12</sup> data are inconclusive.<sup>13</sup> The results of studies of the total  $\alpha$ -synuclein level in CSF and peripheral plasma are also controversial.<sup>10,11</sup> Explanations for such uncertainty may include, but are not limited to, methodologic variables and heterogeneous disease stages across participants in different studies. Moreover, levels of  $\alpha$ -synuclein are exceptionally low in plasma compared with CSF, thereby limiting the capability of enzyme-linked immunosorbent assays to accurately detect plasma  $\alpha$ -synuclein.<sup>14</sup> More recently, immunomagnetic reduction (IMR), which has higher sensitivity than the conventional enzyme-linked immunosorbent assay,<sup>11</sup> has been applied to assay  $A\beta$ s, tau, and  $\alpha$ -synuclein in human plasma<sup>11,15,16</sup> and to confirm PD and AD diagnoses.<sup>11,17,18</sup> These results suggest that IMR may help to clarify the relationship between different misfolding proteins and the progression of PD.

Apart from proteinopathy, inflammation in the CNS and peripheral blood could also contribute to neurodegeneration in PD.<sup>19</sup> Cross-talk between the brain and peripheral inflammatory markers has been implicated in numerous psychologic, behavioral, and physiologic processes.<sup>20</sup> However, research into the association between systemic inflammation and disease progression and their interactions with proteinopathy contributing to regional gray matter volume (GMV) changes is limited and warrants further investigation.

In the present study, we systematically investigated the complex associations among multiple plasma proteinopathies,  $A\beta_{42}$ , total tau (T-tau), and  $\alpha$ -synuclein; nuclear DNA (nDNA), as a marker of inflammation; and regional GMV changes during PD progression. We aimed to identify stage-specific patterns of plasma biomarkers and regional GMVs and stage-specific associations linking GMV patterns, biomarker levels, and clinical status.

## MATERIALS AND METHODS

### Participants

From August 1, 2017, to July 31, 2018, we prospectively enrolled 42 patients with a definitive diagnosis of idiopathic PD (Online Supplemental Data).<sup>21</sup> Disease severity and functional status were

evaluated in the "Off" state using the Unified Parkinson's Disease Rating Scale (UPDRS),<sup>22</sup> the modified Hoehn & Yahr staging scale (HY stage),<sup>23</sup> and the Schwab and England Activities of Daily Living scale (ADL).<sup>24</sup> The Mini-Mental State Examination (MMSE)<sup>25</sup> and Cognitive Abilities Screening Instrument (CASI)<sup>26</sup> were used to assess general cognitive function. In addition, 27 sex- and age-matched healthy controls (HCs) without a medical history of neurologic or psychiatric disorders, alcohol/substance abuse, or head injury with similar education levels were enrolled.

The hospital Ethics Committee on Human Research approved the study protocol (No. 201601519B0) by Chang Gung Medical Foundation Institutional Review Board. All participants or their legally designated proxies provided written informed consent. To investigate the effects of disease stage on plasma biomarker levels and topographic GMV patterns, we further subdivided patients into 2 groups: early-stage PD (PD<sub>E</sub>, HY stage  $\leq 2$ ) or late-stage PD (PD<sub>L</sub>, HY stage  $> 2$ ).

### Blood Sampling and Plasma Biomarker Assays

Plasma  $A\beta_{42}$ , T-tau,  $\alpha$ -Synuclein, and nDNA. At the time of diagnosis of idiopathic PD, potential participants were informed of the study, and those who consented were asked to provide a 10-mL venous blood sample. The levels of multiple proteinopathies and nDNA were quantified using IMR and real-time polymerase chain reaction techniques, respectively. The processing procedures of plasma biomarker assays have been described in our previous studies<sup>11,18,27-29</sup> and documented in the Online Supplemental Data.

### Structural MR Image Acquisition and Analyses

All participants underwent MR imaging within 1 week of peripheral plasma evaluation using a single 3T Signa (GE Healthcare) whole-body MR imaging system with an 8-channel phased array head coil. Whole-brain T1-weighted images were acquired using an axial 3D inversion recovery-prepared fast-spoiled gradient recalled-echo pulse sequence (TR/TE/TI = 9.5/3.9/450 ms; flip angle = 15°; number of excitations = 1; FOV = 24 cm; matrix size = 512 × 512; voxel size = 0.47 × 0.47 × 1.3 mm<sup>3</sup>; 110 contiguous slices without interslice gap and interpolation). To calculate individual regional GMVs, we first preprocessed MR images using the voxel-based morphometry approach and then calculated them with the composite anatomic atlas. The detailed image-preprocessing pipeline is documented in the Online Supplemental Data. Finally, the regional residualized GMVs, which regressed out the nuisance effects of age, sex, and total intracranial volume, were obtained.

### Statistics

All statistical analyses were conducted using SPSS, Version 22.0 (IBM) and Matlab, Version R2010a (MathWorks). Figure 1 shows the analytic workflow, while details of the corresponding image and statistical analyses are as follows: 1) The ANOVA test,  $\chi^2$  test, and ANCOVA were used to compare demographic variables and clinical evaluations between the HCs and the PD<sub>E</sub>/PD<sub>L</sub> groups. Statistical significance was defined as a 2-tailed *P* value  $< .05$ . All the continuous and categorical variables are presented as means and numbers, respectively. 2) For peripheral plasma biomarkers, we used the general linear model to adjust for the

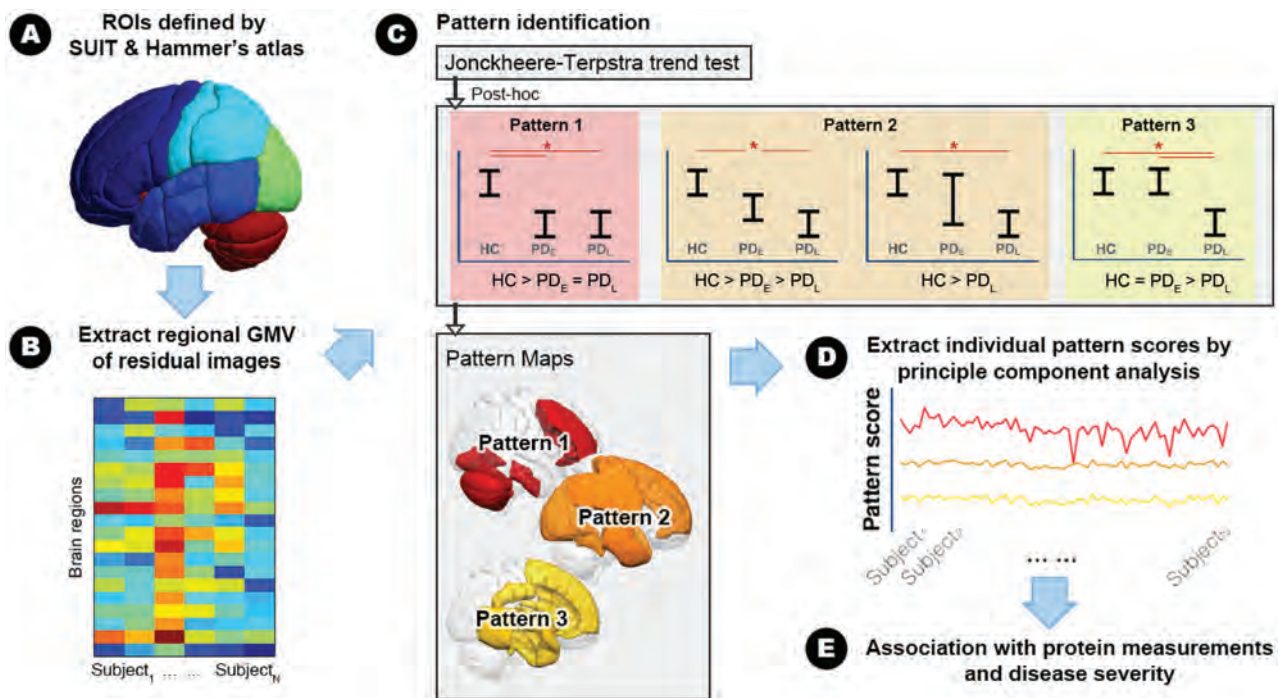


**FIG 1.** Analytic workflow. *A*, Whole-brain composite atlas generated from the SUIT and Hammer's Maximum Probability Atlas. *B*, Regional gray matter volume extracted with the composite atlas. *C*, The Jonckheere-Terpstra test and pair-wise Mann-Whitney *U* test are used to identify stage-specific patterns. *D*, Principal component analysis is used to extract weighting scores of the stage-specific GMV pattern. *E*, Spearman rank-order correlation tests are used to examine the potential associations among weighting scores of the stage-specific GMV pattern, peripheral plasma biomarkers, general cognitive performance, and disease severity. SUIT indicates Spatially Unbiased Infratentorial Template.

confounding effects of age and sex. The resulting residual value of each peripheral plasma biomarker was used for further analysis. We hypothesized that changes in peripheral plasma biomarkers and regional GMVs are associated with disease severity that would be most pronounced in patients with PD<sub>L</sub> and intermediate in those with PD<sub>E</sub> compared with HCs. We, thus, used the nonparametric Jonckheere-Terpstra test to determine the ordered differences among the 3 study groups. The significance threshold for the nonparametric Jonckheere-Terpstra test was set at the false discovery rate (FDR)-corrected *P* value  $< .05$ .<sup>30, 31</sup> Having established possible ordered differences in peripheral plasma biomarkers and regional GMVs, we then used pair-wise Mann-Whitney *U* tests to subdivide changing patterns of plasma biomarkers and regional GMVs into 3 categories each: plasma biomarkers, pattern 1 (control  $<$  PD<sub>E</sub> = PD<sub>L</sub>); pattern 2 (control  $<$  PD<sub>E</sub>  $<$  PD<sub>L</sub> and control  $<$  PD<sub>L</sub>); pattern 3 (control = PD<sub>E</sub>  $<$  PD<sub>L</sub>); and GMV, pattern 1 (control  $>$  PD<sub>E</sub> = PD<sub>L</sub>); pattern 2 (control  $>$  PD<sub>E</sub>  $>$  PD<sub>L</sub> and control  $>$  PD<sub>L</sub>); pattern 3 (control = PD<sub>E</sub>  $>$  PD<sub>L</sub>). This analysis revealed a high degree of collinearity between the GMV of different anatomic regions within the same stage-specific pattern; therefore, we used principal component analysis to identify the component accounting for the largest variances of GMVs in each of the 3 stage-specific patterns and calculated its weighting score for each participant. 4) Finally, we used nonparametric Spearman rank-order correlation tests to investigate associations among weighting scores of stage-specific GMV changes, peripheral plasma biomarkers, general cognitive ability, and disease severity.<sup>31</sup> The significance threshold for the

nonparametric Spearman rank-order correlation tests was set at the FDR-corrected *P* value  $< .05$ .

## RESULTS

### Demographic and Clinical Characteristics

The study cohorts included 42 patients with PD (26 PD<sub>E</sub> and 16 PD<sub>L</sub>) and 27 HCs. The demographic and clinical data for each group are shown in the Online Supplemental Data. Each group had a similar average age and male/female ratio. The HCs had significantly better MMSE and CASI than patients with PD<sub>E</sub> and PD<sub>L</sub> (mean [SD], MMSE: 28.0 [1.5] versus 25.3 [3.7] versus 23.6 [5.1], respectively,  $P < .001$ ; CASI: 92.1 [3.9] versus 81.6 [14.3] versus 78.7 [14.2],  $P < .001$ ). The patients with PD had lower total GMV and higher CSF volume compared with HCs while the patients with PD<sub>L</sub> had lower total GMV compared with the those with PD<sub>E</sub>.

### Stage-Specific Plasma Biomarker Patterns

The Jonckheere-Terpstra test results retained all plasma biomarkers for post hoc tests that confirmed significantly higher  $\alpha$ -synuclein, T-tau, and A $\beta$ <sub>42</sub> levels in patients with PD compared with the HCs (Fig 2A–C, Online Supplemental Data), but no difference between PD<sub>E</sub> and PD<sub>L</sub>, corresponding to pattern 1 (Control  $<$  PD<sub>E</sub> = PD<sub>L</sub>). In contrast, plasma nDNA levels were significantly higher in PD<sub>L</sub> than in PD<sub>E</sub> or controls, but similar between controls and PD<sub>E</sub>, corresponding to pattern 3 (control = PD<sub>E</sub>  $<$  PD<sub>L</sub>) (Fig 2D, Online Supplemental Data).

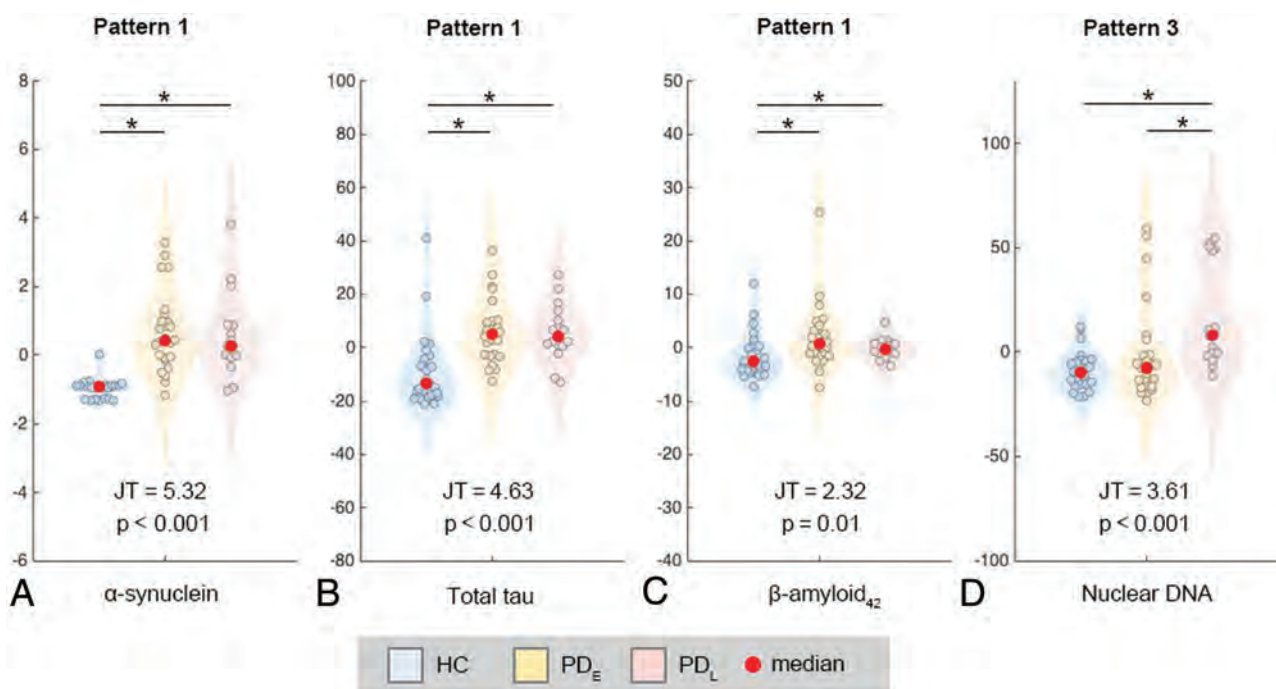


**FIG 2.** Stage-specific patterns of plasma biomarkers. Violin plots demonstrate residual values of each biomarker adjusted for age and sex in healthy controls (blue), patients with PD<sub>E</sub> (yellow), and PD<sub>L</sub> (pink). Red circles of in the violin plots show the median value of each plasma biomarker of each study group. Asterisks indicate statistically significant differences among study groups using pair-wise Mann-Whitney U tests (FDR-corrected,  $P < .05$ ). JT indicates Jonckheere-Terpstra test.

### Stage-Specific Pattern of Gray Matter Volume

Most regions in GMV analyses passed the Jonckheere-Terpstra test ( $P_{FDR} < .05$ ); however, those eliminated included part of the frontal, parietal, and occipital lobes; the thalamus; and the insula. Post hoc tests further subdivided regional GMV patterns into 3 categories (Fig 3). Pattern 1 showed significantly lower GMVs in the PD<sub>E</sub> and PD<sub>L</sub> groups compared with controls, but no difference between the PD<sub>E</sub> and PD<sub>L</sub> groups in the right middle-frontal, left-lingual, and bilateral fusiform gyri; left hippocampus; and cerebellum. Pattern 2 featured progressive GMV atrophy with PD progression in the gyri including the bilateral precentral, postcentral, parahippocampal, left superior-temporal, right temporal, right superior-frontal, and left cingulate gyri in the occipital lobe and a small part of the bilateral cerebellum. In pattern 3, GMV was significantly lower in the PD<sub>L</sub> group compared with controls and the PD<sub>E</sub> group, but similar between controls and the PD<sub>E</sub> group, in the left middle-frontal, superior-frontal, temporal, and posterior cingulate gyri and in the bilateral amygdala, caudate nucleus, and putamen.

### Associations of Stage-Specific Patterns between Plasma Biomarkers and Weighting Scores of GMVs

Plasma T-tau exhibited a moderately negative correlation with GMV atrophy in all 3 patterns ( $\rho = -0.331$ ,  $P_{FDR} = .006$ ;  $\rho = -0.334$ ,  $P_{FDR} = .005$ ;  $\rho = -0.410$ ,  $P_{FDR} = .001$ ) (Fig 4), whereas plasma  $\alpha$ -synuclein showed a moderately negative correlation with only pattern 1 GMV atrophy ( $\rho = -0.390$ ,  $P_{FDR} = .001$ ). Meanwhile, plasma nDNA showed a moderately negative correlation with only pattern 3 GMV atrophy ( $\rho = -0.333$ ,  $P_{FDR} = .005$ ).

### Associations of Disease Severity, Cognitive Performance, Plasma Biomarkers, and Weighting Scores of GMVs

UPDRS II and total score were positively correlated with plasma nDNA levels ( $\rho = 0.515$ ,  $P_{FDR} < .001$ ;  $\rho = 0.449$ ,  $P_{FDR} = .003$ ) (Fig 4). The MMSE performance was negatively correlated with T-tau,  $\alpha$ -synuclein, and nDNA levels ( $\rho = -0.263$ ,  $P_{FDR} = .029$ ;  $\rho = -0.341$ ,  $P_{FDR} = .004$ ;  $\rho = -0.241$ ,  $P_{FDR} = .046$ ), while the CASI score was negatively correlated with  $\alpha$ -synuclein and nDNA levels ( $\rho = -0.328$ ,  $P_{FDR} = .006$ ;  $\rho = -0.285$ ,  $P_{FDR} = .018$ ). However, misfolding protein levels exhibited no correlations with disease severity. The GMV atrophy pattern 2 correlated with the UPDRS II, HY stage, and ADL ( $\rho = -0.378$ ,  $P_{FDR} = .013$ ;  $\rho = -0.379$ ,  $P_{FDR} = .013$ ;  $\rho = 0.412$ ,  $P_{FDR} = .007$ ). Pattern 3 correlated with UPDRS II and III, and total score, HY-stage, and ADL score ( $\rho = -0.412$ ,  $P_{FDR} = .007$ ;  $\rho = -0.374$ ,  $P_{FDR} = .015$ ;  $\rho = -0.409$ ,  $P_{FDR} = .007$ ;  $\rho = -0.451$ ,  $P_{FDR} = .004$ ;  $\rho = 0.426$ ,  $P_{FDR} = .005$ ) (Fig 4). Patterns 1, 2, and 3 also correlated with the MMSE ( $\rho = 0.396$ ,  $P_{FDR} = .001$ ;  $\rho = 0.403$ ,  $P_{FDR} = .001$ ;  $\rho = 0.396$ ,  $P_{FDR} = .001$ ). Patterns 1 and 3 correlated with the CASI ( $\rho = 0.274$ ,  $P_{FDR} = .023$ ;  $\rho = 0.249$ ,  $P_{FDR} = .039$ ).

### DISCUSSION

The results of this study reveal that changes in proteinopathy and inflammation biomarkers are associated with GMV atrophy during PD progression. This finding indicates that elucidation of the associations among plasma biomarkers, GMV changes, and clinical status in PD may facilitate earlier diagnosis and improve prognostic accuracy.

Both the PD<sub>E</sub> and PD<sub>L</sub> groups had higher plasma levels of  $\alpha$ -synuclein, T-tau, and A $\beta$ <sub>42</sub> compared with the HCs, while



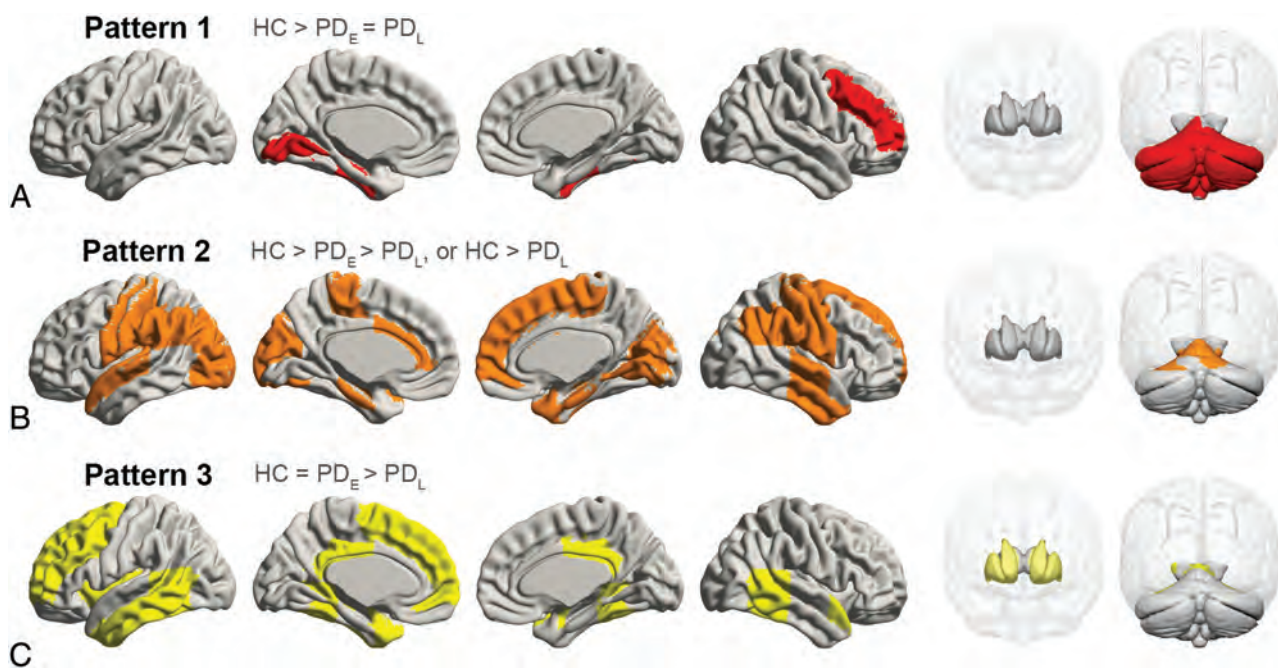


**FIG 3.** Spatial regions of stage-specific gray matter volume patterns. A, Pattern 1, red. B, Pattern 2, orange. C, Pattern 3, yellow.

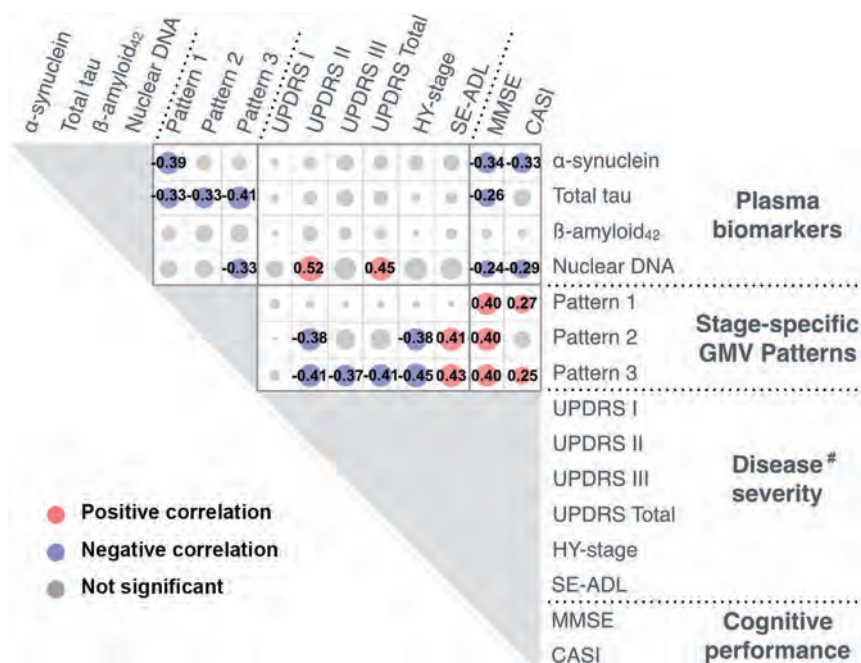


**FIG 4.** Associations among plasma biomarkers, weighting scores of stage-specific GMV patterns, disease severity, and cognitive performance. The hash tag indicates Spearman rank-order correlation analyses between disease severity and peripheral plasma biomarkers/weighting-score of stage-specific GMV patterns were conducted in patients with PD (PD<sub>E</sub> and PD<sub>L</sub>). SE-ADL indicates Schwab and England Activities of Daily Living scale.

nDNA levels were higher in the PD<sub>L</sub> than in PD<sub>E</sub> or HCs. Of note, levels of  $\alpha$ -synuclein, T-tau, and A $\beta$ <sub>42</sub> were not associated with disease severity, and only UPDRS II and total score correlated with nDNA levels. GMV atrophy is pervasive as PD severity increases and can be temporally classified into 3 distinct patterns.

These results are consistent with the hypothesis that  $\alpha$ -synuclein, which is associated with GMV atrophy in the frontal lobe, hippocampus, and cerebellum, plays a potential pathogenic role in early PD, while nDNA may signify GMV atrophy in the late stage of PD. Most important, the plasma T-tau level is a cardinal marker of characteristic brain degeneration patterns in different stages of PD.

The elevated  $\alpha$ -synuclein and T-tau levels noted in patients with PD herein are consistent with those in previous reports.<sup>2-5</sup>  $\alpha$ -synuclein is pathognomonic in the etiology of PD and is found in both CSF and plasma after exocytosis from neurons. Our findings support the growing evidence that elevated plasma  $\alpha$ -synuclein offers potential as a biomarker to identify patients with PD.<sup>18</sup> In a mouse model study, radiolabeled  $\alpha$ -synuclein from an intracerebroventricular injection was diverted to the blood via exosome efflux.<sup>10</sup> Higher plasma levels of  $\alpha$ -synuclein in PD may be partially attributable to increased exosomal elimination

of toxic  $\alpha$ -synuclein buildup from the brain to peripheral blood. Previous studies have demonstrated an inverse relationship between  $\alpha$ -synuclein levels in CSF versus plasma.<sup>32</sup> This observation may reflect the deteriorating ability of the central nervous system to clear  $\alpha$ -synuclein and increased sequestration of pathologic

soluble  $\alpha$ -synuclein in the brain, with consequently lower levels in CSF. However, further research is needed to clarify precisely how  $\alpha$ -synuclein is transported from the central nervous system to peripheral blood.

Numerous A $\beta$  plaques and tau-containing neurofibrillary tangles develop in up to 50% of patients with PD<sub>L</sub>, which may act synergistically with  $\alpha$ -synuclein pathology to worsen prognosis. However, current data on CSF tau levels in PD are inconclusive.<sup>32</sup> Our study results are consistent with a recent report of a high plasma T-tau level in parkinsonism, indicating a potential role for plasma tau IMR in screening for neurodegenerative diseases.<sup>27</sup> Plasma A $\beta$ <sub>42</sub>, which was also elevated in our PD cohorts, has been extensively studied in CSF.<sup>32</sup> There is evidence that lower baseline CSF A $\beta$ <sub>42</sub> may predict subsequent cognitive decline and dementia in patients with PD.<sup>12,33</sup> Although misfolded  $\alpha$ -synuclein aggregation is considered a critical mechanism, the pathophysiology of PD is multifactorial. The comorbid associations of A $\beta$ <sub>42</sub> and tau deposition may be associated with cognitive deficits in PD.<sup>34</sup> In terms of pathogenesis, amyloid- $\beta$  (A $\beta$ <sub>40</sub> and A $\beta$ <sub>42</sub>) is secreted by many types of cells and is normally found in the CSF; notably, studies have shown that A $\beta$ <sub>42</sub> can induce neuronal death.<sup>35,36</sup> Thus, the elevated A $\beta$ <sub>42</sub> in this study indicates that potentially neurotoxic A $\beta$ <sub>42</sub> indeed increased in patients with PD.<sup>34-36</sup>

The  $\alpha$ -synuclein, T-tau, and A $\beta$ <sub>42</sub> levels in our study neither differentiated between PD<sub>E</sub> and PD<sub>L</sub> nor correlated with disease severity; however,  $\alpha$ -synuclein and T-tau have been correlated with cognitive function, possibly implicating AD neuropathology in the cognitive deterioration of patients with PD. Thus, further IMR assay investigation of plasma misfolding-associated proteins may identify potential biomarkers for diagnosing PD and evaluating related cognitive deficits.<sup>11</sup>

Although progressive GMV atrophy has been well-documented in patients with PD, the topographic disposition during the disease course was hitherto unclear. Our systematic investigation revealed alterations in the right frontal lateral lobe, hippocampus, and bilateral cerebellum, in both PD<sub>E</sub> and PD<sub>L</sub> in pattern 1, with no significant differences between groups. The frontostriatal and limbic circuits, which are involved in dopaminergic activity, are commonly affected in early-stage PD but are not associated with a higher risk of subsequent dementia.<sup>37</sup> A recent study also demonstrated widespread early changes in the structure and function of motor and cognitive cerebellar regions in patients with PD,<sup>38</sup> though Braak staging does not specifically address such cerebellar features. These neuroanatomic changes are also correlated with plasma  $\alpha$ -synuclein and T-tau levels, corroborating the role of synucleinopathy in PD and further indicating the possibility of tau co-pathology. Regardless of the cause of neuronal death, the areas in pattern 1 affected from PD<sub>E</sub> to PD<sub>L</sub> implicate the involvement of dopamine neuron substrates during the development of parkinsonian symptoms. Our results indicate that plasma  $\alpha$ -synuclein may play a major pathophysiologic role in early GMV atrophy, particularly in the frontal lobe, hippocampus, and cerebellum. Therefore,  $\alpha$ -synuclein-associated anatomies could act as markers of PD status.

The spatiotemporal progressive atrophic pattern 2 largely involves the posterior neocortices. Different neurotransmitters

could also malfunction secondary to dopaminergic neuron loss or dopaminergic treatment, which may account for subsequent nonmotor impairment.<sup>39</sup> Of note, this atrophy pattern was associated with plasma T-tau but not A $\beta$ <sub>42</sub>. A study of AD has reported a weak association of A $\beta$  with neurodegeneration, despite a strong link between A $\beta$  and tau; however, tau was associated with brain atrophy.<sup>40</sup> Correlations with higher plasma tau in all 3 patterns that we identified suggest that this biomarker is associated with characteristic topographic degeneration throughout the course of PD. Furthermore, PET studies in patients with dementia with Lewy bodies and PD<sup>41</sup> have revealed abnormal tau binding distributions similar to those noted in our pattern 2 GMV atrophy. This finding suggests that the neuropathologic processes that drive tau deposition in PD reflect the same regional vulnerabilities as those driving tau deposition in AD. Thus, pattern 2 atrophy and the associated cognitive symptoms may be effective PD staging biomarkers.

In this study, the pattern 3 areas are mainly located in areas least involved in PD progression until the late stage. Their topographic distribution was consistent with those neocortices less affected in Braak stages V–VI, for both  $\alpha$ -synuclein and tau pathology.<sup>1</sup> We further demonstrated associations between plasma tau and nDNA levels. Oxidative stress and elevated neuroinflammation are considered important etiologies in PD<sup>19</sup> and can be revealed by a marker of cell death, such as plasma DNA levels. The breakdown of the blood-brain barrier may release DNA into the plasma, which has been shown to correlate with structural changes in early-onset PD.<sup>42</sup> Although prion transfection is the prevailing hypothesis in PD pathogenesis, there is growing evidence suggesting that misfolded protein accumulation is necessary but not sufficient to cause neurodegeneration, because the neurodegeneration occurs only in the environment of a specific innate immune response.<sup>43</sup> Our plasma nDNA and tau findings are indicative of neurodegeneration in PD<sub>L</sub>.

Notwithstanding the strengths of this study, our findings should be interpreted in light of some limitations. Our study groups were selected to be as homogeneous as possible, and the relatively small age- and sex-matched PD cohorts may not fully represent the disease spectrum of PD. Given the exploratory design of this study, analyses were based on a simple grouping scheme according to the HY stage, which, though acceptable for general evaluation of disease status, may preclude investigation of subgroup patterns corresponding to different clinical phenotypes with similar disease severity. Elucidating potential relationships between stage-specific atrophic patterns and plasma biomarkers was also hindered by the cross-sectional design. Longitudinal studies may provide further insight into the vulnerability of distinct brain regions as well as their atrophy trajectories during the course of PD.

## CONCLUSIONS

As with most neurodegenerative diseases, the clinicopathology of PD involves complex and dynamic interactions between several underlying etiologic mechanisms. This study revealed that multiple markers of proteinopathy and inflammation are associated with regional GMV atrophy. We herein identified plasma biomarkers that characterize stage-specific GMV atrophy patterns

and clinical features in PD. Such biomarkers, possibly identified from different modalities and following validation in large, longitudinal cohorts may facilitate early diagnosis and improved accuracy of prognostic evaluation.

## ACKNOWLEDGMENTS

This research was financially supported by the Brain Research Center, National Yang Ming Chiao Tung University from The Featured Areas Research Center Program within the framework of the Higher Education Sprout Project by the Ministry of Education (MOE) in Taiwan.

Dr David Neil, PhD, of Full Universe Integrated Marketing provided professional editorial services, and his colleague Pei Chi Kuo assisted with project management for manuscript preparation.

## REFERENCES

- Braak H, Del Tredici K, Rüb U, et al. **Staging of brain pathology related to sporadic Parkinson's disease.** *Neurobiol Aging* 2003;24:197–211 CrossRef Medline
- Burke RE, Dauer WT, Vonsattel JP. **A critical evaluation of the Braak staging scheme for Parkinson's disease.** *Ann Neurol* 2008;64:485–91 CrossRef Medline
- Braak H, Rub U, Jansen SE, et al. **Cognitive status correlates with neuropathologic stage in Parkinson disease.** *Neurology* 2005;64:1404–10 CrossRef Medline
- Irwin DJ, White MT, Toledo JB, et al. **Neuropathologic substrates of Parkinson disease dementia.** *Ann Neurol* 2012;72:587–98 CrossRef Medline
- Gerhard A, Pavese N, Hotton G, et al. **In vivo imaging of microglial activation with [11C](R)-PK11195 PET in idiopathic Parkinson's disease.** *Neurobiol Dis* 2006;21:404–12 CrossRef Medline
- Paola D, Domenicotti C, Nitti M, et al. **Oxidative stress induces increase in intracellular amyloid beta-protein production and selective activation of betaI and betaII PKCs in NT2 cells.** *Biochem Biophys Res Commun* 2000;268:642–46 CrossRef Medline
- Petrout M, Dwamena BA, Foerster BR, et al. **Amyloid deposition in Parkinson's disease and cognitive impairment: a systematic review.** *Mov Disord* 2015;30:928–35 CrossRef Medline
- Kotzbauer PT, Cairns NJ, Campbell MC, et al. **Pathologic accumulation of alpha-synuclein and Abeta in Parkinson disease patients with dementia.** *Arch Neurol* 2012;69:1326–31 CrossRef Medline
- Mollenhauer B, Locascio JJ, Schulz-Schaeffer W, et al.  **$\alpha$ -Synuclein and tau concentrations in cerebrospinal fluid of patients presenting with parkinsonism: a cohort study.** *Lancet Neurol* 2011;10:230–40 CrossRef Medline
- Shi M, Liu C, Cook TJ, et al. **Plasma exosomal alpha-synuclein is likely CNS-derived and increased in Parkinson's disease.** *Acta Neuropathol* 2014;128:639–50 CrossRef Medline
- Yang SY, Chiu MJ, Lin CH, et al. **Development of an ultra-high sensitive immunoassay with plasma biomarker for differentiating Parkinson disease dementia from Parkinson disease using antibody functionalized magnetic nanoparticles.** *J Nanobiotechnology* 2016;14:41 CrossRef Medline
- Siderowf A, Xie SX, Hurtig H, et al. **CSF amyloid {beta} 1-42 predicts cognitive decline in Parkinson disease.** *Neurology* 2010;75:1055–61 CrossRef Medline
- Kang JH, Irwin DJ, Chen-Plotkin AS, et al. **Parkinson's Progression Markers Initiative. Association of cerebrospinal fluid beta-amyloid 1-42, T-tau, P-tau181, and alpha-synuclein levels with clinical features of drug-naïve patients with early Parkinson disease.** *JAMA Neurol* 2013;70:1277–87 CrossRef Medline
- Atik A, Stewart T, Zhang J.  **$\alpha$ -synuclein as a biomarker for Parkinson's disease.** *Brain Pathol* 2016;26:410–18 CrossRef Medline
- Yang CC, Yang SY, Chieh JJ, et al. **Biofunctionalized magnetic nanoparticles for specifically detecting biomarkers of Alzheimer's disease in vitro.** *ACS Chem Neurosci* 2011;2:500–505 CrossRef Medline
- Chiu MJ, Chen YF, Chen TF, et al. **Plasma tau as a window to the brain-negative associations with brain volume and memory function in mild cognitive impairment and early Alzheimer's disease.** *Hum Brain Mapp* 2014;35:3132–42 CrossRef Medline
- Chiu MJ, Yang SY, Horng HE, et al. **Combined plasma biomarkers for diagnosing mild cognition impairment and Alzheimer's disease.** *ACS Chem Neurosci* 2013;4:1530–36 CrossRef Medline
- Lin CH, Yang SY, Horng HE, et al. **Plasma  $\alpha$ -synuclein predicts cognitive decline in Parkinson's disease.** *J Neurol Neurosurg Psychiatry* 2017;88:818–24 CrossRef Medline
- Makin S. **Pathology: the prion principle.** *Nature* 2016;538:S13–16 CrossRef Medline
- Pavlov VA, Tracey KJ. **Neural circuitry and immunity.** *Immunol Res* 2015;63:38–57 CrossRef Medline
- Hughes AJ, Daniel SE, Kilford L, et al. **Accuracy of clinical diagnosis of idiopathic Parkinson's disease: a clinico-pathological study of 100 cases.** *J Neurol Neurosurg Psychiatry* 1992;55:181–84 CrossRef Medline
- Gasser T, Bressman S, Durr A, et al. **State of the art review: molecular diagnosis of inherited movement disorders: Movement Disorders Society Task Force on molecular diagnosis.** *Mov Disord* 2003;18:3–18 CrossRef Medline
- Goetz CG, Poewe W, Rascol O, et al. **Movement Disorder Society Task Force report on the Hoehn and Yahr staging scale: status and recommendations of the Movement Disorder Society Task Force on rating scales for Parkinson's disease.** *Mov Disord* 2004;19:1020–28 CrossRef Medline
- Bjornestad A, Tysnes OB, Larsen JP, et al. **Reliability of three disability scales for detection of independence loss in Parkinson's disease.** *Parkinsons Dis* 2016;2016:1941034 CrossRef Medline
- Folstein MF, Folstein SE, McHugh PR. **"Mini-mental state". A practical method for grading the cognitive state of patients for the clinician.** *J Psychiatr Res* 1975;12:189–98 CrossRef Medline
- Chang CC, Liu JS, Chang YY, et al. **(99m)Tc-ethyl cysteinate dimer brain SPECT findings in early stage of dementia with Lewy bodies and Parkinson's disease patients: a correlation with neuropsychological tests.** *Eur J Neurol* 2008;15:61–66 CrossRef Medline
- Yang SY, Chiu MJ, Chen TF, et al. **Analytical performance of reagent for assaying tau protein in human plasma and feasibility study screening neurodegenerative diseases.** *Sci Rep* 2017;7:9304 CrossRef Medline
- Lin CH, Yang SY, Horng HE, et al. **Plasma biomarkers differentiate parkinson's disease from atypical parkinsonism syndromes.** *Front Aging Neurosci* 2018;10:123 CrossRef Medline
- Wang HC, Yang TM, Lin WC, et al. **The value of serial plasma and cerebrospinal fluid nuclear and mitochondrial deoxyribonucleic acid levels in aneurysmal subarachnoid hemorrhage.** *J Neurosurg* 2013;118:13–19 CrossRef Medline
- Zhang Y, Cabilio P. **A generalized Jonckheere test against ordered alternatives for repeated measures in randomized blocks.** *Stat Med* 2013;32:1635–45 CrossRef Medline
- Pernet CR, Wilcox R, Rousselet GA. **Robust correlation analyses: false positive and power validation using a new open source Matlab toolbox.** *Front Psychol* 2012;3:606 CrossRef Medline
- Magdalinou N, Lees AJ, Zetterberg H. **Cerebrospinal fluid biomarkers in parkinsonian conditions: an update and future directions.** *J Neurol Neurosurg Psychiatry* 2014;85:1065–75 CrossRef Medline
- Compta Y, Pereira JB, Rios J, et al. **Combined dementia-risk biomarkers in Parkinson's disease: a prospective longitudinal study.** *Parkinsonism Rel Disord* 2013;19:717–24 CrossRef Medline
- Jellinger KA, Seppi K, Wenning GK, et al. **Impact of coexistent Alzheimer pathology on the natural history of Parkinson's disease.** *J Neural Transm (Vienna)* 2002;109:329–39 CrossRef Medline



35. Zou K, Gong JS, Yanagisawa K, et al. **A novel function of monomeric amyloid beta-protein serving as an antioxidant molecule against metal-induced oxidative damage.** *J Neurosci* 2002;22:4833–41 Medline
36. Zou K, Kim D, Kakio A, et al. **Amyloid beta-protein (Abeta)1-40 protects neurons from damage induced by Abeta1-42 in culture and in rat brain.** *J Neurochem* 2003;87:609–19 CrossRef Medline
37. Uribe C, Segura B, Baggio HC, et al. **Cortical atrophy patterns in early Parkinson's disease patients using hierarchical cluster analysis.** *Parkinsonism Relat Disord* 2018;50:3–9 CrossRef Medline
38. O'Callaghan C, Hornberger M, Balsters JH, et al. **Cerebellar atrophy in Parkinson's disease and its implication for network connectivity.** *Brain* 2016;139:845–55 CrossRef Medline
39. Roy R, Niccolini F, Pagano G, et al. **Cholinergic imaging in dementia spectrum disorders.** *Eur J Nucl Med Mol Imaging* 2016;43:1376–86 CrossRef Medline
40. Jagust W. **Imaging the evolution and pathophysiology of Alzheimer disease.** *Nat Rev Neurosci* 2018;19:687–700 CrossRef Medline
41. Gomperts SN, Locascio JJ, Makaretz SJ, et al. **Tau positron emission tomographic imaging in the Lewy body diseases.** *JAMA Neurol* 2016;73:1334–41 CrossRef Medline
42. Chen YS, Chen MH, Lu CH, et al. **Associations among cognitive functions, plasma DNA, and white matter integrity in patients with early-onset Parkinson's Disease.** *Front Neurosci* 2017;11:9 CrossRef Medline
43. Alibhai J, Blanco RA, Barria MA, et al. **Distribution of misfolded prion protein seeding activity alone does not predict regions of neurodegeneration.** *PLoS Biol* 2016;14:e1002579 CrossRef Medline

# A Multicenter Preliminary Study of Cangrelor following Thrombectomy Failure for Refractory Proximal Intracranial Occlusions

G. Marnat, F. Delvoe, S. Finitis, B. Lapergue, F. Gariel, A. Consoli, J.-P. Desilles, M. Mazighi, C. Dargazanli, R. Bourcier, J. Darcourt, V. Chalumeau, M. Elhorany, F. Clarençon, S. Richard, B. Gory, and I. Sibon, on behalf of the ETIS Investigators



## ABSTRACT

**BACKGROUND AND PURPOSE:** Rescue endovascular and pharmacologic approaches are increasingly being adopted after recanalization failure of acute large-vessel occlusion strokes with mechanical thrombectomy, with encouraging results. The safety and efficacy of glycoprotein IIb/IIIa inhibitors in ischemic stroke have been investigated, though cangrelor, a recent intravenous P2Y<sub>12</sub>-receptor inhibitor with a rapid onset/offset of action and a short half-life, may be a valuable option. We compared the safety and efficacy of cangrelor with those of glycoprotein IIb/IIIa inhibitors for refractory occlusions.

**MATERIALS AND METHODS:** We performed a retrospective analysis of the ongoing prospective, multicenter, observational Endovascular Treatment in Ischemic Stroke Registry in France between May 2012 and February 2020. Refractory intracranial occlusions of the anterior and posterior circulation were included and defined as recanalization failure of large-vessel occlusion stroke, perioperative target artery reocclusion, or high risk of early reocclusion related to an arterial wall lesion. The primary end point was a favorable outcome, defined as a 90-day mRS of 0–2. Secondary end points were reperfusion, intracranial hemorrhage, and procedural complications.

**RESULTS:** Among 69 patients, 15 were treated with cangrelor, and 54, with glycoprotein IIb/IIIa inhibitors. The favorable outcome (adjusted OR = 2.22; 95% CI, 0.42–11.75;  $P = .348$ ) and mortality (adjusted OR = 0.44; 95% CI, 0.06–3.16;  $P = .411$ ) rates were similar in both groups. There was no difference in the rates of any intracranial hemorrhage (adjusted OR = 0.40; 95% CI, 0.08–2.09;  $P = .280$ ), symptomatic intracranial hemorrhage (6.7% versus 0.0%,  $P = .058$ ), or procedural complications (6.7% versus 20.4%,  $P = .215$ ). Reperfusion rates were higher in the cangrelor group, though the difference did not reach statistical significance (93.3% versus 75.0% for modified TICI 2b–3; adjusted OR = 10.88; 95% CI, 0.96–123.84;  $P = .054$ ).

**CONCLUSIONS:** Cangrelor seems to be as safe as glycoprotein IIb/IIIa inhibitors for managing refractory intracranial occlusion and leads to satisfactory brain reperfusion. Cangrelor is a promising agent in this setting, and additional studies are warranted to confirm our findings.

**ABBREVIATIONS:** ASA = acetylsalicylic acid; GPIIb/IIIa = glycoprotein IIb/IIIa; ICH = intracranial hemorrhage; mTICI = modified TICI; sICH = symptomatic intracranial hemorrhage

**B**ridging therapy is the standard approach for acute large-vessel occlusion strokes.<sup>1</sup> Successful recanalization is

achieved in 70%–80% of cases, and this has been improving continuously in recent years.<sup>1–3</sup> However, mechanical thrombectomy failure remains problematic, and the optimal approach in this setting is unknown. In many cases, reperfusion failure may be related to underlying intracranial atherosclerosis with local acute thrombosis.<sup>4–7</sup> In this context, adjunct pharmacologic and mechanical strategies with promising results are being reported.<sup>8–11</sup> Anti-thrombotic agents such as acute antiplatelet therapy are often considered alone or in combination with intracranial

Received January 11, 2021; accepted after revision March 9.

From the Neuroradiology Department (G.M., F.G.) and Neurology (I.S.), Bordeaux University Hospital, Bordeaux, France; Department of Interventional Neuroradiology (F.D., J.-P.D., M.M.), Rothschild Foundation, Paris, France; Aristotle University of Thessaloniki (S.F.), Ahepa Hospital, Thessaloniki, Greece; Departments of Neuroradiology (A.C.) and Neurology (B.L.), Foch Hospital, Versailles Saint-Quentin en Yvelines University, Suresnes, France; Department of Neuroradiology (C.D.), Centre Hospitalier Régional Universitaire Gui de Chauliac, Montpellier, France; Department of Neuroradiology (R.B.), University Hospital of Nantes, Nantes, France; Department of Neuroradiology (J.D.), University Hospital of Toulouse, Toulouse, France; Department of Interventional Neuroradiology (V.C.), Bicêtre University Hospital, Le Kremlin-Bicêtre, Paris, France; Department of Neuroradiology (M.E., F.C.), Pitié-Salpêtrière Hospital, Paris, France; Departments of Neurology (S.R.) and Diagnostic and Therapeutic Neuroradiology (B.G.), Université de Lorraine, Centre Hospitalier Régional Universitaire-Nancy, Stroke Unit, Nancy, France; Institut National de la Santé et de la Recherche Médicale U116 (S.R.), Centre Hospitalier Régional Universitaire-Nancy, Nancy, France; and Institut National de la Santé et de la Recherche Médicale U1254 (B.G.), Université de Lorraine, Imagerie Adaptative Diagnostique et Interventionnelle, Nancy, France.

Please address correspondence to Gaultier Marnat, MD, Department of Neuroradiology, Bordeaux University Hospital, Place Amélie Raba-Léon, 33000 Bordeaux, France; e-mail: gaultier.marnat@chu-bordeaux.fr

Indicates article with online supplemental data.  
<http://dx.doi.org/10.3174/ajnr.A7180>

angioplasty or stent placement. Acute antiplatelet therapy has been reported in association with a rescue strategy after standard thrombectomy failure, incomplete recanalization, or lesions considered to have a high risk of early reocclusion.<sup>8–10</sup> Such acute antiplatelet therapy is most often deemed essential in the case of rescue intracranial stent placement.

Glycoprotein IIb/IIIa (GPIIb/IIIa) inhibitors are used most often, but the optimal antithrombotic strategy is unknown. In this situation, cangrelor (Kengreal), a new P2Y<sub>12</sub> inhibitor recently added to the standard pharmacologic arsenal for treating acute myocardial infarction,<sup>12</sup> might be used for intracranial reperfusion, given its interesting pharmacologic properties (immediate platelet inhibition, quick platelet function recovery after treatment interruption, and easy transition to oral antiplatelet therapy).<sup>13</sup> There are few reports on the use of cangrelor in acute stroke,<sup>14–18</sup> and none have compared it with GPIIb/IIIa inhibitors. GPIIb/IIIa inhibitors, which are frequently used in this setting, have a slower onset of antiplatelet action.<sup>8,10,11,19,20</sup> Their effect duration is longer, which can be unsafe in the case of intracranial bleeding or any hemorrhagic risk. The role of GPIIb/IIIa inhibitors on intracranial hemorrhage (ICH) risk in the setting of ischemic stroke is controversial.<sup>21</sup> Therefore, this preliminary study compared the safety and efficacy of cangrelor with GPIIb/IIIa inhibitors after mechanical thrombectomy failure for intracranial large-vessel occlusion stroke.

## MATERIALS AND METHODS

The data used in this study are available from the corresponding author on reasonable request.

### Study Population

We performed a retrospective study of the Endovascular Treatment of Ischemic Stroke (ETIS) Registry from May 2012 to February 2020 (NCT03776877). ETIS is an ongoing prospective, multicenter, observational study that includes all consecutive patients undergoing endovascular treatment for large-vessel occlusion stroke at 13 comprehensive stroke centers in France. The local institutional review boards approved the data collection and analysis. All data in the ETIS registry were collected, stored, and accessed locally following the recommendations of the Comité consultatif sur le traitement de l'information en matière de recherche dans le domaine de santé. This study included patients presenting with refractory occlusion of the anterior or posterior circulation. Refractory occlusion was defined as recanalization failure of a large-vessel occlusion stroke after the optimal standard mechanical thrombectomy approach, perioperative reocclusion of the target artery, or a high risk of early reocclusion due to underlying angiographically identified arterial wall disease after mechanical thrombectomy (mostly underlying intracranial atherosclerotic stenosis but also other possible pathologies such as intracranial dissection or large-artery vasculitis). The exclusion criteria were cangrelor or GPIIb/IIIa inhibitor use for any indication other than those mentioned above, such as cervical carotid artery stent placement, distal embolus, or embolus in a new territory. Tandem occlusions, thrombosis of an underlying previously implanted intracranial stent, and iatrogenic occlusion after a

cerebral endovascular procedure (aneurysm or arteriovenous shunt embolization) were also excluded.

### Treatments

Mechanical thrombectomy was performed according to the clinical context, timeframe, imaging data, and guidelines. Intravenous thrombolysis was administered within 4.5 hours after stroke onset according to international recommendations, using recombinant tissue plasminogen activator in the absence of contraindications. The endovascular procedure was performed with the patient under conscious sedation or general anesthesia, depending on the patient's condition and local protocol. The initial thrombectomy approach was left to the discretion of the interventionist. Pharmacologic or mechanical adjunctive treatments were used for refractory occlusions according to patient comorbidities, imaging data (potentially completed with additional perioperative flat panel detector CT), and prior or previously administered thrombolysis and antithrombotic treatments. Perioperative adjunctive acute antiplatelet therapy was decided on a case-by-case basis after a multidisciplinary discussion. The cangrelor administration protocol consisted of a 30- $\mu$ g/kg intravenous bolus continued with a 4- $\mu$ g/kg/min infusion. The GPIIb/IIIa inhibitors were tirofiban (Agrastat), abciximab (ReoPro), or eptifibatide (Intergrilin) given following their respective standard administration protocols and dose (intravenous bolus first followed by intravenous infusion via a syringe pump). An intravenous bolus of 250 mg of acetylsalicylic acid (ASA; aspirin) was also given at the clinician's discretion. During the endovascular procedure, intracranial angioplasty or stent placement was performed optionally in association with pharmacologic therapy. Mid- and long-term antiplatelet therapy was given depending on the clinical and imaging evolution. Ideally, dual antiplatelet therapy with ASA plus clopidogrel or ticagrelor was initiated during the first 24 hours after endovascular treatment after no evidence of ICH seen on day 1 CT or MR imaging. The dual antiplatelet therapy was continued for 3 months and followed by long-term single antiplatelet therapy with ASA. Illustrative cases are presented in Figs 1 and 2.

### Outcomes

Clinical, imaging, timeline, and angiographic data were recorded prospectively. Trained research nurses determined the mRS scores at 90 days during face-to-face interviews or phone conversations with the patients, their relatives, or their general practitioners. Favorable outcome was defined as a 90-day mRS of 0–2. Early neurologic changes (24-hour NIHSS score) were recorded. Successful reperfusion was defined as modified TICI (mTICI) 2b, 2c, or 3. Near-complete reperfusion was defined as a final mTICI 2c or 3, and complete reperfusion, as a final mTICI 3. Intracranial recanalization of the target artery was also assessed with the arterial occlusive lesion score. Favorable reperfusion of the target vessel was defined as a score of 2 or 3. Procedural complications (dissection, embolus in a new territory, perforation, and local puncture-site complication) and 90-day mortality were collected. ICH was assessed according to the European Cooperative Acute Stroke Study (ECASS II) classification. Symptomatic ICH (sICH) was defined as neurologic deterioration (NIHSS worsening



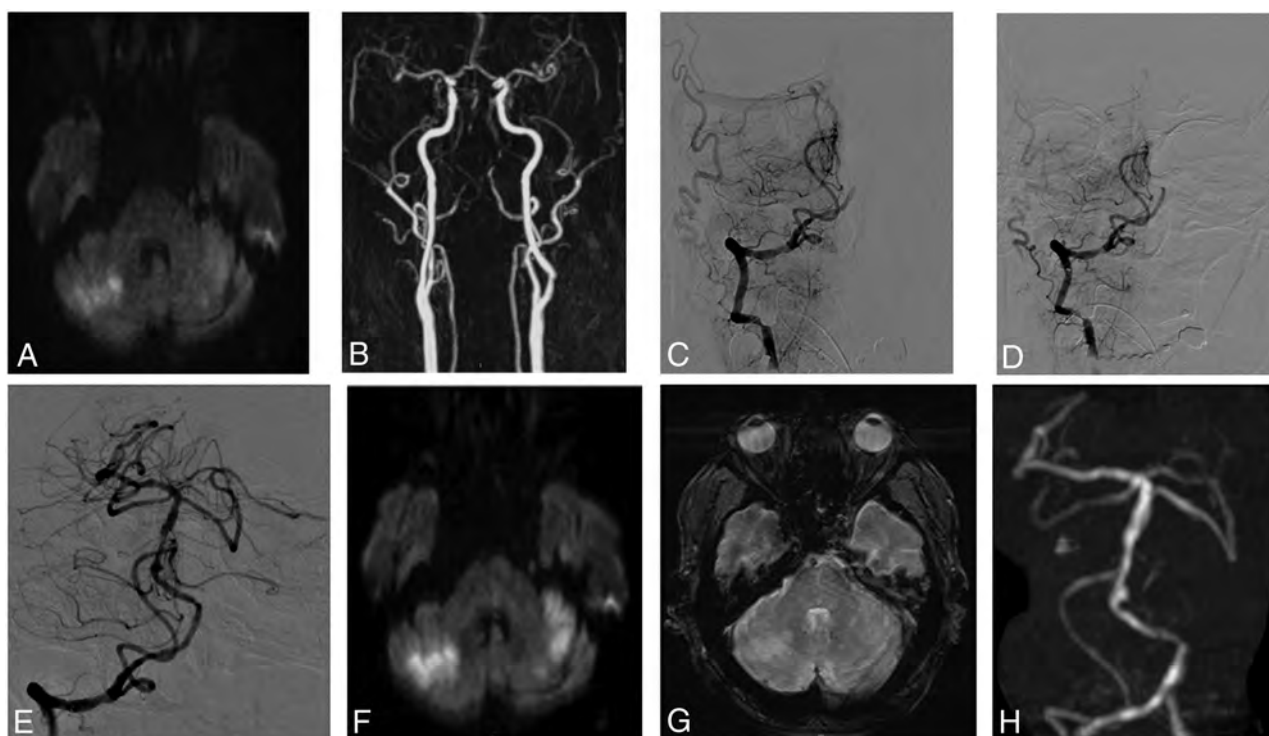


**FIG 1.** Illustrative case 1. *A* and *B*, A 67-year-old patient who presented with a rapidly progressive coma associated with a right hemiplegia. Initial MR imaging demonstrates a basilar artery occlusion with a relatively small infarct core (posteriori circulation posterior circulation-ASPECTS = 8). The patient underwent intravenous thrombolysis combined with endovascular treatment. Considering the absence of recanalization of the basilar artery after 2 mechanical thrombectomy passes with a standard approach (*C* and *D*), intracranial angioplasty associated with cangrelor intravenous infusion was performed, allowing complete reperfusion (*E*). Day 1 MR imaging shows stability of the cerebellar infarction and patency of basilar artery without intracranial hemorrhage (*F–H*). The patient progressively recovered, and after 3 months, the mRS score was 0.

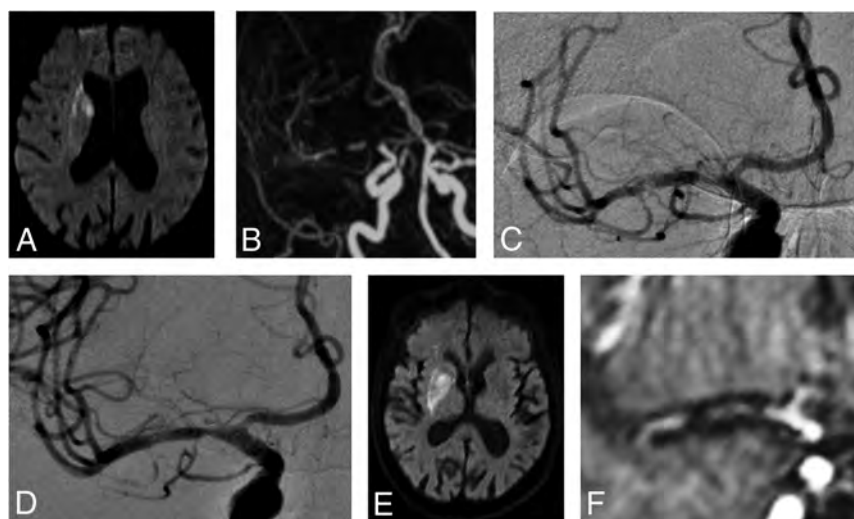


**FIG 2.** Illustrative case 2. *A* and *B*, This 81-year-old woman had acute left hemiparesis and dysarthria (initial NIHSS score = 8) secondary to an occlusion of the right M1 segment of the MCA, likely due to an underlying intracranial stenosis. Intravenous thrombolysis and endovascular treatment were performed. *C*, The first angiographic run confirms the pattern of intracranial acute thrombosis associated with an underlying stenosis (intracranial atherosclerosis). *D*, Considering the poor expected efficacy of a standard mechanical thrombectomy in such occlusion etiology, the limited infarct core, and the absence of intracranial hemorrhage at baseline, intracranial angioplasty and stent placement combined with cangrelor intravenous administration were performed as a first-line strategy. *E* and *F*, Clinical evolution and day 1 imaging have favorable results. At 90 days, the mRS score was 2.

of  $\geq 4$  points) along with ICH. The ASPECTS and patency of the intracranial artery were evaluated on day 1 of imaging.

### Statistical Analysis

Quantitative variables are expressed as the mean (SD) when the distribution is normal or the median (interquartile range) otherwise. Categorical variables are expressed as numbers (percentage). The patients were divided into 2 groups according to the antithrombotic treatment type (GPIIb/IIIa inhibitors and cangrelor). Baseline characteristics were compared between these 2 groups using the Student *t* test for Gaussian continuous variables, the Mann-Whitney *U* test for non-Gaussian continuous variables, or the  $\chi^2$  test (or Fisher exact test when the expected cell frequency was  $<5$ ) for categorical variables, as appropriate. For outcome parameters, multivariate logistic regression models were adjusted for age, ASA treatment, NIHSS and ASPECTS at presentation, infarct

**Table 1: Clinical and imaging outcomes**

	GPIIb/IIIa Inhibitors (n = 54)	Cangrelor (n = 15)	Total (n = 69)	P Value
Arterial occlusion lesion score 2–3	44/54 (81.5%)	15/15 (100.0%)	59/69 (85.5%)	.071
Final mTICI 2b–3	39/54 (75.0%)	14/15 (93.3%)	53/69 (79.1%)	.124
Final mTICI 2c–3	16/52 (30.8%)	12/15 (80.0%)	28/67 (41.8%)	<.001
Final mTICI 3	11/52 (21.2%)	7/15 (46.7%)	18/67 (26.9%)	.050
Puncture-to-recanalization delay (median) (IQR)	80 (55–133)	107 (82–149)	87 (58–135)	.573
Perioperative complication	11/54 (20.4%)	1/15 (6.7%)	12/69 (17.4%)	.215
Day 1 NIHSS (median) (IQR) <sup>a</sup>	12 (7–16)	11 (5–16)	12 (6–16)	.462
Day 1 ASPECTS (median) (IQR)	6 (4–7)	7 (6–8)	6 (4–7)	.089
Intracranial artery patency on day 1 imaging follow-up	42/54 (79.2%)	13/15 (86.7%)	55/69 (80.9%)	.519
Any ICH	20/54 (37.0%)	4/15 (26.7%)	24/69 (34.8%)	.456
sICH	0/53 (0.0%)	1/15 (6.7%)	1/68 (1.5%)	.058
ECASS hemorrhage subtypes				.798
HI-1	8/53 (15.1%)	2/15 (13.3%)	10/68 (14.7%)	
HI-2	7/53 (13.2%)	1/15 (6.7%)	8/68 (11.8%)	
PH-1	1/53 (1.9%)	1/15 (6.7%)	2/68 (2.9%)	
PH-2	0/53 (0%)	0/15 (0%)	0/69 (0%)	
Remote ICH	1/53 (1.9%)	0/15 (0.0%)	1/68 (1.5%)	
Subarachnoid hemorrhage	2/53 (3.8%)	0/15 (0.0%)	2/68 (2.9%)	
90-Day mRS 0–2	17/54 (31.5%)	6/15 (40.0%)	23/69 (33.3%)	.536
90-Day mortality	16/54 (29.6%)	3/15 (20.0%)	19/69 (27.5%)	.460

**Note:**—IQR indicates interquartile range; HI-1, hemorrhagic infarction type 1; HI-2, hemorrhagic infarction type 2; PH-1, parenchymal hematoma type 1; PH-2, parenchymal hematoma type 2.

<sup>a</sup> Missing values in 26 patients.

**Table 2: Multivariate analysis of main outcomes**

	GPIIb/IIIa Inhibitor	Cangrelor	Adjusted ORs <sup>a</sup>	95% CI	P Value
90-Day mRS 0–2	31.5%	40.0%	2.22	0.42–11.75	.348
90-Day mortality	29.6%	20.0%	0.44	0.06–3.16	.411
Any ICH	37.0%	26.7%	0.40	0.08–2.09	.280
Final mTICI 2b–3	75.0%	93.3%	10.88	0.96–123.84	.054
Final mTICI 2c, 3	30.8%	80.0%	5.33	0.97–29.38	.055
Final mTICI 3	21.2%	46.7%	2.77	0.59–13.02	.198

<sup>a</sup> Adjusted for age, initial NIHSS score, initial ASPECTS, infarct topography (anterior versus posterior circulation), aspirin administration, and rescue intracranial stent placement.

location, and intracranial stent placement using complete case analysis. Statistical testing was conducted at a 2-tailed  $\alpha$  level of .05. Data were analyzed using STATA, Version 16.1 (StataCorp).

## RESULTS

During the study period, 7527 patients underwent endovascular therapy in the participating centers. Of these, 69 met the inclusion criteria, of whom 15 received cangrelor and 54 received GPIIb/IIIa inhibitors (abciximab,  $n = 38$ ; tirofiban,  $n = 11$ ; and eptifibatide,  $n = 5$ ). The Online Supplemental Data present the patients' baseline characteristics according to the type of acute antiplatelet therapy and global population. The 2 groups were balanced except for the admission diastolic blood pressure (mean, 77.66 versus 100.71 mm Hg;  $P = .002$ ). Procedural and therapeutic main characteristics were also comparable between groups. ASA administration differed significantly between groups with higher use in the cangrelor group than in the GPIIb/IIIa inhibitors group (93.3% versus 29.6%,  $P < .001$ ). Table 1 presents the main clinical, angiographic, and radiologic outcomes of the univariate analysis. Favorable outcome was comparable between groups (40.0% versus 31.5%,  $P = .536$ ). There was also no difference in the mortality rate (20.0% versus 29.6%,  $P = .460$ ).

Successful reperfusion was achieved without a significant difference between groups (93.3% versus 75.0%,  $P = .124$ ), but the near-complete and complete reperfusion rates significantly favored the cangrelor group (80.0% versus 30.8%,  $P < .001$ , and 46.7% versus 21.2%,  $P = .050$ , respectively).

The difference in the rate of target occlusion recanalization (arterial occlusion lesion score of 2 or 3) did not reach significance (100% versus 81.5%,  $P = .071$ ). Safety criteria did not differ significantly between the 2 groups. Day 1 imaging outcomes were also balanced because no differences were observed in day 1 ASPECTS (median, 7 versus 6;  $P = .089$ ) or patency of the target artery (86.7% versus 79.2%,  $P = .519$ ). The multivariate analysis adjusting for major confounding factors revealed improved reperfusion rates in the cangrelor group, but the difference did not reach significance (final mTICI 2b–3, 93.3% versus 75.0%; adjusted OR = 10.88; 95% CI, 0.96–123.84;  $P = .054$ ) (Table 2). Similarly, we found improved functional outcomes and mortality rates and less ICH in the cangrelor group, without significant differences. Figure 3 presents the distribution of mRS scores at 90 days.

In the cangrelor group, 1 patient presented with intraventricular hemorrhage, considered sICH in our study. He initially presented with basilar artery occlusion secondary to underlying

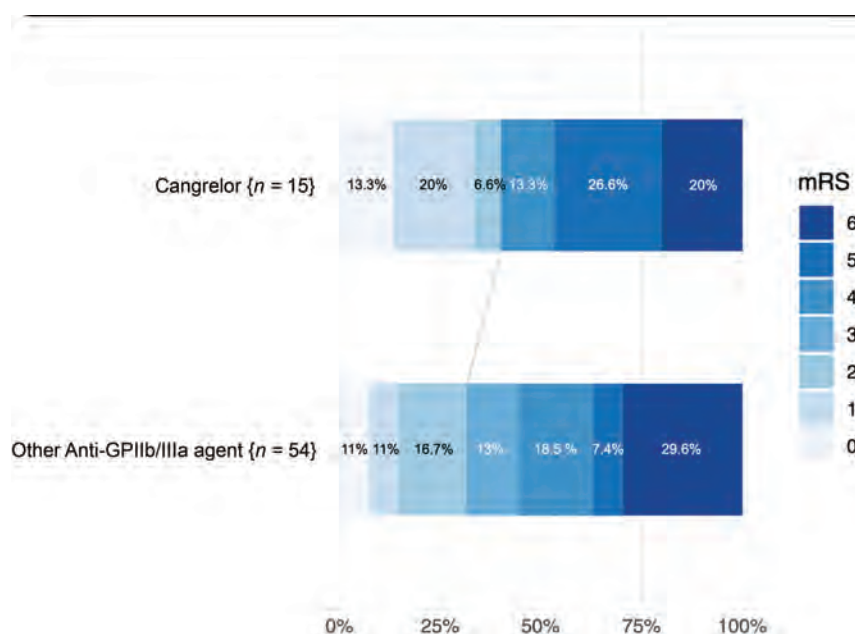


**FIG 3.** Distribution of mRS scores at 90 days according to the antiplatelet therapy type.

stenosis (initial posterior circulation-ASPECTS = 6), treated with stent placement and cangrelor infusion). Day 1 imaging revealed posterior fossa extensive infarction and intraventricular hemorrhage. The patient died at day 3 after stroke onset.

## DISCUSSION

Despite growing reports in the literature, our study presents substantial results of cangrelor use in the setting of intracranial thrombectomy. We found that cangrelor is safe, with no increased risk of mortality or ICH whether symptomatic or not compared with GPIIb/IIIa inhibitors. Reperfusion rates were higher with cangrelor than with GPIIb/IIIa inhibitors, though this difference did not reach statistical significance.

With the expansion of thrombectomy indications, complex angiographic presentations remain improvement targets. In particular, more complementary treatments for failed intracranial recanalization are being proposed. There are 2 possible scenarios: distal fragmentation impairing reperfusion or proximal nonrecanalization. In the second scenario, thrombectomy failure is frequently related to underlying arterial wall disease, mostly atherosclerotic, albeit not exclusively.<sup>4-6</sup> In this setting, aggressive management, including acute antiplatelet therapy and intracranial angioplasty or stent placement, has been reported.<sup>8-10,19,22-25</sup> These pharmacologic and mechanical approaches are most often combined with promising results, considering the specific large-vessel occlusion stroke subtype. To date, the optimal pharmacologic adjunctive therapy for this recently described rescue approach for refractory intracranial occlusion is yet to be determined.

GPIIb/IIIa inhibitors are usually administered for refractory intracranial occlusion. In this setting, the reported ICH risk seems comparable with the observed rates in thrombectomy for

embolic causes.<sup>8,10,11,19,20</sup> The neurologic outcome, intracranial reperfusion, and midterm artery patency are also promising. However, in the setting of large-vessel occlusion stroke, antithrombotic management, especially if intracranial stent placement has been performed, always involves a compromise between hemorrhagic risk and arterial patency. In this sense, reports with GPIIb/IIIa inhibitors are encouraging. However, the specific features of cangrelor might be advantageous in cerebral ischemia.<sup>13,17</sup> Its immediate antiplatelet effect and quicker restoration of platelet function after treatment interruption allow safer management in the context of ischemic stroke, as observed here. Indeed, sICH or emergent craniotomy is not unusual and requires rapid restoration of platelet function. This might be much easier with a rapidly active, reversible drug such as cangrelor than with a GPIIb/IIIa inhibitor. The pharmacodynamics of GPIIb/IIIa inhibitors differ substantially, with a more prolonged onset of action time (10–30 minutes) and a substantially longer duration of the antiplatelet effect (4–12 hours).<sup>16</sup> Improving the pharmacologic characteristics of antiplatelet therapy without impairing the antithrombotic effect and increasing ICH risk are the ideal goals. Cangrelor has been previously reported in several case series, including acute-phase endovascular treatments (cervical or intracranial stent placement) with an encouraging hemorrhagic risk and arterial patency results.<sup>16,18</sup>

We found a trend toward a higher risk of sICH in the cangrelor group with univariate analysis ( $P = .058$ ). However, in our population, ASA use was more frequent in the cangrelor group than in the GPIIb/IIIa inhibitor group. This more frequent ASA use in the cangrelor group might be related to the lack of confidence in its indications. ASA might have been a confounding factor. With the multivariate analysis, after adjusting for ASA use, the ICH risk remained nonsignificant. However, this may indicate that cangrelor should not be systematically associated with ASA in the acute phase. This hypothesis has to be explored with more extensive studies.

Our study revealed that cangrelor might have safety and efficacy profiles similar to those of GPIIb/IIIa inhibitors. Reperfusion rates, including proximal (arterial occlusive lesion score) and global (mTICI score) reperfusion evaluations, favored the cangrelor group, even if statistical significance was not reached. This trend also has to be confirmed.

Our study had several limitations. First, although we presented the largest population of refractory intracranial occlusions treated with rescue therapy and cangrelor, the study sample remains small. The lack of power of the statistical analysis probably explains the absence of a significant difference on



multivariate analysis. Still, given the lack of studies on cangrelor for this indication, we believe that our data provide reassurance regarding the potential safety and efficacy of this pharmacologic management. Moreover, considering the specific subtype of large-vessel occlusion stroke, the lack of validated guidelines in its management, and the retrospective nature of our work, the endovascular procedure and perioperative management in our study were not completely standardized. Aggressive rescue management for refractory intracranial occlusions is still not widely applied by operators of the participating centers to date, partly explaining the small sample size. Biologic data regarding aspirin and the P2Y<sub>12</sub> response were not available. The study period was also quite extended with potential evolutions in endovascular approaches with time. Our small study sample also reflects the recent introduction of cangrelor; therefore, our results are only preliminary. More extensive studies are necessary to evaluate the value of cangrelor in the treatment of refractory intracranial occlusions.

## CONCLUSIONS

In this preliminary study, cangrelor use in the management of intracranial refractory occlusions was associated with encouraging safety and efficacy profiles in comparison with GPIIb/IIIa inhibitors. Due to the limited sample size, no significant influence on 90-day clinical outcome was observed. Given its ease of handling and favorable pharmacodynamics, cangrelor may be a promising alternative to other intravenous acute antiplatelet therapies. Larger studies are mandatory to determine the optimal acute antiplatelet therapy strategy for refractory intracranial large-vessel occlusion stroke.

Disclosures: Gaultier Marnat—UNRELATED: Payment for Lectures Including Service on Speakers Bureaus: Medtronic, MicroVention. Bertrand Lapergue—UNRELATED: Grants/Grants Pending: MicroVention, Phenox.\* Mikael Mazighi—UNRELATED: Consultancy: Air Liquide, Amgen, Boehringer Ingelheim, Acticor Biotech; Grants/Grants Pending: RHU BOOSTER, Agence Nationale pour la Recherche, funding from French Ministry of Health.\* Frédéric Clarençon—UNRELATED: Board Membership: ArteDrone; Consultancy: Medtronic; Payment for Lectures Including Service on Speakers Bureaus: Balt, Penumbra, Stryker. Sébastien Richard—UNRELATED: Grants/Grants Pending: French Ministry. Comments: grants for 2 academic studies\*; Payment for Development of Educational Presentations: Boehringer Ingelheim. \*Money paid to the institution.

## REFERENCES

- Goyal M, Menon BK, Van Zwam WH, et al. HERMES collaborators. Endovascular thrombectomy after large-vessel ischaemic stroke: a meta-analysis of individual patient data from five randomised trials. *Lancet* 2016;387:1723–31 CrossRef Medline
- Lapergue B, Blanc R, Gory B, et al. Effect of endovascular contact aspiration vs stent retriever on revascularization in patients with acute ischemic stroke and large-vessel occlusion: the ASTER randomized clinical trial. *JAMA* 2017;318:443–52 CrossRef Medline
- Turk AS, Siddiqui A, Fifi JT, et al. Aspiration thrombectomy versus stent retriever thrombectomy as first-line approach for large-vessel occlusion (COMPASS): a multicentre, randomised, open label, blinded outcome, non-inferiority trial. *Lancet* 2019;393:998–1008 CrossRef Medline
- Yeo LLL, Bhogal P, Gopinathan A, et al. Why does mechanical thrombectomy in large-vessel occlusion sometimes fail?: a review of the literature. *Clin Neuroradiol* 2019;29:401–14 CrossRef Medline
- Li H, Zhang Y, Zhang L, et al. Endovascular treatment of acute ischemic stroke due to intracranial atherosclerotic large-vessel

occlusion: a systematic review. *Clin Neuroradiol* 2020;30:777–87 CrossRef Medline

- Kim BM. Causes and solutions of endovascular treatment failure. *J Stroke* 2017;19:131–42 CrossRef Medline
- Kaesmacher J, Gralla J, Mosimann PJ, et al. Reasons for reperfusion failures in stent-retriever-based thrombectomy: registry analysis and proposal of a classification system. *AJNR Am J Neuroradiol* 2018;39:1848–53 CrossRef Medline
- Premat K, Dechartres A, Lenck S, et al. Rescue stenting versus medical care alone in refractory large-vessel occlusions: a systematic review and meta-analysis. *Neuroradiology* 2020;62:629–37 CrossRef Medline
- Baek JH, Kim BM, Kim DJ, et al. Stenting as a rescue treatment after failure of mechanical thrombectomy for anterior circulation large artery occlusion. *Stroke* 2016;47:2360–67 CrossRef Medline
- Chang Y, Kim BM, Bang OY, et al. Rescue stenting for failed mechanical thrombectomy in acute ischemic stroke: a multicenter experience. *Stroke* 2018;49:958–64 CrossRef Medline
- Maingard J, Phan K, Lamanna A, et al. Rescue intracranial stenting after failed mechanical thrombectomy for acute ischemic stroke: a systematic review and meta-analysis. *World Neurosurg* 2019;132:e235–45 CrossRef Medline
- Bhatt DL, Stone GW, Mahaffey KW, et al. Effect of platelet inhibition with cangrelor during PCI on ischemic events. *N Engl J Med* 2013;368:1303–13 CrossRef Medline
- Sible AM, Nawarskas JJ. Cangrelor: a new route for P2Y<sub>12</sub> inhibition. *Cardiol Rev* 2017;25:133–39 CrossRef Medline
- Elhorany M, Lenck S, Degos V, et al. Cangrelor and stenting in acute ischemic stroke: monocentric case series. *Clin Neuroradiol* 2020 May [Epub ahead of print] CrossRef Medline
- Abdenmour L, Sourour N, Drir M, et al. Preliminary experience with cangrelor for endovascular treatment of challenging intracranial aneurysms. *Clin Neuroradiol* 2020;30:453–61 CrossRef Medline
- Aguilar-Salinas P, Agnoletto GJ, Brasiliense LBC, et al. Safety and efficacy of cangrelor in acute stenting for the treatment of cerebrovascular pathology: preliminary experience in a single-center pilot study. *J NeuroInterv Surg* 2019;11:347–51 CrossRef Medline
- Godier A, Mesnil M, De Mesmay M, et al. Bridging antiplatelet therapy with cangrelor in patients with recent intracranial stenting undergoing invasive procedures: a prospective case series. *Br J Anaesth* 2019;123:e2–5 CrossRef
- Cervo A, Ferrari F, Barchetti G, et al. Use of cangrelor in cervical and intracranial stenting for the treatment of acute ischemic stroke: a “real life” single-center experience. *AJNR Am J Neuroradiol* 2020;41:2094–99 CrossRef Medline
- Peng F, Wan J, Liu W, et al. Efficacy and safety of rescue stenting following failed mechanical thrombectomy for anterior circulation large-vessel occlusion: propensity score analysis. *J Neurointerv Surg* 2020;12:271–73 CrossRef Medline
- Yang J, Wu Y, Gao X, et al. Intraarterial versus intravenous tirofiban as an adjunct to endovascular thrombectomy for acute ischemic stroke. *Stroke* 2020;51:2925–33 CrossRef Medline
- Ciccone A, Motto C, Abraha I, et al. Glycoprotein IIb/IIIa inhibitors for acute ischaemic stroke. *Cochrane Database Syst Rev* 2014; CD005208 CrossRef Medline
- Park H, Baek JH, Kim BM. Endovascular treatment of acute stroke due to intracranial atherosclerotic stenosis-related large-vessel occlusion. *Front Neurol* 2019;10:308 CrossRef Medline
- Baek JH, Kim BM, Heo JH, et al. Outcomes of endovascular treatment for acute intracranial atherosclerosis-related large-vessel occlusion. *Stroke* 2018;49:2699–705 CrossRef Medline
- Zhang G, Ling Y, Zhu S, et al. Direct angioplasty for acute ischemic stroke due to intracranial atherosclerotic stenosis-related large-vessel occlusion. *Interv Neuroradiol* 2020;26:602–06 CrossRef Medline
- Tsang ACO, Orru E, Klostranec JM, et al. Thrombectomy outcomes of intracranial atherosclerosis-related occlusions: a systematic review and meta-analysis. *Stroke* 2019;50:1460–66 CrossRef Medline

# Interobserver Agreement in Scoring Angiographic Results of Basilar Artery Occlusion Stroke Therapy

 M. Findler,  A.S. Turjman,  J. Raymond,  P.M. White,  U. Sadeh-Gonik,  C.A. Taschner,  M. Mazighi,  A. Biondi,  B. Gory, and  F. Turjman



## ABSTRACT

**BACKGROUND AND PURPOSE:** The modified TICI Infarction grading system is a metric currently used to evaluate angiographic results of thrombectomy for large-vessel occlusion in ischemic stroke. Originally designed for evaluating MCA territories, it is currently used for other vessel occlusions, including the posterior circulation. We postulate that the modified TICI use for the posterior circulation is not accurate due to the different vascular territories supplied by vertebrobasilar vasculature, making grading more complex.

**MATERIALS AND METHODS:** We collected angiographic results from 30 patients who presented with acute posterior circulation occlusions between 2015 and 2018 and underwent thrombectomy in our institution. Eight observers were asked to evaluate the TICI scores before and after thrombectomy. The multirater statistics were computed using Fleiss  $\kappa$  analysis. Further data were collected regarding the potential brain territories at risk and the existence of atherosclerotic disease in the basilar artery.

**RESULTS:** The overall agreement  $\kappa$  reached 0.277 (SD, 0.013), which suggests a “fair” agreement among the raters. On average, 45% of observers achieved a high accuracy in predicting brain areas at risk of ischemia. As for the existence of basilar atherosclerotic disease, a high agreement (defined as at least 5 of 6 observers) was seen in 20 of the 30 patients.

**CONCLUSIONS:** Despite TICI being ubiquitous in stroke diagnostics, the high variability of posterior circulation TICI scores calls into question its use in these strokes. Other methods should be developed to assess recanalization in the posterior circulation.

**ABBREVIATIONS:** LVO = large-vessel occlusion; mTICI = modified TICI

The TICI grading system is a metric developed by Higashida et al<sup>1</sup> to evaluate the response of thrombolytic agents in acute ischemic strokes. Following the demonstration in controlled randomized studies that mechanical thrombectomy is superior to pharmacologic management in anterior ischemic strokes, the 5-point modified TICI (mTICI) scale became

instrumental in analyzing pre- and postintervention cerebral perfusion and assessing procedural effectiveness. In the anterior circulatory system, the mTICI score may be a bona fide metric, which strongly correlates with the patient's prognosis and can be effectively used as a guide for clinical decision-making. However, does it make sense to talk about mTICI score in basilar artery occlusions?

Recent advances in endovascular therapies for stroke treatment allow rapid clot retrieval and restoration of perfusion to ischemic brain tissue.<sup>2</sup> While patient recovery depends on myriad factors such as the time to reperfusion, the size of the infarct, and the location of the occluded vessel, the ability to achieve rapid and complete flow restoration to ischemic tissues is currently the primary goal of stroke treatment. The assessment of vessel patency not only guides the physician's operative plan, namely deciding on additional attempts at extracting clot versus ending the procedure, but is also a metric used posttreatment to gauge the patient's prognosis and the efficacy of the treatment.<sup>3,4</sup> The mTICI scoring system is widely used to encode and compare angiographic results in acute stroke therapies.<sup>5</sup> Despite much debate regarding its accuracy and precision and although

Received January 19, 2021; accepted after revision March 9.

From the Department of Neurology and Interventional Neuroradiology (M.F.), Rabin Medical Center, Petah Tikva, Israel; Cognition Medical Corporation (Alexis S. Turjman), Boston, Massachusetts; Département de Radiologie, Radio-Oncologie et Médecine Nucléaire (J.R.), Université de Montréal, Montreal, Quebec, Canada; Department of Neuroradiology (P.M.W.), Royal Victoria Infirmary, Newcastle, UK; Department of Radiology and Interventional Neuroradiology (U.S.-G.), Tel Aviv Medical Center, Tel-Aviv, Israel; Department of Neuroradiology (C.A.T.), University Medical Centre Freiburg, Freiburg, Germany; Department of Interventional Neuroradiology (M.M.), Fondation Rothschild Hospital, Paris, France; Department of Neuroradiology and Endovascular Therapy (A.B.), Besancon University Hospital, Besancon, France; Department of Diagnostic and Therapeutic Neuroradiology (B.G.), Centre Hospitalier Régional Universitaire Nancy, Nancy, France; and Department of Interventional Neuroradiology (Francis Turjman), Hospices Civils de Lyon, Lyon, France.

Please address correspondence to Michael Findler, MD, 11 Helsingi St Tel Aviv, Israel; e-mail: findlerm@gmail.com

 Indicates article with online supplemental data.

<http://dx.doi.org/10.3174/ajnr.A7182>

modifications were suggested, the mTICI score is still the most widely used metric among interventional neuroradiologists.<sup>6,7</sup>

While the mTICI scoring system is mostly used to assess recanalization in the anterior circulation, recent technologic advances, such as low-profile stent retrievers and hypercompliant, atraumatic aspiration systems, have helped improve the effectiveness of mechanical thrombectomy in the posterior circulation.<sup>8–11</sup> Although not yet demonstrated in a randomized trial, posterior vessel thrombectomy is promising, and several trials of the efficacy and safety of thrombectomy for acute basilar artery occlusions are ongoing.

For a lack of a better metric, the mTICI score is widely used for the assessment of the anterior and posterior circulation, but its popularity hides an ugly truth: The mTICI framework is an ill-adapted yardstick in the evaluation of the posterior circulation because the cerebrovascular anatomy is too convoluted, too diverse, and often incompletely rendered by conventional imaging to achieve either accuracy or precision. In the anterior system, some major interobserver variability is reported<sup>12</sup> and the posterior side is even more complex. First, within posterior occlusions, there is ample variability, depending on the location of the occlusion, that translates into a variety of clinical presentations and, in turn, causes difficulty in scoring blood flow. For example, there are some critical differences between proximal and distal occlusions of the basilar artery. The prognosis of lateral medullary infarction due to PICA occlusion is more benign, mainly due to the absence of important motor dysfunction.<sup>13</sup> Persistent top of the basilar occlusion after a failed thrombectomy attempt might lead to downward extension of thrombi, resulting in catastrophic bilateral midbrain or pontine infarction.<sup>14</sup>

Second, the multiple etiologies of the posterior circulation stroke<sup>15</sup> add a layer of complexity in the scoring. Acute on chronic occlusion of a severely atherosclerotic basilar artery might be more difficult to treat, while it is less clinically devastating due to the development of collaterals.<sup>16</sup> Cardioembolic basilar strokes typically lead to larger infarcts, due to larger clots and insufficiently developed collateral circulation.<sup>17</sup> Third, often the severity of the disease does not follow the intuition gained from imaging, rendering the scoring moot. For example, the lack of the posterior cerebral artery on angiographic images might lead the operator to assign a low mTICI score because the posterior cerebral artery is a major artery of the posterior system and predicts a devastating stroke. However, the occlusions of the basilar perforators, which look more benign and would be scored higher on the mTICI scale, lead to far more serious conditions. We postulate that these major considerations are regarded differently by different operators, resulting in different mTICI grading.

The aim of this work was to examine whether the mTICI score is a bona fide metric of posterior vascularization states and whether it can reliably guide the clinical intent: attempt another pass for better recanalization or stop. Even though numerous outside parameters can influence the progression of the disease postintervention, we framed the decision to continue to treat or stop as a prediction of the likely course of postendovascular treatment. To test our hypotheses, we measured the interobserver reliability with the Fleiss  $\kappa$  of mTICI scoring of 8 trained raters in

adjudicating outcomes of endovascular treatment for ischemic strokes of the posterior circulation.

## MATERIALS AND METHODS

### Patients

We collected angiographic results from 30 patients (men/women = 19:11, mean age = 68 years) who presented with acute posterior circulation occlusions between the 2015 and 2018 and were treated endovascularly in our institution (Department of Interventional Neuroradiology, Hospices Civils de Lyon, Lyon, France). The inclusion criteria were a clinical presentation with a basilar artery occlusion, at least 1 thrombectomy attempt, and proper pre- and postthrombectomy imaging.

### Image Acquisition

DSA images from angiograms of the vertebrobasilar system were acquired during the thrombectomies using a biplane angiography system (Axiom Artis dBA; Siemens). Consecutive anterior-posterior and lateral angiographic images before and after thrombectomy from several consecutive arterial phases were obtained in JPEG format and converted to a movie file format. When they were available, we included images acquired from previous CT or MR imaging scans to assess the existence of patent collaterals, most notably posterior communicating arteries. The images were uploaded to an online survey.

### Image Interpretation and mTICI Scoring

Eight observers were asked to assess pairs of angiographic images taken from 30 patients and to evaluate the mTICI scores before and after thrombectomy. They were instructed to use the modified 5-point mTICI scoring system defined as the following: grade 0, no perfusion; grade 1, contrast penetration with minimal perfusion; grade 2a, partial filling (less than half) of the entire vascular territory; grade 2b, perfusion of half or greater of the vascular territory; grade 3, complete and normal rate of perfusion. The mTICI guidelines were available to the graders before presentation of the cases.

Further questions concerned the potential brain territories at risk. The observers were asked to evaluate whether  $\geq 1$  of the following territories was at risk of ischemia: the occipital lobes, the thalamus, the brainstem, or the cerebellum. Six of the 8 observers were asked to evaluate the brain territories that were likely to be injured by the stroke because the other 2 observers were familiar with the postthrombectomy images and were excluded from this part of the study. Postthrombectomy imaging (brain CT or MR imaging) was analyzed by a single interpreter and was compared with the formal interpretation in the radiology report. Ischemic zones were defined as CT hypodensities or MR imaging hyperintensities on DWI or FLAIR imaging. We also asked the observers whether they found evidence of basilar atherosclerotic disease (basilar artery stenosis or vessel irregularities) for each case.

### Statistical Analysis

Interrater variability is a mathematic analysis tool that measures the degree of agreement among observers and can be used to evaluate the level of consensus and homogeneity of a ranking system. It is useful because it allows rating scale systems, such as mTICI, and quantifying their precision. We used the Fleiss  $\kappa$  to



# Fleiss $\kappa$ test<sup>a</sup>

	Rater 1	Rater 2	Rater 3	Rater 4	Rater 5	Rater 6	Rater 7	Rater 8
Rater 1		0.514 <sup>b</sup>	0.003	0.519 <sup>b</sup>	0.650 <sup>b</sup>	0.476 <sup>b</sup>	0.319 <sup>b</sup>	0.234 <sup>b</sup>
Rater 2			0.007	0.460 <sup>b</sup>	0.652 <sup>b</sup>	0.632 <sup>b</sup>	0.363 <sup>b</sup>	0.273 <sup>b</sup>
Rater 3				0.080	0.014	0.052	0.001	0.094
Rater 4					0.502 <sup>b</sup>	0.350 <sup>b</sup>	0.188 <sup>b</sup>	0.228 <sup>b</sup>
Rater 5						0.501 <sup>b</sup>	0.383 <sup>b</sup>	0.168 <sup>c</sup>
Rater 6							0.403 <sup>b</sup>	0.131 <sup>c</sup>
Rater 7								0.048
Rater 8								

<sup>a</sup> Overall  $\kappa = 0.277$ .

<sup>b</sup>  $P < .05$ .

<sup>c</sup>  $P = .000$ .

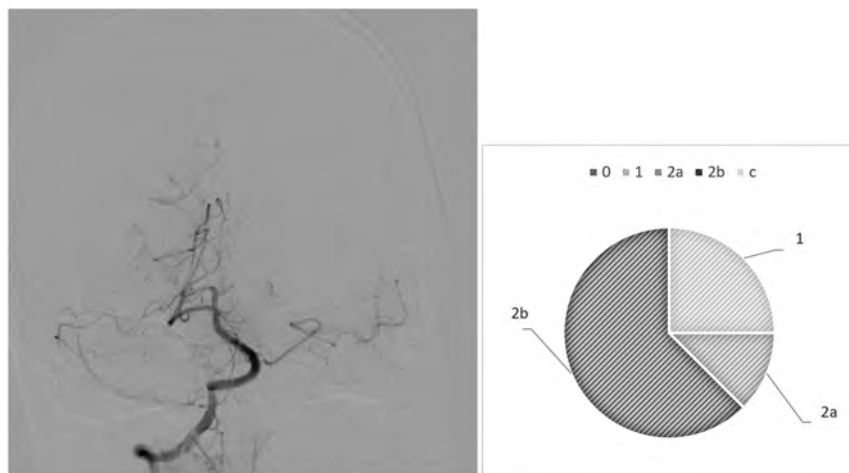


**FIG 1.** Case 6. After thrombectomy, interobserver variability.

assess how closely related 8 trained neurointerventionalists grade the perfusion status of patients with stroke pre- and post-thrombectomy on the 5-step mTICI scale: 1) 0, 2) 1, 3) 2a, 4) 2b, and 5) 3. The Fleiss  $\kappa$  is a number computed from the observation data that describes the degree of agreement over that achieved by randomly assigning grades. Fleiss  $\kappa$  is computed from the following formula:

$$\kappa = \frac{\bar{P} - \bar{P}_e}{1 - \bar{P}_e},$$

where  $\bar{P} - \bar{P}_e$  measures the degree of agreement obtained above chance, and  $1 - \bar{P}_e$  is a normalization coefficient that represents the maximum attainable degree of agreement. If the data are completely in agreement, meaning that all the reviewers graded all the cases exactly the same, then  $\bar{P}$  equals 1 and  $\kappa$  equals 1. In another scenario, if the judges select their answers randomly,  $\bar{P}$  equals  $\bar{P}_e$  and  $\kappa$  equals 0. Note that  $\kappa$  can become negative when raters are in disagreement more times than when the grades are assigned randomly.

The multirater statistics were computed using Fleiss  $\kappa$  analysis with the statistics software SPSS, Version 24 (IBM). The encoded macro takes the grades assigned by the trained observers as input and implements the methodology of Fleiss et al<sup>18</sup> to compute the agreement among raters when the number of raters is  $>2$ . The output of the software package is the values of the  $\kappa$

coefficient, which can assume numeric values between  $-1$  and  $1$ . The Fleiss  $\kappa$  coefficients can be interpreted according to the guidelines proposed by Landis and Koch: 0 indicating poor, 0.01–0.20 slight, 0.21–0.40 fair, 0.41–0.60 moderate, 0.61–0.80 substantial, and 0.81–1.0 almost perfect agreement.

In addition, for every case, we computed the percentage of raters who agreed on predicting the potential brain territories at risk, and we defined a high degree of agreement when raters identified correctly at least 3 of the 4 zones of possible ischemia.

## RESULTS

The interobserver agreement among the 8 observers is demonstrated in the Table.  $\kappa$  values are summarized for our observers'

scores of angiographic outcomes according to the mTICI score. The overall agreement  $\kappa$  reached 0.277 (SD, 0.013), which suggests a "fair" agreement among the raters. Most interesting, 1 rater (rater 3) had a significantly lower agreement rate compared with the other 7 observers. We, therefore, retested the overall agreement excluding rater 3, which resulted in a rise of the overall  $\kappa$  to a value of 0.456 (SD, 0.018), indicating a "moderate" agreement among the observers.

Our analysis highlights diverging behaviors from the raters: In most cases, we observed drastic variability from clusters of raters, which directly questions the existence of a defined mTICI score. For example, case 6 (Fig 1) is an occlusion of the proximal basilar artery with a bilateral fetal configuration of the posterior communicating arteries, which divided the observers. Five of 8 observers (62.5%) assigned the score 2b, 1 (12.5%) gave it a 2a, and 2 (25%) assigned it a score of 1. On the contrary, we observed examples of more consistent analyses, in which the scores were equal or close. This result is demonstrated in case 26 (Fig 2), in which a patent posterior vasculature was achieved following thrombectomy and the analysis was more consensual: mTICI 2b (75%) and 3 (25%).

The Online Supplemental Data show the accuracy of assessment of territory damage. Almost all the cases had follow-up imaging (brain CT or MR imaging scans) (28/30). Twenty patients had follow-up CT scans, and 18, MR imaging scans (some had images available from  $>1$  technique). One patient had

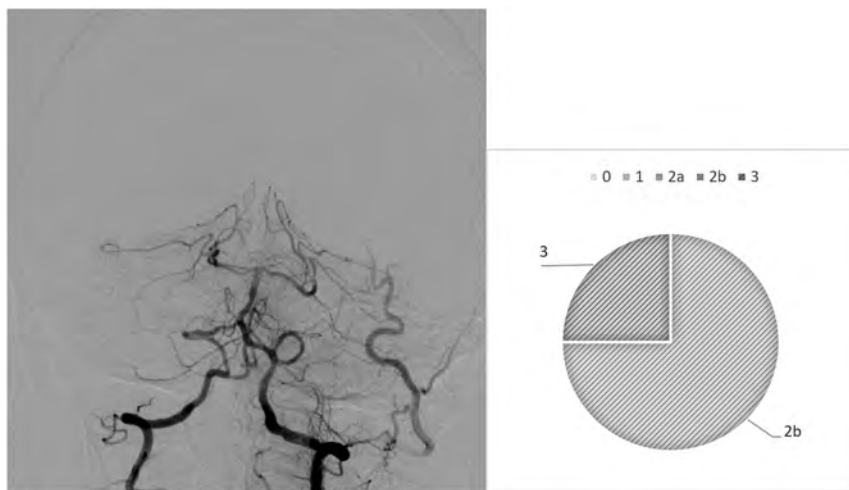


**FIG 2.** Case 26, After thrombectomy, interobserver variability.

no postthrombectomy follow-up available, and another patient had a massive subarachnoid hemorrhage, which did not allow proper evaluation of ischemia. We defined high accuracy as correctly identifying the postthrombectomy ischemic status of at least 3 of 4 potential zones (occipital lobes, thalamus, brainstem, and cerebellum). On average, 45% of observers achieved a high accuracy, meaning that they were able to correctly predict at least 75% of the brain areas at risk. In 6 of 28 thrombectomy cases, no observer reached high accuracy, and in 3 of 28 cases, all observers reached high accuracy.

Basilar artery atherosclerotic disease was graded by 6 of 8 observers. In 23 of 30 cases, at least 1 observer mentioned the existence of basilar atherosclerotic disease. A majority agreement of the existence of basilar atherosclerotic disease (at least 4 of 6 observers) was noted in 8 of the 30 cases. A high agreement (defined as at least 5 of 6 observers) for the existence or the lack of basilar atherosclerotic disease was seen in 20 of the 30 cases.

## DISCUSSION

Recent advances in mechanical thrombectomy for the treatment of acute ischemic stroke with large-artery occlusion have made this treatment safe and extremely effective. Although the efficacy of mechanical thrombectomy for basilar artery occlusion has not yet been proved in a large, randomized, controlled study, it has become a preferred treatment strategy in many centers. The need for a reliable angiographic scale to assess the recanalization status of posterior strokes stems from the hypothesis—proved in anterior infarcts—that a higher grade of reperfusion leads to less ischemic damage and better functional outcomes. Therefore, such a scale might predict the outcome of patients undergoing posterior thrombectomy. Furthermore, a reliable angiographic scale is needed to quantify the efficacy and complication rates of different treatment methods as well as to compare the treatment options.

Our study shows that the interrater agreement among 8 experienced raters is only “fair,” which seriously questions the usefulness and existence of a reliable metric for posterior strokes.

Our study demonstrates the existence of major discrepancies in mTICI grading among experienced interventionalists, a conclusion that we somehow anticipated, considering that the mTICI score was designed to assess MCA strokes and may not be suited to the posterior system.

These results add to a prior study among 3 raters that failed to find substantial mTICI interrater agreement for posterior circulation strokes.<sup>19</sup> In the anterior vascular territory, the interrater agreement of mTICI scores is low as well, a finding that may call for the emergence of a new metric altogether.<sup>7</sup> There is much debate over the proper way to use the mTICI scale in analyses, ranging from clinical stratifying to the comparison of interventional techniques.

There is also a growing consensus among clinicians that the mTICI needs to evolve to improve its clinical relevance and usefulness. Several groups proposed modified or refined versions of the mTICI scoring system: mTICI 2c that adds an additional level to the original scale and mTICI 67 (expanded mTICI 2b67).<sup>6,20–22</sup>

Assessing patent arteries in the vertebrobasilar territory is even more difficult than in its anterior pendant for several reasons: First, the collateral circulation from the posterior communicating arteries makes the flow pattern more complex to visualize and analyze; second, the existence of vital perforating arteries that are not DSA-visible, such as the perforating arteries of the basilar artery, adds inherent uncertainty to the grading; and third, the significance of vascular territories is greater than in the anterior circulation. Notable examples are posterior strokes in which major arteries are irrigated, but small perforants supplying critical zones of the brain are occluded and can easily be missed on imaging because of either their size or larger arteries that are themselves irrigated through fluid redundancies of the circle of Willis. Specifically, strokes of the superior part of the basilar artery with occluded thalamic perforants but patent posterior cerebral arteries fed by the posterior communicating arteries are silent killers because they often lead to misdiagnoses.

The major differences of mTICI scoring among different operators is important because successful recanalization (mTICI 2b or 3) has been associated with good outcome and survival in basilar artery occlusions.<sup>23</sup>

Another interesting finding from our work is the inability of our experienced interventionists to predict follow-up MR imaging diffusion lesions or endangered territories. This has several possible explanations: the existence of collaterals, the existence of varied vascular architectures, and the different pathologies of brainstem strokes or the lack of data regarding time to recanalization and baseline perfusion. Given the difficulty in predicting ischemic lesions, as demonstrated by our data, we suggest including MR imaging diffusion imaging as a routine for posterior circulation postthrombectomy evaluations.

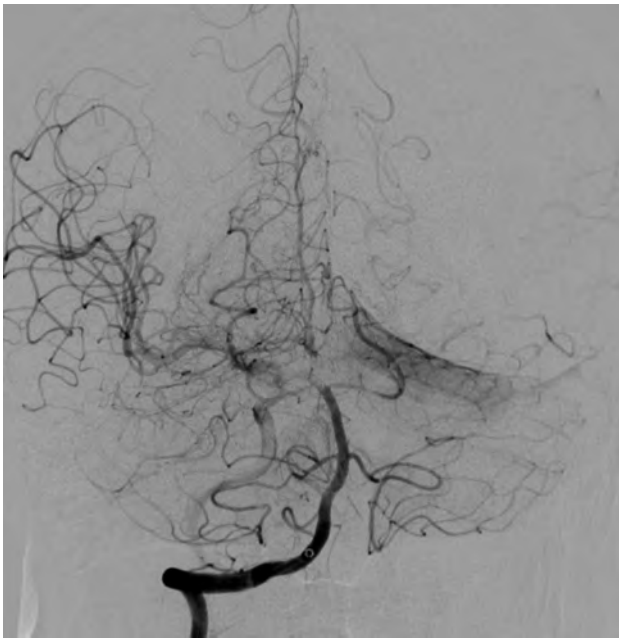


**FIG 3.** Case 1. Fifty percent of reviewers marked basilar atherosclerotic disease.



**FIG 4.** Case 16. All reviewers marked basilar atherosclerotic disease.

We noticed that in almost all cases, the observers overestimated the number of damaged territories. An interesting example is shown in case 15, in which most reviewers marked multiple territories at risk, while the control MR imaging and CT scan did not show any residual ischemia in the vertebrobasilar territory.

We also saw differences regarding the existence of basilar atherosclerotic disease. There was a high accordance of at least 5 of 6 observers regarding the existence of basilar atherosclerotic disease in only two-thirds of cases. Figures 3 and 4 show 2 cases

that illustrate the variability of basilar atherosclerosis diagnostics. In case 1, there was an even split between reviewers on the existence of atherosclerosis in the basilar artery, and no clear diagnostic could be established. In stark contrast, all the reviewers agreed on the presence of atherosclerosis in the basilar artery in another case (case 16).

Basilar atherosclerosis might be determined when stenosis of 50%–99% is seen on initial or postthrombectomy angiography as defined by the Warfarin–Aspirin Symptomatic Intracranial Disease (WASID) study.<sup>24</sup> Occlusion of the more proximal segment of the basilar artery is often associated with basilar artery atherosclerotic disease, while more distal occlusion usually results from the embolic source.<sup>25</sup> Operators might look for vessel wall irregularities or changes in vessel diameter when defining atherosclerotic disease. The importance of correctly identifying basilar artery atherosclerosis might influence the thrombectomy method (the use of intracranial balloon angioplasty and stent placement for example) as well as the following choice of antiplatelet therapy.

### Limitations

Our study has some limitations. We used electronic surveys to facilitate the access to our images of interventionalists from different centers. Not all images of the original DSA were available to the reviewers, and not all cases had data regarding collateral circulation. Data regarding the time from onset and time to recanalization were missing. This issue may have affected the reviewers' judgment regarding brainstem areas at risk. Last, our study did not test intrarater agreement, namely whether images with a defined "true score" are consistently graded similarly by the same grader, but this agreement would greatly complement the present study. Given that there is no "true value" for a particular case, the best surrogate that the authors can envision is a large consensus of experts—if it can be reached.

### CONCLUSIONS

Despite being ubiquitous in stroke diagnostics, the mTICI score is an antiquated metric designed for the anterior cerebrovasculature that fails to describe the status of blood flow in the posterior circulation because it is both inaccurate and imprecise. Our data show that the interrater reliability among 8 experts is low for attributes such as occlusion severity, recanalization status, endangered territories, and the existence of basilar atherosclerotic disease. The high variability of posterior mTICI scores calls into question the very essence of the mTICI scale and its clinical relevance. A more suitable grading system should consider the territories involved (brainstem, cerebellum, thalamus, and occipital lobes), the occlusion site (proximal versus distal), and the lumen patency of the basilar artery (including clots, atherosclerosis, stent placement, and angioplasty attempts). To more accurately assess the success and infarct size of a procedure, we suggest routine MR imaging as an adjunctive technique.

**Disclosures:** Jean Raymond—*UNRELATED: Employment:* Center hospitalier de l'Université de Montréal. Philip M. White—*UNRELATED: Consultancy:* MicroVention, Terumo; *Grants/Grants Pending:* Stryker, Penumbra, Medtronic, MicroVention\*; *Payment for Development of Educational Presentations:* European Society of Minimally Invasive Neurological Therapy. Christian A.



Taschner—UNRELATED: *Employment*: Universitätsklinikum Freiburg; *Expert Testimony*: Expert Panel for medical device regulation, Commission of the European Union. Mikael Mazighi—UNRELATED: *Consultancy*: Acticor Biotech; *Grants/Grants Pending*: Agence Nationale pour la Recherche\*; *Payment for Development of Educational Presentations*: Boehringer Ingelheim. Francis Turjman—UNRELATED: *Consultancy*: Balt; *Medtronic*; *Payment for Development of Educational Presentations*: Medtronic, Balt. \*Money paid to the institution.

## REFERENCES

- Higashida RT, Furlan AJ, Roberts H, et al. Technology Assessment Committee of the American Society of Interventional and Therapeutic Neuroradiology. **Trial design and reporting standards for intra-arterial cerebral thrombolysis for acute ischemic stroke.** *Stroke* 2003;34:e109–37 CrossRef Medline
- Chen CJ, Ding D, Starke RM, et al. **Endovascular vs medical management of acute ischemic stroke.** *Neurology* 2015;85:1980–90 CrossRef Medline
- Kent TA, Mandava P. **Recanalization rates can be misleading.** *Stroke* 2007;38:e103 CrossRef Medline
- Rha JH, Saver JL. **The impact of recanalization on ischemic stroke outcome: a meta-analysis.** *Stroke* 2007;38:967–73 CrossRef Medline
- Fugate JE, Klunder AM, Kallmes DF. **What is meant by ‘TICI’?** *AJNR Am J Neuroradiol* 2013;34:1792–97 CrossRef Medline
- Tomsick T. **TIMI, TIBI, TICI: I came, I saw, I got confused.** *AJNR Am J Neuroradiol* 2007;28:382–84 Medline
- Kallmes DF. **TICI: if you are not confused, then you are not paying attention.** *AJNR Am J Neuroradiol* 2012;33:975–76 CrossRef Medline
- Sun X, Tong X, Gao F, et al. **Endovascular treatment for acute basilar artery occlusion: a single center retrospective observational study.** *BMC Neurol* 2019;19:315 CrossRef Medline
- Chen PM, Pirastehfar M, Hailey L, et al. **PREMISE: Posterior Circulation Results Comparing Embolectomy to Medical Intervention in Stroke Emergencies.** *Cureus* 2019;11:e6000 CrossRef Medline
- Gory B, Eldesouky I, Sivan-Hoffmann R, et al. **Outcomes of stent retriever thrombectomy in basilar artery occlusion: an observational study and systematic review.** *J Neurol Neurosurg Psychiatry* 2016;87:520–25 CrossRef Medline
- Quan T, Hou H, Xue W, et al. **Endovascular treatment of acute intracranial vertebrobasilar artery occlusion: a multicenter retrospective observational study.** *Neuroradiology* 2019;61:1477–84 CrossRef Medline
- Gaha M, Roy C, Estrade L, et al. **Inter- and intraobserver agreement in scoring angiographic results of intra-arterial stroke therapy.** *AJNR Am J Neuroradiol* 2014;35:1163–69 CrossRef Medline
- Kim JS. **Pure lateral medullary infarction: clinical-radiological correlation of 130 acute, consecutive patients.** *Brain* 2003;126:1864–72 CrossRef Medline
- Mendelow AD, Grotta JC, Albers GW, et al. *Stroke E-Book: Pathophysiology, Diagnosis, and Management.* Elsevier; 2015
- Mattle HP, Arnold M, Lindsberg PJ, et al. **Basilar artery occlusion.** *Lancet Neurol* 2011;10:1002–14 CrossRef Medline
- Kim JS, Caplan LR, Wong KS, eds. *Intracranial Atherosclerosis.* John Wiley & Sons; 2009
- Kim HJ, Yun SC, Cho KH, et al. **Differential patterns of evolution in acute middle cerebral artery infarction with perfusion-diffusion mismatch: atherosclerotic vs. cardioembolic occlusion.** *J Neurol Sci* 2008;273:93–98 CrossRef Medline
- Landis JR, Koch GG. **The measurement of observer agreement for categorical data.** *Biometrics* 1977;33:159–74 CrossRef Medline
- Jung C, Yoon W, Ahn SJ, et al. **The revascularization scales dilemma: is it right to apply the treatment in cerebral ischemia scale in posterior circulation stroke?** *AJNR Am J Neuroradiol* 2016;37:285–89 CrossRef Medline
- Dargazanli C, et al. **Modified thrombolysis in cerebral infarction 2c/thrombolysis in cerebral infarction 3 reperfusion should be the aim of mechanical thrombectomy: insights from the ASTER Trial (Contact Aspiration Versus Stent Retriever for Successful Revascularization).** *Stroke* 2018;49:1189–96 CrossRef Medline
- Volny O, Cimflova P, Szeder V. **Inter-rater reliability for thrombolysis in cerebral infarction with MTICI 2c category.** *J Stroke Cerebrovasc Dis* 2017;26:992–94 CrossRef Medline
- Behme D, Tsogkas I, Colla R, et al. **Validation of the extended thrombolysis in cerebral infarction score in a real-world cohort.** *PLoS One* 2019;14:e0210334 CrossRef Medline
- Ravindren J, et al. **Predictors of outcome after endovascular thrombectomy in acute basilar artery occlusion and the 6hr time window to recanalization.** *Front Neurol* 2019;10:923 CrossRef Medline
- Prognosis of patients with symptomatic vertebral or basilar artery stenosis: the Warfarin-Aspirin Symptomatic Intracranial Disease (WASID) Study Group. *Stroke* 1998;29:1389–92 CrossRef Medline
- Lee YY, Yoon W, Kim SK, et al. **Acute basilar artery occlusion: differences in characteristics and outcomes after endovascular therapy between patients with and without underlying severe atherosclerotic stenosis.** *AJNR Am J Neuroradiol* 2017;38:1600–04 CrossRef Medline

# Clinical and Procedural Outcomes with or without Balloon Guide Catheters during Endovascular Thrombectomy in Acute Ischemic Stroke: A Systematic Review and Meta-analysis with First-line Technique Subgroup Analysis

 A. Podlasek,  P.S. Dhillon,  G. Jewett,  A. Shahein,  M. Goyal, and  M. Almekhlafi



## ABSTRACT

**BACKGROUND:** Balloon guide catheters are increasingly used to improve clot retrieval by temporarily stopping proximal blood flow during endovascular thrombectomy.

**PURPOSE:** Our aim was to provide a summary of the literature comparing the procedural and clinical outcomes of endovascular thrombectomy with or without balloon guide catheters, depending on the first-line technique used.

**DATA SOURCES:** We used PubMed/MEDLINE, EMBASE, and the Cochrane Database of Systematic Reviews.

**STUDY SELECTION:** We chose studies that compared using balloon guide catheters with not using them.

**DATA ANALYSIS:** Random effects meta-analysis was performed to compare the procedural outcomes measured as the first-pass effect, successful reperfusion, number of passes, procedural duration, arterial puncture to reperfusion time, distal emboli, and clinical outcomes.

**DATA SYNTHESIS:** Overall, a meta-analysis of 16 studies (5507 patients, 50.8% treated with balloon guide catheters and 49.2% without them) shows that the use of balloon guide catheters increases the odds of achieving a first-pass effect (OR = 1.92; 95% CI, 1.34–2.76;  $P < .001$ ), successful reperfusion (OR = 1.85; 95% CI, 1.42–2.40;  $P < .001$ ), and good functional outcome (OR = 1.48; 95% CI, 1.27–1.73;  $P < .001$ ). Balloon guide catheters reduce the number of passes (mean difference =  $-0.35$ ; 95% CI,  $-0.65$  to  $-0.04$ ;  $P = .02$ ), procedural time (mean difference =  $-19.73$ ; 95% CI,  $-34.63$  to  $-4.83$ ;  $P = .009$ ), incidence of distal or new territory emboli (OR = 0.5; 95% CI, 0.26–0.98;  $P = .04$ ), and mortality (OR = 0.72; 95% CI, 0.62–0.85;  $P < .001$ ). Similar benefits of balloon guide catheters are observed when the first-line technique was a stent retriever or contact aspiration, but not for a combined approach.

**LIMITATIONS:** The analysis was based on nonrandomized trials with a moderate risk of bias.

**CONCLUSIONS:** Current literature suggests improved clinical and procedural outcomes associated with the use of balloon guide catheters during endovascular thrombectomy, especially when using the first-line stent retriever.

**ABBREVIATIONS:** eTICI = extended TICI score; sICH = symptomatic intracranial hemorrhage

Acute stroke management changed drastically after 2015, when endovascular thrombectomy became the standard-of-care treatment for large-vessel occlusion.<sup>1–3</sup> Shorter procedural time and successful recanalization were the independent

procedural predictors of favorable clinical outcome after endovascular thrombectomy.<sup>4–6</sup> Currently, there is no consensus on the optimal procedural techniques or devices to achieve fast and complete endovascular reperfusion. Stand-alone strategies of stent retriever and contact aspiration have emerged as the most popular approaches for endovascular thrombectomy<sup>7</sup> without definite differences in clinical and procedural outcomes.<sup>8–12</sup>

Received January 16, 2021; accepted after revision March 16.

From the Department of Neuroscience and Vascular Simulation (A.P.), School of Medicine, Anglia Ruskin University, Chelmsford, Essex, UK; National Institute of Health Research Nottingham Biomedical Research Centre (A.P., P.S.D.), University of Nottingham, Nottingham, UK; Department of Clinical Radiology (A.P., P.S.D.), Queens Medical Centre, Nottingham University Hospitals National Health Service Trust, Nottingham, UK; and Departments of Clinical Neurosciences (G.J., A.S., M.G., M.A.) and Radiology (M.G., M.A.), University of Calgary, Calgary, Alberta, Canada.

Paper previously presented as an interim analysis on 8 studies in poster format at: European Stroke Organisation–World Stroke Organization 2020, Joint Stroke Virtual Conference, November 7–9, 2020.

Please address correspondence to Anna Podlasek, MD, NIHR-BRC Nottingham, Queen's Medical Centre, Derby Road, Nottingham NG7 2UH, United Kingdom; e-mail: podlaseka@gmail.com; @annapodlasek; @AlmekhlafiMa; @mayank\_Go

 Indicates article with online supplemental data.

<http://dx.doi.org/10.3174/ajnr.A7164>

Combined techniques of stent retriever and contact aspiration have also been shown to result in high rates of successful reperfusion and good functional outcomes and are now increasingly used.<sup>13,14</sup>

During endovascular thrombectomy, using a balloon guide catheter has been associated with higher recanalization rates and better functional outcomes in early clinical studies.<sup>15,16</sup> Balloon guide catheters offer transient proximal flow arrest and decrease the forward pressure impacting the clot, which has been shown to prevent distal thrombus migration or embolization to new vascular territories during retrieval.<sup>17,18</sup> Despite level 2A evidence suggesting benefits of stent retrievers in conjunction with proximal balloon guide catheters,<sup>2</sup> there is continued debate over their use in everyday clinical practice, especially when used in conjunction with contact aspiration.

Two previous meta-analyses suggested that the use of balloon guide catheters during endovascular thrombectomy is associated with improved clinical and angiographic outcomes.<sup>19,20</sup> However, a few larger registries have since been published in addition to many endovascular thrombectomy procedural modifications. Thus, we conducted this updated systematic review to investigate the effects of balloon guide catheters on the clinical and procedural outcomes following endovascular thrombectomy and considering the first-line endovascular thrombectomy technique: stent retriever, contact aspiration, or a combination (stent retriever + contact aspiration).

## MATERIALS AND METHODS

### Search Strategy, Study Selection, and Eligibility Criteria

The study was performed per the Preferred Reporting Items for Systematic Reviews and Meta-Analyses (PRISMA) guidelines.<sup>21</sup> We systematically searched electronic data bases up to December 2020, including PubMed/MEDLINE, EMBASE, and the Cochrane Database of Systematic Reviews. The following keywords were used in combination or individually using the Boolean operators “OR” and “AND”: “thrombectomy,” “endovascular procedures,” “stroke,” “retrievable stent,” “stent retriever,” “stentriever,” “aspiration,” “suction,” and “balloon guided catheter.” The articles were selected in 2 stages. First, the titles and abstracts were screened for relevant studies. Second, the full texts were downloaded and assessed for eligibility. The reference lists of included publications were then hand-searched for additional relevant studies. This process was performed by 4 assessors independently (A.P., G.J., A.S., P.S.D.). Any differences were resolved by consensus.

Studies evaluating  $\geq 1$  procedural and clinical outcome of endovascular thrombectomy were included. Randomized and nonrandomized controlled (retrospective and prospective) trials, observational studies, or post hoc analyses of observational data in trials were included when a control group was reported. Exclusion criteria included studies published before 2009, review articles and meta-analyses, guidelines, technical notes, studies on animals, and studies in languages other than English.

In the case of an overlapping patient population, only the series with the largest number of patients or the most detailed data were included.

### Data Extraction

The variables were, if available, the following: use of balloon guide catheters, the first-line endovascular thrombectomy technique used, study type (retrospective, prospective), study period, anatomic region (anterior/posterior circulation), sample size, mean age, number of women, presence of comorbidities (atrial fibrillation, hypertension, diabetes, coronary artery disease, dyslipidemia, smoking), tandem occlusion, clot location, baseline NIHSS score, IV-tPA, use of general anesthesia, use of a distal-access catheter, use of intra-arterial thrombolysis, onset to arterial puncture time, arterial puncture to reperfusion time, total procedural time (the time from the sheath insertion until the sheath is out), number of passes, successful reperfusion rate (defined as extended TICI [eTICI] 2b<sup>22</sup> or higher), first-pass effect defined as eTICI 2b or higher<sup>16,18,23-25</sup> or eTICI 2c or higher<sup>25-27</sup> or eTICI 3<sup>28-30</sup> or complete reperfusion<sup>18,28</sup> after the first pass, good functional outcome defined as functional independence described as mRS  $\leq 2$  at 90 days, symptomatic intracranial hemorrhage (sICH) defined as any ICH with an increase of the NIHSS score of  $\geq 4$  within 24 hours or death, and mortality at 90 days.

### Outcome Measures

Study characteristics and extracted variables were summarized using standard descriptive statistics. Continuous variables were expressed as means (SD), and categorical variables were expressed as frequencies or percentages. The primary outcomes were procedural (the first-pass effect, successful recanalization, procedural time, arterial puncture to reperfusion time, number of passes, distal embolization, or embolization in the new territory) and clinical (good functional outcome [mRS  $\leq 2$ ] at 90 days, sICH, mortality at 90 days).

### Statistical Analysis

Binary outcomes are reported as ORs with 95% confidence intervals. Continuous outcomes are analyzed as mean difference with a 95% CI. Tests of heterogeneity were conducted with the Q-statistic distributed as a  $\chi^2$  variate (assumption of homogeneity of effect sizes). The extent of between-study heterogeneity was assessed with the  $I^2$  statistic.<sup>31,32</sup> A random effects model was used. The ROBINS-I<sup>33,34</sup> tool was used to evaluate and visualize the individual risk of bias of each study. *P* values were 2-tailed with values  $< .05$  considered statistically significant. All analyses were conducted in Statistica 13.1 (StatSoft Poland), online calculators, and Review Manager 5.4.1 software ([https://www.advanceduninstaller.com/Review-Manager-5\\_4\\_1-509a434684edfe58c850c849ab795eca-application.htm](https://www.advanceduninstaller.com/Review-Manager-5_4_1-509a434684edfe58c850c849ab795eca-application.htm)).<sup>35</sup>

### Ethics

This study is a systematic review and meta-analysis, and no human-participant procedure was involved. Informed consent and ethics approval were not essential for this study.

## RESULTS

### Literature Search Results

We screened 8930 titles and abstracts and 877 full-text articles (Online Supplemental Data). Of those, data were extracted from



**Table 1: Baseline characteristics of the included studies**

Feature	BGC (No.) (%)	Non-BGC (No.) (%)	P
Baseline characteristics			
Mean age (yr)	68.2 (SD, 14.2)/2796	69.7 (SD, 14.0)/2711	<.001
Sex (female)	1318/2748 (48.0)	1314/2672 (49.2)	.37
IV t-PA	1598/2748 (58.2)	1487/2672 (55.7)	.06
Baseline NIHSS (mean)	16.3 (SD, 8.1)/2646	16.2 (SD, 8.8)/2591	.67
Comorbidities			
Atrial fibrillation	1064/2369 (44.9)	755/1972 (38.3)	<.001
Hypertension	1600/2516 (63.6)	1533/2346 (65.3)	.20
Diabetes	561/2516 (22.3)	544/2346 (23.2)	.46
Coronary artery disease	407/1891 (21.5)	388/1883 (20.6)	.49
Dyslipidemia	909/2516 (36.1)	798/2346 (34.0)	.12
Smoking	770/2492 (30.9)	673/2308 (29.2)	.19
Localization			
Tandem occlusions	136/1305 (10.4)	136/1423 (9.6)	.45
Distal ICA	716/2621 (27.3)	581/2604 (22.3)	<.001
M1 segment	1169/1976 (59.1)	1026/1776 (57.7)	.39
M2 segment	255/1918 (13.3)	256/1703 (15.0)	.13
Unspecified MCA segment	492/740 (66.5)	384/884 (43.4)	<.001
Periprocedural			
Onset to arterial puncture (min)	278.1 (SD, 171.7)/2563	280.3 (SD, 162.4)/2279	.65
General anesthesia	432/1705 (25.3)	391/1677 (23.3)	.17
Distal access catheter use	35/827 (4.2)	124/763 (16.3)	<.001
Intra-arterial thrombolysis	149/1389 (10.7)	191/1185 (16.1)	<.001

Note:—BGC indicates balloon guide catheter.

**Table 2: Summary of balloon guide catheter effects on procedural and clinical outcomes of endovascular thrombectomy**

Impact of BGC on/during	Overall	SR	Combined (SR + CA)	CA
Procedural outcomes				
First-pass effect	↑	↑	—	NA
Successful reperfusion	↑	↑	—	↑
Procedural time	↓	↓	NA	NA
Arterial puncture to reperfusion	—	—	—	—
No. of passes	↓	—	—	NA
Distal or new territory emboli	↓	—	—	—
Clinical outcomes				
Good functional outcome	↑	↑	—	↑
sICH	—	—	—	—
Mortality	↓	↓	NA	—

Note:—NA indicates not available; SR, stent retriever; CA, contact aspiration; ↑, increase; ↓, decrease; —, no difference.

16 studies that met inclusion criteria.<sup>15,16,18,23–28,30,36–41</sup> Eight hundred sixty-one studies were excluded due to not reporting balloon guide catheter versus non-balloon guide catheter, not reporting the desired variables, or lack of full text.

### Characteristics of Included Studies

The 16 studies published between 2010 and 2020 described 5507 patients (2796 with balloon guide catheters and 2711 patients without balloon guide catheters) undergoing endovascular thrombectomy due to occlusion in the anterior circulation (5472 patients)<sup>16,18,23–30,36–38,40,41</sup> or posterior circulation (35 patients).<sup>1</sup> Nine studies of 3213 patients (1875 balloon guide catheters versus

1338 non-balloon guide catheters) reported on outcomes with a stent retriever–first approach,<sup>15,16,18,25,30,37–40</sup> four studies of 1107 patients (464 balloon guide catheters versus 643 non-balloon guide catheters) with a contact aspiration–first approach,<sup>18,23,37,41</sup> and 4 studies of 1023 patients (377 balloon guide catheters versus 646 non-balloon guide catheters) with a combined first approach.<sup>24,26,28,36</sup> The studies are summarized in the Online Supplemental Data, and the baseline characteristics are presented in Table 1.

### Procedural Outcomes

Eleven studies of 4000 patients reported the first-pass effect (Table 2).<sup>16,18,23–28,30,39,40</sup> It was achieved among 829/1962 (42.3%) patients undergoing endovascular thrombectomy using balloon guide catheters and 572/2038 (28.1%) patients undergoing endovascular thrombectomy without balloon guide catheters (OR = 1.92; 95% CI, 1.34–2.76;  $P < .001$ ) (Online Supplemental Data). Final successful reperfusion (eTICI 2b or more) was reported in 15 studies (5207 patients).<sup>15,16,18,23–28,36–41</sup> This was higher in patients undergoing endovascular thrombectomy using balloon guide catheters (2258/2676, 84.8%) versus without balloon guide catheters (2007/2617, 76.7%) (OR = 1.85; 95% CI, 1.42–2.40;  $P < .001$ ) (Online Supplemental Data).

Total procedural time was reported in 6 studies (1345 patients).<sup>15,16,30,38–40</sup> Procedures using balloon guide catheters were shorter (mean, 73.7 [SD, 47.9] minutes) than those that did not use balloon guide catheters (98.7 [SD 61.9] minutes), corresponding to a

mean difference of –19.73 minutes (95% CI, –34.63 to –4.83 minutes;  $P = .009$ ) (Online Supplemental Data). In 7 studies (2602 patients) that reported arterial puncture–reperfusion time,<sup>18,23–25,28,36,41</sup> this was also shorter using balloon guide catheters with a mean of 51.2 (SD, 28.6) versus 57.8 (SD, 38.6) minutes without balloon guide catheters (mean difference = –7.57 minutes; 95% CI, –17.50 to 2.37 minutes;  $P = .14$ ) (Online Supplemental Data). Similarly, the number of passes needed to achieve successful reperfusion was lower in procedures using balloon guide catheters by a mean difference of –0.35 (95% CI, –0.65 to –0.04;  $P = .02$ ). This was reported in 13 studies (3927 patients) (Online Supplemental Data).

Distal embolization or emboli in a new territory were reported in 9 studies (2063 patients).<sup>15,23-25,28,36,38,40,41</sup> They complicated 77/1028 (7.5%) procedures using balloon guide catheters and 119/1035 (11.5%) without balloon guide catheters (OR = 0.5; 95% CI, 0.26–0.98;  $P = .04$ ) (Online Supplemental Data). Symptomatic ICH was reported in 10 studies (4469 patients).<sup>15,18,25,28,37-41,42</sup> It occurred in 119/2345 (5.1%) patients undergoing endovascular thrombectomy using balloon guide catheters and 155/2124 without (7.3%) (OR = 0.76; 95% CI, 0.55–1.05;  $P = .09$ ) (Online Supplemental Data).

### Clinical Outcomes

Twelve studies of 4718 patients reported 90-day functional outcomes (Table 2).<sup>15,18,23,25-27,30,36,37,39-41</sup> Favorable outcome (mRS 0–2) was higher in patients undergoing endovascular thrombectomy using balloon guide catheters (1253/2426, 51.6%) versus those without balloon guide catheters (971/2292, 42.4%) (OR = 1.48; 95% CI, 1.27–1.73;  $P < .001$ ) (Online Supplemental Data). On the other hand, mortality occurred in 364/2470 (14.7%) patients undergoing endovascular thrombectomy using balloon guide catheter versus 454/2335 (19.4%) patients undergoing endovascular thrombectomy without balloon guide catheters (OR = 0.72; 95% CI, 0.62–0.85;  $P < .001$ ) (Online Supplemental Data). This was reported in 12 studies (4805 patients).<sup>15,18,23,25-27,30,36-40</sup>

### Procedural Outcomes in Subgroup Analysis Based on the First-line Endovascular Thrombectomy Technique

A balloon guide catheter increases the odds of first-pass effect when the stent retriever is used as a first approach (OR = 2.18; 95% CI, 1.56–3.06;  $P < .001$ ) (Table 2),<sup>16,18,25,30,39,40</sup> but not when a combined approach of stent retriever + contact aspiration was used (OR = 1.03; 95% CI, 0.72–1.46;  $P = .87$ ).<sup>24,26,28</sup> The contact aspiration subgroup was not included because only 1 study population reported this subgroup outcome (Online Supplemental Data).<sup>18,23</sup>

The use of balloon guide catheters increased the odds of successful reperfusion when a stent retriever–first approach was used (OR = 1.7; 95% CI, 1.27–2.27;  $P < .001$ )<sup>15,16,18,25,37-40</sup> or when a contact aspiration–first approach was used (OR = 2.47; 95% CI, 1.35–4.52;  $P = .003$ ).<sup>18,23,41</sup> It had no influence when the combined approach was used (OR = 1.69; 95% CI, 0.76–3.77;  $P = .2$ ) (Online Supplemental Data).<sup>24,26,28,36</sup>

The use of balloon guide catheters was not associated with a change in arterial puncture to reperfusion time in any of the first-approach subgroups (OR for stent retriever =  $-9.63$ ; 95% CI,  $-28.35$ – $9.08$ ;  $P = 0.31$ ;<sup>18,43</sup> OR for combined =  $2.82$ ; 95% CI,  $-15.13$ – $20.77$ ;  $P = 0.76$ ;<sup>24,28,36</sup> and OR for contact aspiration =  $-23$ ; 95% CI,  $-52.69$ – $6.69$ ;  $P = .13$ ) (Online Supplemental Data).<sup>18,41</sup>

While overall balloon guide catheter use reduced the number of passes required to achieve reperfusion, this effect did not reach statistical significance, neither in the stent retriever–first approach (OR =  $-0.26$ ; 95% CI,  $-0.59$ – $0.06$ ;  $P = .11$ )<sup>15,16,18,25,30,38-40</sup> nor in the combined approach (OR =  $-0.36$ ; 95% CI,  $-0.99$ – $0.27$ ;  $P = .26$ ).<sup>28,36</sup> The contact aspiration subgroup was not included because only 1 study reported these outcomes (Online Supplemental Data).<sup>18,23</sup> Similarly, while overall the balloon guide catheter reduced the

incidence of distal embolization or new-territory emboli, this effect was not significant in the first-approach subgroups (OR for stent retriever = 0.51; 95% CI, 0.17–1.5;  $P = 0.22$ ;<sup>15,25,38,40</sup> OR for combined = 0.59; 95% CI, 0.11–3.1;  $P = 0.53$ ;<sup>24,28,35</sup> OR for contact aspiration = 0.4; 95% CI, 0.11–1.38;  $P = .15$ ) (Online Supplemental Data).<sup>23,41</sup>

There was no difference in the incidence of sICH with regard to the use of balloon guide catheters in any of the subgroups (OR for stent retriever = 0.73; 95% CI, 0.4–1.33;  $P = 0.30$ ;<sup>15,37-40</sup> OR for combined = 0.77; 95% CI, 0.42–1.42;  $P = 0.41$ ;<sup>26,28</sup> OR for contact aspiration = 0.8; 95% CI, 0.25–2.54;  $P = .71$ ) (Fig 1B).<sup>37,41</sup>

### Clinical Outcomes in Subgroup Analysis Based on the First-line Endovascular Thrombectomy Technique

Use of a balloon guide catheter improves the odds of good functional outcome in the stent retriever–first approach (OR = 1.6; 95% CI, 1.23–2.09;  $P < .001$ ) (Table 2)<sup>15,25,30,37,39,40</sup> and contact aspiration–first approach (OR = 1.75; 95% CI, 1.26–2.44;  $P < .001$ ).<sup>23,37,41</sup> while there was no statistically significant difference in the combined approach (OR = 1.26; 95% CI, 0.91–1.75;  $P = .16$ ) (Fig 1A).<sup>26,36</sup>

A balloon guide catheter is associated with decreased odds of death in the stent retriever–first approach (OR = 0.72; 95% CI, 0.59–0.89;  $P < .001$ )<sup>15,25,30,37-40</sup> but not in the contact aspiration–first approach (OR = 0.75; 95% CI, 0.41–1.38;  $P = .36$ ).<sup>23,37,41</sup> The combined-approach subgroup was not included because only 1 study reported these outcomes (Fig 1C).<sup>26</sup>

### Risk of Bias

The risk of bias was moderate in 13 studies and low in 3 studies (Online Supplemental Data).

## DISCUSSION

Our systematic review and meta-analysis of 5507 patients suggests that the use of a balloon guide catheter increases the odds of achieving the first-pass effect and successful reperfusion and reduces the procedural time, the number of passes, and distal embolization or emboli in a new vascular territory. Furthermore, the use of a balloon guide catheter increases the odds of achieving good functional outcome and reduces the risk of death, without influencing the risk of sICH. This updated review, which includes recent large patient cohort registries, is among the largest meta-analysis on this topic to date.<sup>18,25,26,37,39</sup> Our findings validate the results of previous meta-analyses<sup>20,44</sup> and expand to report the procedural and clinical outcomes according to the first-line endovascular thrombectomy technique.

A longer procedural time is associated with a lower likelihood of a good functional outcome and a higher probability of sICH. Some observed a transition point at 30 minutes when the cumulative rate of good functional outcome drops by 40%.<sup>45</sup> Similar to the results of endovascular thrombectomy workflow analysis studies,<sup>46</sup> our findings show that the use of a balloon guide catheter is associated with a shorter total procedural time. This likely corresponds to fewer passes required and an increased first-pass effect. In accordance with the Trevo Acute Ischemic Stroke (TRACK) Multicenter Registry analysis, high-volume centers use balloon guide catheters most often.<sup>47</sup>

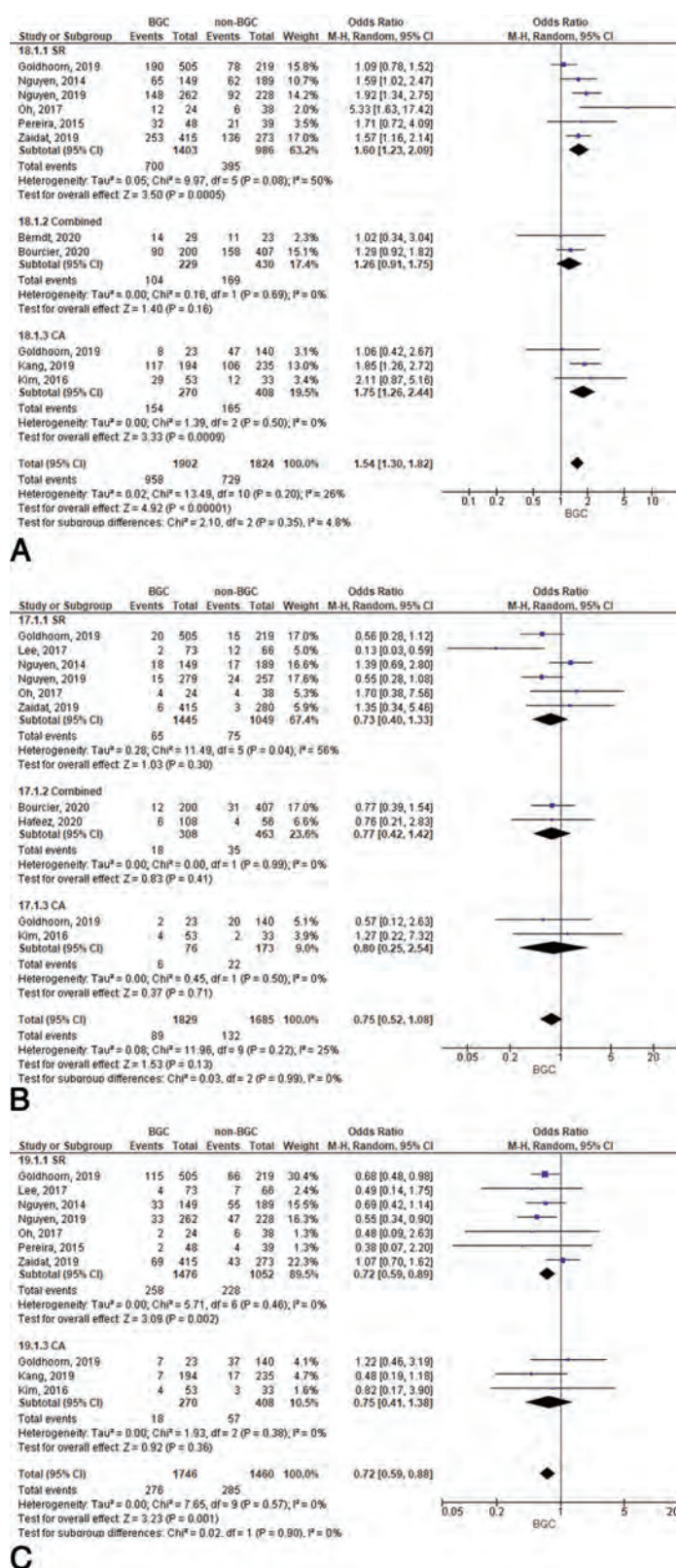


**FIGURE.** Clinical outcomes. This figure is a summary of random effects forest plots showing studies divided into the 3 groups depending on the first-line endovascular thrombectomy technique. A, Good functional outcome at 90 days. B, sICH. C, Mortality at 90 days. SR indicates stent retriever versus combined versus contact aspiration (CA).

Our findings confirmed a reduction in distal clot embolizations, including those to new vascular territories. Previous studies have also demonstrated that the balloon guide catheter reduces clot fragmentation and distal embolic shower and provides more effective revascularization,<sup>48</sup> but this was not reported in previous meta-analyses.<sup>19,20</sup> In vitro studies have also reported that the use of proximal flow control by a balloon guide catheter significantly reduced the formation of large distal emboli with a diameter of  $>1$  mm.<sup>49</sup>

There remains ambiguity over the best first-line endovascular thrombectomy technique (stent retriever, contact aspiration, or combined) when used in conjunction with a balloon guide catheter. For instance, Baek et al<sup>18</sup> analyzed 955 participants and reported that the positive influence of a balloon guide catheter on procedural and clinical outcomes is independent of the first-line treatment technique, whereas Goldhoorn et al<sup>37</sup> reported no difference in the clinical outcome in each stent-retriever and contact-aspiration group, with or without a balloon guide catheter. Bourcier et al<sup>26</sup> also observed no difference between balloon guide catheters and conventional guide catheters when the stent-retriever technique was combined with contact aspiration. The recent Contact Aspiration vs Stent Retriever for Successful Revascularization (ASTER2) trial compared the use of the combined approach versus stent retriever only; both used balloon guide catheters. The authors demonstrated no significant differences in the procedural and functional outcomes, though there was a tendency toward the combined technique.<sup>50,51</sup> Our subgroup analysis suggests that the most significant benefit of a balloon guide catheter is in conjunction with the first-line stent-retriever approach. Balloon guide catheters also improve successful reperfusion rates and good clinical outcomes. However, there is currently insufficient



evidence regarding their use during a combined-approach technique.

Balloon guide catheters have limitations related to their construction: 1) a larger outer diameter requiring larger introductory sheaths, 2) larger aspiration catheters not compatible with most balloon guide catheters, and 3) a relatively more rigid construct rendering endovascular navigation with balloon guide catheter more challenging. However, new balloon guide catheters with larger internal diameters of up to 0.087 inches are able to accommodate large-bore aspiration catheters and can still be used through an 8F sheath.<sup>52,53</sup> Concerns have also been raised about potential groin complications, especially among patients on anti-coagulants or IV-tPA.<sup>17</sup> However, a recent study of 472 patients reported only a 0.4%–0.8% risk of sheath-related groin complications for balloon guide catheters.<sup>54</sup>

### Limitations and Further Directions

None of the included studies were randomized, and most of them were weighted with a moderate risk of bias. Furthermore, the included studies had a high heterogeneity level except for the overall clinical outcomes ( $I^2$  was 30% for good clinical outcome, 28% for sICH, and 0% for mortality).

There were differences in the baseline characteristics of the population. Atrial fibrillation and ICA occlusions were more frequently identified in the balloon guide catheter group. Most interesting, data from the ASTER2 trial suggest better efficacy in a subset of patients with distal ICA occlusions when balloon guide catheters with the combined technique were used.<sup>50,51</sup> Periprocedurally, distal access catheter use and intra-arterial thrombolysis administration were less frequently observed in the balloon guide catheter group (Table 2.) While we extracted the baseline characteristics of the clot location, the studies did not report the outcome measures in these subgroups, precluding direct comparison.

A small number of posterior circulation strokes ( $n = 35$ ) from a single study were included in our meta-analysis.<sup>15</sup> However, it was not possible to extract the outcome measures for this cohort of patients or exclude this cohort from the analysis because the relevant outcomes were not separately reported.

Additional factors that may influence the outcome of endovascular thrombectomy with balloon guide catheter use are its position and the adequacy of the balloon inflation. The latter could not be reliably assessed in the included studies. Jeong et al<sup>55</sup> compared proximal and distal positions of balloon guide catheters in the carotid artery among 102 patients. They reported that a shorter procedural time and higher recanalization rates were associated with a more distal balloon guide catheter position. Another factor is the size and positioning of the stent retriever. The Systematic Evaluation of Patients Treated with Neurothrombectomy Devices for Acute Ischemic Stroke (STRATIS) registry showed that the size of the stent retriever may have a positive influence on successful recanalization rates, regardless of the use of a balloon guide catheter.<sup>56</sup> However, information concerning the size of the stent retriever used was not provided by all studies.

A uniform assessment of emboli in new territories was lacking in most studies, mainly due to the lack of subsequent MR

imaging after the procedure. For example, Schönfeld et al<sup>27</sup> studied 37 patients with successful reperfusion (TICI 2b or higher) following endovascular thrombectomy (with or without a balloon guide catheter) who had subsequent MR imaging with a DWI sequence within 24 hours. They reported that the use of a balloon guide catheter led to a significant reduction in the number and volume of peripheral emboli, with a median number/volume of peripheral emboli of 4.5/287 versus 12/938  $\mu\text{L}$ .<sup>27</sup> However, the assessment of embolic showers in new territories is generally difficult because its definition often varies among studies.

Further randomized trials<sup>57</sup> are needed to evaluate our findings while taking into account other factors such as clot localization and composition and the first-line endovascular thrombectomy technique. While a large proportion of the included studies investigated and highlighted the benefits of balloon guide catheters with stent retrievers, the use of stent retrievers only in modern day endovascular thrombectomy is diminishing. Instead, the combined approach or contact aspiration–only first-line techniques are increasingly adopted in many centers. However, there is a lack of data on the efficacy of balloon guide catheter use in both groups, which are under-represented in our study.

### CONCLUSIONS

Current literature and our meta-analysis confirm the benefits of balloon guide catheters in achieving shorter total procedural times. The balloon guide catheter improves the successful reperfusion rate and good clinical outcomes when used during first-line contact aspiration or stent retrieval but not with a combined approach.

Disclosures: Mayank Goyal—UNRELATED: Consultancy: Stryker, Medtronic, MicroVention, Mentice.

### REFERENCES

1. Goyal M, Menon BK, van Zwam WH, et al. **Endovascular thrombectomy after large-vessel ischaemic stroke: a meta-analysis of individual patient data from five randomised trials.** *Lancet* 2016;387:1723–31 CrossRef Medline
2. Powers WJ, Rabinstein AA, Ackerson T, et al. **Guidelines for the Early Management of Patients with Acute Ischemic Stroke: 2019 update to the 2018 Guidelines for the Early Management of Acute Ischemic Stroke—a guideline for healthcare professionals from the American Heart Association/American Stroke Association.** *Stroke* 2019;50:E344–418 CrossRef Medline
3. Turc G, Bhogal P, Fischer U, et al. **European Stroke Organisation (ESO) – European Society for Minimally Invasive Neurological Therapy (ESMINT) Guidelines on Mechanical Thrombectomy in Acute Ischaemic Stroke Endorsed by Stroke Alliance for Europe (SAFE).** *Eur Stroke J* 2019;4:6–12 CrossRef Medline
4. Deb-Chatterji M, Pinnschmidt H, Flottmann F, et al. **Stroke patients treated by thrombectomy in real life differ from cohorts of the clinical trials: a prospective observational study.** *BMC Neurol* 2020;20:81 CrossRef Medline
5. Ozdemir O, Giray S, Arlier Z, et al. **Predictors of a good outcome after endovascular stroke treatment with stent retrievers.** *Scientific World Journal* 2015;2015:403726 CrossRef Medline
6. Yoon W, Kim SK, Park MS, et al. **Predictive factors for good outcome and mortality after stent-retriever thrombectomy in patients with acute anterior circulation stroke.** *J Stroke* 2017;19:97–103 CrossRef Medline

7. Munich SA, Vakharia K, Levy EI. **Overview of mechanical thrombectomy techniques.** *Clin Neurosurg* 2019;85:S60–67 CrossRef Medline
8. Phan K, Maingard J, Kok HK, et al. **Contact aspiration versus stent-retriever thrombectomy for distal middle cerebral artery occlusions in acute ischemic stroke: meta-analysis.** *Neurointervention* 2018;13:100–09 CrossRef Medline
9. Primiani CT, Vicente AC, Brannick MT, et al. **Direct aspiration versus stent retriever thrombectomy for acute stroke: a systematic review and meta-analysis in 9127 patients.** *J Stroke Cerebrovasc Dis* 2019;28:1329–37 CrossRef Medline
10. Qin C, Shang K, Xu S-B, et al. **Efficacy and safety of direct aspiration versus stent-retriever for recanalization in acute cerebral infarction.** *Medicine (Baltimore)* 2018;97:e12770 CrossRef Medline
11. Ye G, Lu J, Qi P, et al. **Firstline a direct aspiration first pass technique versus first-line stent retriever for acute basilar artery occlusion: a systematic review and meta-analysis.** *J Neurointerv Surg* 2019;11:740–46 CrossRef Medline
12. Zafar M, Mussa M, Memon RS, et al. **Aspiration thrombectomy versus stent retriever thrombectomy alone for acute ischemic stroke: a systematic review and meta-analysis.** *Cureus* 2020;12:1–15 CrossRef Medline
13. Maus V, Behme D, Kabbasch C, et al. **Maximizing first-pass complete reperfusion with SAVE.** *Clin Neuroradiol* 2018;28:327–38 CrossRef Medline
14. McTaggart RA, Tung EL, Yaghi S, et al. **Continuous aspiration prior to intracranial vascular embolectomy (CAPTIVE): a technique which improves outcomes.** *J Neurointerv Surg* 2017;9:1154–59 CrossRef Medline
15. Nguyen TN, Malisch T, Castonguay AC, et al. **Balloon guide catheter improves revascularization and clinical outcomes with the Solitaire device: analysis of the North American Solitaire Acute Stroke Registry.** *Stroke* 2014;45:141–45 CrossRef Medline
16. Velasco A, Buerke B, Stracke CP, et al. **Comparison of a balloon guide catheter and a non-balloon guide catheter for mechanical thrombectomy.** *Radiology* 2016;280:169–76 CrossRef Medline
17. Chueh JY, Kang DH, Kim BM, et al. **Role of balloon guide catheter in modern endovascular thrombectomy.** *J Korean Neurosurg Soc* 2020;63:14–25 CrossRef Medline
18. Baek JH, Kim BM, Kang DH, et al. **Balloon guide catheter is beneficial in endovascular treatment regardless of mechanical recanalization modality.** *Stroke* 2019;50:1490–96 CrossRef Medline
19. Brinjikji W, Murad H, Fiorella D, et al. **Impact of balloon guide catheter on technical and clinical outcomes: a systematic review and meta-analysis.** *J Neurointerv Surg* 2018;10:335–39 CrossRef Medline
20. Ahn JH, Cho SS, Kim SE, et al. **The effects of balloon-guide catheters on outcomes after mechanical thrombectomy in acute ischemic strokes: a meta-analysis.** *J Korean Neurosurg Soc* 2019;62:389–97 CrossRef Medline
21. Hutton B, Salanti G, Caldwell DM, et al. **The PRISMA extension statement for reporting of systematic reviews incorporating network meta-analyses of health care interventions: checklist and explanations.** *Ann Intern Med* 2015;162:777 CrossRef Medline
22. Liebeskind DS, Bracad S, Guillemin F, et al. **ETICI reperfusion: defining success in endovascular stroke therapy.** *J Neurointerv Surg* 2019;11:433–38 CrossRef Medline
23. Kang DH, Kim BM, Heo JH, et al. **Effect of balloon guide catheter utilization on contact aspiration thrombectomy.** *J Neurosurg* 2019;131:1494–500 CrossRef Medline
24. Maegerlein C, Mönch S, Boeckh-Behrens T, et al. **PROTECT: PProximal balloon Occlusion ToGether with direCt Thrombus aspiration during stent retriever thrombectomy—evaluation of a double embolic protection approach in endovascular stroke treatment.** *J Neurointerv Surg* 2018;10:751–55 CrossRef Medline
25. Zaidat OO, Mueller-Kronast NH, Hassan AE, et al. **Impact of balloon guide catheter use on clinical and angiographic outcomes in the STRATIS stroke thrombectomy registry.** *Stroke* 2019;50:697–704 CrossRef Medline
26. Bourcier R, Marnat G, Labreuche J, et al. **Balloon guide catheter is not superior to conventional guide catheter when stent retriever and contact aspiration are combined for stroke treatment.** *Neurosurgery* 2020;88:E88–90 CrossRef Medline
27. Schönfeld MH, Kabiri R, Kniep HC, et al. **Effect of balloon guide catheter utilization on the incidence of sub-angiographic peripheral emboli on high-resolution DWI after thrombectomy: a prospective observational study.** *Front Neurol* 2020;11:1–8 CrossRef Medline
28. Hafeez MU, Kan P, Srivatsan A, et al. **Comparison of first-pass efficacy among four mechanical thrombectomy techniques: a single-center experience.** *World Neurosurg* 2020;144:e533–40 CrossRef Medline
29. Johnson CO, Nguyen M, Roth GA, et al. **Global, regional, and national burden of stroke, 1990–2016: a systematic analysis for the Global Burden of Disease Study 2016.** *Lancet Neurol* 2019;18:439–58 CrossRef Medline
30. Pereira V, Siddiqui A, Jovin T, et al. **Role of balloon guiding catheter in Mechanical Thrombectomy Using Stent Retrievers subgroup analysis of SWIFT-PRIME.** *J Neurointerv Surg* 2015;7:A30 CrossRef
31. Higgins JP, Thompson SG, Deeks JJ, et al. **Measuring inconsistency in meta-analyses Testing for heterogeneity.** *BMJ* 2003;327:557–60 CrossRef Medline
32. Higgins JPT, Thompson SG. **Quantifying heterogeneity in a meta-analysis.** *Stat Med* 2002;21:1539–58 [Database] CrossRef Medline
33. Sterne JA, Hernán MA, Reeves BC, et al. **ROBINS-I: a tool for assessing risk of bias in non-randomised studies of interventions.** *BMJ* 2016;355:4919 CrossRef Medline
34. McGuinness LA, Higgins JP. **Risk-of-bias VISualization (ROBVIS): an R package and Shiny web app for visualizing risk-of-bias assessments.** *Res Synth Methods* 2021;12:55–61 CrossRef Medline
35. Cochrane. **Revman.** <https://training.cochrane.org/online-learning/core-software-cochrane-reviews/revman>. Accessed December 15, 2020
36. Berndt MT, Goyal M, Psychogios M, et al. **Endovascular stroke treatment using balloon guide catheters may reduce penumbral tissue damage and improve long-term outcome.** *Eur Radiol* 2021;31:2191–98 CrossRef Medline
37. Goldhoorn RJ, Duijsters N, Majoie CB, et al. **MR CLEAN Registry Investigators. Balloon guide catheter in endovascular treatment for acute ischemic stroke: results from the MR CLEAN Registry.** *J Vasc Interv Radiol* 2019;30:1759–64 CrossRef Medline
38. Lee DH, Sung JH, Kim SU, et al. **Effective use of balloon guide catheters in reducing incidence of mechanical thrombectomy related distal embolization.** *Acta Neurochir (Wien)* 2017;159:1671–77 CrossRef Medline
39. Nguyen TN, Castonguay AC, Nogueira RG, et al. **Effect of balloon guide catheter on clinical outcomes and reperfusion in Trevo thrombectomy.** *J Neurointerv Surg* 2019;11:861–65 CrossRef Medline
40. Oh JS, Yoon SM, Shim JJ, et al. **Efficacy of balloon-guiding catheter for mechanical thrombectomy in patients with anterior circulation ischemic stroke.** *J Korean Neurosurg Soc* 2017;60:155–56 CrossRef Medline
41. Kim YS, Kang DH, Hwang YH, et al. **Efficacy of proximal aspiration thrombectomy for using balloon-tipped guide catheter in acute intracranial internal carotid artery occlusion.** *J Korean Neurosurg Soc* 2016;59:379–84 CrossRef Medline
42. Di Maria F, Kyheng M, Consoli A, et al. **ETIS Investigators. Identifying the predictors of first-pass effect and its influence on clinical outcome in the setting of endovascular thrombectomy for acute ischemic stroke: results from a multicentric prospective registry.** *Int J Stroke* 2021;16:20–28 CrossRef Medline
43. Zaidat OO, Castonguay AC, Linfante I, et al. **First pass effect: a new measure for stroke thrombectomy devices.** *Stroke* 2018;49:660–66 CrossRef Medline
44. Brinjikji W, Starke RM, Murad MH, et al. **Impact of balloon guide catheter on technical and clinical outcomes: a systematic review and meta-analysis.** *J Neurointerv Surg* 2018;10:335–39 CrossRef Medline

45. Alawieh A, Vargas J, Fargen KM, et al. **Impact of procedure time on outcomes of thrombectomy for stroke.** *J Am Coll Cardiol* 2019;73:879–90 CrossRef Medline
46. Goyal M, Jadhav AP, Bonafe A, et al. SWIFT PRIME investigators. **Analysis of workflow and time to treatment and the effects on outcome in endovascular treatment of acute ischemic stroke: results from the SWIFT PRIME randomized controlled trial.** *Radiology* 2016;279:888–97 CrossRef Medline
47. Nogueira RG, Haussen DC, Castonguay A, et al. **Site experience and outcomes in the Trevo Acute Ischemic Stroke (TRACK) multicenter registry: higher volumes translate in better outcomes.** *Stroke* 2019;50:2455–60 CrossRef Medline
48. Blanc R, Escalard S, Baharvadhath H, et al. **Recent advances in devices for mechanical thrombectomy.** *Expert Rev Med Devices* 2020;17:697–706 CrossRef Medline
49. Chueh JY, Kühn AL, Puri AS, et al. **Reduction in distal emboli with proximal flow control during mechanical thrombectomy: a quantitative in vitro study.** *Stroke* 2013;44:1396–401 CrossRef Medline
50. Lapergue B, Blanc R, Labreuche J. **Combined use of contact aspiration and stent retriever technique versus stent retriever alone for recanalisation in acute cerebral infarction: ASTER 2 combined.** *J Neurointerv Surg* 2020;12:471–76 CrossRef Medline
51. Lapergue B, Fischer UR, . **Looking at the ASTER 2 Trial Results at ESOC 2019.** **YouTube.** 2019. [https://www.youtube.com/watch?v=h5B9nZ\\_wePw](https://www.youtube.com/watch?v=h5B9nZ_wePw). Accessed January 03, 2021
52. FDA. **BOBBY Balloon Guide Catheter. Premarket Notification Results.** 2020. <https://www.accessdata.fda.gov/scripts/cdrh/cfdocs/cfpmn/pmn.cfm?ID=K193607>. Accessed January 03, 2021
53. Fiorella. **Walrus 087 Balloon Guide Catheter System; Premarket Notification Results.** 2019. <https://www.youtube.com/watch?v=fZOtqwVGsEw>. Accessed January 03, 2021
54. Shah VA, Martin CO, Hawkins AM, et al. **Groin complications in endovascular mechanical thrombectomy for acute ischemic stroke: a 10-year single center experience.** *J Neurointerv Surg* 2016;8:568–70 CrossRef Medline
55. Jeong DE, Kim JW, Kim BM, et al. **Impact of balloon-guiding catheter location on recanalization in patients with acute stroke treated by mechanical thrombectomy.** *AJNR Am J Neuroradiol* 2019;40:840–44 CrossRef Medline
56. Zaidat OO, Haussen DC, Hassan AE, et al. **Impact of stent retriever size on clinical and angiographic outcomes in the STRATIS stroke thrombectomy registry.** *Stroke* 2019;50:441–47 CrossRef Medline
57. **Efficacy and Safety of Balloon Guide Catheter in Mechanical Thrombectomy Patients.** ESCAPE. <https://clinicaltrials.gov/ct2/show/NCT03754738>. Accessed January 03, 2021



# Infarct Growth despite Successful Endovascular Reperfusion in Acute Ischemic Stroke: A Meta-analysis

F. Bala, J. Ospel, B. Mulpur, B.J. Kim, J. Yoo, B.K. Menon, M. Goyal, C. Federau, S.-I. Sohn, M.S. Hussain, and M.A. Almekhlafi



## ABSTRACT

**BACKGROUND:** Infarct volume inversely correlates with good recovery in stroke. The magnitude and predictors of infarct growth despite successful reperfusion via endovascular treatment are not known.

**PURPOSE:** We aimed to summarize the extent of infarct growth in patients with acute stroke who achieved successful reperfusion (TICI 2b–3) after endovascular treatment.

**DATA SOURCES:** We performed a systematic review and meta-analysis by searching MEDLINE and Google Scholar for articles published up to October 31, 2020.

**STUDY SELECTION:** Studies of >10 patients reporting baseline and post-endovascular treatment infarct volumes on MR imaging were included. Only patients with TICI 2b–3 were included. We calculated infarct growth at a study level as the difference between baseline and follow-up MR imaging infarct volumes.

**DATA ANALYSIS:** Our search yielded 345 studies, and we included 10 studies reporting on 973 patients having undergone endovascular treatment who achieved successful reperfusion.

**DATA SYNTHESIS:** The mean baseline infarct volume was 19.5 mL, while the mean final infarct volume was 37.5 mL. A TICI 2b reperfusion grade was achieved in 24% of patients, and TICI 2c or 3 in 76%. The pooled mean infarct growth was 14.8 mL (95% CI, 7.9–21.7 mL). Meta-regression showed higher infarct growth in studies that reported higher baseline infarct volumes, higher rates of incomplete reperfusion (modified TICI 2b), and longer onset-to-reperfusion times.

**LIMITATIONS:** Significant heterogeneity among studies was noted and might be driven by the difference in infarct growth between early- and late-treatment studies.

**CONCLUSIONS:** These results suggest considerable infarct growth despite successful endovascular treatment reperfusion and call for a faster workflow and the need for specific therapies to limit infarct growth.

**ABBREVIATIONS:** EVT = endovascular treatment; mTICI = modified TICI

Final infarct volume is a known predictor of clinical outcome in acute ischemic stroke: The larger the infarcted area on follow-up imaging, the worse the outcome is.<sup>1–3</sup> The goal of reperfusion therapies like intravenous alteplase and endovascular

treatment (EVT) is to minimize infarct progression as much as possible, thereby ultimately improving clinical outcomes. Arterial occlusion leads to hypoperfusion of downstream brain tissue. The area of irreversible damage will grow unless recanalization is achieved and normal blood flow is restored. Restoration of blood flow would, in theory, arrest infarct growth. It is, however, increasingly recognized that infarcted brain keeps growing even after blood flow has been restored; this is reperfusion injury.<sup>4</sup> To

Received February 11, 2021; accepted after revision March 25.

From the Calgary Stroke Program (F.B., J.O., B.K.M., M.G., M.A.A.), Departments of Clinical Neurosciences (F.B., B.K.M., M.A.A.), and Radiology (B.K.M., M.A.A.), University of Calgary, Calgary, Alberta, Canada; Department of Neuroradiology, Clinic of Radiology, and Nuclear Medicine (J.O.), University Hospital Basel, Basel, Switzerland; Cerebrovascular Center and Department of Neurology (B.M., M.S.H.), Neurological Institute, Cleveland Clinic, Cleveland, Ohio; Department of Neurology and Cerebrovascular Center (B.J.K.), Seoul National University Bundang Hospital, Seongnam-si, Gyeonggi-do, Korea; Yonsei University College of Medicine (J.Y.), Yonjin Severance Hospital, Yonjin, Korea; Institute for Biomedical Engineering (C.F.), Swiss Federal Institute of Technology in Zürich, Zürich, Switzerland; and Department of Neurology (S.-I.S.), Keimyung University School of Medicine, Daegu, Korea.

Please address correspondence to Mohammed Almekhlafi, MD, MSc, FRCP, 1403 29th St NW, University of Calgary, Calgary, AB, T2N 2T9, Canada; e-mail: mohammed.almekhlafi@ucalgary.ca; @AlmekhlafiMa

Indicates article with online supplemental data.  
<http://dx.doi.org/10.3174/ajnr.A7177>

date, it is not entirely clear to what extent infarct growth occurs after reperfusion because serial brain imaging after reperfusion is not feasible in clinical routine.<sup>5,6</sup> Quantifying infarct growth following successful reperfusion would allow a better understanding of these different mechanisms of infarct growth and provide valuable information for studies on neuroprotective agents that aim to reduce infarct growth.

Thus, we aimed to summarize published evidence on the extent of infarct growth measured on MR imaging from baseline imaging to posttreatment follow-up imaging in patients with acute ischemic stroke who achieved successful reperfusion after EVT.

## MATERIALS AND METHODS

### Search Strategy

We conducted a systematic review and meta-analysis according to the Preferred Reporting Items for Systematic Reviews and Meta-Analyses (PRISMA) guidelines.<sup>7</sup> Using MEDLINE and the Google Scholar data base, we reviewed clinical studies published in full length from inception to April 2020 and updated on October 31, 2020. Keywords included “stroke” AND (“thrombectomy” OR “endovascular” OR “aspiration” OR “stent-retriever” or “recanalization”) AND (“infarct” OR “core” OR “lesion”) AND (“growth” OR “volume” OR “change”). Bibliographies of key articles were reviewed to identify additional relevant publications.

### Study Selection

Studies were included if they enrolled  $\geq 10$  patients with acute ischemic stroke, were published in English, and reported infarct volume on MR imaging performed at baseline (before or within 12 hours post-EVT) and after EVT ( $\geq 24$  hours) according to endovascular reperfusion quality using the modified TIC1 (mTICI) score. Only patients with mTICI 2b–3 were eligible for inclusion in this analysis. We included studies that reported baseline volumes on early post-EVT MR imaging because we hypothesized that infarct growth would be minimal between pre- and immediate post-EVT MR imaging in patients who achieved rapid and successful reperfusion.

Three reviewers (F.B., J.O., M.A.A.) independently screened the identified abstracts and jointly extracted the following information for each study: first author's name, year of publication, study design (prospective versus retrospective), number of patients, number of male/female patients, mean/median age, median NIHSS score, proportion of occlusion of the first segment of the middle cerebral artery (M1), proportion of tandem occlusion, treatment with intravenous alteplase, reperfusion quality (final mTICI score on the last angiography run), and final infarct volume at baseline and on follow-up imaging. We directly contacted the corresponding authors of the studies that did not report complete details.

### Outcome

The primary outcome of this analysis was the assessment of infarct growth, defined as infarct volume on MR imaging follow-up minus infarct volume at baseline MR imaging in patients with successful reperfusion (mTICI 2b–3).

### Statistical Analysis

The estimates of mean infarct growth (in milliliters) were calculated from the baseline and final mean infarct volumes and pooled across all studies using random effects analysis. If the mean volumes were not reported, we obtained them directly from the study authors or calculated their closest approximation using the methods of Luo et al<sup>8</sup> and Shi et al.<sup>9</sup> In addition, percentage infarct volume change from baseline was calculated  $[(\text{final baseline} / \text{baseline}) \times 100]$ .

Subgroup and sensitivity analyses were performed for studies according to the time of baseline imaging in relation to the start of EVT for patients with complete reperfusion (mTICI 3) and for patients with onset-to-reperfusion  $\leq 6$  hours versus  $> 6$  hours.

Heterogeneity among studies was assessed using the  $I^2$  index. Meta-regression models were fitted to explore sources of heterogeneity and associations of infarct growth with baseline infarct volume, speed of treatment, completeness of reperfusion, and intravenous tPA use.

Publication bias was assessed with the Egger test and illustrated with a funnel plot. Two-tailed  $P$  values  $< .05$  were considered statistically significant. Statistical analysis was conducted in STATA MP 15.1 (StataCorp).

**Risk of Bias and Quality Assessment.** The risk of bias was assessed by 2 authors independently using the Risk Of Bias in Non-Randomized Studies of Interventions assessment tool. In case of disagreement, a consensus was reached.<sup>10,11</sup>

The tool addresses preintervention (confounding and selection bias), at-intervention (misclassification of interventions), and postintervention features of the study, which cover biases due to deviations from intended interventions, missing data, measurement of outcomes, and selection of the reported result. The risk of bias judgment for each bias domain and for the overall risk of bias was low, moderate, serious, or critical risk of bias, with a supplementary option of “no information.”<sup>10,11</sup>

## RESULTS

### Study and Participant Characteristics

A total of 10 studies ( $n = 973$  patients) were identified.<sup>6, 12–20</sup> The Online Supplemental Data show the selection flow chart.

Three studies were prospective and 7 were retrospective analyses of prospectively collected data (Online Supplemental Data). Six of the included studies (60%) were multicenter. The mean age was 68 years, and the median NIHSS score was 16. Women represented 48% of participants. All patients had anterior circulation strokes with occlusion of the terminal ICA and/or MCA. Isolated MCA occlusion was described in 54% of cases (reported in 8 studies). Tandem cervical occlusion was noted in 15% of patients (reported in 4 studies). The mean time from symptom onset to baseline imaging was 246.3 minutes (reported in 7 studies).

### Treatment Characteristics

Intravenous tPA was administered in 46% of patients. All patients in this analysis received endovascular therapy and achieved successful reperfusion (mTICI 2b–3 scores). Complete or near-complete reperfusion (mTICI 3 or expanded TIC1 2c, 3) was achieved in 76% of patients. Three studies reported  $\geq 90$  reperfusion status

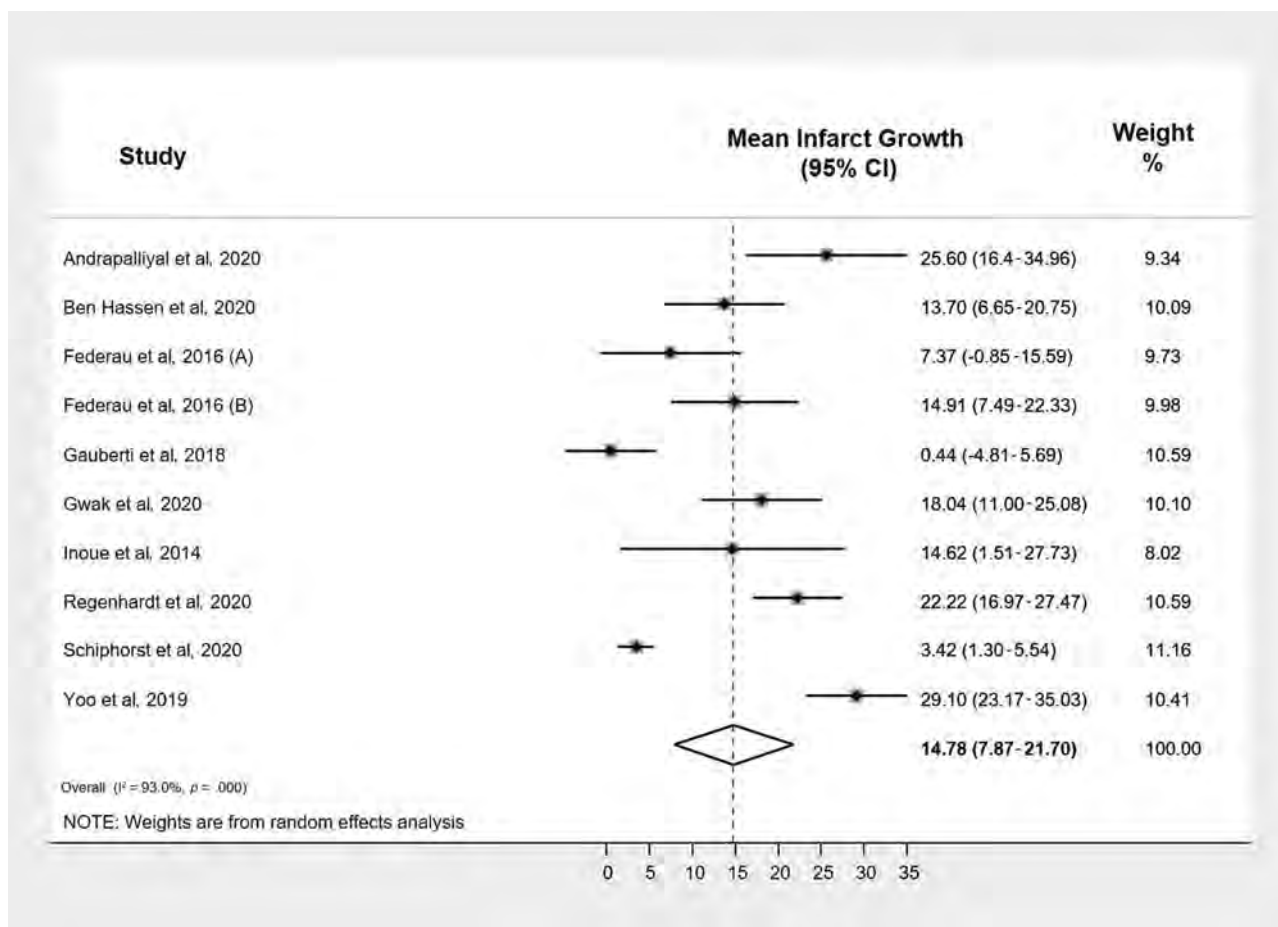


**FIG 1.** Forest plot with a random effects model showing the overall mean infarct growth.

on perfusion-weighted imaging performed post-EVT. The mean time from symptom onset to the start of the endovascular procedure was 295 minutes (reported in 8 studies).

#### **Times of Baseline and Follow-up Imaging Assessments**

All included studies assessed infarct volumes (baseline and follow-up) on diffusion-weighted MR imaging except 1 study<sup>14</sup> that used 5-day follow-up FLAIR to estimate the final infarct volume. Baseline volumes were measured on MR imaging performed before the EVT procedures in all studies except 2 that used early post-EVT (within 12 hours) for baseline infarct volumes. The median time from onset to imaging was 135 minutes in the studies that used pre-EVT scans versus 714 minutes for studies with early post-EVT studies. Final infarct volumes were assessed at a median of 24 hours post-EVT. Three studies used 5-day follow-up MR imaging, while 1 study used 2-week follow-up for final infarct volumes.

**Meta-analysis of Infarct Growth and Sensitivity Analyses.** The mean baseline infarct volume was 19.5 (SD, 7) mL, while the mean final infarct volume was 37.5 (SD, 15.4) mL. The pooled mean infarct growth was 14.8 mL (95% CI, 7.9–21.7 mL) (Fig 1). There was no difference in the mean infarct growth between the studies that performed the follow-up MR imaging in the first 24 hours (18.8 mL; 95% CI, 14.7–22.8 mL) versus in the

first 5 days post-EVT (19.7 mL; 95% CI, 15.6–23.7 mL) versus within 2 weeks (18.0 mL; 95% CI, 11.0–25.1 mL).

Significant heterogeneity existed among the included studies ( $I^2 = 93\%$ ). However, subgroup analyses according to the onset-to-reperfusion time suggest that the heterogeneity is driven by the variability of infarct growth in the early-treatment studies (onset to reperfusion <6 hours) (pooled mean growth: 9.7 mL; 95% CI, 4.3–15.0 mL) compared with those with an onset-to-reperfusion time of  $\geq 6$  hours (pooled mean growth: 25.4 mL; 95% CI, 20.9–30.0 mL) (Fig 2).

When the analysis was restricted to studies that included only patients with complete reperfusion (reperfusion  $\geq 90\%$ ;  $n = 6$ ), the pooled mean infarct growth was relatively lower than the overall pooled growth at 11.6 mL (95% CI, 5.3–17.8 mL). In the studies that assessed final infarct volumes within 24 hours post-EVT, the pooled mean infarct growth was not notably different, with a pooled mean infarct growth of 13.3 mL (95% CI, 2.3–24.3 mL). On the basis of the time of baseline MR imaging, mean infarct growth did not significantly differ between studies reporting initial infarct volume on MR imaging performed immediately post-EVT versus those with pre-EVT MR imaging ( $P = .6$ ).

The percentage infarct growth from baseline also varied among the included studies (pooled mean growth: 80.4%; 95% CI, 57.8%–103.0%) and was lower in the studies in the early (<6 hours) treatment window (pooled mean growth: 69.4%; 95%



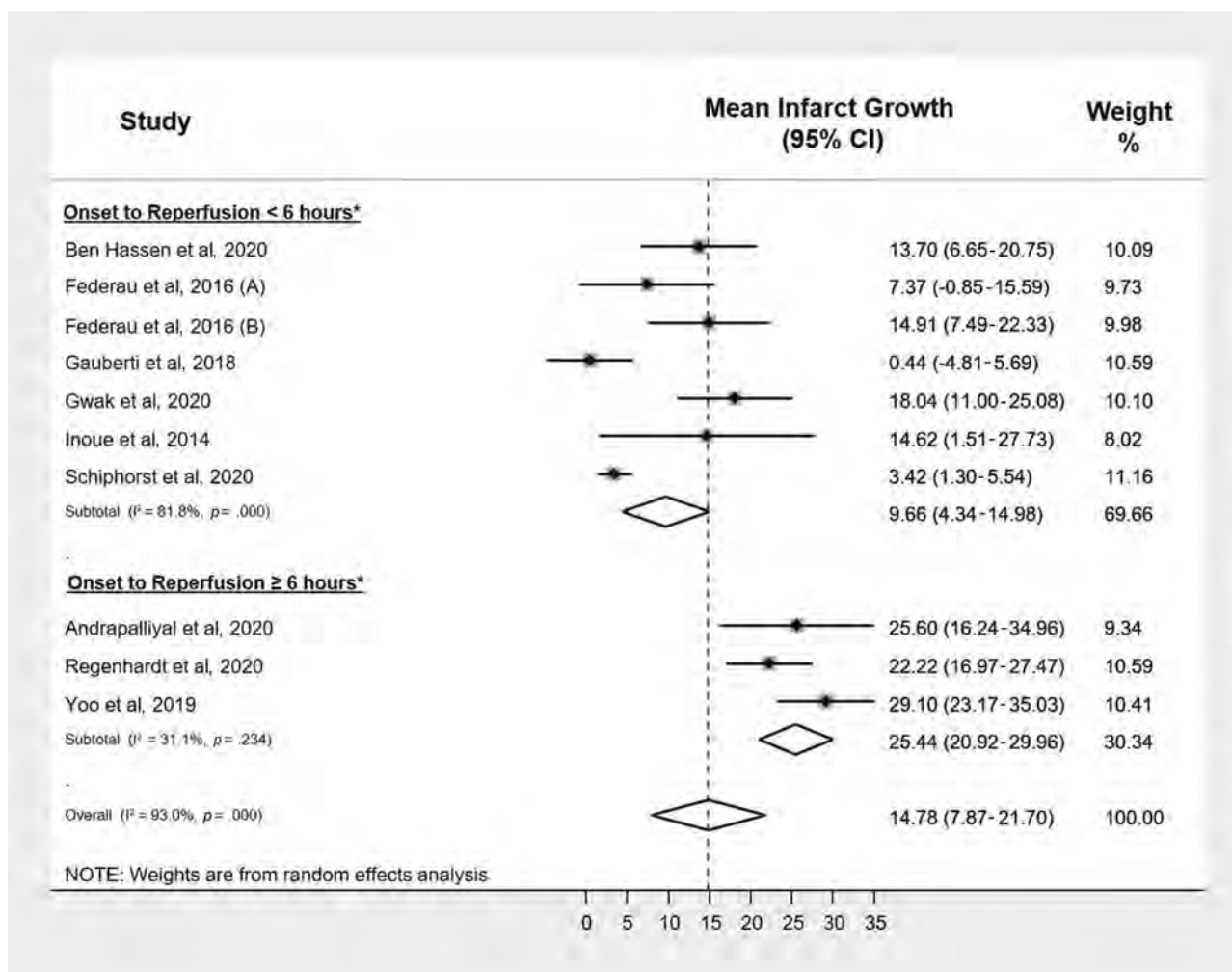


**FIG 2.** Forest plot with a random effects model for mean infarct volume according to dichotomized onset-to-reperfusion time (<6 versus  $\geq 6$  hours).

CI, 41.2%–97.6%) versus studies with onset to reperfusion of  $\geq 6$  hours (pooled mean growth: 107.8%; 95% CI, 78.6%–137.0%).

### Meta-regression

To assess the potential effects of various predictors on infarct growth, we conducted a series of random effects meta-regression analyses. These showed a significant association between the pooled mean infarct growth and the baseline infarct volume (coefficient = 1.02; 95% CI, 0.2–1.9;  $P = .022$ ), indicating increasing infarct growth in studies with higher baseline infarct volumes (Fig 3).

There was a higher mean infarct growth in the studies that reported higher proportions of patients with incomplete reperfusion (mTICI 2b) (coefficient = 0.22; 95% CI, 0.1–0.4;  $P = .019$ ), while studies with higher complete reperfusion (mTICI 3 or  $\geq 90\%$  reperfusion) reported lower mean infarct growth (coefficient = 0.21; 95% CI,  $-0.4$  to  $-0.03$ ;  $P = .026$ ). Similarly, the mean infarct growth increased in the studies that reported longer onset-to-reperfusion times (coefficient = 0.1; 95% CI, 0.01–0.2;  $P = .028$ ). Other factors such as onset-to-imaging time and the use of intravenous tPA did not influence infarct growth in the included studies.

**Study Quality and Risk of Bias.** The quality of included studies ranged between moderate and high (Online Supplemental Data).

Testing for publication bias showed significant small-study effects (Egger statistic,  $P = .045$ ). The funnel plot also suggests skewing of studies, indicative of publication bias toward reporting higher mean infarct growth (Online Supplemental Data).

### DISCUSSION

We summarized available estimates of infarct growth despite successful endovascular reperfusion in patients with acute stroke. Our findings suggest that ischemic stroke evolves despite successful reperfusion. The degree of infarct growth appears to positively correlate with the initial stroke volume and negatively with the completeness and speed of reperfusion. The observed heterogeneity among the included studies was partially explained by the difference in the onset-to-reperfusion times.

In a pooled individual patient data meta-analysis of 7 randomized clinical trials, reduction of final infarct volume explained only 12% of the treatment effect of EVT.<sup>21</sup> Our finding of continued infarct growth despite successful recanalization might be 1 explanation for this phenomenon. Possible mechanisms of infarct growth

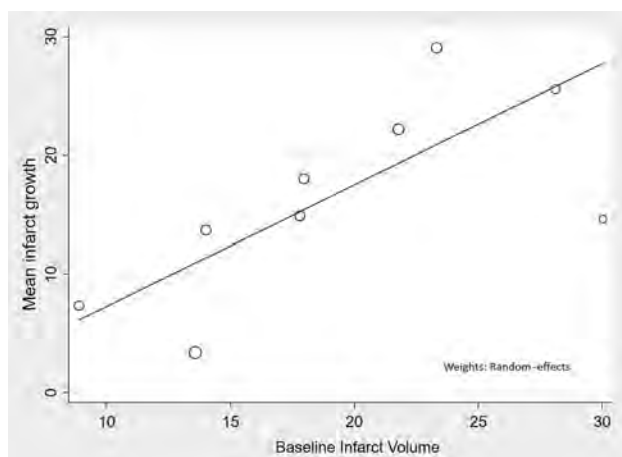


**FIG 3.** The relationship between infarct growth and baseline infarct volume using meta-regression analysis.

include ischemic reperfusion injury, overestimation of final infarct due to edema, progression of infarction due to delays or failure to achieve complete reperfusion, or vascular reocclusion post-EVT. Ischemic reperfusion injury is thought to result from numerous processes, including endothelium activation, oxidative stress, inflammatory responses causing leukocyte infiltration, platelet activation, and blood-brain barrier breakdown, engendering apoptosis, brain edema, and hemorrhagic transformation.<sup>22,23</sup> While the restoration of blood flow mitigates hypoxia, subsequent irreversible cell death might still occur. This mechanism plays an important role in experimental stroke models,<sup>24,25</sup> despite discrepant results between animal models and human studies.<sup>26,27</sup> Our findings are in line with the results of a serial MR imaging study after endovascular treatment that described secondary infarct growth despite good recanalization.<sup>28</sup>

Infarct growth may be biased by brain edema, leading to the overestimation of the final infarct volume.<sup>29</sup> A recent study of Harston et al<sup>30</sup> found that edema was responsible for 20% and 36% of lesion expansion at 24 hours and 1 week after acute stroke, respectively. Vasogenic edema occurs because of blood-brain barrier breakdown and may lead to hemorrhagic transformation.<sup>31</sup> Recently, net water uptake was described on CT to discriminate between infarct lesion and edema.<sup>32</sup> Results showed that edema-corrected volumes of early follow-up imaging were in agreement with the true final infarct volume.<sup>33</sup> Another study by the same group reinforced this view and found that infarct volume was overestimated within the first 24 hours owing to edema.<sup>34</sup> Therefore, therapies targeting cerebral edema before reperfusion could be a potential neuroprotective strategy to slow down infarct growth postreperfusion in patients with large-vessel occlusion.

Successful angiographic reperfusion encompasses TICI 2b, TICI 2c, and TICI 3 grades. However, TICI 2c and 3 reperfusion are associated with better outcome than TICI 2b reperfusion.<sup>35</sup> The area of infarct in patients with TICI 2b may continue to grow after EVT. Several studies reported reduced infarct growth in patients with TICI 2c and 3 compared with TICI 2b reperfusion; this finding was confirmed by our analysis.<sup>36,37</sup> Early reocclusion is an infrequent event, with a prevalence estimated between 2% and 11%.<sup>38,39</sup> However, it should still be taken into

account when explaining the infarct growth after endovascular treatment. This has been demonstrated by Santana et al,<sup>40</sup> who found that reocclusion is associated with an increased infarct growth (adjusted OR = 8.5; 95% CI, 2.04–34.70). Similarly, distal embolization and infarction in new territory can contribute to the infarct growth.<sup>41,42</sup>

### Potential Strategies to Slow Down Infarct Growth

Our analysis confirms the need for therapies to limit the infarct expansion after successful endovascular reperfusion and improve the clinical outcomes of these patients. Strategies targeting the possible pathways leading to infarct growth have been described, including slowing down the ischemic reperfusion process and/or enhancing the collateral blood flow. Novel approaches have demonstrated the ability to enhance collateral blood flow, including sphenopalatine ganglion stimulation and remote ischemic conditioning.<sup>43–45</sup>

Some agents (nerinetide and uric acid) showed encouraging results in large clinical trials of patients with acute stroke treated by reperfusion therapy.<sup>46,47</sup> In addition, therapeutic hypothermia has shown promising results in reducing infarct volume and, therefore, improving clinical outcome.<sup>48</sup> A recent study of intra-arterial selective cooling infusion showed a lower average final infarct volume (63.7 [SD, 31.8] mL) compared with controls (77.9 [SD, 44.7] mL) ( $P = .038$ ).<sup>49</sup>

### Limitations

Our analysis has several limitations. First, we did not include studies that used CT to estimate the initial and/or final stroke volumes; however, it is well-known that MR imaging is more accurate than CT for infarct detection.<sup>50</sup> Second, we used aggregate patient data, which may lead to ecologic bias. Third, the collateral status was not always available in the included studies, and the mean baseline infarct volume in the included studies was relatively low; therefore, our results might not be generalizable to patients with large baseline volumes. Fourth, serial imaging was not available in the included studies, thus, raising the possibility that infarct growth noted in these studies could have happened during the time from baseline imaging to reperfusion. Fifth, not all covariables were reported in the included studies. Thus, we were unable to account for some differences in unreported confounders, which may impact some of our results of analyses. Sixth, the definition of infarcted-versus-noninfarcted tissue on MR imaging might be less accurate owing to the high variability of interindividual tissue vulnerability and to selective neuronal loss.<sup>51</sup> Recently the term “severely ischemic tissue of uncertain viability” was introduced to replace the erstwhile “ischemic core” to account for its uncertainty in determining tissue state.<sup>52</sup>

### CONCLUSIONS

This meta-analysis reported substantial infarct growth in patients with acute stroke despite successful reperfusion after EVT. Patients with low baseline infarct volume, those who achieve fast complete or near-complete reperfusion, and those presenting in the early time window had lower infarct growth. Continuous

effort is needed to improve treatment workflow and to develop therapies that aim to reduce infarct growth postreperfusion.

Disclosures: Fouzi Bala—UNRELATED: Grants/Grants Pending: Société Française de Neuroradiologie and Société Française de Radiologie, Comments: I had 2 scholarships from the French Society of Neuroradiology and the French Society of Radiology. Bhageeradh Mulpur—UNRELATED: Employment: Cleveland Clinic Foundation. Bijoy K. Menon—UNRELATED: Board Membership: Circle NVI; Stock/Stock Options: Circle NVI. Mayank Goyal—UNRELATED: Consultancy: Medtronic, Stryker, Mentice, MicroVenting; Patents (Planned, Pending or Issued): GE Healthcare; Royalties: GE Healthcare. Muhammad Shazam Hussain—UNRELATED: Consultancy: Cerenovus, Comments: Advisory Board; Other: Rapid Medical, Cerenovus, Comments: Data and Safety Monitoring Board, Rapid Medical; Clinical Events Committee, Cerenovus. Mohammed Almekhlafi—UNRELATED: Board Membership: Palmera Medical Inc, Comments: Scientific Advisory Board; Stock/Stock Options: Palmera Medical Inc.

## REFERENCES

- Yoo AJ, Chaudhry ZA, Nogueira RG, et al. **Infarct volume is a pivotal biomarker after intra-arterial stroke therapy.** *Stroke* 2012;43:1323–30 CrossRef Medline
- Zaidi SF, Aghaebrabim A, Urta X, et al. **Final infarct volume is a stronger predictor of outcome than recanalization in patients with proximal middle cerebral artery occlusion treated with endovascular therapy.** *Stroke* 2012;43:3238–44 CrossRef Medline
- Regenhardt RW, Etherton MR, Das AS, et al. **White matter acute infarct volume after thrombectomy for anterior circulation large vessel occlusion stroke is associated with long term outcomes.** *J Stroke Cerebrovasc Dis* 2021;30:105567 CrossRef Medline
- De Meyer SF, Denorme F, Langhauser F, et al. **Thromboinflammation in stroke brain damage.** *Stroke* 2016;47:1165–72 CrossRef Medline
- Desilles JP, Mazighi M, Ho-Tin-Noé B. **Letter by Desilles regarding article, “Ischemia-Reperfusion Injury After Endovascular Thrombectomy for Ischemic Stroke.”** *Stroke* 2019;50:e98 CrossRef Medline
- Gauberti M, Lapergue B, Martinez de Lizarrondo S, et al. **Ischemia-reperfusion injury after endovascular thrombectomy for ischemic stroke.** *Stroke* 2018;49:3071–74 CrossRef Medline
- Moher D, Liberati A, Tetzlaff J, et al. for the PRISMA Group. **Preferred reporting items for systematic reviews and meta-analyses: the PRISMA statement.** *PLoS Med* 2009;6:e1000097 CrossRef Medline
- Luo D, Wan X, Liu J, et al. **Optimally estimating the sample mean from the sample size, median, mid-range, and/or mid-quartile range.** *Stat Methods Med Res* 2018;27:1785–1805 CrossRef Medline
- Shi J, Luo D, Weng H, et al. **Optimally estimating the sample standard deviation from the five-number summary.** *Res Synth Methods* 2020;11:641–54 CrossRef Medline
- Sterne JA, Hernán MA, Reeves BC, et al. **ROBINS-I: a tool for assessing risk of bias in non-randomised studies of interventions.** *BMJ* 2016;355:i4919 CrossRef Medline
- McGuinness LA, Higgins JP. **Risk-of-bias VISualization (robvis): an R package and Shiny web app for visualizing risk-of-bias assessments.** *Res Synth Methods* 2021;12:55–61 CrossRef Medline
- Andrapalliyal N, Handshoe Lacy S, Mulpur B, et al. **Abstract WP44: less infarct volume growth in early window mechanical thrombectomy compared to late window in emergent large vessel occlusion.** In: *Proceedings of the International Stroke Conference*, Los Angeles, California. February 18–21, 2020
- Ben Hassen W, Tordjman M, Boulouis G, et al. **Benefit of first-pass complete reperfusion in thrombectomy is mediated by limited infarct growth.** *Eur J Neurol* 2021;28:124–31 CrossRef Medline
- Federau C, Mlynash M, Christensen S, et al. **Evolution of volume and signal intensity on fluid-attenuated inversion recovery MR images after endovascular stroke therapy.** *Radiology* 2016;280:184–192 CrossRef Medline
- Federau C, Christensen S, Mlynash M, et al. **Comparison of stroke volume evolution on diffusion-weighted imaging and fluid-attenuated inversion recovery following endovascular thrombectomy.** *Int J Stroke* 2017;12:510–18 CrossRef Medline
- Gwak DS, Park HK, Jung C, et al. **Infarct growth patterns may vary in acute stroke due to large vessel occlusion and recanalization with endovascular therapy.** *Eur Radiol* 2020;30:6432–40 CrossRef Medline
- Inoue M, Mlynash M, Christensen S, et al. **Early diffusion-weighted imaging reversal after endovascular reperfusion is typically transient in patients imaged 3 to 6 hours after onset.** *Stroke* 2014;45:1024–28 CrossRef Medline
- Regenhardt RW, Etherton MR, Das AS, et al. **Infarct growth despite endovascular thrombectomy recanalization in large vessel occlusive stroke.** *J Neuroimaging* 2021;31:15564 CrossRef Medline
- Schiphorst AT, Charron S, Hassen WB, et al. **Tissue no-reflow despite full recanalization following thrombectomy for anterior circulation stroke with proximal occlusion: a clinical study.** *J Cereb Blood Flow Metab* 2021;41:253–66 CrossRef Medline
- Yoo J, Choi JW, Lee SJ, et al. **Ischemic diffusion lesion reversal after endovascular treatment.** *Stroke* 2019;50:1504–09 CrossRef Medline
- Boers AM, Jansen IG, Brown S, et al. **Mediation of the relationship between endovascular therapy and functional outcome by follow-up infarct volume in patients with acute ischemic stroke.** *JAMA Neurol* 2019;76:194–202 CrossRef Medline
- Choi JH, Pile-Spellman J. **Reperfusion changes after stroke and practical approaches for neuroprotection.** *Neuroimaging Clin N Am* 2018;28:663–82 CrossRef Medline
- Khatri R, McKinney AM, Swenson B, et al. **Blood-brain barrier, reperfusion injury, and hemorrhagic transformation in acute ischemic stroke.** *Neurology* 2012;79:S52–57 CrossRef Medline
- Xu W, Zhang Y, Su J, et al. **Ischemia reperfusion injury after gradual versus rapid flow restoration for middle cerebral artery occlusion rats.** *Sci Rep* 2018;8:1638 CrossRef Medline
- Sutherland BA, Neuhaus AA, Couch Y, et al. **The transient intraluminal filament middle cerebral artery occlusion model as a model of endovascular thrombectomy in stroke.** *J Cereb Blood Flow Metab* 2016;36:363–69 CrossRef Medline
- Pillai DR, Dittmar MS, Baldaranov D, et al. **Cerebral ischemia-reperfusion injury in rats—a 3 T MRI study on biphasic blood-brain barrier opening and the dynamics of edema formation.** *J Cereb Blood Flow Metab* 2009;29:1846–55 CrossRef Medline
- Nour M, Scalzo F, Liebeskind DS. **Ischemia-reperfusion injury in stroke.** *Interv Neurol* 2012;1:185–99 CrossRef Medline
- Sah RG, d’Este CD, Hill MD, et al. **Diffusion-weighted imaging lesion growth occurs despite recanalization in acute ischemic stroke: implications for future treatment trials.** *Int J Stroke* 2019;14:257–64 CrossRef Medline
- Tipirneni-Sajja A, Christensen S, Straka M, et al. **Prediction of final infarct volume on subacute MRI by quantifying cerebral edema in ischemic stroke.** *J Cereb Blood Flow Metab* 2017;37:3077–84 CrossRef Medline
- Harston GW, Carone D, Sheerin F, et al. **Quantifying infarct growth and secondary injury volumes: comparing multimodal image registration measures.** *Stroke* 2018;49:1647–55 CrossRef Medline
- Simard JM, Kent TA, Chen M, et al. **Brain oedema in focal ischaemia: molecular pathophysiology and theoretical implications.** *Lancet Neurol* 2007;6:258–68 CrossRef Medline
- Broocks G, Flottmann F, Ernst M, et al. **Computed tomography-based imaging of voxel-wise lesion water uptake in ischemic brain: relationship between density and direct volumetry.** *Invest Radiol* 2018;53:207–13 CrossRef Medline
- Broocks G, Faizy TD, Flottmann F, et al. **Subacute infarct volume with edema correction in computed tomography is equivalent to final infarct volume after ischemic stroke: improving the comparability of infarct imaging endpoints in clinical trials.** *Invest Radiol* 2018;53:472–76 CrossRef Medline
- Broocks G, Hanning U, Faizy TD, et al. **Ischemic lesion growth in acute stroke: water uptake quantification distinguishes between**



- edema and tissue infarct. *J Cereb Blood Flow Metab* 2020;40:823–32 CrossRef Medline
35. Kaesmacher J, Dobrocky T, Heldner MR, et al. **Systematic review and meta-analysis on outcome differences among patients with TICI2b versus TICI3 reperfusions: success revisited.** *J Neurol Neurosurg Psychiatry* 2018;89:910–17 CrossRef Medline
  36. Chamorro A, Blasco J, López A, et al. **Complete reperfusion is required for maximal benefits of mechanical thrombectomy in stroke patients.** *Sci Rep* 2017;7:11636 CrossRef Medline
  37. Rangaraju S, Aghaebrahim A, Streib C, et al. **Abstract T MP7: TICI 2B vs. TICI 3: differences in infarct volumes and clinical outcomes in proximal intracranial large vessel occlusions treated with endovascular therapy.** In: *Proceedings of the International Stroke Conference*, Los Angeles, California. January 23–26, 2018
  38. Marto JP, Strambo D, Hajdu SD, et al. **Twenty-four-hour reocclusion after successful mechanical thrombectomy: associated factors and long-term prognosis.** *Stroke* 2019;50:2960–63 CrossRef Medline
  39. Mosimann PJ, Kaesmacher J, Gautschi D, et al. **Predictors of unexpected early reocclusion after successful mechanical thrombectomy in acute ischemic stroke patients.** *Stroke* 2018;49:2643–51 CrossRef Medline
  40. Santana D, Laredo C, Renú A, et al. **Incidence and clinico-radiological correlations of early arterial reocclusion after successful thrombectomy in acute ischemic stroke.** *Transl Stroke Res* 2020;11:1314–21 CrossRef Medline
  41. Almekhlafi MA, Modi J, Menon B, et al. **Abstract 3232: distal embolization predicts infarct growth and futile recanalization after endovascular stroke therapy.** In: *Proceedings of the International Stroke Conference*, New Orleans, Louisiana. February 1–3, 2012
  42. Kaesmacher J, Kurmann C, Jungi N, et al. **Infarct in new territory after endovascular stroke treatment: a diffusion-weighted imaging study.** *Sci Rep* 2020;10:8366 CrossRef Medline
  43. Shuaib A, Butcher K, Mohammad AA, et al. **Collateral blood vessels in acute ischaemic stroke: a potential therapeutic target.** *Lancet Neurol* 2011;10:909–21 CrossRef Medline
  44. An JQ, Cheng YW, Guo YC, et al. **Safety and efficacy of remote ischemic postconditioning after thrombolysis in patients with stroke.** *Neurology* 2020;95:e3355–63 CrossRef Medline
  45. England TJ, Hedstrom A, O'Sullivan SE, et al. **Remote ischemic conditioning after stroke trial 2: a Phase IIb randomized controlled trial in hyperacute stroke.** *J Am Heart Assoc* 2019;8:e013572 CrossRef Medline
  46. Hill MD, Goyal M, Menon BK, et al. ESCAPE-NA1 Investigators. **Efficacy and safety of nerinetide for the treatment of acute ischaemic stroke (ESCAPE-NA1): a multicentre, double-blind, randomised controlled trial.** *Lancet* 2020;395:878–87 CrossRef Medline
  47. Chamorro A, Amaro S, Castellanos M, et al. URICO-ICTUS Investigators. **Safety and efficacy of uric acid in patients with acute stroke (URICO-ICTUS): a randomised, double-blind phase 2b/3 trial.** *Lancet Neurol* 2014;13:453–60 CrossRef Medline
  48. Kuczynski AM, Demchuk AM, Almekhlafi MA. **Therapeutic hypothermia: applications in adults with acute ischemic stroke.** *Brain Circ* 2019;5:43–54 CrossRef Medline
  49. Wu C, Zhao W, An H, et al. **Safety, feasibility, and potential efficacy of intraarterial selective cooling infusion for stroke patients treated with mechanical thrombectomy.** *J Cereb Blood Flow Metab* 2018;38:2251–60 CrossRef Medline
  50. Chalela JA, Kidwell CS, Nentwich LM, et al. **Magnetic resonance imaging and computed tomography in emergency assessment of patients with suspected acute stroke: a prospective comparison.** *Lancet* 2007;369:293–98 CrossRef Medline
  51. Baron JC, Yamauchi H, Fujioka M, et al. **Selective neuronal loss in ischemic stroke and cerebrovascular disease.** *J Cereb Blood Flow Metab* 2014;34:2–18 CrossRef Medline
  52. Goyal M, Ospel JM, Menon B, et al. **Challenging the ischemic core concept in acute ischemic stroke imaging.** *Stroke* 2020;51:3147–55 CrossRef Medline

# Impact of A1 Asymmetry on the Woven EndoBridge Device in Anterior Communicating Artery Aneurysms

J. Cortese, J. Caroff, J.-B. Girot, C. Mihalea, V. Da Ros, G. Aguiar, A. Elawady, L. Ikka, S. Gallas, A. Ozanne, V. Chalumeau, A. Rouchaud, J. Moret, and L. Spelle



## ABSTRACT

**BACKGROUND AND PURPOSE:** Woven EndoBridge (WEB) devices are increasingly used to treat intracranial aneurysms. A1 asymmetry contributes to anterior communicating artery aneurysm formation and to treatment instability after coiling. We sought to evaluate whether A1 asymmetry had an impact on angiographic outcome in anterior communicating artery aneurysms treated with the WEB.

**MATERIALS AND METHODS:** Anterior communicating artery aneurysms treated between July 2012 and July 2020 with the WEB from an institutional review board–approved database were reviewed. A1 asymmetry was categorized as the following: absence of the A1 segment on 1 side (unilateral A1) versus bilateral A1. Univariate and multivariable analyses assessed independent predictors of adequate (WEB Occlusion Scale A, B, and C) and complete occlusion (WEB Occlusion Scale A and B).

**RESULTS:** Forty-eight individual aneurysms (47 patients) were included in the final analysis, of which 16 (33%) were acutely ruptured. The mean size was 6.5 (SD, 2.2) mm. Adequate and complete occlusion was achieved in 33 (69%) and 30 (63%) cases, respectively. Unilateral A1 was associated with significantly higher rates of adequate (92% versus 60% for bilateral A1;  $P = .03$ ) and complete occlusion (92% versus 50% for bilateral A1;  $P < .01$ ). Multivariable logistic regression confirmed unilateral A1 as an independent predictor of both adequate (OR = 10.6; 95% CI, 1.6–220.7;  $P = .04$ ) and complete occlusion (OR = 9.5, 95% CI, 1.5–190.2;  $P = .04$ ). A sensitivity analysis comparing unilateral “functional” A1 with bilateral “functional” A1 showed similar results. WEB shape modification was not influenced by the unilateral A1 configuration ( $P = .70$ ).

**CONCLUSIONS:** Anterior communicating artery aneurysms with a unilateral A1 configuration treated with WEB devices are associated with better angiographic outcome than those with bilateral A1. This finding supports the hypothesis that WEB devices are resistant to unilateral flow in the aneurysm as opposed to coils.

**ABBREVIATIONS:** ACoA = anterior communicating artery; WOS = WEB Occlusion Scale; WShM = WEB shape modification

The efficacy and safety of the Woven EndoBridge device (WEB; MicroVention) have been widely reported in several observational studies and in prospective trials.<sup>1,2</sup> The device is now a reliable option for the treatment of wide-neck aneurysms. Two recent meta-analyses of WEB device use found that overall

rates of complete and adequate occlusion were 53% and 80%–83.3%, respectively.<sup>3,4</sup>

The anterior communicating artery (ACoA) is a preferred site for aneurysms,<sup>5</sup> and aneurysms in this location tend to have a higher risk of rupture than aneurysms in other locations.<sup>6,7</sup> Because of the wide variety and complexity of the anterior communicating artery anatomy, ACoA aneurysms are usually considered the most complex ones to treat. Several endovascular devices (coils, stent-assisted coiling, and flow diverters) have been specifically reported in this location to overcome this challenge.<sup>8–10</sup> Most pointed out the role of A1 asymmetry on the angiographic outcome.<sup>8,10</sup> In this situation, the WEB device appears to be an appealing solution: It can be used in wide-neck aneurysms without a stent. However, the influence of the ACoA anatomy on WEB devices is not known.

Here, we aimed to report the angiographic outcomes of ACoA aneurysms treated with the WEB and to determine whether A1 asymmetry has an impact on the treatment outcome.

Received February 8, 2021; accepted after revision March 16.

From the Department of Interventional Neuroradiology (J. Cortese, J. Caroff, J.-B.G., C.M., G.A., A.E., L.I., S.G., A.O., V.C., J.M., L.S.), NEURI Brain Vascular Center, Bicêtre Hospital, APHP, Paris Saclay University, Le Kremlin-Bicêtre, France; Department of Radiology (J.-B.G.), Angers University Hospital, Angers, France; Department of Biomedicine (V.D.R.), Fondazione PTV Policlinico Tor Vergata, Roma, Italy; Department of Interventional Neuroradiology (A.R.), Limoges University Hospital, Limoges, France; and University of Limoges (A.R.), XLIM UMR CNRS 7252, Limoges, France.

Please address correspondence to Jildaz Caroff, MD, PhD, Department of Interventional Neuroradiology (NEURI), Hôpital Bicêtre-APHP, 78 Rue du Général Leclerc, 94270, Bicêtre, France; e-mail: jildaz.caroff@aphp.fr



Indicates article with online supplemental data.

<http://dx.doi.org/10.3174/ajnr.A7189>

## MATERIALS AND METHODS

### Data-Sharing Statement

Study data are available from the corresponding author on reasonable request.

### Ethical Statement

The French Ethical Committee for Research in Medical Imaging approved this study (institutional review board number CRM-2101-127). Informed consent was obtained for every patient.

### Study Design

In our tertiary care center (Neuri center, Bicêtre Hospital, France), we retrospectively queried the prospectively acquired database of patients with aneurysms treated with WEB devices between July 2012 and July 2020. Consecutive, ruptured or unruptured ACoA aneurysms treated with WEB were included. Patients were excluded under the following circumstances: No follow-up angiograms for at least 3 months after treatment were available; treatment with a WEB was used as a retreatment strategy in a recanalized coiled aneurysm; or the aneurysm was secondary to another vascular malformation (eg, brain arteriovenous malformation).

The primary outcome was adequate angiographic occlusion, defined as a score on the WEB Occlusion Scale (WOS) of A, B or C. The secondary outcome was angiographic complete occlusion (WOS A or B).

### A1 Asymmetry Assessment

We classified A1 asymmetry using a 4-point grading scale, inspired by previous studies,<sup>8,10</sup> on the basis of A1 segment size and functionality (Fig 1) as follows: grade H1, both A1 segments are the same size (ie, symmetric A1s); grade H2, the A1 segment is smaller (hypoplastic) on 1 side but large enough for an opacification of the A2 segment with an ipsilateral injection (ie, asymmetric sizes but both functional A1s); grade H3, the A1 segment is very hypoplastic on 1 side, the A2 segment on that side is not opacified following ipsilateral injection of contrast agent, and both A2 segments are only opacified following injection from the dominant side (ie, asymmetric size and a nonfunctional hypoplastic side); and grade Y, the A1 segment is absent on 1 side (aplastic).

A1 segment anatomy was reported as “unilateral A1” (ie, grade Y) or otherwise “bilateral A1” (ie, grade H1 + H2 + H3). For a sensitivity analysis, we also dichotomized A1 segment anatomy using a more functional approach: unilateral “functional” A1 (grade H3 + Y) versus bilateral functional A1 (grade H1 + H2).

### Imaging Analysis

Angiographic results were analyzed by 2 expert interventional radiologists (blinded to the clinical data) including 1 working in a different hospital and not involved in the treatment or follow-up. For this study, we used the WOS 4-point grading scale,<sup>11</sup> as follows: complete occlusion (WOS A), near-complete occlusion (WOS B), neck remnant (WOS C), and aneurysm remnant (WOS D). Discrepancies were resolved by a third neuroradiologist not involved in the treatment.

We report the following aneurysm characteristics: size (including width/neck ratio and aspect ratio [height/neck]) and

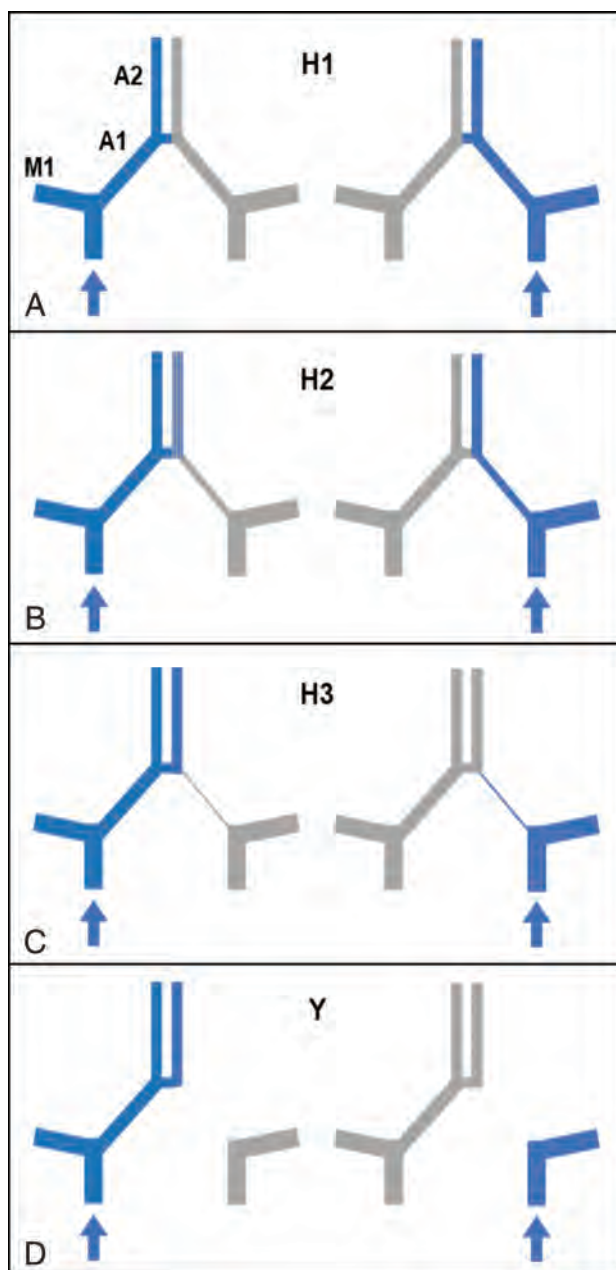


**FIG 1.** Grading scale for A1 segments. A, Grade H1: A1 segments are symmetric. B, Grade H2: The A1 segment is smaller on 1 side, but opacification of the A2 segment on that side is observed following ipsilateral injection (ie, asymmetric A1s but both functional). C, Grade H3: The A1 segment is very hypoplastic on 1 side, the A2 segment is not opacified from the ipsilateral injection, and A2 segments are only opacified with injection from the dominant side (ie, asymmetric A1s and a nonfunctional hypoplastic side). D, Grade Y: The A1 segment is absent on 1 side (aplastic). Blue filling represents opacification after injection from the side with the blue arrow. Grade Y corresponds to unilateral A1, and grade H3 + Y, to unilateral functional A1.

shape (rated as regular [smooth aneurysm surface on 3D] versus irregular [in case of a bleb or multilobar shape]).

WEB shape modification (WSHM) refers to a loss of device height occurring during the follow-up.<sup>12,13</sup> WSHM was quantitatively defined as a ratio (percentage) defined as



$$WShM(\%) = \left(1 - \left[\frac{d(\text{final})}{d(\text{initial})}\right]\right) \times 100,$$

with “ $d(\text{initial})$ ” the distance between the WEB proximal and distal markers after detachment, and “ $d(\text{final})$ ” the distance between the same 2 markers on last follow-up. The distance between the markers of the WEB was measured on cross-sectional images obtained with conebeam CT (VasoCT; Philips Healthcare) performed after WEB detachment and at each follow-up.<sup>14</sup>

### Antiplatelet Regimen

In unruptured cases, patients received aspirin (160 mg per day) and ticagrelor (90 mg twice per day) the day before WEB implantation, and oral treatment was discontinued if not needed (depending on eventual WEB protrusion or use of a stent). In ruptured aneurysms, no antiplatelet regimen was used. For either ruptured or unruptured aneurysms, treatment was performed with the patient under systemic heparinization (50-UI/kg intravenous bolus followed by 20–40 IU/kg/h) that was stopped at the end of the procedure.

### WEB Indication and Selection

The decision for WEB treatment of unruptured aneurysms was made by multidisciplinary consensus. For acutely ruptured aneurysms, selection of the treatment strategy was left to the operator. The main indication for using a WEB was a wide-neck bifurcation aneurysm.

In our database, 5 generations of WEB devices were used,<sup>15,16</sup> corresponding to the different evolutions of the WEB device. We separated the “previous generation” (ie, generations 1–4), from the “fifth generation” (newest generation available). We also reported WEB devices: Double-Layer (WEB-DL), Single-Layer (WEB-SL), or Single Layer Sphere (WEB-SLS) as chosen by the operator. Devices were delivered through VIA catheters (MicroVention): VIA-17 or 27 depending on the size, or VIA-21–33 for older procedures. The operator used measurements (width, height, and neck of the aneurysm in at least 2 orthogonal projections) from 3D rotational angiograms to select the WEB size and followed the usual guidelines for the sizing: oversizing the width by 1 or 2 mm.<sup>17</sup>

### Statistical Analysis

Continuous variables are reported as mean (SD) if normally distributed or as median (interquartile range), while categorical variables are expressed as frequency (percentage). We explored the following: 1) “adequate occlusion” (WOS A, B, and C) versus “aneurysm remnant” (WOS D), and 2) “complete occlusion” (WOS A and B) versus “incomplete occlusion” (WOS C and D). A  $\chi^2$  or Fisher exact test was used to evaluate qualitative factors as appropriate, and a Student  $t$  test or Wilcoxon  $U$  test was used to assess quantitative variables as appropriate.

Multivariable logistic regression analysis was performed using all candidate variables ( $P < .2$  in the univariate analysis). For selected variables, ORs with 95% CIs and a  $P$  value of the likelihood-ratio test are given. No adjustment for multiple testing was performed, and analyses are regarded as explorative. To further

**Table 1: Baseline characteristics and angiographic outcomes<sup>a</sup>**

Baseline Aneurysm Characteristics	All (n = 48)
Age (mean) (yr)	58.4 (SD, 11.2)
Women	26 (54.2)
Cardiovascular risk factor	25 (52.1)
Current smoker	7 (14.6)
Acutely ruptured	16 (33.3)
Irregular aneurysm	19 (39.6)
Maximum diameter (mean) (mm)	6.5 (SD, 2.2)
Aneurysm height (mean) (mm)	5.0 (SD, 1.8)
Aneurysm neck (mean) (mm)	3.8 (SD, 1.1)
Aneurysm width (mean) (mm)	5.1 (SD, 1.7)
Aspect ratio (height/neck) (mean)	1.27 (SD, 0.39)
Width/neck ratio (mean)	1.28 (SD, 0.27)
Unilateral A1 (grade Y)	13 (27.1)
Unilateral functional A1 (grade H3+Y)	19 (39.6)
Baseline treatment characteristics	
Type of WEB	
WEB-DL	2 (4.2)
WEB-SL	37 (77.1)
WEB-SLS	9 (18.8)
WEB device generation	
Fifth generation	30 (62.5)
Previous generations	18 (37.5)
Additional stent	2 (4.7)
Angiographic outcomes	
Adequate occlusion	33 (68.8)
Complete occlusion	30 (62.5)
Aneurysm remnant	15 (31.2)
WShM (median) (IQR) (%)	31 (11–51)

**Note:**—IQR indicates interquartile range.

<sup>a</sup> Data are presented as number (%) unless otherwise indicated.

test the impact of A1 asymmetry, we assessed a sensitivity analysis to test unilateral functional A1 (grades H3 + Y) versus bilateral functional A1 (grades H1 + H2).  $P$  values  $< .05$  were considered statically significant. All statistical analyses were performed using R statistical and computing software (Version 3.6.1; <http://www.r-project.org/>).

## RESULTS

### Patient, Aneurysm, and Anatomic Characteristics

A total of 48 independent ACoA aneurysms treated with WEB devices in 47 patients were included in the analysis (Table 1 and Fig 2, patient flow chart). There were no missing data in the analysis. The mean age was 58.4 (SD, 11.2) years (range, 37–90 years), and 26 patients (54.2%) were women. Sixteen aneurysms (33.3%) were acutely ruptured cases. The mean maximum aneurysm diameter was 6.5 (SD, 2.2) mm (range, 3.1–13.1 mm).

A unilateral A1 segment (grade Y) was noted in 13 cases (27.1%), whereas 20 cases (41.7%) had symmetric A1 segments (grade H1). Grades H2 and H3 were noted in 9 (18.8%) and 6 (12.5%) cases, respectively. Both groups, unilateral A1 and bilateral A1, had similar aneurysm sizes: 7.1 (SD, 2.5) mm and 6.0 (SD, 1.9) mm, respectively. The aneurysm was systematically treated from the side with the largest A1 segment. If the sides were symmetric, the side with the more direct angle to the aneurysm was chosen (11 of 20 procedures were from the right side).

### Treatment Characteristics and Outcomes

The WEB-SL was used in most cases (37/48, 77.1%), and 30/48 (62.5%) of devices used were fifth generation. Two aneurysms (4.2%) were also stented due to protrusion of the WEB into the parent artery. In both cases, a stent was used as a rescue technique because of WEB protrusion in the parent artery; 1 patient had a grade H1 ACoA configuration, and the other had a grade Y.

The median last follow-up was 12.2 months (range, 3–65 months). Adequate occlusion and complete occlusion were observed in 33/48 (68.8%) and 30/48 (62.5%) cases, respectively. The median WEB shape modification ratio at last follow-up was

31% (interquartile range = 11%–50.8%) and was similar in both adequate occlusion (30%) and aneurysm remnant groups (35%,  $P = .40$ ). Angiographic outcome was also similar between ruptured and unruptured aneurysms ( $P = .99$ ).

### A1 Asymmetry as a Predictor of Angiographic Outcome

Unilateral A1 was associated with significantly higher rates of adequate (92.3% versus 60.0% for bilateral A1;  $P = .03$ ) and complete occlusion (92.3% versus 51.4% for bilateral A1;  $P < .01$ ). Other candidate variables for adequate occlusion were irregular shape ( $P = .19$ ) and aspect ratio ( $P = .19$ ), and for complete occlusion, they were irregular shape ( $P = .08$ ) and age ( $P = .11$ ).

Finally, unilateral A1 was not associated with WEB shape modification ( $P = .70$ ).

Unilateral A1 was confirmed as an independent predictor for both adequate (OR = 10.6; 95% CI, 1.6–220.7;  $P = .04$ ) and complete occlusion (OR = 9.5; 95% CI, 1.5–190.2;  $P = .04$ ). None of the other variables were independent predictive factors of adequate or complete occlusion in this population. Detailed results of univariate and multivariable analyses for adequate and complete occlusion are presented in Table 2 and the Online Supplemental Data, respectively.

A sensitivity analysis comparing unilateral functional A1 (grade H3 + Y) versus bilateral functional A1 (grade H1 + H2) showed similar results. The adequate occlusion rate was 58.6% in grade H1 + H2 versus 84.2% in grade H3 + Y ( $P = .06$ ), and the complete occlusion rate was 48.3% in grade H1 + H2 versus 84.2% in grade H3 + Y ( $P = .01$ ), leading to an adjusted OR = 4.2; 95% CI, 1.01–22.87 ( $P = .06$ ) for adequate

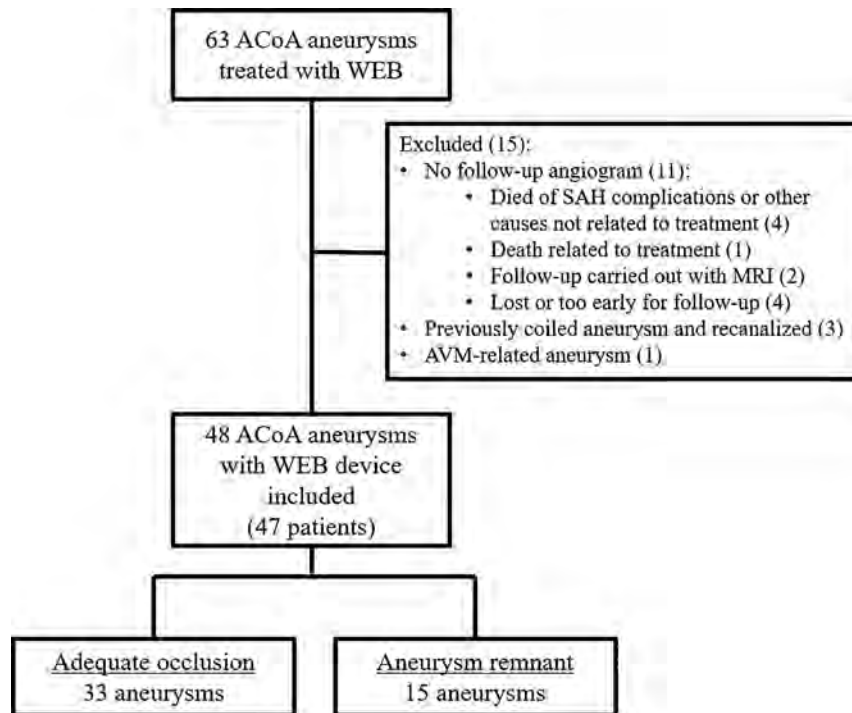


FIG 2. Patient flow chart.

Table 2: Univariate analysis and multivariable logistic regression for angiographic adequate occlusion of ACoA aneurysms treated with WEB<sup>a</sup>

Variables	Univariate Analysis			Multivariable Analysis	
	Adequate Occlusion (n = 33)	Aneurysm Remnant (n = 15)	P Value	ORa (95% CI)	P Value
Age (mean) (yr)	59.1 (SD, 12)	56.9 (SD, 8)	.45		
Women	19 (58)	8 (53)	.78		
Cardiovascular risk factors	17 (52)	8 (53)	.91		
Current smoker	5 (15)	2 (13)	.87		
Ruptured aneurysm	11 (33)	5 (33)	.99		
Irregular aneurysm	11 (33)	8 (53)	.19	0.54 (0.13–2.17)	.38
Aspect ratio (mean)	1.32 (SD, 0.37)	1.15 (SD, 0.40)	.19	5.98 (0.84–64.79)	.10
Width/neck ratio (mean)	1.27 (SD, 0.27)	1.29 (SD, 0.28)	.84		
Neck (mean) (mm)	3.77 (SD, 1.13)	3.79 (SD, 1.20)	.97		
Unilateral A1	12 (36)	1 (7)	.03	10.6 (1.6–220.7)	.04
WEB-SL	27 (82)	10 (67)	.39		
Fifth-generation WEB device	20 (61)	10 (67)	.69		
WShM (median) (IQR) (%)	30 (11–48)	35 (19–52)	.40		

Note:—ORa indicates adjusted odds ratio.

<sup>a</sup> Data are presented as number (%) unless otherwise indicated.

occlusion and an adjusted OR = 5.5; 95% CI, 1.31–30.42 ( $P = .03$ ) for complete occlusion. Table 3 presents the rate of angiographic adequate occlusion at each step of the 4-point grading scale that we used to describe A1 asymmetry.

## DISCUSSION

### Impact of ACoA Anatomic Configuration on WEB Devices

Our study of 48 ACoA aneurysms treated with the WEB device, in which we eliminated potential confounding factors using multivariate analysis, showed that unilateral A1 is a strong independent predictor of both adequate and complete occlusion (Fig 3, illustrative case). When an A1 segment was aplastic on 1 side (grade Y), leading to a unique unilateral blood flow entering the aneurysm, complete occlusion reached 93%. As intended by the sensitivity analysis, it seems that the definition of unilateral A1

could be extended to the absence of a functional A1 segment, which includes grade H3 in the definition.

Absence of an A1 segment on one side or the other of the ACoA shifts the anterior communicating complex from an “H-shape” to a “Y-shape.” It is possible that the angle between the aneurysm and the A1 segment on the side used for treatment may also partly explain the better results achieved in the Y-shaped ACoA. Like other termination locations (eg, basilar artery, middle cerebral artery bifurcation), Y-shaped “true bifurcation” aneurysms are more “straightforward,” enabling better positioning of the WEB device and subsequent sealing of the neck, which plays a important role in aneurysm occlusion.<sup>18</sup> However, in our experience, complex anatomy with unfavorable angles of approach can be overcome with the balloon-assisted WEB remodeling technique.<sup>19</sup>

Another interesting result was the absence of significant difference in WEB shape modification between the unilateral A1 and bilateral A1 groups. This supports the hypothesis that this phenomenon is not only correlated to outside arterial flow but is under the influence of multifactorial events like the biologic healing response inside the WEB device.<sup>12,20</sup>

### Comparison with Other Devices

An asymmetric A1 segment of the anterior cerebral arteries, with 1 side dominating the other, is a known risk factor for ACoA aneurysm formation and rupture.<sup>21–23</sup>

Several hypotheses have been proposed to explain the role of the anterior communicating complex anatomy in the formation of aneurysms, including wall shear stress and arterial blood flow.<sup>21,24</sup>

In contrast to our findings using WEB devices, Tarulli et al<sup>10</sup> demonstrated that an asymmetric A1 was associated with unstable occlusion in coiled aneurysms, leading to higher rates of incomplete occlusion at follow-up. They hypothesized that substantial blood flow in 1 spot at a bifurcation may lead to formation of aneurysms that, after treatment with coils, are predisposed to molding and flattening of coil masses, resulting in an increased incidence of aneurysm remnants. The paradigm shift offered by extra- and intrasaccular flow-diversion devices may be of interest in this situation because it prevents the blood flow from entering the aneurysm. Pagiola et al<sup>8</sup> recommended avoiding flow-diverter stents in grade Y ACoA aneurysms because of the risk of thromboembolic complications. Moreover, they also reported higher complication rates and lower rates of aneurysm occlusion when the A1 segments were highly asymmetric (grade H3). Here, our results suggest that the WEB, an intrasaccular

**Table 3: Angiographic aneurysm occlusion depending on A1 asymmetry grading**

A1 Asymmetry Grading Scale	Adequate Occlusion No. (%)
Bilateral functional A1	17/29 (59)
H1 ( $n = 20$ )	12 (60)
H2 ( $n = 9$ )	5 (55)
Unilateral functional A1	16/19 (84)
H3 ( $n = 6$ )	4 (67)
Y ( $n = 13$ )	12 (92)

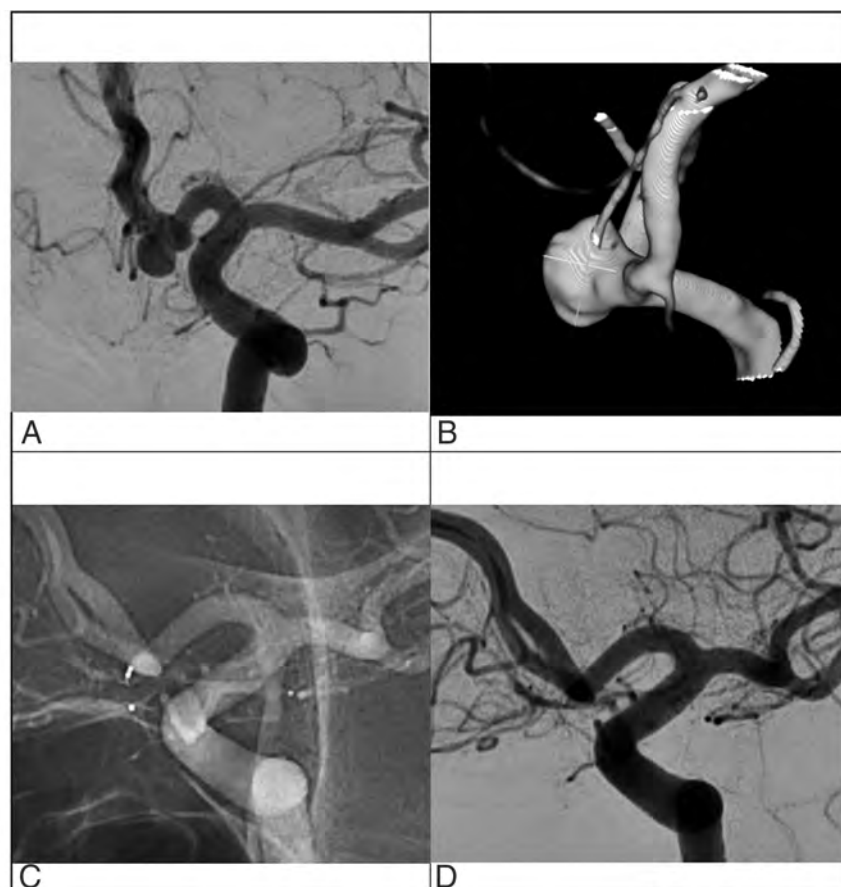


**FIG 3.** Illustrative case of a ACoA aneurysm treated with a WEB device (A and B). The contralateral A1 segment is absent, rendering a Y-shape to the ACoA anatomy. Last control angiogram at 1-year follow-up demonstrates complete occlusion (C and D).



flow-diversion device, could prevent the 1-sided blood flow from entering the aneurysm sac, without risking the patency of covered arterial branches.

To summarize, the WEB device could represent the best option for the treatment of a wide-neck ACoA aneurysm with a unilateral A1 configuration (especially if acutely ruptured): 1) It is resistant to unilateral blood flow, so it is more stable than coils across time, and 2) it avoids the deployment of a stent in the parent artery and, thus, the use of antiplatelet therapy.

### Other Predictive Factors of Occlusion

In this study focusing on ACoA aneurysms treated with WEB, we observed rates of adequate occlusion similar to those found in a prospective study at midterm follow-up.<sup>25</sup> Cagnazzo et al,<sup>26</sup> evaluating a series of 86 aneurysms treated with a WEB in any location, found that an irregular shape and wide neck (>4 mm) were independent predictors of aneurysm remnants. Although not statistically significant, our results could suggest a role of the aneurysm irregular shape and aspect ratio (height/neck) on the angiographic outcome. We acknowledge that because the number of included aneurysms was relatively small, it is possible that some variables could not reach statistical significance in the multivariable analysis. However, we present, to date, the largest cohort of ACoA aneurysms treated with WEB.

### Limitations

There are other limitations to our analysis. It was a retrospective study performed at a single academic center, and further prospective studies are needed to confirm our results. Also, the follow-up period seems limited (median: 1 year). However, the WEB is considered a stable device across time with most remnant aneurysms detected during the first year.<sup>27</sup> Finally, a standardized definition of A1 asymmetry, dominance, and hypoplasia is lacking in the literature, making it difficult to compare studies. To this end, we chose first a consensual definition for the A1 asymmetry (absent or present). Then, we updated a previous grading system by focusing on the functional aspect of the A1 segments, which further confirmed our results.

### CONCLUSIONS

A1 asymmetry favors better angiographic outcomes in ACoA aneurysms treated with the WEB device. Here, approximately 70% of ACoA aneurysms were adequately occluded after WEB implantation; however, this reached >92% in the unilateral A1 group, with an adjusted odds ratio of 11. This finding supports the hypothesis that WEB devices are less impacted by unilateral A1 flow, as opposed to other endovascular devices. This could be of interest when planning for a wide-neck ACoA aneurysm with a unilateral A1, particularly if the aneurysm is acutely ruptured. Further prospective studies comparing coils, flow-diverters, and the WEB device in this location are needed.

Disclosures: Jacques Moret—UNRELATED: Consultancy: Medtronic, MicroVention, Stryker, Balt. Laurent Spelle—UNRELATED: Consultancy: MicroVention, Medtronic, Balt; Grants/Grants Pending: hospital grant from Philips Healthcare.

### REFERENCES

1. Arthur AS, Molyneux A, Coon AL, et al. The safety and effectiveness of the Woven EndoBridge (WEB) system for the treatment of wide-necked bifurcation aneurysms: final 12-month results of the pivotal WEB Intracascular Therapy (WEB-IT) Study. *J Neurointerv Surg* 2019;11:924–30 CrossRef Medline
2. Pierot L, Szikora I, Barreau X, et al. Aneurysm treatment with WEB in the cumulative population of two prospective, multicenter series: 3-year follow-up. *J Neurointerv Surg* 2021;13:363–68 CrossRef Medline
3. van Rooij S, Sprengers ME, Peluso JP, et al. A systematic review and meta-analysis of Woven EndoBridge single layer for treatment of intracranial aneurysms. *Interv Neuroradiol* 2020;26:455–60 CrossRef Medline
4. Zhang SM, Liu LX, Ren PW, et al. Effectiveness, safety and risk factors of Woven EndoBridge device in the treatment of wide-neck intracranial aneurysms: systematic review and meta-analysis. *World Neurosurg* 2020;136:e1–23 CrossRef Medline
5. Brismar JL, Song JK, Newell DW. Cerebral aneurysms. *N Engl J Med* 2006;355:928–39 CrossRef Medline
6. Bijlenga P, Ebeling C, Jaegersberg M, et al. @neurIST Investigators. Risk of rupture of small anterior communicating artery aneurysms is similar to posterior circulation aneurysms. *Stroke* 2013;44:3018–26 CrossRef Medline
7. Suárez Mira JM, De Oliveira Costa FA, Horta BL, et al. Risk of rupture in unruptured anterior communicating artery aneurysms: meta-analysis of natural history studies. *Surg Neurol* 2006;66:S12–19; discussion S19 CrossRef Medline
8. Pagiola I, Mihalea C, Caroff J, et al. Flow diversion treatment of aneurysms of the complex region of the anterior communicating artery: which stent placement strategy should “I” use? A single center experience. *J Neurointerv Surg* 2019;11:1118–22 CrossRef Medline
9. Huang Q, Xu Y, Hong B, et al. Stent-assisted embolization of wide-neck anterior communicating artery aneurysms: review of 21 consecutive cases. *AJNR Am J Neuroradiol* 2009;30:1502–06 CrossRef Medline
10. Tarulli E, Sneade M, Clarke A, et al. Effects of circle of Willis anatomic variations on angiographic and clinical outcomes of coiled anterior communicating artery aneurysms. *AJNR Am J Neuroradiol* 2014;35:1551–55 CrossRef Medline
11. Fiorella D, Arthur A, Byrne J, et al. Interobserver variability in the assessment of aneurysm occlusion with the WEB aneurysm embolization system. *J Neurointerv Surg* 2015;7:591–95 CrossRef Medline
12. Caroff J, Mihalea C, Da Ros V, et al. A computational fluid dynamics (CFD) study of WEB-treated aneurysms: can CFD predict WEB “compression” during follow-up? *J Neuroradiol* 2017;44:262–68 CrossRef Medline
13. Cognard C, Januel AC. Remnants and recurrences after the use of the WEB intracascular device in large-neck bifurcation aneurysms. *Neurosurgery* 2015;76:522–30; discussion 530 CrossRef Medline
14. Caroff J, Mihalea C, Neki H, et al. Role of C-arm VasoCT in the use of endovascular WEB flow disruption in intracranial aneurysm treatment. *AJNR Am J Neuroradiol* 2014;35:1353–57 CrossRef Medline
15. Mihalea C, Caroff J, Pagiola I, et al. Safety and efficiency of the fifth generation Woven EndoBridge device: technical note. *J Neurointerv Surg* 2019;11:511–15 CrossRef Medline
16. Caroff J, Mihalea C, Klisch J, et al. Single-Layer WEBs: intracascular flow disrupters for aneurysm treatment: feasibility results from a European study. *AJNR Am J Neuroradiol* 2015;36:1942–46 CrossRef Medline
17. Goyal N, Hoit D, DiNitto J, et al. How to WEB: a practical review of methodology for the use of the Woven EndoBridge. *J Neurointerv Surg* 2020;12:512–20 CrossRef Medline
18. Vardar Z, King RM, Kraitem A, et al. High-resolution image-guided WEB aneurysm embolization by high-frequency optical coherence tomography. *J Neurointerv Surg* 2020 Sept 28 [Epub ahead of print] CrossRef Medline

19. Mihalea C, Escalard S, Caroff J, et al. **Balloon remodeling-assisted Woven EndoBridge technique: description and feasibility for complex bifurcation aneurysms.** *J Neurointerv Surg* 2019;11:386–89 CrossRef Medline
20. Ding Y, Dai D, Rouchaud A, et al. **WEB Device shape changes in elastase-induced aneurysms in rabbits.** *AJNR Am J Neuroradiol* 2021;42:334–39 CrossRef Medline
21. Castro MA, Putman CM, Sheridan MJ, et al. **Hemodynamic patterns of anterior communicating artery aneurysms: a possible association with rupture.** *AJNR Am J Neuroradiol* 2009;30:297–302 CrossRef Medline
22. Krasny A, Nensa F, Sandalcioglu IE, et al. **Association of aneurysms and variation of the A1 segment.** *J Neurointerv Surg* 2014;6:178–83 CrossRef Medline
23. Tarulli E, Fox AJ. **Potent risk factor for aneurysm formation: termination aneurysms of the anterior communicating artery and detection of A1 vessel asymmetry by flow dilution.** *AJNR Am J Neuroradiol* 2010;31:1186–91 CrossRef Medline
24. Alnaes MS, Isaksen J, Mardal K-A, et al. **Computation of hemodynamics in the circle of Willis.** *Stroke* 2007;38:2500–05 CrossRef Medline
25. Pierot L, Gubucz I, Buhk JH, et al. **Safety and efficacy of aneurysm treatment with the WEB: results of the WEBCAST 2 Study.** *AJNR Am J Neuroradiol* 2017;38:1151–55 CrossRef Medline
26. Cagnazzo F, Ahmed R, Zannoni R, et al. **Predicting factors of angiographic aneurysm occlusion after treatment with the Woven EndoBridge Device: a single-center experience with midterm follow-up.** *AJNR Am J Neuroradiol* 2019;40:1773–78 CrossRef Medline
27. Fujimoto M, Lylyk I, Bleise C, et al. **Long-term outcomes of the WEB device for treatment of wide-neck bifurcation aneurysms.** *AJNR Am J Neuroradiol* 2020;41:1031–36 CrossRef Medline

# Dural Arteriovenous Fistulas of the Foramen Magnum Region: Clinical Features and Angioarchitectural Phenotypes

M.T. Caton, K.H. Narsinh, A. Baker, C.F. Dowd, R.T. Higashida, D.L. Cooke, S.W. Hetts, V.V. Halbach, and M.R. Amans



## ABSTRACT

**BACKGROUND AND PURPOSE:** AVFs of the foramen magnum region, including fistulas of the marginal sinus and condylar veins, have complex arterial supply, venous drainage, symptoms, and risk features that are not well-defined. The purpose of this study was to present the angioarchitectural and clinical phenotypes of a foramen magnum region AVF from a large, single-center experience.

**MATERIALS AND METHODS:** We retrospectively reviewed cases from a 10-year neurointerventional data base. Arterial and venous angioarchitectural features and clinical presentation were extracted from the medical record. Venous drainage patterns were stratified into 4 groups as follows: type 1 = unrestricted sinus drainage, type 2 = sinus reflux (including the inferior petrosal sinus), type 3 = reflux involving sinuses and cortical veins, and type 4 = restricted cortical vein outflow or perimedullary congestion.

**RESULTS:** Twenty-eight patients (mean age, 57.9 years; 57.1% men) had 29 foramen magnum region AVFs. There were 11 (37.9%) type 1, nine (31.0%) type 2, six (20.7%) type 3, and 3 (10.3%) type 4 fistulas. Pulsatile tinnitus was the most frequent symptom (82.1%), followed by orbital symptoms (31.0%), subarachnoid hemorrhage (13.8%), cranial nerve XII palsy (10.3%), and other cranial nerve palsy (6.9%). The most frequent arterial supply was the ipsilateral ascending pharyngeal artery (93.1% ipsilateral, 55.5% contralateral), vertebral artery (89.7%), occipital artery (65.5%), and internal carotid artery branches (48.3%).

**CONCLUSIONS:** We present the largest case series of foramen magnum region AVFs to date and show that clinical features relate to angioarchitecture. Orbital symptoms are frequent when sinus reflux is present. Hemorrhage was only observed in type 3 and 4 fistulas.

**ABBREVIATIONS:** FMR = foramen magnum region; IJV = internal jugular vein

Dural AVFs of the foramen magnum region (FMR) comprise a rare subgroup of intracranial arteriovenous shunts occurring at the marginal sinus and condylar veins.<sup>1</sup> These FMR AVFs are thought to represent between 1.5% and 4.2% of cranial shunting lesions.<sup>2,3</sup> These lesions are anatomically complex, owing to the functional and anatomic variability of venous drainage at the craniocervical junction.<sup>4-6</sup> The marginal sinus is an inconstant

ringlike intradural sinus along the rim of the foramen magnum and is frequently undetectable on noninvasive imaging in normal physiologic states.<sup>7</sup> The marginal sinus communicates with a network of venous channels, including the condylar veins (anterior, posterior, and lateral), the condylar confluence, and the inferior petrosal sinus, serving to redirect blood flow between the parallel venous egress pathways of the jugular vein and vertebral venous plexus (Fig 1). As a consequence, pressurization of this FMR venous network can manifest with a spectrum of symptoms ranging from pulsatile tinnitus to myelopathy. Retrograde pressurization of the cavernous sinus via the inferior petrosal sinus may also generate orbital chemosis and extraorbital muscle palsies that may masquerade as carotid cavernous fistulas.<sup>8</sup>

An FMR AVF at high risk of hemorrhage or causing debilitating symptoms can be treated endovascularly with low morbidity.<sup>1</sup> Both transvenous and transarterial approaches have been described.<sup>9-12</sup> Successful treatment of FMR AVFs demands rigorous preparation and knowledge of both the arterial supply and venous drainage patterns to achieve a durable cure and avoid nontarget embolization.

Received January 10, 2021; accepted after revision February 26.

From the Department of Radiology and Biomedical Imaging, Interventional Neuroradiology Section, University of California, San Francisco, San Francisco, California.

This work was supported by National Heart Lung-Blood Institute of the National Institutes of Health under award No. R56 HL149124-01.

Paper previously presented, in part, at: Annual Meeting of the American Society of Neuroradiology, May 22–26, 2021; virtual.

Please address correspondence to M. Travis Caton Jr, MD, University of California, San Francisco, 505 Parnassus Ave, Room L349, San Francisco, CA 94143; e-mail: michael.caton2@ucsf.edu; @traviscaton

Indicates open access to non-subscribers at www.ajnr.org

Indicates article with online supplemental data.

<http://dx.doi.org/10.3174/ajnr.A7152>



However, as with other classes of AVF, observation is appropriate for low-risk lesions.<sup>13</sup> Therefore, knowledge of the holistic structure and behavior of the shunt, including comprehensive evaluation of the arterial and venous anatomy of the fistula, is essential for treatment planning and complication avoidance.

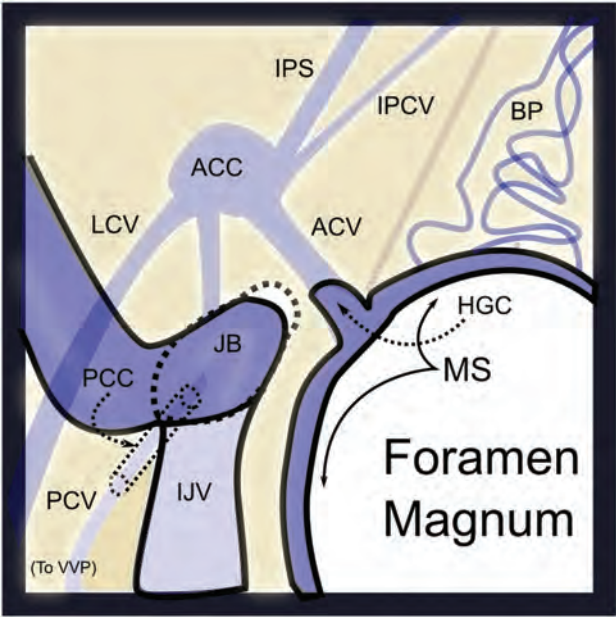


**FIG 1.** Venous anatomy of the FMR from above. The marginal sinus (MS) lines the margin the foramen magnum and connects to the basilar plexus (BP) anteriorly, the anterior condylar vein (ACV) laterally via the hypoglossal canal (HGC), and the suboccipital cavernous sinus inferiorly (not shown). The anterior condylar vein (ACV) connects with the anterior condylar confluence (ACC), which, in turn, communicates with the inferior petrosal sinus (IPS) and inferior petroclival vein (IPCV) and posteriorly with the lateral condylar vein (LCV), and the jugular bulb and internal jugular vein (JB/IJV). The posterior condylar (emissary) vein (PCV) exits via the posterior condylar canal (PCC).

McDougall et al<sup>1</sup> at the University of California, San Francisco proposed a grading system for FMR AVF, classifying shunts by their pattern of venous drainage. In this model, low-risk shunts (grade I) have unrestricted antegrade drainage via the internal jugular vein (IJV) system, whereas intermediate (grade II) lesions show partial or restricted IJV outflow. High-risk shunts (grade III) drain exclusively via superficial venous channels. Spittau et al<sup>14</sup> proposed a modification to this taxonomy based on the dominant pattern of drainage, type 1: dominant antegrade flow (jugular or vertebral venous plexus), type 2: dominant retrograde flow (petrosal→cavernous), and type 3: dominant pial/perimedullary reflux. Because the current neuroendovascular literature is confined to small case reports and series, the validity of these proposed angiographic-clinical relationships is uncertain.

The purpose of this study was to elucidate the relationship between vascular angioarchitecture and clinical presentation by retrospectively evaluating a large single-institution case series.

### MATERIALS AND METHODS

#### Data Acquisition

The neurointerventional data base of a single, large, tertiary hospital (University of California, San Francisco) was retrospectively reviewed between January 2010 and November 2020 under an institutional review board–approved protocol in which informed consent was waived. Search inclusion criteria were confined to patients who underwent conventional angiography at our hospital and who were diagnosed with fistulas of the marginal sinus, condylar veins (anterior, lateral, posterior, and condylar confluence), or foramen magnum during the prespecified time interval. Inclusion mandated complete angiography including selective DSA of the bilateral internal and external carotid arteries and bilateral subclavian arteries including the deep and ascending cervical branches, and dedicated angiography of the posterior fossa (vertebral artery injection). Cases in which the original angiographic diagnosis was equivocal or discordant with intraoperative

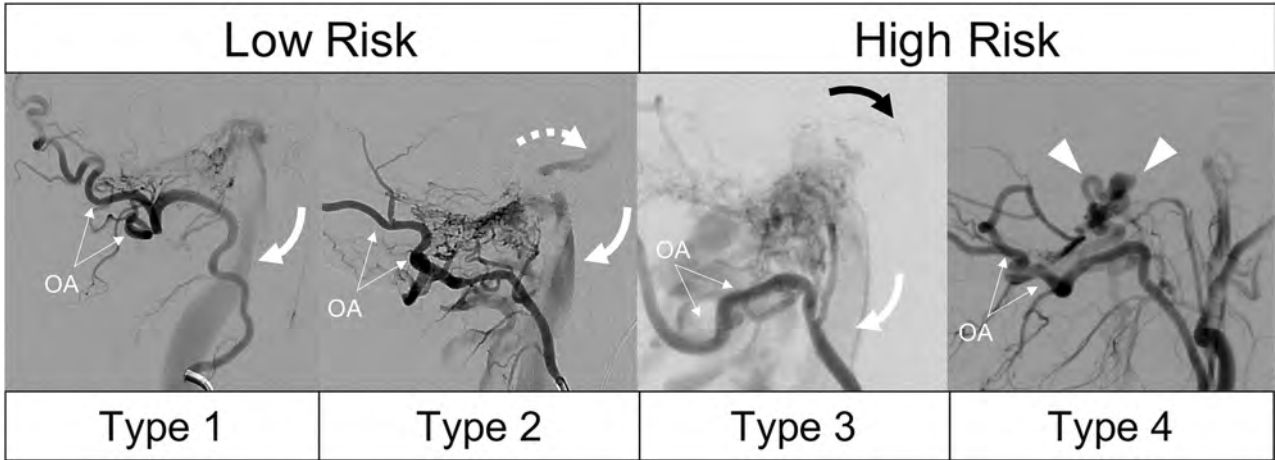


**FIG 2.** Modified grading system for FMR-AVFs shown in 4 patients having undergone lateral occipital artery (OA) injection DSA. Type 1 shows unrestricted drainage via the IJV (curved arrow) without reflux. Type 2 shows both antegrade drainage (curved arrow) and sinus reflux (dashed arrow, inferior petrosal sinus). Type 3 lesions are differentiated by the presence of cortical venous reflux, in this case, pontine perforating veins (black arrow) in addition to sinus drainage (white arrow). Type 4 lesions have restricted, exclusive drainage via cortical veins (arrowheads) without a coexisting sinus drainage pathway.

## Venous drainage patterns in FMR AVF

Venous Angioarchitectural Type	Clinical Presentation (% of Cases)					
	Pulsatile Tinnitus and/or Bruit	Orbital Symptoms	CN XII Palsy	Myelopathy	Hemorrhage	Headache
Type 1 (n = 11)	90.9%	9.1%	0.0%	0.0%	0.0%	27.3%
Type 2 (n = 9)	100.0%	44.4%	22.2%	0.0%	0.0%	44.4%
Type 3 (n = 6)	66.7%	33.3%	0.0%	0.0%	16.7%	50.0%
Type 4 (n = 3)	33.3%	33.3%	0.0%	33.3%	66.7%	66.7%

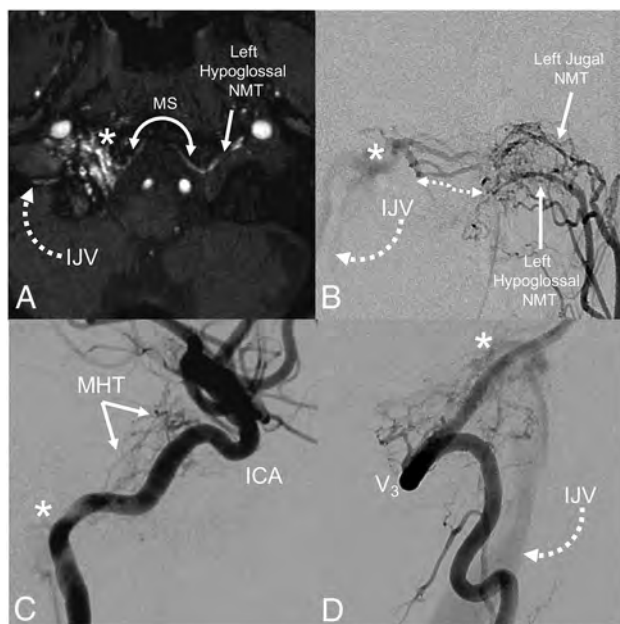


**FIG 3.** Arterial anatomy of a typical type 1 FMR AVF. TOF-MRA (A) of the skull base shows abnormal flow-related enhancement in the right hypoglossal canal, corresponding to a fistula (asterisk). Arterial supply from the contralateral ascending pharyngeal artery (hypoglossal branch) crosses the foramen magnum and drains via the IJV. Relative anatomy: an anterior-posterior DSA with injection of the left ascending pharyngeal artery (B) shows hypertrophied arterial channels (double-sided arrow). Lateral DSA of the right ICA (C) shows supply to the fistula (asterisk) from the meningo-hypophyseal trunk (MHT). D, Lateral DSA of the right vertebral artery ( $V_3$ ) shows direct contribution to fistula (asterisk) and drainage via the IJV. NMT indicates neuro-meningeal trunk; MS, marginal sinus.

findings were reviewed by an experienced neurointerventionalist (M.R.A.) and were excluded if a shunt of the FMR was not definitely identified. Patients with angiographic work-up at other hospitals were excluded.

Demographic characteristics including clinical presentation were extracted from the clinical and procedural notes. For this purpose, we defined “orbital symptoms” as including exophthalmos, chemosis, episcleral venous engorgement, or extraorbital muscle palsy. Each cerebral angiogram was reviewed to gather arterial feeder vessels and venous drainage patterns. Fistulas were subclassified as marginal sinus, anterior condylar vein, posterior condylar vein, or lateral condylar vein on the basis of the venous location of the shunt. Venous drainage was classified according to a modified version of the McDougall grading system: type 1 = unrestricted sinus drainage, type 2 = sinus reflux (including inferior petrosal sinus), type 3 = reflux involving sinuses and cortical

veins, and type 4 = restricted cortical vein outflow or perimedullary congestion (Fig 2). All values are reported as mean (SD).

Statistical comparison of symptom prevalence between groups was performed using a 2-tailed Fisher exact test, and comparison of mean arterial feeder numbers across groups was performed using the Kruskal-Wallis test, with  $P$  values  $< .05$  considered significant.

## RESULTS

Retrospective review of neuroangiographic reports obtained between January 2010 and November 2020 initially identified 36 patients with a possible FMR AVF. We excluded 8 patients: Of these, 2 were patients initially treated outside the prespecified time interval, 1 patient’s final diagnosis was a small medullary arteriovenous malformation confirmed on resection, and 5 patients with possible FMR AVF were excluded after review by the senior author (M.R.A.) due to the uncertainty of the fistulous site or incomplete angiographic characterization after review of DSA images. We, therefore, included 28 patients with 29 FMR AVFs in the final analysis (1 patient had 2 discrete fistulas involving the marginal sinus and lateral condylar vein). The mean patient age was 57.9 (SD, 15.2) years, and 57.1% of patients were men.

### Venous Drainage Patterns, Risk Stratification, and Clinical Presentation

The most common fistulous sites were the marginal sinus (21/29, 72.4%), anterior condylar vein, (4/29, 13.8%), posterior condylar vein (2/29, 6.9%), and lateral condylar vein (2/29, 6.9%). Using the modified University of California, San Francisco criteria (Fig 2), we classified 11/29 (37.9%) FMR AVFs as type one, 9/29 (31.0%) as type two, 6/29 (20.7%) as type 3, and 3/29 (10.3%) as type 4. The most frequent clinical symptoms among all patients included pulsatile tinnitus (82.8%) and orbital symptoms (27.6%). Less frequent clinical presentations included subarachnoid hemorrhage (10.3%), hypoglossal nerve palsy (6.9%), trigeminal nerve palsy (6.9%), and myelopathy (3.4%). One patient in this series (1/29, 3.4%) was asymptotically diagnosed during routine angiographic follow-up of a resected AVM. Headache was common in all groups, with an overall prevalence of 48.3%, increasing in frequency at higher venous angioarchitectural types, ranging from 27.3% of patients (type 1) to 66.7% (type 4).

The relationship of clinical presentation to venous angioarchitectural risk type is summarized in the Table. Orbital symptoms were present in 40% of cases associated with some degree of venous sinus reflux (type 2 or 3) compared with 9.1% of patients with intact antegrade sinus drainage, though this difference was not significant ( $P = .13$ ). Hypoglossal palsy was seen in 2/9 (22.2%) cases of type 2 FMR AVF as was trigeminal nerve palsy

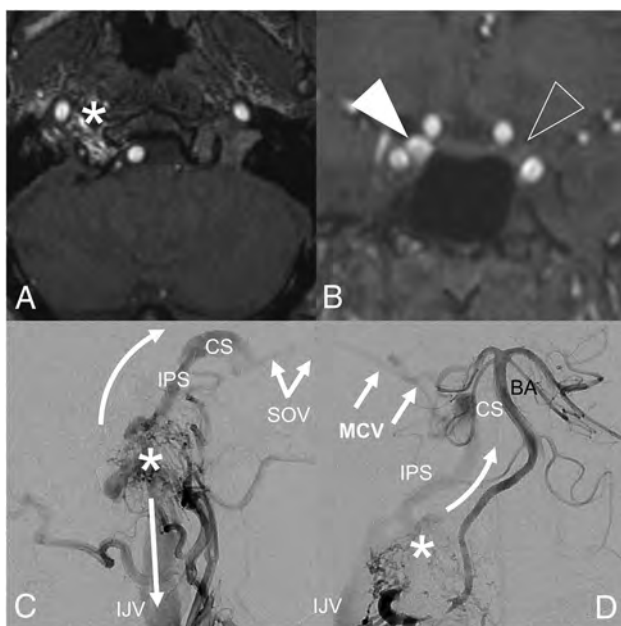


**FIG 4.** A type 3 FMR-AVF with clinical features mimicking a carotid cavernous fistula. MRA of the FMR (A) shows flow-related enhancement in the right hypoglossal canal, corresponding to an anterior condylar vein fistula site. Coronal MRA (B) shows asymmetric flow-related enhancement of the right (white arrowhead) relative to left (clear arrowhead) cavernous sinuses. Lateral-projection DSA of the right ascending pharyngeal artery (C) shows the fistula (asterisk) with antegrade drainage via the IJV (straight arrow) and reflux via the inferior petrosal sinus (IPS, curved arrow) extending to the cavernous sinus (CS) and superior ophthalmic vein (SOV), resulting in proptosis and chemosis. Anterior-posterior DSA of the right vertebral artery (D) shows reflux via the IPS and CS, which continues to the middle cerebral vein (MCV), making this a high-risk type 3 fistula. The asterisk represents the fistulous shunt site. BA indicates the basilar artery.

(2/9, 22.2%). Hemorrhage was seen exclusively in FMR AVFs with cortical vein reflux (type 3 or 4). One patient with a type 4 FMR AVF presented with cervical myelopathy.

### Arterial Supply

The overall mean number of arterial feeders per fistula was 5.7 (SD, 3.00). The frequency of each arterial feeder is summarized in the Online Supplemental Data, and an illustrative example of a type 1 lesion is shown in Fig 3. Eighteen of 29 (62.1%) FMR AVFs derived supply from at least 1 contralateral artery. Arterial feeders present in >50% of all patients with FMR AVF included the ipsilateral ascending pharyngeal artery (93.1%), ipsilateral vertebral artery (89.7%), ipsilateral occipital artery 65.5%, and contralateral ascending pharyngeal artery (55.2%). Other frequent arterial feeders included the meningohypophyseal and inferolateral trunks of the internal carotid artery (48.3% ipsilateral and 31.0% contralateral), ipsilateral middle meningeal artery (31.0%), posterior auricular artery (31.0%), and contralateral vertebral artery (28.6%). There was no significant difference in the number of arterial feeders by venous risk group ( $P = .18$ ): The mean number of feeders for type 1 was 5.6 (SD, 3.4), type two, 6.8 (SD, 2.1), type three, 6.2 (SD, 3.1), and type four, 2.3 (SD, 1.5). The fraction of cases with at least 1 contralateral arterial

feeder was 63.6% for type one, 77.8% for type two, 50.0% for type 3, and 33.0% for type 4.

### DISCUSSION

This study represents the largest series of FMR AVFs to date and clarifies the behavior of this uncommon form of intracranial shunt, revealing 4 distinct clinical-angiographic phenotypes. FMR AVFs were under-represented in previous studies, for example, comprising only 1.5% of cases in the cohort from which the Cognard classification was derived.<sup>2</sup> This study, therefore, builds on prior work<sup>1,3,14</sup> by establishing a classification system specific to FMR AVF, incorporating both risk and symptoms toward appropriate therapy selection.

McDougall et al<sup>1</sup> were the first to systematically describe fistulas of the marginal sinus in a series of 14 patients. They defined 3 clinical phenotypes based on the restriction of jugular outflow and the presence of cortical venous reflux. More recently, Choi et al<sup>3</sup> described 10 fistulas of the hypoglossal canal (anterior condylar vein), noting that orbital symptoms and myelopathy were present only in cases with restriction of antegrade sinus outflow, extending the notion that clinical presentation is a manifestation of venous drainage and therefore an overall risk. In a case series and in a systematic review of 120 cases of FMR AVF (115/120, 95.8% from the literature), Spittau et al<sup>14</sup> modified the McDougall taxonomy on the basis of clinical phenotypes, emphasizing the dominant pattern of venous drainage: 1 = antegrade sinus, 2 = retrograde sinus with or without antegrade drainage/cortical venous reflux, and 3 = dominant cortical venous or perimedullary reflux. They showed that this angiographic classification schema corresponds well with clinical manifestations. However, due to inclusion of a subjective element (dominance) and lack of primary angiographic data in >90% of included cases, the reproducibility and generalizability of this scale are uncertain. In addition, the Spittau criteria do not differentiate the binary presence or absence of cortical venous reflux, a feature that has important implications for hemorrhagic risk and mortality.<sup>15,16</sup> We, therefore, differentiated type 2 (60%) and 3 lesions (40%) on the basis of the presence of cortical venous reflux despite a similar prevalence of orbital symptoms (44.3% versus 33.3%,  $P = 1.0$ , Fisher exact test) among patients with sinus reflux (Fig 4).

The principal finding of this study is that nearly all FMR AVFs present symptomatically (96.5%), most with pulsatile tinnitus (82.3%). While AVFs of the sigmoid and transverse sinuses are known causes of pulsatile tinnitus, the correlation of FMR AVF and pulsatile tinnitus is less established. Turbulence in the pressurized condylar veins and petrosal sinuses could plausibly result in conduction across the petrous bone, accounting for a high-pitched, pulse-synchronous tinnitus. In our experience, direct auscultation of the mastoid bone often reveals audible bruit in patients with FMR AVF. Given the observed association of pulsatile tinnitus and FMR AVF, vigilance of the posterior skull base is warranted on noninvasive imaging studies performed to evaluate pulsatile tinnitus. Advanced MR imaging techniques including contrast MR angiography, susceptibility mapping of deoxygenated hemoglobin, and arterial spin-labeling may aid in the diagnosis but care should be taken to avoid misinterpretation of artifactual signal in this



region.<sup>17</sup> Our findings also support results of previous work showing that the orbital symptoms are frequent in an FMR AVF with sinus reflux (40% of patients with type 2 or 3), a finding that may clinically mimic carotid cavernous fistula (Fig 4).<sup>8</sup>

In this series, high-risk presenting symptoms (myelopathy, hemorrhage) were seen exclusively in type 3 and 4 lesions. Type 1 and 2 FMR AVFs may, therefore, be considered low-risk when evaluating patients for treatment. This finding corroborates previously well-established risk features from the Borden and Cognard classification systems, in which cortical venous reflux is the key mediator of risk.<sup>2,18</sup> Although the overall incidence of hemorrhage and myelopathy was low (13.7%) relative to other cranial AVFs, the presence of orbital symptoms in >25% of cases has important therapeutic implications. Left untreated, pressurization of the cavernous sinus can result in permanent vision loss and represents an urgent indication for therapy for the FMR AVF.<sup>19</sup> We find that the presence (or absence) of orbital symptoms is a useful heuristic for stratifying patients. Although we did not find statistical difference, orbital symptoms were seen in 40% of patients with angiographic evidence of venous reflux (type 2/3) compared with 14.3% with none (type 1/4). Still, the considerable overlap in orbital symptoms between ostensibly low-risk (type 2) and high-risk (type 3) lesions stresses the importance of angiography in the initial diagnostic work-up.

Djindjian and Merland<sup>20</sup> first recognized the disproportionate impact of venous drainage over arterial supply in their taxonomy of cranial AVFs. Subsequent work has confirmed this as a tenet of risk stratification.<sup>15,21,22</sup> Despite the emphasis on venous angioarchitecture, knowledge of the arterial supply is critical to inform treatment strategies. Curative endovascular treatment requires total obliteration of the network of arterial feeders; failure to recognize the contribution of a contralateral feeding artery could result in treatment failure and preclude repeat treatment. Our findings show that a contralateral arterial supply is present in 62.5% of cases. We found that dural supply from the internal carotid artery (48.3% ipsilateral, 31.0% contralateral) and direct vertebral artery supply (89.7% ipsilateral, 27.6% contralateral) were common. Recognition of these and other potential hazardous collaterals is critical to prevent inadvertent reflux if transarterial liquid embolics are used. While this study is insufficiently powered to detect statistical differences in arterial supply across venous angioarchitectural types, we noted a general increase in the number of arterial feeders from type 1 through type 3, with the notable exception of type 4 FMR AVFs, which typically have fewer arterial feeders at presentation. These findings again emphasize the importance of meticulous pretreatment control angiograms to delineate the full extent of the arterial supply in FMR AVFs.

There are several important limitations of the current study. First, although this is the largest comprehensive angiographic review of FMR AVFs, our analysis is underpowered to detect robust differences among angioarchitectural groups. Moreover, we cannot define the natural history of FMR AVFs or the propensity for lesions to attain higher risk features across time, a phenomenon that was reported in 2% of patients in 1 study.<sup>13</sup> We elected to aggregate fistulas of the FMR, including the condylar veins and marginal sinus, because these share many interconnections and

common final drainage pathways.<sup>4,5,7,23</sup> However, it is plausible that subgroups of FMR AVFs (eg, lateral-versus-posterior condylar veins) behave differently.

## CONCLUSIONS

We report the clinical characteristics and detailed arteriovenous angioarchitecture of 29 FMR AVFs, defining 4 clinical-angiographic phenotypes. These fistulas have a wide range of clinical presentations that correlate to, but may not reliably predict, angiographic risk. The arterial supply and venous drainage patterns of FMR AVFs are equally variable; we, therefore, recommend thorough diagnostic angiography before treatment.

Disclosures: Christopher F. Dowd—UNRELATED: Other: Stryker, Comments: Chief Adjudicator for the EVOLVE Flow Diverter Clinical Trial.\* Steven W. Hett—UNRELATED: Consultancy: Stryker Neurovascular, Route 92, Johnson & Johnson, Siemens, Comments: Core Lab or Clinical Endpoints Committee for clinical trials, contract for angiography suite evaluation\*; Stock/Stock Options: ThrombX Medical, Comments: equity in stroke device startup company. Matthew R. Amans—RELATED: Grant: National Institutes of Health; UNRELATED: Board Membership: MindRhythm Inc; Consultancy: Covidien, Stryker, MicroVention, Comments: Pipeline proctor, consultant, Precipitating Hydrophobic Injectable Liquid (PHIL), Data and Safety Monitoring Board. \*Money paid to the institution.

## REFERENCES

1. McDougall CG, Halbach VV, Dowd CF, et al. **Dural arteriovenous fistulas of the marginal sinus.** *AJNR Am J Neuroradiol* 1997;18:1565–72 Medline
2. Cognard C, Gobin YP, Pierot L, et al. **Cerebral dural arteriovenous fistulas: clinical and angiographic correlation with a revised classification of venous drainage.** *Radiology* 1995;194:671–80 CrossRef Medline
3. Choi JW, Kim BM, Kim DJ, et al. **Hypoglossal canal dural arteriovenous fistula: incidence and the relationship between symptoms and drainage pattern: clinical article.** *J Neurosurg* 2013;119:955–60 CrossRef Medline
4. San Millán Ruiz D, Gailloud P, Rüfenacht DA, et al. **The craniocervical venous system in relation to cerebral venous drainage.** *AJNR Am J Neuroradiol* 2002;23:1500–08 Medline
5. de Oliveira E, Rhoton AL, Peace D. **Microsurgical anatomy of the region of the foramen magnum.** *Surg Neurol* 1985;24:293–352 CrossRef Medline
6. Takahashi S, Sakuma I, Omachi K, et al. **Craniocervical junction venous anatomy around the suboccipital cavernous sinus: evaluation by MR imaging.** *Eur Radiol* 2005;15:1694–700 CrossRef Medline
7. Tubbs RS, Ammar K, Liechty P, et al. **The marginal sinus.** *J Neurosurg* 2006;104:429–31 CrossRef Medline
8. Turner RD, Gonugunta V, Kelly ME, et al. **Marginal sinus arteriovenous fistulas mimicking carotid cavernous fistulas: diagnostic and therapeutic considerations.** *AJNR Am J Neuroradiol* 2007;28:1915–18 CrossRef Medline
9. Tanoue S, Goto K, Oota S. **Endovascular treatment for dural arteriovenous fistula of the anterior condylar vein with unusual venous drainage: report of two cases.** *AJNR Am J Neuroradiol* 2005;26:1955–59 Medline
10. Takemoto K, Tateshima S, Rastogi S, et al. **Onyx embolization of anterior condylar confluence dural arteriovenous fistula.** *J Neurointerv Surg* 2014;6:e13 CrossRef Medline
11. Choi HS, Kim DI, Kim BM, et al. **Endovascular treatment of dural arteriovenous fistula involving marginal sinus with emphasis on the routes of transvenous embolization.** *Neuroradiology* 2011;54:163–69 CrossRef Medline
12. Cyril C, Ofélia M, Hervé D. **Dural arteriovenous fistula involving the anterior condylar canal.** *J Neuroimaging* 2013;23:425–28 CrossRef Medline
13. Satomi J, van Dijk JM, Terbrugge KG, et al. **Benign cranial dural arteriovenous fistulas: outcome of conservative management based**

- on the natural history of the lesion. *J Neurosurg* 2002;97:767–70 CrossRef Medline
14. Spittau B, Millán DS, El-Sherifi S, et al. **Dural arteriovenous fistulas of the hypoglossal canal: systematic review on imaging anatomy, clinical findings, and endovascular management.** *J Neurosurg* 2015;122:883–903 CrossRef Medline
  15. van Dijk JM, terBrugge KG, Willinsky RA, et al. **Clinical course of cranial dural arteriovenous fistulas with long-term persistent cortical venous reflux.** *Stroke* 2002;33:1233–36 CrossRef Medline
  16. Davies MA, TerBrugge K, Willinsky R, et al. **The validity of classification for the clinical presentation of intracranial dural arteriovenous fistulas.** *J Neurosurg* 1996;85:830–37 CrossRef Medline
  17. Caton MT, Callen AL, Copelan AZ, et al. **Jugular venous reflux can mimic posterior fossa dural arteriovenous fistulae on MRI/MRA.** *Am J Roentgenol* 2020 Sep 2. [Epub ahead of print] CrossRef Medline
  18. Borden JA, Wu JK, Shucart WA. **A proposed classification for spinal and cranial dural arteriovenous fistulous malformations and implications for treatment.** *J Neurosurg* 1995;82:166–79 CrossRef Medline
  19. Halbach V, Hieshima G, Higashida R, et al. **Carotid cavernous fistulae: indications for urgent treatment.** *AJR Am J Roentgenol* 1987;149:587–93 CrossRef Medline
  20. Djindjian R, Merland JJ. **Normal super-selective arteriography of the external carotid artery.** In: Djindjian R, Merland JJ. *Super-Selective Arteriography of the External Carotid Artery.* Springer-Verlag: Berlin Heidelberg; 1978:1–123
  21. Awad IA, Little JR, Akarawi WP, et al. **Intracranial dural arteriovenous malformations: factors predisposing to an aggressive neurological course.** *J Neurosurg* 1990;72:839–50 CrossRef Medline
  22. Kim MS, Han DH, Kwon OK, et al. **Clinical characteristics of dural arteriovenous fistula.** *J Clin Neurosci* 2002;9:147–55 CrossRef Medline
  23. Matsushima K, Kawashima M, Matsushima T, et al. **Posterior condylar canals and posterior condylar emissary veins: a microsurgical and CT anatomical study.** *Neurosurg Rev* 2014;37:115–26 CrossRef Medline

# Transradial Neuroendovascular Procedures in Adolescents: Initial Single-Center Experience

 H. Alshehri,  A.A. Dmytriw,  K. Bhatia,  S. Bickford,  V. Rea,  N. Shkumat, and  P. Muthusami

## ABSTRACT

**BACKGROUND AND PURPOSE:** The feasibility and safety of transradial angiography is not established outside the adult literature. The objective of this study was to assess the feasibility and safety of transradial access for neuroangiography in adolescents.

**MATERIALS AND METHODS:** A retrospective case-control study was performed, comparing transradial neuroendovascular procedures in adolescents (age range, 10–18 years) with an age- and procedure-matched cohort of transfemoral neuroendovascular procedures. Clinical and procedural details, including type of procedure, conversion rate, fluoroscopy time, radiation dose, complications, and readmissions, were reported by descriptive statistics or measures of central tendency and compared using a *t* test or nonparametric equivalent. A *P* value < .05 was considered statistically significant.

**RESULTS:** Twenty adolescents (mean age, 14.6 [SD, 1.7] years, M/F ratio = 9:11) who underwent transradial neuroangiography were compared against 20 adolescents (mean age, 14.4 [SD, 2.1] years, M/F ratio = 12:8) who underwent transfemoral neuroangiography. We found no significant difference in procedural success (0% conversion rate), fluoroscopy times (33.7 [SD, 40.2] minutes versus 23.3 [SD, 26.2] minutes, *P* = .34) and radiation dose (150.9 [SD, 133.7] Gy×cm<sup>2</sup> and 122.9 [SD, 79.7] Gy×cm<sup>2</sup>, *P* = .43). There were 2 self-limiting postprocedural complications in the transradial group. There were no major hemorrhages, need for further interventions, or readmissions in either group.

**CONCLUSIONS:** The benefits of transradial angiography described for adults can likely be safely extended to adolescents. These are important data before transitioning to smaller children and should be prospectively evaluated in a larger cohort.

Several randomized controlled trials in cardiovascular intervention have shown the superiority of transradial angiography over transfemoral access for procedural safety, outcomes, and health care costs in adults, with the American Heart Association supporting a “radial-first” strategy for patients with acute coronary syndrome.<sup>1–3</sup> A lower rate of access-site complications, including life-threatening hemorrhage, pseudoaneurysms, and ischemic limbs and a lower rate of procedural adverse events, including death, myocardial infarction, and stroke, have resulted in this paradigm clinical shift.<sup>2</sup> In the past few years, there has also been increased adoption of the transradial approach for neurointerventional procedures, with substantially increased patient preference and reduced hospital costs in the adult neurointerventional

literature.<sup>4–9</sup> In the Patient Preference for Radial versus Femoral Vascular Access for Elective Coronary Procedures (PREVAS) trial, >70% of patients preferred transradial access over transfemoral access.<sup>10</sup> Similarly, in a recent study in 25 patients having undergone neurointerventional procedures who received transradial access after previous transfemoral access, 96% reported preference for the former.<sup>4</sup>

In contrast to its increasing acceptance in adults, radial arterial access for neuroangiography in children and adolescents has traditionally been performed via the femoral route. Some recent reports describe specific cases in which transradial cerebral and coronary angiographic procedures were performed successfully and safely in children.<sup>5,6,11</sup> However, concerns regarding arterial size and an increased incidence of spasm, dissection, and occlusion have led to modest adoption of this technique for angiography outside adult populations. It was recently shown that radial arteries approach adult dimensions by adolescence.<sup>12</sup> In addition, the recently described distal radial access technique in adults (ie, the “snuffbox” technique) for coronary and neuroangiography procedures uses the distal radial artery branch, which is comparable in size with a pediatric radial artery at the wrist.<sup>13–15</sup> However, there is no study reporting the feasibility and safety of transradial

Received December 21, 2020; accepted after revision February 23, 2021.

From the Divisions of Neuroradiology and Image-Guided Therapy (H.A., A.A.D., S.B., V.R., N.S., P.M.), Department of Diagnostic Imaging, The Hospital for Sick Children, University of Toronto, Toronto, Ontario, Canada; and Department of Medical Imaging (K.B.), Children's Hospital at Westmead, Westmead, New South Wales, Australia.

Please address correspondence to Prakash Muthusami, MD, Divisions of Neuroradiology & Image-Guided Therapy, The Hospital for Sick Children, Toronto, ON M5G 1X8 Canada; e-mail: prakash.muthusami@sickkids.ca; @PMuthusami; @AdamDmytriw  
<http://dx.doi.org/10.3174/ajnr.A7142>



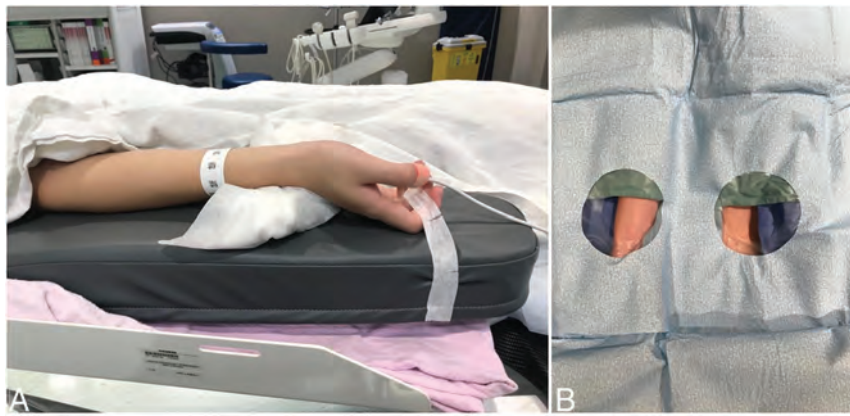


**FIG 1.** Arm position for radial angiography. *A*, Right arm positioned at the same height as the groin during transradial neuroangiography, with the wrist slightly hyperextended and a saturation probe on the thumb. *B*, Postdraping appearance, showing the wrist and right groin exposed. For the operator's working position, this is akin to bilateral groin access.

access for angiography in larger cohorts of patients younger than 18 years of age. In our practice, we started offering transradial access for neuroendovascular procedures in adolescents (10–18 years of age) in November 2019. We, therefore, began to evaluate and report this experience, as well as compare this technique with transfemoral access.

## MATERIALS AND METHODS

An institutional review board–approved retrospective analysis of cerebral angiography in adolescents, during a 1-year period from November 2019 to October 2020, was performed. Procedures were categorized as “cases” (consecutive procedures of neuroangiography performed via radial access) and “controls” (consecutive age- and procedure-matched patients who underwent neuroangiography via femoral access in the same period), all of whom were age- and procedure-matched. Procedures performed via brachial or axillary artery access were excluded. All neuroangiographic procedures were performed by the same neuroradiologist (P.M.) in a biplane angiography suite (Artis Q BA Twin; Siemens) with the patient under general anesthesia or local anesthesia with or without mild sedation or anxiolysis. Sonography-guided access was performed in all cases, using an out-of-plane method with a single-wall puncture followed by a standard Seldinger technique for sheath insertion.

### Transfemoral Neuroangiography and Embolization

Transfemoral neuroangiography was performed under systemic heparinization (50 IU/kg up to a maximum of 3000 IU), using a 4F Glidesheath (Terumo) and a 4F diagnostic catheter with standard projections. The catheter system was maintained on a continuous flush of heparinized saline. Digital subtraction angiography was performed using an iodinated contrast agent (Iohexol, Omnipaque, 300 mg I/mL; GE Healthcare) injected through a power injector at 3–5 mL/s, depending on the age and arterial size. Rotational angiography was performed in the vessels of interest at the discretion of the operator. Embolization procedures, if any, were performed following diagnostic angiography, after upsizing the sheath if required. Postprocedural hemostasis was achieved

with manual compression or a vascular closure device, followed by local instillation of 2–6 mL of 0.25% bupivacaine. Patients were asked to remain supine for 5 hours following the procedure, after which they were slowly ambulated, and, if uneventful, discharged home at 6–7 hours. Some patients required additional postprocedural sedation to prevent movement. In the event of hematoma or new bleeding at the arteriotomy site, additional manual compression was applied until hemostasis was achieved. Following discharge, patients could resume daily activities but avoid strenuous physical activity or sports for 1 week.

### Transradial Neuroangiography and Embolization

Procedures were performed with the arm supported as close to the body as possible, with the wrist supinated and slightly hyperextended, and a saturation probe on the ipsilateral thumb (Fig 1). Access was obtained using a 5F Glidesheath Slender (Terumo), which is 25-cm in length. A radial cocktail consisting of heparin (1000 IU), verapamil (1 mg), and nitroglycerin (1.5 mcg/kg up to a maximum of 150 mcg) was given as a slow intra-arterial injection. Initial access into the subclavian artery was performed over a Glidewire Baby-J (Terumo). Diagnostic angiography was performed using a 5F Sim-1 Glide catheter (Terumo), using hand injections and rotational angiography if considered relevant. Postprocedural hemostasis was performed using an inflatable wrist TR Band (Terumo). Patients were ambulated after 30 minutes of observation, were discharged following wrist band removal 2–3 hours following the procedure, and could resume all activities the following day except lifting heavy objects.

Patient demographics and clinical details including complications, follow-up, further admissions, consults, or procedures needed were retrieved from electronic patient charts (Table 1). Procedural details were obtained from the radiology PACS report and image review. These included procedural and technical details, parameters for procedural safety (complications, type, and severity), fluoroscopy time, procedural time, procedural completion, and conversion rate to another site. Complications were graded according to the Clavien-Dindo classification.<sup>13</sup> Clinical and procedural details were reported as descriptive or as means (SDs). Fluoroscopy times and radiation doses were compared using 2-tailed *t* tests or their nonparametric equivalents. *P* < .05 was considered statistically significant.

## RESULTS

A total of 40 adolescents were included, of whom 20 (mean age, 14.6 [SD, 1.7] years, M/F ratio = 9:11) underwent transradial angiography, and 20 age- and procedure-matched adolescents (mean age, 14.4 [SD, 2.1] years, M/F ratio = 12:8) underwent transfemoral angiography. Clinical and demographic details are shown in Table 1.

**Table 1: Demographics of our cohorts (n = 40) and clinical features**

	Transradial Neuroangiography (n = 20)	Transfemoral Neuroangiography (n = 20)	P Value
Age (mean) (yr)	14.6 (SD, 1.7)	14.4 (SD, 2.1)	.69
M/F	9:11	12:8	.35
Indication (No.)			
Ischemic stroke work-up	6	10	
Arteriovenous malformation/ fistula	14	9	
Other	0	1 (Ruptured aneurysm)	
Procedures (No.)			
Diagnostic cerebral angiography	18	18	
Endovascular embolization	2	2	
General anesthesia (%)	95	95	1.0
Preprocedural hemoglobin (mean) (g/dL)	132.8 (SD, 18.5)	123.8 (SD 9.5)	.21
Preprocedural INR (mean)	1.1 (SD, 0.1)	1.1 (SD, 0.1)	1.0
Preprocedural routine use of anticoagulants/antiplatelets (No.) (%)	4, 20	6, 30	.47

Note:—INR indicates international normalized ratio.

**Table 2: Comparison of transradial (n = 20) and transfemoral (n = 20) cohorts**

	Transradial Neuroangiography (n = 20)	Transfemoral Neuroangiography (n = 20)	P Value
Conversion rate to another site (%)	0	0	1.0
Fluoroscopy time (mean) (min)	33.7 (SD, 40.2)	23.3 (SD, 26.2)	.34
Total radiation dose (mean) (Gy × cm <sup>2</sup> )	150.9 (SD, 133.7)	122.9 (SD, 79.7)	.43
Complications, grade I (No.)	2	0	.15
Complications, grades I–V (No.)	0	0	
Readmissions (No.)	0	0	1.0

### Procedural and Technical Success

Under sonographic guidance, successful catheterization was achieved in all cases. The mean radial artery diameter was 2.6 [SD, 0.4] mm (range, 2.0–3.3 mm), and all showed a type A Barbeau response to radial artery test occlusion. The right radial artery was used in 19/20 (95%) cases, and left radial arterial access, in 1 case. Radial-to-femoral conversion was not required in any case for procedure completion. Mean fluoroscopy duration in the transradial and transfemoral groups was 33.7 [SD 40.2] minutes versus 23.3 [SD, 26.2] minutes in the transfemoral group ( $P = .34$ ), whereas the mean fluoroscopy doses for the transradial and transfemoral groups were 150.9 [SD, 133.7] Gy × cm<sup>2</sup> and 122.9 [SD, 79.7] Gy × cm<sup>2</sup>, respectively ( $P = .43$ ) (Table 2).

### Closure and Complications

Hemostasis in all transradial procedures was achieved using the TR Band; in transfemoral cases, using manual compression in 19/20 cases, and a closure device (Angio-Seal Vascular Closure Device; Terumo) in 1 case. One patient in the transradial group developed forearm swelling and pain requiring conservative management. Sonography and Doppler sonography showed no radial arterial

thrombosis or occlusion. There was 1 instance of hemorrhage after TR Band removal, which required manual compression. There were no instances of major hemorrhage or pseudoaneurysm formation in either group and no readmissions for delayed complications. There were no significant vascular access-site complications that required surgical or image-guided interventions in either group.

## DISCUSSION

There are robust data favoring transradial angiography in adults. These include data on procedural outcomes, hospital costs, and patient preference in the cardiac and neurologic literature.<sup>15–17</sup> Although the transradial approach for angiography has been described in a few reports in children, there is still controversy about safety, feasibility, cost, and patient preference.<sup>12,18</sup> Our early experience with transradial neuroangiography confirms the safety and feasibility in adolescents and shows that the benefits of this technique over transfemoral neuroangiography can be extended to this population. These data form the basis for designing a randomized controlled trial for assessing patient preference and procedure-associated costs and also serve as the first step toward a discussion of the merits and demerits of transradial neuroangiog-

raphy in smaller children.

Similar to the proved benefit in adults, radial artery access for angiography could also have several potential advantages over femoral artery access for angiography in children. Because the radial artery is a superficial artery, access and monitoring hemostasis are more straightforward. The median nerve is relatively distant, there are no major veins in the vicinity, and these are well-visualized under sonography, thereby minimizing the risk of neurovascular complications or arteriovenous fistula formation. The transradial approach allows early ambulation and discharge, reducing hospital costs.<sup>1–4,10</sup> If proved feasible and safe in future studies, small children can particularly benefit from a transradial approach due to sedation or immobilization not being required, the small risk of hemorrhage, and early return to sports and school activities.<sup>6</sup> In addition, transradial angiography is likely well-suited for systemic angiography in children, which often requires a cephalad approach due to the smaller diameter of the aorta. In our radial cohort, there were 2 adolescents who required systemic angiography in addition to cerebral angiography for the work-up of vasculopathy. Traditionally, this procedure has been performed via a brachial or

axillary artery approach, with concomitant high morbidity and access-site complications.<sup>18</sup>

Radiation exposure during transradial angiography has not yet been investigated in children. Studies in adults have shown that transradial procedures may result in more radiation to both the patient and operator than transfemoral procedures.<sup>19,20</sup> However, it has also been shown that as operator experience increases, radiation exposure decreases to levels comparable with those seen in transfemoral procedures.<sup>21-23</sup> In the present study in adolescents, though the fluoroscopic times and doses were higher in the transradial cohort, the differences, we believe, were not statistically nor clinically significant.

It has been shown that failure to access the radial artery is typically due to puncture error or radial artery spasm.<sup>24</sup> In our experience, the routine use of sonography for radial artery access eliminated access failure and spasm in all patients. Radial artery spasm has been reported in the adult literature in 10%–30% of cases.<sup>21</sup> Spasm has been shown to be related to arterial size, initial wire or catheter manipulation, and patient anxiety.<sup>18,23</sup> A radial cocktail of verapamil, nitroglycerin, and heparin given intra-arterially immediately after sheath insertion has been shown to reduce the rates of spasm.<sup>22,23,25</sup> Longer sheaths may also reduce the development of radial artery spasm,<sup>18</sup> by covering a greater length of the artery and offering more protection from catheter manipulations during vessel selection.<sup>6</sup> We did not observe any cases of intraprocedural radial artery spasm because all patients received either a general anesthetic or anxiolysis, and we routinely used a long radial sheath advanced above the elbow joint.

The risk of radial artery occlusion following cannulation in adults has been reported as 0.8%–38%.<sup>21,26</sup> This has been shown to be related to patient characteristics such as high body mass index and diabetes, as well as intraprocedural precautions like sheath size, use of anticoagulants, and postprocedural patent hemostasis. Whereas testing in adults for ulnar patency before radial puncture with the Allen or Barbeau test is no longer recommended, we still perform this check in adolescents, in whom it is possible that the 2 major arteries have not yet achieved their full adult dimensions. Although we did not see any instances of radial artery occlusion in our cohort, this would require a forward-looking study with delayed sonographic follow-up to definitively exclude it, being usually a clinically quiescent condition. Because the radial artery is 1 of 2 arteries to the hand, there is no major ischemic risk from occlusion of the radial artery, as opposed to femoral occlusion,<sup>27-29</sup> albeit the likelihood and frequency of the latter is arguably less.

The only complications in our series were minor and self-limiting, occurring during diagnostic angiography. The first was swelling of the forearm and hand, which subsided with arm elevation and encouraging finger movement. This occurred early in our transradial experience, presumably related to the use of a flush at the side arm of the sheath, similar to our transfemoral practice. We have since abandoned using this flush for transradial procedures and have not seen this complication since. The second was a postprocedural small hematoma immediately after removing the TR Band. This subsided with manual compression with no significant clinical sequelae. We have since moved from a single-step deflation of the TR Band to a 2-step process. Of note,

this transradial cohort represents our learning curve with the radial approach to angiography in adolescents, and we expect reduced postprocedural complications going forward.<sup>30</sup> We had no instances of having to switch to femoral access due to the inability to catheterize the neck arteries in adolescents, despite the narrower arch and acute angles of arterial origin compared with adults.

Our study had certain limitations. Being retrospective in design, it has associated biases. However, all procedures were performed by the same operator using standardized protocols. The cohorts were small-but-adequate to assess feasibility and procedural safety. We did not have data regarding procedure-related costs, patient preference, or long-term data regarding radial artery occlusion rates, but this information was not within the scope of this study and requires a prospectively designed trial to satisfactorily evaluate it. Although the cohorts did not include children younger than 10 years of age, this study represents the next logical step in assessing the benefits of transradial neuroangiography documented in the adult literature when balanced against a potential risk to pediatric radial arteries. Finally, this study represents our early experience with transradial angiography, naturally skewing results in favor of the more established transfemoral technique. Nevertheless, the lack of major differences in procedural efficacy, radiation doses, and major complications is a testament to the safety of the transradial technique in adolescents.

## CONCLUSIONS

Transradial neuroangiography is feasible and safe in adolescents. As shown in adult practice, success rates are likely to be high, with increasing operator experience. Evidence from prospective studies is required to compare patient preference and long-term occlusion rates, as well as for extending the benefit of this technique to smaller children.

## REFERENCES

1. Mason PJ, Shah B, Tamis-Holland JE, et al. American Heart Association Interventional Cardiovascular Care Committee of the Council on Clinical Cardiology; Council on Cardiovascular and Stroke Nursing; Council on Peripheral Vascular Disease; and Council on Genomic and Precision Medicine. **An update on radial artery access and best practices for transradial coronary angiography and intervention in acute coronary syndrome: a scientific statement from the American Heart Association.** *Circ Cardiovasc Interv* 2018;11:e000035 CrossRef Medline
2. Ferrante G, Rao SV, Jüni P, et al. **Radial versus femoral access for coronary interventions across the entire spectrum of patients with coronary artery disease: a meta-analysis of randomized trials.** *JACC Cardiovasc Interv* 2016;9:1419–34 CrossRef Medline
3. Catapano JS, Ducruet AF, Koester SW, et al. **Propensity-adjusted cost analysis of radial versus femoral access for neuroendovascular procedures.** *J Neurointerv Surg* 2020 Oct 26. [Epub ahead of print] CrossRef Medline
4. Satti SR, Vance AZ, Golwala SN, et al. **Patient preference for transradial access over transfemoral access for cerebrovascular procedures.** *J Vasc Interv Neurol* 2017;9:1–5 Medline
5. Srinivasan VM, Hadley CC, Prablek M, et al. **Feasibility and safety of transradial access for pediatric neurointerventions.** *J Neurointerv Surg* 2020;12:893–96 CrossRef Medline



6. Irving C, Zaman A, Kirk R. **Transradial coronary angiography in children and adolescents.** *Pediatr Cardiol* 2009;30:1089–93 CrossRef Medline
7. Liu LB, Cedillo MA, Bishay V, et al. **Patient experience and preference in transradial versus transfemoral access during transarterial radioembolization: a randomized single-center trial.** *J Vasc Interv Radiol* 2019;30:414–20 CrossRef Medline
8. Franchi E, Marino P, Biondi-Zoccai GG, et al. **Transradial versus transfemoral approach for percutaneous coronary procedures.** *Curr Cardiol Rep* 2009;11:391–97 CrossRef
9. Jo KW, Park SM, Kim SD, et al. **Is transradial cerebral angiography feasible and safe? A single center's experience.** *J Korean Neurosurg Soc* 2010;47:332–37 CrossRef Medline
10. Kok MM, Weernink MG, von Birgelen C, et al. **Patient preference for radial versus femoral vascular access for elective coronary procedures: the PREVAS study.** *Catheter Cardiovasc Interv* 2018;91:17–24 CrossRef Medline
11. Majmundar N, Patel P, Dodson V, et al. **First case series of the transradial approach for neurointerventional procedures in pediatric patients.** *J Neurosurg Pediatr* 2020 Jan 31. [Epub ahead of print] CrossRef Medline
12. Alehaideb A, Ha W, Bickford S, et al. **Can children be considered for transradial interventions? Prospective study of sonographic radial artery diameters.** *Circ Cardiovasc Interv* 2020;13:e009251 CrossRef Medline
13. Roh JH, Lee JH. **Distal radial approach through the anatomical snuff box for coronary angiography and percutaneous coronary intervention.** *Korean Circ J* 2018;48:1131–34 CrossRef Medline
14. Rajah G, Garling RJ, Hudson M, et al. **Snuff box radial access: a technical note on distal radial access for neuroendovascular procedures.** *Brain Circ* 2019;5:36–40 CrossRef Medline
15. Kühn AL, de Macedo Rodrigues K, Singh J, et al. **Distal radial access in the anatomical snuffbox for neurointerventions: a feasibility, safety, and proof-of-concept study.** *J Neurointerv Surg* 2020;12:798–801 CrossRef Medline
16. Dindo D, Demartines N, Clavien P-A. **Classification of surgical complications: a new proposal with evaluation in a cohort of 6336 patients and results of a survey.** *Ann Surg* 2004;240:205–13 CrossRef Medline
17. Levy EI, Boulos AS, Fessler RD, et al. **Transradial cerebral angiography: an alternative route.** *Neurosurgery* 2002;51:335–40; discussion 40–42 Medline
18. Schindler E, Kowald B, Suess H, et al. **Catheterization of the radial or brachial artery in neonates and infants.** *Paediatr Anaesth* 2005;15:677c82 CrossRef Medline
19. Mann JT 3rd, Cubeddu G, Arrowood M. **Operator radiation exposure in PTCA: comparison of radial and femoral approaches.** *J Invasive Cardiol* 1996;8(Suppl D):22D–25D Medline
20. Hess CN, Peterson ED, Neely ML, et al. **The learning curve for transradial percutaneous coronary intervention among operators in the United States: a study from the National Cardiovascular Data Registry.** *Circulation* 2014;129:2277–86 CrossRef
21. Greenwood MJ, Della-Siega AJ, Fretz EB, et al. **Vascular communications of the hand in patients being considered for transradial coronary angiography: is the Allen's test accurate?** *J Am Coll Cardiol* 2005;46:2013–17 CrossRef Medline
22. Vuurmans T, Hilton D. **Brewing the right cocktail for radial intervention.** *Indian Heart J* 2010;62:221–25
23. Xiaolong L, Bin W. **Analysis of radial artery spasm and vasodilator intervention study.** *Heart* 2012;98(Suppl 2):E164 CrossRef
24. Brunet MC, Chen SH, Peterson EC. **Transradial access for neurointerventions: management of access challenges and complications.** *J Neurointerv Surg* 2020;12:82–86 CrossRef Medline
25. Sandhu K, Butler R, Nolan J. **Expert opinion: transradial coronary artery procedures—tips for success.** *Interv Cardiol* 2017;12:18–24 CrossRef Medline
26. Rashid M, Kwok CS, Pancholy S, et al. **Radial artery occlusion after transradial interventions: a systematic review and meta-analysis.** *J Am Heart Assoc* 2016;5:e002686 CrossRef Medline
27. Taylor LM, Troutman R, Feliciano P, et al. **Late complications after femoral artery catheterization in children less than five years of age.** *J Vasc Surg* 1990;11:297–304; discussion 304–06 CrossRef Medline
28. Hoffman CE, Santillan A, Rotman L, et al. **Complications of cerebral angiography in children younger than 3 years of age.** *J Neurosurg Pediatr* 2014;13:414–19 CrossRef Medline
29. Andraska EA, Jackson T, Chen H, et al. **Natural history of iatrogenic pediatric femoral artery injury.** *Ann Vasc Surg* 2017;42:205–13 CrossRef Medline
30. Goldberg SL, Renslo R, Sinow R, et al. **Learning curve in the use of the radial artery as vascular access in the performance of percutaneous transluminal coronary angioplasty.** *Cathet Cardiovasc Diagn* 1998;44:147–52 CrossRef

# Prevalence of Cervical Artery Abnormalities on CTA in Patients with Spontaneous Coronary Artery Dissection: Fibromuscular Dysplasia, Dissection, Aneurysm, and Tortuosity

J.C. Benson, V.T. Lehman, J.T. Verdoorn, D.P. Shlapak, S.N. Hayes, and M.S. Tweet



## ABSTRACT

**BACKGROUND AND PURPOSE:** Little is known about associations between spontaneous coronary artery dissection and cervical artery abnormalities. This study sought to assess the prevalence of cervical artery abnormalities among patients with spontaneous coronary artery dissection.

**MATERIALS AND METHODS:** A retrospective analysis was completed of patients who underwent CTA neck imaging as part of arterial assessment following the diagnosis of spontaneous coronary artery dissection. The internal carotid and vertebral arteries were evaluated for the presence of fibromuscular dysplasia, dissection and/or pseudoaneurysm, ectasia and/or aneurysmal dilation, atherosclerosis, and webs. Carotid tortuosity was categorized into kinks, loops, coils, and retrojugular and/or retropharyngeal carotid courses; vertebral tortuosity was classified by subjective analysis of severity.

**RESULTS:** Two hundred fourteen patients were included in the final cohort, of whom 205 (95.8%) were women; the average age was 54.4 years. Fibromuscular dysplasia was the most frequently observed abnormality (83 patients; 38.8%), followed by dissections and/or pseudoaneurysms ( $n = 28$ ; 13.1%), ectasia and/or aneurysmal dilation ( $n = 22$ ; 10.3%), and carotid webs ( $n = 10$ ; 4.7%). At least 1 type of carotid tortuosity was present in 99 patients (46.3%). The majority ( $n = 185$ ; 86.4%) of patients had no carotid atherosclerosis; and 26 (12.2%) had mild; 3 (1.4%), moderate; and 0, severe carotid atherosclerosis.

**CONCLUSIONS:** The most common abnormality in the cervical artery vasculature of patients with spontaneous coronary artery dissection is fibromuscular dysplasia. Cervical dissections were higher than previously reported but were not observed in most patients.

**ABBREVIATIONS:** ACS = acute coronary syndrome; CTD = connective tissue disorder; FMD = fibromuscular dysplasia; SCAD = spontaneous coronary artery dissection

Spontaneous coronary artery dissection (SCAD) is an increasingly recognized cause of acute coronary syndrome (ACS), predominantly affecting otherwise healthy young and middle-aged women.<sup>1,2</sup> By definition, it refers to dissection of the coronary artery wall in the absence of trauma, atherosclerosis, or iatrogenic causes.<sup>3</sup> The resultant intramural hematoma and/or intimal flap can cause substantial luminal narrowing, leading to myocardial ischemia and infarction. Once considered rare, SCAD is now thought to be the cause of up to 4% of cases of ACS and up to 35% of cases of ACS in women younger than of 50 years of age.<sup>4,5</sup> Furthermore, there is evidence that the incidence of SCAD has increased during the past decades.<sup>6</sup>

Prior work has reported an association of SCAD with fibromuscular dysplasia (FMD) in various arteries. Less frequently, there may be an association with connective tissue disorders (CTDs) and vasculitides.<sup>7,8</sup> Peripartum or postpartum women are also thought to be at risk, and both emotional stress and exercise have been offered as precipitating factors.<sup>9,10</sup> These associations suggest that patients with SCAD have an underlying susceptibility to dissection, related to structural and/or hormonal alterations. Thus, patients are advised to undergo additional imaging to assess additional vascular abnormalities, such as asymptomatic dissection, aneurysms, or evidence of CTDs.<sup>3,11</sup>

Within the cervical carotid vasculature specifically, the aforementioned arterial anomalies have the potential to cause neurologic symptoms. To date, however, little is known about the prevalence of cervical artery anomalies in patients with SCAD. This study aimed to systematically evaluate the cervical artery vasculature in patients with a documented history of SCAD.

Received December 18, 2020; accepted after revision February 26, 2021.

From the Departments of Radiology (J.C.B., V.T.L., J.T.V., D.P.S.) and Cardiovascular Medicine (S.N.H., M.S.T.), Mayo Clinic, Rochester, Minnesota.

Please address correspondence to John C. Benson, MD, Mayo Clinic, Department of Radiology, 723 6th St. SW, Rochester, MN 55902; e-mail: benson.john3@mayo.edu

Indicates open access to non-subscribers at [www.ajnr.org](http://www.ajnr.org)

<http://dx.doi.org/10.3174/ajnr.A7151>

## MATERIALS AND METHODS

### Patient Selection

This study was approved by the local institutional review board. A retrospective review was completed of adult (18 years of age or older) patients included in the Mayo Clinic SCAD Registry and evaluated at our institution between September 2011 and January 2015 who had CTA imaging of the neck vasculature as part of recommended screening for arteriopathy (patients with SCAD, after being stabilized, typically undergo CTA screening for additional arterial abnormalities).<sup>3,11</sup> SCAD was nearly always diagnosed when a patient presenting with ACS was found to have a dissection at the time of coronary angiography, which is the criterion standard for diagnosis. The diagnosis of SCAD was confirmed by review of coronary angiograms by at least 2 experienced interventional cardiologists. Patients with atherosclerotic, traumatic, or iatrogenic dissection were excluded, as were patients with nondiagnostic imaging (eg, due to artifacts). Patients who did not survive sudden cardiac death and were diagnosed at postmortem examination were not included. The Mayo Clinic SCAD Registry is described in more detail elsewhere.<sup>12</sup> Repeat and follow-up CTAs were not included as part of this analysis. MRAs were also not included to optimize the homogeneity of imaging interpretation.

### CTA Protocol

Most imaging was performed on a 128-section multidetector scanner (Somatom Definition Flash; Siemens). For all examinations, Omnipaque 350 (GE Healthcare) was used, administered at 4 mL/s, (total volume, 100 mL). Contrast administration was followed by a flush of normal saline, administered at 4 mL/s (total volume, 35 mL). Bolus tracking at the level of the aortic arch was used for automatic contrast administration. Anatomic coverage for CTA of the neck was from the carina to the sella; for CTA of the head and neck, the coverage was from the carina to the vertex. Tube current was set to 194 mAs, and tube voltage was set to 120 kV. Section thickness was 0.75 mm; FOV, 250 mm; and pitch, 0.6. Images were reconstructed and evaluated in all 3 planes (axial, sagittal, and coronal).

### Imaging Analysis

Each CTA neck examination was assessed for multiple findings by 1 of 4 neuroradiologists (J.C.B., V.T.L., J.T.V., D.P.S.); 55–56 examinations were evaluated by each neuroradiologist. Reviewers were not blinded to the diagnosis of SCAD at the time of imaging assessment. The reviewers agreed on the assessment of all imaging characteristics before review to ensure interobserver consistency.

The carotid arteries were evaluated for the presence or absence of FMD, dissection and/or pseudoaneurysm, aneurysm/ectasia, atherosclerosis, tortuosity, a retrojugular or retropharyngeal course, or intraluminal web. Identification of FMD was based on observation of either focal FMD (focus of nonatherosclerosis narrowing, often with distal/poststenotic arterial dilation) or multifocal FMD (segmental luminal irregularity, the so-called string of beads sign).<sup>13</sup> The presence or absence of “multivessel” FMD (defined by the international consensus as being focal or multifocal FMD in one vascular bed, with FMD, aneurysm, dissection,

or tortuosity in another vascular bed) was not assessed in this study.<sup>13</sup> Instead, the study specifically assessed whether various abnormalities were present in specific vascular beds.

Dissections, particularly when chronic, share many imaging features with pseudoaneurysms. Thus, the term “dissecting pseudoaneurysm” is often used to describe such findings, explaining why these findings were combined. Dissections and/or pseudoaneurysms were defined as being either an intimal flap, sudden arterial caliber change with distal irregularity, or tapering occlusion (“flame sign”) or a focal outpouching of the artery (typically along 1 side of the lumen) in addition to at least 1 of the aforementioned findings. Aneurysms and ectasia were defined as either focal areas of arterial dilation of >50% of the adjacent luminal diameter (ie, either ectasia or “fusiform” aneurysms) or a focal outpouching along an arterial wall (“saccular” aneurysm).

Webs were presumed on the basis of a classic imaging appearance: a thin, noncalcified focus of tissue projecting into the vessel lumen from the posterior wall of the carotid artery (typically within the carotid bulb). Although webs are thought to represent a variant of FMD, as discussed below, they were considered to be distinct from FMD for the purposes of this review. Carotid atherosclerosis was based on the severity of luminal stenosis: “mild” was <25% narrowing, “moderate” was 25%–74.9%, and “severe” was ≥75%, while “none” referred to the absence of any identifiable plaque.

Arterial tortuosity was divided into 3 previously described subtypes, as the following: “Kink” was a singular acute angulation of the ICA (≤90°), a “loop” was an S- or C-shaped curvature in which 2 adjacent turns both had acute angulations (≤90°), and a “coil” was a complete 360° turn in the vessel.<sup>14,15</sup> Retrojugular and retropharyngeal pathways of the ICA were also considered subtypes of tortuosity because their presence implied a greater degree of horizontal distortion of the arterial pathway. Both pathways were similarly evaluated on the basis of prior definitions: A “retrojugular” ICA took a course in which >50% of the cross-sectional area of the artery was behind or lateral to the adjacent internal jugular vein, while a “retropharyngeal” ICA had ≥50% of its cross-sectional lumen located behind or medial to the lateral edge of the pharynx.<sup>14,16</sup> Vertebral arteries were assessed for FMD, dissection and/or pseudoaneurysm, aneurysm/ectasia, and a subjective degree of tortuosity (categorized as none, mild, moderate, and severe). In cases of asymmetric severity of either carotid atherosclerosis or vertebral tortuosity, the side with greater severity was considered for purposes of statistical assessment (eg, if atherosclerosis severity was moderate on the right and mild on the left, the overall severity was considered moderate).

### Electronic Medical Review and Data Analysis

Patient demographics and comorbidities were assessed through retrospective review of patients’ electronic medical records. Documentation of extracoronary FMD (outside the cerebrovascular system) was also noted, typically diagnosed at the time of coronary angiography. All data were analyzed using the statistical software package JMP, Version 13.0 (SAS Institute). Continuous data are summarized as mean (SD), while categorical variables are expressed as frequency (percentage).



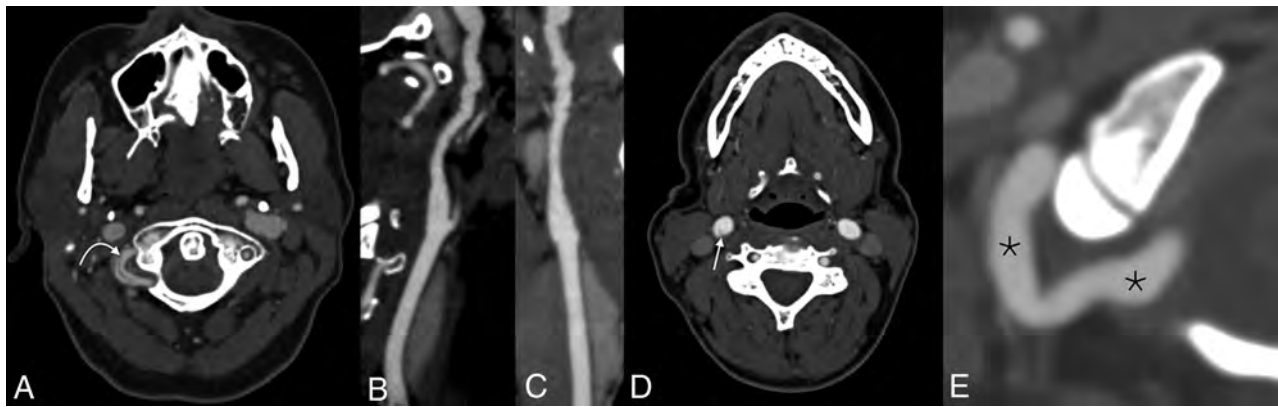


**FIG 1.** Examples of cervical artery abnormalities noted in patients with SCAD. Axial CTA (A) demonstrates a right vertebral artery dissection (curved arrow). Reformatted sagittal (B) and coronal (C) images show multifocal FMD of the right ICA. Axial CTA (D) demonstrates a web in the right ICA bulb (straight arrow). Reformatted axial CTA (E) shows ectasia of the distal right vertebral artery (asterisks).

**Table 1: Prevalence of various imaging findings in patients with SCAD<sup>a</sup>**

Findings	No. (%)
FMD	83/214 (38.8%)
Dissection and/or pseudoaneurysm	28/214 (13.1%)
Aneurysm/ectasia	22/214 (10.3%)
Carotid web	10/214 (4.7%)
1+ type of carotid tortuosity	99/214 (46.3%)
Atherosclerosis	
None	185/214 (86.4%)
Mild	26/214 (12.2%)
Moderate	3/214 (1.4%)
Severe	0/214 (0.0%)
Vertebral tortuosity	
None	124/214 (57.9%)
Mild	64/214 (29.9%)
Moderate	22/214 (10.3%)
Severe	4/214 (1.9%)

<sup>a</sup>FMD, dissection, pseudoaneurysm, and aneurysm/ectasia numbers reflect the number of patients with those findings in either the carotid or vertebral artery. Webs were only assessed in the carotid arteries because they are considered to be rarely present in the vertebral arteries. Subtypes of carotid tortuosity include kinks, loops, coils, and retropharyngeal and retrojugular courses. Carotid atherosclerosis and vertebral tortuosity reflect the more severe side, if asymmetry existed.

## RESULTS

### Patient Characteristics

Of 221 patients with SCAD and CTA neck imaging, 7 were excluded because the obtained images were nondiagnostic. The final cohort, therefore, comprised 214 patients, 205 (95.8%) of whom were women. The average age was 54.4 (SD, 10.6) years. The average time between the initial SCAD event and CTA neck imaging was 27.9 (SD, 43.8) months.

The most common comorbidities were a documented history of hypertension and hyperlipidemia (both in 71 patients [33.2%]). Three patients (1.4%) had diabetes, 60 patients (28.2%) had either current or prior tobacco use, and 9 patients had a known connective tissue disorder (4 with Raynaud's phenomenon, 1 mixed connective tissue disorder, 1 Ehlers-Danlos syndrome, 1 rheumatoid arthritis, 1 Sjogren syndrome, and 1 undefined).

Regarding a documented history of extracoronary FMD outside the cerebrovascular system, 108 (50.5%) had imaging evidence

of FMD, 18 (8.4%) had a type of non-FMD extracoronary vascular abnormality (dissection, aneurysm, ectasia/dilation, or tortuosity that did not meet the criteria for multifocal FMD), and the remainder had no FMD noted or documented. The most common location of extracoronary, extracerebrovascular FMD was the renal arteries (69; 32.2%), followed by the iliac arteries (common, internal, or external) (51; 23.8%), femoral arteries (11; 5.1%), celiac artery (10; 4.7%), superior mesenteric artery (5; 2.3%), splenic artery (5; 2.3%), and brachial artery (1; 0.5%).

### Imaging Analysis

Examples of various abnormalities are shown in Fig 1. The most common abnormality found within the arterial vasculature of patients with SCAD was FMD (Tables 1 and 2). One hundred seven (50.0%) patients had no web, FMD, dissection and/or pseudoaneurysm, or aneurysm and/or ectasia in any of the neck vessels. Although the severity of FMD was not formally graded, some cases were subjectively mild. Similarly, some webs were subjectively subtle. Among patients with SCAD, the majority (185/214; 86.4%) had no atherosclerosis and 26/214 (12.2%) had mild, 3 (1.4%) had moderate, and no patients had severe atherosclerotic narrowing.

A subtype of tortuosity (kink, loop, or coil) was present in either carotid artery in 56/214 (26.2%) patients (Fig 2). When we considered retropharyngeal and retrojugular courses as additional phenotypes of tortuosity, some tortuosity subtype (kink, loop, coil, retropharyngeal, retrojugular) was present in either carotid artery in 99/214 (46.3%) patients. Of these, kinks were the most common and observed in 15/214 (7.0%) right carotid arteries and 14/214 (6.5%) left carotid arteries. These were followed by loops (present in 9.3% of both right and left carotid arteries) and coils (present in 2.8% of right carotid and 2.3% of left carotid arteries). Eight patients (3.7%) had kinks of both ICAs, 14 patients (6.5%) had loops of both ICAs, and 1 patient (0.5%) had coils in both ICAs. The right ICA followed a retrojugular course in 17 patients and a retropharyngeal course in 8 patients; the left ICA followed a retrojugular course in 54 patients and a retropharyngeal course in 4 patients. Most patients with SCAD had no vertebral tortuosity (124/214; 57.9%); 64/214

**Table 2: Prevalence of FMD, dissection and/or pseudoaneurysm, aneurysm/ectasia, and webs based on arterial involvement<sup>a</sup>**

	Right Carotid Artery	Left Carotid Artery	Both Carotid Arteries	Right Vertebral Artery	Left Vertebral Artery	Both Vertebral Arteries
FMD	56 (25.2%)	49 (22.9%)	39 (18.2%)	30 (14.0%)	32 (15.0%)	22 (10.3%)
Dissection and/or pseudoaneurysm	5 (2.3%)	8 (3.7%)	0 (0.0%)	8 (3.7%)	12 (5.6%)	1 (0.5%)
Aneurysm/ectasia	16 (7.5%)	13 (6.1%)	8 (3.7%)	4 (1.9%)	3 (1.4%)	1 (0.5%)
Web	6 (2.8%)	6 (2.8%)	0 (0.0%)	NA		

**Note:**—NA indicates not applicable.

<sup>a</sup> The presence or absence of webs within the vertebral arteries was not assessed because they are classically found in the carotid bulbs. Data are No. (%).

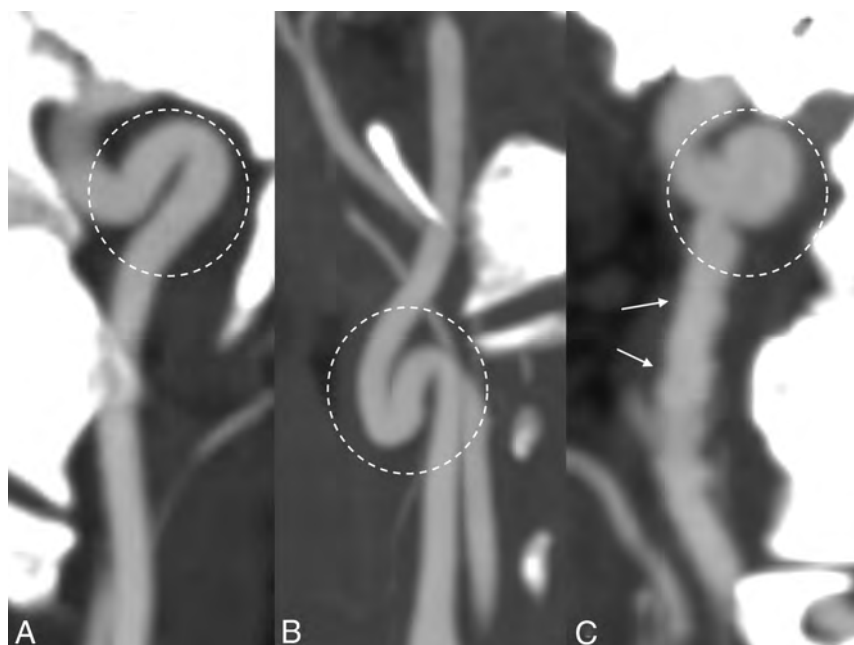


**FIG 2.** Examples of tortuosity subtypes. Arterial kink (A) (a single arterial angulation of  $\leq 90^\circ$ ), loop (B) (2 adjacent acute angulations of the vessel), and coil (C) (complete  $360^\circ$  turn) are all shown. Also note the beaded irregularity of the vessel in C, compatible with FMD (arrows).

(29.9%) had mild, 22/214 (10.3%) had moderate, and 4/214 (1.9%) had severe vertebral tortuosity.

## DISCUSSION

This study is the most robust analysis of detailed cervical imaging findings among patients with SCAD and establishes the prevalence of cervical artery vasculature abnormalities among such patients on CTA. Pertinent findings of this study include finding a high prevalence of cervical FMD among patients with SCAD, identifying a subset of patients with isolated cervical artery dissection, and finding a high prevalence of arterial webs, ectasia, and/or aneurysms in the absence of cervical FMD. These findings have implications for patient counseling and image interpretation, offer insight into the pathogenesis of SCAD-related arterial manifestations, and reinforce the importance of cervical artery imaging surveillance in patients with SCAD.

The current study found that nearly 40% of patients with SCAD had imaging evidence of cervical FMD. Prior work has indicated that noncoronary FMD exists in as many as 72%–86% of patients with SCAD.<sup>1,17,18</sup> However, these evaluations have

come from angiography, particularly of the iliac and renal arteries.<sup>19</sup> Prior data dedicated to analysis of the cervical artery vasculature, conversely, are relatively scant. For example, Saw et al<sup>9</sup> found imaging evidence of cerebrovascular (not specifically defined as extra- or intracranial) FMD in 46.5% of 43 patients. A separate study by Saw et al<sup>20</sup> included 327 patients. The authors found that 62.7% of patients had FMD. Approximately 49% of the observed FMDs involved the cerebrovasculature.

The high prevalence of FMD in patients with SCAD offers an alluring prospect for explaining the pathogenesis of coronary artery dissections. Histologically, FMD is considered a nonatherosclerotic, noninflammatory thickening of arterial wall layers that predisposes the vessel to both dissection and aneurysms and vascular ectasia.<sup>21,22</sup> Furthermore, Olin et al<sup>23</sup> found that nearly 20% of patients with FMD had a history of TIA or stroke. Thus, the prevalence of cervical FMD in patients with SCAD suggests that this patient subset

may be at increased risk of such cerebrovascular manifestation, though additional work will be needed to further characterize the association.

The higher rate of carotid webs among patients with SCAD is important because this finding may also be related to FMD and is increasingly associated with otherwise cryptogenic strokes.<sup>24,25</sup> Some authors have suggested that webs represent rare variants of the intimal subtype of FMD.<sup>26,27</sup> However, an international consensus article reinforced webs as being likely distinct entities from FMD.<sup>13</sup> Nevertheless, the nearly 5% prevalence of webs in this study suggests that radiologists should carefully scrutinize CTA examinations in this population for this finding and clinicians should note the potential risk for stroke. Additional work with even larger numbers of patients would be needed to confirm this association because this was identified in only a handful of patients and the prevalence of webs in a typical population is around 1%.<sup>25,28–30</sup>

While prior work has found the presence of carotid dissection in SCAD to be in the range of 2.5%–5%, the current study demonstrates a prevalence of more than twice that, suggesting that

dissection is more common than previously suspected.<sup>31,32</sup> Nonetheless, the relatively low prevalence of dissection compared with FMD at a single time point examination in the current study may provide some reassurance of cerebrovascular risk for patient counseling for many patients. However, further evaluation is needed regarding the rate of dissection and related neurologic sequelae, with long-term longitudinal data specific to patients with SCAD. Current studies focused on patients with FMD show that clinical complications from cerebrovascular FMD are uncommon.<sup>33,34</sup>

The lack of arterial tortuosity in patients with SCAD is interesting, because coronary tortuosity has been shown in prior studies to be highly prevalent in patients with SCAD and exists at higher rates in patients with SCAD than in age- and sex-matched controls.<sup>35,36</sup> Although a relatively nonspecific finding, arterial tortuosity is increased in patients with many types of CTD to varying degrees.<sup>37</sup> CTDs, in turn, are associated with arterial dissections.<sup>15</sup> It is, therefore, reasonable that the higher level of tortuosity seen in coronary arteries in patients with SCAD is related to underlying CTDs and plays a role in the pathogenesis of dissection. Although it remains uncertain why the current study did not demonstrate a higher prevalence of tortuosity in the patients with SCAD, this topic could be further addressed in future analyses.

Finally, moderate and severe atherosclerosis was extremely rare in patients with SCAD, occurring in 1.4% and 0% of patients, respectively. Prior studies have shown patients with SCAD to have a low prevalence of atherosclerotic disease.<sup>38</sup> Certainly, the relatively young age and female predominance of patients with SCAD may play a role. However, recent studies have also offered a genetic explanation. SCAD is related to the *PHACTR1/EDN1* genetic locus, and a risk allele at this locus is associated with both SCAD and FMD and is opposite to the risk allele at this locus that increases the risk of coronary artery disease and myocardial infarction.<sup>38,39</sup> Genetic susceptibility to FMD and SCAD could, therefore, confer protection against the atherosclerotic changes that lead to coronary artery disease/myocardial infarction.

This study shares the limitations of all retrospective analyses. In addition, though CTA is a noninvasive approach to studying the prevalence of arteriopathy in SCAD, this study is limited by the sole reliance on CTA imaging evidence rather than histologic confirmation or invasive angiography. There is also an inevitable selection bias among those patients who were imaged, even though performance of comprehensive arterial imaging is encouraged at least once among all patients with history of SCAD. Next, although most imaging characteristics were defined by specific criteria, vertebral artery tortuosity was subjectively evaluated by different reviewers, thus raising the possibility that such assessments were limited by interobserver variability. In addition, because a history of neurologic events was not assessed, it is uncertain to what degree the observed abnormalities were associated with symptomatology. Finally, the lack of clinical data in this article prevents discussion on whether the observed findings were symptomatic or incidental. This type of analysis could be a topic of future studies.

## CONCLUSIONS

This study represents the most robust comprehensive review of cervical artery abnormalities in patients with SCAD. CTA evidence of carotid and/or vertebral artery FMD was found in a substantial subset of patients with SCAD, offering a possible mechanism by which the coronary arteries of such patients are prone to dissection. Some patients with SCAD also demonstrate cervical artery webs (likely a subset of FMD) and ectasia and aneurysms. The burden of dissection was higher than that in prior studies but still affected just >10% of patients. Half of patients with SCAD will not have any of these findings on CTA, which may provide reassurance. Nevertheless, the prevalence of abnormalities supports the practice of routine screening for arterial abnormalities in this population.

## ACKNOWLEDGMENTS

The authors thank the Mayo Clinic “Virtual” Multicenter SCAD Registry participants who volunteered their data for this study.

Disclosures: Marysia S. Tweet—RELATED: Grant: National Institutes of Health Building Interdisciplinary Research Careers in Women's Health, Comments: National Institutes of Health Building Interdisciplinary Research Careers in Women's Health Scholar during part of the time spent on this project.\* \*Money paid to the institution.

## REFERENCES

- Gilhofer TS, Saw J. Spontaneous coronary artery dissection: update 2019. *Curr Opin Cardiol* 2019;34:594–602 CrossRef Medline
- Rashid HN, Wong DT, Wijesekera H, et al. Incidence and characterisation of spontaneous coronary artery dissection as a cause of acute coronary syndrome: a single-centre Australian experience. *Int J Cardiol* 2016;202:336–38 CrossRef Medline
- Hayes SN, Kim ES, Saw J, et al. American Heart Association Council on Peripheral Vascular Disease; Council on Clinical Cardiology; Council on Cardiovascular and Stroke Nursing; Council on Genomic and Precision Medicine; and Stroke Council. Spontaneous coronary artery dissection: current state of the science: a scientific statement from the American Heart Association. *Circulation* 2018;137:e523–57 CrossRef Medline
- Saw J. Spontaneous coronary artery dissection. *Can J Cardiol* 2013;29:1027–33 CrossRef Medline
- Saw J, Aymong E, Mancini GB, et al. Nonatherosclerotic coronary artery disease in young women. *Can J Cardiol* 2014;30:814–19 CrossRef Medline
- Kronzer VL, Tarabochia AD, Lobo Romero AS, et al. Lack of association of spontaneous coronary artery dissection with autoimmune disease. *J Am Coll Cardiol* 2020;76:2226–34 CrossRef Medline
- Henkin S, Negrotto SM, Tweet MS, et al. Spontaneous coronary artery dissection and its association with heritable connective tissue disorders. *Heart Br Heart* 2016;102:876–81 CrossRef Medline
- Kaadan M, Ihsan MacDonald C, Ponzini F, et al. Prospective cardiovascular genetics evaluation in spontaneous coronary artery dissection. *Circ Genom Precis Med* 2018;11:e001933 CrossRef Medline
- Saw J, Ricci D, Starovoytov A, et al. Spontaneous coronary artery dissection: prevalence of predisposing conditions including fibromuscular dysplasia in a tertiary center cohort. *JACC Cardiovasc Interv* 2013;6:44–52 CrossRef Medline
- Pabla JS, John L, McCrea WA. Spontaneous coronary artery dissection as a cause of sudden cardiac death in the peripartum period. *BMJ Case Rep* 2010;2010:bcr0520102994 CrossRef Medline
- European Society of Cardiology, Acute Cardiovascular Care Association. SCAD study group: a position paper on spontaneous coronary artery dissection. *European Heart Journal*. Oxford Academic.



<https://academic.oup.com/eurheartj/article/39/36/3353/4885368>. Accessed November 16, 2020.

12. Tweet MS, Young KA, Best PJ, et al. **Association of pregnancy with recurrence of spontaneous coronary artery dissection among women with prior coronary artery dissection.** *JAMA Netw Open* 2020;3:e2018170 CrossRef Medline
13. Gornik HL, Persu A, Adlam D, et al. **First international consensus on the diagnosis and management of fibromuscular dysplasia.** *Vasc Med Lond Med* 2019;24:164–89 CrossRef Medline
14. Barbour PJ, Castaldo JE, Rae-Grant AD, et al. **Internal carotid artery redundancy is significantly associated with dissection.** *Stroke* 1994;25:1201–06 CrossRef Medline
15. Kim ST, Brinjikji W, Lehman VT, et al. **Association between carotid artery tortuosity and carotid dissection: a case-control study.** *J Neurosurg Sci* 2018;62:413–17 CrossRef Medline
16. Benson JC, Brinjikji W, Messina SA, et al. **Cervical internal carotid artery tortuosity: A morphologic analysis of patients with acute ischemic stroke.** *Interv Neuroradiol* 2020;26:216–21 CrossRef Medline
17. Saw J, Poulter R, Fung A, et al. **Spontaneous coronary artery dissection in patients with fibromuscular dysplasia: a case series.** *Circ Cardiovasc Interv* 2012;5:134–37 CrossRef Medline
18. Gilhofer TS, Saw J. **Spontaneous coronary artery dissection: a review of complications and management strategies.** *Expert Rev Cardiovasc Ther* 2019;17:275–91 CrossRef Medline
19. Rogowski S, Maeder MT, Weilenmann D, et al. **Spontaneous coronary artery dissection: angiographic follow-up and long-term clinical outcome in a predominantly medically treated population.** *Catheter Cardiovasc Interv Off Interv* 2017;89:59–68 CrossRef Medline
20. Saw J, Humphries K, Aymong E, et al. **Spontaneous coronary artery dissection: clinical outcomes and risk of recurrence.** *J Am Coll Cardiol* 2017;70:1148–58 CrossRef Medline
21. Varennes L, Tahon F, Kastler A, et al. **Fibromuscular dysplasia: what the radiologist should know: a pictorial review.** *Insights Imaging* 2015;6:295–307 CrossRef Medline
22. Harriott AM, Zimmerman E, Singhal AB, et al. **Cerebrovascular fibromuscular dysplasia.** *Neurol Clin Pract* 2017;7:225–36 CrossRef Medline
23. Olin JW, Froehlich J, Gu X, et al. **The United States Registry for Fibromuscular Dysplasia: results in the first 447 patients.** *Circulation* 2012;125:3182–90 CrossRef Medline
24. Vercelli GG, Campeau NG, Macedo TA, et al. **De novo formation of a carotid web: case report.** *J Neurosurg* 2018 Nov 1. [Epub ahead of print] CrossRef Medline
25. Haussen DC, Grossberg JA, Bouslama M, et al. **Carotid web (intimal fibromuscular dysplasia) has high stroke recurrence risk and is amenable to stenting.** *Stroke* 2017;48:3134–37 CrossRef Medline
26. Priyadarshni S, Neralla A, Reimon J, et al. **Carotid webs: an unusual presentation of fibromuscular dysplasia.** *Cureus* 2020;12:e9549 CrossRef Medline
27. Zhang AJ, Dhruv P, Choi P, et al. **A systematic literature review of patients with carotid web and acute ischemic stroke.** *Stroke* 2018;49:2872–76 CrossRef Medline
28. Sajedi PI, Gonzalez JN, Cronin CA, et al. **Carotid bulb webs as a cause of “cryptogenic” ischemic stroke.** *AJNR Am J Neuroradiol* 2017;38:1399–1404 CrossRef Medline
29. Wojcik K, Milburn J, Vidal G, et al. **Carotid webs: radiographic appearance and significance.** *Ochsner J* 2018;18:115–20 CrossRef Medline
30. Choi PM, Singh D, Trivedi A, et al. **Carotid webs and recurrent ischemic strokes in the era of CT angiography.** *AJNR Am J Neuroradiol* 2015;36:2134–39 CrossRef Medline
31. Prasad M, Tweet MS, Hayes SN, et al. **Prevalence of extracoronary vascular abnormalities and fibromuscular dysplasia in patients with spontaneous coronary artery dissection.** *Am J Cardiol* 2015;115:1672–77 CrossRef Medline
32. McGrath-Cadell L, McKenzie P, Emmanuel S, et al. **Outcomes of patients with spontaneous coronary artery dissection.** *Open Heart* 2016;3:e000491 CrossRef Medline
33. Touzé E, Southerland AM, Boulanger M, et al. **Fibromuscular dysplasia and its neurologic manifestations: a systematic review.** *JAMA Neurol* 2019;76:217–26 CrossRef Medline
34. Kadian-Dodov D, Goldfinger JZ, Gustavson S, et al. **Natural history of cervical artery fibromuscular dysplasia and associated neurovascular events.** *Cerebrovasc Dis Basel Dis* 2018;46:33–39 CrossRef Medline
35. Eleid MF, Guddeti RR, Tweet MS, et al. **Coronary artery tortuosity in spontaneous coronary artery dissection: angiographic characteristics and clinical implications.** *Circ Cardiovasc Interv* 2014;7:656–62 CrossRef Medline
36. Ciurică S, Lopez-Sublet M, Loeys BL, et al. **Arterial tortuosity.** *Hypertension* 2019;73:951–60 CrossRef Medline
37. Welby JP, Kim ST, Carr CM, et al. **Carotid artery tortuosity is associated with connective tissue diseases.** *AJNR Am J Neuroradiol* 2019;40:1738–43 CrossRef Medline
38. Adlam D, Olson TM, Combaret N, et al. **CARDIoGRAMPlusC4D Study Group. Association of the PHACTR1/EDN1 genetic locus with spontaneous coronary artery dissection.** *J Am Coll Cardiol* 2019;73:58–66 CrossRef Medline
39. Kiando SR, Tucker NR, Castro-Vega LJ, et al. **PHACTR1 is a genetic susceptibility locus for fibromuscular dysplasia supporting its complex genetic pattern of inheritance.** *PLoS Genet* 2016;12:e1006367 CrossRef Medline

## Look beyond the Heart: Extracoronary Vascular Manifestations of Spontaneous Coronary Artery Dissection

Spontaneous coronary artery dissection (SCAD) accounts for 1%–4% of all acute coronary syndromes and is the culprit in up to 35% of myocardial infarctions (MIs) in women younger than 50 years of age.<sup>1</sup> An association between fibromuscular dysplasia (FMD), other nonatherosclerotic arteriopathies, pregnancy, systemic inflammatory conditions, and SCAD has been reported.<sup>1</sup> For many patients, SCAD may be the first manifestation of an underlying disease that could put them at increased risk of repeat coronary and extracoronary ischemic events. Among these is the risk of cervical artery involvement, making patients susceptible to stroke leading to increased morbidity and mortality. Unfortunately, there is little information on the presence of aneurysms, dissection, or tortuosity in the cervical arteries of those with SCAD.

The article by Benson et al<sup>2</sup> provides complete angiographic details of cervical artery abnormalities in patients with spontaneous coronary artery dissection. In a retrospective review, Benson et al examined 214 patients who were enrolled in the Mayo Clinic SCAD registry from 2011 to 2015. All patients had CTA of the neck after the initial SCAD event. As in other published data, patients were almost exclusively women (95.8%), with an average age of 54 years. Similar to prior studies, there was a low prevalence of common cardiovascular risk factors, hypertension and hyperlipidemia (both 33%), compared with patients with atherosclerotic MI.<sup>2–4</sup>

Prior studies with a thorough screening of head-to-pelvis imaging with either high-resolution CTA or MR angiography or conventional angiography have reported a >50% prevalence of concomitant multifocal FMD.<sup>1,3–5</sup> Not surprisingly, Benson et al<sup>2</sup> corroborated the known association between FMD and SCAD because 50.5% of patients were found to have FMD in at least 1 noncoronary arterial bed. Specifically, 39% of patients were found to have cervical artery FMD, which was also the most common location, followed by renal FMD in 32% of patients. This finding also mirrors the findings of the US Registry for fibromuscular dysplasia, in which renal and cerebrovascular beds are the most commonly reported locations of FMD.<sup>6</sup> Additionally, Benson et al reported significant tortuosity in the carotid arteries such as a kink, loop, coil, or a retropharyngeal or retrojugular course in

46% of patients.<sup>2</sup> These findings have been reported in other studies as well. McNair et al,<sup>3</sup> similarly, showed that FMD was highly prevalent in the SCAD population (63%), with similar rates of carotid (38%) and renal (50%) FMD when imaged. They also reported that 70% of patients had additional non-FMD vascular abnormalities albeit their imaging included vessels from the head to pelvis.<sup>3</sup> Saw et al<sup>7</sup> reported FMD in 63% of patients with SCAD, of whom 49% had involved cerebrovascular anatomy. Additionally, 5% and 12% of patients had other connective tissue disorders and systemic inflammatory disorders, respectively. These conditions were rarely reported by Benson et al<sup>2</sup> (9/221 patients). A multicenter study from Saw et al<sup>4</sup> involving 750 patients with SCAD reported FMD in 31.1% (45.2% had no or incomplete screening), systemic inflammatory diseases in 4.7%, peripartum conditions in 4.5%, and connective tissue disorders in 3.6% of patients.

The findings of FMD and other extracoronary vascular abnormalities can be clinically vital. Patients with FMD have a high incidence of cervical artery dissection (16% in carotid and 5% in vertebral arteries) and intracranial aneurysms (13%), often manifest as a cerebrovascular ischemic event.<sup>8,9</sup> Other studies have reported a 5%–23% prevalence of cerebral aneurysms in patients with SCAD.<sup>3,4,7,10</sup>

Benson et al<sup>2</sup> make a clear distinction between cervical artery FMD and non-FMD cervical arterial abnormalities, but this distinction may not be that clear. Specific forms of tortuosity, specifically the S-curve and cervical artery dissections, can be considered FMD equivalents, particularly if FMD is present in other vascular beds.<sup>6</sup> Reclassifying these may further increase the prevalence of FMD in patients SCAD.

Researchers, clinicians, and patients seek to know whether these other noncoronary systemic arterial abnormalities are part of the same disease process. Most interesting, genome-wide association studies recognize the increased risk for SCAD, FMD, cervical artery dissection, and migraine headaches in patients who have a single nucleotide polymorphism rs9349379 (A) of the *PHACTR1* gene (locus 6p24).<sup>11,12</sup>

It does appear that SCAD is not a solitary disease. The publication by Benson et al<sup>2</sup> substantially adds to the existing literature,

which underscores the systemic nature of SCAD and the need to screen vascular beds beyond the coronary arteries in these patients. The clinical conundrum is whether all these conditions, SCAD, FMD, cervical artery dissection, pseudoaneurysms, and others, are a part of a larger syndrome with underlying similar genetic and clinical findings.

## REFERENCES

1. Hayes SN, Kim ES, Saw J, et al. American Heart Association Council on Peripheral Vascular Disease; Council on Clinical Cardiology; Council on Cardiovascular and Stroke Nursing; Council on Genomic and Precision Medicine; and Stroke Council. **Spontaneous coronary artery dissection: current state of the science: a scientific statement from the American Heart Association.** *Circulation* 2018;137:e523–57 CrossRef Medline
2. Benson JC, Lehman VT, Verdoorn JT, et al. **Prevalence of cervical artery abnormalities on CTA in patients with spontaneous coronary artery dissection: fibromuscular dysplasia, dissection, aneurysm, and tortuosity.** *AJNR Am J Neuroradiol* 2021 May 13. [Epub ahead of print]. CrossRef Medline
3. McNair PW, Parker A, Taylor A, et al. **Spontaneous coronary artery dissection and its association with fibromuscular dysplasia and other vascular abnormalities.** *Am J Cardiol* 2020;125:34–39 CrossRef Medline
4. Saw J, Starovoytov A, Humphries K, et al. **Canadian spontaneous coronary artery dissection cohort study: in-hospital and 30-day outcomes.** *Eur Heart J* 2019;40:1188–97 CrossRef Medline
5. Kim ES. **Spontaneous coronary-artery dissection.** *N Engl J Med* 2020;383:2358–70 CrossRef Medline
6. Gornik HL, Persu A, Adlam D, et al. **First International Consensus on the diagnosis and management of fibromuscular dysplasia.** *Vasc Med* 2019;24:164–89 CrossRef Medline
7. Saw J, Humphries K, Aymong E, et al. **Spontaneous coronary artery dissection: clinical outcomes and risk of recurrence.** *J Am Coll Cardiol* 2017;70:1148–45 CrossRef Medline
8. Lather HD, Gornik HL, Olin JW, et al. **Prevalence of intracranial aneurysm in women with fibromuscular dysplasia: a report from the US Registry for Fibromuscular Dysplasia.** *JAMA Neurol* 2017;74:1081–87 CrossRef Medline
9. Touzé E, Southerland AM, Boulanger M, et al. **Fibromuscular dysplasia and its neurologic manifestations: a systematic review.** *JAMA Neurol* 2019;76:217–26 CrossRef Medline
10. Prasad M, Tweet MS, Hayes SN, et al. **Prevalence of extracoronary vascular abnormalities and fibromuscular dysplasia in patients with spontaneous coronary artery dissection.** *Am J Cardiol* 2015;115:1672–77 CrossRef Medline
11. Warchol-Celinska E, Berrandou T, Prejbisz A, et al. **Genetic study of PHACTR1 and fibromuscular dysplasia, meta-analysis and effects on clinical features of patients: the ARCADIA-POL study.** *Hypertension* 2020;76:e4–e7 CrossRef Medline
12. Adlam D, Olson TM, Combaret N, et al. CARDIoGRAMPlusC4D Study Group. **Association of the PHACTR1/EDN1 genetic locus with spontaneous coronary artery dissection.** *J Am Coll Cardiol* 2019;73:58–66 CrossRef Medline

R. Ramcharitar

✉ A.M. Sharma

Division of Cardiovascular Medicine  
University of Virginia  
Charlottesville, Virginia

<http://dx.doi.org/10.3174/ajnr.A7212>



# Functional MRI Shows Altered Deactivation and a Corresponding Decrease in Functional Connectivity of the Default Mode Network in Patients with Gliomas

Y.M. Maniar, K.K. Peck, M. Jenabi, M. Gene, and A.I. Holodny



## ABSTRACT

**BACKGROUND AND PURPOSE:** The default mode network normally decreases in activity during externally directed tasks. Although default mode network connectivity is disrupted in numerous brain pathologies, default mode network deactivation has not been studied in patients with brain tumors. We investigated default mode network deactivation with language task-based fMRI by measuring the anticorrelation of a critical default mode network node, the posterior cingulate cortex, in patients with gliomas and controls; furthermore, we examined default mode network functional connectivity in these patients with task-based and resting-state fMRI.

**MATERIALS AND METHODS:** In 10 healthy controls and 30 patients with gliomas, the posterior cingulate cortex was identified on task-based fMRI and was used as an ROI to create connectivity maps from task-based and resting-state fMRI data. We compared the average correlation in each default mode network region between patients and controls for each correlation map and stratified patients by tumor location, hemisphere, and grade.

**RESULTS:** Patients with gliomas ( $P = .001$ ) and, in particular, patients with tumors near the posterior default mode network ( $P < .001$ ) showed less posterior cingulate cortex anticorrelation in task-based fMRI than controls. Patients with both left- and right-hemisphere tumors, as well as those with grade IV tumors, showed significantly lower posterior cingulate cortex anticorrelation than controls ( $P = .02$ ,  $.03$ , and  $< .001$ , respectively). Functional connectivity in each default mode network region was not significantly different between task-based and resting-state maps.

**CONCLUSIONS:** Task-based fMRI showed impaired deactivation of the default mode network in patients with gliomas. The functional connectivity of the default mode network in both task-based and resting-state fMRI in patients with gliomas using the posterior cingulate cortex identified in task-based fMRI as an ROI for seed-based correlation analysis has strong overlap.

**ABBREVIATIONS:** BOLD = blood oxygen level-dependent; DMN = default mode network; FC = functional connectivity; IPL = inferior parietal lobule; LIPL = left inferior parietal lobule; mPFC = medial prefrontal cortex; PCC = posterior cingulate cortex; RIPL = right inferior parietal lobule; rs-fMRI = resting-state fMRI; tb-fMRI = task-based fMRI

The default mode network (DMN) is a functionally connected brain network<sup>1,2</sup> that demonstrates deactivation during tasks that require external attention relative to nontask conditions.<sup>3–5</sup> The functions of the DMN appear to be central in spontaneous

cognition,<sup>6</sup> stimulus-independent thoughts,<sup>7</sup> and self-referential mental activity.<sup>8</sup> DMN deactivation has been correlated with functions such as memory-encoding<sup>9</sup> and goal-directed external task performance.<sup>10</sup>

The DMN has been studied extensively using blood oxygen level-dependent (BOLD) fMRI, both in healthy volunteers and in patients with a variety of neurologic and psychiatric conditions.

Received October 19, 2020; accepted after revision February 19, 2021.

From the Departments of Radiology (Y.M.M., K.K.P., M.J., M.G., A.I.H.) and Medical Physics (K.K.P.), Memorial Sloan Kettering Cancer Center, New York, New York; Department of Radiology (A.I.H.), Weill Medical College of Cornell University, New York, New York; and Department of Neuroscience (A.I.H.), Weill-Cornell Graduate School of the Medical Sciences, New York, New York.

This work was supported by the following grants from the National Institutes of Health: National Institutes of Health–National Cancer Institute P30 CA008748, National Institutes of Health–National Institute of Biomedical Imaging and Bioengineering R01 EB022720 (Holodny AI, Principal Investigator), National Institutes of Health–National Cancer Institute R21 CA220144 (Holodny AI and Peck KK, Principal Investigators), National Institutes of Health–National Cancer Institute U54 CA137788, National Institutes of Health–National Cancer Institute R25CA020449.

The content is solely the responsibility of the authors and does not necessarily represent the official views of the National Institutes of Health.

Previously presented as an abstract at: Annual Meeting of the American Society of Neuroradiology, May 18–23, 2019; Boston, Massachusetts.

Please address correspondence to Kyung K. Peck, PhD, Department of Medical Physics, Memorial Sloan Kettering Cancer Center, 1275 York Ave, New York, NY 10065; e-mail: peckk@mskcc.org

Indicates open access to non-subscribers at [www.ajnr.org](http://www.ajnr.org)

<http://dx.doi.org/10.3174/ajnr.A7138>

## Clinical data and tumor pathology

Characteristic	Patients (n = 30)
Age (mean, range) (yr)	46.1, 19–79
Sex	
Male	19
Female	11
Handedness	
Right	25
Left	5
Tumor hemisphere	
Right	7
Left	23
Tumor location	
Posterior DMN	14
Anterior DMN	8
Outside DMN	8
Tumor grade	
II	11 (5 Astrocytomas, 6 oligodendrogliomas)
III	7 (3 Anaplastic astrocytomas, 3 anaplastic oligodendrogliomas, 1 anaplastic ganglioglioma)
IV	12 Glioblastomas

Because DMN deactivation is known to be important for cognitive function,<sup>10</sup> exploring the impact of brain tumors on DMN deactivation could help elucidate the underpinnings of accelerated cognitive decline in patients with brain tumors.<sup>11</sup> Subclinical cognitive decline in middle-aged healthy men has been associated with decreased deactivation of the posterior DMN during a visual-motor task paradigm.<sup>12</sup> Decreased DMN deactivation has also been demonstrated in patients with schizophrenia during a semantic and perceptual encoding task paradigm,<sup>13</sup> in patients with Alzheimer disease during a face-name recognition paradigm,<sup>14</sup> and in patients with stroke during a motor-task paradigm.<sup>15</sup> However, task-induced deactivation of the DMN has not yet been studied with fMRI in patients with gliomas.

Functional connectivity (FC) refers to the degree of the correlation of simultaneous activity of disparate brain regions, either during a task or at rest, as measured by fMRI.<sup>16</sup> Disruptions in the FC of the DMN have been associated with cognitive impairment in patients with focal lesions, including patients with stroke<sup>17</sup> and brain tumors,<sup>18–20</sup> as well as in patients with autism,<sup>21</sup> schizophrenia,<sup>22</sup> and neurodegenerative diseases such as Alzheimer disease<sup>23</sup> and Parkinson disease.<sup>24</sup> However, while decreases in the FC of the DMN have been found in patients with brain tumors, the data are varied regarding the impact of tumor location, grade, and hemisphere.<sup>18–20</sup> Additionally, there are no data comparing the FC of the DMN using both task-based fMRI (tb-fMRI) and resting-state fMRI (rs-fMRI) in the same cohort of patients with gliomas.

Thus, the purpose of this study was to investigate the effect of gliomas on DMN deactivation using tb-fMRI with a language task paradigm and DMN FC using a seed-based correlation analysis in both tb-fMRI and rs-fMRI. To measure DMN deactivation during tb-fMRI, we recorded the degree of negative correlation (anticorrelation) in the posterior cingulate cortex (PCC), a major node of the DMN, relative to the language task waveform in both healthy volunteers and patients with gliomas. Then, we measured the FC to the PCC of the other major nodes of the DMN: the

medial prefrontal cortex (mPFC) and the left and right inferior parietal lobules (LIPL and RIPL).<sup>3</sup> We also compared these 2 different methods of measuring tumor-induced functional changes in the DMN. We hypothesized that DMN regions impacted by tumors would demonstrate less anticorrelation in tb-fMRI and a correspondingly reduced resting-state connectivity compared with healthy volunteers.

## MATERIALS AND METHODS

### Subject Selection

This retrospective study was approved by the institutional review board of Memorial Sloan Kettering Cancer Center and was conducted in compliance with the Health Insurance Portability and Accountability Act. We analyzed the fMRI scans of 10 healthy controls and 30 patients diagnosed with gliomas who underwent both language tb-fMRI and rs-fMRI in the same sitting between 2017 and 2018. The control subjects gave consent for a funded study. Patient data were all acquired for the purpose of the pre-surgical planning protocol in addition to routine MR imaging. A summary of patient clinical data, including tumor type, location, and grade, is shown in the Table.

### MR Imaging Acquisition

Both tb-fMRI and rs-fMRI were performed using a 3T scanner (Discovery 750W, GE Healthcare) with 24-channel head coils. fMRI was acquired with single-shot EPI (TR/TE = 2500/32 ms, section thickness = 4 mm, matrix = 64 × 64, FOV = 240 mm, scanning duration = 6 minutes 55 seconds). fMRI coverage matching FLAIR parameters (TR/TE = 10,000/106 ms, TI = 220 ms, matrix = 256 × 256), T1 postcontrast (TR/TE = 600/20 ms, matrix = 256 × 256), and 3D T1-weighted anatomic images using a spoiled gradient recalled-echo sequence (TR/TE = 22/4 ms, matrix = 256 × 256, section thickness = 1 mm) were acquired as routine clinical scans.

### Tb-fMRI and rs-fMRI Paradigms

The fMRI examination consisted of 8 cycles of alternating task (20 seconds) and rest periods (30 seconds). During the phonemic fluency task, subjects were presented with different letters and were asked to silently generate words starting with that letter. During the rs-fMRI scan, subjects were instructed to relax, fixate on a central cross, and try not to think during the scan. Brain activity and head motion were monitored in real-time during the scan using BrainWave software (Medical Numerics).

### fMRI Data Preprocessing

Images were preprocessed and analyzed with the Analysis of Functional Neuro Images (AFNI; <http://afni.nimh.nih.gov/afni>) software.<sup>25</sup> Images were assessed for noise and artifacts. To correct for head motion, we performed 3D volume registration. Spatial smoothing using a Gaussian filter with 6-mm full width at half maximum was applied to suppress noise and increase the SNR. In addition, rs-fMRI data were filtered (range, 0.01–0.08 Hz) to extract functional integration processes and remove respiratory and cardiac noise during rest.

### DMN Deactivation and FC Analysis

We measured the DMN with 3 different methods in controls and patients: language-task-based deactivation, functional connectivity using the task-based fMRI map, and functional connectivity using the resting-state fMRI map.

1. Deactivation: To assess DMN deactivation in tb-fMRI, we performed a seed-based correlation analysis based on the functional ROI for each subject. For each subject, 3 correlation maps were sequentially generated. First, a correlation map was created from the BOLD response to the word-generation task, depicting both positively correlated and anticorrelated areas (tb-fMRI map). The region of the PCC that was anticorrelated in the tb-fMRI map was then selected as an ROI. A correlation threshold with an absolute value of 0.4 ( $P < .0001$ , and  $Q = .01$ ) was set to minimize the possible false-positive rate. All anticorrelated voxels of less than  $-0.4$  at the level of PCC on the axial view of the functional image were used to generate the PCC ROI.
2. Functional connectivity, task-based: To assess DMN FC, we used this PCC ROI to create a second correlation map from the same task-based functional data (PCC ROI task-based map), to measure the correlation of the other DMN regions (mPFC, LIPL, and RIPL) with the PCC.
3. Functional connectivity, resting-state: The same PCC ROI was transferred to the rs-fMRI data and used to create a third correlation map (PCC ROI resting-state map), again to measure the correlation of the other DMN regions with the PCC.

For quantitative analysis, the number of voxels, average correlation value, maximum correlation value, and correlation threshold were recorded from each DMN region.

For group analysis of controls, the correlation maps generated from PCC ROIs in tb-fMRI and rs-fMRI were normalized to the Montreal Neurological Institute 152 T1\_2-mm template and averaged over the subjects using the FMRIB Software Library (FSL; <http://www.fmrib.ox.ac.uk/fsl>)<sup>26</sup> to create the mean correlation map. The final map was thresholded at  $t > 6$  ( $P < .001$ ) and overlaid on the Montreal Neurological Institute 15 T1\_2-mm template image. Patient data were then separated by tumor location into 3 groups for analysis: tumors near or invading the posterior DMN ( $n = 14$ ), tumors near or invading the anterior DMN ( $n = 8$ ), and tumors outside the DMN ( $n = 8$ ), as indicated by abnormal findings on FLAIR. The tumor-location group classification was supervised by a Certificate of Added Qualification–certified neuroradiologist with 20 years' experience. DMN symmetry was measured with the inferior parietal lobe (IPL) ratio, which was calculated by dividing the correlation of the IPL on the nontumor side by the correlation of the IPL on the tumor side for both tb-fMRI and rs-fMRI. In controls, because the DMN is symmetric, the ratio was arbitrarily calculated as the LIPL correlation divided by the RIPL correlation. Patient data were also separated by tumor hemisphere (right-sided = 7, left-sided = 23) and tumor grade (II = 11, III/IV = 19).

### Statistical Analysis

The 2-tailed Mann-Whitney  $U$  test was used to assess the impact of tumor location, tumor hemisphere, and tumor grade on the average correlation value of the PCC in the tb-fMRI map and of the

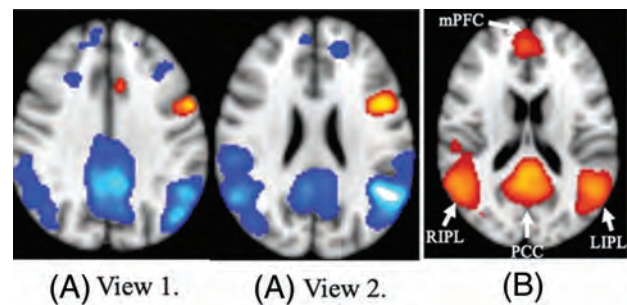


**FIG 1.** Group correlation maps for controls ( $n=10$ ). **A**, Group analysis map created from task-paradigm correlation maps (2 axial views). A positive correlation (orange) in the Broca area can be seen in the left hemisphere. A negative correlation (blue) in the DMN is also apparent. The 4 major DMN regions (PCC, mPFC, LIPL, and RIPL) are clearly anticorrelated, and the left-hemisphere Broca area is positively correlated with the language task. **B**, Mean group analysis map ( $t=6$ ,  $P < .001$ ) created from PCC ROI task-based correlation maps. DMN connectivity is apparent (orange). As expected, the regions of strongest connectivity to the PCC are the other major DMN regions. Thus, this figure illustrates a baseline level of DMN FC in healthy controls that can be visualized using the tb-fMRI correlation map with a PCC ROI.

correlation values of the mPFC, LIPL, and RIPL to the PCC in the PCC ROI task-based and resting-state maps. The Benjamini-Hochberg procedure (Benjamini-Hochberg critical value =  $i/m \times Q$ , where  $i$  = rank order,  $m$  = total number of tests, and  $Q$  = FDR = 0.05) was used to adjust the  $P$  value and control the false discovery rate (FDR). For analyses of tumor location and tumor grade, we used  $m = 3$  because there were 3 control-to-patient comparisons for deactivation and FC in each brain region in tb-fMRI and in rs-fMRI. For analysis of tumor hemisphere, there were 2 patient-to-control comparisons; consequently,  $m = 2$ .  $P$  values lower than their respective critical values were considered significant.

## RESULTS

### DMN Deactivation and the FC of Patients versus Controls

While performing the language task in tb-fMRI, all patients and controls demonstrated anticorrelation in the PCC. Healthy controls demonstrated anticorrelation with the language task in the 4 major DMN regions (PCC, mPFC, LIPL, and RIPL) (Fig 1A), as well as a baseline level of DMN FC on a mean PCC ROI task-based map (Fig 1B).

DMN anticorrelation, FC in tb-fMRI, and FC in rs-fMRI were all similarly disrupted in patients with gliomas compared with controls. Compared with the group of controls ( $n = 10$ ), the group of patients ( $n = 30$ ) showed significantly less anticorrelation in the PCC in tb-fMRI ( $P = .001$ ). Patients also showed significantly lower FC of the other 3 DMN regions to the PCC (mPFC,  $P = .004$ ; LIPL,  $P = .04$ ; RIPL,  $P = .048$ ) in tb-fMRI. While undergoing rs-fMRI, patients also showed lower FC to the PCC compared with controls, but the difference was only significant for the mPFC ( $P = .02$ ).

### Effect of Tumor Location on DMN Deactivation and FC

Figure 2 shows the fMRI maps of 3 patients, 1 from each tumor location group. Patient A, who had a tumor infiltrating the RIPL,



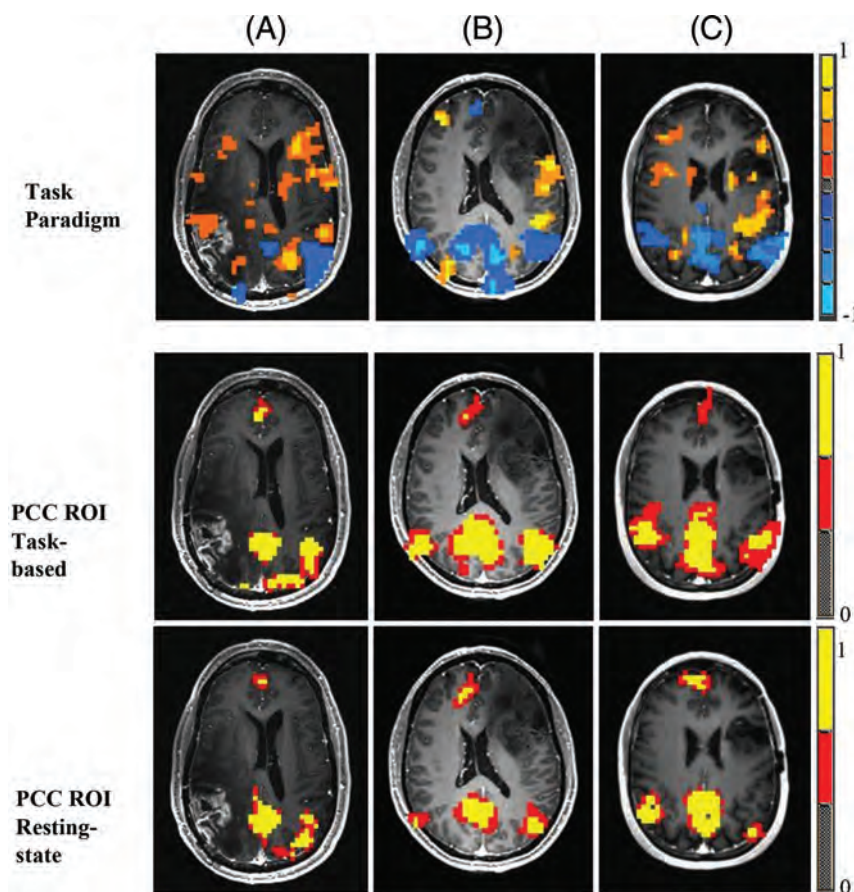


**FIG 2.** Examples of correlation maps in an axial view for patients with gliomas in different locations (patient A, posterior DMN; patient B, anterior DMN; patient C, outside DMN). The first row of images shows task-paradigm correlation maps. Blue represents areas of negative correlation, and orange represents areas of positive correlation to the language task. The second row of images illustrates the PCC ROI task-based fMRI correlation maps. Red and yellow represent areas of increased connectivity to the PCC ROI. The third row of images illustrates PCC ROI resting-state fMRI correlation maps. Patient A has a right-hemisphere glioblastoma invading the posterior DMN. Patient B has a left-hemisphere anaplastic oligodendroglioma invading the anterior DMN. Patient C has a left-hemisphere oligodendroglioma outside the DMN. The first 2 rows demonstrate a decreased anticorrelation in the DMN in the area of the tumor that corresponds to a decrease in both resting-state and task-based fMRI connectivity.

had less anticorrelation of the RIPL (compared with the LIPL) in both tb-fMRI and rs-fMRI. Patient A also showed less FC of the RIPL (compared with the LIPL) to the PCC in both tb-fMRI and rs-fMRI. Patient B had a tumor near the mPFC in the left hemisphere, and patient C had a tumor outside the DMN in the left hemisphere. Notably, across all patients including these 3, no significant differences were found in terms of FC of the mPFC, LIPL, and RIPL to the PCC between tb-fMRI and rs-fMRI. In addition, the ratio of FC values in each DMN region in tb-fMRI versus rs-fMRI was not significantly different between controls and patients.

When we stratified the data by tumor location (Fig 3A, -B), only patients with posterior DMN tumors showed significantly lower anticorrelation in the PCC compared with controls ( $P < .001$ ) in tb-fMRI. In terms of DMN FC, significantly lower FC of the mPFC to the PCC was found in patients with anterior DMN tumors in tb-fMRI ( $P = .001$ ) and rs-fMRI ( $P = .01$ ). Patients with posterior

DMN tumors also demonstrated significantly lower FC to the LIPL in tb-fMRI ( $P = .02$ ) and rs-fMRI ( $P = .02$ ).

The IPL ratio of patients with posterior DMN tumors was significantly greater than that of controls (tb-fMRI,  $P = .006$ ; rs-fMRI,  $P = .008$ ) (Fig 4). The IPL ratio of patients with anterior DMN tumors was significantly greater than that of controls in rs-fMRI ( $P = .004$ ), but not in tb-fMRI. Patients with tumors outside the DMN showed no significant differences from controls.

#### **Effect of Tumor Hemisphere on DMN Deactivation and FC**

Significantly lower PCC anticorrelation was found for patients with both left tumors ( $P = .003$ ) and right tumors ( $P = .015$ ) compared with controls (Fig 3C, -D). The FC of the mPFC to the PCC was significantly lower for patients with both left ( $P = .02$ ) and right ( $P = .03$ ) tumors in tb-fMRI, but not in rs-fMRI. No hemispheric differences in PCC anticorrelation or FC were found when directly comparing patients with left tumors with those with right tumors.

#### **Effect of Tumor Grade on DMN Deactivation and FC**

After we stratified by tumor grade (Fig 3E, -F), only patients with grade IV tumors showed significantly lower PCC anticorrelation ( $P < .001$ ) compared with controls. Only patients with grade III tumors showed significantly lower mPFC connectivity in tb-fMRI ( $P = .005$ ) compared with

controls, while rs-fMRI revealed no significant differences in FC compared with controls. No significant differences in PCC anticorrelation or mPFC connectivity were found when directly comparing grade II with high-grade (grades III and IV) tumors.

## **DISCUSSION**

Our study has 2 major findings: First, we showed that patients with gliomas have significantly less anticorrelation in the PCC on tb-fMRI than healthy controls. Second, our study successfully used the PCC identified in tb-fMRI as an ROI for seed-based correlation analysis to examine the FC of the DMN in both task-based and resting-state fMRI in patients with gliomas. We found strong overlap between the task-based and resting-state maps.

We found significantly lower anticorrelation in the PCC as well as significantly lower FC of the 3 regions of the DMN (mPFC, LIPL, and RIPL) to the PCC in patients compared



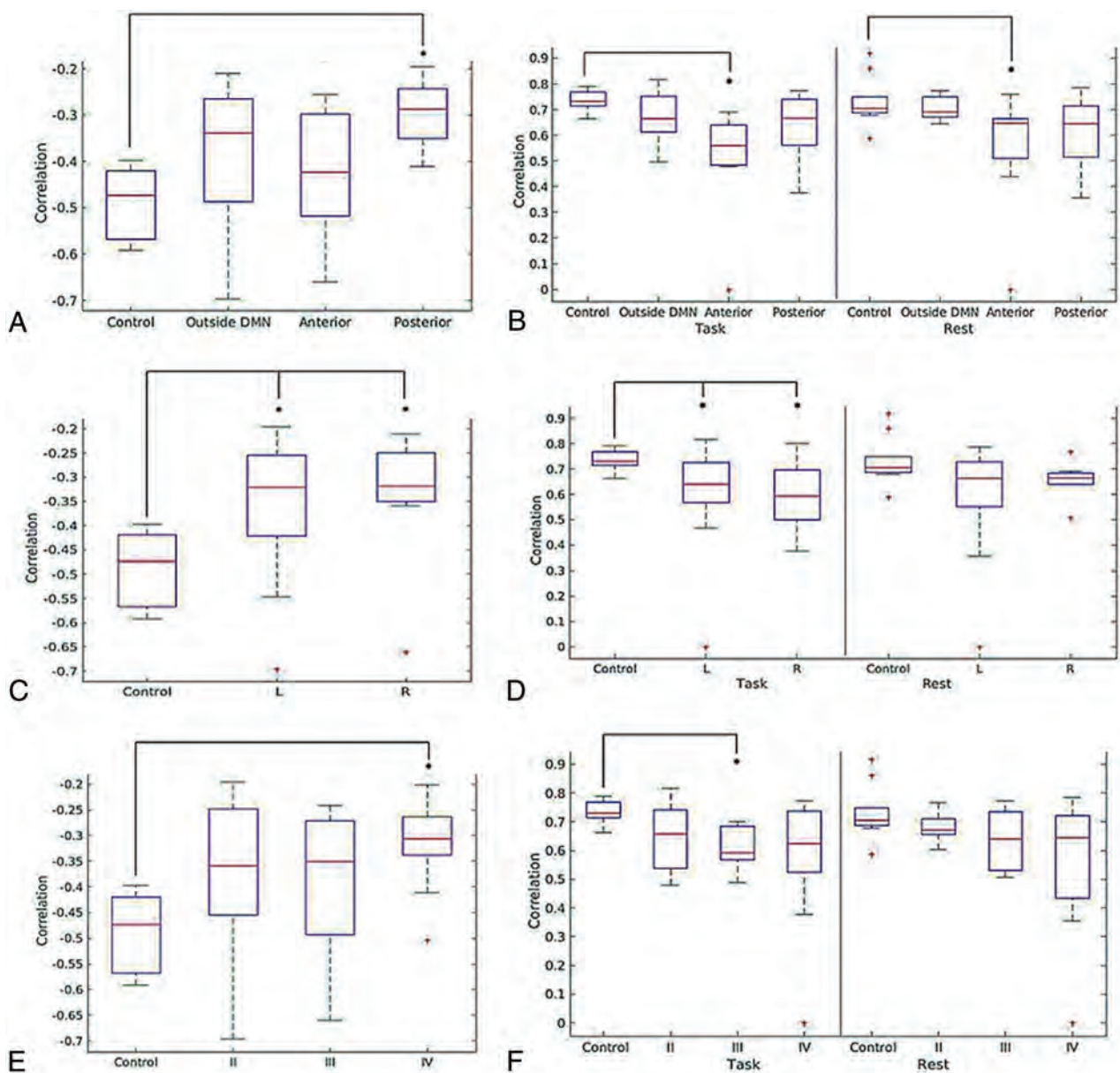


**FIG 3.** Box-and-whisker plots illustrating the distribution of average correlation values in the term of task-induced deactivation of PCC region of the DMN for controls and patients by tumor location (A), tumor hemisphere (C), and tumor grade (E) and average correlation values of the mPFC region of the DMN for controls and patients in both the PCC ROI task-based correlation map and the PCC ROI resting-state correlation map by tumor location (B), tumor hemisphere (D), and tumor grade (F).

with controls during task-based fMRI. The decrease in anticorrelation was more pronounced for patients with tumors in or near the posterior regions of the DMN (including the PCC, LIPL, and RIPL). When patients were stratified by tumor hemisphere or tumor grade, both patients with left- and right-hemisphere tumors as well as patients with grade IV tumors demonstrated decreased anticorrelation in the PCC compared with controls. No significant differences were found for either anticorrelation in the PCC or FC when comparing left- with right-hemisphere tumors or grade II tumors with high-grade (grades III and IV) tumors. Due to the relatively small sample size of the overall study, especially of each subgroup, and the statistical adjustments for multiple

comparisons, underpowering may have contributed to these negative results.

While DMN deactivation has not been previously studied in patients with brain tumors, alterations in DMN connectivity have been shown. Esposito et al<sup>18</sup> used independent component analysis to show globally reduced DMN connectivity in patients with left-hemisphere gliomas during a language task. Our results not only affirm their findings but also show the same results in right-hemisphere gliomas. Furthermore, we showed decreased DMN FC for right- and left-hemisphere gliomas in the resting state.

The PCC has been described as a critical node of the DMN.<sup>17</sup> The location-dependent change in PCC anticorrelation indicates that tumors near or directly infiltrating the posterior DMN

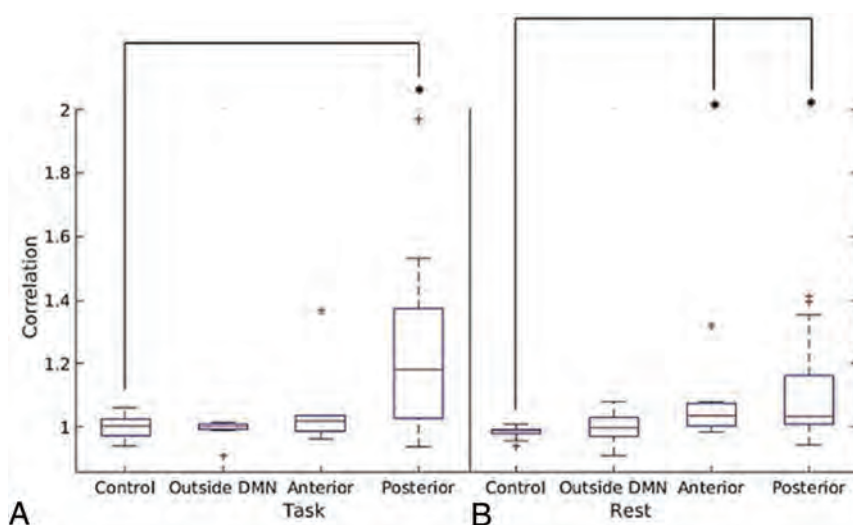


**FIG 4.** Box-and-whisker plots illustrating the ratio of the average correlation values of nontumor/tumor IPL versus tumor location for patients and of left/right IPL versus tumor location for controls in task-based fMRI (A) and resting-state fMRI (B).

regions have a greater impact on PCC anticorrelation. The physical proximity of these tumors to the PCC is likely part of the explanation. Anterior DMN tumors showed a smaller difference in PCC anticorrelation than tumors outside the DMN; overall, tumors outside the DMN were closer in distance to the PCC than anterior DMN tumors.

Meanwhile, the location-dependent asymmetry of IPL connectivity means that posterior DMN tumors affect the ipsilateral IPL more than the contralateral IPL; therefore, these tumors have a greater impact on ipsilateral connectivity. Again, this may be largely due to proximity, given that many of the posterior DMN tumors were near the ipsilateral IPL.

Local tumor effects, such as parenchymal infiltration, local necrosis, and tumor neoangiogenesis, may result in neurovascular uncoupling. Neurovascular uncoupling has been shown to cause false-negative results in both tb-fMRI and rs-fMRI data.<sup>27-38</sup> It remains unclear whether our findings are due to a global decrease in DMN function, neurovascular uncoupling, or some combination thereof. Our data showed—in patients with both left- and right-hemisphere tumors, compared with controls—lower PCC anticorrelation and lower FC of the mPFC to the PCC in tb-fMRI. In contrast, a rs-fMRI study by Ghumman et al<sup>20</sup> found decreased overall DMN connectivity in patients with left-hemisphere cerebral tumors, but not in patients with right-hemisphere tumors. Their study included gliomas along with other tumor pathologies such as meningiomas and metastases, which may impact DMN connectivity differently. However, Ghumman et al<sup>20</sup> did not find a significant difference among histologic types of tumor. Again, we studied connectivity of individual regions to the PCC, not overall network connectivity, but this difference likely does not explain the discrepancy in our findings.

In another study, Harris et al<sup>19</sup> showed that brain tumors of higher grades corresponded to a greater reduction in global DMN connectivity in pseudo-resting-state fMRI. However, after false discovery rate correction, our data did not corroborate this

finding, with lower FC found only in grade III tumors between the PCC and mPFC. An important difference is that their study also measured global DMN connectivity, while our study directly measured connectivity between individual regions and the PCC. Additionally, their data were acquired using pseudo-resting-state fMRI, which analyzes residual tb-fMRI signals after taking into account activation due to the task. On the other hand, 1 possible explanation for our negative results is underpowering due to false discovery rate correction for multiple comparisons and a smaller sample size. Esposito et al<sup>18</sup> actually found increased correspondence in the global DMN spatial pattern of controls and patients with high-grade gliomas compared with those with low-grade gliomas; they attributed this finding to the slow-growing nature of low-grade gliomas, which allows time for network reorganization due to neuronal plasticity.

The decreased DMN deactivation and connectivity have clinical implications for cognitive decline in patients with brain tumors. Deficits in behavioral and cognitive function in patients with tumors in or near the posterior DMN may be explained by the location-dependent effects of brain tumors. Deficits in activities such as memory-encoding and external task performance may be at least partially due to the disruption of DMN deactivation and connectivity by the tumor. Because our patients' scans were all preoperative, comparison with postoperative fMRI could assess whether resection or debulking is associated with restoration of DMN deactivation and FC.

Our study was limited by a number of factors. Although ROIs were systematically placed in each patient by 1 investigator, they were selected manually, which creates the possibility of human variation in ROI placement. At the same time, manual selection allowed us to better account for small variations in the location of positive or negative correlations in each region, especially because tumors and their accompanying edema often induce mass effect that distorts regional anatomy. Another limitation is the variation in the precise location of each tumor; the reduced number of patients with tumors in each DMN region necessitated grouping tumors in the PCC or bilateral IPLs into the broader "posterior DMN" group. Each tumor that was classified as in or near the anterior or posterior DMN was determined by the investigators visually, and the amount of overlap between the DMN region and the tumor or surrounding edema was variable. Limited patient volume also prohibited further analysis of tumors "outside the DMN" by a more specific location.

Our study was limited by a number of factors. Although ROIs were systematically placed in each patient by 1 investigator, they were selected manually, which creates the possibility of human variation in ROI placement. At the same time, manual selection allowed us to better account for small variations in the location of positive or negative correlations in each region, especially because tumors and their accompanying edema often induce mass effect that distorts regional anatomy. Another limitation is the variation in the precise location of each tumor; the reduced number of patients with tumors in each DMN region necessitated grouping tumors in the PCC or bilateral IPLs into the broader "posterior DMN" group. Each tumor that was classified as in or near the anterior or posterior DMN was determined by the investigators visually, and the amount of overlap between the DMN region and the tumor or surrounding edema was variable. Limited patient volume also prohibited further analysis of tumors "outside the DMN" by a more specific location.

## CONCLUSIONS

Task-based fMRI shows impaired deactivation in patients with gliomas. In particular, patients with posterior DMN tumors and grade IV tumors showed decreased anticorrelation in the PCC.

Our study also, for the first time, directly examined the FC of the DMN in both task-based and resting-state fMRI in patients with gliomas, using the PCC identified in tb-fMRI as an ROI for seed-based correlation analysis. DMN maps created from a PCC ROI using the tb-fMRI and rs-fMRI waveforms are strongly correlated. Hence, in DMN regions impacted by tumors, the decrease in anticorrelation in tb-fMRI corresponds to a reduced resting-state connectivity compared with healthy volunteers.

## ACKNOWLEDGMENT

The authors would like to acknowledge Joanne Chin, Senior Editor/Grant Writer of the Department of Radiology at Memorial Sloan Kettering Cancer Center, for her valuable contributions.

Disclosures: Yash M. Maniar—RELATED: Support for Travel to Meetings for the Study or Other Purposes: Icahn School of Medicine at Mount Sinai Medical Student Research Office, Comments: funding for the national meeting of the American Society of Neuroradiology, poster submission/registration. Andrei I. Holodny—UNRELATED: Other: fMRI Consultants, LLC, Comments: a purely educational entity.

## REFERENCES

- Greicius MD, Krasnow B, Reiss AL, et al. **Functional connectivity in the resting brain: a network analysis of the default mode hypothesis.** *Proc Natl Acad Sci U S A* 2003;100:253–58 CrossRef Medline
- Fox MD, Snyder AZ, Vincent JL, et al. **The human brain is intrinsically organized into dynamic, anticorrelated functional networks.** *Proc Natl Acad Sci U S A* 2005;102:9673–78 CrossRef Medline
- Buckner RL, Andrews-Hanna JR, Schacter DL. **The brain's default network: anatomy, function, and relevance to disease.** *Ann N Y Acad Sci* 2008;1124:1–38 CrossRef Medline
- Raichle ME, MacLeod AM, Snyder AZ, et al. **A default mode of brain function.** *Proc Natl Acad Sci U S A* 2001;98:676–82 CrossRef Medline
- Shulman GL, Fiez JA, Corbetta M, et al. **Common blood flow changes across visual tasks, II: decreases in cerebral cortex.** *J Cogn Neurosci* 1997;9:648–63 CrossRef Medline
- Andrews-Hanna JR, Reidler JS, Sepulcre J, et al. **Functional-anatomic fractionation of the brain's default network.** *Neuron* 2010;65:550–62 CrossRef Medline
- Mason MF, Norton MI, Van Horn JD, et al. **Wandering minds: the default network and stimulus-independent thought.** *Science* 2007;315:393–95 CrossRef Medline
- Gusnard DA, Akbudak E, Shulman GL, et al. **Medial prefrontal cortex and self-referential mental activity: relation to a default mode of brain function.** *Proc Natl Acad Sci U S A* 2001;98:4259–64 CrossRef Medline
- Daselaar SM, Prince SE, Cabeza R. **When less means more: deactivations during encoding that predict subsequent memory.** *Neuroimage* 2004;23:921–27 CrossRef Medline
- Anticevic A, Cole MW, Murray JD, et al. **The role of default network deactivation in cognition and disease.** *Trends Cogn Sci* 2012;16:584–92 CrossRef Medline
- Ali FS, Hussain MR, Gutierrez C, et al. **Cognitive disability in adult patients with brain tumors.** *Cancer Treat Rev* 2018;65:33–40 CrossRef Medline
- Hansen NL, Lauritzen M, Mortensen EL, et al. **Subclinical cognitive decline in middle-age is associated with reduced task-induced deactivation of the brain's default mode network.** *Hum Brain Mapp* 2014;35:4488–98 CrossRef Medline
- Jeong B, Kubicki M. **Reduced task-related suppression during semantic repetition priming in schizophrenia.** *Psychiatry Res* 2010;181:114–20 CrossRef Medline
- Pihlajamaki M, Sperling RA. **Functional MRI assessment of task-induced deactivation of the default mode network in Alzheimer's disease and at-risk older individuals.** *Behav Neurol* 2009;21:77–91 CrossRef Medline
- Lariviere S, Ward NS, Boudrias MH. **Disrupted functional network integrity and flexibility after stroke: relation to motor impairments.** *Neuroimage Clin* 2018;19:883–91 CrossRef Medline
- Rogers BP, Morgan VL, Newton AT, et al. **Assessing functional connectivity in the human brain by fMRI.** *Magn Reson Imaging* 2007;25:1347–57 CrossRef Medline
- Dacosta-Aguayo R, Grana M, Iturria-Medina Y, et al. **Impairment of functional integration of the default mode network correlates with cognitive outcome at three months after stroke.** *Hum Brain Mapp* 2015;36:577–90 CrossRef Medline
- Esposito R, Mattei PA, Briganti C, et al. **Modifications of default-mode network connectivity in patients with cerebral glioma.** *PLoS One* 2012;7:e40231 CrossRef Medline
- Harris RJ, Bookheimer SY, Cloughesy TF, et al. **Altered functional connectivity of the default mode network in diffuse gliomas measured with pseudo-resting state fMRI.** *J Neurooncol* 2014;116:373–79 CrossRef Medline
- Ghumman S, Fortin D, Noel-Lamy M, et al. **Exploratory study of the effect of brain tumors on the default mode network.** *J Neurooncol* 2016;128:437–44 CrossRef Medline
- Kennedy DP, Courchesne E. **The intrinsic functional organization of the brain is altered in autism.** *Neuroimage* 2008;39:1877–85 CrossRef Medline
- Bluhm RL, Miller J, Lanius RA, et al. **Spontaneous low-frequency fluctuations in the BOLD signal in schizophrenic patients: anomalies in the default network.** *Schizophr Bull* 2007;33:1004–12 CrossRef Medline
- Hohenfeld C, Werner CJ, Reetz K. **Resting-state connectivity in neurodegenerative disorders: is there potential for an imaging biomarker?** *Neuroimage Clin* 2018;18:849–70 CrossRef Medline
- Chen Y, Yang W, Long J, et al. **Discriminative analysis of Parkinson's disease based on whole-brain functional connectivity.** *PLoS One* 2015;10:e0124153 CrossRef Medline
- Cox RW. **AFNI: software for analysis and visualization of functional magnetic resonance neuroimages.** *Comput Biomed Res* 1996;29:162–73 CrossRef Medline
- Woolrich MW, Jbabdi S, Patenaude B, et al. **Bayesian analysis of neuroimaging data in FSL.** *Neuroimage* 2009;45:S173–86 CrossRef Medline
- Holodny AI, Schulder M, Liu WC, et al. **Deceased BOLD functional MR activation of the motor and sensory cortices adjacent to a glioblastoma multiforme: implications for fMRI guided neurosurgery.** *AJNR Am J Neuroradiol* 1999;20:609–12 Medline
- Holodny AI, Schulder M, Liu WC, et al. **The effect of brain tumors on BOLD fMRI activation in the adjacent motor cortex: implications for image-guided neurosurgery.** *AJNR Am J Neuroradiol* 2000;21:1415–22 Medline
- Chen C, Hou BL, Holodny AI. **Effect of age and tumor grade on BOLD fMRI in preoperative assessment of patients with gliomas.** *Radiology* 2008;248:971–78 CrossRef Medline
- Peck KK, Bradbury M, Brennan N, et al. **Presurgical evaluation of language using fMRI in brain tumor patients with prior surgery.** *Neurosurgery* 2009;64:644–52 CrossRef Medline
- Abreu VH, Peck KK, Petrovich-Brennan NM, et al. **Brain tumors: the influence of tumor type and routine MR imaging characteristics at BOLD functional MR imaging in the primary motor gyrus.** *Radiology* 2016;281:876–83 CrossRef Medline
- Mallela AN, Peck KK, Petrovich-Brennan NM, et al. **Altered resting state functional connectivity in the hand motor network in patients with gliomas.** *Brain Connect* 2016;6:587–95 CrossRef Medline
- un H, Vachha B, Laino ME, et al. **Decreased hand-motor resting-state functional connectivity in patients with glioma: analysis of factors**

- including neurovascular uncoupling. *Radiology* 2020;294:610–21 CrossRef Medline
34. Agarwal S, Sair HI, Gujar S, et al. Functional magnetic resonance imaging activation optimization in the setting of brain tumor-induced neurovascular uncoupling using resting-state blood oxygen level-dependent amplitude of low frequency fluctuations. *Brain Connect* 2019;9:241–50 CrossRef Medline
  35. Agarwal S, Lu H, Pillai JJ. Value of frequency domain resting-state functional magnetic resonance imaging metrics amplitude of low-frequency fluctuation and fractional amplitude of low-frequency fluctuation in the assessment of brain tumor-induced neurovascular uncoupling. *Brain Connect* 2017;7:382–89 CrossRef Medline
  36. Pak RW, Hadjiabadi DH, Senarathna J, et al. Implications of neurovascular uncoupling in functional magnetic resonance imaging (fMRI) of brain tumors. *J Cereb Blood Flow Metab* 2017;37:3475–87 CrossRef Medline
  37. Agarwal S, Sair HI, Pillai JJ. The resting-state functional magnetic resonance imaging regional homogeneity metrics–Kendall’s coefficient of concordance–regional homogeneity and coherence–regional homogeneity–are valid indicators of tumor-related neurovascular uncoupling. *Brain Connect* 2017;7:228–35 CrossRef Medline
  38. Agarwal S, Sair HI, Airan R, et al. demonstration of brain tumor-induced neurovascular uncoupling in resting-state fMRI at ultra-high field. *Brain Connect* 2016;6:267–72 CrossRef Medline



# Convolutional Neural Network to Stratify the Malignancy Risk of Thyroid Nodules: Diagnostic Performance Compared with the American College of Radiology Thyroid Imaging Reporting and Data System Implemented by Experienced Radiologists

G.R. Kim, E. Lee, H.R. Kim, J.H. Yoon, V.Y. Park, and J.Y. Kwak



## ABSTRACT

**BACKGROUND AND PURPOSE:** Comparison of the diagnostic performance for thyroid cancer on ultrasound between a convolutional neural network and visual assessment by radiologists has been inconsistent. Thus, we aimed to evaluate the diagnostic performance of the convolutional neural network compared with the American College of Radiology Thyroid Imaging Reporting and Data System (TI-RADS) for the diagnosis of thyroid cancer using ultrasound images.

**MATERIALS AND METHODS:** From March 2019 to September 2019, seven hundred sixty thyroid nodules ( $\geq 10$  mm) in 757 patients were diagnosed as benign or malignant through fine-needle aspiration, core needle biopsy, or an operation. Experienced radiologists assessed the sonographic descriptors of the nodules, and 1 of 5 American College of Radiology TI-RADS categories was assigned. The convolutional neural network provided malignancy risk percentages for nodules based on sonographic images. Sensitivity, specificity, accuracy, positive predictive value, and negative predictive value were calculated with cutoff values using the Youden index and compared between the convolutional neural network and the American College of Radiology TI-RADS. Areas under the receiver operating characteristic curve were also compared.

**RESULTS:** Of 760 nodules, 176 (23.2%) were malignant. At an optimal threshold derived from the Youden index, sensitivity and negative predictive values were higher with the convolutional neural network than with the American College of Radiology TI-RADS (81.8% versus 73.9%,  $P = .009$ ; 94.0% versus 92.2%,  $P = .046$ ). Specificity, accuracy, and positive predictive values were lower with the convolutional neural network than with the American College of Radiology TI-RADS (86.1% versus 93.7%,  $P < .001$ ; 85.1% versus 89.1%,  $P = .003$ ; and 64.0% versus 77.8%,  $P < .001$ ). The area under the curve of the convolutional neural network was higher than that of the American College of Radiology TI-RADS (0.917 versus 0.891,  $P = .017$ ).

**CONCLUSIONS:** The convolutional neural network provided diagnostic performance comparable with that of the American College of Radiology TI-RADS categories assigned by experienced radiologists.

**ABBREVIATIONS:** ACR = American College of Radiology; AUC = area under the curve; AI = artificial intelligence; CNB = core needle biopsy; CNN = convolutional neural network; FNA = fine-needle aspiration; ROC = receiver operating characteristic; TI-RADS = Thyroid Imaging and Reporting and Data System; TR = category of TI-RADS; US = ultrasound

Thyroid ultrasound (US) is the best tool to evaluate thyroid nodules for ultrasound-guided fine-needle aspiration (US-FNA).<sup>1,2</sup> However, the diagnostic performance of US varies because it is operator-dependent, and interobserver variability is inevitable.<sup>3,4</sup> To overcome this limitation, studies have been

conducted on the computerized diagnosis of thyroid cancer with US images.<sup>5-8</sup> The convolutional neural network (CNN) is a deep learning technique that incorporates fully trainable models and can potentially cover various medical imaging tasks.<sup>9</sup> Recently, multiple CNN models have been investigated for the diagnosis of thyroid cancer.<sup>10-17</sup> Computerized algorithms were designed to

Received August 5, 2020; accepted after revision March 6, 2021.

From the Department of Radiology (G.R.K., J.H.Y., V.Y.P., J.Y.K.), Severance Hospital, Research Institute of Radiological Science, Center for Clinical Imaging Data Science, and Biostatistics Collaboration Unit (H.R.K.), Department of Biomedical Systems Informatics, Yonsei University College of Medicine, Seoul, Korea; and Department of Computational Science and Engineering (E.L.), Yonsei University, Seoul, Korea.

This study was supported by the National Research Foundation of Korea grant funded by the Korean government (Ministry of Science and ICT) (2019R1A2C1002375) and a CMB-Yuhan research grant of Yonsei University College of Medicine (6-2017-0170).

The funders had no role in study design, data collection and analysis, decision to publish, or preparation of the manuscript.

Please address correspondence to Jin Young Kwak, MD, PhD, Department of Radiology, Research Institute of Radiological Science, Center for Clinical Imaging Data Science, Yonsei University College of Medicine, 50 Yonsei-ro, Seodaemun-gu, Seoul, Republic of Korea, 120-752; e-mail: docjin@yuhs.ac

Indicates open access to non-subscribers at [www.ajnr.org](http://www.ajnr.org)

<http://dx.doi.org/10.3174/ajnr.A7149>

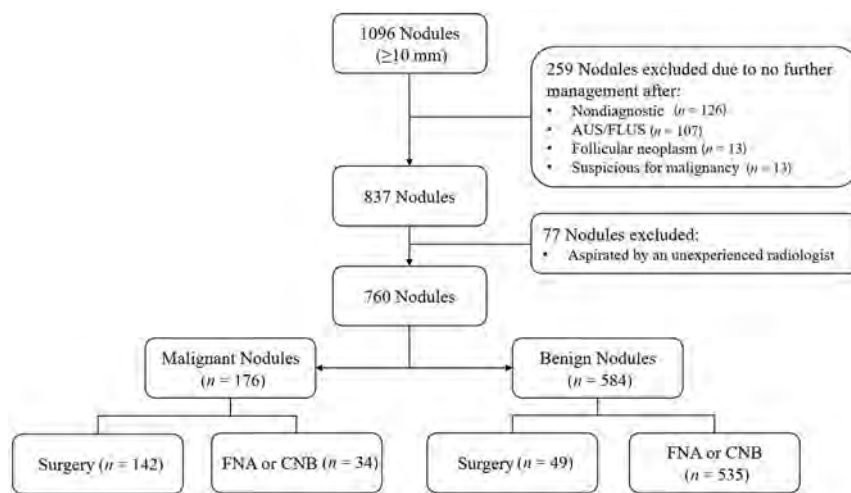


**FIG 1.** Flowchart of the study population. AUS/FLUS indicates atypia of undetermined significance/follicular lesion of undetermined significance.

predict thyroid cancer, and the deep CNN was used to differentiate malignant and benign thyroid nodules on the basis of US images.

Findings of past studies have been inconsistent when the diagnostic performance of the CNN was compared with visual assessment by radiologists. Even when US images were assessed according to published guidelines, the diagnostic performance of the CNN could be inferior to or favorable compared with that of radiologists, and in some studies even superior.<sup>10-12,15</sup> This variation might be due to unpredictable human judgment as well as differing algorithms that were developed by researchers or corporations individually; radiologists have been known to make their own final assessment, with guidelines being simply a point of reference. Thus, we aimed to compare the diagnostic performance of a CNN with a well-established guideline, the American College of Radiology (ACR) Thyroid Imaging Reporting and Data System (TI-RADS), which reduces benign FNAs with high specificity and accuracy in an era when the overdiagnosis and overtreatment of thyroid cancer have become issues of concern.<sup>18-22</sup> ACR TI-RADS guides the diagnosis of thyroid cancer through a summation of points assigned to each US feature and then classifies nodules into 5 categories, TI-RADS (TR) 1 to TR5.<sup>23</sup> In our institution, the radiologist performing the US prospectively records the US features of all thyroid nodules expected to undergo US-FNA or US-guided core needle biopsy (US-CNB), and each thyroid nodule is assigned to 1 of the 5 ACR TI-RADS categories, TR1 to TR5, according to the recorded US features.

Therefore, the aim of this study was to evaluate the diagnostic performance of the CNN compared with ACR TI-RADS for the diagnosis of thyroid cancer using US images.

## MATERIALS AND METHODS

### Study Population

From March 2019 to September 2019, US-FNA or US-CNB was initially performed on 1096 thyroid nodules measuring  $\geq 10$  mm in 1087 patients 19 years of age or older in Severance Hospital. Of

the original 1096 nodules, 259 were excluded because they did not receive further management such as repeat FNA or an operation after US-FNA showed the results as nondiagnostic ( $n = 125$  in FNA;  $n = 1$  in CNB). Exclusions were also due to atypia of undetermined significance/follicular lesion of undetermined significance ( $n = 107$  in FNA), indeterminate ( $n = 6$  in CNB), follicular neoplasm ( $n = 3$  in FNA;  $n = 4$  in CNB), or suspicion for malignancy ( $n = 13$ ). Seventy-seven nodules were also excluded because they were aspirated by an inexperienced radiologist who had  $< 1$  year of experience dedicated to thyroid imaging. The remaining 760 nodules met 1 of the following criteria: 1) nodules with benign or malignant results on US-FNA or US-CNB ( $n = 551$ ), 2) nodules that underwent an operation ( $n = 191$ ), and 3) nodules that were confirmed as benign on repeat US-FNA or US-CNB after initial cytology results of nondiagnostic ( $n = 4$ ) or atypia of undetermined significance/follicular lesion of undetermined significance ( $n = 14$ ). Finally, 760 thyroid nodules in 757 patients were included (Fig 1). Three patients had 2 nodules that were aspirated from both sides of the thyroid gland.

### US Image Acquisition

All US examinations were performed using a 7- to 17-mHz linear transducer (EPIQ 7; Phillips Healthcare). One of 5 radiologists dedicated to thyroid imaging with 6–21 years of experience performed the US examinations and subsequent US-FNAs. The radiologist who performed the US-FNA prospectively recorded the US features of each thyroid nodule with respect to composition, echogenicity, shape, margin, and calcifications.<sup>2,24</sup> Composition was assessed as solid, predominantly solid (solid component  $\geq 50\%$ ), or predominantly cystic (solid component  $< 50\%$ ) or spongiform. Echogenicity was assessed as hyperechoic (hyperechogenicity compared with the surrounding thyroid parenchyma), isoechoic (isoechochogenicity compared with the surrounding thyroid parenchyma), hypoechoic (hypoechochogenicity compared with the surrounding thyroid parenchyma), or markedly hypoechoic (hypoechochogenicity compared with the strap muscles). Shape was assessed as parallel or nonparallel (greater in the anteroposterior dimension than the transverse dimension, taller-than-wide). Margin was assessed as well-defined, microlobulated, or irregular. Calcifications were classified as eggshell calcifications, macrocalcifications, microcalcifications, mixed calcifications, or no calcifications.

### Image Analyses

A representative US image of each thyroid nodule was selected by an experienced radiologist (J.Y.K. with 18 years of experience dedicated to thyroid imaging), and the chosen images were stored as JPEG images in the PACS. The radiologist (J.Y.K.) drew a square ROI to cover the targeted thyroid nodule entirely using the Windows 10 Paint program. The extracted ROIs were analyzed by

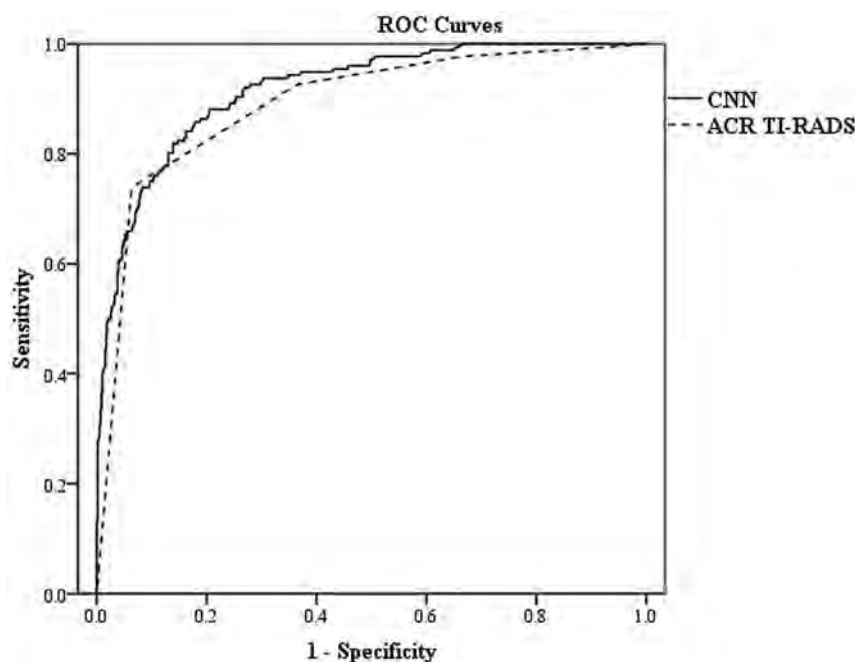


**FIG 2.** Comparison of ROC curves between the CNN (solid line) and ACR TI-RADS categories (dotted line). The area under the ROC curve of the CNN (0.917; 95% confidence interval, 0.895–0.936) was higher than that in the ACR TI-RADS categories (0.891; 95% confidence interval, 0.867–0.912) ( $P = .017$ ). The areas under the ROC curve of the CNN using a malignancy risk percentage between 0 and 100 and ACR TI-RADS categories using a TR category from 1 to 5 were compared as continuous values.

the deep CNN, and malignancy risk was shown as a percentage between 0 and 100 for each thyroid nodule (Fig 2). The deep CNN implementation was based on an algorithm that was trained (fine-tuned) with 589 thyroid nodule datasets from our institution.<sup>10</sup> Using 3 pretrained CNNs, AlexNet, GoogLeNet, and InceptionResNetV2, we created thyroid classifiers and collected the area under the receiver operating characteristic (ROC) curve (AUC) corresponding to each CNN using Matlab 2019a (MathWorks). These classifiers and AUCs were then used to produce the mean of classification scores expressed as posterior probability in which the AUCs were used as weights. This process yields more objective results by gathering various opinions and tends to hold the final result if predictions are the same and follows the higher score if predictions contradict (see more details in the previous studies).<sup>10,25</sup>

One radiologist (G.R.K.) with 7 years of experience dedicated to thyroid imaging arranged the previously recorded US features to match the US descriptors used in the ACR TI-RADS and summed up the score of each nodule as follows: TR1 (0–1 point), TR2 (2 points), TR3 (3 points), TR4 (4–6 points), and TR5 ( $\geq 7$  points).<sup>21</sup> Regarding the US features of ACR TI-RADS, “predominantly cystic” nodules were considered to have cystic or almost completely cystic composition, and “predominantly solid” nodules were considered to have mixed cystic and solid composition. “Solid” nodules were considered to have solid or almost completely solid composition. An echogenicity of “marked hypoechoic” was regarded as “very hypoechoic.” “Well-defined” margins were regarded as smooth and microlobulated, and “irregular” margins were regarded as lobulated or

irregular. “Eggshell calcifications” were regarded as peripheral (rim) calcifications, and “mixed calcification” and “microcalcifications” were regarded as punctate echogenic.

### Data and Statistical Analysis

Benign results on US-FNA or US-CNB and benign or malignant histopathologic results from an operation and follow-up US-FNA or US-CNB were the reference standards for analysis. On the basis of these results, we calculated the malignancy risk of the 5 categories of ACR TI-RADS, respectively. Each nodule that had its percentage of malignancy risk calculated by the CNN was re-categorized into 1 of the 5 TR categories according to the malignancy risk range suggested for each TR category by ACR TI-RADS.<sup>22,26</sup> Malignancy risk was also calculated for those TR categories created from the CNN (CNN-TR).

Variables were compared between the benign and malignant nodules using the Mann-Whitney  $U$  test and the  $\chi^2$  test or the Fisher exact test. Diagnostic performances including sensitivity, specificity, accuracy, posi-

tive predictive value, and negative predictive value for predicting thyroid malignancy were calculated for the CNN and ACR TI-RADS with 95% confidence intervals. The cutoff value to diagnose thyroid malignancy was defined using the Youden index in the CNN (malignancy risk percentage as a continuous variable) and ACR TI-RADS (TR category as an ordinal variable).<sup>27</sup> Logistic regression using the generalized estimating equation method was used to test the significance of comparisons with adjustments for correlated observations of clustered data. The AUCs of the CNN using a malignancy risk percentage between 0 and 100 and ACR TI-RADS categories using a TR category from 1 to 5 were compared as continuous values using the DeLong method.<sup>28</sup>

All statistical analyses were performed with SAS (Version 9.4; SAS Institute) and SPSS 25.0 for Windows (IBM). Statistical significance was defined with  $P$  values  $< .05$ .

## RESULTS

### Study Population and Nodule Characteristics

In 760 thyroid nodules, 176 (23.2%) were malignant. Final diagnoses of the 176 malignant nodules were confirmed through surgical resection ( $n = 142$ ; one hundred thirty-two papillary thyroid carcinomas, 5 follicular carcinomas, 2 poorly differentiated carcinomas, 1 medullary carcinoma, 1 Hurthle cell carcinoma, and 1 squamous cell carcinoma) and US-FNA ( $n = 34$ ; 33 papillary thyroid carcinomas and 1 small-cell carcinoma). The median size of all 176 nodules was 20 mm (interquartile range, 14–30 mm). The median age of the 757 patients was 51 years (interquartile range,

**Table 1: Patient demographics and distribution of ACR TI-RADS features in benign and malignant thyroid nodules (n = 760)<sup>a</sup>**

Characteristics	All (n = 760)	Benign Nodules (n = 584)	Malignant Nodules (n = 176)	P Value
Sex				.035
Women	587	462 (79.4%)	125 (71.4%)	
Men	170	120 (20.6%)	50 (28.6%)	
Age (median) (interquartile range) (yr)	51 (39–61)	52 (41–61)	45 (34–60)	<.001
Nodule size (median) (interquartile range) (mm)	20 (14–30)	23 (15–32)	14 (11–20)	<.001
Nodule features				
Composition				<.001
Cystic or almost completely cystic	50	47 (8.0%)	3 (1.7%)	
Spongiform	1	1 (0.2%)	0	
Mixed cystic and solid	234	222 (38.0%)	12 (6.8%)	
Solid or almost completely solid	475	314 (53.8%)	161 (91.5%)	
Echogenicity				<.001
Anechoic		0	0	
Hyperechoic or isoechoic	410	387 (66.3%)	23 (13.1%)	
Hypoechoic	329	191 (32.7%)	138 (78.4%)	
Very hypoechoic	21	6 (1.0%)	15 (8.5%)	
Shape				<.001
Wider-than-tall	671	554 (94.9%)	117 (66.5%)	
Taller-than-wide	89	30 (5.1%)	59 (33.5%)	
Margin				<.001
Smooth	579	535 (91.6%)	44 (25.0%)	
Ill-defined	0	0	0	
Lobulated or irregular	181	49 (8.4%)	132 (75.0%)	
Extrathyroidal extension	0	0	0	
Echogenic foci				<.001
None or large comet-tail artifacts	536	477 (81.7%)	59 (33.5%)	
Macrocalcifications	91	69 (11.8%)	22 (12.5%)	
Peripheral (rim) calcifications	10	10 (1.7%)	0	
Punctate echogenic foci	123	28 (4.8%)	95 (54.0%)	

<sup>a</sup>Data are numbers of nodules, with percentages in parentheses.

**Table 2: Calculated malignancy risk of each category according to the risk stratification of ACR TI-RADS**

	TR1	TR2	TR3	TR4	TR5	Total
Suggested risk of malignancy (%) <sup>20,24</sup>	≤2	≤2	2< and ≤5	5< and ≤20	>20	
ACR TI-RADS category						
No. of malignant nodules	0	4	9	33	130	176
Assigned total nodules	41	158	185	209	167	760
Calculated risk of malignancy (%)	0	2.5	4.9	15.8	77.8	23.2
CNN <sup>a</sup>						
No. of malignant nodules	0	0	0	9	167	176
Assigned total nodules	0	5	45	307	403	760
Calculated risk of malignancy (%)	0	0	0	2.9	41.4	23.2

<sup>a</sup>Malignancy percentages provided by the CNN were re-categorized according to the suggested cancer risk levels of ACR TI-RADS.

39–61 years). Of the 757 patients, 587 (77.5%) were women and 170 (22.5%) were men.

The US features of the benign and malignant nodules according to ACR TI-RADS and their distributions are described in Table 1. The median size of the benign nodules was 23 mm, which was larger than the that of malignant nodules (median, 14 mm;  $P < .001$ ). Solid or almost completely solid composition (161 of 176, 91.5%), hypoechoic or very hypoechoic echogenicity (153 of 176, 86.9%), taller-than-wide shape (59 of 176, 33.5%), lobulated or irregular margins (132 of 176, 75.0%), and punctate echogenic foci (95 of 176, 54.0%) were frequently seen in the malignant nodules ( $P < .001$ , respectively).

#### Malignancy Risk According to ACR TI-RADS Category

Table 2 summarizes the malignancy risk of each category in ACR TI-RADS and CNN-TR that was calculated after nodules were

re-categorized according to the malignancy-risk ranges suggested by ACR TI-RADS.<sup>22,26</sup> The malignancy risk of ACR TR5 was 77.8% (130 of 167), which was much higher than the suggested malignancy risk of 20%. The malignancy risks of ACR TR1 to TR4 were within the risk ranges suggested by the ACR. According to the CNN, 403 thyroid nodules had malignancy risks higher than 20% and were re-categorized as CNN-TR5. Among 403 nodules, 167 were thyroid cancers (41.4%). Of 760 nodules, 307 nodules that had a 5%–20% range of malignancy risk according to the CNN were re-categorized to CNN-TR4 and 9 of these 307 (2.9%) nodules were thyroid cancers.

#### Comparing the Diagnostic Performances of CNN and ACR TI-RADS

According to the cutoff value found using the Youden index in the CNN and ACR TR categories, respectively, thyroid nodules



**Table 3: Comparison of diagnostic performance between CNN and ACR TI-RADS**

	CNN (95% CI)	ACR TI-RADS (95% CI)	P Value
Sensitivity	81.8% (76.1–87.5)	73.9% (67.4–80.4)	.009
Specificity	86.1% (83.3–88.9)	93.7% (91.7–95.6)	<.001
Accuracy	85.1% (82.6–87.7)	89.1% (86.9–91.3)	.003
Positive predictive value	64.0% (57.7–70.3)	77.8% (71.6–84.1)	<.001
Negative predictive value	94.0% (92–96)	92.2% (90.1–94.4)	.046
AUC <sup>a</sup>	0.917 (0.895–0.936)	0.891 (0.867–0.912)	.017

<sup>a</sup> The AUCs of the CNN using a malignancy risk percentage between 0 and 100 and ACR TI-RADS categories using a TR category from 1 to 5 were compared as continuous values.

with a malignancy risk of 52.6% or higher in the CNN or nodules equal to or higher than TR5 according to ACR TI-RADS were considered malignant. The diagnostic performances of the ACR TI-RADS and CNN are summarized in Table 3. Sensitivity was significantly higher with the CNN than with ACR TI-RADS (81.8% versus 73.9%,  $P = .009$ ). Specificity, accuracy, and positive predictive values were significantly lower with the CNN than with ACR TI-RADS (86.1% versus 93.7%,  $P < .001$ ; 85.1% versus 89.1%,  $P = .003$ ; and 64.0% versus 77.8%,  $P < .001$ , respectively). The negative predictive value was significantly higher with the CNN than with ACR TI-RADS (94.0% versus 92.2%,  $P = .046$ ). Figure 2 shows the ROC curves for the diagnosis of thyroid cancer with the CNN and ACR TI-RADS. The AUC of the CNN (0.917; 95% CI, 0.895–0.936) was higher than that of the ACR TI-RADS categories (0.891; 95% CI, 0.867–0.912) ( $P = .017$ ).

## DISCUSSION

Our study demonstrates that the CNN shows diagnostic performance comparable with that of ACR TI-RADS when experienced radiologists assigned US descriptors and scored their observations. The malignancy risk of each ACR TR category in our study was within the range suggested by ACR TI-RADS. In our study, the sensitivity (81.8%), specificity (86.1%), and accuracy (85.1%) of the CNN were within ranges similar to those reported in previous publications on the deep CNN for the diagnosis of thyroid cancer.<sup>10,11,16,17</sup> At an optimal threshold derived from the Youden index, our CNN was more sensitive but less specific and accurate compared with the ACR TI-RADS (sensitivity, 81.8% versus 73.9%; specificity, 86.1% versus 93.7%; and accuracy, 85.1% versus 89.1%). The AUC was higher in the CNN than in ACR TI-RADS (0.917 versus 0.891,  $P = .017$ ).

Past studies have shown different results for the diagnostic performance of the CNN compared with visual assessment by radiologists. According to Ko et al,<sup>10</sup> the CNN showed favorable diagnostic performances for predicting thyroid cancer on US, with sensitivities of 84.0%–91.0%, specificities of 82.0%–90.0%, accuracies of 86.0%–88.0%, and AUCs of 0.835–0.850, values that were like those of experienced radiologists. Li et al<sup>11</sup> reported somewhat higher performances for the CNN with AUCs of 0.908–0.947; compared with experienced radiologists, the CNN showed similar sensitivity (84.3%–93.4%) and significantly higher specificity (86.1%–87.3%) and accuracy (85.7%–89.8%). Unlike the favorable performances of the CNN observed in the above-mentioned studies, the CNN in the study of Kim et al<sup>12</sup> had lower specificity (68.2%) and accuracy (73.4%) compared with radiologists for the diagnosis of thyroid cancer, even though it achieved

similar sensitivity (81.4%). In our study, the specificity and accuracy of the CNN were somewhat higher than those reported in Kim et al. The different frequencies of punctate echogenic foci (considered as microcalcifications) in malignant nodules (54.0% in our study versus 72.1% in Kim et al) might be 1 explanation because Kim et al suggested the recognition of microcalcifications as a cause of inaccuracy for the CNN in their study. In addition, the inferior performance of the CNN in their study was thought to originate from manual manipulation for segmentation and human-designed features applied to the computer-aided diagnosis system. Moreover, the experience level of the performing operator had an effect on the performance of computer-aided diagnosis because of the manual manipulation required for computer-aided diagnosis.<sup>29</sup>

Unlike the traditional machine learning algorithm or the traditional commercial system that is connected to US machines and already applied in clinical practice,<sup>5,12,29</sup> the recently introduced deep CNN is not limited to or influenced by human-designed features known to represent thyroid cancer on US, though its operational principles for diagnosing thyroid malignancy are not yet completely explained by humans. In our study, the radiologist just drew a square ROI covering the entire targeted nodule without any human interference with the diagnostic process of the CNN. Instead of using features engineered by humans, the deep CNN extracts image information directly from imaging data, and the CNN might be able to recognize cancer-specific US features that are not identified explicitly by the naked eye.<sup>30</sup>

Because US is performed and interpreted by humans, any diagnosis of thyroid cancer based on US images is subjective, thus requiring experience and expertise.<sup>3,4</sup> Recent studies have evaluated the computer-aided diagnosis of thyroid cancer, which incorporates texture analysis and machine learning and deep learning techniques for US images; the authors reported that computer-aided diagnosis showed comparable and even higher diagnostic performance compared with radiologists.<sup>5,6,11,29</sup> While artificial intelligence (AI) is not yet considered ready for a clinical setting,<sup>31</sup> computer software is already thought to have several strong advantages over radiologists because its use can overcome human variation and provide diagnostic reproducibility and consistency in image interpretation. However, past studies have shown greatly differing results when the diagnostic performance of the CNN is compared with human interpretation. This might be due to the diversity of assessments possible by radiologists as well as the different algorithms developed by individual researchers or corporations. Despite referring to guidelines, radiologists might eventually reach diagnoses independently on the basis of their individual expertise and experience.

On the other hand, we intended to directly compare the performances of our CNN with that of an established guideline, ACR TI-RADS, which is known to have a high specificity and positive predictive value without sacrificing sensitivity, and to further use this knowledge to help radiologists achieve optimal performances with the ACR TI-RADS.<sup>20,21,32,33</sup> We used results found with prospectively recorded descriptors that were obtained during real-time evaluations of entire 3D nodules instead of those collected through a retrospective human review of single US images. This choice might represent ACR TI-RADS more properly and objectively than a new individual human review. The experienced radiologists in the study of Li et al<sup>11</sup> showed a less specific and accurate performance than the CNN; the radiologists in the study of Li et al showed low specificities of 57.1%–68.6% and low accuracies of 72.7%–78.8% compared with the previous studies and our study. Regarding this matter, Li et al replied that their reviewers were burdened due to the larger subject sample and subsequent large amounts of image reviews needed.<sup>11,34,35</sup>

In this study, the malignancy risk of each ACR TR category was within the theoretic percentage of malignancy risk, which meant that nodules had been assessed appropriately with ACR TI-RADS. The ACR TR categories of our study showed enough specificity and accuracy for diagnosis, fulfilling the original goals of ACR TI-RADS to decrease biopsies with benign findings and improve accuracy. On the other hand, radiologists have shown a wide range in diagnostic performance with ACR TI-RADS because sensitivity has been reported to be 81.7%–96.7%; specificity, 47.7%–77.3%; and accuracy, 69.3%–84.9%.<sup>20,21,32,36</sup> This inconsistency in performance might be caused by the different experience levels of the radiologists or by the different cutoff values of each study. In our study, we were able to conduct a relatively objective validation of ACR TI-RADS by experienced radiologists using US features and to compare its diagnostic performance with that of the AI diagnosis. The diagnostic performance of the CNN was comparable with that of ACR TI-RADS with a somewhat higher AUC for thyroid cancer. Given that a recent study reported that alteration of ACR TI-RADS by AI led to improvement in specificity, the adequate modification and fusion of the settled guidelines and AI, ie, AI-powered US, might be a potential aid to better diagnostic performance and implementation of AI.<sup>36,37</sup>

This study has several limitations. First, US examinations are performed in real-time. The process of image acquisition such as capturing 2D-US images and selecting a representative image from the acquired images is inevitably operator-dependent. Additionally, there are limits to how much 2D US images can represent the entire thyroid nodule. AI studies that analyze 3D-US images might be of more help in the future.<sup>37</sup> Second, we used data prospectively recorded in our institutional data base, in which US features were described with different terminology than that suggested by the ACR guidelines. Because information about “anechoic,” “ill-defined” or “extrathyroidal,” and large comet-tail artifacts was not collected during the study period, despite being listed in the ACR guidelines, this issue might be a limitation of our study. However, we did not conduct an intentional retrospective review for this study because we aimed to investigate ACR TI-RADS itself and not the man-made final

assessments. Third, our institution is a tertiary center, and we included thyroid nodules that underwent US-FNA or US-CNB only, which meant that surgical histopathology was unavailable. Thus, there might be false-negative or false-positive results, even though the rates would be very low with a false-negative rate of <3% and a false-positive rate of about 3%–4%.<sup>38</sup> Fourth, the ROC-derived cutoff value that we used to calculate diagnostic performance cannot be accepted as a diagnostic standard in real clinical practice without further validation.

## CONCLUSIONS

The CNN provided diagnostic performance comparable with that of the ACR TI-RADS categories assigned by experienced radiologists. Before AI can be used to diagnose thyroid cancer, a thorough evaluation of AI diagnosis compared with pre-existing guidelines is needed, and our study should be able to present a relatively objective comparison of diagnostic performances between the ACR TI-RADS and CNN for thyroid cancer. Adequate modification and fusion of the ACR TI-RADS and CNN that takes advantage of their unique characteristics will help optimize overall diagnostic performance.

Disclosures: Jin Young Kwak—*RELATED: Grant:* National Research Foundation of Korea grant funded by the Korean government (Ministry of Science and ICT) (2019RIA2C1002375).

## REFERENCES

1. Haugen BR, Alexander EK, Bible KC, et al. **2015 American Thyroid Association Management Guidelines for Adult Patients with Thyroid Nodules and Differentiated Thyroid Cancer: The American Thyroid Association Guidelines Task Force on Thyroid Nodules and Differentiated Thyroid Cancer.** *Thyroid* 2016;26:1–133 CrossRef Medline
2. Kwak JY, Han KH, Yoon JH, et al. **Thyroid imaging reporting and data system for US features of nodules: a step in establishing better stratification of cancer risk.** *Radiology* 2011;260:892–99 CrossRef Medline
3. Choi SH, Kim EK, Kwak JY, et al. **Interobserver and intraobserver variations in ultrasound assessment of thyroid nodules.** *Thyroid* 2010;20:167–72 CrossRef Medline
4. Park SH, Kim SJ, Kim EK, et al. **Interobserver agreement in assessing the sonographic and elastographic features of malignant thyroid nodules.** *AJR Am J Roentgenol* 2009;193:W416–23 CrossRef Medline
5. Chang Y, Paul AK, Kim N, et al. **Computer-aided diagnosis for classifying benign versus malignant thyroid nodules based on ultrasound images: a comparison with radiologist-based assessments.** *Med Phys* 2016;43:554 CrossRef Medline
6. Choi YJ, Baek JH, Park HS, et al. **A computer-aided diagnosis system using artificial intelligence for the diagnosis and characterization of thyroid nodules on ultrasound: initial clinical assessment.** *Thyroid* 2017;27:546–52 CrossRef Medline
7. Acharya UR, Swapna G, Sree SV, et al. **A review on ultrasound-based thyroid cancer tissue characterization and automated classification.** *Technol Cancer Res Treat* 2014;13:289–301 CrossRef Medline
8. Gopinath B, Shanthi N. **Computer-aided diagnosis system for classifying benign and malignant thyroid nodules in multi-stained FNAB cytological images.** *Australas Phys Eng Sci Med* 2013;36:219–30 CrossRef Medline
9. Shin HC, Roth HR, Gao M, et al. **Deep convolutional neural networks for computer-aided detection: CNN architectures, dataset characteristics and transfer learning.** *IEEE Trans Med Imaging* 2016;35:1285–98 CrossRef Medline

10. Ko SY, Lee JH, Yoon JH, et al. **Deep convolutional neural network for the diagnosis of thyroid nodules on ultrasound.** *Head Neck* 2019;41:885–91 CrossRef Medline
11. Li X, Zhang S, Zhang Q, et al. **Diagnosis of thyroid cancer using deep convolutional neural network models applied to sonographic images: a retrospective, multicohort, diagnostic study.** *Lancet Oncol* 2019;20:193–201 CrossRef Medline
12. Kim HL, Ha EJ, Han M. **Real-world performance of computer-aided diagnosis system for thyroid nodules using ultrasonography.** *Ultrasound Med Biol* 2019;45:2672–78 CrossRef Medline
13. Ma J, Wu F, Zhu J, et al. **A pre-trained convolutional neural network based method for thyroid nodule diagnosis.** *Ultrasonics* 2017;73:221–30 CrossRef Medline
14. Ma J, Wu F, Jiang T, et al. **Cascade convolutional neural networks for automatic detection of thyroid nodules in ultrasound images.** *Med Phys* 2017;44:1678–91 CrossRef Medline
15. Buda M, Wildman-Tobriner B, Hoang JK, et al. **Management of thyroid nodules seen on US images: deep learning may match performance of radiologists.** *Radiology* 2019;292:695–701 CrossRef Medline
16. Koh J, Lee E, Han K, et al. **Diagnosis of thyroid nodules on ultrasonography by a deep convolutional neural network.** *Sci Rep* 2020;10:15245 CrossRef Medline
17. Jin Z, Zhu Y, Zhang S, et al. **Ultrasound computer-aided diagnosis (CAD) based on the thyroid imaging reporting and data system (TI-RADS) to distinguish benign from malignant thyroid nodules and the diagnostic performance of radiologists with different diagnostic experience.** *Med Sci Monit* 2020;26:e918452 CrossRef Medline
18. Park S, Oh CM, Cho H, et al. **Association between screening and the thyroid cancer “epidemic” in South Korea: evidence from a nationwide study.** *BMJ* 2016;355:i5745 CrossRef Medline
19. Jegerlehner S, Bulliard JL, Aujesky D, et al. **NICER Working Group. Overdiagnosis and overtreatment of thyroid cancer: a population-based temporal trend study.** *PLoS One* 2017;12:e0179387 CrossRef Medline
20. Wu XL, Du JR, Wang H, et al. **Comparison and preliminary discussion of the reasons for the differences in diagnostic performance and unnecessary FNA biopsies between the ACR TIRADS and 2015 ATA guidelines.** *Endocrine* 2019;65:121–31 CrossRef Medline
21. Yoon JH, Lee HS, Kim EK, et al. **Pattern-based vs. score-based guidelines using ultrasound features have different strengths in risk stratification of thyroid nodules.** *Eur Radiol* 2020;30:3793–3802 CrossRef Medline
22. Tappouni RR, Itri JN, McQueen TS, et al. **ACR TI-RADS: pitfalls, solutions, and future directions.** *Radiographics* 2019;39:2040–52 CrossRef Medline
23. Tessler FN, Middleton WD, Grant EG, et al. **ACR thyroid imaging, reporting and data system (TI-RADS): White Paper of the ACR TI-RADS Committee.** *J Am Coll Radiol* 2017;14:587–95 CrossRef Medline
24. Kim EK, Park CS, Chung WY, et al. **New sonographic criteria for recommending fine-needle aspiration biopsy of nonpalpable solid nodules of the thyroid.** *AJR Am J Roentgenol* 2002;178:687–91 CrossRef Medline
25. Lee E, Ha H, Kim HJ, et al. **Differentiation of thyroid nodules on US using features learned and extracted from various convolutional neural networks.** *Sci Rep* 2019;9:19854 CrossRef Medline
26. Middleton WD, Teefey SA, Reading CC, et al. **Comparison of performance characteristics of American College of Radiology TI-RADS, Korean Society of Thyroid Radiology TIRADS, and American Thyroid Association Guidelines.** *AJR Am J Roentgenol* 2018;210:1148–54 CrossRef Medline
27. Youden WJ. **Index for rating diagnostic tests.** *Cancer* 1950;3:32–35 CrossRef Medline
28. DeLong ER, DeLong DM, Clarke-Pearson DL. **Comparing the areas under two or more correlated receiver operating characteristic curves: a nonparametric approach.** *Biometrics* 1988;44:837–45 Medline
29. Jeong EY, Kim HL, Ha EJ, et al. **Computer-aided diagnosis system for thyroid nodules on ultrasonography: diagnostic performance and reproducibility based on the experience level of operators.** *Eur Radiol* 2019;29:1978–85 CrossRef Medline
30. LeCun Y, Bengio Y, Hinton G. **Deep learning.** *Nature* 2015;521:436–44 CrossRef Medline
31. Park SH, Han K. **Methodologic guide for evaluating clinical performance and effect of artificial intelligence technology for medical diagnosis and prediction.** *Radiology* 2018;286:800–09 CrossRef Medline
32. Ruan JL, Yang HY, Liu RB, et al. **Fine needle aspiration biopsy indications for thyroid nodules: compare a point-based risk stratification system with a pattern-based risk stratification system.** *Eur Radiol* 2019;29:4871–78 CrossRef Medline
33. Ha EJ, Na DG, Baek JH, et al. **US fine-needle aspiration biopsy for thyroid malignancy: diagnostic performance of seven society guidelines applied to 2000 thyroid nodules.** *Radiology* 2018;287:893–900 CrossRef Medline
34. Ha EJ, Baek JH, Na DG. **Deep convolutional neural network models for the diagnosis of thyroid cancer.** *Lancet Oncol* 2019;20:e130 CrossRef Medline
35. Li X, Zhang S, Zhang Q, et al. **Deep convolutional neural network models for the diagnosis of thyroid cancer: authors’ reply.** *Lancet Oncol* 2019;20:e131 CrossRef Medline
36. Wildman-Tobriner B, Buda M, Hoang JK, et al. **Using artificial intelligence to revise ACR TI-RADS risk stratification of thyroid nodules: diagnostic accuracy and utility.** *Radiology* 2019;292:112–19 CrossRef Medline
37. Akkus Z, Cai J, Boonrod A, et al. **A survey of deep-learning applications in ultrasound: artificial intelligence-powered ultrasound for improving clinical workflow.** *J Am Coll Radiol* 2019;16:1318–28 CrossRef Medline
38. Cibas ES, Ali SZ. **The 2017 Bethesda System for reporting thyroid cytopathology.** *Thyroid* 2017;27:1341–46 CrossRef Medline

# Neuroaxial Infantile Hemangiomas: Imaging Manifestations and Association with Hemangioma Syndromes

T. Feygin, A.E. Goldman-Yassen, D.J. Licht, J.E. Schmitt, A. Mian, A. Vossough, L. Castelo-Soccio, J.R. Treat, A. Bhatia, and A.N. Pollock



## ABSTRACT

**BACKGROUND AND PURPOSE:** Infantile hemangiomas are common lesions in the pediatric population; in rare cases, an infantile hemangioma can be detected along the neural axis. The purposes of our study included determination of the incidence, location, and imaging appearance of neuroaxial infantile hemangiomas and their syndromic association. We also assessed additional features of cerebral and cardiovascular anomalies that may be associated with neuroaxial lesions.

**MATERIALS AND METHODS:** A retrospective cohort study was performed, searching the radiology database for patients with segmental infantile hemangiomas referred for assessment of possible hemangioma syndromes. We retrospectively reviewed brain and spine MR imaging studies, with particular attention paid to neuroaxial vascular lesions, as well as the relevant clinical data. Neuroaxial hemangioma imaging findings were described, and comparison of segmental cutaneous infantile hemangioma location with the imaging findings was performed in patients with confirmed hemangioma syndromes and in patients with isolated skin infantile hemangioma.

**RESULTS:** Ninety-five patients with segmental infantile hemangioma were included in the study, 42 of whom had a hemangioma syndrome; of those, 41 had posterior fossa brain malformations, hemangioma, arterial lesions, cardiac abnormalities, and eye abnormalities (PHACE) syndrome and 1 had diffuse neonatal hemangiomatosis. Neuroaxial involvement was detected in 20/42 patients (48%) with hemangioma syndromes and in no subjects with isolated segmental infantile hemangioma ( $P < .001$ ). The most common intracranial hemangioma location was within the ipsilateral internal auditory canal (83%).

**CONCLUSIONS:** Many pediatric patients with segmental infantile hemangioma in the setting of hemangioma syndromes, especially those with PHACE, had neuroaxial hemangiomas. This finding may potentially lead to requiring additional clinical evaluation and management of these patients.

**ABBREVIATIONS:** IAC = internal auditory canal; IH = infantile hemangioma; MC = Meckel cave; PHACE = posterior fossa brain malformations, hemangioma, arterial lesions, cardiac abnormalities, and eye abnormalities

Infantile hemangiomas (IHs) are benign vascular tumors common in infants.<sup>1-3</sup> IHs express endothelial glucose transporter 1, differentiating them from other pediatric vascular tumors.<sup>4</sup> Unlike congenital hemangiomas, IHs are not

discernable prenatally because they are known to proliferate and evolve after birth.<sup>5</sup> The clinical evolution of all IHs progresses through several predictable phases: faint pink/red patches during the nascent phase (shortly after birth), rapid proliferation (for the first 3–6 months), a plateau phase until approximately 12 months, followed by slow involution.<sup>6</sup>

Infantile hemangioma lesions may differ by clinical presentation, location, and morphology; therefore, each lesion may require a different approach. According to the latest update of the International Society for the Study of Vascular Anomalies (2018), IHs are characterized by their distribution pattern: focal, multifocal, segmental, and indeterminate types.<sup>7-9</sup> Of the 4 types, focal IHs are the most common, with a round or oval shape representing the most common morphology. Segmental IHs appear as broader geometric lesions that correspond to the embryonic boundaries that exist among the various facial primordia derived

Received November 24, 2020; accepted after revision January 14, 2021.

From the Division of Neuroradiology (T.F., A.V., A.N.P.), Department of Radiology; Department of Neurology (D.J.L.); and Department of Dermatology (L.C.-S., J.R.T.), The Children's Hospital of Philadelphia, Philadelphia, Pennsylvania; Department of Radiology (A.E.G.-Y.), Children's Healthcare of Atlanta, Atlanta, Georgia; Division of Neuroradiology (J.E.S.), Department of Radiology, Hospital of the University of Pennsylvania, Philadelphia, Pennsylvania; Division of Neuroradiology (A.M.), Department of Radiology, Mallinckrodt Institute of Radiology, St. Louis, Missouri; and Department of Radiology (A.B.), Children's Hospital of Pittsburgh, Pittsburgh, Pennsylvania.

Please address correspondence to Tamara Feygin, MD, Children's Hospital of Philadelphia, Department of Radiology, Division of Neuroradiology, 3401 Civic Center Blvd, Philadelphia, PA 19104; e-mail: feygin@email.chop.edu



Indicates article with online supplemental data.

<http://dx.doi.org/10.3174/ajnr.A7204>



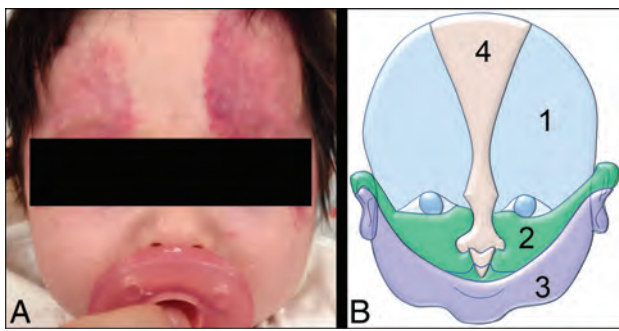


**FIG 1.** Segmental IH. **A**, A 3-month-old girl with PHACE syndrome. Clinical photograph shows a bilateral segmental IH in an S1 distribution predominantly and with minimal S2 involvement. **B**, Diagram of the Haggstrom classification, used for clinical assessment of superficial IH distribution. It divides the face on the 4 following segments: S1 = frontotemporal, S2 = maxillary, S3 = mandibular, S4 = frontonasal.

from neural crest cells.<sup>10</sup> Segmental IHs that cover a broad cutaneous territory (Fig 1) may be associated with hemangioma syndromes and may be detected immediately after birth.<sup>11</sup> Deep cutaneous lesions may be diagnosed at several months of age, and they may appear as nonspecific soft-tissue masses.<sup>11,12</sup> Segmental IHs may occur in multiple locations within the head and neck, extremities, and/or body.<sup>13</sup>

Segmental IHs are a requisite for the diagnosis of hemangioma syndromes, such as posterior fossa brain malformations, hemangioma, arterial lesions, cardiac abnormalities, and eye abnormalities (PHACE).<sup>14,15</sup> PHACE syndrome denotes the following: posterior fossa and other structural brain malformations; large hemangiomas of the face, neck, and/or scalp; anatomic anomalies of the cerebral or cervical arteries; cardiac anomalies/coarctation of the aorta; and eye abnormalities.<sup>16-19</sup> If sternal anomalies are present, the term “PHACES syndrome” is used, with S standing for sternal anomalies. PHACE syndrome is associated with segmental IHs in the head and neck region with a trigeminal nerve distribution.<sup>11,16,17</sup> IHs within the lower body, especially involving the perineal region, may be a marker of the relatively recently defined LUMBAR, SACRAL, or PELVIS association/syndrome.<sup>20-25</sup> Hemangioma syndromes are now perceived as a spectrum of manifestations rather than fixed imaging and clinical features.<sup>17</sup> The exact criteria for these complex heterogeneous conditions are still under debate, though consensus guidelines for definite-versus-possible PHACE syndrome were introduced in 2016 (Online Supplemental Data).<sup>14,26</sup> These consensus criteria may evolve with time as more data on etiology and pathophysiology become available. Nonetheless, the presence of a superficial segmental IH remains the dominant essential feature of these syndromes. Diffuse neonatal hemangiomatosis is another less common hemangioma syndrome with numerous IHs in the skin of the neonate, and it has a high association with visceral and neuroaxial lesions.

Although neuroaxial (intracranial and/or intra-/paraspinal) IHs are rare in the general population, occurring in 1% of all patients with skin hemangiomas,<sup>12</sup> several studies have described an increased frequency in patients with hemangioma syndromes.<sup>12,27-31</sup> Additional intracranial abnormalities

have also been described in PHACE syndrome, including midline anomalies, neuronal migration disorders, and asymmetric enlargement of Meckel's cave.<sup>14,32,33</sup>

The purposes of our retrospective study include determination of the incidence, location, imaging appearance, and natural history of neuroaxial infantile hemangiomas and their syndromic association. We also assessed additional cerebral and/or cardiovascular abnormalities that were associated with neuroaxial hemangiomas.

## MATERIALS AND METHODS

### Cohort Selection

After obtaining institutional review board approval, we searched the Children's Hospital of Philadelphia radiology database, Illuminate search software (Softek Illuminate), for patients with segmental IH referred to our institution for imaging and clinical evaluation of suspected underlying systemic hemangioma syndromes between 2002 and 2017. We performed Boolean searches using the keywords “segmental,” “infantile hemangioma,” “hemangioma,” “PHACE,” “PELVIS syndrome,” and “MR imaging.” All patients were referred for initial imaging because of cutaneous hemangiomas. Inclusion criteria were the following: 1) the presence of subcutaneous/cutaneous vascular segmental lesions in the head, neck, or trunk; 2) available MR imaging of the brain and spine with contrast administration; and 3) younger than 12 months of age at the time of first imaging (the known timeframe for regression of superficial infantile hemangiomas). Exclusion criteria included technically suboptimal studies due to excessive motion and absence of contrast administration.

### Image Interpretation

All imaging was performed on 1.5 or 3T MR imaging scanners, including Skyra, Prisma and Vario Scanners, (Siemens) during the course of routine clinical care. All patients were imaged with standard MR imaging protocol using multiplanar T1- and T2-weighted sequences, FLAIR, diffusion-weighted, arterial spin-labeling perfusion imaging, and multiplanar postcontrast T1-weighted sequences. Specific acquisition parameters varied across time and scanners. Vascular imaging was performed using TOF-MRA. Three pediatric neuroradiologists, blinded to the clinical history, independently retrospectively reviewed MR imaging of the brain and spine for all cases and recorded imaging findings, with a special focus on the following: 1) the presence and imaging characteristics of neuroaxial vascular lesions; 2) abnormalities of the posterior fossa; 3) head and neck vascular anomalies; and 4) additional brain anomalies, including the symmetry of the Meckel cave (MC). A consensus reading was then performed for potential discrepancies. In addition, in those cases that had serial imaging, the temporal evolution of neuroaxial and superficial IHs was assessed.

### Clinical Evaluation

Cutaneous IHs involving the head and neck were evaluated by pediatric dermatologists, who used the classification described by Haggstrom et al<sup>10,34</sup> (S1 = frontotemporal, S2 = maxillary, S3 = mandibular, S4 = frontonasal, Fig 1B), which corresponds with the embryonic boundaries that exist among the various

**Table 1: Characteristics of subjects with IH as part of a hemangioma syndrome compared with isolated IH**

	Hemangioma Syndrome (n = 42)	Isolated Superficial IH (n = 53)	P Value
Age (median) (IQR) (mo)	2 (3–2)	2 (3–2)	.53
Female sex (%) (n)	74% (31)	86% (46)	.12
Side/location of cutaneous IH (%) (n)			.78
Right face only	45% (19)	40% (21)	
Left face only	33% (14)	41% (22)	
Bilateral face	14% (6)	15% (8)	
Other	7% (3)	4% (2)	
Facial segment (%) (n)			
S1	65% (27)	30% (16)	.002
S2	50% (21)	66% (35)	.14
S3	43% (18)	28% (15)	.19
S4	21% (9)	4% (2)	.010
Multiple facial segments	57% (24)	34% (18)	.037
All facial segments	14% (6)	0% (0)	.006
Intracranial IH (%) (n)	45% (19)	0% (0)	<.001
Paraspinal IH (%) (n)	12% (5)	0% (0)	.015
MC enlargement (%) (n)	67% (28)	0% (0)	<.001
Posterior fossa abnormality (%) (n)	48% (20)	0% (0)	<.001
Cardiovascular abnormalities (%) (n)	95% (40)	0% (0)	<.001

Note:—IQR indicates Interquartile range.

**Table 2: Locations of neuroaxial IH and agreement between 3 readers**

Neuroaxial IH Location (n = 95)	Reader 1	Reader 2	Reader 3	$\kappa$	P Value	Consensus
IAC	15	15	15	1.00	<.001	15
Cochlea	3	4	3	0.85	<.001	3
Cerebellopontine angle	5	5	5	1.00	<.001	5
MC	2	2	2	1.00	<.001	2
Cavernous sinus	2	2	2	1.00	<.001	2
Pterygopalatine fossa	1	1	1	1.00	<.001	1
Vidian canal	1	1	1	1.00	<.001	1
Leptomeningeal	10	10	8	0.89	<.001	10
Dural base	4	4	4	1.00	<.001	4
Intra-/paraspinal	5	5	5	1.00	<.001	5

facial primordia derived from neural crest cells. Additionally, the electronic medical record was queried to obtain relevant clinical and demographic data, specifically age, sex, cardiac history, and the diagnosis of systemic vascular hemangioma syndrome. Available information about the presence of developmental or hearing issues was obtained from patients' charts.

### Statistical Analysis

We compared the imaging and clinical findings between the subjects with diagnosed hemangioma syndromes and those with isolated superficial segmental IHs. Continuous variables were not normally distributed and were, therefore, compared using the non-parametric Mann-Whitney *U* test. Categorical variables were compared using the Fisher exact test. Comparisons within the syndrome group were similarly analyzed. To assess the degree of agreement among the 3 readers, we calculated the Fleiss  $\kappa$  coefficients and interpreted them according to Landis and Koch.<sup>35</sup> Statistical analysis

was performed on STATA, Version 12.1 (StataCorp) and R statistical and computing software (<http://www.r-project.org>). A 2-tailed *P* value <.05 was used for statistical significance.

## RESULTS

### Subject Characteristics

Ninety-eight subjects with superficial IHs in a segmental distribution were identified from 2002 to 2017. We excluded 3 patients: 2 subjects, both with vascular lesions within the lower spinal canal and diagnoses of LUMBAR/PELVIS syndrome, did not have brain imaging, and 1 who was older than the defined inclusion criteria age range (3 years of age) at initial imaging. The final cohort, therefore, contained 95 subjects, including 42 subjects with diagnosed hemangioma syndromes (41 with a diagnosis of PHACE syndrome and 1 with diffuse neonatal hemangiomatosis) and 53 subjects with isolated segmental skin hemangiomas. The final diagnoses had been made on the basis of a multidisciplinary clinical team specializing in vascular malformations. Subject characteristics are summarized in Table 1.

Seventy-seven subjects (81%) were female, without a significant difference in rates between subjects with syndromic and isolated segmental IH (74% versus 86%, *P* = .12). The median age of the subjects at the time of imaging was 2 months (range, 0.5–11 months), and it was not significantly different between syndromic and nonsyndromic subjects (*P* = .53). Among the patients with identified hemangioma syndromes, 93% of patients (39/42) had segmental facial hemangiomas, 2 (5%) had body truncal surface hemangiomas, and 3 (8%) had hemangiomas of the tongue, subglottis, or upper airway (2 patients had IHs in multiple locations).

Nonsyndromic subjects had a similar proportion of facial hemangiomas (96% [51/53], *P* = .65), with neck IHs in 4 subjects and a midchest IH in 1.

### Neuroaxial IH

Twenty subjects were found to have neuroaxial IH, all of whom had identified hemangioma syndromes (20/42): 15 with only intracranial IHs, 1 with only a paraspinal IH, and 4 with both. The agreement among the 3 readers for the presence and location of neuroaxial IH was almost perfect for all locations, with  $\kappa$  ranging from 0.85 to 1.00 (Table 2).

All intracranial lesions were ipsilateral to the cutaneous hemangiomas. Intracranial IHs were more prevalent in patients with S1 segment lesions compared with subjects without S1 segment IHs (59% versus 20%, *P* = .023). There were no significant differences in the prevalence of intracranial IH in subjects with S2 (62% versus 29%, *P* = .06), S3 (39% versus 50%, *P* = .54), or S4 (67% versus 39%, *P* = .26) segment IHs compared with those without those

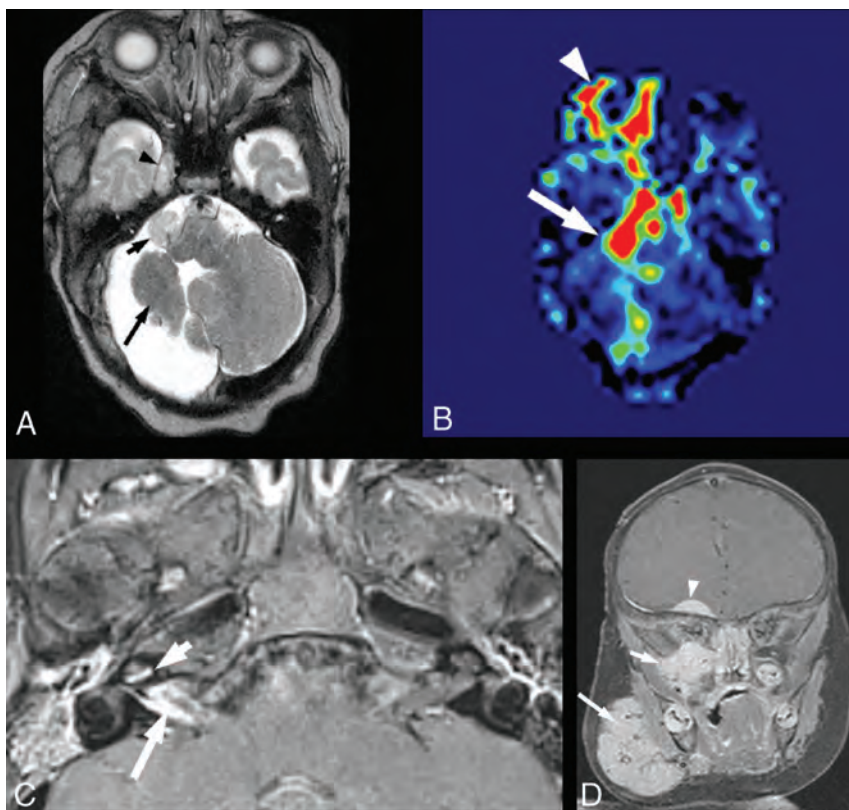


**FIG 2.** Intracranial infantile hemangioma. A and B, A 1.5-month-old girl with segmental IH of the right face and PHACE syndrome. A, Axial T2-weighted image shows an extra-axial T2-hyperintense mass in the right cerebellopontine angle cistern (*small arrow*) and a similar lesion in the enlarged right MC (*arrowhead*). A *long arrow* points to an asymmetrically small right cerebellar hemisphere, which is an additional common manifestation of PHACE syndrome. Both lesions reveal diffuse enhancement on postcontrast imaging and markedly increased perfusion on arterial spin-labeling imaging (B). C, A 3-month-old girl with right orbital segmental IH and PHACE syndrome. Axial postcontrast T1-weighted image with fat suppression shows linear enhancement in the right IAC (*large arrow*) and linear enhancement of the cochlear basal turn (*arrowhead*). D, A 2-month-old girl with segmental IH of the right face and PHACE syndrome. Coronal postcontrast T1-weighted image with fat suppression shows a dural base extra-axial enhancing mass in the right frontal lobe undersurface (*arrowhead*). Additional IHCs are demonstrated in the right face (*large arrow*) and the right skull base and inferior orbit (*small arrow*).

segmental lesions. The prevalence of intracranial IHCs in syndromic subjects with all 4 facial segments involved unilaterally was found to be 83% compared with subjects with  $\leq 3$  segments (39%), though this was not statistically significant ( $P = .08$ ).

### Imaging Features

Imaging features of neuroaxial mass lesions were similar to those of superficial infantile hemangiomas. Briefly, the lesions were T1 isointense, T2 hyperintense compared with brain parenchyma, and enhanced diffusely, with markedly increased perfusion on arterial spin-labeling sequences (Fig 2 A, -B). None of the lesions demonstrated reduced diffusion.

Intracranial IHCs most often presented as enhancing extra-axial masses in variable locations. The distribution of intracranial IHCs is summarized in Table 2. Of the 19 subjects, the most common intracranial IHCs were located within the internal auditory canals (IACs) ( $n = 15$ ) and at the cerebellopontine angle ( $n = 5$ ). There was substantial variation in size, ranging from a few

millimeters of focal enhancement to rounded 1.5-cm tumors. Three of the lesions within the IAC demonstrated cochlear involvement of varying degrees (Fig 2C). Three of the 15 patients (20%) with IAC involvement had hearing loss. One had severe ipsilateral sensorineural hearing loss, 1 had mild sensorineural hearing loss at 6 months of age that resolved by 4 years of age, and 1 had early conductive hearing loss that resolved later. The cause of the conductive hearing loss is unknown. Five patients (33%) had normal hearing, and the hearing results of the remaining 8 patients were not available in our retrospective review.

The other intracranial masses were dural-based lesions in the anterior and middle cranial fossa ( $n = 4$ ), extending along the anterior surface of the frontal or the temporal lobes (Fig 2D). Small masses in the sella turcica and basal cisterns were seen in 4 patients. In several cases, there was extension of vascular masses through the skull base foramina, which included MC ( $n = 2$ ), cavernous sinus ( $n = 2$ ), pterygopalatine fossa ( $n = 1$ ), and vidian canal. One patient with an isolated large IH of the forehead in the S4 segment had complete agenesis of the corpus callosum and an interhemispheric vascular mass (Fig 3A, -B). An additional pattern of intracranial IHC consisted of foci of leptomeningeal enhancement (Fig 3C), observed in 10 subjects. Intracranial IHCs were found in multiple locations in 11/19 subjects. No definite connection between intracranial

and superficial IHCs was demonstrated in all cases, though skull base foramina lesions involving the ipsilateral cavernous sinus, vidian canal, hypoglossal canal, or orbital fissures were in close proximity to the superficial cutaneous lesions (Fig 3D).

The intra-/paraspinal vascular masses were all extradural and varied from small unilateral lesions, spanning 1 or 2 vertebral segments, to large bilateral masses causing cord compression on imaging in 1 patient (Fig 4). None of the neuroaxial lesions originated in or invaded the cerebral parenchyma or the spinal cord.

### Neuroaxial IH Follow-up

Of the 19 subjects with intracranial IHCs, 10 underwent follow-up MR imaging with contrast and 3 underwent follow-up MR imaging without contrast. Of those 10, the median follow-up was 5 years (interquartile range, 2–7 years). Five intracranial IHCs resolved completely, 4 demonstrated partial resolution, and 1 lesion in the IAC had no change during 2 years of monitoring. In the 1 subject with only a paraspinal IH, resolution was



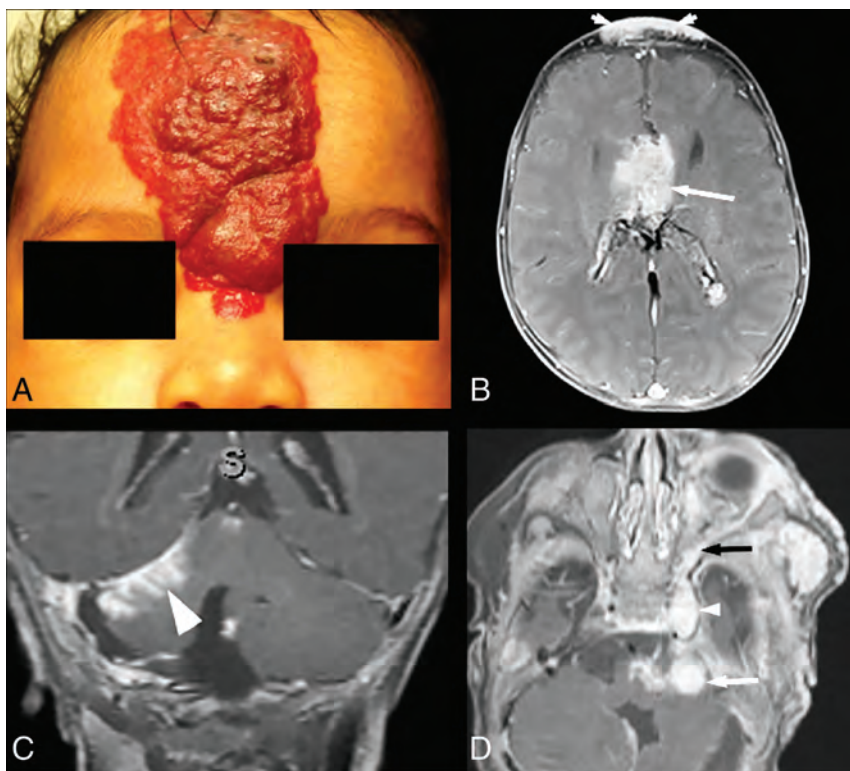


**FIG 3.** Intracranial infantile hemangioma. *A* and *B*, A 2-month-old girl, born with a very large segmental IH of the forehead. *A*, Clinical photograph shows an IH in the S4 segment (according to the Haggstrom classification). *B*, Axial postcontrast T1-weighted image with fat suppression of the same patient shows a lobulated enhancing interhemispheric mass (arrow). A superficial forehead IH is indicated by arrowheads. *C*, A different 2-month-old girl with right facial IH and PHACE syndrome. Coronal postcontrast T1-weighted image with fat suppression shows focal leptomeningeal enhancement along the right tentorium (arrowhead). *D*, A 1.5-month-old boy with left facial IH. Axial postcontrast T1-weighted image with fat suppression shows enhancing hemangiomas in the left cerebellopontine angle cistern (white arrow) and in the enlarged left MC (small white arrowhead) and enhancing vascular tissue along the lateral orbital wall (black arrow), which seems to communicate between the intra- and extracranial components.

demonstrated after 12 years. Only 1 case of recurrence of an intracranial IH was demonstrated, which occurred simultaneous to the recurrence of skin lesions occurring after propranolol (beta blocker) therapy was weaned.

### Meckel Cave Asymmetry

Unilateral asymmetric enlargement of the MC (Figs 2A, 3D, and 5A) was observed in 28/42 cases with an identified syndrome (67%), in 17/20 cases with neuroaxial vascular lesions (85%), and in no patients without an identified syndrome (0%) ( $P < .001$ ). MC enlargement was associated with S1 segmental facial hemangiomas, occurring in 85% (23/27) of syndromic subjects with S1 IH, compared with 33% (5/15) of those with segments other than S1 ( $P = .001$ ). No significant association was found with MC enlargement and S2–S4 segment involvement. MC enlargement was not noted in subjects with only para-/intrapinal neuroaxial IHs.

### Posterior Fossa Abnormalities

Twenty of 42 subjects with syndromic hemangiomas (48%) demonstrated anomalies of the posterior fossa. Those included

inferior vermal hypoplasia ( $n = 14$ ), hypoplasia of a cerebellar hemisphere ( $n = 13$ ), and Dandy-Walker malformation ( $n = 4$ ) (Fig 5B). No posterior fossa abnormalities were identified in the nonsyndromic patients ( $P < .001$ ), which would be expected because they are part of the definition of PHACE. In patients with identified hemangioma syndromes, the prevalence of posterior fossa abnormalities was similar between patients with and without neuroaxial IHs (40% versus 50%,  $P = .55$ ). No association was found between the location of the segmental facial IH or intracranial IH and the presence of posterior fossa abnormalities ( $P > .05$  for all comparisons). Unilateral MC enlargement was found more frequently in syndromic subjects with posterior fossa abnormalities than in those without posterior fossa anomalies (85% versus 48%,  $P = .020$ ) (Fig 5).<sup>33</sup> Sex was not associated with the presence of intracranial IHs, an enlarged MC, or posterior fossa abnormalities ( $P > .05$ ).

### Cardiovascular Abnormalities

Ninety-five percent (40/42) of patients with hemangioma syndromes had cardiovascular anomalies, ranging from minor developmental variants to severe dysplastic vasculopathy of the large arteries (Fig 5B), including aortic arch anomalies and cardiac defects. We did not observe serious vascular events or ischemic lesions in our group, though 1

patient was treated with pial synangiosis in response to developing Moyamoya vasculopathy identified after presenting with headaches on presymptomatic brain MR imaging.

### DISCUSSION

Most authors agree that infants presenting with large segmental hemangiomas of the head, neck, chest, and lower body may be manifesting an underlying hemangioma syndrome; hence, careful patient work-up is recommended.<sup>36</sup> We found that 42% of patients referred to our institution with segmental IHs who underwent brain and/or neck and spine imaging were ultimately diagnosed with an underlying hemangioma syndrome, PHACE, and diffuse neonatal hemangiomatosis.

We detected a high rate of neuroaxial lesions in the group with confirmed hemangioma syndromes (48% of our subjects), substantially higher than reported in the general population.<sup>29–31</sup> The reason for this higher prevalence is not entirely clear, but possible reasons include the resolution of our multiplanar imaging, the presence of multiplanar postcontrast imaging in all cases, and the focus of the study team on the detection of neuroaxial



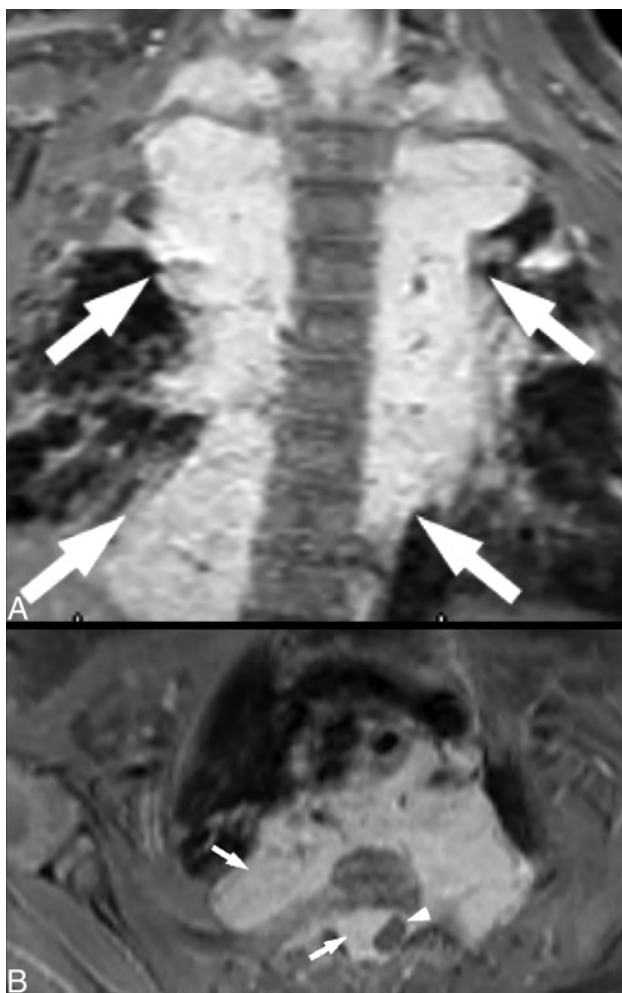


**FIG 4.** Paraspinal IH. A 2-month-old girl with face and neck segmental IH. Coronal (A) and axial (B) postcontrast T1-weighted images with fat suppression show extensive bilateral enhancing paraspinal masses along the thoracic spine (arrows), with extension into the spinal canal and focal cord compression (arrowhead).

lesions. The lesions were extra-axial without parenchymal involvement and extradural in location within the spine, corresponding to the existing literature.<sup>3,11,12,16,18,27-30,37</sup> The most common location of intracranial hemangiomas in our cohort was the auditory apparatus. The degree of involvement varied from subtle linear enhancement of the vestibulocochlear nerve or basal turn of the cochlea to large masses extending from the cerebello-pontine angle and filling the IAC and cochlea. Duffy et al<sup>38</sup> reported an under-recognized association of hearing loss with PHACE syndrome in 6 patients, emphasizing the variety of clinical manifestations in patients with auditory lesions. The data from our series indicating a high prevalence of internal auditory canal involvement add to this literature. Some authors suggest dedicated imaging of the auditory apparatus, as well as thorough assessment of auditory functions in patients with superficial hemangiomas involving the external ear,<sup>27,39</sup> though as we have shown, IAC hemangiomas can be seen in patients having segmental hemangiomas in segments not involving the external ear. Even subtle imaging findings of auditory apparatus involvement with hemangiomas may, therefore, result in a monitoring strategy toward a more detailed clinical evaluation and imaging follow-up. In one of our patients, there was improvement of sensorineural hearing loss. It is possible to speculate that the timing of auditory testing may influence the hearing test results because there are changes in the size of the IAC hemangiomas with time. The long-term effect of internal auditory apparatus involvement by IH is not fully known, to our knowledge.

Enhancing dural-based masses were present in approximately 12% of subjects, which demonstrated imaging features in some ways similar to meningiomas. This type of vascular lesion should be added to a list of differential lesions mimicking meningioma if visualized in the appropriate clinical setting.<sup>37</sup> In 1 case, the small dural-based hemangioma was the only intracranial vascular mass present, representing the pertinent feature contributing to the diagnosis of PHACE syndrome.

Wright and Wycoco<sup>32</sup> reported asymmetric MC enlargement as an imaging marker highly supportive a diagnosis of PHACE

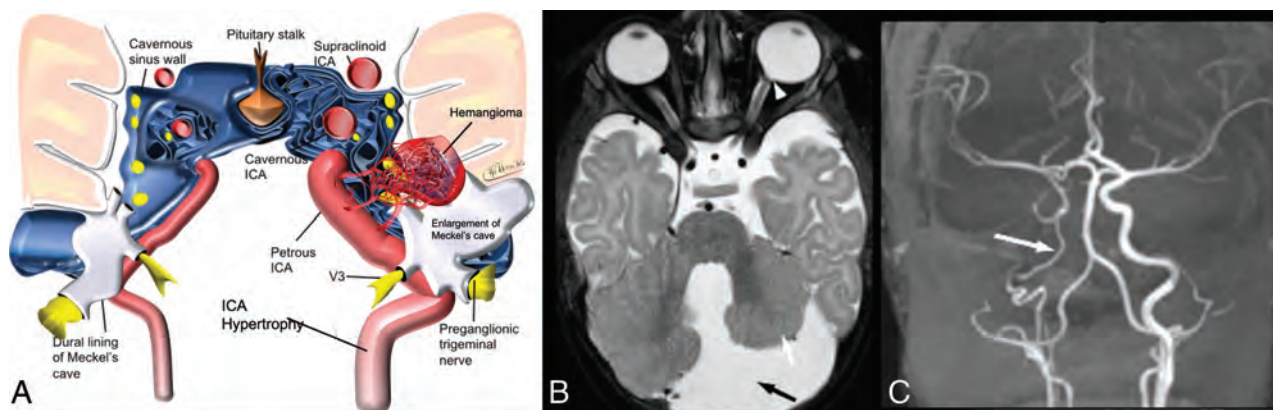


**FIG 5.** A, Asymmetrical enlargement of Meckel's cave in patients with PHACE syndrome, an illustration showing a relationship between skull base hemangioma and adjacent nerves and vascular structures. Modified from a previously published image.<sup>33</sup> B, Posterior fossa abnormality in patients with PHACE syndrome. A 6-week-old girl with a left facial IH. An axial T2-weighted image shows an enlarged retrocerebellar CSF space (black arrow), an asymmetrically small left cerebellar hemisphere (white arrow), and a small posterior vitreous coloboma in the left globe (arrowhead), which is another infrequent feature of PHACE syndrome. C, Arteriopathy of PHACE syndrome. A 6-month-old girl with a right-face IH and PHACE syndrome. Coronal TOF-MRA reconstructed image shows the diffusely small caliber of intracranial right ICA (arrow). Fig 5A courtesy of Malhotra, A., Tu, L., Kalra, V.B. et al. Neuroimaging of Meckel's cave in normal and disease conditions. Insights Imaging 9, 499–510 (2018). <https://doi.org/10.1007/s13244-018-0604-7>.

syndrome. They reported that 82% of patients with confirmed PHACE syndrome revealed asymmetric MC enlargement and that this finding has a positive predictive value of 100%, a negative predictive value of 91%, and an accuracy of 93% in predicting a clinical diagnosis of PHACE or possible PHACE syndrome. We found MC asymmetry in 67% (28/42) of patients with hemangioma syndromes, noting a particularly high frequency (85%) of unilateral MC enlargement in patients with coexisting intracranial lesions, without MC asymmetry in the isolated superficial IH group. We observed a statistically significant association of MC enlargement with superficial segmental facial IH in the distribution involving the frontotemporal segment (S1); this observation is concordant with the literature.<sup>32</sup> Several theories have been suggested to explain this finding. Early hemangioma involvement of the trigeminal V1 division traversing the MC, which may be small or have regressed by the time of imaging, could influence fluid dynamics and may cause remodeling of the affected MC. Additionally, IHs secrete numerous signaling factors that affect multiple cell types, including osteoblasts and meningeal cells, as well as changes in local endothelial proliferation via the vascular endothelial growth factor, Insulin-like growth factor and other growth factors.<sup>40</sup>

Another theory of MC enlargement proposes an aberrant/deficient migration of the cephalic neural crest in a metamer distribution, noting a common origin of skull base tissues and trigeminal nerve ganglia. It assumed that a postzygotic mutation or early prenatal insult to the fetal skull base may cause dysplasia of the MC.<sup>32</sup> Although being highly suggestive of the diagnosis of PHACE, this sign was not seen in all cases, especially in patients with symmetric or midline face or neck lesions. Most interesting, we found a higher rate of MC enlargement than posterior fossa abnormalities in PHACE syndrome. An additional study with follow-up monitoring of imaging findings and clinical data may elucidate the significance of an asymmetric MC. Overall, our findings support asymmetric enlargement of the MC as highly suggestive of an underlying diagnosis of PHACE syndrome in the appropriate clinical setting.

The pattern of facial segmental IH distribution may help in predicting underlying structural defects.<sup>41</sup> We observed a high frequency of intracranial hemangiomas in patients with S1 segmental facial hemangiomas, as well as multiple segments involved, which is in concordance with literature data.<sup>17</sup> Therefore, the presence of S1 and/or multisegmental superficial segmental IH mandates a careful imaging search for even subtle neuroaxial hemangiomas. Viswanathan et al<sup>12</sup> reported clear continuity of neuroaxial lesions with subcutaneous/cutaneous lesions. In our cohort, a definite connection between intracranial vascular masses and its superficial counterpart was not demonstrated in all cases, though skull base foramina lesions were seen in close proximity to the superficial cutaneous lesions.

A high percentage of all patients had cardiovascular anomalies, ranging from minor developmental variants to severe dysplastic vasculopathy of large arteries, including aortic arch anomalies and cardiac defects. However, PHACE syndrome is rarely associated with progressive vascular disease, and we did not observe serious vascular events or ischemic lesions in our group, though 1 patient was treated with synangiosis in response

to the development of Moyamoya vasculopathy (this patient had been treated with systemic steroids, not propranolol).<sup>42</sup> Although the intracranial lesions mostly regressed on available follow-up imaging, some of the residual lesions remained visible at 4–5 years of age. One patient did have recurrence of intracranial IH at 3 years of age, which was simultaneous with the recurrence of skin lesions. Decisions regarding the scheduling of follow-up imaging may, therefore, be considered on a case-by-case basis rather than only in the event of new neurologic signs or symptoms.

Our study has limitations inherent to the retrospective design. Because our institution is a referral center, the overall rate of subjects with facial segmental IH with hemangioma syndromes may have been higher in our study compared with the general population. However, it is unlikely that this rate affected the differences in rates of neuroaxial IH and other findings associated with such syndromes. Imaging studies were retrospectively reviewed and could not be tailored to specific indications as needed. Neuroimaging of 2 subjects with LUMBAR/PELVIS syndrome was not available; therefore, these patients were excluded from the study. Additionally, follow-up imaging in the retrospective cohort was inconsistent, and a formal assessment of the longitudinal pattern of neuroaxial lesions was not possible. Clinical data were limited to what was available in the electronic medical record.

The results of our study suggest the necessity of a methodic approach in the evaluation of patients with segmental IH. These patients require a thorough imaging search for vascular lesions involving the neural axis. Imaging usually begins with brain MR imaging, occasionally neck MR imaging (if the superficial lesion involves the neck), and vascular MR imaging, including head and neck MRA with TOF or dynamic MRA with contrast if indicated. Contrast administration may be considered in cases of S1 and/or multisegmental distribution of IH, which is notable for a higher association of intracranial or intraspinal lesions. We demonstrate spinal involvement by neuroaxial hemangiomas in a subset of the patients. However at this point, beyond increasing awareness of spinal involvement, no firm conclusion can be drawn for changing clinical practice or the necessity of spinal imaging in this group of patients without further knowledge of the short- and long-term clinical implications of these spinal neuroaxial hemangiomas.

## CONCLUSIONS

Although CNS involvement by IH is an overall unusual occurrence, a substantial number of pediatric patients with hemangioma syndromes, especially PHACE syndrome, have a high rate (48%) of neuroaxial lesions. Therefore, detection of neuroaxial IHs may be potentially considered as one of the criteria for diagnosis of this hemangioma syndrome. The neuroaxial lesions appear to behave similar to superficial lesions (imaging features and clinical course of development and regression). The neuroaxial IHs were not demonstrated in patients with isolated cutaneous segmental IHs. Further studies would be necessary to determine how these findings may influence the management and potential implications of neuroaxial lesions on patient development.

Disclosures: Tamara Feygin—UNRELATED: Employment: The Children's Hospital of Philadelphia. Aashim Bhatia—UNRELATED: Consultancy: Guerbet. Avrum Pollock—UNRELATED: expert testimony A. Pollock MD, LLC.

## REFERENCES

- Mulliken JB, Glowacki J. Hemangiomas and vascular malformations in infants and children: a classification based on endothelial characteristics. *Plast Reconstr Surg* 1982;69:412–22 CrossRef Medline
- Leaute-Labreze C, Harper JJ, Hoeger PH. Infantile haemangioma. *Lancet* 2017;390:85–94 CrossRef Medline
- Pascual-Castroviejo I. Vascular and nonvascular intracranial malformation associated with external capillary hemangiomas. *Neuroradiology* 1978;16:82–84 CrossRef Medline
- van Vugt LJ, van der Vleuten CJ, Flucke U, et al. The utility of GLUT1 as a diagnostic marker in cutaneous vascular anomalies: a review of literature and recommendations for daily practice. *Pathol Res Pract* 2017;213:591–97 CrossRef Medline
- Dadras SS, North PE, Bertoncini J, et al. Infantile hemangiomas are arrested in an early developmental vascular differentiation state. *Mod Pathol* 2004;17:1068–79 CrossRef Medline
- Donnelly LF, Adams DM, Bisset GS 3rd. Vascular malformations and hemangiomas: a practical approach in a multidisciplinary clinic. *AJR Am J Roentgenol* 2000;174:597–608 CrossRef Medline
- Wassef M, Blei F, Adams D, et al. on behalf of the ISSVA Board and Scientific Committee. Vascular anomalies classification: recommendations from the International Society for the Study of Vascular Anomalies. *Pediatrics* 2015;136:e203–14 CrossRef Medline
- Morrow AC, Gupta A, Patel MN, et al. 2014 Revised Classification of Vascular Lesions from the International Society for the Study of Vascular Anomalies: Radiologic-Pathologic Update. *Radiographics* 2016;36:1494–1516 CrossRef Medline
- International Society for the Study of Vascular Anomalies. Classification. 2018. issva.org/classification. Accessed October 9, 2020
- Haggstrom AN, Lammer EJ, Schneider RA, et al. Patterns of infantile hemangiomas: new clues to hemangioma pathogenesis and embryonic facial development. *Pediatrics* 2006;117:698–703 CrossRef Medline
- Melnick LE, Yan AC, Licht DJ, et al. PHACE syndrome: a retrospective review of 23 patients. *Pediatr Dermatol* 2014;31:390–92 CrossRef Medline
- Viswanathan V, Smith ER, Mulliken JB, et al. Infantile hemangiomas involving the neuraxis: clinical and imaging findings. *AJNR Am J Neuroradiol* 2009;30:1005–13 CrossRef Medline
- Darrow DH, Greene AK, Mancini AJ, et al. Section on Dermatology, Section on Otolaryngology–Head and Neck Surgery, and Section on Plastic Surgery. Diagnosis and management of infantile hemangioma. *Pediatrics* 2015;136:e1060–1104 CrossRef Medline
- Metry D, Heyer G, Hess C, et al. PHACE Syndrome Research Conference. Consensus Statement on Diagnostic Criteria for PHACE syndrome. *Pediatrics* 2009;124:1447–56 CrossRef Medline
- Girard C, Bigorre M, Guillot B, et al. PELVIS syndrome. *Arch Dermatol* 2006;142:884–88 CrossRef Medline
- Metry DW, Dowd CF, Barkovich AJ, et al. The many faces of PHACE syndrome. *J Pediatr* 2001;139:117–23 CrossRef Medline
- Metry DW, Garzon MC, Drolet BA, et al. PHACE syndrome: current knowledge, future directions. *Pediatr Dermatol* 2009;26:381–98 CrossRef Medline
- Oza VS, Wang E, Berenstein A, et al. PHACES association: a neuro-radiologic review of 17 patients. *AJNR Am J Neuroradiol* 2008;29:807–13 CrossRef Medline
- Restrepo R, Palani R, Cervantes LF, et al. Hemangiomas revisited: the useful, the unusual and the new, Part 1: overview and clinical and imaging characteristics. *Pediatr Radiol* 2011;41:895–904 CrossRef Medline
- Balaci E, Sumner TE, Auringer ST, et al. Diffuse neonatal hemangiomatosis with extensive involvement of the brain and cervical spinal cord. *Pediatr Radiol* 1999;29:441–43 CrossRef Medline
- Glick ZR, Frieden IJ, Garzon MC, et al. Diffuse neonatal hemangiomatosis: an evidence-based review of case reports in the literature. *J Am Acad Dermatol* 2012;67:898–903 CrossRef Medline
- Schumacher WE, Drolet BA, Maheshwari M, et al. Spinal dysraphism associated with the cutaneous lumbosacral infantile hemangioma: a neuroradiological review. *Pediatr Radiol* 2012;42:315–20 CrossRef Medline
- Verma SB, Wollina U. Infantile perianal pyramidal protrusion with coexisting perineal and perianal hemangiomas: a fortuitous association or incomplete PELVIS syndrome? *Indian J Dermatol* 2014;59:71–74 CrossRef Medline
- Ganapathy S, Kleiner LI, Mirkin LD, et al. Intradural capillary hemangioma of the cauda equina. *Pediatr Radiol* 2008;38:1235–38 CrossRef Medline
- Luu M, Frieden IJ. Infantile hemangiomas and structural anomalies: PHACE and LUMBAR syndrome. *Semin Cutan Med Surg* 2016;35:117–23 CrossRef Medline
- Garzon MC, Epstein LG, Heyer GL, et al. PHACE syndrome: consensus-derived diagnosis and care recommendations. *J Pediatr* 2016;178:24–33 CrossRef Medline
- Judd CD, Chapman PR, Koch B, et al. Intracranial infantile hemangiomas associated with PHACE syndrome. *AJNR Am J Neuroradiol* 2007;28:25–29 Medline
- Poindexter G, Metry DW, Barkovich AJ, et al. PHACE syndrome with intracerebral hemangiomas, heterotopia, and endocrine dysfunction. *Pediatr Neurol* 2007;36:402–06 CrossRef Medline
- Tortori-Donati P, Fondelli MP, Rossi A, et al. Intracranial contrast-enhancing masses in infants with capillary haemangioma of the head and neck: intracranial capillary haemangioma? *Neuroradiology* 1999;41:369–75 CrossRef Medline
- Ersoy S, Mancini AJ. Hemifacial infantile hemangioma with intracranial extension: a rare entity. *Pediatr Dermatol* 2005;22:309–13 CrossRef Medline
- Karikari IO, Selznick LA, Cummings TJ, et al. Capillary hemangioma of the fourth ventricle in an infant: case report and review of the literature. *J Neurosurg* 2006;104:188–91 CrossRef Medline
- Wright JN, Wycoco V. Asymmetric Meckel cave enlargement: a potential marker of PHACES syndrome. *AJNR Am J Neuroradiol* 2017;38:1223–27 CrossRef Medline
- Malhotra A, Tu L, Kalra VB, et al. Neuroimaging of Meckel's cave in normal and disease conditions. *Insights Imaging* 2018;9:499–510 PMC CrossRef Medline
- Haggstrom AN, Beaumont JL, Lai JS, et al. Measuring the severity of infantile hemangiomas: instrument development and reliability. *Arch Dermatol* 2012;148:197–202 CrossRef Medline
- Landis JR, Koch GG. The measurement of observer agreement for categorical data. *Biometrics* 1977;33:159–174 Medline
- Hartemink DA, Chiu YE, Drolet BA, et al. PHACES syndrome: a review. *Int J Pediatr Otorhinolaryngol* 2009;73:181–87 CrossRef Medline
- Chourmouzi D, Potsi S, Moutzouoglou A, et al. Dural lesions mimicking meningiomas: a pictorial essay. *World J Radiol* 2012;4:75–82 CrossRef Medline
- Duffy KJ, Runge-Samuelson C, Bayer ML, et al. Association of hearing loss with PHACE syndrome. *Arch Dermatol* 2010;146:1391–96 CrossRef Medline
- Polanski JF, Veras RO, Lucinda LR, et al. PHACE syndrome and hearing loss. *An Bras Dermatol* 2019;94:489–90 CrossRef Medline
- Ji Y, Chen S, Li K, et al. Signaling pathways in the development of infantile hemangioma. *J Hematol Oncol* 2014;7:13 CrossRef Medline
- Patil SJ, Moray AA, Kiran VS, et al. PHACE/S syndrome: a syndromic infantile segmental hemangioma. *Indian J Pediatr* 2010;77:911–13 CrossRef Medline
- Heyer GL, Dowling MM, Licht DJ, et al. The cerebral vasculopathy of PHACES syndrome. *Stroke* 2008;39:308–16 CrossRef Medline



# The Fetus with Ganglionic Eminence Abnormality: Head Size and Extracranial Sonographic Findings Predict Genetic Diagnoses and Postnatal Outcomes

 S.K. Goergen,  E. Alibrahim,  J. Christie,  A. Dobrotwir,  M. Fahey,  L. Fender,  K. Frawley,  S.A. Manikkam,  J.R. Pinner,  S. Sinnott,  R. Romaniello,  S.A. Sandaradura,  J. Taylor,  A. Vasudevan, and  A. Righini



## ABSTRACT

**BACKGROUND AND PURPOSE:** Ganglionic eminence abnormalities on fetal MR imaging are associated with cerebral malformations. Their presumed genetic basis and associated postnatal outcomes remain largely unknown. We aimed to elucidate these through a multicenter study.

**MATERIALS AND METHODS:** Between January 2010 and June 2020, seven hospitals in 2 countries performing fetal MR imaging examinations identified fetal MR imaging studies demonstrating ganglionic eminence enlargement, cavitation, or both. Cases with no genetic diagnosis, no whole exome sequencing, or no outcome of a liveborn child were excluded. Head size was classified as large (fronto-occipital diameter > 95th centile), small (fronto-occipital diameter < 5th centile), or normal.

**RESULTS:** Twenty-two fetuses with ganglionic eminence abnormalities were identified. Of 8 with large heads, 2 were diagnosed with *MTOR* mutations; 1 with *PIK3CA* mutation—producing megalencephaly, polymicrogyria, polydactyly, hydrocephalus (MPPH) syndrome; 3 with *TSC* mutations; 1 with megalencephaly capillary malformation syndrome; and 1 with hemimegalencephaly. Cardiac rhabdomyoma was present prenatally in all cases of *TSC*; mutation postaxial polydactyly accompanied megalencephaly capillary malformation and MPPH. Of 12 fetuses with small heads, 7 had *TUBA1A* mutations, 1 had a *TUBB3* mutation, 2 had cobblestone lissencephaly postnatally with no genetic diagnosis, 1 had a *PDHA1* mutation, and 1 had a fetal akinesia dyskinesia sequence with no pathogenic mutation on trio whole exome sequencing. One of the fetuses with a normal head size had an *OPHN1* mutation with postnatal febrile seizures, and the other had peri-Sylvian polymicrogyria, seizures, and severe developmental delay but no explanatory mutation on whole exome sequencing.

**CONCLUSIONS:** Fetal head size and extracranial prenatal sonographic findings can refine the phenotype and facilitate genetic diagnosis when ganglionic eminence abnormality is diagnosed with MR imaging.

**ABBREVIATIONS:** GE = ganglionic eminence; WES = whole exome sequencing; TSC = tuberous sclerosis complex

The human ganglionic eminence (GE) is a focal thickening in the proliferative neuroepithelium lining the ventricles of the

telencephalic lobes, situated inferolateral to the frontal horns of the lateral ventricles, and persists throughout nearly all of fetal life, longer than other proliferative areas.<sup>1,2</sup> It is thickest at 20 weeks, decreases in size by approximately 50% between 26 and 28 weeks' gestation, and involutes by 34–36 weeks' gestation; this period of rapid involution of the GE through fibrinolysis has been theorized as a contributing factor to the selective vulnerability of preterm neonates to hemorrhage in this region.<sup>2</sup> Most cortical GABAergic


Received December 10, 2020; accepted after revision February 17, 2021.

From the Monash Imaging (S.K.G.) and Neurogenetics Unit (M.F.), Monash Health, Victoria, Australia; Departments of Imaging and Surgery (S.K.G.) and Paediatrics (M.F.), School of Clinical Sciences, Monash University, Clayton, Victoria, Australia; Departments of Radiology (E.A., A.D.) and Clinical Genetics (A.V.), Royal Women's Hospital, Parkville, Victoria, Australia; PRP Imaging (J.C.), Sydney, New South Wales, Australia; Department of Radiology (L.F.), King Edward Memorial Hospital, Perth, Western Australia, Australia; Department of Medical Imaging and Nuclear Medicine (K.F., S.A.M.), Queensland Children's Hospital, Brisbane, Queensland, Australia; Centre for Clinical Genetics (J.R.P.), Sydney Children's Hospital, Sydney, New South Wales, Australia; School of Women's and Children's Health (J.R.P.), University of New South Wales, Sydney, Australia; SO + GI Scan I-MED Radiology (S.S.), Department of Medical Imaging, Royal Brisbane and Women's Hospital, Brisbane, Queensland, Australia; Child Neuropsychiatry and Neurorehabilitation Department (R.R.), Scientific Institute Eugenio Medea, La Nostra Famiglia, Bosiso Parini, Lecco, Italy; Discipline of Child and Adolescent Health (S.A.S.), Faculty of Medicine and Health, The University of Sydney, Westmead, New South Wales, Australia; Department of Clinical Genetics (S.A.S.), Children's Hospital at Westmead, Westmead, New South Wales, Australia; Department of Radiology (J.T.), Prince of Wales Hospital, Sydney, New South Wales, Australia; and Department of Pediatric Radiology and Neuroradiology (A.R.), Vittore Buzzi Children's Hospital, Milan, Italy.

This work was supported by the Research Grant for Clinical Radiology awarded by The Royal Australian and New Zealand College of Radiologists (2020/RANZCR/004).

Paper previously presented in part at: Virtual World Congress of the International Society of Ultrasound in Obstetrics and Gynaecology, October 16–18, 2020; Virtual

Please address correspondence to Stacy K. Goergen, MD, Monash Imaging, Monash Health, Departments of Imaging and Surgery, School of Clinical Sciences, Monash University, 246 Clayton Rd, Clayton, Victoria 3168, Australia, e-mail: stacy.goergen@monashhealth.org

 Indicates article with online supplemental data.

<http://dx.doi.org/10.3174/ajnr.A7131>



interneurons are generated in the GE, and they migrate to the cortex by first tangential and then radial migration. The GE also contributes to a population of thalamic neurons and is responsible for forming most of the basal ganglia. Furthermore, the GE represents an intermediate target for thalamocortical and corticothalamic axons and is a source of oligodendrocyte precursors.<sup>1-3</sup>

Abnormal persistence, enlargement, and cavitation of GEs on fetal MR imaging have been associated with markedly reduced fetal head size and underdevelopment of sulcation (microlissencephaly),<sup>4</sup> as well as a range of other brain malformations, including mild partial callosal agenesis, vermis hypoplasia and rotation, cerebellar hypoplasia, ventriculomegaly, enlarged subarachnoid spaces, and molar tooth malformation.<sup>5</sup>

Although the normal GE is demonstrable with sonography using an endovaginal 3D technique between 9 and 13 weeks' gestation,<sup>6</sup> the pathologic GE has been identified at or after the mid-trimester only recently in isolated case reports,<sup>7,8</sup> without postnatal outcome or genetic diagnosis. Coexistence of GE abnormalities with other brain malformations of the corpus callosum, cerebellum, or microcephaly may be the impetus for fetal MR imaging in which the GE abnormality is first recognized.

A very recent report<sup>9</sup> on a large cohort of fetuses with GE alterations at MR imaging highlighted the more frequently associated brain anomalies. However, the authors themselves stressed that a scarcity of knowledge on the genetic substrate of such GE anomalies is the major drawback for the correct characterization and understanding of the pathophysiology. We have also noted an association of fetal GE abnormalities with extremely large and small head sizes.

Better understanding of the intracranial and extracranial associations of this abnormality, its genetic causes, and postnatal outcomes for liveborn children is pivotal for the following reasons:

- 1) Genetic diagnosis requires accurate fetal phenotyping; lack thereof is one of the greatest barriers to the use of prenatal whole genome and exome sequencing.<sup>10,11</sup>
- 2) Given the current lack of wide availability of fetal exome and genome sequencing during pregnancy, an understanding of the causes of GE abnormalities would facilitate prenatal counseling and decision-making within a clinically realistic timeframe.

We hypothesized that a multi-institutional study of prenatal sonographic findings, genetic analyses, and postnatal outcomes of fetuses with prenatal MR imaging showing an abnormality of the GE would enable us to do the following:

1. Establish the genetic abnormalities most often associated with GE abnormalities
2. Narrow the range of differential diagnoses for a given fetus by categorization based on cranial biometry and specific extracranial structural abnormalities
3. Develop a less biased picture of the relative likelihood of various genetic causes for the GE abnormalities by involving multiple subspecialist fetal MRI centers in case identification.

## **MATERIALS AND METHODS**

### **Study Setting**

Hospitals in all states of Australia and New Zealand involved in providing fetal MR imaging clinical services and the Vittore Buzzi

Children's Hospital in Milan, Italy, were invited by e-mail from the principal investigator to participate in the study by contributing cases from their institutional fetal MR imaging databases. Participating sites provided deidentified sample JPEG images of candidate cases to the principal investigator to determine whether the images demonstrated a GE abnormality before applying other inclusion criteria and final enrollment of the subject.

### **Study Period**

January 2010 to June 2020 was chosen due to the lesser availability of genomic testing before January 2010 at the participating sites.

### **Inclusion**

We included all women older than 18 years of age with a singleton or multiple pregnancies who had fetal MR imaging for a suspected fetal cranial abnormality as a result of a referral for abnormal findings on a prior tertiary sonography during the study period (January 2010 to June 2020), on which the fetus had a GE abnormality reported in the initial clinical report or discovered on review of the case. Postnatal MR imaging with clinical outcome data or composite clinoradiologic diagnosis (based on extracranial prenatal sonography and MR imaging findings specific for a disorder) or genomic testing (gene panel, singleton whole exome sequencing [WES], trio exome sequencing, or any combination of these) was a further requirement for inclusion. All fetuses had tertiary prenatal ultrasound imaging that resulted in their referral for fetal MR imaging. Before submitting cases for consideration, participating centers were provided with 4 sample cases of fetuses with abnormal ganglionic eminence enlargement or cavitation, with the gestational ages of the fetuses as well as references<sup>4,5</sup> with cases of GE abnormalities on fetal MR images.

### **Case Ascertainment**

Searches of radiology reports (using the radiology information system search functions) or local fetal MR imaging case databases (maintained by radiologists at their institutions) were conducted using the following search terms: "ganglionic eminence," "lissencephaly," "Walker Warburg," "dystroglycanopathy," "cobblestone," "germinolytic," "tuberous sclerosis," "TSC," "megalocephaly," "microcephaly," "hemimegalocephaly," "SEGA (subependymal giant cell astrocytoma), and "polymicrogyria." The rationale for these terms is that these conditions and abnormalities have been previously shown to be associated with abnormal GEs. This search would potentially help identify cases with abnormal GEs, not appreciated or reported in the original clinical report, even if the correct diagnosis had been provided on the basis of other criteria and abnormal findings.

### **Exclusion**

Submitted cases that, in the opinion of the lead authors, did not demonstrate GE abnormalities were excluded. The criterion for determining that the GEs were abnormally enlarged for gestational age or cavitated was a qualitative, visual assessment of size and assessment for any cavitation; currently there are no published data for fetal GE measurements by gestational age. Cases that had no genomic testing and also no postnatal

imaging or clinical follow up that provided a genetic diagnosis were excluded.

For example, an infant with typical tuberous sclerosis complex (TSC) features on postnatal MR imaging would be included even if no genetic test results were available or genetic testing had not been performed. Similarly, a fetus of a terminated pregnancy, in which a cardiac rhabdomyoma was identified along with abnormal fetal cranial MR imaging findings consistent with tuberous sclerosis complex, would also be eligible for inclusion in the absence of genetic confirmation.

Finally, in all cases diffusion-weighted and T2\* images were reviewed, and if the GE enlargement was attributable to hemorrhage based on this evaluation, the case was excluded.

### Data Collection

**Demographics.** The following data were collected: Gestational age at sonography before MR imaging; prenatal sonographic findings; gestation at the first fetal MR imaging examination demonstrating GE abnormality; gestation at any subsequent MRI; the nature of GE abnormality (uni- or bilateral, enlargement, cavitation); other abnormal cranial findings on MR imaging; fronto-occipital dimension of the fetal head on the first MR imaging demonstrating GE abnormality; brain stem and cerebellar biometry; and clinical outcomes and postnatal MR imaging findings for liveborn children. The radiologist collected identified patient and imaging data at the site where the study was performed, and all patient identification was removed before the subject was matched with a unique study identification number. An Excel (Microsoft) spreadsheet case report form containing this deidentified data was submitted to the coordinating site.

**Genomic Data Collection.** The results of all genomic testing (panel and single-gene testing, singleton WES, trio WES) performed for study subjects were provided by genetics departments affiliated with participating sites. Variants were classified according to the American College of Medical Genetics and Genomics criteria.<sup>12</sup>

**Fetal MR Image Acquisition Technique and Analysis.** Deidentified JPEG images were sent from the participating sites, including full axial, coronal, and sagittal single-shot T2-weighted HASTE or fast spin-echo as well as single-plane echo-planar diffusion-weighted sequences. Imaging was performed on both 1.5T and 3T MR imaging units with a variety of scanning platforms. A torso-array coil with or without a spinal array was used to acquire image data, and section thickness was typically 3–4 mm with in-plane resolution ranging from 0.5 to 1.2 mm. Other imaging sequences may have been acquired at the participating sites, as per local protocol, but these were not provided for this study. However, hemorrhage as the sole cause of GE enlargement was excluded by the participating sites by reviewing the acquired T2\* gradient-echo sequences.

The fronto-occipital diameter of the fetal brain was measured at the participating sites as were transverse cerebellar diameter, vermis height, anteroposterior diameter of the pons, and maximum ventricular atrial diameters; centile was calculated at the

coordinating site on the basis of gestational age and standard tables of biometric data for normal fetuses.<sup>13</sup>

### Ethics

A site-specific waiver of formal ethics application was granted at all participating sites on the basis of audit methodology to permit sending deidentified clinical and imaging data to the coordinating site.

### Key Outcome Measures

The key outcome measures were the following:

1. Final clinical outcome and imaging diagnoses and/or
2. Results of genomic testing
3. Fetal cranial biometry
4. Associated non-GE findings intra- and extracranial.

## RESULTS

Individual institutional data bases with a total of 4135 fetal MR imaging studies were searched by the participating sites for cases meeting all the inclusion criteria, and these cases were submitted for consideration. No submitted case was excluded following review of the provided images by the coordinating site, resulting in 22 study subjects. Their gestational ages at the time of MR imaging ranged from 21 to 33 weeks. There were 9 pregnancy terminations and 13 live births. Genomic testing was performed in 17 of the 22. In 13/22, this was WES; in 2, it was trio exome sequencing; in 1, a prenatal microarray that identified a pathogenic mutation causing tuberous sclerosis; and in the final subject, neuromuscular gene panel testing was performed (More detailed information regarding associated malformations and clinical outcomes is found in the Online Supplemental Data).

### Head Size and Genetic/Clinicoradiologic Diagnoses

Subjects 1–8 had fronto-occipital head dimension measurements of  $\geq 2$  SDs greater than the mean. Of 5 cases with genetic testing, an *MTOR* or *PI3KCA* mutation was identified in 3, with megalencephaly, polymicrogyria, polydactyly, and hydrocephalus syndrome diagnosed prenatally in case 2 because of sonographically demonstrated postaxial polydactyly (Figs 1 and 2). Tuberous sclerosis was confirmed on genetic testing in 2 cases with cardiac rhabdomyoma, and a putative diagnosis was made in a third case with fetal hemimegalencephaly, a markedly enlarged ipsilateral GE, and a cardiac rhabdomyoma (Fig 3). In 2 subjects with large head sizes and no genetic testing, megalencephaly and hemimegalencephaly were present on postnatal imaging.

Of 12 fetuses with small head sizes, 8 had tubulin mutations and 7 of these were mutations involving the *TUBA1A* gene; 2 had clinical and imaging findings consistent with Walker-Warburg syndrome and cobblestone lissencephaly postnatally; 1 had a *PDHAI1* mutation; and 1 had a fetal akinesia dyskinesia sequence (Fig 4).

Two fetuses had normal head size, one with an *OPHN1* mutation and the other with no genetic diagnosis following WES, but severe developmental delay and seizures.

In no case were the GE abnormalities identified on sonography. Subjects were referred due to a wide variety of abnormalities on sonography, including ventriculomegaly, a small cerebellum, and agenesis of the corpus callosum.

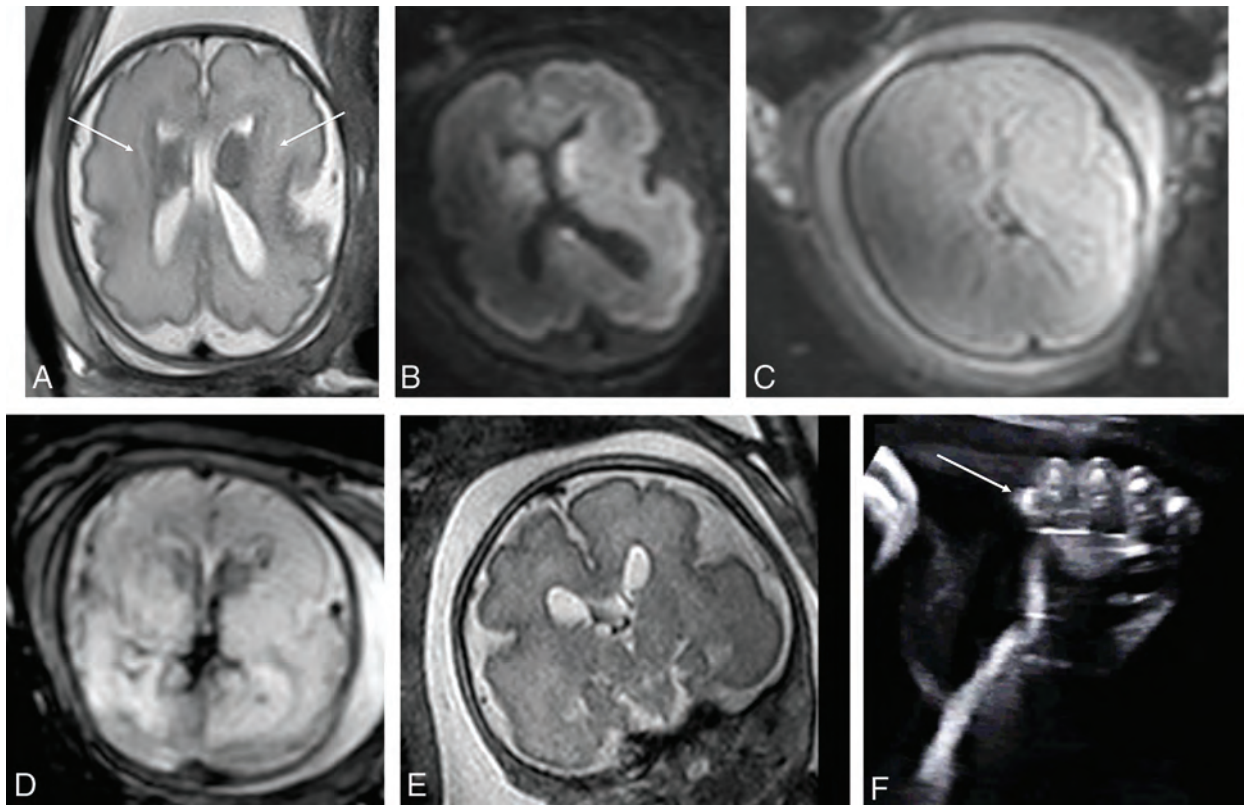


**FIG 1.** *PIK3CA* pathogenic variant. Case 2 at 31 weeks 3 days' gestation. Megalencephaly, polymicrogyria, polydactyly hydrocephalus syndrome due to a *PIK3CA* heterozygous pathogenic variant. The fronto-occipital diameter is  $>6$  SDs above the mean for gestation. Enlarged bilateral ganglionic eminences (arrows, A) are seen on T2-weighted single-shot FSE and DWI (A and B). Diffusion-weighted  $b = 0$  image (C) and T2\*-weighted EPI (D) confirm the absence of hemorrhage as the cause for ganglionic eminence enlargement. Abnormal opercularization is present with Sylvian fissures lined by peri-Sylvian polymicrogyria (E). Postaxial polydactyly is seen on sonography with arrow indicating a rudimentary sixth digit medial to the fifth digit of the hand (F).

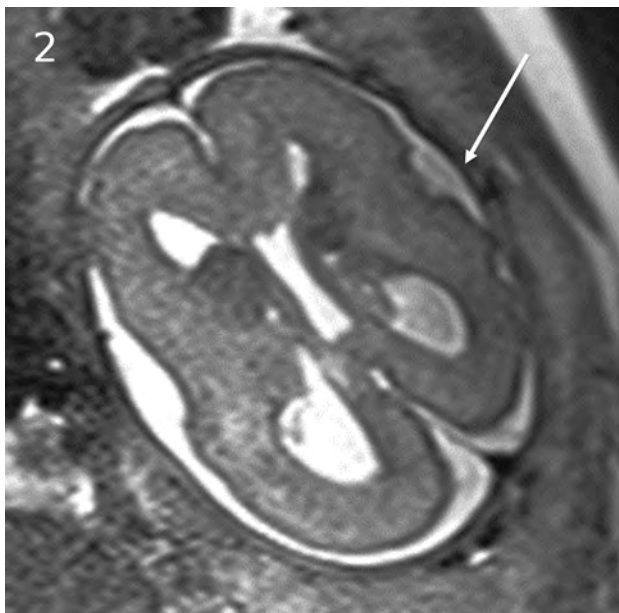


**FIG 2.** *MTOR/PROS* pathway mutations. Smith-Kingsmore syndrome (case 5) at 25 weeks' gestation demonstrates enlarged GEs on DWI and T2-weighted single-shot FSE. There is bilateral underopercularization and left peri-Sylvian polymicrogyria (arrow). The right hemisphere is mildly overgrown.

## DISCUSSION

Our work has gathered international data from centers performing fetal MR imaging to provide information about the genetic causes and postnatal outcomes of fetuses with GE abnormalities on prenatal MR imaging. We have identified a strong association between *MTOR-PIK3CA (PROS) AKT* pathway mutations, including tuberous sclerosis, and fetal head size greater than the 97th centile. *TUBA1A* mutations were the dominant cause of GE abnormalities when frontal-occipital dimensions were less than the third centile, with frequent absence or severe hypoplasia of the corpus callosum and Walker-Warburg imaging phenotype in some cases. Postaxial polydactyly and cardiac rhabdomyoma are useful findings in the fetus with megalencephaly (Frontooccipital diameter =  $+2$  SDs or more) in separating fetuses with tuberous sclerosis from those with *MTOR/PROS* spectrum disorders. Also, extreme increases in head size were most often due to *MTOR-PIK3CA* mutations rather than *TSC* mutations in our cohort.

Caution needs to be exercised with regard to the major differential diagnosis of pathologic GE enlargement, germinal matrix hemorrhage, which, when isolated in the fetus, does not have the severe neurodevelopmental implications that many of the conditions associated with GE enlargement have. T2\*-weighted imaging and DWI should be a routine part of fetal brain imaging, and the  $b = 0$  DWI and T2\*-weighted images must be evaluated for hemorrhage before concluding that the GE is abnormally prominent due to another



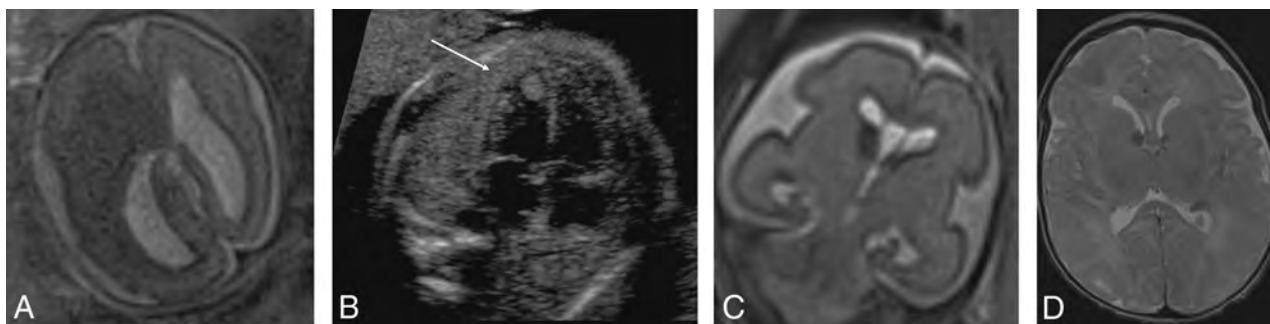


**FIG 3.** Tuberosclerosis complex (A and B). Case 1. Dichorionic diamniotic twin at 22 weeks 5 days' gestation. T2-weighted single-shot FSE image demonstrates hemimegalencephaly and marked enlargement of the ipsilateral GE, which merges with a hypointense masslike lesion in the enlarged right cerebral hemisphere. The fetus had left ventricular cardiac rhabdomyoma on prenatal sonography (arrow, B); the findings likely represent tuberosclerosis complex with an associated hemispheric malformation or, less likely, coexistent subependymal giant cell astrocytoma. No postmortem data or confirmatory genetic testing was available. Case 8. T2 single-shot FSE at 25 weeks gestation (C) and T2 FSE at 1-week postnatal imaging (D) demonstrate mild enlargement of the right GE, ipsilateral and mild ventriculomegaly on fetal MR imaging, and typical changes of tuberosclerosis complex postnatally. The fetus' father also had tuberosclerosis complex.

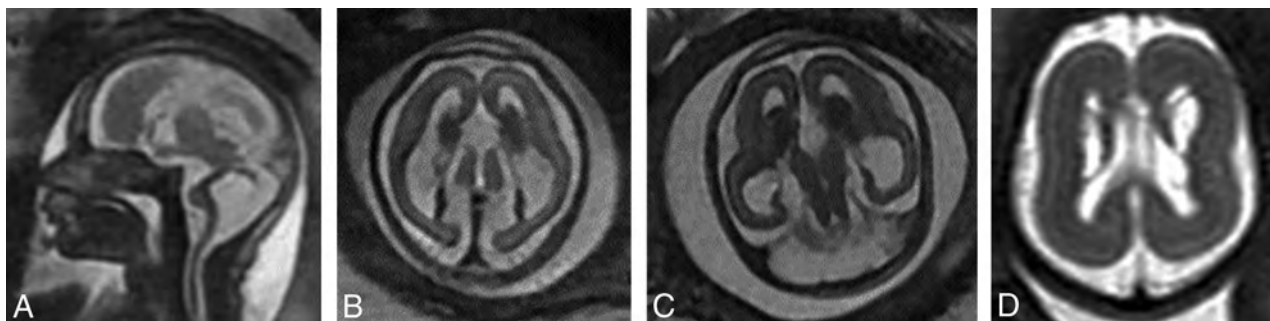


**FIG 4.** *TUBA1A* mutations (A–C). Case 18. T2-weighted single-shot FSE at 24 weeks 4 days' gestation. *TUBA1A* pathogenic heterozygous variant. The bilateral GEs are enlarged. The fronto-occipital diameter is 2.5, standard deviations below the mean. The corpus callosum and cerebellum are severely hypogenetic/hypoplastic. Underopercularization, severe ventriculomegaly, a thin kinked brainstem (A), a ventral pontine cleft suggestive of a Walker-Warburg phenotype, and apparent diencephalic-mesencephalic fusion or dysplasia (C) are also noted. D, Case 19 at 33 weeks. *TUBA1A* mutation with enlarged, cavitated GEs and abnormal persistence of hemispheric lamination.

cause. Notably, in no patient in our series was a GE abnormality seen in the absence of other major structural malformations involving one or more of the corpus callosum, cerebellum, brainstem, microcephaly, or megalencephaly, or a malformation of cortical development. No case of GE abnormality in fetuses with tuberosclerosis complex was seen in the absence of cardiac rhabdomyoma.

Several findings that lay outside our intended aims are worthy of mention:

1. In 1 fetus with tuberosclerosis complex, the only cranial abnormalities were mild ventriculomegaly and subtle asymmetric enlargement of 1 GE (Fig 3). The fetus also had a father with tuberosclerosis complex and a cardiac rhabdomyoma on prenatal sonography, and it would have been possible to dismiss the subtle GE abnormality or perhaps attribute it to germinal matrix hemorrhage without this clinical and sonographic information that increases the pretest probability of such an abnormality reflecting tuberosclerosis complex. This finding underlines the importance of the acquisition of T2\*-weighted sequences to exclude hemorrhage as the cause of asymmetric GE enlargement and the importance of knowledge of the prenatal sonographic findings and family history at the time of MR imaging interpretation.

2. The imaging of our single case of pyruvate dehydrogenase deficiency (Fig 5) manifested as bilateral cavitated GE and agenesis of the corpus callosum with microcephaly, superficially resembling findings in some fetuses with tubulinopathy. The combination of ACC with germinolytic cysts is well-recognized as the postnatal imaging phenotype of *PDHA1* mutations causing pyruvate dehydrogenase deficiency.<sup>14</sup> It may be that the GE cavitations “collapse” with physiologic resolution of the cavitated GE, resulting in germinolytic cysts postnatally.
3. We have confirmed that the Walker-Warburg imaging phenotype with cobblestone lissencephaly may be due to tubulinopathy. To our knowledge, there is only a single case report of this in the literature<sup>15</sup> in which a *TUBB3* mutation was found to be the causative pathogenic variant, but no images were provided. Cobblestone lissencephaly is considered pathognomonic of a group of autosomal recessive disorders characterized by ocular and muscular deficits, including Walker-Warburg syndrome, muscle-eye-brain disease, and Fukuyama muscular dystrophy. All these conditions grouped under the term “ $\alpha$ -dystroglycanopathies” result in neuroglial overmigration and the typical cobblestone appearance of the cortex seen on postnatal but often not on fetal MR imaging examinations. Two-thirds of the cases

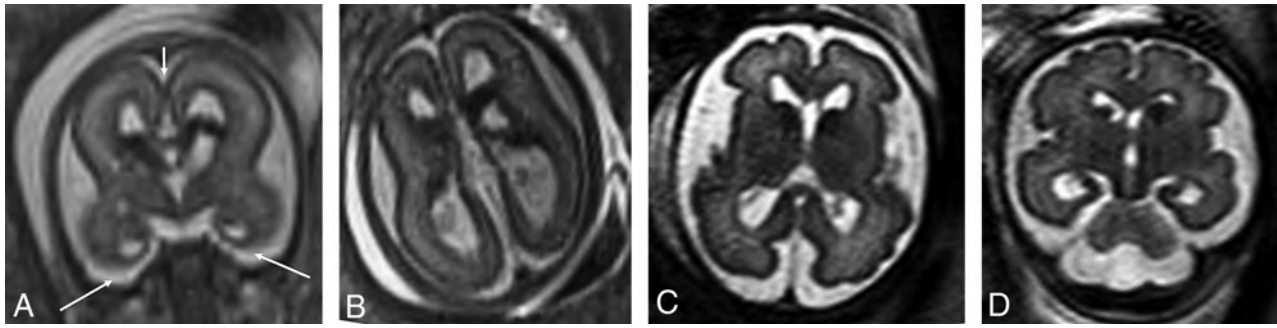


**FIG 5.** *PDHAI* and *OPHN1* mutations. *A* and *B*, *PDHAI* mutation. Case 20 at 23 weeks 3 days' gestation. *PDHAI* mutation. Agenesis of the corpus callosum with the anterior commissure present (*short arrow*), cavitated enlarged GEs, and anterior temporal pole subependymal pseudocysts (germinolitic cysts) (*long arrows*). *C* and *D*, Case 21 at 29 weeks. *OPHN1* mutation with mild ventriculomegaly (11 mm) and bilaterally enlarged GEs.

of cobblestone lissencephaly can be attributed to mutations in 1 of 6 genes, particularly *POMT1*, *POMT2*, and *FKPR*, which are involved in the most severe form of  $\alpha$ -dystroglycanopathy, Walker-Warburg syndrome.<sup>16</sup> However, if a dystroglycanopathy or muscular dystrophy panel is used to identify the causative genetic variant in cobblestone lissencephaly, the diagnosis may be missed.<sup>15</sup> Indeed, one of our subjects with postnatal cobblestone lissencephaly had muscular dystrophy gene panel testing, not including all of the tubulin genes, which was negative for an explanatory mutation; this case is now the subject of re-evaluation with WES. Another (case 16) had initially negative genomic testing findings following pregnancy termination, with cobblestone lissencephaly diagnosed at postmortem examination; a diagnosis of a *TUBA1A* pathogenic variant in this fetus was only made later, following the neonatal death of a younger sibling diagnosed with this pathogenic variant (case 17). In this case, the presumption is that one of the parents has germline mosaicism, but this has not yet been investigated with genomic testing. Genetic re-evaluation of fetuses with structural brain abnormalities is important.

Our study has limitations. The retrospective methodology of case identification and search terms used may have biased our results by finding what we were suspecting, and there was the risk that other less common causes of GE abnormality have been overlooked. However, it was not feasible for participating sites to review their entire fetal MR imaging database in search of potential cases for this exploratory study. We sought to maximize the yield of database review by directing our search. In addition, fetuses with GE abnormalities but no genetic testing or postnatal outcome data were, a priori, not included in the study, introducing possible selection bias.

## CONCLUSIONS

Our work will raise awareness of the radiologic appearance of the abnormal fetal GE and the associated malformations. It will thus facilitate prenatal counseling and identification of further genetic causes for this disorder. Increasing access to genomic testing for prenatal cases will increase genetic diagnoses in fetuses presenting with features suggestive of a GE disorder, and improvements in turnaround time of results of such testing will allow genomic testing results in this setting to guide decision-making in pregnancy. Information on the genotype-phenotype correlation in this group of patients will continue to improve and inform future work in this area.

Disclosures: Stacy K. Goergen—*RELATED: Grant:* Royal Australian and New Zealand College of Radiologists, *Comments:* We received a grant of A\$5000 (3860.50 US dollars) from the 2020 Royal Australian and New Zealand College of Radiologists Research Grant funding round to support the conduct and publication of this study. The grant disbursement will be managed by the Monash University School of Clinical Sciences at Monash Medical Center, Clayton, Victoria, Australia.\* Michael Fahey—*UNRELATED: Board Membership:* Australian New Zealand Child Neurology Society, *Comments:* voluntary board membership; *Expert Testimony:* multiple expert testimonies with no influence over the work; *Grants/Grants Pending:* NHMRC, CPA, *Comments:* no influence over the work; *Stock/Stock Options:* Sigma Pharmaceuticals, *Comments:* of no influence over the work. Laura Fender—*UNRELATED: Employment:* hospital consultant radiologist, *Comments:* full-time employment at Public Hospital; Sir Charles Gairdner Hospital, Perth, Western Australia, Australia; King Edward Memorial Hospital, Perth, Western Australia, Australia. Jason R. Pinner—*UNRELATED: Employment:* Sydney Children's Hospital. Andrea Righini—*UNRELATED: Expert Testimony:* 2396.39 US dollars paid to the author's institution, *Comments:* Expert testimony in medicolegal cases. \*Money paid to the institution.

## REFERENCES

1. Ulfig N. **Ganglionic eminence of the human fetal brain: new vistas.** *Anat Rec* 2002;267:191–95 CrossRef Medline
2. Del Bigio MR. **Cell proliferation in human ganglionic eminence and suppression after prematurity-associated haemorrhage.** *Brain* 2011;134:1344–61 CrossRef Medline
3. Vasung L, Lepage C, Rados M, et al. **Quantitative and qualitative analysis of transient fetal compartments during prenatal human brain development.** *Front Neuroanat* 2016;10:11 CrossRef Medline
4. Righini A, Frasson C, Inverardi F, et al. **Bilateral cavitations of ganglionic eminence: a fetal MR imaging sign of halted brain development.** *AJNR Am J Neuroradiol* 2013;34:1841–45 CrossRef Medline
5. Righini A, Cesaretti C, Conte G, et al. **Expanding the spectrum of human ganglionic eminence region anomalies on fetal magnetic resonance imaging.** *Neuroradiology* 2016;58:293–300 CrossRef Medline
6. Boitor-Borza D, Kovacs T, Stamatiou F. **Ganglionic eminence within the early developing brain visualised by 3D transvaginal ultrasound.** *Med Ultrason* 2015;17:289–94 CrossRef Medline
7. Prefumo F, Petrilli G, Palumbo G, et al. **Prenatal ultrasound diagnosis of cavitation of the ganglionic eminence.** *Ultrasound Obstet Gynecol* 2019;54:558–60 CrossRef Medline
8. Pooh RK. **Normal ganglionic eminence and blighted ganglionic eminence in neuronal migration disorder cases detected by transvaginal neuroscan.** In: *Proceedings of 27th World Congress on Ultrasound in Obstetrics and Gynecology*, Vienna, Austria; September 16–19, 2017
9. Scarabello M, Righini A, Severino M, et al. **Ganglionic eminence anomalies and coexisting cerebral developmental anomalies on fetal MR imaging: Multicenter-based review of 60 cases.** *AJNR Am J Neuroradiol* 2021;42:1151–56 CrossRef Medline
10. Best S, Wou K, Vora N, et al. **Promises, pitfalls and practicalities of prenatal whole exome sequencing.** *Prenat Diagn* 2018;38:10–19 CrossRef Medline

11. Pratt M, Garritty C, Thuku M, et al. **Application of exome sequencing for prenatal diagnosis: a rapid scoping review.** *Genet Med* 2020;22:1925–34 CrossRef Medline
12. Richards S, Aziz N, Bale S, et al. ACMG Laboratory Quality Assurance Committee. **Standards and guidelines for the interpretation of sequence variants: a joint consensus recommendation of the American College of Medical Genetics and Genomics and the Association for Molecular Pathology.** *Genet Med* 2015;17:405–24 CrossRef Medline
13. Kline-Fath B, Bulas D, Bahado-Singh R. *Fundamental and Advanced Fetal Imaging Ultrasound and MRI.* Wolters Kluwer Health; 2015
14. Poretti A, Blaser SI, Lequin MH, et al. **Neonatal neuroimaging findings in inborn errors of metabolism.** *J Magn Reson Imaging* 2013;37:294–312 CrossRef Medline
15. Powis Z, Chamberlin AC, Alamillo CL, et al. **Postmortem diagnostic exome sequencing identifies a de novo TUBB3 alteration in a newborn with prenatally diagnosed hydrocephalus and suspected Walker-Warburg syndrome.** *Pediatr Dev Pathol* 2018;21:319–23 CrossRef Medline
16. Devisme L, Bouchet C, Gonzalès M, et al. **Cobblestone lissencephaly: neuropathological subtypes and correlations with genes of dystroglycanopathies.** *Brain* 2012;135:469–82 CrossRef Medline



# Diffusion MRI Microstructural Abnormalities at Term-Equivalent Age Are Associated with Neurodevelopmental Outcomes at 3 Years of Age in Very Preterm Infants

M.N. Parikh, M. Chen, A. Braimah, J. Kline, K. McNally, J.W. Logan, L. Tamm, K.O. Yeates, W. Yuan, L. He, and N.A. Parikh



## ABSTRACT

**BACKGROUND AND PURPOSE:** Microstructural white matter abnormalities on DTI using Tract-Based Spatial Statistics at term-equivalent age are associated with cognitive and motor outcomes at 2 years of age or younger. However, neurodevelopmental tests administered at such early time points are insufficiently predictive of mild-moderate motor and cognitive impairment at school age. Our objective was to evaluate the microstructural antecedents of cognitive and motor outcomes at 3 years' corrected age in a cohort of very preterm infants.

**MATERIALS AND METHODS:** We prospectively recruited 101 very preterm infants (<32 weeks' gestational age) and performed DTI at term-equivalent age. The Differential Ability Scales, 2nd ed, Verbal and Nonverbal subtests, and the Bayley Scales of Infant and Toddler Development, 3rd ed, Motor subtest, were administered at 3 years of age. We correlated DTI metrics from Tract-Based Spatial Statistics with the *Bayley Scales of Infant and Toddler Development*, 3rd ed, and the Differential Ability Scales, 2nd ed, scores with correction for multiple comparisons.

**RESULTS:** Of the 101 subjects, 84 had high-quality DTI data, and of these, 69 returned for developmental testing (82%). Their mean (SD) gestational age was 28.4 (2.5) weeks, and birth weight was 1121.4 (394.1) g. DTI metrics were significantly associated with Nonverbal Ability in the corpus callosum, posterior thalamic radiations, fornix, and inferior longitudinal fasciculus and with Motor scores in the corpus callosum, internal and external capsules, posterior thalamic radiations, superior and inferior longitudinal fasciculi, cerebral peduncles, and corticospinal tracts.

**CONCLUSIONS:** We identified widespread microstructural white matter abnormalities in very preterm infants at term that were significantly associated with cognitive and motor development at 3 years' corrected age.

**ABBREVIATIONS:** Bayley-III = Bayley Scales of Infant and Toddler Development, 3rd ed; CA = corrected age; DAS-II = Differential Ability Scales, 2nd ed; FA = fractional anisotropy; IFOF = inferior fronto-occipital fasciculi; ILF = inferior longitudinal fasciculus; MD = mean diffusivity; PTR = posterior thalamic radiations

Premature birth is associated with a significantly increased risk of brain abnormalities and long-term neurodevelopmental impairment. Injuries or maturational delays affecting the WM are observed in 50%–80% of very preterm infants.<sup>1–3</sup> These abnormalities are associated with serious neurodevelopmental impairment.<sup>1,3,4</sup> However, such abnormalities are challenging to detect using

conventional MR imaging techniques alone. Fortunately, DTI, a specialized form of MR imaging that can sensitively query the brain's microstructure, offers a novel approach for identifying these WM injuries. In preterm brains, the evolution of fractional anisotropy (FA) and mean diffusivity (MD), 2 metrics derived from DTI, varies from that of normative populations, and underlying brain injury may lead to neurodevelopmental impairment later in life.<sup>4–6</sup>

Functional MR imaging with the FMRIB Tract-Based Spatial Statistics (TBSS; <http://fsl.fmrib.ox.ac.uk/fsl/fslwiki/TBSS>) tool uses observer-independent voxelwise statistical analysis to process the complex information contained within

Received October 16, 2020; accepted after revision February 18, 2021.

From the Perinatal Institute (M.N.P., J.K., L.H., N.A.P.), Imaging Research Center (M.C., A.B., W.Y.), and Center for ADHD (L.T.), Cincinnati Children's Hospital Medical Center, Cincinnati, Ohio; Department of Electronic Engineering and Computer Science (M.C.), College of Engineering and Applied Science, University of Cincinnati, Cincinnati, Ohio; Center for Perinatal Research (K.M., J.W.L.), The Research Institute at Nationwide Children's Hospital, Columbus, Ohio; Department of Psychology (K.O.Y.), Alberta Children's Hospital Research Institute and Hotchkiss Brain Institute, University of Calgary, Alberta, Canada; and Departments of Radiology (W.Y.) and Pediatrics (L.T., L.H., N.A.P.), University of Cincinnati College of Medicine, Cincinnati, Ohio.

This work was supported by National Institutes of Health grants R01NS094200 (to N.A.P.), R01NS096037 (to N.A.P.), and R21HD094085 and a Trustee Grant from the Cincinnati Children's Hospital Medical Center (to L.H.).

Please address correspondence to Nehal A. Parikh, DO, MS, Cincinnati Children's Hospital, 3333 Burnet Ave, MLC 7009, Cincinnati, OH 45229; e-mail: [Nehal.Parikh@cchmc.org](mailto:Nehal.Parikh@cchmc.org)

Indicates open access to non-subscribers at [www.ajnr.org](http://www.ajnr.org)

Indicates article with online supplemental data.

<http://dx.doi.org/10.3174/ajnr.A7135>

diffusion-weighted images.<sup>4-16</sup> TBSS can be used to identify specific WM tracts and structures in the infant brain that correlate with later developmental outcomes.<sup>8,10,13-15</sup> Previous studies have used TBSS to objectively assess WM microstructure following clinical events such as infection, sports injury, or preterm brain injury (eg, intraventricular hemorrhage) and to relate the associated WM alterations to outcomes.<sup>9,11,16-19</sup> In addition, studies have used TBSS to identify brain regions and tracts in which FA significantly correlates with cognitive and motor outcomes at 2 years of age or younger.<sup>10,13,15</sup> These studies have consistently concluded that higher FA is associated with better motor, cognitive, and language functioning.

Past studies emphasizing the value of TBSS correlated DTI parameters with neurodevelopmental outcomes derived from the Bayley Scales of Infant and Toddler Development, 3rd ed (Bayley-III) collected at 2 years of age or younger. Such standardized assessments are administered between 18 and 24 months of age, representing the earliest time point at which cognitive, language, and motor development can be reliably ascertained. However, assessment at these earliest ages is not necessarily predictive of school age outcomes.<sup>20-22</sup> For example, the Bayley-III Motor subscale at 2 years of age significantly underestimates rates of motor impairment at 4 years of age in preterm infants.<sup>22</sup> Spencer-Smith et al<sup>23</sup> showed that cognitive delay, as assessed by the Bayley-III administered at 2 years of age, was not strongly associated with cognitive impairment at 4 years of age as assessed by the Differential Ability Scales, 2nd ed (DAS-II).<sup>24</sup> We propose that correlating FA from term-equivalent age MR imaging with 3-year outcomes may provide a more robust understanding of the early changes in WM microstructure that are also significantly associated with cognitive development.

Our objective was to test the hypothesis that WM microstructure, assessed using TBSS at term-corrected age (CA), is associated with neurodevelopmental performance at 3 years' CA in a regional cohort of very preterm infants.

## MATERIALS AND METHODS

### Participants

All infants born at 31 weeks' gestational age or earlier between November 2014 and March 2016 who were cared for in 1 of 4 level III neonatal intensive care units in the Columbus, Ohio, region were eligible for inclusion, with a few exceptions. Infants with congenital or chromosomal anomalies that affected their central nervous system and infants who remained hospitalized at 44 weeks' postmenstrual age unless cared for at the Nationwide Children's Hospital, the sole site of imaging, were excluded ( $n=7$ ). We also excluded infants with severe ventriculomegaly, because it can interfere with proper MR imaging registration ( $n=9$ ). We prospectively enrolled 101 infants from the Nationwide Children's Hospital, Ohio State University Medical Center, Riverside Hospital, and Mount Carmel St. Ann's Hospital, which together care for approximately 80% of all infants born very preterm in the Columbus, Ohio, region. Data were collected between January 2015 and July 2018. The institutional review board of the Nationwide Children's Hospital approved the study. Written informed consent was obtained from a parent or guardian of every study infant.

### MR Imaging Acquisition

For all infants, structural MR imaging was performed at the Nationwide Children's Hospital using a 3T Magnetom Skyra MR imaging scanner (Siemens) and a 32-channel phased array head coil. All scans were completed between 39 and 44 weeks' postmenstrual age. Inpatients were transported to MR imaging by a skilled neonatal nurse and neonatologist. Infant heart rate and oxygen saturation were monitored during every scan. All imaging was performed during natural sleep and without sedation by feeding infants immediately before the scan, providing hearing protection, and using an immobilization device. All infants were imaged safely without any adverse events using the following parameters—axial T2-weighted: TE = 147 ms, TR = 9500 ms, flip angle = 150°, resolution =  $0.93 \times 0.93 \times 1.0 \text{ mm}^3$ , scan time = 4 minutes 9 seconds.

Single-shot echo-planar diffusion MR imaging with 64 noncollinear gradient directions was performed with parameters that varied among subjects. To mitigate the variability in the FA/MD maps caused by unwanted variability arising from the different b-shells and TE/TR values across subjects, we used an advanced harmonization method using ComBat, a batch-effect correction tool with an open-source Matlab (MathWorks) implementation.<sup>25,26</sup> Each subject was assigned a "batch" value based on having the same b-shell ( $b=800$  or  $b=2000$ ) and highly similar TE/TR parameters (maximum difference of  $\pm 3/1600$  for TE/TR parameters within the same batch). We used 3 batches: batch 1 (TR = 7500 ms, TE = 77 ms, flip angle = 90°, resolution =  $1.97 \times 1.97 \times 2.00 \text{ mm}$ , b-value = 800 s/mm<sup>2</sup>); batch 2 (mean TR = 9553 ms, mean TE = 89 ms, flip angle = 90°, resolution =  $2.23 \times 2.23 \times 2.00 \text{ mm}$ , b-value = 2000 s/mm<sup>2</sup>); and batch 3 (mean TR = 3996 ms, TE = 104 ms, flip angle = 80°, resolution =  $2 \times 2 \times 2 \text{ mm}$ , b-value = 2000 s/mm<sup>2</sup>).

### Baseline Clinical and MR Imaging Variables

As previously described,<sup>27</sup> all MR imaging scans were read by pediatric neuroradiologists qualitatively for the degree of brain injury/maturation and objective quantitative biometric measurements, using a standardized scoring system per Kidokoro et al.<sup>28</sup> This approach yielded a global brain abnormality score, which was categorized as normal (total score, 0–3), mild (total score, 4–7), moderate (total score, 8–11), or severe abnormality (total score,  $\geq 12$ ). All readings were unblinded to clinical history but blinded to outcomes.

Severe bronchopulmonary dysplasia was defined using the National Institutes of Health definition:<sup>29</sup> the need for  $>30\%$  effective fractional inspiratory oxygen concentration via nasal cannula or the need for any positive-pressure support at 36 weeks' postmenstrual age. We defined severe retinopathy of prematurity as any of the following: stage 3 retinopathy of prematurity (international classification<sup>30</sup>), any stage retinopathy of prematurity with plus disease (presence of dilated and tortuous posterior pole vessels), or any prethreshold retinopathy of prematurity requiring treatment with laser ablation or bevacizumab intraocular injections.

### Data Preprocessing and Harmonization

For each subject, eddy current distortions were corrected by registering the diffusion-weighted images to the B0 image, and skulls were removed using the FSL Brain Extraction Tool ([1536 Parikh Aug 2021 www.ajnr.org](http://</a></p></div><div data-bbox=)

# Clinical characteristics for very preterm infants with neurodevelopmental assessments at 3 years' CA

Baseline Characteristics <sup>a</sup>	Final Cohort (n = 69)	Excluded (n = 32)	P
Maternal age (mean) (SD) (yr)	30.2 (6.0)	30.1 (6.1)	.96
Antenatal corticosteroid therapy (any)	64 (92.8%)	23 (71.9%)	.01
Multiple gestation	24 (34.8%)	9 (28.1%)	.51
Male sex	39 (56.5%)	15 (46.9%)	.37
Gestational age (mean) (SD) (wk)	28.4 (2.5)	28.1 (2.5)	.68
Birth weight (mean) (SD) (g)	1121.4 (394.1)	1131.6 (398.1)	.91
5-Minute Apgar score <5	12 (17.4%)	9 (29.0%) <sup>b</sup>	.20
Late-onset sepsis (culture-positive)	9 (13.0%)	4 (12.5%)	1.00
Severe bronchopulmonary dysplasia	22 (31.9%)	10 (31.3%)	1.00
Severe retinopathy of prematurity	8 (11.6%)	1 (3.1%)	.27
Surgery requiring general anesthesia	9 (13.0%)	7 (21.9%)	.26
MR imaging global brain abnormality score (median) (range)	2 (0–9)	3 (0–23)	.51
Postmenstrual age at MR imaging (mean) (SD) (wk)	40.4 (0.6)	40.6 (0.8)	.35
Cerebral palsy diagnosis, cases/total (%)	7/65 (10.8%)	2/20 (10.0%)	1.00

<sup>a</sup> All data are No. (%) unless otherwise stated.

<sup>b</sup> Data missing for 1 subject born at home.

fsl.fmrib.ox.ac.uk/fsl/fslwiki/BET).<sup>31,32</sup> For all subjects before ComBat, we first nonlinearly warped their FA and MD maps to a common neonatal template image using Advanced Normalization Tools (ANTs; <http://stnava.github.io/ANTs/>).<sup>33</sup> This step was necessary because ComBat performs batch harmonization by fitting a model at the voxel level. After ComBat harmonization of the FA/MD plots between batches was complete, we verified that the FA/MD histograms between batches were aligned and that the skew of Bland-Altman plots of the FA/MD values across batches had been significantly reduced, similar to Fortin et al.<sup>25</sup>

## Neurodevelopmental Outcomes

At 3 years' CA, the DAS-II was administered by a psychometrician blinded to the child's history and imaging results. The administered DAS-II subtests included Verbal Comprehension, Naming Vocabulary, Picture Similarities, and Pattern Construction. Verbal Comprehension and Naming Vocabulary are combined to derive the Verbal Ability score, which evaluates verbal concepts and knowledge. Picture Similarities and Pattern Construction make up the Nonverbal Ability score, which estimates nonverbal inductive reasoning. The DAS-II yields age-standardized scores (mean = 100 [SD, 15]), with higher scores indicating better cognitive functioning.<sup>24</sup> The psychometric properties of the DAS-II are strong in the 3- to 3.5-year age range, with high internal reliability coefficients and test-retest reliability.<sup>34</sup> In terms of validity, DAS-II scores are highly consistent with other standardized cognitive measures.

The Bayley-III is also a widely used and validated test that yields age-standardized scores (mean = 100; [SD, 15]), with higher scores indicating better motor functioning.<sup>35</sup>

## Tract-Based Spatial Statistics

Voxelwise statistical analyses of the FA data were performed using TBSS. TBSS projects all subjects' FA data onto a mean FA tract skeleton, before applying voxelwise cross-subject statistics. Each subject's brain was aligned to a neonatal-optimized study-specific template created from all 84 study subjects.<sup>12</sup> The FA template was created using the multivariate template construction 2 protocol in ANTs, in which symmetric group normalization is used to create a group template and deform each image to that template, updating the group template after each

deformation.<sup>33</sup> We repeated this procedure until all registrations to the group template yielded minimally deformed transformations.<sup>36</sup> Next, we produced a mean FA skeleton representing the centers of all tracts common to the group. Each subject's aligned FA data were then projected onto this skeleton with a threshold of 0.15, and the resulting data were fed into voxelwise cross-subject statistics, which determined the correlation between FA and continuous scores from the Bayley-III and DAS-II, adjusted for postmenstrual age at MR imaging and sex. This was done using the FSL Randomize tool (<https://fsl.fmrib.ox.ac.uk/fsl/fslwiki/Randomize>) with the threshold-free cluster enhancement option with 5000 permutations, followed by correction for multiple comparisons. Significant voxels were defined via a *P* value of <.05 following this correction. The same analysis was performed for MD.

## Statistical Analysis

We compared the baseline characteristics of infants with and without 3 years' CA data using independent samples *t* tests, Mann-Whitney *U* tests, or Fisher exact tests, as appropriate. Following TBSS, we verified the associations shown using linear regression. For each image, we extracted the mean FA/MD for all voxels that were significantly associated with each developmental score. A linear regression was then used to examine the relationship between the mean FA/MD values from all these significant voxels combined and the associated outcome score. All analyses were also corrected for multiple comparisons. We used the traditional 2-sided *P* value < .05 to indicate statistical significance. All analyses were performed using STATA 16.0 (StataCorp).

## RESULTS

Of the original 101 subjects, a total of 17 were excluded due to unusable scans: Fourteen did not fit into the 3 established harmonized batches, 2 had missing T2 images, and 1 was excluded due to poor image quality. Of the 84 subjects with harmonized DTI data, 69 returned for developmental testing (82%). Their mean (SD) gestational age was 28.4 (2.5) weeks, and birth weight was 1121.4 (394.1) g (Table). Of these 69 infants, 7 (10.1%) had moderate brain abnormalities (global brain abnormality score = 8–11), 15 (21.7%) had mild abnormalities (score = 4–7), and 47 infants (68.1%) had normal (score = 0–3) structural MR imaging findings. Within that



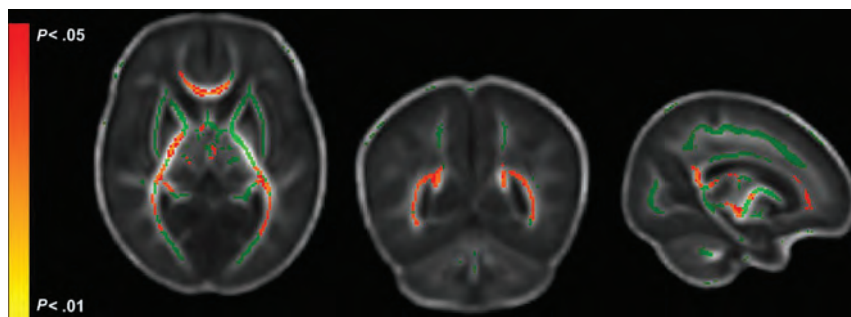


**FIG 1.** FA regions significantly correlated with DAS-II Nonverbal scores. The mean FA skeleton is shown in green with regions of significant correlations highlighted in red. Regions significantly correlated with Nonverbal outcome include the genu, splenium, and body of the corpus callosum; the posterior thalamic radiations; the posterior limb of the internal capsule; and the inferior longitudinal fasciculi.

same 69 infants, 7 (10.8%) were diagnosed with cerebral palsy: 4 with spastic diplegia, 1 with spastic hemiplegia, 1 with spastic quadriplegia, and 1 for whom a classification was not made. Infants with neurodevelopmental outcome data did not differ significantly from those without outcomes except on maternal antenatal steroids status (Table). At 3 years' CA, the mean (SD) DAS-II Nonverbal and Verbal scores were 98.04 (18.05) and 89.16 (22.01), respectively. Bayley-III Motor outcomes were assessed at 3 years' CA in most infants, except for 10 who were tested between 25.8 and 30.8 months' CA. The mean (SD) age at follow-up was 35.6 (3.7) months' CA in the 67 infants with Motor scores. The mean (SD) Bayley-III Motor score was 90.87 (13.03).

In TBSS analyses correlating whole-brain FA with DAS-II developmental scores at 3 years' CA, adjusted for sex and postmenstrual age at MR imaging and corrected for the false discovery rate, several significant positive correlations between FA and Nonverbal Ability scores were identified. Nonverbal scores were significantly correlated with FA in the genu, splenium, and body of the corpus callosum; the posterior thalamic radiations (PTR); the fornix; and the inferior longitudinal fasciculus (ILF)/inferior fronto-occipital fasciculi (IFOF) (Fig 1, Online Supplemental Data). Verbal scores were not significantly correlated with FA in any brain voxels. There were no significant negative correlations with either outcome. Whole-brain MD was not significantly associated with DAS-II scores after adjustment for covariates. The linear regression analyses showed that the mean FA from all significant TBSS voxels explained 15% ( $P = .001$ ) of the variance in the DAS-II Nonverbal scores at 3 years' CA (Fig 2).

Bayley-III Motor scores were significantly positively correlated with FA in the genu, splenium, and body of the corpus callosum; posterior limb of the internal capsule; anterior limb of the internal capsule; external capsule; PTR; superior longitudinal fasciculi; ILF/IFOF; cerebral peduncles; and corticospinal tracts (Fig 3, Online Supplemental Data). FA was not negatively correlated with Motor scores in any region. We also identified several significant negative correlations between MD and motor development in approximately the same regions as those correlated with FA (Fig 3, Online Supplemental Data). There were no positive correlations between MD in any region and Motor scores. Linear regression analysis showed that the mean FA and MD from all significant voxels,

respectively, explained 20% ( $P < .001$ ) and 25% ( $P < .001$ ) of the variance in Bayley-III Motor outcomes at 3 years' CA (Fig 2).

## DISCUSSION

We used TBSS, a well-established, objective, whole-brain tool, to quantify microstructural development in infants born very preterm at term-equivalent age and to identify brain regions in which 2 DTI metrics were associated with cognitive and motor development at 3 years' CA. Using voxelwise correlations between FA/MD and DAS-II Nonverbal and Bayley-III Motor scores, we identified several WM regions in

which FA and MD were associated with neurodevelopmental outcomes. In comparison with prior studies that evaluated neurodevelopment at an earlier age (18–24 months' CA),<sup>10,13,15,37</sup> we were able to correlate early WM development with more reliable measures of cognitive and motor outcomes at 3 years' CA. We identified several regions of WM in which FA at term was significantly positively correlated with 3-year cognitive and motor development in very preterm infants. This finding validates prior findings correlating increased FA with better cognitive and motor outcomes, confirming that greater microstructural development and integrity is associated with better function even at older ages. Previous studies have shown that decreased MD or its components, axial and radial diffusivity, were associated with better motor development.<sup>10,15</sup> However, in this study, we did not identify any significant relationship between MD and cognitive development. FA is known to be a useful metric in neonates due to its ability to assess regional myelination. MD, being an aggregate of both myelination and axonal integrity, has not been strongly associated with cognitive development, which has been significantly more difficult to predict than motor development.

The DAS-II is a standardized, well-validated test of verbal and nonverbal abilities, both of which are keys to outcomes such as academic success and behavioral functioning.<sup>38</sup> We found that the genu, splenium, and body of the corpus callosum; PTR; posterior limb of the internal capsule; fornix; and ILF/IFOF are important for nonverbal cognitive abilities as assessed by the DAS-II at 3 years' CA. Our findings are generally consistent with studies that examined Bayley-III cognitive subscores in younger children at or before 2 years' CA. Specifically, the 3 largest studies reported an association between FA of the corpus callosum,<sup>10,13,15</sup> posterior limb of the internal capsule,<sup>13,15</sup> and/or PTR<sup>13</sup> with Bayley-III cognitive outcomes at 18–24 months of age. However, neither the FA of the ILF/IFOF nor the fornix was explicitly linked to cognitive development, as in our study. The ILF/IFOF fibers overlap posteriorly and are, therefore, not easy to distinguish using TBSS, and it is still debated whether the IFOF is a distinct pathway or just a portion of a bigger bundle that includes the ILF.<sup>39</sup> Functionally, both tracts are known to be important for several higher-order cognitive processes.<sup>34,35</sup> The fornix is considered a part of the limbic system and is associated with memory and emotions.<sup>36</sup>

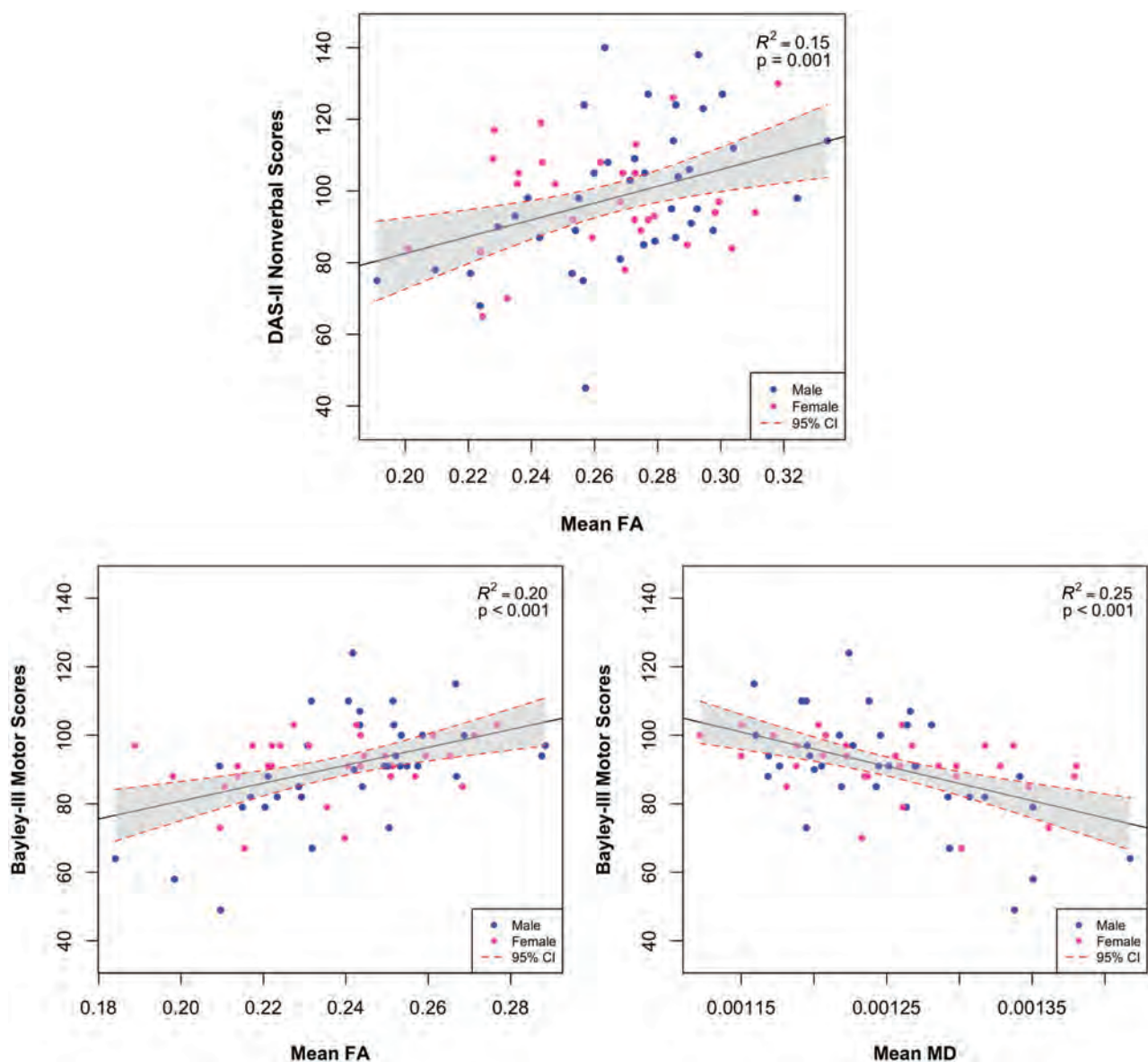


**FIG 2.** Relationships between diffusion metrics and neurodevelopmental outcomes. The linear relationship between mean FA or MD of all voxels identified by TBSS is significantly associated with developmental outcomes, including the Nonverbal score on the DAS-II or Motor scores on the Bayley-III at 3 years' corrected age. The *dashed red lines* and *shaded region* represent the 95% confidence intervals for the linear relationship.

For the DAS-II Verbal Abilities outcome, we did not identify any correlations with white matter microstructure. Two prior studies of TBSS-derived DTI metrics and language development at earlier ages also did not find significant associations.<sup>15,37</sup> In a large cohort, Barnett et al<sup>13</sup> identified limited regions where FA was significantly associated with Bayley language scores. Our findings, using arguably more accurate testing at 3 years of age, suggest that TBSS-assessed microstructure is not a strong predictor of language outcome.

We identified several significant WM regions that correlated with Bayley-III Motor scores at 3 years of age that have known associations with sensorimotor function, including the corpus callosum, corticospinal tract, corona radiata, PTR, and superior longitudinal fasciculi. All these regions, except the PTR, were also identified by a prior neonatal TBSS study that followed infants until 24 months' CA.<sup>10</sup> The other 2 neonatal studies with follow-up before 24

months' CA also did not identify the PTR or the superior longitudinal fasciculi.<sup>13,15</sup> In older children with cerebral palsy, injury to the PTR appears to be as common or more common than injury to the corticospinal tract.<sup>37,38</sup> However, some studies have found no relationship between FA in the PTR at term-equivalent age and motor outcomes.<sup>40,41</sup> Similarly, prior studies have not shown consistently significant relationships between superior longitudinal fasciculi integrity and cerebral palsy.<sup>42,43</sup> Because up to 50% of children with cerebral palsy also have associated cognitive impairment, it is possible that tracts such as the PTR and superior longitudinal fasciculi are identified as significant because of their overlap and known association with cognitive impairment.<sup>42,43</sup> Indeed, FA in the PTR at term was also associated with nonverbal scores in our cohort. Similarly, the ILF and IFOF were significantly associated with Motor and Nonverbal scores.

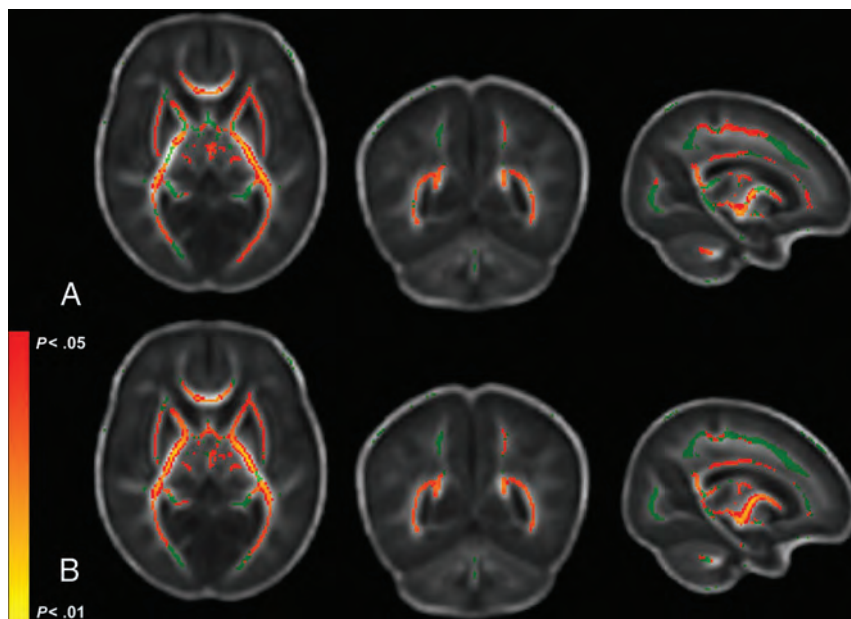


**FIG 3.** FA and MD regions significantly correlated with Bayley-III Motor scores. The mean FA skeleton is shown in green with regions of significant correlations highlighted in red. *A*, Significant FA regions include the corona radiata, corpus callosum, posterior and anterior limbs of the internal capsule, external capsule, posterior thalamic radiation, fornix, superior longitudinal fasciculus, inferior fronto-occipital fasciculus, cerebral peduncles, and corticospinal tracts. *B*, Significant MD regions closely match significant FA regions.

We speculate that some of the inconsistencies in the literature result from differences between the Bayley-III and the DAS-II. In a study of extremely preterm infants, the Bayley-III cognitive and language scores at 2 years of age were not strongly predictive of scores on the DAS-II at 4 years of age (24%–37% variance explained) or on the Wechsler Intelligence Scale for Children at 6 years of age (24%–26% variance explained).<sup>23,44</sup> The DAS-II generally has high correlations with the Wechsler scales in infants, while the Bayley-III has been shown to be a poor predictor of school-age cognitive impairment in extremely preterm children.<sup>20,21,34</sup> These findings are not surprising considering that cognitive/language functions are just beginning to manifest at 2 years of age; therefore, they are difficult to accurately evaluate at this early time point, and the Bayley-III underestimates scores and impairment as assessed by the Bayley-II.<sup>45,46</sup> Even the Bayley-III Motor subscale at 2 years of age significantly underestimates rates of motor impairment at 4 years of age in preterm infants.<sup>22</sup> Overall, these prior studies suggest a need to shift to more accurate test instruments and increase the follow-up testing period to at least 3 years of age for studies of preterm infants.

A strength of our study is that it is population-based, unlike most prior neonatal studies that have been derived only from tertiary care referral hospitals, thus increasing the generalizability of our findings. We also performed developmental testing at 36 months' CA. This allowed us to identify more robust structure-function relationships than neonatal studies that reported outcomes before 36 months. A weakness of our study is that we did not examine the effect of the postnatal environmental factors on developmental outcomes. Prior studies have shown a strong relationship between maternal education and socioeconomic status

and neurodevelopmental scores. In addition, the heterogeneity of our sample with regard to imaging parameters, even with extensive harmonization, may still have impacted our results. A larger study, such as the one we are currently performing, is needed to validate our findings and improve the prediction of neurodevelopmental impairment using diffusion MR imaging and other advanced MR imaging modalities. Additionally, while TBSS offers a significant advantage in reliability and whole-brain assessment over ROI-based techniques, it is still based on tensor models, which can result in erroneously lower FA measurements in regions of crossing fibers (eg, the centrum semiovale). Automated, whole-brain, probabilistic tractography methods using higher-order diffusion models, which are currently lacking for neonates, are needed to overcome this limitation.

## CONCLUSIONS

In a cohort of very preterm infants, we validated the presence of widespread

microstructural perturbations, particularly in FA, from several brain regions that were associated in previous studies with neurodevelopmental outcomes at 2 years of age or younger. We used the DAS-II scores at 3 years' CA to validate these findings and also identified significant associations in a few previously unreported white matter regions. These diffusion MR imaging biomarkers can be potentially combined with additional promising biomarkers from other advanced MR imaging modalities to enhance the prediction of long-term neurodevelopmental outcomes in very preterm infants.

## ACKNOWLEDGMENTS

We thank Jennifer Notestine, RN, and Valerie Marburger, NNP, for serving as the study coordinators; Josh Goldberg, MD, for assisting with recruitment; and Mark Smith, MS, for serving as the study MR imaging technologist. We are also grateful to the families, neonatal intensive care unit personnel, and High-Risk Clinic staff who made this study possible.

**Disclosures:** Milan N. Parikh—*RELATED:* Grant: National Institutes of Health.\* Kelly McNally—*RELATED:* Other: Cincinnati Children's Hospital, *Comments:* A subcontract was set up from the study Principal Investigator at Cincinnati Children's Hospital to support the cost of data collection at my site, Nationwide Children's Hospital.\* John W. Logan—*RELATED:* Grant: The Nationwide Children's Hospital received grant support to conduct neurodevelopmental follow-up for this study, *Comments:* no conflict of interest.\* *UNRELATED:* Expert Testimony: I once provided expert testimony in a case in Florida, unrelated to this work; no conflict of interest. Leanne Tamm—*UNRELATED:* Employment: Cincinnati Children's Hospital Medical Center. Keith O. Yeates—*RELATED:* Grant: National Institutes of Health, *Comments:* The work was supported by the National Institute of Child Health and Human Development network.\* Lili He—*RELATED:* Grant: This study was supported by



the National Institutes of Health grant R21-HD094085.\* Nehal A. Parikh—RELATED: Grant: This study was supported by the National Institutes of Health grants R01-NS094200 and R01-NS096037.\* \*Money paid to the institution.

## REFERENCES

- Woodward LJ, Anderson PJ, Austin NC, et al. Neonatal MRI to predict neurodevelopmental outcomes in preterm infants. *N Engl J Med* 2006;355:685–94 CrossRef Medline
- Dyet LE, Kennea N, Counsell SJ, et al. Natural history of brain lesions in extremely preterm infants studied with serial magnetic resonance imaging from birth and neurodevelopmental assessment. *Pediatrics* 2006;118:536–48 CrossRef Medline
- Hintz SR, Barnes PD, Bulas D, et al. SUPPORT Study Group of the Eunice Kennedy Shriver National Institute of Child Health and Human Development Neonatal Research Network. Neuroimaging and neurodevelopmental outcome in extremely preterm infants. *Pediatrics* 2015;135:e32–42 CrossRef Medline
- Dudink J, Kerr JL, Paterson K, et al. Connecting the developing preterm brain. *Early Hum Dev* 2008;84:777–82 CrossRef Medline
- Qiu A, Mori S, Miller MI. Diffusion tensor imaging for understanding brain development in early life. *Annu Rev Psychol* 2015;66:853–76 CrossRef Medline
- Caldinelli C, Froudust-Walsh S, Karolis V, et al. White matter alterations to cingulum and fornix following very preterm birth and their relationship with cognitive functions. *Neuroimage* 2017;150:373–82 CrossRef
- Adamson C, Yuan W, Babcock L, et al. Diffusion tensor imaging detects white matter abnormalities and associated cognitive deficits in chronic adolescent TBI. *Brain Inj* 2013;27:454–63 CrossRef Medline
- Anjari M, Srinivasan L, Allsop JM, et al. Diffusion tensor imaging with tract-based spatial statistics reveals local white matter abnormalities in preterm infants. *Neuroimage* 2007;35:1021–27 CrossRef Medline
- Myer GD, Yuan W, Barber FK, et al. The effects of external jugular compression applied during head impact exposure on longitudinal changes in brain neuroanatomical and neurophysiological biomarkers: a preliminary investigation. *Front Neurol* 2016;7:74 CrossRef Medline
- Van Kooij BJ, De Vries LS, Ball G, et al. Neonatal tract-based spatial statistics findings and outcome in preterm infants. *AJNR Am J Neuroradiol* 2012;33:188–94 CrossRef Medline
- Yuan W, Barber Foss KD, Thomas S, et al. White matter alterations over the course of two consecutive high-school football seasons and the effect of a jugular compression collar: a preliminary longitudinal diffusion tensor imaging study. *Hum Brain Mapp* 2018;39:491–508 CrossRef Medline
- Ball G, Counsell SJ, Anjari M, et al. An optimised tract-based spatial statistics protocol for neonates: applications to prematurity and chronic lung disease. *Neuroimage* 2010;53:94–102 CrossRef Medline
- Barnett ML, Tumor N, Ball G, et al. Exploring the multiple-hit hypothesis of preterm white matter damage using diffusion MRI. *Neuroimage Clin* 2018;17:596–606 CrossRef Medline
- Counsell SJ, Edwards AD, Chew AT, et al. Specific relations between neurodevelopmental abilities and white matter microstructure in children born preterm. *Brain* 2008;131:3201–08 CrossRef Medline
- Duerden EG, Foong J, Chau V, et al. Tract-based spatial statistics in preterm-born neonates predicts cognitive and motor outcomes at 18 months. *AJNR Am J Neuroradiol* 2015;36:1565–71 CrossRef Medline
- Glass TJ, Chau V, Grunau RE, et al. Multiple postnatal infections in newborns born preterm predict delayed maturation of motor pathways at term-equivalent age with poorer motor outcomes at 3 years. *J Pediatr* 2018;196:91–97.e1 CrossRef Medline
- Hollund IM, Olsen A, Skranes J, et al. White matter alterations and their associations with motor function in young adults born preterm with very low birth weight. *Neuroimage Clin* 2018;17:241–50 CrossRef Medline
- Merhar SL, Gozdas E, Tkach JA, et al. Functional and structural connectivity of the visual system in infants with perinatal brain injury. *Pediatr Res* 2016;80:43–48 CrossRef Medline
- Mürner-Lavanchy IM, Kelly CE, Reidy N, et al. White matter microstructure is associated with language in children born very preterm. *Neuroimage Clin* 2018;20:808–22 CrossRef Medline
- Hack M, Taylor HG, Drotar D, et al. Poor predictive validity of the Bayley Scales of Infant Development for cognitive function of extremely low birth weight children at school age. *Pediatrics* 2005;116:333–41 CrossRef Medline
- O'Shea TM, Joseph RM, Allred EN, et al. ELGAN Study Investigators. Accuracy of the Bayley-II mental development index at 2 years as a predictor of cognitive impairment at school age among children born extremely preterm. *J Perinatol* 2018;38:908–16 CrossRef Medline
- Spittle AJ, Spencer-Smith MM, Eeles AL, et al. Does the Bayley-III Motor Scale at 2 years predict motor outcome at 4 years in very preterm children? *Dev Med Child Neurol* 2013;55:448–52 CrossRef Medline
- Spencer-Smith MM, Spittle AJ, Lee KJ, et al. Bayley-III cognitive and language scales in preterm children. *Pediatrics* 2015;135:e1258–65 CrossRef Medline
- Elliott CD. Contemporary intellectual assessment: theories, tests, and issues. In: *Third*. New Guilford Press; 2012:336–56
- Fortin JP, Parker D, Tunç B, et al. Harmonization of multi-site diffusion tensor imaging data. *Neuroimage* 2017;161:149–70 CrossRef Medline
- Johnson WE, Li C, Rabinovic A. Adjusting batch effects in microarray expression data using empirical Bayes methods. *Biostatistics* 2007;8:118–27 CrossRef Medline
- Logan JW, Tan J, Skalak M, et al. Adverse effects of perinatal illness severity on neurodevelopment are partially mediated by early brain abnormalities in infants born very preterm. *J Perinatol* 2021;41:519–27 CrossRef Medline
- Kidokoro H, Neil JJ, Inder TE. New MR imaging assessment tool to define brain abnormalities in very preterm infants at term. *AJNR Am J Neuroradiol* 2013;34:2208–14 CrossRef Medline
- Jobe AH, Bancalari E. Bronchopulmonary dysplasia. *Am J Respir Crit Care Med* 2001;163:1723–29 CrossRef Medline
- International Committee for the Classification of Retinopathy of Prematurity. The international classification of retinopathy of prematurity. *Arch Ophthalmol* 2005;123:991–99 CrossRef Medline
- Andersson JL, Sotiropoulos SN. An integrated approach to correction for off-resonance effects and subject movement in diffusion MR imaging. *Neuroimage* 2016;125:1063–78 CrossRef Medline
- Smith SM. Fast robust automated brain extraction. *Hum Brain Mapp* 2002;17:143–55 CrossRef Medline
- Avants BB, Tustison NJ, Song G, et al. A reproducible evaluation of ANTs similarity metric performance in brain image registration. *Neuroimage* 2011;54:2033–44 CrossRef Medline
- Elliot CD. *Differential Ability Scales, 2nd ed: Introductory and Technical Handbook*. Psychological Corporation; 2007
- Bayley NB. *Bayley Scales of Infant and Toddler Development, 3rd ed: Technical Manual*. Psychological Corporation; 2006
- Avants BB, Yushkevich P, Pluta J, et al. The optimal template effect in hippocampus studies of diseased populations. *Neuroimage* 2010;49:2457–66 CrossRef Medline
- Skiöld B, Alexandrou G, Padilla N, et al. Sex differences in outcome and associations with neonatal brain morphology in extremely preterm children. *J Pediatr* 2014;164:1012–18 CrossRef Medline
- McGrew KS. CHC theory and the human cognitive abilities project: standing on the shoulders of the giants of psychometric intelligence research. *Intelligence* 2009;37:1–10 CrossRef
- Wahl M, Li YO, Ng J, et al. Microstructural correlations of white matter tracts in the human brain. *Neuroimage* 2010;51:531–41 CrossRef Medline
- Jiang H, Li X, Jin C, et al. Early diagnosis of spastic cerebral palsy in infants with periventricular white matter injury using diffusion tensor imaging. *AJNR Am J Neuroradiol* 2019;40:162–68 CrossRef Medline



41. Parikh NA, Hershey A, Altaye M. **Early detection of cerebral palsy using sensorimotor tract biomarkers in very preterm infants.** *Pediatr Neurol* 2019;98:53–60 CrossRef Medline
42. Thomas B, Eyssen M, Peeters R, et al. **Quantitative diffusion tensor imaging in cerebral palsy due to periventricular white matter injury.** *Brain* 2005;128:2562–77 CrossRef Medline
43. Arrigoni F, Peruzzo D, Gagliardi C, et al. **Whole-brain DTI assessment of white matter damage in children with bilateral cerebral palsy: evidence of involvement beyond the primary target of the anoxic insult.** *AJNR Am J Neuroradiol* 2016;37:1347–53 CrossRef Medline
44. Månsson J, Stjernqvist K, Serenius F, et al. **Agreement between Bayley-III measurements and WISC-IV measurements in typically developing children.** *J Psychoeduc Assess* 2019;37:603–16 CrossRef
45. Jary S, Whitelaw A, Walløe L, et al. **Comparison of Bayley-2 and Bayley-3 scores at 18 months in term infants following neonatal encephalopathy and therapeutic hypothermia.** *Dev Med Child Neurol* 2013;55:1053–9 CrossRef Medline
46. Sharp M, DeMauro SB. **Counterbalanced comparison of the BSID-II and Bayley-III at Eighteen to Twenty-two months corrected age.** *J Dev Behav Pediatr* 2017;38:322–9 CrossRef Medline

# Cystlike Lesions as a Late Sequela of Radiotherapy in Pediatric Patients

M.G.D. Veiga, I. Fragata, J. Passos, M. Alves, A.L. Papoila, and D. Salgado

## ABSTRACT

**BACKGROUND AND PURPOSE:** The developing nervous system is particularly vulnerable to late adverse effects of cranial radiation therapy, such as leukoencephalopathy, microbleeds, and cavernomas. Cystlike lesions have been rarely described and characterized in the literature. We aimed to characterize cystlike lesions, their risk factors, and association with other late adverse effects.

**MATERIALS AND METHODS:** Children treated for brain tumors during a 30-year period ( $n = 139$ ) were included. We documented imaging findings, focusing on cystlike lesion development and its relationship with clinical history and other imaging findings. Multivariable analysis was performed using logistic regression and negative binomial regression models.

**RESULTS:** Cystlike lesions developed in 16.5% of patients treated with radiotherapy, with a median of 2 years until the development of the first lesion. For every 4-year age increase, there were 50% decreased odds of developing lesions and a 50% decrease in the average count of lesions. Females demonstrated a 4.00 rate ratio of developing a higher number of lesions. Patients who underwent chemoradiotherapy had 3.20 increased odds of developing cystlike lesions compared with patients with radiation therapy alone. A larger proportion of patients treated with methotrexate (25%) developed cystlike lesions, but this was not statistically significant. Cystlike lesions tended to develop in cerebral locations where leukoencephalopathy was worse. A strong relationship was found between the development of cystlike lesions and leukoencephalopathy severity.

**CONCLUSIONS:** Cystlike lesions are frequent and under-reported late adverse effects of cranial radiation therapy in children. Younger age, chemoradiotherapy, and the severity of leukoencephalopathy represent risk factors for the development of cystlike lesions.

**ABBREVIATIONS:** CLL = cystlike lesions; LE = leukoencephalopathy; MTX = methotrexate; RT = radiotherapy

Central nervous system tumors are the most common solid tumors in children, accounting for up to 22% of tumors in patients between 0 and 14 years of age.<sup>1</sup> The 5-year relative cancer survival rate in these patients has been increasing in the past decades.<sup>2</sup> Childhood cancer therapy causes chronic health problems in almost 75% of survivors, which can become clinically visible several years after treatment and are frequently irreversible and progressive.<sup>1</sup>

Received January 12, 2021; accepted after revision March 8.

From the Department of Neuroradiology (M.G.D.V., I.F.), Hospital de São José, Centro Hospitalar Universitário de Lisboa Central, Lisboa, Portugal; Department of Epidemiological Analysis and Statistics (M.A., A.L.P.), Hospital Dona Estefânia, Centro Hospitalar Universitário de Lisboa Central, Lisboa, Portugal; and Department of Neurology (J.P., D.S.), Instituto Português de Oncologia de Lisboa Francisco Gentil, Lisboa, Portugal.

Please address correspondence to M.G.D. Veiga, MD, Department of Neuroradiology, Hospital de São José, Centro Hospitalar Universitário de Lisboa Central, R. José António Serrano, 1150-199 Lisboa, Portugal; e-mail: marcos.gil.d.veiga@gmail.com  
<http://dx.doi.org/10.3174/ajnr.A7156>

Late adverse effects are related to chemotherapy, radiation therapy (RT), or a combination of both.<sup>1,3,4</sup> These adverse effects of treatment are additive, with a higher disease burden in patients who had more aggressive therapies or were younger at diagnosis.<sup>5,6</sup> The developing nervous system of young children is particularly vulnerable to cancer treatment, especially to the effects of radiation.<sup>4,7,8</sup> One of the chemotherapy agents with more significant CNS adverse effects is methotrexate (MTX). Concomitant brain radiation and young age represent risk factors for MTX-associated adverse effects.<sup>3,4</sup>

Neuroimaging abnormalities after chemotherapy, RT, or multimodal therapy are described in several studies, ranging from the common leukoencephalopathy (LE), microbleeds, and cavernomas to the rarely described cystlike lesions (CLL).<sup>4,8</sup> In fact, only 3 cohort studies describe these lesions.<sup>9-11</sup> This study aimed to characterize the risk factors and associations of CLL with other late adverse effects.

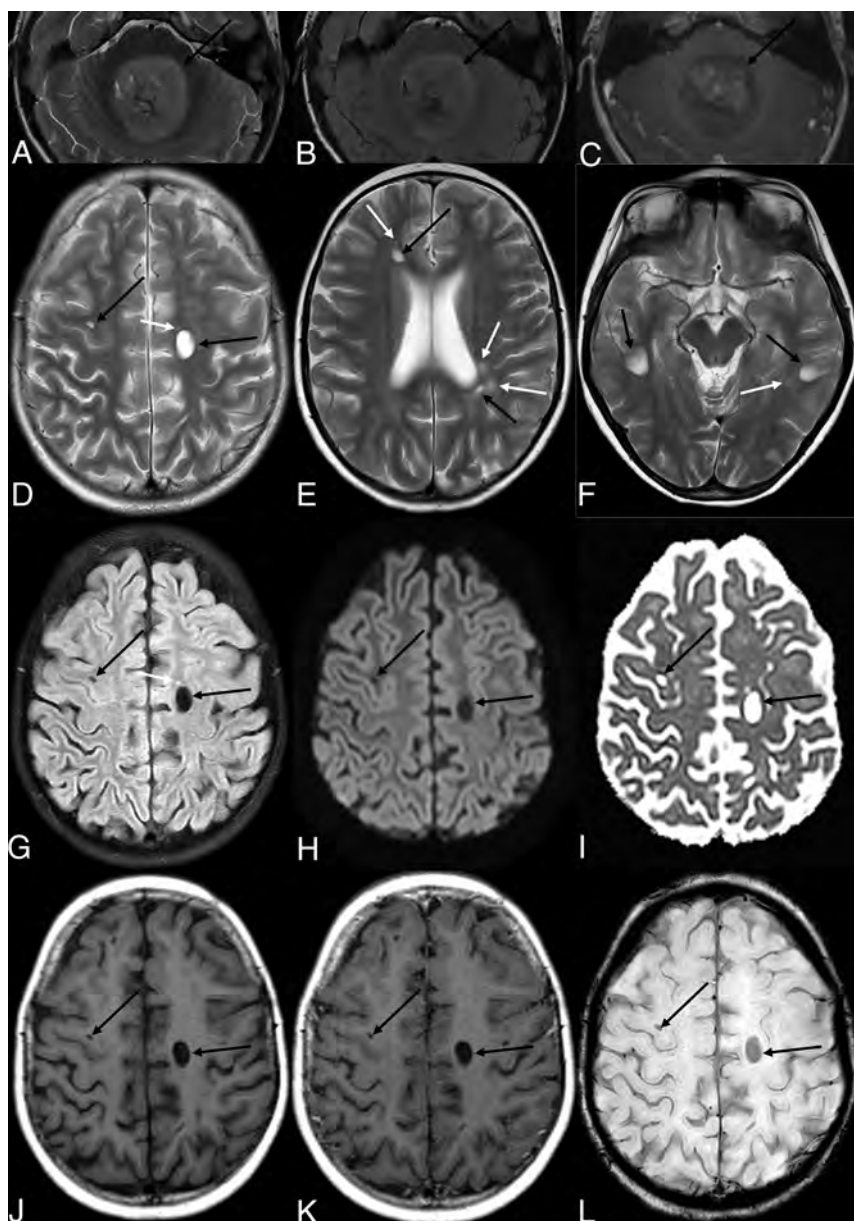


**FIG 1.** Patient 10 was treated for medulloblastoma (A–C) (T2WI, T2 FLAIR, T1WI after gadolinium administration). D–L, Three T2WIs, T2 FLAIR, DWI/ADC map, T1WI, T1WI after gadolinium, and SWI, all obtained 7 years after treatment. The patient underwent whole-brain RT; consequently, CLL developed diffusely in both cerebral hemispheres (D–F). CLL (black arrows) are cystlike cavities of the cerebrum white matter with MR signal equal to that of CSF on all sequences, which frequently develop in proximity to LE (white arrows), represented by T2 and T1 prolongation of white matter signal.

## MATERIALS AND METHODS

### Sample Characteristics

Between January 1990 and June 2020, one hundred seventy-five children with brain tumors were treated with cranial RT at Instituto Português de Oncologia de Lisboa Francisco Gentil, Lisbon, Portugal. Most patients underwent multimodality treatment with different therapy regimens, including surgery, chemotherapy, and RT.

According to previous studies, only pediatric patients treated with cranial RT develop CLL, with a median time from cranial RT

to imaging findings of 2 years (range, 0.26–5.7 years); thus, a minimum of 5 years of follow-up was considered adequate.<sup>9–11</sup>

The inclusion criteria for case enrollment in this retrospective cohort study were cranial RT, 17 years of age or younger at the time of cranial RT, and a minimum of 5 years of follow-up after cranial RT with serial MR imaging. Thirty-six patients without a minimum of 5 years of follow-up were excluded. This retrospective study was approved by the institution's ethics committee.

### Data Collection

All patients were regularly followed in a dedicated outpatient consultation. The clinical files from neuro-oncology, radiation therapy, and pediatrics were reviewed. The pertinent clinical data were retrieved from patients' clinical charts, including demographic information (age, age at cranial RT, sex), tumor characteristics (location, histology), and treatment (treatment protocol, RT technique and total dose [Gy], and the chemotherapy regimen).

### MR Imaging Evaluation

Patients underwent MR imaging at the time of diagnosis and during routine follow-up examinations. By protocol, after treatment completion, the patients underwent sequential MR imaging studies with 6-month intervals during the first 4 years and every year after that. MR imaging protocols included the following sequences: T2WI, FLAIR, DWI, and T1WI after gadolinium administration. Most of the performed examinations also included an iron-sensitive sequence, eg, T2\* and SWI.

Neuroimaging studies of these patients were retrospectively reviewed for the presence of cystlike lesions, leukoencephalopathy, microbleeds, and cavernomas.

All the examinations were previously reported by staff radiologists trained in neuroradiology, with a mean of 20 years of experience in neuro-oncology imaging. A neuroradiologist (with 4 years of experience) blinded to the clinical status and imaging report reviewed all the examinations twice. Discrepancies between the 2 observers were reviewed for consensus.

CLL (Fig 1) were defined as cystlike cavities of the cerebrum white matter with MR signal equal to that of CSF in all sequences, without enhancement after gadolinium, at any time of follow-up (Fig 2). All the observed cysts had a minimum



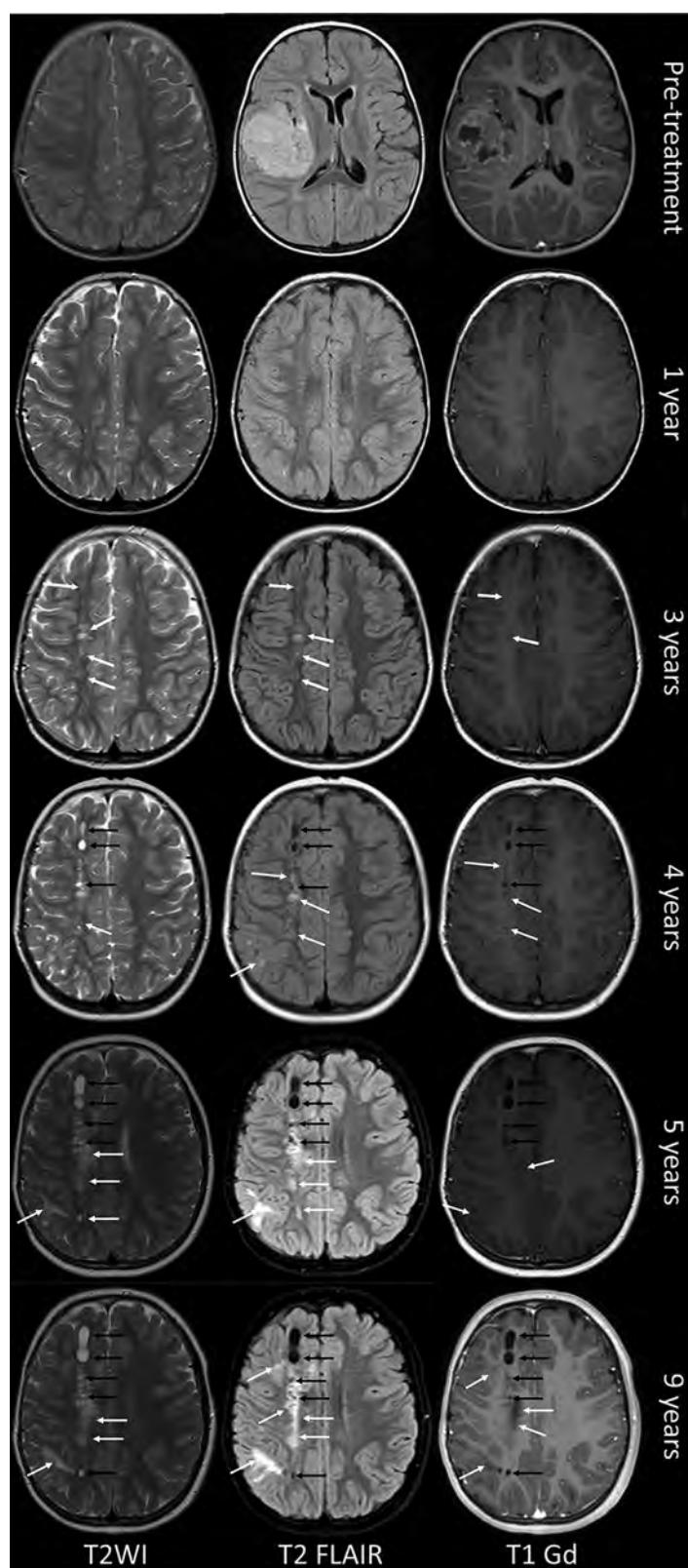


**FIG 2.** Patient 24 underwent all the MR imaging examinations of the protocol. Pretreatment images are shown in the first row, depicting a frontotemporal anaplastic ependymoma (T2 FLAIR and T1WI after gadolinium) and the corona radiata (T2WI). CLL developed between 3 and 4 years of follow-up. CLL (black arrows) mainly evolved from previous LE, represented by noncystic white matter lesions, with T2 and T1 prolongation, without gadolinium enhancement (white arrows). Only the right cerebral hemisphere was irradiated; consequently, the left cerebral hemisphere was spared from LE and CLL.

distance of 1 cm from the tumor site or surgical bed. The number, size, and distribution of the WM cysts were recorded in each examination.

LE was classified according to the Fazekas scale on the basis of the distribution and size of white matter T2WI hyperintensities, as previously described in the study by Yamasaki et al<sup>11</sup> (Fig 3A–C).<sup>12</sup>

Microbleeds were defined by small, round or ovoid, well-defined hypointense lesions on T2\* and SWI, not seen on T1WI and T2WI, with a maximum diameter of 3 mm (Fig 3D). The potential mimickers (calcium deposits, vessel flow void, and traumatic brain injury) were excluded by imaging or clinical history.<sup>5,13</sup> All lesions within a 1-cm margin of the surgical resection site were excluded.

Cavernomas were defined as all T2\* and SWI hypointense lesions with signal changes in T1WI and/or T2WI that could be categorized using the Zabramski classification as type I, II, or III (Figs 3E, -F).<sup>14</sup>

### Statistical Analysis

Categorical data are presented as frequencies and percentages, and quantitative variables, as median and range (minimum-maximum). Groups of patients (with and without CLL) were compared using  $\chi^2$  or Fisher exact tests for categorical variables (sex, tumor location and histology, treatment protocol, chemotherapy regimen, and RT technique) and Mann-Whitney tests for quantitative variables (age at cranial RT and RT total dose).

Hurdle models were used to identify factors associated with CLL development and associated with the number of cystlike lesions, such as sex, tumor histology, tumor location, age during radiation therapy, treatment protocol, radiation therapy technique and dose (Gy), and chemotherapy agents. All variables that attained a *P* value of  $\leq .25$  were considered for the multivariable analysis. The hurdle model is a 2-component model useful when there is an excess of zeroes, as is the case in our study in which many of the children did not have CLL. The first part (hurdle model) is a logistic

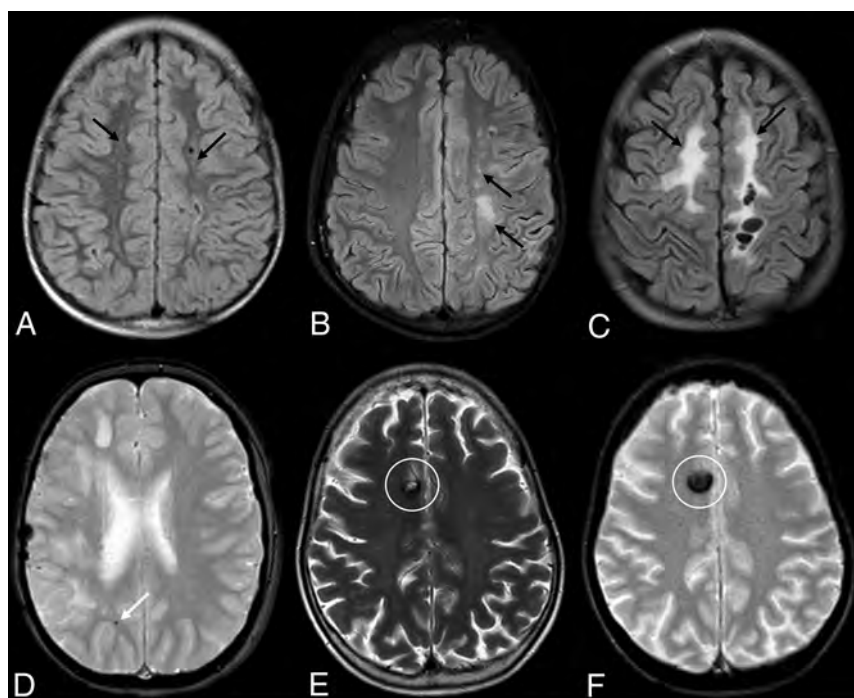


**FIG 3.** A, Patient 42. LE (Fazekas grade 1) is shown, with punctate white matter T2-hyperintense lesions (black arrows). B, Patient 43. LE (Fazekas grade 2), with a slight confluence of T2-hyperintense lesions of the white matter (black arrows). C, Patient 26. LE (Fazekas grade 3), with large confluent areas of white matter T2 hyperintensities (black arrows). D, Patient 24. Small cerebral microbleeds, with a T2\* blooming black dot (white arrow), not visible on T2WI. E and F, Patient 107 demonstrates a cavernoma with a classic “popcorn” appearance on T2WI and a large hypointensity on T2\* with blooming (white circles).

**Table 1: Demographic, clinical, and imaging characteristics of the studied sample with CLL compared with those without CLL**

	Total (n = 139)	Patients with CLL (n = 23)	Patients without CLL (n = 116)	P Value
Age at cranial RT (median) (minimum-maximum) (yr)		6 (0–15)	9 (1–17)	.004 <sup>a</sup>
Primary CNS tumor, No. (%)				.044 <sup>a</sup>
Medulloblastoma	52	14 (26.9)	38 (73.1)	
Ependymoma	22	4 (18.2)	18 (82.8)	
Germinal cell tumor	19	2 (10.5)	17 (89.5)	
Others	46	3 (6.5)	43 (93.5)	
Location, No. (%)				.725 <sup>b</sup>
Infratentorial	80	14 (17.5)	66 (82.5)	
Supratentorial	59	9 (15.3)	50 (84.7)	
RT technique, No. (%)				.341 <sup>a</sup>
WBRT	3	0 (0)	3 (100)	
Focal	64	8 (79.2)	56 (87.5)	
WBRT + focal	72	15 (20.8)	57 (79.2)	
RT total dose (median) (minimum-maximum) (Gy)		54 (20–90)	54 (50–60)	.294 <sup>a</sup>
Treatment protocol, No. (%)				.027 <sup>a</sup>
No chemoradiotherapy	109	14 (12.8)	95 (87.2)	
Chemoradiotherapy	29	9 (31.0)	20 (69.0)	
Chemotherapy regimen, No. (%)				.584 <sup>b</sup>
No Chemotherapy	41	5 (12.2)	36 (87.8)	
Chemotherapy with MTX	8	2 (25.0)	6 (75.0)	
Chemotherapy without MTX	90	16 (17.8)	74 (82.2)	

**Note:**—WBRT indicates whole-brain RT.

<sup>a</sup> Fisher exact test; and for quantitative variables, the Mann-Whitney test.

<sup>b</sup>  $\chi^2$  test.

regression model, and it is used to estimate the odds of developing CLL through the estimation of the OR, while the second part (count model) is a negative binomial regression model, which is used to estimate rate ratios regarding the number of cysts.

A level of significance  $\alpha = .05$  was considered. The analysis was performed using R statistical and computing software (<http://www.r-project.org/>).

## RESULTS

### Patient Characteristics

Table 1 summarizes baseline demographic and clinical data by groups of patients (with and without CLL). A total of 139 patients met the inclusion criteria, 82 (59.0%) of whom were male. Patients’ ages at the time of cranial RT varied between 0 and 17 years, with a median of 8 years.

Medulloblastomas (37.4%), ependymomas (15.8%), and germinal cell tumors (13.7%) were the most represented tumors. Eighty (57.6%) tumors were infratentorial.

Concerning the RT technique, 72 (51.8%) patients were treated with combined whole-brain RT and focal RT, 64 (46.0%) were treated with isolated focal RT, and 3 (2.2%), with isolated whole-brain RT. Twenty-nine (20.9%) patients underwent chemoradiotherapy (chemotherapy-RT).

Ninety-eight patients (70.5%) underwent chemotherapy. Only 8 patients (5.8%) had MTX included in their chemotherapy regimen. The RT median total dose was similar in both subgroups, but the CLL group’s minimum dose was 50 Gy.

Twenty-three (16.5%) individuals of the sample of 139 patients developed CLL. The median time to the first appearance of CLLs after radiation therapy was 2 years (mean, 2.1 [SD, 0.64] years; minimum, 1 year; maximum, 3.5 years). Seventeen of 23 patients (73.9%) had >1 cystlike lesion, with a median of 4 per patient (minimum, 2; maximum, 45). No CLLs were observed in the infratentorial compartment or outside the radiation field (Fig 2).

**Table 2: Posttreatment imaging characterization of the studied sample comparing patients with and without CLL**

	Total (n = 139)	Patients with CLL (n = 23)	Patients without CLL (n = 116)	P Value <sup>a</sup>
LE, No. (%)				<.001
No	81	4 (4.9)	77 (95.1)	
Yes	58	19 (32.8)	39 (67.2)	
Fazekas scale, No. (%)				.001
Grade 0	81	4 (4.9)	77 (95.1)	
Grade 1	32	4 (12.5)	28 (87.5)	
Grade 2	13	7 (53.8)	6 (46.2)	
Grade 3	13	8 (61.5)	5 (38.5)	
Microbleeds, No. (%)				.248
Yes	88	17 (19.3)	71 (80.7)	
No	51	6 (11.8)	45 (88.2)	
Cavernomas, No. (%)				.129
Yes	53	12 (22.6)	41 (77.4)	
No	86	11 (12.8)	75 (87.2)	

<sup>a</sup> P values were obtained by the  $\chi^2$  test.

**Table 3: Prevalence of CLL in age groups (4-year gap)**

Age Group	Total	Patients with CLL	Prevalence of CLL
0–3 yr	17	6	35.3%
4–7 yr	47	10	21.3%
8–11 yr	35	6	17.1%
12–15 yr	35	1	2.9%
16–17 yr (2-yr gap)	5	0	0.0%

**Table 4: Results of the multivariable regression model for CLL<sup>a</sup>**

Estimate (95% CI)	P Value
RR	
Count model coefficients	
Female sex	3.99 (1.53–10.41)
Age at cranial RT <sup>b</sup>	0.51 (0.27–0.97)
OR	
Zero hurdle model coefficients	
Age at cranial RT <sup>b</sup>	0.51 (0.30–0.88)
Treatment protocol (CT-RT)	3.20 (1.17–8.75)

**Note:**—RR indicates rate ratio; CT, chemotherapy.

<sup>a</sup> Reference categories are male sex, no chemoradiotherapy. P values were obtained by the hurdle regression model.

<sup>b</sup> For each 4-year increase.

Fifty-eight (41.7%) patients developed LE, while 88 (63.3%) patients developed microbleeds and 53 (38.1%) developed cavernomas. A significantly higher proportion of patients developed CLL, depending on the severity of LE (according to the Fazekas scale). These data are summarized in Table 2. The development of CLLs was not related to acute or subacute clinical manifestations.

### Risk Factors Associated with the Development of Cystlike Lesions

Regarding risk factors for the development of CLL, results of the univariable study depicted in Table 1 showed that a statistically significant association was found with chemotherapy-RT ( $P = .027$ ) and younger age ( $P = .004$ ). One-third (31%) of the patients who underwent chemotherapy-RT developed CLL, compared with 12.8% of patients with a single therapy. Younger patients

demonstrated higher susceptibility when considering CLL prevalence in age groups with 4-year gaps (Table 3). Histology was also associated with development of CLL ( $P = .044$ ).

Both variables (age, chemotherapy-RT) remained significant in the multivariable analysis (Table 4). Children exposed to chemotherapy-RT had increased odds of 3.20 of developing CLL compared with those not exposed to chemotherapy-RT ( $P = .024$ ; 95% CI, 1.17–8.75). It was also demonstrated that for each 4-year increase in a child's growth, there was a 49% decrease in the odds of developing CLL (OR = 0.51;  $P = .015$ ; 95% CI, 0.30–0.88). The remaining factors, such as sex ( $P = .841$ ), tumor location ( $P = .725$ ), chemotherapy regimen ( $P = .584$ ), and RT total dose ( $P = .294$ ), were not found to be associated with CLL (Table 1).

Among those who had positive counts, the CLL average count was 1.61. The number of lesions decreased by 0.5 times (95% CI, 0.27–0.97;  $P = .041$ ) for each 4-year age increase, and it was increased 4 times in females (95% CI, 1.53–10.41;  $P = .005$ ).

### Associated RT Late Adverse Effects

A strong association was found between the development of CLL and LE ( $P < .001$ ), but no significant association was found with microbleeds or cavernomas (Table 2). However, 52.2% of patients with CLL developed cavernomas, and only 35.3% of patients without CLL had cavernomas. A strong relationship was also found between the development of CLL and the severity of LE, measured by the Fazekas scale ( $P = .001$ ).

## DISCUSSION

Most scientific literature has classically described children's radiation therapy brain toxicity as a replication of the adult toxicity, but with increased incidence and/or severity of the adverse effects.<sup>3,15</sup> The vulnerability of developing tissues to radiation determines a range of adverse events in children, different from those seen in the adult population.<sup>16</sup>

The reviews of neuroimaging findings in pediatric cancer survivors include brain volume loss, leukoencephalopathy, mineralizing microangiopathy, microbleeds, and cavernomas.<sup>1,3,15</sup> However, in previous literature reviews, CLL<sup>9–11</sup> have not been mentioned as RT adverse effects in the pediatric brain.<sup>1,3,15</sup>

To the present date, only 3 studies have been published relating to these types of late-induced lesions from radiation therapy.<sup>9–11</sup> The first, the only one in the Western population, was published in 2000 and included the largest number of patients.<sup>9</sup> The last 2 articles, published in 2007 and 2017, were based on much smaller populations from Japan (33 and 41 patients, respectively).<sup>10,11</sup> The 3 studies attributed different names to these lesions: silent lacunar lesions, cystic malacia, and asymptomatic cystic lesions.<sup>9–11</sup> Because no histology was obtained in any of the studies and the nature of the lesions is unknown, we opted to name them cystlike lesions, which represent the imaging phenotype. To our best knowledge, our study is the second with >100 patients in a Western population.

### Characterization of CLL and Risk Factors

The percentage of patients who developed CLL (16.5%) is similar to that reported by Kitajima et al<sup>10</sup> (18%) but is considerably higher than that of Fouladi et al<sup>9</sup> (6%). This latter study included the use of CT, which might have contributed to decreased



sensitivity. Similar to the results of previous studies, CLL appeared a median of 2 years after cranial RT.<sup>9-11</sup> This finding supports the evidence that these lesions develop only in the first years after cranial RT.

As previously described in the literature, late adverse effects of cranial RT depend on several factors, such as patient age, radiation dose, type of irradiation, and concomitant antineoplastic or radiosensitizing agents.<sup>3</sup> Our analysis demonstrated that for each 4-year age increase, there are 50% decreased odds of developing CLL and a 50% decrease in the average lesion count. In line with previous studies, this finding suggests that increasing age has an attenuating effect on disease burden.

We hypothesized that the RT dose could be a risk factor; however, the significant overlap of radiation doses between the subgroups, namely in patients subject to  $\geq 50$  Gy, precluded a statistically significant result. However, none of the patients irradiated with  $< 50$  Gy developed CLL, which appears to be a cutoff value below which patients tend to not develop CLL.

Given the neurotoxicity of MTX, we also hypothesized that it could represent an independent risk factor.<sup>3,4,10</sup> In fact, a larger proportion of patients treated with MTX (25%) developed CLL, compared with the patients who underwent chemotherapy without MTX (18%) and the ones treated without any chemotherapy (12%). These results suggest that chemotherapy could be a risk factor, eventually aggravated by the inclusion of MTX. However, the small number of patients treated with MTX limits the statistical significance of the results.

The patients who underwent chemotherapy-RT had 3.20 increased odds of developing CLL, showing that concomitant chemotherapy also acts as a radiosensitizing agent in healthy brain tissue.

The patient's sex does not seem to relate to CLL development, but females demonstrated a 4.00 rate ratio of developing a higher number of lesions. This has not been previously described, and the reasons for this finding are unknown. As in previous studies, no relationship was established with tumor location.

Similar to what happens with other RT late adverse effects, CLL seem to develop only in the radiation field.<sup>15,17</sup>

#### **Association of CLL with Other Late Adverse Effects**

Younger age at treatment has a detrimental effect on the development of CLL, LE, microbleeds, and cavernomas.<sup>6,8</sup> We hypothesized that there could be an association in the susceptibility to develop these 4 types of injuries.

We demonstrated an association between LE and the development of CLL. In fact, the lesions tend to develop in cerebral locations where LE is worse, and a strong relationship was also found between the development of CLL and the global severity of LE, measured by the Fazekas scale. This finding suggests that the pathophysiologic processes of LE and CLL could be related. Similar to what happens with LE<sup>8</sup> and in line with previous studies,<sup>9-11</sup> we also demonstrated that infratentorial WM is less susceptible to the development of CLLs.

#### **Nature and Clinical Significance of CLL**

The study of Fouladi et al<sup>9</sup> described the lesions as cerebral lacunes, in direct analogy to typical adult small ischemic infarcts. Radiation

therapy-induced vasculopathy was inferred as the pathophysiologic mechanism.<sup>9</sup> As stated, none of the children presented with acute neurologic deficits, the lesions were regular cystic lesions located in the cerebral WM, and some of the lesions demonstrated growth. All these characteristics argue against the possibility of cerebral ischemic lacunes, which are widely described in the scientific literature as irregular lesions without growth, commonly located in the deep gray matter and pons and frequently associated with acute neurologic deficits.<sup>9,18,19</sup>

Yamasaki et al<sup>11</sup> coined the term "cystic malacia" as the final result of WM necrosis. Indeed, the development of cerebral malacia lesions has been described as a later stage of radionecrosis.<sup>1,3</sup> However, these lesions are different from CLL, presenting as pseudotumoral masses with contrast enhancement mimicking tumor progression, frequently presenting with clinical manifestations such as seizures or signs of intracranial hypertension.<sup>15</sup>

None of the patients presented with clinical symptoms that could be related to the location of CLL. All lesions had well-defined, regular margins, oval or rounded, with CSF-isointense MR signal in all sequences, without hemosiderin deposits or gadolinium enhancement (Figs 1 and 2). Most of them evolved in deep and periventricular WM, demonstrated some growth, and subsequently stabilized (Fig 2). Like Kitajima et al,<sup>10</sup> we consider these characteristics to be consistent with dilated perivascular spaces.<sup>19</sup> Incidentally, some anecdotal reports have reported growing dilated perivascular spaces as late cranial RT effects in the adult population.<sup>20</sup> Post-RT pathologic findings such as hyalinization and fibrinoid necrosis of small arteries and arterioles, demyelination, gliosis, or brain atrophy could contribute to the growing dilated perivascular spaces.<sup>10,17</sup>

There is no reference to cystic lesions in the literature other than as a result of radionecrosis, which, as argued before, does not represent CLL.<sup>21</sup> The reason may be the paucity of post-RT pathology studies in the pediatric population or the interpretation of these lesions as enlarged perivascular spaces, unrelated to RT.

The differentiation between therapy toxicity and recurrent disease is sometimes difficult but is critical to therapeutic management and prognosis.<sup>3,20</sup> Thus, the knowledge of all late adverse effects of cancer treatment is crucial, including the described CLL. We consider that the clinical significance of these lesions remains unknown and that long-term follow-up and pathologic studies are necessary.

#### **Limitations**

There are several limitations to our study, the first being its retrospective nature. This is a 30-year-long cohort, during which different RT and multimodality protocols have been used.<sup>6,22</sup> Some of the differences between protocols were not considered, such as the type of irradiation or chemotherapy regimens. Radiation-induced brain injury is probably multifactorial, but the pathophysiology of late CNS radiation cytotoxicity remains unclear.<sup>8</sup> We hypothesized that CLL represent dilated perivascular spaces; however, we did not perform histologic analysis of any specimen, so the nature and pathogenesis of these lesions remain unknown.

Pediatric cranial RT is associated with a decline in intelligence quotient, and the most significant cognitive decline happens in patients treated at younger than 5 years of age.<sup>5</sup> Specifically, it is



known that LE and microbleeds are related to poorer neurocognitive performance.<sup>5,8</sup> Cognitive tests were not administered to the studied population; thus, the cognitive impact of CLL remains unknown.

## CONCLUSIONS

This study illustrates CLL as a frequent but less studied and under-reported late toxicity of cranial RT in the pediatric population. We demonstrated that CLL developed in the first 4 years after irradiation of the pediatric brain with  $\geq 50$  Gy, irrespective of sex, tumor location, and radiation protocol. Particularly, younger children were at higher risk of developing CLL, with a higher lesion count, with a progressive risk reduction for older children and teenagers. Patients who underwent chemotherapy-RT had a 3-fold higher risk of developing CLL. Female patients had a higher risk of developing a higher number of CLL. Postradiation LE was associated with a higher risk of the development of CLL.

Our data reinforce iatrogenic sequelae differing among age groups, even in pediatric patients, suggesting higher radiosensitivity of tissues in younger patients.

RT-induced acute and late effects on normal tissue limit the delivery of therapeutically optimal RT doses for a variety of pediatric and adult cancers; thus, a sound knowledge of all adverse effects is essential.

Disclosures: Joao Passos—UNRELATED: Employment: Clinica de Santo António, Comments: payment related to the provision of services of neurology consultation.

## REFERENCES

- Vázquez E, Delgado I, Sánchez-Montañez A, et al. **Side effects of oncologic therapies in the pediatric central nervous system: update on neuroimaging findings.** *Radiographics* 2011;31:1123–39 CrossRef Medline
- Howlader N, Noone AM, Krapcho M, et al, eds. **Previous Version: SEER Cancer Statistics Review 1975–2013 National Cancer Institute. Natl Cancer Institute.** Updated September 12, 2016. [https://seer.cancer.gov/archive/csr/1975\\_2013/](https://seer.cancer.gov/archive/csr/1975_2013/). Accessed May 5, 2020
- Rossi Espagnet MC, Pasquini L, Napolitano A, et al. **Magnetic resonance imaging patterns of treatment-related toxicity in the pediatric brain: an update and review of the literature.** *Pediatr Radiol* 2017;47:633–48 CrossRef Medline
- Ikonomidou C. **Chemotherapy and the pediatric brain.** *Mol Cell Pediatr* 2018;5:8 CrossRef Medline
- Roddy E, Sear K, Felton E, et al. **Presence of cerebral microbleeds is associated with worse executive function in pediatric brain tumor survivors.** *Neuro Oncol* 2016;18:1548–58 CrossRef Medline
- Paulino AC. **Treatment strategies to reduce radiotherapy late effects in children.** *J Radiat Oncol* 2013;2:121–28 CrossRef
- Perry A, Schmidt RE. **Cancer therapy-associated CNS neuropathology: an update and review of the literature.** *Acta Neuropathol* 2006;111:197–212 CrossRef Medline
- Partap S, Russo S, Esfahani B, et al. **A review of chronic leukoencephalopathy among survivors of childhood cancer.** *Pediatr Neurol* 2019;101:2–10 CrossRef Medline
- Fouladi M, Langston J, Mulhern R, et al. **Silent lacunar lesions detected by magnetic resonance imaging of children with brain tumors: a late sequela of therapy.** *J Clin Oncol* 2000;18:824–31 CrossRef Medline
- Kitajima M, Hirai T, Maruyama N, et al. **Asymptomatic cystic changes in the brain of children after cranial irradiation: frequency, latency, and relationship to age.** *Neuroradiology* 2007;49:411–17 CrossRef Medline
- Yamasaki F, Takayasu T, Nosaka R, et al. **Development of cystic malacia after high-dose cranial irradiation of pediatric CNS tumors in long-term follow-up.** *Childs Nerv Syst* 2017;33:957–64 CrossRef Medline
- Fazekas F, Chawluk JB, Alavi A. **MR signal abnormalities at 1.5 T in Alzheimer's dementia and normal aging.** *AJNR Am J Neuroradiol* 1987;8:421–26 CrossRef Medline
- Charidimou A, Krishnan A, Werring DJ, et al. **Cerebral microbleeds: a guide to detection and clinical relevance in different disease settings.** *Neuroradiology* 2013;55:655–74 CrossRef Medline
- Passos J, Nzwalu H, Valente M, et al. **Microbleeds and cavernomas after radiotherapy for paediatric primary brain tumours.** *J Neurol Sci* 2017;372:413–16 CrossRef Medline
- Martino A, Krainik A, Pasteris C, et al. **Neurological imaging of brain damages after radiotherapy and/or chemotherapy.** *J Neuroradiol* 2014;41:52–70 CrossRef Medline
- Constine LS, Ronckers CM, Hua CH, et al. **Pediatric Normal Tissue Effects in the Clinic (PENTEC): an international collaboration to analyse normal tissue radiation dose–volume response relationships for paediatric cancer patients.** *Clin Oncol (R Coll Radiol)* 2019;31:199–207 CrossRef Medline
- Remes TM, Suo-Palosaari MH, Koskenkorva PKT, et al. **Radiation-induced accelerated aging of the brain vasculature in young adult survivors of childhood brain tumors.** *Neurooncology Pract* 2020;34:1–13 CrossRef Medline
- Caplan LR. **Lacunar infarction and small vessel disease: pathology and pathophysiology.** *J Stroke* 2015;17:2–6 CrossRef Medline
- Kwee RM, Kwee TC. **Virchow-Robin spaces at MR imaging.** *Radiographics* 2007;27:1071–86 CrossRef Medline
- Mark IT, Carr CM, Ruff MW, et al. **Enlarging perivascular spaces following radiation therapy in the brain: a report of 2 cases and literature review.** *World Neurosurg* 2020;138:436–39 CrossRef Medline
- Lai R, Abrey LE, Rosenblum MK, et al. **Treatment-induced leukoencephalopathy in primary CNS lymphoma: a clinical and autopsy study.** *Neurology* 2004;62:451–56 CrossRef Medline
- De Ruyscher D, Niedermann G, Burnet NG, et al. **Radiotherapy toxicity.** *Nat Rev Dis Prim* 2019;5:13 CrossRef Medline

# Diagnostic Accuracy and Failure Mode Analysis of a Deep Learning Algorithm for the Detection of Cervical Spine Fractures

A.F. Voter, M.E. Larson, J.W. Garrett, and J.-P.J. Yu



## ABSTRACT

**BACKGROUND AND PURPOSE:** Artificial intelligence decision support systems are a rapidly growing class of tools to help manage ever-increasing imaging volumes. The aim of this study was to evaluate the performance of an artificial intelligence decision support system, Aidoc, for the detection of cervical spinal fractures on noncontrast cervical spine CT scans and to conduct a failure mode analysis to identify areas of poor performance.

**MATERIALS AND METHODS:** This retrospective study included 1904 emergent noncontrast cervical spine CT scans of adult patients (60 [SD, 22] years, 50.3% men). The presence of cervical spinal fracture was determined by Aidoc and an attending neuroradiologist; discrepancies were independently adjudicated. Algorithm performance was assessed by calculation of the diagnostic accuracy, and a failure mode analysis was performed.

**RESULTS:** Aidoc and the neuroradiologist's interpretation were concordant in 91.5% of cases. Aidoc correctly identified 67 of 122 fractures (54.9%) with 106 false-positive flagged studies. Diagnostic performance was calculated as the following: sensitivity, 54.9% (95% CI, 45.7%–63.9%); specificity, 94.1% (95% CI, 92.9%–95.1%); positive predictive value, 38.7% (95% CI, 33.1%–44.7%); and negative predictive value, 96.8% (95% CI, 96.2%–97.4%). Worsened performance was observed in the detection of chronic fractures; differences in diagnostic performance were not altered by study indication or patient characteristics.

**CONCLUSIONS:** We observed poor diagnostic accuracy of an artificial intelligence decision support system for the detection of cervical spine fractures. Many similar algorithms have also received little or no external validation, and this study raises concerns about their generalizability, utility, and rapid pace of deployment. Further rigorous evaluations are needed to understand the weaknesses of these tools before widespread implementation.

**ABBREVIATIONS:** AI = artificial intelligence; ASiR = adaptive statistical iterative reconstruction; DSS = decision support system; CSFx = cervical spinal fractures

Cervical spinal fractures (CSFx) are devastating injuries that can cause severe morbidity and mortality from damage to the

enclosed spinal cord, the craniocervical junction, and cervical vasculature.<sup>1</sup> Failure of the osseous spinal column can lead to instability and impingement of the underlying spinal cord;<sup>2</sup> therefore, timely identification and stabilization of CSFx are crucial to prevent further disability.<sup>1,3</sup> In the acute clinical setting, NCCT of the cervical spine is the recommended method for detecting CSFx;<sup>4</sup> however, with diagnostic imaging volumes dramatically increasing,<sup>5,6</sup> these increased imaging volumes place a burden on radiologists who must maintain diagnostic accuracy and efficiency.<sup>7</sup> While there has been great effort to reduce the number of unnecessary scans ordered, including the use and implementation of the National Emergency X-Radiography Utilization Study Group<sup>8</sup> criteria and the Canadian C-Spine Rule<sup>9</sup> to reduce the number of unnecessary cervical spinal NCCTs, their effectiveness appears to be modest,<sup>10,11</sup> and diagnostic imaging volumes continue to increase.

To assist radiologists in managing these rising case volumes, artificial intelligence (AI) decision support systems (DSSs) have been developed to help prioritize imaging studies with critical

Received December 9, 2020; accepted after revision March 14, 2021.

From the School of Medicine and Public Health (A.F.V.) and Departments of Radiology (M.E.L., J.W.G., J.-P.J.Y.), Biomedical Engineering (J.-P.J.Y.), College of Engineering, and Psychiatry (J.-P.J.Y.), University of Wisconsin School of Medicine and Public Health, Madison, Wisconsin; and

A.F.V. was supported by National Institutes of Health F30 CA210465 and T32 GM008692; J.W.G. was supported by National Institutes of Health R01 LM013151; and J.-P.J.Y. was supported by the Clinical and Translational Science Award program, through the National Institutes of Health National Center for Advancing Translational Sciences, grant UL1TR002373.

The content is solely the responsibility of the authors and does not necessarily represent the official views of the National Institutes of Health.

Please address correspondence to John-Paul J. Yu, MD, PhD, Department of Radiology, University of Wisconsin-Madison, 600 Highland Ave, D4-352, Madison, Wisconsin; e-mail: jpyu@uwhealth.org

Indicates open access to non-subscribers at www.ajnr.org

Indicates article with online supplemental data.

<http://dx.doi.org/10.3174/ajnr.A7179>

findings.<sup>12,13</sup> These DSSs identify and subsequently flag studies with actionable results, allowing radiologists to prioritize them over scans with likely negative findings to speed the reporting of critical findings. However, DSSs that incorrectly flag an excessive number of studies with negative findings or conversely miss critical findings might slow the radiologist's performance. Rigorous analysis is, therefore, crucial. AI algorithms are known to have numerous limitations, including the need for large, diverse, and unbiased datasets,<sup>14</sup> which can be difficult to acquire or curate<sup>15</sup> and operate in a manner that precludes direct interrogation of the decision process itself. These issues can lead to poor performance, which is difficult or impossible to troubleshoot, especially when the algorithms are implemented in settings beyond their initial training environment.<sup>16–18</sup> While the rapid development and clinical implementation of DSSs are exciting, this proliferation risks outstripping our ability to rigorously assess and validate their performance. This validation and assessment have not been extensively performed or reported in the literature. Furthermore, site-specific performance differences without obvious etiologies have been observed for AI DSSs.<sup>16–18</sup> Thus, rigorous studies to guide AI DSS installations in varied clinical settings and a greater understanding of the generalizability (or lack thereof) of AI DSSs are needed to safely translate this important tool into widespread clinical practice.

Our institution recently implemented Aidoc (Aidoc Medical), an FDA-cleared, commercially available AI DSS for the detection of CSFx.<sup>19</sup> While several spine fracture DSSs have been developed,<sup>19–23</sup> their diagnostic accuracy and overall performance remain unknown. To gain insight into the performance of this system specifically and AI DSSs more generally, we conducted a retrospective review of Aidoc as clinically implemented in our institution. The aim of this study was to characterize the performance of Aidoc for the detection of CSFx and conduct a failure mode analysis to identify areas of poor diagnostic performance.

## MATERIALS AND METHODS

This Health Insurance Portability and Accountability Act–compliant retrospective study was approved by the institutional review board. The requirement for informed consent was waived. The data were analyzed and controlled by the authors exclusively, none of whom are employees of or consultants to Aidoc Medical or its competitors.

### Study Population, Data Collection, Imaging Parameters, and AI System

Adult (older than 18 years of age) CT cervical spine studies without contrast from January 20, 2020, to October 8, 2020, in our radiology information system were identified and contemporaneously processed by Aidoc. Pediatric (younger than 18 years of age) studies and examinations with intrathecal contrast were excluded from this study. Scans were performed at an academic level I trauma center and associated outreach imaging centers with a fleet of 9 models of scanners (GE Healthcare) (summarized in Online Supplemental Data). A total of 1904 adult, noncontrast cervical spine CT scans were identified in 1923 emergent neck CT scans (mean age, 60 [SD, 22] years; 50.3% men). Acquisition parameters for noncontrast CT examinations of the cervical spine are as follows: 120 kV(peak); axial helical acquisition; pitch = 0.625 mm;

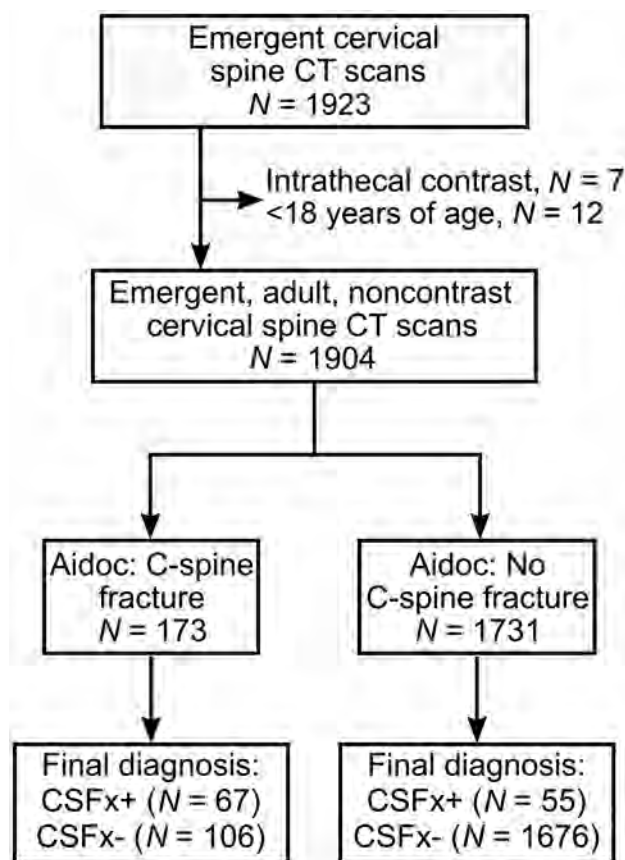


**FIG 1.** Standards for reporting diagnostic accuracy studies (STARD) patient flow diagram.

rotation speed = 5.6 mm/rotation; rotation time = 0.5 seconds; automatic exposure control = smart mA (230–750 mA); section thickness = 1.25 mm; interval = 0.625 mm. Standard soft-tissue and bone window (Bone Plus algorithm [GE Healthcare]) reconstructions were contemporaneously generated for review by radiologists (1.25-mm section thickness, sagittal and coronal; 0.625-mm interval; no adaptive statistical iterative reconstruction [ASiR]). Immediately following study acquisition, axial thin bone (Bone Plus reconstruction; 0.625-mm section thickness; 0.312-mm interval; no ASiR) and sagittal bone (Bone Plus reconstruction; 1.5-mm section thickness; 0.98-mm interval; no ASiR) series were generated and analyzed by the Aidoc algorithm, which then classifies each scan as positive or negative for CSFx. Aidoc-specific image series were not available to the interpreting radiologist for review. However, because the algorithm was evaluated as clinically implemented, the final Aidoc classification and key image indicating the flagged pathology were available to the radiologist at the time of initial study interpretation. For the purposes of this study, the final neuroradiologist interpretation serves as ground truth data and is in keeping with prior approaches evaluating the diagnostic performance of AI-related systems.<sup>24,25</sup>

### Data Processing and Analysis

The presence of a cervical spine fracture, type of fracture, vertebra fractured, estimate of fracture age, and study indication were manually extracted from the attending neuroradiologist imaging



**Table 1: The impact of patient characteristics on Aidoc performance**

Factor		Aidoc Incorrect (No.)	%	P Value
Total (No.) (%)	1904, 100	161	100	
Indication (No.) (%)				.97
Trauma	1796, 94	155	96	
Critical	511, 27	45	28	
Minor	888, 47	74	46	
Not specified	397, 21	36	22	
Neck pain	27, 1	1	1	
Neurologic deficit	33, 2	2	1	
Postoperative	10, 1	1	1	
Other	38, 2	2	1	
Sex (No.) (%)				.08
Male	958, 50	92	57	
Female	946, 50	69	43	
Imaging location (No.) (%)				.86
Academic center	1659, 87	141	88	
Outreach center	245, 13	20	12	
History of cervical spine surgery (No.) (%)				.57
Prior surgery	67, 4	7	4	
No prior surgery	1837, 96	154	96	
Age (mean) (yr)				.03
Overall	60 (SD, 22)			
Aidoc incorrect	64 (SD, 21)			
Aidoc correct	60 (SD, 22)			

**Table 2: Etiology of the false-positive flagged studies**

False-Positive Etiology	Count	Percentage of All Flagged Studies (n = 173)
Degeneration	55	31.8
Degenerative ossicle	18	10.4
Facet degeneration	14	8.1
Calcified ligament	6	3.5
Cortical irregularity	7	4.0
Osteopenia	4	2.3
Cystic degeneration	4	2.3
Atlantodental joint	1	0.6
Osteophyte	1	0.6
Noncervical pathology	15	8.7
Rib fracture	8	4.6
Degeneration, thoracic	4	2.3
Skull fracture	2	1.2
Carotid calcification	1	0.6
Anatomic variant	10	5.8
Nonunion vertebrae	4	2.3
Transitional anatomy	2	1.2
Limbus	2	1.2
Bifid spinous process	1	0.6
Secondary transverse foramen	1	0.6
Nutrient foramen	9	5.2
Artifact	7	4.0
Unknown	8	4.6
Other	2	1.7
DISH	1	0.6
Occipital suture	1	0.6
Total	106	61.3

**Note:**—DISH indicates diffuse idiopathic skeletal hyperostosis.

report of each study. To establish the ground truth of the presence or absence of an CSFx, we compared the interpretations of the neuroradiologist and Aidoc. Concordant interpretations were

assumed to be correct; studies with discordant interpretations were reviewed by a third independent reviewer not involved in the initial interpretation (radiology resident and attending neuroradiologist with 6 years of experience) to make a final ground truth determination. Study indication was inferred from the report body and imaging order. Critical traumas included motor vehicle collisions, falls from heights or stairs, sporting accidents, assaults, and hangings. Minor traumas largely involved falls from standing height or lower. Last, traumas were categorized as “not specified” if there was insufficient information regarding the mechanism of trauma.

### Statistical Analysis

$\chi^2$  tests and 2-sided paired *t* tests were used for statistical testing for categoric and quantitative comparisons, respectively, with a significance threshold of .05. Diagnostic accuracy (sensitivity, specificity, positive predictive value, negative predictive value, and tests for statistical significance were all performed in Excel 365 [Microsoft]).

### RESULTS

To gauge the diagnostic accuracy of Aidoc as clinically implemented in our institution, we identified

1904 noncontrast cervical spine CTs for inclusion during our study. A total of 173 (9.1%) of the total studies were flagged by Aidoc as positive for CSFx, and CSFx were identified on 38.7% (67/173) of the flagged studies. Of the studies not flagged by Aidoc, 3.2% (55/1731) contained fractures (Fig 1). Diagnostic performance characteristics with 95% confidence intervals were determined as follows: sensitivity, 54.9% (95% CI, 45.7%–63.9%); specificity, 94.1% (95% CI, 92.9%–95.1%); positive predictive value, 38.7% (95% CI, 33.1%–44.7%); and negative predictive value, 96.8% (95% CI, 96.2%–97.4%).

First, we sought to understand how patient factors might impact the diagnostic accuracy of Aidoc (Table 1). Because the mechanism of injury can determine the type and severity of injury, we calculated the Aidoc false-negative rate based on the indication for the CT examination of the cervical spine (eg, trauma, neck pain, neurologic deficit). No significant differences in Aidoc performance were noted for any of the study indications, study location (ie, academic center or outreach imaging center), or model of CT scanner (Online Supplemental Data, *P* = .82). Similarly, the diagnostic error rate of Aidoc was not impacted by either patient sex or history of cervical spine surgery. We did observe, however, that patients incorrectly classified by Aidoc were older than those correctly classified (mean 64 [SD, 21] years versus 60 [SD, 22] years, respectively; *P* = .03).

Next, we examined whether characteristics of the individual fractures impacted algorithm performance (Online Supplemental Data). Aidoc performance was found to be independent of the number of vertebrae fractured (single versus multiple) and the identity of the fractured vertebrae. However, while they were not significant as a category, we observed a lower rate of incorrect Aidoc calls with injuries of C2 and a higher rate at C5. We also

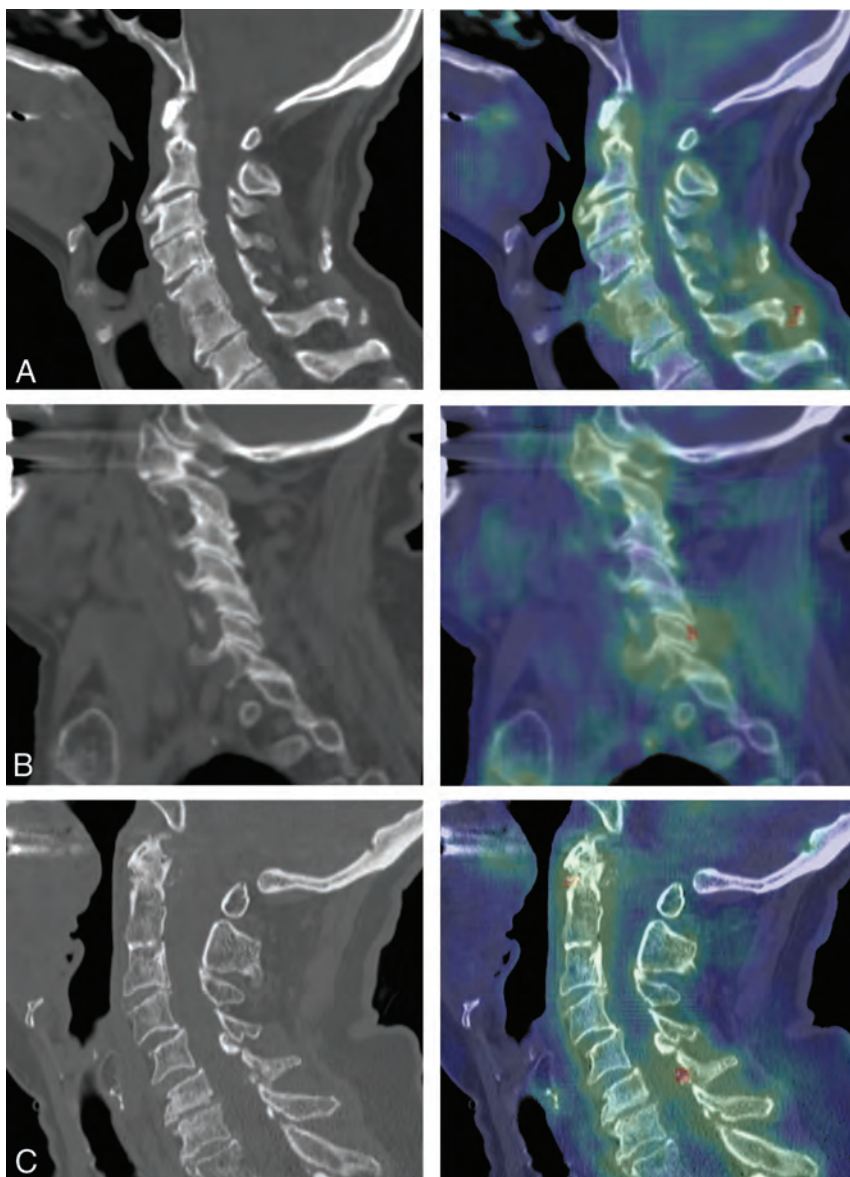


**FIG 2.** Examples of degenerative findings falsely flagged by Aidoc. Each panel shows the sagittal noncontrast cervical spine CT (*left*) and the Aidoc key image indicating the flagged pathology in red (*right*). A, A chronic ossicle falsely flagged by Aidoc. B, False-positive findings triggered by facet degeneration. C, Ossification of the ligamentum flavum incorrectly identified as a fracture by Aidoc.

observed that the algorithm was significantly more successful at identifying acute fractures than nonacute fractures (ie, chronic or age-indeterminate). Furthermore, location of the fracture within each vertebra was a significant contribution to algorithm performance, with fractures of osteophytes or the vertebral body overrepresented in the false-negative studies.

The timely identification of new fractures is of particular clinical importance, so we explored the performance of Aidoc in the detection of acute fractures. We did not find any significant differences between the acute fractures correctly flagged by Aidoc and those it missed, though our analysis was limited by the relatively small number of acute fractures (Online Supplemental

Data). However, the algorithm missed 50% (5 of 10) of acute fractures involving the transverse foramen.

Because the number of false-positive flagged studies exceeded the number of true-positives (106 versus 67), we next sought to understand the poor positive predictive value of Aidoc by exploring possible failure modes of the false-positive studies. Each study flagged by Aidoc is accompanied by a probability heat map highlighting the suspected fracture identified by Aidoc, thus allowing us to identify the etiology of each false-positive finding (Table 2). The most common etiology was the presence of degenerative structures such as a degenerative ossicle (Fig 2A), facet degeneration (Fig 2B), ossification of the ligamentum flavum (Fig 2C), or other degenerative cortical irregularities. The next most common sources of false-positive findings were pathologies outside the cervical spine and scope of the algorithm, such as rib or skull fractures (Fig 3A), and nonpathologic anatomic variants (Fig 2B, -C). False-positives were also found to have been triggered by motion artifacts or normal anatomy, and in a small number of cases, we were unable to identify any abnormality.

## DISCUSSION

A wide range of AI DSSs have been developed to reduce the risk of missing or delaying the reporting of time-sensitive findings.<sup>12,13</sup> However, AI algorithms are known to have limitations and can be difficult to generalize to clinical sites with disease prevalence and imaging protocols that differ from training datasets. Because poorly performing DSSs can hinder radiologists, it is crucial that these tools undergo rigorous evaluation before widespread implementation. While the imple-

mentation of Aidoc for CSFx has excellent reported diagnostic characteristics (sensitivity of 91.7% and specificity of 88.6%, as reported in the initial FDA disclosure),<sup>19</sup> to our knowledge, no independent evaluations of its performance have been published or, more generally, any data evaluating the diagnostic accuracy of AI DSSs in detecting cervical spine fractures. To this end, we conducted a retrospective study to evaluate the diagnostic accuracy of Aidoc, an FDA-cleared AI DSS for the evaluation of CSFx as clinically implemented at our institution.

At our institution, Aidoc fared poorly, with a notably lower sensitivity and positive predictive value than initially reported to the FDA.<sup>19</sup> To understand this unexpected



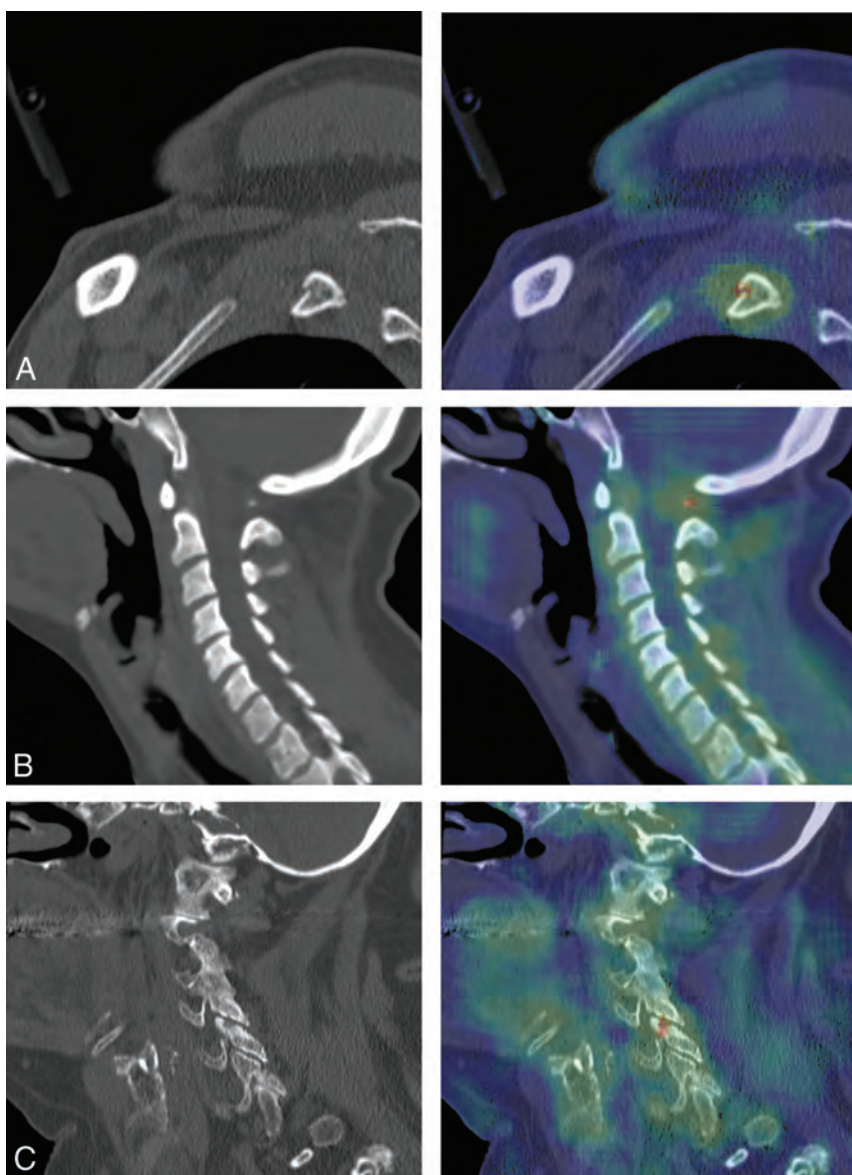


**FIG 3.** Examples of nondegenerative findings falsely flagged by Aidoc. Sagittal noncontrast cervical spine CT (left) and the Aidoc key image indicating the flagged pathology in red (right). A, Rib fracture outside of the cervical spine incorrectly flagged by Aidoc. B, Congenital hypoplasia of the posterior arch of the atlas flagged as a fracture. C, A nonpathologic nutrient foramen with degenerative changes identified as a fracture by Aidoc.

performance gap, we conducted a failure mode analysis to identify possible sources of this impaired performance. Neither imaging location, scanner model, nor study indications were found to be significantly associated with the diagnostic performance of Aidoc. However, the sensitivity was affected by patient age and characteristics of the underlying fracture, specifically the fracture acuity and location of the fracture, with chronic fractures and fractures of osteophytes and the vertebral body overrepresented among the missed fractures. Osteophyte formation and compression fractures are degenerative in nature, so underperformance in their detection may contribute to the worsened algorithm performance in older patients.

Because the value of this and similar algorithms stems from the faster detection of findings that can alter clinical management, it is especially important to consider the performance in the detection of acute fractures. We did not find any differences between the acute fractures correctly identified or missed by Aidoc, though our statistical analysis was limited by the relatively small number of acute fractures missed by the algorithm. However, it is notable that the 50% of the acute fractures involving the transverse foramen were missed by Aidoc. These fractures can indicate compromise of the underlying vertebral artery, so rapid detection by the algorithm is especially valuable and more examples should be included in the algorithm training set.

In cases with multiple fractures, the algorithm needs to correctly identify only a single fracture to score as correct. Therefore, we hypothesized that these studies would have a lower false-negative rate. However, we observed that the miss rate did not depend on the total number of fractures present in an imaging examination, suggesting that fracture identification may have been precluded by other features of the study rather than fracture characteristics themselves.

We noted a significant and unexpected number of false-positive studies in our dataset, outnumbering the flagged true CSFx. Spine degeneration was the most common etiology of false-positives observed. This is perhaps not surprising because degeneration occurs with aging and generates abnormalities such as ossicles or irregularities in the bony surface that could be mistaken for fractures. Accordingly, the age of patients misclassified by Aidoc was

higher than that in the correctly classified group, and we hypothesize that the increased burden of degeneration may have led to impaired performance. Our dataset lacked an accessible way to assess the extent of degeneration directly, but this could be explored in future studies. We speculate that greater representation of nonfractured examples of both degeneration and anatomic variants in the training set would likely reduce the false-positive burden, given their overrepresentation here in our analysis as false-positives. In addition, differences in diagnostic accuracy may also be attributed to institution-specific differences and would be difficult to disentangle. However, in the FDA 510(k) application, the number of cases positive and negative for CSFx were adjusted to be roughly equal. Because

diagnostic performance is strongly influenced by disease prevalence, this also likely contributes to the observed differences in the reported diagnostic accuracy of Aidoc and our clinical observations.<sup>19</sup> Our observed rate of positive findings is 6.4%, which reflects the true rate of CSFx at our institution. Because positive and negative predictive values depend on the underlying prevalence of the disease, we believe our measurements will more closely reflect the experience of other users. This discrepancy highlights an emerging need to standardize study design to allow rigorous and unbiased comparisons across different sites and for accurate reporting and evaluation of AI DSS algorithms in the imaging literature.

Our study has limitations that must be considered. First, because Aidoc has already been clinically implemented at our institution, the interpretation by Aidoc of each study was available to the neuroradiologist during the initial read. While this may have inflated the accuracy of the neuroradiologist's read, the diagnostic accuracy of Aidoc is unaffected. Additionally, while the Aidoc algorithm is available to all radiologists at our institution, there is marked variation in how it has been incorporated into their individual workflow. We were, therefore, unable to assess whether the algorithm reduced time to image analysis in cases flagged for CSFx. Nevertheless, given the poor positive predictive value, we suspect that any time savings would be diluted by the number of false-positives. Last, this single-institution study was performed at an academic center equipped with GE Healthcare scanners, potentially limiting the generalizability of our findings to institutions in other practice settings or those with a different fleet of scanners from other vendors.

## CONCLUSIONS

We examined the diagnostic performance of Aidoc for the detection of CSFx as implemented at our institution and observed meaningful worse diagnostic accuracy than previously reported. Although the nature of neural network algorithms obscures a full understanding of this impairment, our failure mode analysis has identified several potential areas for improvement. Nevertheless, the overall performance of this AI DSS at our institution is different enough and raises potential concerns about the generalizability of AI DSSs across heterogeneous clinical environments and motivates the creation of data-reporting standards and standardized study design, the lack of which precludes unbiased comparisons of AI DSS performance across both institutions and algorithms. Adoption of a standardized design for all AI DSS algorithms will help speed the development and safe implementation of this promising technology as we aim to integrate this important tool into clinical workflow.

Disclosures: Andrew F. Voter—RELATED: Grant: National Institutes of Health.\* John W. Garrett—RELATED: Grant: National Institutes of Health.\* John-Paul J. Yu—RELATED: Grant: National Institutes of Health.\* \*Money paid to the institution.

## REFERENCES

- Copley D, Tilliridou D, Jamjoom M. **Traumatic cervical spine fractures in the adult.** *Br J Hosp Med (Lond)* 2016;77:530–35 CrossRef Medline
- Denis F. **The three-column spine and its significance in the classification of acute thoracolumbar spinal injuries.** *Spine (Phila Pa 1976)* 1983;8:817–31 CrossRef Medline
- Fischer PE, Perina DG, Delbridge TR, et al. **Spinal motion restriction in the trauma patient: a joint position statement.** *Prehosp Emerg Care* 2018;22:659–61 CrossRef Medline
- Beckmann NM, West OC, Nunez D Jr, et al. Expert Panel on Neurological Imaging and Musculoskeletal Imaging. **ACR Appropriateness Criteria® Suspected Spine Trauma.** *J Am Coll Radiol* 2019;16:S264–85 CrossRef Medline
- Hess EP, Haas LR, Shah ND, et al. **Trends in computed tomography utilization rates: a longitudinal practice-based study.** *J Patient Saf* 2014;10:52–58 CrossRef Medline
- Kocher KE, Meurer WJ, Fazel R, et al. **National trends in use of computed tomography in the emergency department.** *Ann Emerg Med* 2011;58:452–62 CrossRef Medline
- McDonald RJ, Schwartz KM, Eckel LJ, et al. **The effects of changes in utilization and technological advancements of cross-sectional imaging on radiologist workload.** *Acad Radiol* 2015;22:1191–98 CrossRef Medline
- Hoffman JR, Mower WR, Wolfson AB, et al. **Validity of a set of clinical criteria to rule out injury to the cervical spine in patients with blunt trauma: National Emergency X-Radiography Utilization Study Group.** *N Engl J Med* 2000;343:94–99 CrossRef Medline
- Mower WR, Wolfson AB, Hoffman JR, et al. **The Canadian C-spine rule.** *N Engl J Med* 2004;350:1467–69 CrossRef Medline
- Sharp AL, Huang BZ, Tang T, et al. **Implementation of the Canadian CT head rule and its association with use of computed tomography among patients with head injury.** *Ann Emerg Med* 2018;71:54–63 CrossRef Medline
- Mower WR, Gupta M, Rodriguez R, et al. **Validation of the sensitivity of the National Emergency X-Radiography Utilization Study (NEXUS) head computed tomographic (CT) decision instrument for selective imaging of blunt head injury patients: an observational study.** *PLoS Med* 2017;14:e1002313 CrossRef Medline
- DSI Home. **FDA Cleared AI Algorithms.** American College of Radiology. 2020. <https://models.acrdsi.org/>. Accessed September 11, 2020
- Benjamins S, Dhunoo P, Mesko B. **The state of artificial intelligence-based FDA-approved medical devices and algorithms: an online database.** *NPJ Digit Med* 2020;3:118 CrossRef Medline
- Alwosheel A, van Cranenburgh S, Chorus CG. **Is your dataset big enough? Sample size requirements when using artificial neural networks for discrete choice analysis.** *J Choice Model* 2018;28:167–82 CrossRef
- Park SH, Han K. **Methodologic guide for evaluating clinical performance and effect of artificial intelligence technology for medical diagnosis and prediction.** *Radiology* 2018;286:800–09 CrossRef Medline
- Kim DW, Jang HY, Kim KW, et al. **Design characteristics of studies reporting the performance of artificial intelligence algorithms for diagnostic analysis of medical images: results from recently published papers.** *Korean J Radiol* 2019;20:405–10 CrossRef Medline
- Liu X, Faes L, Kale AU, et al. **A comparison of deep learning performance against health-care professionals in detecting diseases from medical imaging: a systematic review and meta-analysis.** *Lancet Digit Health* 2019;1:e271–97 CrossRef Medline
- Zech JR, Badgeley MA, Liu M, et al. **Variable generalization performance of a deep learning model to detect pneumonia in chest radiographs: a cross-sectional study.** *PLoS Med* 2018;15:e1002683 CrossRef Medline
- U.S. Food and Drug Administration. **K190896.** 2019 [https://www.accessdata.fda.gov/cdrh\\_docs/pdf19/K190896.pdf](https://www.accessdata.fda.gov/cdrh_docs/pdf19/K190896.pdf). Accessed February 19, 2021
- Burns JE, Yao J, Munoz H, et al. **Automated detection, localization, and classification of traumatic vertebral body fractures in the thoracic and lumbar spine at CT.** *Radiology* 2016;278:64–73 CrossRef Medline



21. Burns JE, Yao J, Summers RM. **Vertebral body compression fractures and bone density: automated detection and classification on CT images.** *Radiology* 2017;284:788–97 CrossRef Medline
22. Tomita N, Cheung YY, Hassanpour S. **Deep neural networks for automatic detection of osteoporotic vertebral fractures on CT scans.** *Comput Biol Med and Med* 2018;98:8–15 CrossRef Medline
23. Roth HR, Wang Y, Yao J, et al. **Deep convolutional networks for automated detection of posterior-element fractures on spine CT.** *Computer Science > Computer Vision and Pattern Recognition* January 29, 2016. <https://arxiv.org/abs/1602.00020>. Accessed September 2, 2020
24. Ginat DT. **Analysis of head CT scans flagged by deep learning software for acute intracranial hemorrhage.** *Neuroradiology* 2020;62:335–40 CrossRef Medline
25. Ojeda PZ, Zawaideh M, Mossa-Basha M, et al. **The utility of deep learning: evaluation of a convolutional neural network for detection of intracranial bleeds on non-contrast head computed tomography studies.** In: *Proceedings of SPIE Medical Imaging, San Diego California*. February 16–21, 2019

# The Updated Neuroradiology Milestones: Synapsing from 1.0 to 2.0

 A.A. Bhatt,  R.M. Kurtz,  T.A. Kennedy,  M.M. Miller-Thomas,  J.C. Anderson,  L. Edgar, and  C.P. Wood

## ABSTRACT

**SUMMARY:** The Accreditation Council for Graduate Medical Education is currently in the process of specialty-by-specialty revision of the Milestones. As a result, the Neuroradiology Milestones 2.0 Workgroup was created to refine a system of competency-based assessments for fellow educational growth and development. Strengths of the new Milestones include decreased complexity and uniformity within a subcompetency as it relates to a specific educational development trajectory. The Supplemental Guide serves to decrease clutter in the Milestones 2.0 document and provides a more practical resource for guidance. This article serves to review the history of the Neuroradiology Milestones, followed by a summary of the timeline of events and discussions of the workgroup for development of Neuroradiology Milestones 2.0 and a synopsis of major changes. The plan is for the updated Neuroradiology Milestones to take effect in 2021 or 2022 based on public commentary.

**ABBREVIATIONS:** ACGME = Accreditation Council for Graduate Medical Education; ICS = interpersonal and communication skills; MK = medical knowledge; PBLI = practice-based learning and improvement; PC = patient care and procedural skills; PROF = professionalism; SBP = system-based practice

First introduced in 1999, the Accreditation Council for Graduate Medical Education (ACGME) and American Board of Medical Specialties jointly approved 6 core competencies to begin an outcomes-based framework to enhance medical education. The goal was to certify physicians based on training outcomes rather than duration spent in training, thus improving the quality of graduate medical education.<sup>1</sup> The 6 core competencies included: patient care and procedural skills (PC), medical knowledge (MK), systems-based practice (SBP), practice-based learning and improvement (PBLI), professionalism (PROF), and interpersonal and communication skills (ICS).<sup>2</sup> These were launched as the Outcomes Project in 2001.<sup>3</sup> The aim was to avoid overspecialization and provide key developmental areas common to all specialties.<sup>2</sup>

Unfortunately, residency and fellowship programs struggled with implementation of the competencies due to uncertainty about

how to integrate the competencies into evaluation models already in place, as well as differences in expectations for each specialty. As a result, in 2009, the ACGME introduced the Milestones, which organized subcompetencies under the 6 core competencies, providing a continuum of outcome guidelines to effectively assess the competency level of a trainee and follow growth and progress through a residency or fellowship training program. The Dreyfus model of skill development was utilized as a framework to assess the level of development of competencies and skills of trainees learning new skills, ideas, and concepts.<sup>2</sup> Subcompetencies were selected to address either a discipline-specific element or disease process to translate core competencies into specialty- or subspecialty-specific competencies.<sup>4</sup> It was expected that individual programs have a set of tools to assess a trainee's progress in achieving each milestone. Under this system, the program's clinical competency committee is tasked with determining each trainee's level of performance by using evaluations and other assessment tools twice a year and reporting results to the ACGME.<sup>5</sup>

It is important to understand that the Milestones represent the essence of a discipline, but it is up to the individual program to develop a robust curriculum, as well as assessment tools to evaluate each trainee's progress. The Milestones are not intended to be used as evaluation forms, but rather a guide for trainee self-assessment by providing explicit expectations for learners, as well as for curriculum development, and assessment of training methods.<sup>6</sup>

From the Department of Radiology (A.A.B.), Mayo Clinic Jacksonville, Jacksonville, Florida; Department of Radiology (R.M.K.), Hospital of the University of Pennsylvania, Philadelphia, Pennsylvania; School of Medicine and Public Health (T.A.K.), The University of Wisconsin, Madison, Wisconsin; Mallinckrodt Institute of Radiology (M.M.M.-T.), Washington University in St. Louis, St. Louis, Missouri; Department of Radiology (J.C.A.), Oregon Health & Science University, Portland, Oregon; Milestones Development (L.E.), Accreditation Council for Graduate Medical Education, Chicago, Illinois; and Department of Radiology (C.P.W.), Mayo Clinic Rochester, Rochester, Minnesota.

Please address correspondence to Alok A. Bhatt, MD, Mayo Clinic Jacksonville, Department of Radiology, 4500 San Pablo Rd S, Jacksonville, FL 32224; e-mail: Bhatt.alok@mayo.edu  
<http://dx.doi.org/10.3174/ajnr.A7123>

## Neuroradiology fellowship Milestones 1.0 compared with Milestones 2.0

	Neuroradiology Milestones 1.0	Neuroradiology Milestones 2.0
Patient care	<ol style="list-style-type: none"> <li>1. Consultant in Neuroradiology</li> <li>2. Competence in Invasive and Noninvasive Procedures</li> <li>3. Patient Safety</li> </ol>	<ol style="list-style-type: none"> <li>1. Reporting</li> <li>2. Consultant in Neuroradiology</li> <li>3. Interpretation of Neuroimaging</li> <li>4. Competence in Neuroradiology Procedures</li> </ol>
Medical knowledge	<ol style="list-style-type: none"> <li>1. Application of Neuroscience in Neuroradiology</li> <li>2. Interpretation of Neuroimaging</li> <li>3. Protocol Selection and Optimization of Images</li> </ol>	<ol style="list-style-type: none"> <li>1. Application of Neuroscience to Neuroradiology</li> <li>2. Protocol Selection, Contrast Agent Selection/Dosing, and Image Optimization</li> </ol>
Systems-based practice	<ol style="list-style-type: none"> <li>1. Health Care Economics</li> </ol>	<ol style="list-style-type: none"> <li>1. Patient Safety</li> <li>2. Quality Improvement</li> <li>3. System Navigation for Patient-Centered Care</li> <li>4. Physician Role in Health Care Systems</li> <li>5. Contrast Agent Safety</li> <li>6. Radiation Safety</li> <li>7. Magnetic Resonance (MR) Safety</li> </ol>
Practice-based learning and improvement	<ol style="list-style-type: none"> <li>1. Self-directed Learning</li> <li>2. Scholarly Activity</li> <li>3. Implements Quality Improvement Project</li> </ol>	<ol style="list-style-type: none"> <li>1. Evidence-Based and Informed Practice</li> <li>2. Reflective Practice and Commitment to Professional Growth</li> </ol>
Professionalism	<ol style="list-style-type: none"> <li>1. Personal</li> <li>2. Systems</li> </ol>	<ol style="list-style-type: none"> <li>1. Professional Behavior and Ethical Principles</li> <li>2. Accountability/Conscientiousness</li> <li>3. Self-Awareness and Help-Seeking</li> </ol>
Interpersonal and communication skills	<ol style="list-style-type: none"> <li>1. Effective Communication with Patients, Families, and Caregivers</li> <li>2. Effective Communication with Members of the Health Care Team (Written and Oral)</li> </ol>	<ol style="list-style-type: none"> <li>1. Patient- and Family-Centered Communication</li> <li>2. Interprofessional and Team Communication</li> <li>3. Communication within Health Care System</li> </ol>

### Harmonized Milestones

The Milestones were not intended to remain a document set in stone, but rather to be reviewed and revised as adequate feedback is obtained, graduate medical education evolves, and the specialty advances and changes. Experts from each specialty or subspecialty creating subcompetencies resulted in marked variability between specialties and subspecialties with respect to content and how educational progression was operationalized across Milestone levels.<sup>6</sup> In 2016 at the 2nd ACGME Milestones Summit, stakeholders from all ACGME core specialties and subspecialties expressed dissatisfaction with inconsistencies in the Milestones and subcompetencies. For example, the subcompetencies tended to detail a variety of differing skills across milestone levels, rather than describing the expected spectrum of growth from beginning to advanced resident or fellow of one particular skill. Additional problems that needed to be addressed were that there were too many subcompetencies for some specialties, the language at times was too complex, some of the guidelines were not practical, and there was too much material in a milestone set. It was reported that these differences had “complicated efforts to share assessment tools across programs and provide comprehensive faculty development across specialties.”<sup>7</sup> In other words, the Milestones needed to have more national stakeholder input and overall simplification.

To evaluate and address these concerns, the ACGME Department of Research, Milestone Development, and Evaluation reviewed data collected from the field, data submitted for the biannual milestone reporting, as well as learning from quantitative and qualitative research. Analysis of non-PC and non-MK domains

showed marked variation between 26 core specialties and the transitional year; there were more than 230 different ways of describing PROF, 171 for PBLI, 176 for ICS, and 122 for SBP.<sup>8</sup> As a result, the ACGME created 4 stakeholder groups consisting of content experts, directors, interprofessional team members, and other faculty; each group was tasked to develop 2 to 3 subcompetencies that applied to all specialties and subspecialties, thus creating Harmonized Milestones. Terminology in these Harmonized Milestones could be modified if needed to pertain to a particular specialty or subspecialty during the Milestones 2.0 workgroup meetings.

### Original Neuroradiology Milestones

The Neuroradiology Fellowship Milestones were initially published in February 2014, followed by a minor edit to the introductory pages in July 2015; however, the content remained the same.<sup>9</sup> The original task force, chaired by Jim Anderson, MD, consisted of a panel of experts from the ACGME Radiology Review Committee, the American Board of Radiology, the American Society of Neuroradiology, and additional volunteers. The group met over 2 days at the ACGME headquarters in Chicago. There were 14 separate subcompetencies included in the initial document that were based in the 6 core competencies (Table). The workgroup focused on those milestones that were specific to neuroradiology training under the PC and MK domains. Those milestones within SBP, PBLI, PROF, and ICS were modelled after the Diagnostic Radiology Residency Milestones, which had been published in December 2012. Following the initial draft and edits, the document was posted for public commentary, approved, and published approximately 1 year later.



The main goal of the original task force was to create a list of subcompetencies that were applicable to all neuroradiology fellowships and representative of the expected abilities of graduating fellows. There was a general interest to keep the number to a minimum, which ultimately led to grouping of subcompetencies under larger headings.

The major criticism of the Neuroradiology Milestones 1.0 is the challenge in assessing a learner in a Milestone when more than one element is included. For example, “Contrast Agents,” “Radiation Safety,” and “Magnetic Resonance Safety” are all included as separate elements under Patient Care 3 in Milestones 1.0. The more elements represented within a single Milestone has made it challenging for programs to accurately assess its learners. The other major shortcoming of the process is inherent in applying a 5-point scale to show Milestone progression in a 1-year fellowship with midpoint and end of year assessment time points.

### **Development of Neuroradiology Milestones 2.0**

The Neuroradiology Milestones 2.0 workgroup was created with the intention of involving neuroradiologists from various backgrounds; as such, representatives were appointed by the ACGME Review Committee and American Board of Radiology, and there was a call for volunteers in late 2019; a total of 9 neuroradiologists and the ACGME Vice President of Milestones Development were part of the working group. The original plan was to have 3 meetings in Chicago, with a target implementation date of the Milestones 2.0 in either 2021 or 2022, based on public commentary. However, due to the COVID-19 pandemic, the ACGME converted from in-person to virtual meetings. The group work was extended to 4 virtual meetings with individual or small group work between meetings. As with in-person meetings, the virtual meetings included development and thorough analysis of the Milestones and Supplemental Guide and individual off-line reviews for accuracy and agreement on the draft.

The first meeting was August 17, 2020, followed by August 18, October 20, and November 5. Before the first meeting, reading materials were provided to serve as background and a basis for discussion in revising the Milestones. Meetings 1 and 2 focused on creating a shared mental model of the task, then selecting topics important to the graduate of 2025 and deciding if they were at the level of a subcompetency, a theme within a subcompetency, something to be used as an example, or if it was not something to be evaluated regularly. The group also started developing subcompetencies. Before meeting 3, the group reviewed the changes discussed and made edits as necessary. Meeting 3 was utilized to complete development of the Milestones and work on the Supplemental Guide. At the end of meeting 3, the team was divided into 4 groups (3 groups of 2 and 1 group of 3) to work on refining or developing examples within each subcompetency, describing the expected growth from beginning to advanced fellow of a particular skill. These smaller groups also reviewed or updated suggested reading material and references included in the Supplemental Guide. Meeting 4 was used for consensus review, minor adjustments, and approval of each group’s examples and suggested reading material, thus completing the Supplemental Guide. Following this meeting, each team member reviewed both the Milestones 2.0 and

Supplemental Guide documents for accuracy and final endorsement, before public commentary.

### **Major Changes Between Milestones 1.0 and 2.0**

The Neuroradiology Milestones 2.0 workgroup was tasked with several areas of improvement to focus upon. First, since many evaluators utilize both the Radiology Milestones and the Neuroradiology Milestones, the workgroup aimed to revise the Neuroradiology Milestones 2.0 such that they align with the Radiology Milestones 2.0 put into effect several months before the Neuroradiology workgroup convened. Radiology Milestones 2.0 was used as a starting point in writing the Neuroradiology Milestones 2.0, which results in commonalities in language and organizational structure between the documents, thus harmonizing and simplifying the radiology specialty and neuroradiology subspecialty Milestones documents. An effort was made to keep the overall number of milestones manageable while still capturing the core assessable components of neuroradiology practice and fellowship training. The Radiology Milestones 2.0 contains 24 milestones, and the Neuroradiology Milestones 2.0 was expanded from the original 14 milestones to 21 milestones. The differences between Radiology Milestones 2.0 and Neuroradiology Milestones 2.0 are primarily under the MK competency. MK2, MK3, and MK4 of the Radiology Milestones 2.0, which assess application of physics to imaging, appropriate selection of protocol and contrast, and knowledge of imaging technology, respectively, were combined to form MK2 of the Neuroradiology Milestones 2.0, assessing knowledge of all 3 topics in a format appropriate for an advanced subspecialty trainee.

The workgroup assessed the current and projected future practice of neuroradiology and training to ensure that the Milestones remain relevant. Using the first Neuroradiology Milestones as a starting point, we identified the most important areas concerning the MK and PC competencies that needed to be included in the Neuroradiology 2.0 Milestones. The increasing adoption of lexicons and structured reporting, skills reflecting the importance of the role of the neuroradiologist as a consultant to subspecialized clinicians, and the need to apply concepts regarding imaging physics, image processing, and image acquisition to optimize imaging were incorporated into Neuroradiology Milestones 2.0 as changes from the original version. The non-PC, non-MK milestones are derived from the harmonized milestones across all medical specialties in the Neuroradiology Milestones 2.0 document, with additional milestones specific to medical imaging added to the Radiology and Neuroradiology SBP domain (SBP5, SBP6, SBP7).

The workgroup simplified the Milestones by reducing the number of rows within each milestone set and the complexity of the milestone wording. Subcompetencies were limited to no more than 3 rows, with most only containing 1 or 2. Also, within each subcompetency, there are no longer any random milestones (evaluation or introduction of a different skill at a different level within a particular subcompetency), meaning that each subcompetency follows expected growth of 1 particular skill from level 1 to level 5 (Figure). While limiting the number of subcompetencies led to an increase in overall

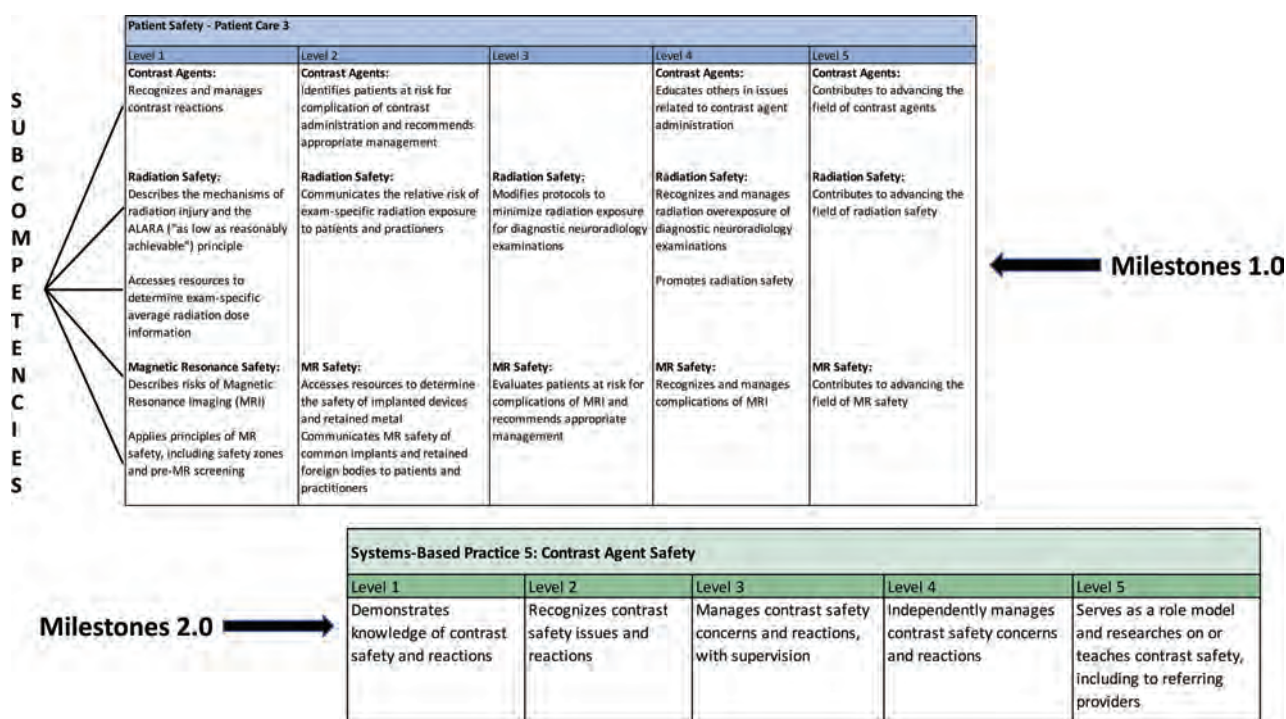


**FIGURE.** Comparison between Neuroradiology Milestones 1.0 and 2.0. This figure shows some of the major differences between the original Neuroradiology Milestones and the Neuroradiology Milestones 2.0. The original milestone (top left) for Patient Care 3 contains up to 5 subcompetencies, some of which did not follow through each of the levels of the milestone. In the Neuroradiology Milestones 2.0, the milestone is more simplified, with the evaluation of only 1 subcompetency and with the single subcompetency having a skillset under each level, followed through level 1 to 5.

number of Milestones, the new Milestones create concise benchmarks. Often with the original milestones, the separate subcompetencies may have been attained at different levels of training for individual trainees. This led to difficulties in assigning a single Milestone level to any given trainee. With the more granular milestones, while there are overall more milestones to score by the Clinical Competency Committee, the time spent deciding between Milestone levels will be decreased due to the uniformity of each Milestone.

The Supplemental Guide for Neuroradiology Milestones 2.0 is a separate document available through the ACGME website that replaces the footnotes at the bottom of the original Neuroradiology Milestones. The Supplemental Guide was created to provide insights into the intent of the subcompetencies, with examples for each level, sample assessment methods, and other resources. The Supplemental Guide for the Radiology Milestones 2.0 was also used as a starting point for the Neuroradiology Milestone 2.0 Supplemental Guide, with general radiology clinical examples replaced with neuroradiology subspecialty-specific content.

## CONCLUSIONS

The ACGME is currently in the process of specialty-by-specialty revision of the Milestones. The Neuroradiology Milestones 2.0 Workgroup is part of this project and has taken a step forward in refining a system of competency-based assessments for fellow educational growth and development. Strengths of the new Milestones include improved usability, decreased complexity,

less redundancy, and uniformity within a subcompetency as it relates to a specific educational development trajectory. The Supplemental Guide serves to decrease clutter in the Milestones 2.0 document and provides a more practical resource for guidance and examples of expected progress within a subcompetency. These milestones will be reviewed and updated as necessary with a plan for Milestones 3.0 in an appropriate time period after national experience and stakeholder feedback and comments have been obtained.

## ACKNOWLEDGMENTS

The Neuroradiology Milestones 2.0 workgroup would like to thank Braden Harsy and Sydney McLean from the ACGME for their efforts in organizing our meetings on the virtual platform.

Disclosures: Tabassum A. Kennedy—UNRELATED: Payment for Lectures Including Service on Speakers Bureaus: The National Diagnostic Imaging Symposium, Comments: honorarium for lectures given as part of a virtual imaging symposium. Michelle M. Miller-Thomas—UNRELATED: Grants/Grants Pending: Biogen, Comments: MS PATHS, grant to study feasibility of imaging platform in patients with multiple sclerosis\*; Payment for Lectures Including Service on Speakers Bureaus: University of Texas Medical Branch, Comments: honorarium and travel expenses for visiting professorship February 2020 and May 2019, \$1500 total. James C. Anderson—UNRELATED: Board Membership: Member of Association of Program Directors in Radiology Board, Comments: no monetary relationship; Travel/Accommodations/Meeting Expenses Unrelated to Activities Listed: Accreditation Council for Graduate Medical Education, Comments: Reimbursement for meeting travel as member of the Radiology Review Committee at Accreditation Council for Graduate Medical Education before June 2020. Laura Edgar—UNRELATED: Employment: Accreditation Council for Graduate Medical Education, Comments: I am a paid employee of Accreditation Council for Graduate Medical Education. \*Money paid to the institution.

## REFERENCES

1. Cate O, Billett S. **Competency-based medical education: origins, perspectives and potentialities.** *Med Educ* 2014;48:325–32 CrossRef Medline
2. Batalden P, Leach D, Swing S, et al. **General competencies and accreditation in graduate medical education.** *Health Aff (Millwood)* 2002;21:103–11 CrossRef Medline
3. Swing SR. **The ACGME outcome project: retrospective and prospective.** *Med Teach* 2007;29:648–54 CrossRef Medline
4. Nasca TJ, Philibert I, Brigham T, et al. **The Next ACGME accreditation system: rationale and benefits.** *N Engl J Med* 2012;366:1051–56 CrossRef Medline
5. Carter WA Jr. **Milestone myths and misperceptions.** *J Grad Med Educ* 2014;6:18–20 CrossRef Medline
6. Holmboe ES, Yamazaki K, Edgar L, et al. **Reflections of the first 2 years of milestone implementation.** *J Grad Med Educ* 2015;7:506–11 CrossRef Medline
7. Edgar L, Roberts S, Yaghmour NA, et al. **Competency cross-walk: a multispecialty review of the Accreditation Council for Graduate Medical Education Milestones across four competency domains.** *Acad Med* 2018;93:1035–41 CrossRef Medline
8. Edgar L, Roberts S, Holmboe E. **Milestones 2.0: a step forward.** *J Grad Med Educ* 2018;10:367–69 CrossRef Medline
9. The Neuroradiology Milestone Project. <https://www.acgme.org/Portals/0/PDFs/Milestones/NeuroradiologyMilestones.pdf>. Accessed February 22, 2021

# COVID-19 Stroke Apical Lung Exam Study: Is it Really an Accurate Diagnostic Method?



We have read with great interest the article by Dr J. Siddiqui et al,<sup>1</sup> titled “COVID-19 Stroke Apical Lung Examination Study: A Diagnostic and Prognostic Imaging Biomarker in Suspected Acute Stroke,” which was published in January 2021. We want to congratulate you in advance for addressing an important issue, such as the association between infection with Severe Acute Respiratory Syndrome coronavirus 2 (SARS-CoV-2) and a cerebrovascular accident, because of the impact that the latter has on both mortality and quality of life for patients. As the literature has shown, so far, the incidence of stroke in these patients is up to 5%.<sup>2</sup>

As we know, the standard reference test to establish the diagnosis of coronavirus disease 2019 (COVID-19) is reverse transcription-polymerase chain reaction. However, it is also widely known that its diagnostic accuracy is not 100%, which is why other diagnostic methods such as chest tomography scans have been used because of their wide availability, speed in acquisition and interpretation, and diagnostic performance.

CT is not approved as a diagnostic method for COVID-19 and its main function is to classify the degree of pulmonary involvement instead of being a detection tool. In no circumstances does it replace the administration of the reverse transcription-polymerase chain reaction test in individuals who are suspected of having an infection.<sup>3</sup>

From the studies carried out so far and our experiences with patients with COVID-19, it is known that the main pulmonary involvement (especially in patients in the initial phase of the infection who probably do not yet present symptoms) is found

in the posterior aspect and the pulmonary bases and is much smaller in the apices. The latter may even be respected in the initial stages of the disease.<sup>4</sup> Therefore, we believe that using only the presence of ground-glass opacities in the lung apices is not a reliable or accurate biomarker for the diagnosis of COVID-19 and should not replace the acquisition of a complete chest tomography, much less the performance of reverse transcription-polymerase chain reaction testing.

Finally, we consider that it would have been interesting and accurate to include in the article which underlying diseases and other risks factors these patients had that could have influenced the occurrence of a cerebrovascular event.

## REFERENCES

1. Siddiqui J, Bala F, Sciacca S, et al. COVID-19 stroke apical lung examination study: a diagnostic and prognostic imaging biomarker in suspected acute stroke. *AJNR Am J Neuroradiol* 2021;42:138–43 CrossRef Medline
2. Ortiz M, Valencia N, Moreno E, et al. ACV y COVID-19: una revisión de los estudios observacionales publicados en época de pandemia. *Acta Neurológica Colombiana* 2020;36:63–74 CrossRef
3. Khatami F, Saatchi M, Zadeh S.S. et al. A meta-analysis of accuracy and sensitivity of chest CT and RT-PCR in COVID-19 diagnosis. *Scientific Reports* 2020;10:22402 CrossRef Medline
4. Kwee T, Kwee R. Chest CT in COVID-19: what the radiologist needs to know. *Radiographics* 2020;40:1848–65 CrossRef Medline

© S. Marquez

© J. Campaña

© N. Bedoya

Diagnostic Imaging Department  
Fundacion Santa Fe De Bogota University Hospital  
Bogotá, Colombia

Indicates open access to non-subscribers at [www.ajnr.org](http://www.ajnr.org)  
<http://dx.doi.org/10.3174/ajnr.A7141>



# REPLY:



We thank Marquez et al for their interest in our study.<sup>1</sup> Their points are worthy of a discussion. Our article demonstrates a highly sensitive and specific biomarker, namely apical ground-glass opacification (GGO) seen on carotid CTA, in a cohort of patients with suspected stroke during the pandemic (sensitivity, 75% [95% CI, 56–87]; specificity, 81% [95% CI, 71–88]; OR = 11.65 [95% CI, 4.14–32.78];  $P = .001$ ). The sample was accrued continuously from March through April 2020 from a population scanned for the indication of suspected acute stroke, not for suspected coronavirus disease 2019 (COVID-19). This study simply highlights the importance of vigilance in assessment of the lung apices when reporting carotid CTAs in the population with suspected acute stroke. Most patients in our study were without typical symptoms of COVID-19. We used other information readily available at the time of the carotid CTA acquisition but were unable to find any other additional biomarkers. This included demographics, clinical history, symptoms and signs, as well as chest radiographs<sup>2</sup> (which are typically obtained shortly after the admission of patients with acute stroke). In summary, we recommend routinely analyzing lung apices in patients with stroke undergoing carotid CTA, because this rapid and easy assessment of apices is valuable, opportunistic, and “free” information in a routine and unmodified scan. The apical analysis simply identifies patients likely to have COVID-19 with early downstream benefits such as limiting disease transmission.

We reiterate that reverse transcriptase polymerase chain reaction (RT-PCR) should not be omitted or replaced. Such patients still require formal RT-PCR testing according to hospital policy. In some hospitals, RT-PCR testing may be required for all emergency admissions; in others, it may be just for those patients who have clinical features suggestive of COVID-19. Regardless of RT-PCR indication, we again point out that RT-PCR takes hours to process. In the interim, the opportunistic and free information we describe in analyzing the lung apices is of benefit. In our hospitals, apical analysis is now articulated in reports to good effect, for example, changing staff personal protective equipment requirements (eg, from a fluid-repellant surgical mask to an FFP3 or N95 mask), and directing a patient to a side room instead of an open ward, pending RT-PCR results.

We agree that chest CT findings of COVID-19 are useful when found; however, we highlight that guidance from both the Royal College of Radiologists (UK) and the American College of Radiology do not recommend routine chest CT scanning as a means of diagnosing Severe Acute Respiratory Syndrome coronavirus 2 (SARS-CoV-2).<sup>3,4</sup>

It remains challenging to draw definitive conclusions from any index test (apical GGO analysis) compared with a reference standard (RT-PCR), which itself is not of optimal sensitivity.<sup>5</sup> However, our study showed that apical GGO alone is a prognostic biomarker of 30-day mortality. In other words, regardless of

whether RT-PCR had been performed, and regardless of the RT-PCR result if performed, the absence of apical GGO confers a survival advantage compared with those with the presence of apical GGO (5.7% versus 18.0% mortality,  $P = .017$ ; hazard ratio = 3.51 [95% CI, 1.42–8.66];  $P = .006$ ). This would further support the use of an opportunistic and free biomarker in a routine scan as being valuable.

We concur and mention in our article that the inferior and posterior pulmonary segments are more often affected in SARS-CoV-2 infection; however, we do not recommend routinely scanning the entire lungs with chest CT, without clinical indication, in keeping with the published guidance mentioned above.

Regarding the suggestion to include comorbidities and risk factors for stroke, we refer the authors to Online Table 4. Here it shows that key stroke risk factors were included in our study (hypertension, diabetes mellitus, atrial fibrillation, hyperlipidemia, history of stroke/TIA, and smoking status) and were incorporated as covariates in the bivariate and multivariate analyses.

Our primary objective was to determine candidate diagnostic biomarkers for COVID-19, but we agree there were some interesting additional findings from our study regarding the association between SARS-CoV-2 infection and stroke. For example, a contributory mechanism to COVID-19-related excess mortality might be thromboembolic because increased carotid occlusion was associated with GGO (16.0% versus 3.4%,  $P = .004$ ; OR = 6.82 [95% CI, 1.97–23.53];  $P = .002$ ), and our multivariate analysis suggested carotid occlusion was likely to be an independent predictor of death.

While this study was based in London, United Kingdom, and included 3 hospitals with a nonwhite population ranging from 10% to 40%, with patients from a variety of socioeconomic status in the catchment area, we believe the biomarker would benefit from further rigorous temporal and spatial validation. In other words, having developed the biomarker, we should now test it on a cohort of patients from hospitals throughout an entire nation with prospective data collection at a subsequent time point in the pandemic. Such a study to obtain highly representative samples of the populations with acute stroke during the COVID-19 pandemic is currently underway.<sup>6</sup>

## REFERENCES

1. Siddiqui J, Bala F, Sciacca S, et al. **COVID-19 stroke apical lung examination study: a diagnostic and prognostic imaging biomarker in suspected acute stroke.** *AJNR Am J Neuroradiol* 2021;42:138–43 CrossRef Medline
2. Siddiqui J, Bala F, Sciacca S, et al. **A comparison of chest radiograph and CTA apical pulmonary findings in patients presenting with suspected acute stroke during the COVID-19 pandemic.** *AJNR Am J Neuroradiol* 2021;42:E13–14 CrossRef Medline
3. American College of Radiology (ACR). **ACR Recommendations for the Use of Chest Radiography and Computed Tomography (CT) for Suspected COVID-19 Infection.** <https://www.acr.org/Advocacy-and-Economics/ACR-Position-Statements/Recommendations-for-Chest-Radiography-and-CT-for-Suspected-COVID19-Infection> Accessed March 25, 2021.
4. The Royal College of Radiologists. **The role of CT in patients suspected with COVID-19 infection.** <https://www.rcr.ac.uk/college/>

Indicates open access to non-subscribers at [www.ajnr.org](http://www.ajnr.org)

This work was supported by the Wellcome/Engineering and Physical Sciences Research Council Center for Medical Engineering (WT 203148/Z/16/Z). <http://dx.doi.org/10.3174/ajnr.A7161>


coronavirus-covid-19-what-rcr-doing/clinical-information/role-ct-chest/role-ct-patients Accessed March 25, 2021.

5. Jarrom D, Elston L, Washington J, et al. **Effectiveness of tests to detect the presence of SARS-CoV-2 virus, and antibodies to SARS-CoV-2, to inform COVID-19 diagnosis: a rapid systematic review.** *BMJ Evidence-Based Medicine* 2020 Oct 1. [Epub ahead of print] CrossRef Medline
6. King's College Hospital National Health Service Trust. **COVID-19 Stroke Apical Lung Examination Study - A Multi-Centre Prospective Study.** ClinicalTrials.gov; 2021. <https://clinicaltrials.gov/ct2/show/NCT04640428> Accessed March 24, 2021.

 **F. Bala**

 **J. Siddiqui**

Department of Neuroradiology  
King's College Hospital, National Health Service Foundation Trust  
London, United Kingdom

 **S. Sciacca**

 **A.M. Falzon**

Lysholm Department of Neuroradiology National Hospital for Neurology and Neurosurgery  
University College London Hospitals, National Health Service Foundation Trust  
London, United Kingdom

 **M. Bengier**


Department of Neurology  
King's College Hospital, National Health Service Foundation Trust  
London, United Kingdom

 **S.A. Matloob**

Department of Neurosurgery National Hospital for Neurology and Neurosurgery  
University College London Hospitals, National Health Service Foundation Trust  
London, United Kingdom

 **F.N.A.C. Miller**

Department of Radiology  
King's College Hospital National Health Service Foundation Trust  
London, United Kingdom

 **R.J. Simister**


Comprehensive Stroke Service  
University College London Hospitals, National Health Service Foundation Trust,  
Stroke Research Centre, University College London Queen Square Institute of  
Neurology  
London, United Kingdom

 **L.K. Sztriha**

Department of Neurology  
King's College Hospital National Health Service Foundation Trust  
London, United Kingdom

 **I. Chatterjee**

Comprehensive Stroke Service  
University College London Hospitals, National Health Service Foundation Trust  
London, United Kingdom

 **I. Davagnanam**

Lysholm Department of Neuroradiology National Hospital for Neurology and Neurosurgery  
University College London Hospitals, National Health Service Foundation Trust  
London, United Kingdom  
Brain Repair & Rehabilitation Unit University College London Queen Square  
Institute of Neurology  
London, United Kingdom

 **T.C. Booth**

Department of Neuroradiology  
King's College Hospital, National Health Service Foundation Trust  
London, United Kingdom  
School of Biomedical Engineering and Imaging Sciences  
King's College London  
London, United Kingdom

## Do Prior Iodine Contrast Injections Affect Cerebral Blood Flow Measurement on CT Perfusion Studies of Patients with Large-Vessel Occlusions?

We read with great interest the recent study by Copelan et al<sup>1</sup> in which the authors concluded that recent administration (< 8 hours) of iodinated contrast renders infarct estimations inaccurate using a commercial CTP processing software. We believe that the conclusions suffer from unassessed confounders and misinterpretations deserving of clarification for the prospective reader.

First, the small cohort ( $n = 38$ ) differs not only in the use of iodine, but also in presentation time and infarct size. The transfer patient group arrived approximately 3.2 hours later than the direct presenters. In our experience, this delay increases the likelihood of distal clot migration (eg, from the ICA terminus to the M1 or M2 segment), which may explain the reported core underestimation using CBF. It is unclear whether this confounder was excluded after comparison of the emergent large-vessel occlusion location on each patient's baseline and post-transfer CTAs.

Second, both core under- and overestimations are well-described limitations of CTP that are inherent to using perfusion as a surrogate of the core.<sup>2</sup> As shown in Fig 7,<sup>1</sup> the authors compared a delay-insensitive CTP processing method (RAPID processing of Perfusion and Diffusion [RAPID; iSchemaView]) with a delay-compensated (but not delay-insensitive) parametric CTP processing method (Advanced-Visualization Workstation; GE Healthcare). The apparent CBF reduction on the parametric deconvolution methods is not easily disambiguated from artifactual changes arising from delay-estimation and compensation errors between the arterial input function and the tissue. Prior studies have shown that CBF observed with delay-compensated deconvolution methods can be underestimated by as much as 40% for delays of 5 seconds.<sup>2</sup>

Third, CTP maps are derived from dynamic attenuation changes caused by the iodine bolus, relative to the prebolus baseline attenuation values. Provided that a reliable prebolus baseline attenuation measurement is obtained, any attenuation offset caused by persistent intravascular or extravascular tissue iodine (from preceding injections) is negligible. It is unclear if the authors' CTP acquisitions had an adequate baseline measurement. The authors also acquired their CTP in 2 sequential slabs,

each with a separate bolus injection, to achieve the desired 80-mm coverage. This means that the second CTP slab is, by definition, a postcontrast scan in both patient groups. Thus, any confounding effects from prior iodine administration should be observed in the second CTP slab in both groups. However, when allowing at least 90 seconds between the 2 CTP acquisitions, we have not encountered such issues in our experience with either dual slab protocols or cases in which the CTA is acquired before the CTP. If leakage is the culprit (either first pass or at a steady-state from an earlier injection for the CTP or the outside CTA study), then this would affect CBV and, to a much lesser extent, CBF. Although the authors reference contrast leakage as a potential explanation for core underestimation, they did not report on whether, or to what extent, patients demonstrated contrast staining on their pre- and postcontrast head CTs.

Last, the authors state that "rather than delay the reporting of such a clinically relevant pitfall to augment our sample size, we thought it pertinent to alert our [...] colleagues to our finding." While the effort to bring urgent findings to the attention of the broader scientific community is laudable, doing so at the expense of scientific rigor is fraught with danger. On the basis of the reported number of cases, we are uncertain whether meaningful conclusions can be drawn regarding the association between CBF-derived core and the robustness of collaterals. Specifically, only 2 and 3 cases with "poor collaterals" were reported in the iodine and noniodine groups, respectively, while "intermediate collaterals" were reported only in 6 and 3 cases, respectively. Moreover, the initial power analysis was based on a 50% core overestimation, not underestimation. Therefore, we are concerned for the potential conflation of correlation with causality.

In summary, we thank Copelan et al<sup>1</sup> for sharing their findings and we agree with their conclusion that CBF can underestimate (or overestimate) core, and critically, that one should always cross-reference CTP with an unenhanced CT. We believe, however, that the authors' conclusions are excessively extrapolated and potentially without attention to well-recognized confounders. Several potential sources of bias may have had further influences upon the results, including the tendency to promote

underestimation of the CBF core. Multiple prior studies, including post hoc analyses in large, prospectively collected cohorts and real-world populations with much larger numbers of patients, have documented accurate core estimations using the tested software, which included “transfer cases” with prior contrast.<sup>3,4</sup>

## REFERENCES

1. Copelan AZ, Smith ER, Drocton GT, et al. **Recent administration of iodinated contrast renders core infarct estimation inaccurate using RAPID software.** *AJNR Am J Neuroradiol* 2020;41:2235–42 CrossRef Medline
2. Kudo K, Christensen S, Sasaki M, et al. **Accuracy and reliability assessment of CT and MR perfusion analysis software using a digital phantom.** *Radiology* 2013;267:201–11 CrossRef Medline
3. Sarraj A, Hassan AE, Savitz S, et al. **Outcomes of endovascular thrombectomy vs medical management alone in patients with large ischemic cores: a secondary analysis of the optimizing patient's selection for endovascular treatment in acute ischemic stroke (SELECT) study.** *JAMA Neurol* 2019;76:1147–56 CrossRef Medline
4. Dehkharghani S, Bammer R, Straka M, et al. **Performance and predictive value of a user-independent platform for CT perfusion analysis:**

**threshold-derived automated systems outperform examiner-driven approaches in outcome prediction of acute ischemic stroke.** *AJNR Am J Neuroradiol* 2015;36:1419–25 CrossRef Medline

 **S.A. Amukotuwa**  
Monash Health Imaging  
Monash Health  
Melbourne, Australia  
Monash University  
Clayton, Australia

 **R. Bammer**  
Department of Radiology, Royal Melbourne Hospital  
University of Melbourne  
Melbourne, Australia

 **S. Dehkharghani**  
Departments of Radiology and Neurology  
NYU Langone  
New York, New York



## REPLY:

**W**e would like to thank Amukotuwa et al for their interest in our article,<sup>1</sup> their expertise in the technical aspects of CTP, and for their important contributions to the development of RAPid processing of Perfusion and Diffusion (RAPID) software and iSchemaView, the company that produces RAPID. Their efforts to automate the interpretation of CTP to facilitate early stroke interventions have been important for acute stroke therapy, and we wish them continued success with their products.

The underlying mechanism for the systematic underestimation of the core infarct by RAPID in patients who previously received intravenous contrast is of important academic interest. As neurointerventionalists and diagnostic neuroradiologists, our goal is to rapidly diagnose and appropriately treat patients with acute ischemic stroke. Using the RAPID software, our team repeatedly observed underestimation of the volume of core infarction in patients with persistent large-vessel occlusions and large MCA infarctions on unenhanced CT. We felt this specific limitation needed to be highlighted for the physicians reliant on such information when deciding to perform interventions. While we take exception to the authors' questioning our "scientific rigor," we will attempt to answer the potential issues raised by Amukotuwa et al point-by-point.

We agree that the sample size is a potential limitation of our study, as we stated in our Discussion. While 38 subjects met inclusion criteria, we excluded several subjects from the analysis who showed distal migration of thrombus. At the authors' request, we confirm that the original thrombus location remained the same on the follow-up posttransfer CTAs for all of the included subjects. In regard to the other covariates that were raised by Amukotuwa et al as potential confounders, our multivariate analysis was designed to account for the potential influence of these variables.

We agree that delay-insensitive and delay-compensated parametric processing methods may result in differing estimates of core infarction volume; however, that was not the point of Figs 3, 4, and 7. Rather, these figures exemplify that RAPID inaccurately calculated a small core infarct in a patient with a large complete MCA infarct and a persistent M1 occlusion, who had previously received iodinated contrast before the transfer to our facility. More specifically, Fig 3 shows a patient with a completed infarct in the right MCA territory with persistent occlusion of the right M1. RAPID correctly identified the prolonged transit time in that territory but estimated a core infarct volume of 0 mL (Fig 4). Figure 7 demonstrates that the underlying raw data were not the problem, but the methods used by RAPID resulted in a gross underestimation of core infarct volume. These figures illustrate the point of the article in its entirety, namely that the method used by RAPID, to a high statistical likelihood ( $P = .04$ ), results in underestimation of core infarct volume in patients who recently received iodinated contrast.

We thank the authors for pointing out that CTP maps are derived from dynamic attenuation changes. We suggested contrast

leakage as a potential mechanism for the observed error, but again, we are not certain. At the authors' request, we reviewed the prebolum CT scans and measured the attenuation manually. Our analysis showed the expected evolution of core infarct after transfer. As time progressed, the infarct became less attenuated (pair-wise  $t$  test,  $P = .004$ ). We also evaluated the 12 patients who had a post-contrast CT obtained as part of the same study, and only 1 of the 12 had contrast enhancement. Again, the mechanism of the error remains unclear, but the data very clearly demonstrate an underestimation of the volume of core infarct in patients who had recently received iodinated contrast as part of a separate pretransfer examination ( $P = .04$ ).

We thank the authors for again pointing out the perils of small sample sizes. It is a valid concern. We did have small samples in some of the statistical groups, and as such, the precision of our estimates was quite poor. For example, the 95% CI for the effect of grade III collaterals was 2.1–34.1. This nonetheless met the threshold of statistical significance ( $P = .004$ ) and indicated the effect very likely exists. More samples are required to satisfactorily determine the true effect size of poor collaterals on CTP estimates produced by RAPID. We also thank the authors for pointing out our typographical error regarding the power analysis. Indeed, it should read "underestimation."

In the concluding paragraph, the authors reference 2 articles they and their colleagues with ties to iSchemaView have co-authored<sup>2,3</sup> as proof of real-world accuracy of RAPID. Overall, we agree that RAPID is an important addition to the diagnosis and treatment of patients with acute ischemic infarction. However, neither of the 2 referenced studies evaluated the accuracy of core estimate in patients with prior contrast administration versus patients who were contrast naïve. In the article by Sarraj et al,<sup>3</sup> a minority of the subjects were transfer patients (only 27 of 105), which is likely insufficient to affect the outcome of the study. In the article by Dehkharghani et al,<sup>2</sup> there was no mention of how many patients had previously received iodinated contrast.

Clinical practice demands that practicing neurointerventionalists and diagnostic neuroradiologists understand both the value and the limitations of software to determine the viability of brain tissue in patients with acute stroke. As scientists and physicians, it is our obligation to identify potential limitations and pitfalls, study them carefully, and report the results in the medical literature regardless of potential financial conflicts. Amukotuwa et al have great experience in CTP. As co-developers of RAPID, shareholders and consultants for iSchemaView (the company that produces RAPID), and in having relationships with the founders of iSchemaView,<sup>4</sup> we feel it is incumbent on them to publicly inform the user community of both the advantages and limitations of their products. As inventors, we thank them for making a product that has helped so many patients. As scientists, we challenge them to further explore the underestimation of core infarct by RAPID in patients who received iodinated contrast as part of a prior study. Should they confirm our findings, we hope they will inform physicians who rely on their software of the pitfalls of prior contrast administration on the estimate of core infarction provided by RAPID and make improvements to the platform for patients in whom contrast has recently been administered.

<http://dx.doi.org/10.3174/ajnr.A7160>


## REFERENCES

1. Copelan AZ, Smith ER, Drocton GT, et al. **Recent administration of iodinated contrast renders core infarct estimation inaccurate using RAPID software.** *AJNR Am J Neuroradiol* 2020;41:2235–42 CrossRef Medline
2. Dehkharghani S, Bammer R, Straka M, et al. **Performance and predictive value of a user-independent platform for CT perfusion analysis: threshold-derived automated systems outperform examiner-driven approaches in outcome prediction of acute ischemic stroke.** *AJNR Am J Neuroradiol* 2015;36:1419–25 CrossRef Medline
3. Sarraj A, Hassan AE, Savitz S, et al. **Outcomes of endovascular thrombectomy vs medical management alone in patients with large ischemic cores: a secondary analysis of the optimizing patient's selection for endovascular treatment in acute ischemic stroke (SELECT) study.** *JAMA Neurol* 2019;76:1147 CrossRef Medline
4. Amukotuwa SA, Straka M, Smith H, et al. **Automated detection of intracranial large vessel occlusions on computed tomography angiography: a single center experience.** *Stroke* 2019;50:2790–98 CrossRef Medline


 **M.R. Amans**  
 **E. Smith**  
 **K.H. Narsinh**  
 **C.F. Dowd**  
 **R.T. Higashida**  
 **V.V. Halbach**  
 **S.W. Hetts**


 **D.L. Cooke**  
 **J. Nelson**  
 **D. McCoy**  
 **M. Ciano**  
 **W.P. Dillon**


Diagnostic and Interventional Neuroradiology  
 University of California, San Francisco  
 San Francisco, California

 **A.Z. Copelan**  
 Neurointerventional Radiology  
 Consulting Radiologists, Ltd  
 Minneapolis, Minnesota

 **G.T. Drocton**  
 **R.S. Khangura**  
 Neurointerventional Radiology  
 Sutter Health  
 Sacramento, California

 **D. Murph**  
 Interventional Neuroradiology  
 Asheville Radiology Associates  
 Asheville, North Carolina

 **Z.J. Hartley**  
 Diagnostic Radiology  
 Brown University  
 Providence, Rhode Island

 **A.A. Abia**  
 Neurosurgery  
 University of California, San Francisco  
 San Francisco, California